THE UNIVERSITY OF SHEFFIELD

ENGD THESIS

UNDERSTANDING THE LINK BETWEEN MACHINING, MICROSTRUCTURE AND PRIMARY PROCESSING FOR A MODERN NICKEL SUPERALLOY

Kyle Marshall

August 2019

Abstract

Powder metallurgy derived nickel superalloys are often subjected to a range of thermomechanical processes, including extrusion, forging and heat treatment in order to produce the required mechanical properties. In this EngD research program, a modern nickel superalloy was processed using two different powder metallurgy routes, with a view to examining the machining response with respect to changes in upstream forging. The conventional route involved hot isostatic pressing (HIP) followed by forging. Small subscale test pieces were used to first examine the variation in microstructure that occurred with varying strain rates and isothermal deformation temperatures, leading to the development of a two-step forging strategy which allowed successful open-die non-isothermal forging to be produce for the purpose of machining trials. In parallel a powder consolidation technique, known as field assisted sintering technology (FAST), was explored, to produce billets with varying microstructures. This is the first time that the FAST technique has been applied to an advanced nickel alloy powder feedstock. Both the HIP+forged and FAST billets were machined to examine the influence of varying microstructure on cutting forces, tool wear and subsurface damage during high performance machining trials. For the as-FAST material, it was found that coarse grain microstructures exhibited lower cutting forces, however this could not be concluded for the HIP+forged material. In both cases, coarser grain microstructures contained more evidence of microstructural damage including observable shear planes and deformed precipitates, irrespective of the measured cutting forces. Comparing cost and complexity, it is suggested that FAST is a more robust method for producing material when examining the correlation between local microstructure and imparted machining damage during the early stages of alloy development.

Acknowledgements

I would like to thank my academic supervisor Dr Martin Jackson for his continual support throughout this research project, without his continual support and encouragement this work would simply not be possible. His commitment to myself and fellow post-graduate students cannot be overstated.

I would also like to thank my supervisors from Industry. Thanks to Dr Mario Epler from Carpenter Technology Corporation who provided technical support particularly during the forging work undertaken and also was an extremely welcoming host during my time spent in Reading Pennsylvania during my visit to Carpenter Technology, which can be said for all staff I met during my time with the company. I also owe a debt of gratitude to colleagues of Mario at Carpenter for operating the Gleeble and Industrial scale forging apparatus.

I am appreciative of the guidance and encouragement from Dr Jamie McGourlay and Andrew Mantle from Rolls-Royce PLC as well as Dr Chris Taylor and Dr Pete Crawforth from the AMRC for all the opportunities they have provided me and for keeping me on the right track. I would like to thank and acknowledge the technical staff the University of Sheffield, the AMRC and from the IDC in machining science for the learning opportunities provided. These skills will surely serve me well in my future. Thanks to my colleagues in D1 for never being shy to put the kettle on and the world to rights.

Thanks to the EPSRC, Carpenter Technology Corporation, Rolls-Royce PLC and the IDC in machining science for funding and supporting this research, and therefore providing an opportunity of immeasurable value.

Finally I would like to thank my father Martin, my brother Reece and my partner Tara. Without you I would have never been on this journey. You have been there through good and bad, my love for you all is the only thing that exceeds your patience in me.

Contents

List of Tables

List of Figures

Nomenclature

Symbol	Meaning
γ	Gamma phase in a nickel superalloy
γ'	Gamma prime phase in a nickel superalloy
γ''	Gamma double prime phase in a nickel superalloy
σ	Sigma phase in a nickel superalloy
$\mathrm{Hv}_{0.5}$	Vickers hardness measured for an applied load of 0.5 Kg
ε	True strain
σ	True stress
h_i	Instantaneous specimen height during hot compression testing
h_o	Initial specimen height prior to hot compression testing
d_i	Instantaneous die displacement during hot compression testing
r_i	Instantaneous specimen height during hot compression testing
V	Compression test specimen volume
$F_\mathrm{corrected}$	Friction corrected die load measured during hot compression testing
F_i	Measured die load during hot compression testing
$\sigma_\mathrm{corrected}$	Friction corrected flow stress
μ	Friction correction coefficient
$\varepsilon_\mathrm{true}$	Friction corrected stress calculated from hot compression test data
σ_iso	Isothermally corrected flow stress
Q_def	Activation energy for hot deformation
β	Isothermal correction coefficient
R	Universal Gas constant
T_i	Instantaneous sample temperature measured during hot compression testing
T_iso	Isothermal deformation temperature
σ_ε	Flow stress value for a fixed strain value

B_ε	Fitting constant defined at a fixed strain value
Z	Zener-Holloman Parameter
$\dot{\varepsilon}$	True strain rate
a_1	Equation coefficient used in the isothermal correction of flow stress data
a_2	Equation coefficient used in the isothermal correction of flow stress data
n	Equation coefficient used in the isothermal correction of flow stress data
a	Equation coefficient used in the isothermal correction of flow stress data
α	Equation coefficient used in isothermal correction of flow stress data
F_{x}	X direction cutting forces
F_{y}	Y direction cutting forces
F_{z}	Z direction cutting forces
$\mathrm{D_s}$	Diameter at the start of tool engagement during facing machining trials
$\mathrm{D_f}$	Diameter at the end of tool engagement for machining facing trials
$\mathrm{t_c}$	Time in cut for the facing machining trials
$\mathrm{A_r}$	Surface area removed during facing machining trials
$\mathrm{V_c}$	Surface speed of the tool during machining
$\mathrm{Z_s}$	Axial position of the tool at the start of tool engagement for outer diameter turning trials
$\mathrm{Z_f}$	Axial position of the tool at the point of disengagement during outer diameter turning trials
$\mathrm{f_d}$	Tool feed distance during a machining pass

Chapter 1

Introduction

1.1 The Role of Superalloys in an Aerospace Environment and Manufacturing Challenges

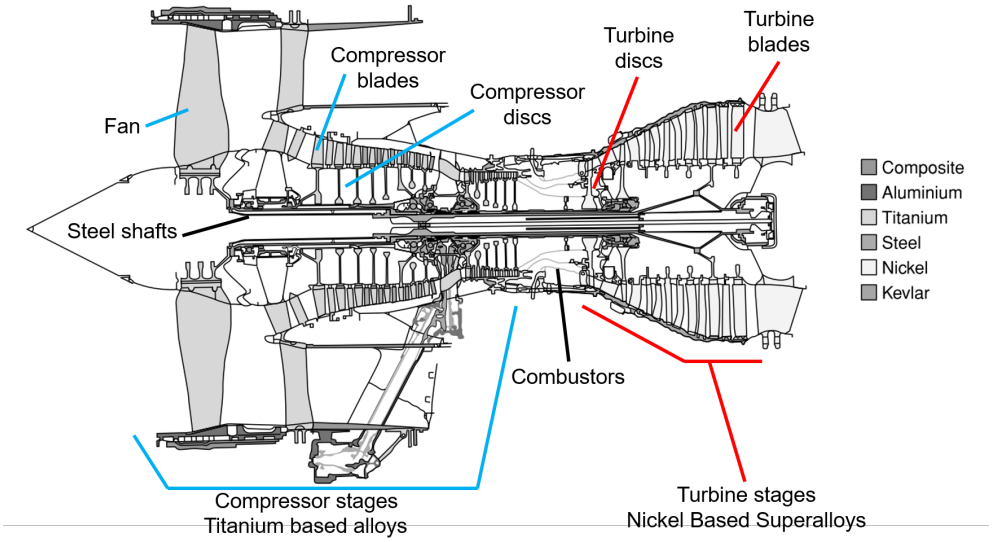

Figure 1.1: Schematic of the Rolls-Royce Trent 800 gas turbine engine, showing the location of the compressor and turbine stages and the various materials used in construction. Adapted from Reed [1].

The typical gas turbine functions by compressing air, adding energy through combustion and then expanding in order to extract some of the energy to drive the compression stage. The compression of air takes place in a series of

compressor stages where the pressure and temperature of the air is increased. The combustion greatly increases the temperature and pressure of the air further before the air reaches the turbine which extracts energy from the heated air, driving the preceding compressor stages. A wide variety of materials are used in a gas turbine engine, with the choice of material influenced by the local temperatures. Traditionally, the shafts which connect the compressor and turbine stages are steel due to torsional strength requirements. In the compressor stages, titanium alloys are used as temperatures are relatively low and in these applications the strength to weight benefits provided by titanium alloys means they are well suited. A schematic showing a typical turbo-fan gas turbine architecture and the materials used in each section is shown in Figure 1.1.

Nickel superalloys are found in two key areas within the average gas turbine engine. One application is within the turbine blades, which extract energy from the flow of combustion products to drive the shaft. These blades are subjected to some of the highest temperatures in the engine and as such are prone to material creep which is undesirable considering the requirements for high tolerance, to maximise the effectiveness and efficiency of energy transfer from the flow to the blade. These blades are also subjected to very high loading and therefore require high strength. The key requirement for these blades is metallurgical stability at the high temperatures seen. The abilities of normal equiaxed polycrystalline nickel superalloys eventually failed to produce the required performance as engine efficiencies and combustion temperatures increased. The next stage of the development was to alter the grain morphology of such alloys to produce directionally solidified and single crystal alloys which resulted in an increase in creep performance. Alloy chemistries were eventually tailored specifically to improve the properties of single crystal nickel superalloy variants removing the elemental additions which strengthen grain boundaries.

The second place where nickel superalloys feature prominently is in the discs to which the blades are mounted, particularly in the turbine sections. These alloys are polycrystalline and equiaxed in nature and are produced via traditional ingot or powder metallurgy routes, in order to produce large discs with excellent mechanical properties which are also uniform in nature. As turbine inlet temperatures increase with each subsequent engine generation, the mechanical property requirements further increase. Alloy chemistries have diversified and become increasing complex to meet property requirements, with the addition of 10 or more elements found in some modern superalloys. Chemical segregation inherent with complex chemistries shifted production of alloys away from traditional casting and ingot methods to power metallurgy methods, where segregation is limited to micron length

scales. As a generalisation, turbine discs require very high strength which is facilitated by a fine grain size. This is achieved through multiple hot working steps to produce high levels of recrystallisation. This is followed by complex heat treatments to produce precipitate morphologies suitable for delivering the required properties. The development of a modern nickel superalloy is extremely expensive given the severity of the application. An un-contained disc failure in flight is more than capable of bringing down an aircraft, which tragically has been proven on a number of occasions. The modern approach to alloy development must include both a strategy for production, maintenance of supply chain, ensuring the longevity of the component and finally its disposal. This holistic approach can lead to extensive lead times for entry into service of nickel superalloy components and therefore the more understanding of superalloys is available before a manufacturer commits to a particular alloy choice the less commercial risk is faced.

The numerous manufacturing steps involved in producing a powder metallurgy superalloy and their purpose are listed Table 1.1. The processes involved in the production of these alloys are extensive and costly and there are multiple instances where deviations from the intended processing routes can occur. Each process can negatively affect a manufacturer's ability to perform the subsequent manufacturing step, particularly during hot working. The prior particle boundaries can negatively affect hot ductility which limits the ability of the material to accept further hot working in order to induce recrystallisation. This then limits the ability of the material to acquire the mechanical properties required in service. The final step in the shaping processes used in manufacturing involves machining the component into its functional form, this step is therefore at great risk from being affected by subsequent steps and it is the aim of the work presented in this thesis to understand how some of the changes that occur during manufacturing can affect the machinability of the material.

Table 1.1: Key processes used in the production of a powder metallurgy derived nickel superalloy aerospace components. Compiled using information from [1–3].

Process	Purpose
Alloy melting	Produce the required stoichiometry from elemental constituents to a high degree of precision
Powder production	Produce pre-alloyed powder via techniques such as gas atomisation
Powder sieving	Ensure tight tolerances on powder size and shape are enforced, as well as removing impurities such as ceramics from furnace linings
Powder consolidation	Consolidate powder into a billet format, with low levels of segregation and porosity
Billet extrusion	Break up prior particle boundaries allowing subsequent processing steps
Forging and heat treatment	Produce near net shape components with the required microstructure
Rectilinear machining	Machine to the required shape for ultrasonic inspection
Finish machining	Machine to the finish component geometry

Before detailing the investigations conducted in this thesis, it is worth first exploring the behaviour of these complex materials and the basic fundamentals. It is worth noting however regardless of the attempts to do so in this thesis, the reader is invited to review the well cited book by Reed [1], who provides all the work that a young researcher could ever need to know regarding superalloys. The following sections can therefore be considered an abridgement of the fundamentals of nickel superalloy behaviour.

1.2 Nickel superalloy metallurgy and behaviour

1.2.1 Basic Nickel Metallurgy

Elemental nickel is a transition metal which exhibits a crystallographic structure with a face centred cubic (FCC) unit cell. In its elemental form nickel is a relative high density metal which exhibits properties such as high hardness and high ductility. Elemental nickel provides a good base for a high strength alloy owed to its ability to accept strengthening via substitutional

and precipitation mechanisms. Substitutional strengthening occurs when the metallic lattice is distorted via the substitution of foreign atoms, this distortion impedes the motion of dislocations resulting in a an increased resistance to plastic deformation through slip mechanisms. A wide variety of elemental additions are used in solid solution and precipitation strengthening of Nickel superalloys.

Alloying additions with similar atomic radii to the nickel matrix include cobalt, iron and chromium. These elements exist within, and stabilise, the matrix phase known as γ. Cobalt is known to improve the hot workability by lowering the activation energy of recrystallisation, lowering the stacking fault energy and by refining γ' precipitates [1]. Elements which typically have a greater atomic radius than nickel partition to the ordered precipitate phase known as γ'. The γ' phase consists of a FCC lattice whereby the corner atoms are replaced by tantalum, titanium, aluminium and niobium. The addition of these elements leads to the stabilisation of the γ' allowing the phase to exist in higher volume fractions and increases the temperature at which the precipitate goes into solution. The γ' precipitates are discussed in detail in section 1.2.3. Another key group of elemental additions includes carbide formers such as boron, carbon and zirconium which aid the formation of carbides precipitates on the grain boundaries which help with properties such as creep resistance and act as further barriers to dislocation motion. Some of the elements mentioned perform multiple roles such as tantalum which both partitions to the γ' as well as forms carbides.

It can be inferred from the previous comments that nickel superalloy metallurgy can be very complex and care must be taken to ensure that the balance of elements results in the optimal quantity and thermal stability of the various phases while a component is operating under in service conditions. Such is the complexity of superalloy chemistries that efforts have been made to predict the mechanical properties of nickel superalloys based on chemistry alone via computer simulations with limited success due to the range of microstructural changes that may occur [4]. The modelling approach to alloy design has also been applied to newer cobalt based superalloys which have similarly complicated chemistries designed for high temperature applications [5]. These tools can be employed at the early stage of the development of a new alloy, however an empirical approach is required in order to fully understand its behaviour, this provides one of the greatest challenges in producing a new superalloy and there is vast expense in doing so.

1.2.2 The γ Phase

the γ phase is the austenitic matrix phase which exists in all nickel superalloys, strengthened by the solid solution strengthening elements mentioned in section 1.2.1; tungsten and hafnium for example provide an increase in the tensile strength of the γ matrix [6]. The γ grains within a superalloy relate to the mechanical properties according the the Hall-Petch effect, with finer grains promoting higher strength. The size of the γ grains also has strong influence over the fatigue properties, with the grain size influencing the initiation point of a fatigue crack and the rate of crack propagation [7–10] with larger grains promoting a reduction of low cycle fatigue life [11,12]. The influence of grain size can also be seen during creep testing, with grain boundaries providing sites for diffusion and facilitating creep [13]. Larger grain sizes have been found to improve creep rupture lives [14].

Nickel superalloys are prone to abnormal grain growth, which as the name suggests manifests as single large grains in and amongst a region of finer grains. The formation of abnormally large grains is related to incomplete recrystallisation post hot working and retained strain energy. This strain energy coupled with the dissolution of the grain boundary pinning γ' precipitates results in grain growth to release said strain energy [15]. Abnormal grain growth can occur while the pinning precipitates are still present in the material [16], which is related to static recrystallisation events during subsolvus heat treatment and the overcoming of the pinning precipitates due to the level of stored energy post deformation. Grains with higher stored energy will grow at the expense of neighbouring finer leading to the formation of abnormally large grains. There appears to be a positive correlation between increasing strain, strain gradient, strain rate and abnormal grain growth during super-solvus annealing [17].

Besides the manipulation of grain size, the promotion of beneficial grain boundary characteristics (know as grain boundary engineering) can also be exploited to improve the properties through the γ phase grains. High levels of grain boundary serration, for example, can increase both the strength and ductility of nickel superalloys [18]. One study suggests that slower cooling rates are optimal for promoting serrated grain boundaries [19]. Addition of boron has been suggested to have a potential benefit in terms of forming serrated grain boundaries which improve ductility [20]. Large incoherent γ' have been shown to result in serrated grain boundaries [21] which are beneficial for creep resistance [22].

1.2.3 The γ' phase

The γ' phase is a precipitate phase which forms through the elemental addition of aluminium, titanium, tantalum or niobium. The two former elements are most commonly used in order to facilitate γ' formation due to the cost of tantalum and niobium. The γ' phase is ordered which is extremely beneficial for strengthening purposes as well as promoting high temperature stability and therefore creep properties. The development of nickel superalloys has focused primarily on the increase in the volume fraction of γ' as well as the optimisation of its morphology. The size and shape of γ' precipitates can vary wildly in superalloys and many research articles aim to understand the interaction between superalloy performance, primary processing and precipitate morphology. γ' precipitates commonly exist in three size distributions in a polycrystalline superalloy referred to as primary, secondary and tertiary γ'. Primary γ' are typically above 0.5 μm and above in size and are intragranular. Secondary and tertiary γ' have sizes between 150-500 nm and 150 nm and below respectively, these precipitates exist within γ grains [2]. A schematic provided by Jackson and Reed shows the typical tri-modal distribution of γ' in Udimet 720 as shown in Figure 1.2, note the size definition of the three size distributions differs amongst publications. The precipitates not only influence the final material properties but also the processing steps involved in material production. The dissolution of these precipitates, allowing grain growth, has been reported to improve hot workability [23]. Although the behaviour of these precipitates is intrinsically linked to high temperature performance, their behaviour at a large range of temperatures is non-trivial. Temperature has been shown to influence the interaction between dislocations passing γ' precipitates, with precipitate shearing occurring at lower temperatures and by-passing occurring at higher temperatures [6].

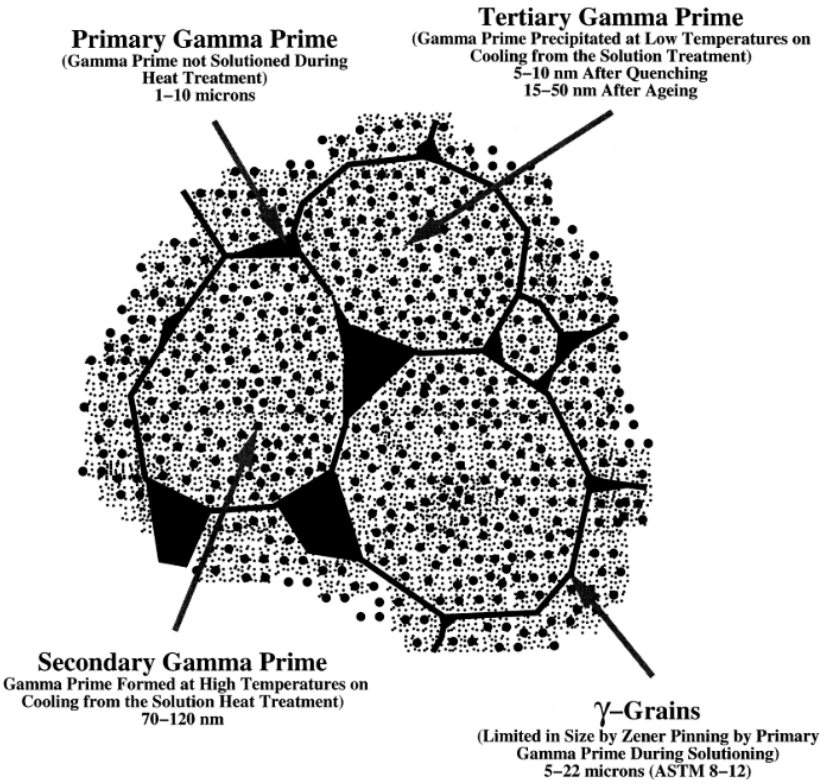

Figure 1.2: Diagram showing the multi-modal γ' precipitate structure commonly found in polycrystalline nickel superalloys. From Jackson and Reed [24].

The γ' phase can exist both coherently and incoherently within the γ matrix phase due to the similarity in lattice parameters [25]. Recent work has shown the γ' phase can exhibit a twin boundary relation within its parent γ grain. The relationship between the lattice parameters of the γ and γ' has implications regarding the mechanical properties in a nickel superalloy. Additions of boron and zirconium result in an increase in the mismatch between γ and γ' resulting in increased elastic strains between the two phases, which results in increased impedance to dislocation motion and increases the driving force for γ' growth at elevated temperatures [26]. During the ageing of RR1000, the lattice misfit has been shown to change over time and is attributed to the diffusion of solute atoms between the γ and γ' phases [27].

The interaction between the γ' phase and dislocations is the main mechanism of strengthening due to the ordered nature of the precipitates, resulting in increased energy requirements in order to penetrate such precipitates. The effect of γ' precipitates can lead to a saw tooth appearance in the tensile stress strain curve, as shown by Rai and Sahn [28]. It was shown that at interme-

diate strain rates and temperatures (10^{-3} s^{-1} and 300°C) these prominent serrations are due to the shearing of precipitates by super-partial dislocations which are bounded by anti-phase boundaries. This may lead to short range disordering and reordering of precipitates which would produce concurrent softening and strengthening mechanisms leading to the saw tooth appearance of the flow stress curves.

The cooling rate is known to particularly affect the size, distribution and morphology of γ'. The sizes of secondary γ' precipitates are shown to vary logarithmically with the cooling rate [29]. An optimum cooling rate was shown in the work of Wu [29] to produce the maximal hardness which is related to an optimal size distribution of γ' precipitates. It has been shown that the volume fraction of larger incoherent γ' precipitates was inversely proportional to the size and volume fraction of secondary γ' precipitates when a two step cooling rate was applied [30]. This involved slow to intermediate cooling rates from super-solvus conditions which was transitioned to faster cooling rates below the solvus temperature. Slower cooling rates through the solvus temperature resulted in larger size and volume fraction of primary γ' precipitates. Higher solution treatment temperatures while still below the solvus temperature are associated with larger secondary γ' precipitation [31]. Faster cooling rates have been shown to limit the coarsening of secondary γ', as well as the occurrence of splitting. Higher cooling rates are associated with finer secondary γ' as well as the formation of regular cubic or spherical morphologies [19]. The cooling rate has been shown to affect the formation of the 3 precipitate size classes. Experimental and computer modelling work has shown that very high cooling rates promote the formation of tertiary γ' only. Slower cooling rates are required to produce secondary γ' and even slower rates are required to form primary γ' [32]. It can be inferred from these findings that the tertiary precipitates are therefore the first to form, followed by the secondary and primary. Heat treatments that combine ageing and differing cooling rates can result in improved mechanical properties via the reduction of spacing between secondary γ' and the coarsening of γ' precipitates results in an increase in the yield strength. This is due to the increase in the effect of the strengthening mechanisms caused by coherency strain and anti-phase boundaries. Coherency strain is produced by the lattice misfit between the γ and γ' which increases as the γ' precipitates increase in size. This misfit produces coherency strains between phases which impedes dislocation motion [33]. Quenching to room temperature and reheating to the ageing temperature produced higher strength material compared to quenching to the ageing temperature and then immediately conducting the ageing. The size of precipitates was also found to be larger for the former. This is explained to be due to greater dislocation density when quenching to room

temperature, which provides more diffusional pathways and therefore coarsening of the γ' precipitates. It has been found that the coarsening of γ' can accelerate the creep process [34]. Tsai et al [35] note that a higher volume fraction of γ' precipitates can result in improved creep properties. Chen et al [36] note that secondary γ' exhibit close to equilibrium compositions while compositional deviations where noted in the smaller tertiary γ'. The same study noted that slow cooling led to higher aluminium content in precipitates. With regards to the development of precipitates during ageing at high temperature exposure, it has been found that γ' can undergo a cycle of coarsening and splitting due to enriched cobalt content at the centre of the precipitates. This segregation results in the instability of the precipitates due to a higher lattice mismatch between the γ and γ' at the interface between the precipitate and matrix phase. This causes the precipitate to split and then coarsen until the segregation is again present in the larger precipitates, resulting in the eventual coarsening and splitting cycle [37].

1.2.4 The Carbide Phases

The formation of metal carbides within a nickel superalloy has been shown to have a profound affect on the microstructure and properties. Generally, carbides precipitate on grain boundaries and triple points. This can provide additional resistance to creep deformation and grain boundary pinning during processing leading to refined microstructures. Tang et al [38] showed that the addition of hafnium led to greater amounts of hafnium carbides which reduced the level of twin formation in a hot isostatically pressed nickel superalloy, due to the slowing of grain boundary motion caused by the presence of MC carbides. Carbides present on the grain boundaries in increasing amounts can improve creep properties due the the hindrance of dislocation motion [39]. Carbides also provide a pinning effect preventing grain coarsening at elevated temperatures [40, 41].

Despite the benefits they provide, carbides have been shown to accelerate the formation and propagation of fatigue cracks [42] with lamellar type carbides providing opportunity for fracture to occur in Inconel 718. It is therefore a requirement to ensure that the size and the morphologies of carbides precipitates are controlled. The carbide phases are also known to be the source of prior particle boundaries (PPBs) which appear as rings of precipitates. Again these are also known to accelerate cracking and limit the scope for hot working due to rupture during deformation. Prior particle boundaries are discussed further in section 3.2.1.

1.2.5 TCP phases

Topologically closed packed (TCP) phases are generally detrimental phases which form in nickel superalloys. The precipitation of TCP phases is generally associated with chemical composition in particular the concentrations of usually creep strengthening elements such as tungsten and tantalum [1] and also excessive chromium. The presence of TCP phases is associated with a reduction in creep strength. ruthenium is a common element additional to single crystal nickel superalloys to suppress the formation of TCP phases [43]. TCP phases are of particularly interest in the field of single crystal nickel superalloys due to their detriment in creep strength and their enhanced formation due to the addition of rhenium [44]

The common TCP phases in nickel superalloys include the σ, μ and laves phases [45]. TCP phases exhibit a crystallographic structure formed of close packed layers of smaller atoms, with larger atoms positioned between layers [46]. The formation of TCP phases is associated with a reduction in mechanical properties due to the depletion of solid solution strengtheners from the matrix phase, particularly chromium [47]. The σ phase exhibits a Tetragonal crystallographic structure and the chemical compositions of FeCr, FeCrMo and Fe_2Ti. This TCP phases is therefore most commonly found in iron containing nickel Superalloys, and appears as elongated globules after high temperature thermal exposure [45]. During solidification the σ phase forms in the inter-dendritic regions where there is an increased presence of aluminium and titanium, upon solution treatment the σ phase transforms in γ phase before again forming σ phase upon the application of heat treatment [48]. The σ phase can result in a reduction in fatigue performance when aligned with the fatigue crack growth direction with crack growth occurring preferentially at the interface between the σ phase and matrix phase.

The μ phase exhibits a rhombohedral structure and has the chemical composition $(Fe,Co)_7(Mo, W)_6$. This TCP phase forms at elevated temperature and is associated with high levels of Mo or W in the alloy composition [45]. The Laves phase has the chemical compositions Fe_2Nb, Co_2Ti and Fe_2Ti [45]. In alloys such as Inconel 718, the formation of Laves phases consumes niobium which is detrimental to mechanical strength [49] and also reduces the amount of titanium which can partition to the γ' phase. The formation of Laves phases is strongly influence by chemistry and an increase in niobium and decrease in aluminium and titanium has been shown to increase the chances of the deleterious phase forming [50].

1.2.6 The γ'' Phase and Other Phases

The γ'' phase is formed in nickel superalloys such as Inconel 718, the precipitation and coarsening of which is said to be controlled by the diffusion of niobium [51]. The γ'' phase is also an ordered precipitate phase and has the composition of Ni_3V or Ni_3Nb. This phase is not present in the latest generation of nickel superalloys such as RR1000 and (formerly Udimet) 720li. The γ'' phase can also provide benefits to material properties similar to the γ' phase. Mignanelli et al [52] used a more simplified composition consisting of 4 elements to produce γ' and γ'' in equal volume fractions resulting in superior properties of that of a more traditional superalloy through the formation of a dual super-lattice of γ' and γ''precipitates, which successfully impedes dislocation motion through the combination of each precipitates respective strengthening mechanism. The presence of γ' is also thought to stabilise the γ'' phase preventing the unwanted transition from γ'' to η phase which precipitates at the expense of γ' and results in a reduction in mechanical properties [52]. The γ'' phase has been shown to improve fatigue resistance through its ability to produce slip bands as opposed to brittle fracture, unlike TCP phases which cannot absorb dislocations leading to rapid brittle fracture [42]. The η phase forms upon the increase of titanium beyond its solubility limit [53] and presents itself as rod shaped precipitates, the orientation was found to affect the ease of material flow as noted in [54], where flow softening was seen as precipitates reorientate parallel to the forging direction.

The γ'' phase transforms into the δ phase at temperatures above 650°C [55]. The δ phase acts in the same manner as γ' and pins grain boundaries during hot working resulting in the production of uniform fine grain sizes which are beneficial to in service properties. The δ phase can form with a uniformly distributed spherical morphology or as basket-weave type structures. The presence of δ phase reduces the yield strength in Inconel 718 due to a depletion of γ'' [56]. The presence of δ has an influence on the hot working characteristics in Inconel 718 at higher temperatures. The δ phase dissolves which permits greater strain without cracking, and thus allowing recrystallisation. At lower temperatures, the δ phase precipitates act as sinks for dislocations and therefore act as nucleation sites allowing dynamic recrystallisation. Although these effects aid the formation of fine grain structures, the presence of δ phase can act as crack initiation sites leading to flow instability [57]. Hot working has been shown to increase the volume fraction of δ phase precipitation [58] and change the morphology of the precipitates from platelet to spherical [59]. The time for δ formation has been shown to reduce with the addition of zirconium and boron, however the temperature at which formation occurs is increased [60].

1.2.7 Strengthening and Deformation Mechanisms in Polycrystalline Nickel Superalloys

The FCC lattice of the γ phase has twelve possible slip systems through which dislocations can move during plastic deformation. Du et al [61] noted that the interaction between dislocations and the superalloy structure is dependant on temperature during tensile deformation. At room temperature, dislocations are shown to be traversing the γ' precipitates through the anti-phase boundary shearing mechanism. At increased temperatures, the formation of dislocation loops are evident indicating a change in the deformation mechanism.

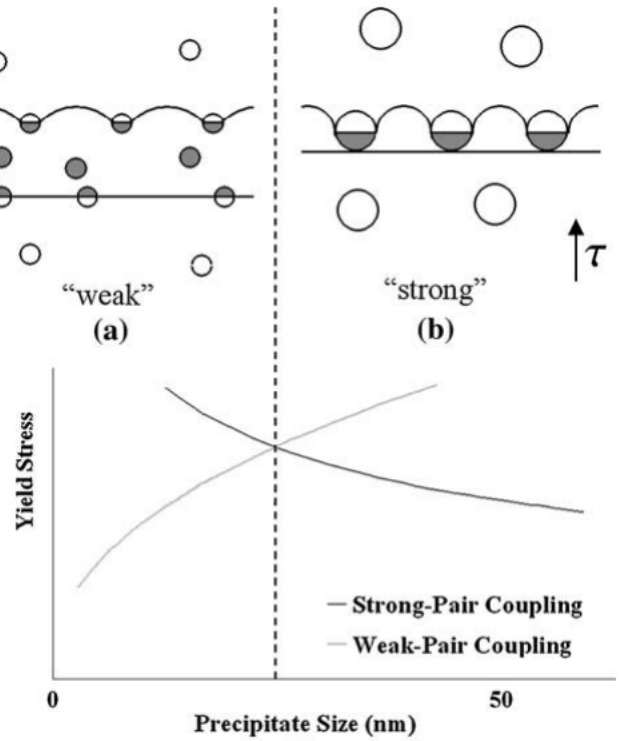

Figure 1.3: Diagram showing (a) weakly coupled and (b) strongly coupled dislocation motion and the variation in the strengthening effect provided by each mechanism as a function of precipitate size. From Huther and Reppich [62].

The γ and γ' phases exhibit greatly different behaviours in terms of dislocation motion during plastic deformation. In the γ matrix, which is not ordered, single dislocations can traverse the material along the $a/2\langle 1\bar{1}1\rangle\{111\}$ slip system. The ordering in the γ' precipitate prevents the passing of a nor-

mal dislocations along the $a/2\langle 1\bar{1}1\rangle\{111\}$ system as dissociations of the lattice is energetically unfavourable and leads to a planar defect known as anti-phase boundary. In order for dislocations to travel along the $a/2\langle 1\bar{1}1\rangle\{111\}$ system, they must therefore travel in pairs known as a super dislocation made up of two super partial dislocations. One dislocation leads to the formation of an anti-phase boundary and second removes it. This allows the passage of dislocations through the γ' precipitates. This is the primary reason for the strengthening effect provided by the γ' precipitates [1].

The described two dislocations can traverse shear the γ' precipitates in what Reed [1] describes as weakly coupled and strongly coupled pairs. Weakly coupled dislocations are described as such due to the large distance between the two dislocations compared to the γ' precipitates. In this deformation behaviour the leading dislocation or super partial dislocation traverses a non-linear path through precipitates due to the leading dislocation being unable to overcome the energy to form an anti-phase boundary (APB). This means that the dislocation effectively travels non linearly from precipitate to precipitate until the precipitate size, the APB energy and the applied shear stress field allows the leading dislocation to shear the precipitates forming an APB. The elastic repulsive force provided by the precipitates within the matrix must also be overcome. The trailing dislocation is aided by the fact that the removal of the APB is energetically favourable and thus the secondary precipitate traverses in a linear fashion, shearing precipitates, and thus restoring short range order via removal of the APB. This interaction mechanism between γ' precipitates and super dislocations relies on the precipitates being small and sparsely spaced, relative to the precipitate size. Note that in this mechanism the two distinct dislocations do not shear the same precipitate.

Strongly coupled dislocations however, exist closer together with respect to the surrounding γ' precipitates, and thus, the two partial dislocations pass through a single precipitate sequentially. The shear stress required for this to occur is determined by the size of the precipitates, with the resistance to strongly coupled dislocations approaching zero as the precipitate size increases. The particle size at which the transition from weakly coupled dislocation motion to strongly coupled dislocation motion is determined by the shear modulus, Burgers vector length and the APB energy, which in turn is determined by the lattice constant between the γ and γ' phases. The optimum strength is exhibited at the transition from strongly coupled dislocation motion. This is described diagrammatically in Figure 1.3.

Chapter 2

Research Motivation and Thesis outline

2.1 Industrial Relevance of Machining of Nickel Superalloys and Potential Opportunities

The usage of nickel superalloys in the civil aerospace sector mandates the requirement for a detailed understanding of the fatigue and the creep resistance of such materials, in order to design and operate critical rotating parts within the typical gas turbine engine. The fatigue of such material is not only determined by the material properties but also by the levels of microstructural damage imparted by the manufacturing process, particularly during machining [63]. The machining process is a subtractive manufacturing technique which relies on high shear forces to remove material on typically small length scales relevant to the component. However, these shear forces impart deformation in the subsurface on a smaller length scale still. Alongside tooling developments, focussed attempts have been made to improve alloy processing and chemistry to reduce the cost of manufacturing, that said, these efforts are often offset by the in service performance requirements which demand increasing properties at the expense of the ease of manufacture.

Another issue when developing a new nickel superalloy is the cost involved in large scale machining trials to determine optimum tooling, geometries and process parameters, while ensuring the level of damage imparted on the material is within expectation for suitable fatigue life. These costs include the tooling and machine time usage which often is required to be outsourced, as well as the baseline material costs. This often involves producing large billets which are often far from the intended shape of the component at large costs and long lead times. If the microstructure needs to be optimised

then several iterations of this process may be required to arrive at a final solution. These considerations present 4 industrial opportunities to aid nickel superalloy development, as follows:

- The production of nickel superalloy material specifically for the use of testing and machining trials is expensive and long lead times can be incurred. Can alternative production techniques be employed to minimise material production costs and lead times in order to speed up alloy development? Do these techniques show any promise in terms of their use in producing production scale components?

- The way different alloy chemistries and microstructures are tested involves the iterative production of billets with different production routes to produce varying microstructure. If dual or even multiple microstructures could be contained within a single billet, this could allow multiple microstructures to be tested, particularly in terms of machining with associated time and cost reductions.

- If a greater understanding between different microstructural features and the microstructural damage imparted during machining could be understood in terms of relationships between precipitate sizes and distributions as well as grain morphologies, then alloy microstructures could be employed to optimise machinability. It is unlikely that this can be achieved without being a detriment to in service properties, however more producible and machinable nickel superalloys open up the possibility of introducing the beneficial high temperature properties to other, less critical and expensive applications.

- The production route for powder metallurgy nickel superalloys is complex and there is much opportunity for variations which would lead to differences in upstream processing and final material microstructure. If knowledge could be gained with regards to how these variations are likely to end processing steps such as machining, the processes could be adapted on a billet by billet basis to optimise production.

The work contained within this thesis aims to produce data and understanding which takes a step towards addressing the listed opportunities. Through the use of a modification of the modern nickel superalloy RR1000 named alloy 131072, the material will be followed from the start of the powder metallurgy production route to final machining trials.

2.2 Thesis Methodology

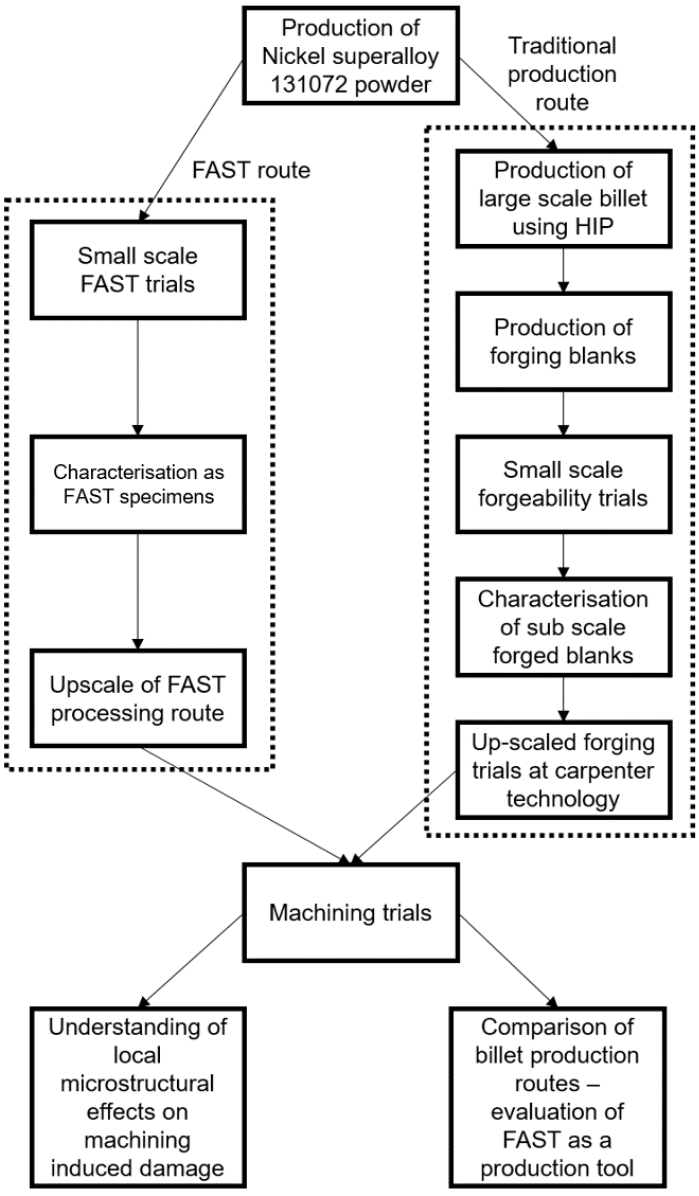

Figure 2.1: Schematic showing the experimental approach taken in this thesis.

A schematic showing the research approach is shown in Figure 2.1. As is described in the figure, two alternative processing techniques were chosen for the production of material eventually used for machining trials. The com-

monality between the two process routes is the desire to produce differing microstructures which can be then evaluated during machining. The two chosen routes are the conventional powder metallurgy route which includes Hot isostatic pressing and forging. Due to the limited availability of hot extrusion apparatus on the length scales required, it was decided that HIP+forge would be employed, which represents the processing route of more legacy powder metallurgy superalloys such as Alloy 720 and Waspaloy. Alongside this, an alternative route was proposed which involves the use of field assisted sintering technology (FAST) which is a technique that is being increasingly used in the production of metallics and ceramics, and more recently aerospace grade titanium alloys [64]. The FAST process is currently capable of producing large plate like billets with large diameters ranging between 100-250 mm and thickness's ranging from 20-40 mm. Due to the relatively low aspect ratio cylinders, upset forging would be difficult due to the large surface areas and high forging loads required. Therefore it was decided that the processing via FAST would be varied via differing process conditions, determined beforehand using small scale trials.

The forging route also took advantage of smaller scale forging trials to first understand the implication of varying forging process parameters on the material response and post forged microstructure. These trials reduced the risk during the more costly large scale trials preventing any loss of material through incorrect forging parameters and therefore preventing subsequent machining trials.

Once the two production routes were explored, materials were prepared for machining trials with the aim to ascertaining how the processing route and material microstructure responded to the machining process. These machining trials then provided a subsurface which was examined for correlations between material, processing route and underlying damage. Once the machining trials had been completed, the large scale billets were sectioned to reveal the comparison in material characteristics for the two routes on a length scale much larger than the sub scale testing performed beforehand.

Chapter 3

Production of a Modern Nickel superalloy via Hot Isostatic Pressing

3.1 Introduction

In order to produce material required to examine the effects of its processing life-cycle on the machinability of a modern nickel alloy, two different consolidation methods were chosen to produce consolidated material from a nickel superalloy powder feedstock.

Alloy	Cr	Co	Mo	W	Nb	Al	Ti	Ta	Fe	Hf	C	B	Zr	Ni
Alloy 10	11.5	15	2.3	5.9	1.7	3.8	3.9	0.75	—	—	0.030	0.020	0.05	Bal
Astroloy	15.0	17.0	5.3	—	—	4.0	3.5	—	—	—	0.06	0.030	—	Bal
Inconel 706	16.0	—	—	—	2.9	0.2	1.8	—	40.0	—	0.03	—	—	Bal
Inconel 718	19.0	—	3.0	—	5.1	0.5	0.9	—	18.5	—	0.04	—	—	Bal
ME3	13.1	18.2	3.8	1.9	1.4	3.5	3.5	2.7	—	—	0.030	0.030	0.050	Bal
MERL-76	12.4	18.6	3.3	—	1.4	0.2	4.3	—	—	0.35	0.050	0.03	0.06	Bal
N18	11.5	15.7	6.5	0.6	—	4.35	4.35	—	—	0.45	0.015	0.015	0.03	Bal
Rene 88DT	16.0	13.0	4.0	4.0	0.7	2.1	3.7	—	—	—	0.03	0.015	0.03	Bal
Rene 95	14.0	8.0	3.5	3.5	3.5	3.5	2.5	—	—	—	0.15	0.010	0.05	Bal
Rene 104	13.1	18.2	3.8	1.9	1.4	3.5	3.5	2.7	—	—	0.030	0.030	0.050	Bal
RR1000	15.0	18.5	5.0	—	1.1	3.0	3.6	2.0	—	0.5	0.027	0.015	0.06	Bal
Udimet 500	18.0	18.5	4.0	—	—	2.9	2.9	—	—	—	0.08	0.006	0.05	Bal
Udimet 520	19.0	12.0	6.0	1.0	—	2.0	3.0	—	—	—	0.05	0.005	—	Bal
Udimet 700	15.0	17.0	5.0	—	—	4.0	3.5	—	—	—	0.06	0.030	—	Bal
Udimet 710	18.0	15.0	3.0	1.5	—	2.5	5.0	—	—	—	0.07	0.020	—	Bal
Udimet 720	17.9	14.7	3.0	1.25	—	2.5	5.0	—	—	—	0.035	0.033	0.03	Bal
Udimet 720LI	16.0	15.0	3.0	1.25	—	2.5	5.0	—	—	—	0.025	0.018	0.05	Bal
Waspaloy	19.5	13.5	4.3	—	—	1.3	3.0	—	—	—	0.08	0.006	—	Bal

Figure 3.1: Chemical composition of widely used nickel superalloys from Reed [1].

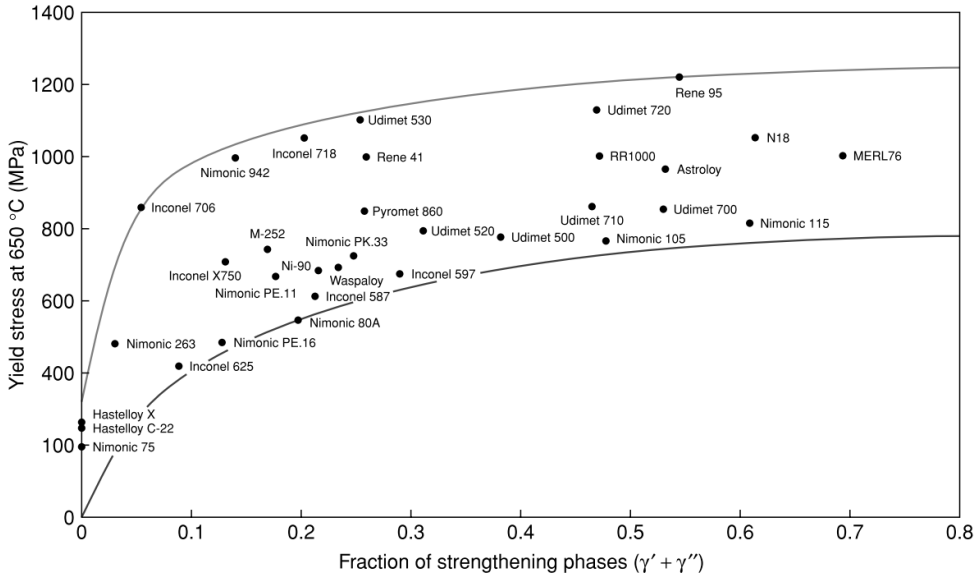

Figure 3.2: Yield strength vs γ' and γ'' volume fraction of common Nickel based superalloys from Reed [1].

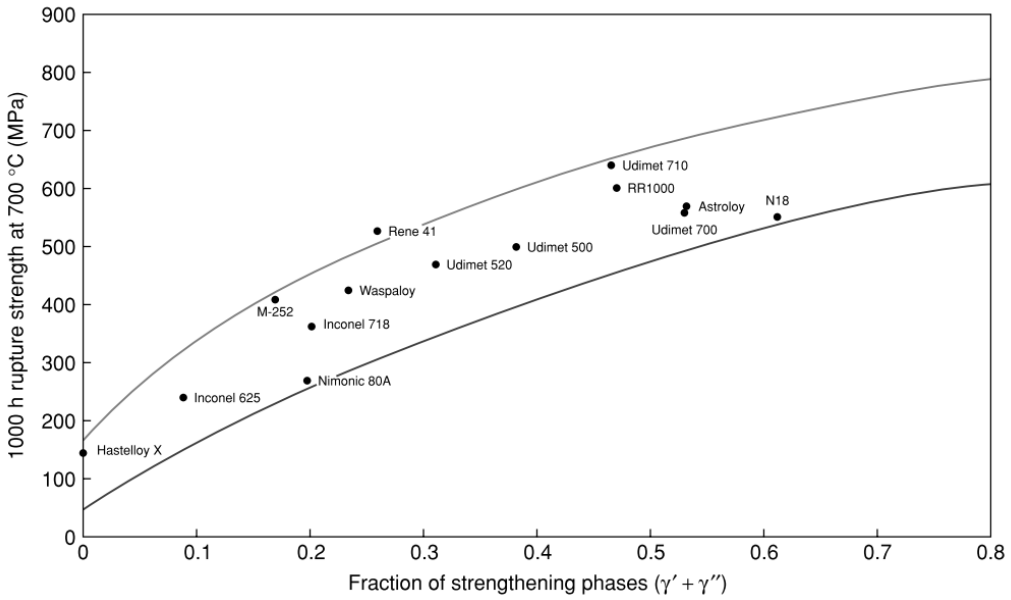

Figure 3.3: 1000 hour creep rupture strength vs γ' and γ'' volume fraction of common Nickel based superalloys from Reed [1].

RR1000, a modern high performance nickel superalloy was chosen to be

the base material used for testing. RR1000 is a modern high performance nickel alloy that contains a highly alloyed chemical composition as shown in Figure 3.1. As shown in Figure 3.2 and Figure 3.3, RR1000 is one of the highest performing modern nickel superalloys in terms of the yield strength and creep resistance. This is due to the high volume fraction of γ' precipitates in the material due to the high levels of titanium and aluminium used in the chemistry. This chemistry was used as a basis to produce powder via gas atomisation to be used in consolidation trials to compare how two different methods of sintering the powder to form a billet would affect the microstructure.

3.2 Literature Review

3.2.1 Consolidation of Nickel Based Superalloys through Hot Isostatic Pressing

For powder metallurgy based superalloys there is a requirement to have near 100% density, as micro-porosity has shown to increase the rate of fatigue failure through accelerating crack initiation and propagation. HIP (hot isostatic pressing) is a process which consolidates powder by the healing of porosity between powder particles through diffusional mechanisms. The combination of an applied stress and high temperature results in accelerated diffusion which closes the porosity between powder particles. Increasing both the stress and temperature results in an increased rate of diffusion [65]. It has also been proposed that the high stresses result in plastic flow which adds to the porosity reduction mechanisms [66]. Densification has been found to increase when the temperatures used exceed the γ' solvus of the material [67]. Efforts have been made to optimise the HIP process through empirical modelling techniques. For example in [68] the power dissipation energy during the HIP process is related to the relative density and strain rate sensitivity of a material. This is then related to microstructural change and by optimising the processing temperature, the input energy during HIP is used mostly for reducing porosity instead of negatively changing the materials underlying microstructure.

In order to ensure that gaseous species are not trapped in the microstructure, degassing and sealing of the HIP container is required prior to the process being conducted. The ability to de-gas the HIP vessel depends on the quality of its construction particularly when welding the HIP container. For cost reduction purposes as well as ease of manufacture, HIP vessels are constructed from mild steel. It is also worth noting that the HIP vessel is

required to deform as the contained powder densifies, leading to a reduction in its volume. The shrinkage of the HIP vessel is non uniform but predictable due to the isostatic pressure applied. The non uniform nature of the shrinkage of the HIP vessel can lead to issues when it comes to can removal and limits the options for the process. One method of removing the HIP can is via corrosive action, normally in high strength nitric acids. Machining is often not allowable due to the level of deformation of the HIP vessel leading to high volumes of material required to be removed in order to produce shapes usable in subsequent manufacturing steps.

Besides the applied pressure and sintering temperature, powder size can affect the final density of the as sintered product, with one study by Ye et al [69] noting that finer particles lead to enhanced densification, however mixed size fractions were optimal for minimising porosity as finer powder particles infill the gaps between larger particles . The powder processing route not only influences the shape and size fraction of the input powder, but also affects the tensile properties. Argon atomised IN600 powder was shown to have lower ductility that equivalent powder produced via the plasma rotating electrode process for equivalent sintering conditions. During consolidation via HIP, diffusional mechanisms between the HIP can and the nickel superalloy powder can lead to complex microstructures in the diffusion zone. In an example study by Bassini et al [70] it was noted that up to nine distinct diffusional layers can exist, with the overall thickness of the diffusion layer being in the region of 500 μm .

One consideration when consolidating nickel powders through HIP is the development of PPBs. These boundaries are a result of oxides and carbides on the powder surface being consolidated into the material leaving these phases entrapped in the microstructure. These oxides produce regions of oxygen and carbon based precipitates in the form of metal carbides formed from titanium or zirconium as well as other alloying additions [71]. These PPBs have been shown to provide a pathway through which cracks can propagate more quickly and are therefore considered to be highly detrimental [72]. The presence of the PPBs has shown to result in cracking during hot working, particularly at low strain rates and high deformation temperatures. The presence of inclusions in powder metallurgy derived material results in reduced fatigue life, particularly if the defects are present near the surface of a fatigue specimen/component which accentuates such effects [73]. PPBs have been thought to produce abnormal stress/strain curves during hot deformation. The PPBs are thought to act as nucleation point for recrystallisation, resulting in the formation of a necklace structure of fine grains around PPBs, with further deformation resulting in further nucleation sites. This produces a continual hardening and softening mechanism which leads to abnormal in-

flections in the flow stress curves [74]. Efforts have been made to reduce PPBs, for example by using a compound HIP cycle which takes advantage of liquid phases to reduce PPBs [75]. During hot deformation processing such as extrusion, PPBs are shown to break up resulting in a more uniform grain structure [71].

More recently, alternative processing routes have been explored for the consolidation of nickel superalloy powders, one such example is a direct forging strategy where loose powder is contained within a vacuum sealed vessel which is then forged as a single entity. This approach produces a range of densities depending on the local strain applied, however when the deformation and temperature are sufficient, full density can be achieved. This method also has the added advantage of dispersing PPBs in the microstructure, thus removing the need for an extrusion step [76].

It should be noted that due to the effective manner in which the material is consolidated, the HIP process can be used to heal porosity and crack defects in a material, such as is presented by Zhang et al [65] where it was demonstrated that the HIP process can heal defects on the millimetre length scales. Casting defects can also be removed via hot pressing, which is particularly important in nickel superalloys which are at high risk in terms of segregation as previously discussed [66]. Modelling work conducted by Zhou et al [77] concludes that the rate of creep cavity healing in a nickel superalloy is increased with both temperature and pressure. It is also possible to combine HIP with additive manufacturing, with one study by Tillmann et al [78] showing that the density of SLM (selective laser melted) additively manufactured parts can be improved by densifying pores with entrapped argon. This study concludes that the temperature has a greater influence over the final HIP density than the applied pressure, however in the case of SLM the pores cannot be completely healed due to entrapped argon gas which originates from the build atmosphere used during SLM manufacture. The HIP process can also be used to refine the microstructure of directionally solidified nickel superalloys without altering the desired crystallographic orientations [79].

3.2.2 Deleterious Effects During Consolidation

Bassini et al [70] characterised the diffusion layer between the can material and underlying nickel superalloy. In their study, a square bar section was produced using a mild steel can and Astroloy powder. Using microscopy and hardness indentations, the authors determined that the nickel superalloy and steel can interface comprises of 9 distinct layers each with distinct microstructural characteristics and properties. In this study a total interface thickness of 500 microns was observed, which the authors suggest can be eas-

ily removed via light machining. Bassini et al [70] suggest that this low level of interface thickness suggests HIP shows promise for a near net processing technique. Within the layer closest to the nickel superalloy, an increase in the PPBs which is related to the level of carbon diffusion across the interface during sintering, forming carbides leading to an enhanced PPB zone.

Tan et al [71] examined the development of PPBs by examining both the powder, as HIP material and HIP+extruded material to determine how various stages in the production of a usable nickel superalloy billet affect the formation of PPBs. Using the alloy FGH96 as a testing base with two different powder size fractions, the authors examined the microstructural and chemical changes at each stage. Examining the microstructure after the HIP process it was found that finer size fractions result in finer grain structures in the as HIP material for equivalent HIP conditions. TEM (Transmission electron microscopy) examination revealed that zirconium and aluminium oxides, as well as MC carbides and γ' precipitates can all be found within the region of PPBs. Comparing before and after the application of extrusion post HIP with an area reduction ratio of 7:1, Tan et al [71] showed that finer microstructures and broken PPBs were observed. This is due to the imparted large strain during extrusion that leads to the elongation of the circular PPBs due to material flow. The strain input allows both refinement of the grain structure due to dynamic recrystallisation and also a reduction in the pinning effect provided by PPBs, increasing ductility. On the development of PPBs during consolidation, Tan et al [71] attributed this to the movement of carbon at high temperature driven by surface free energy. They suggested that if the consolidation time can be reduced, PPB formation will be reduced, by limiting the time allowable for carbon to diffuse and form the PPB species noted.

In the work of Teng et al [80], the effect of HIP temperature on the microstructure, fatigue and mechanical properties were examined for the γ' strengthened superalloy FGH4097. It was found that the HIP temperature, particularly with respect to the solvus temperature can have a clear effect on the material. At 1100°C, the lowest HIP temperature chosen (below the solvus temperature) it was found that incomplete recrystallisation could be observed in the material with PPBs. There was also evidence of a dendrite microstructure left over from the parent powder. When HIP was performed at 1200°C it was found that complete recrystallisation could be observed with lower occurrence of PPBs. This processing condition resulted in the best tensile strength and ductility. At a higher HIP temperature of 1300°C grain and MC carbide coarsening was observed which resulted in reduction of material properties. As the HIP temperature increased it was found that the fatigue failure mode shifted from a ductile to brittle mechanism. The

results of this study indicate that the HIP temperature is vital for PPB management, producing optimal microstructures for further processing.

3.3 Description Of The Feedstock 131072 Powder Used In This Study

An advanced nickel-based superalloy, designated 131072, produced via argon gas atomisation (GA) by Carpenter Technology Corporation (Pennsylvania, USA) under a collaborative research agreement with Rolls-Royce PLC, was used for HIP consolidation. The chemistry of alloy 131072, shown in Table 3.1 is a variation of the Rolls-Royce proprietary alloy RR1000. The chemical of RR1000 is reported in [2] and shown in Table 3.2. The different phases formed in the superalloy 131072 upon cooling, from liquid were calculated using the software ThermoCalc (2017) with the TCNi8 database, see Figure 3.4 .The particle size distribution was measured using laser diffraction with a Malvern Mastersizer 3000 and the dry dispersion method. Measurements were taken in compliance with ISO 13320:2009 and the average particle size distribution is shown in Figure 3.5a. It can be noted that a considerable range in powder sizes was measured, which is typical of the gas atomisation process. The morphology of the powder is shown in Figure 3.5b. In addition, Figure 3.6 shows an example of the internal porosity within the as received material, which again is a typical feature within gas atomised powder.

Table 3.1: Carpenter Technology nickel superalloy 131072 chemistry by weight %. Note this chemistry is based on that of the Rolls-Royce proprietary alloy RR1000.

Element	Ni	Co	Cr	Mo	Ti	Al	Ta	Hf	Trace elements
Wt %	51.87	18.11	14.78	4.91	3.59	3.10	2.00	0.64	1.00

Table 3.2: RR1000 Chemistry by weight %, reported in the work of Qiu [2].

Element	Ni	Co	Cr	Mo	Ti	Al	Ta	Hf	Trace elements
Wt %	52.30	18.50	15.00	5.00	3.60	3.00	2.00	0.50	0.10

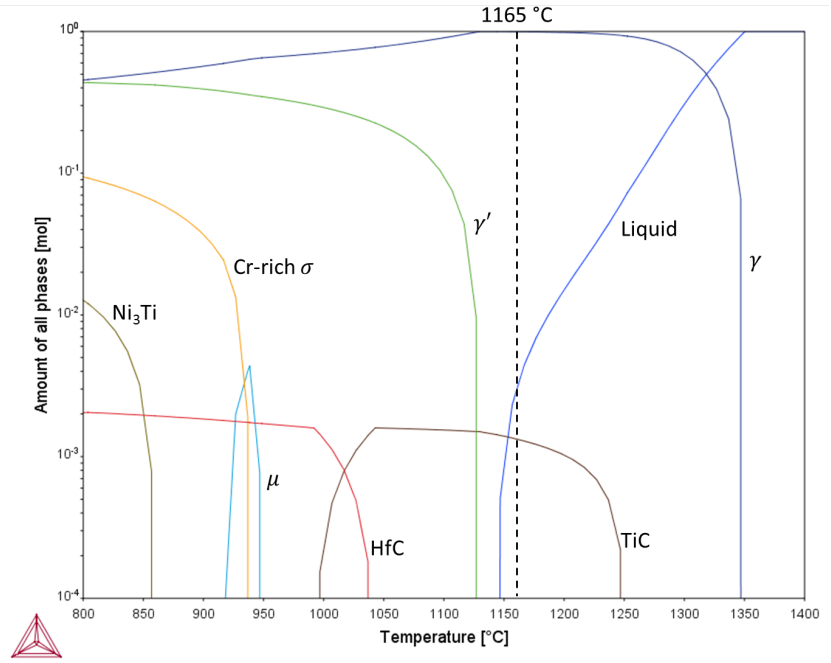

Figure 3.4: Phases in the alloy 131072 after cooling from liquid. Produced using the software ThermoCalc (2017) with the TCNi8 database. Courtesy of Carpenter Technology.

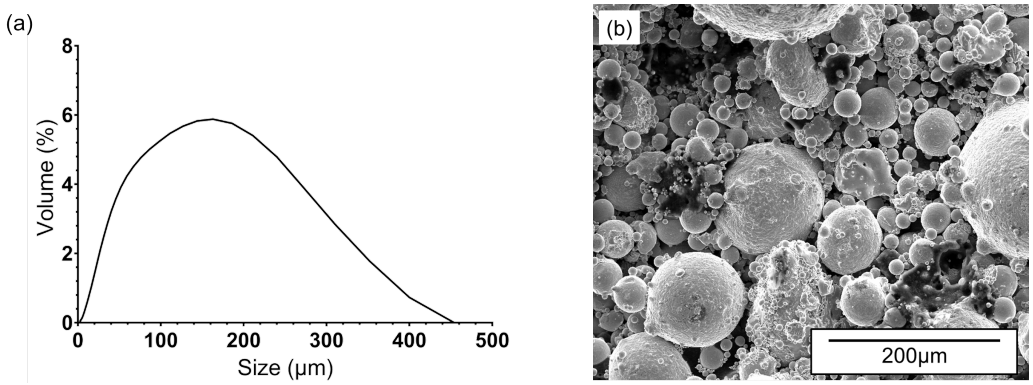

Figure 3.5: (a) Particle size distribution of the feedstock GA Alloy 131072 powder and (b) secondary electron micrograph of the GA Alloy 131072 powder.

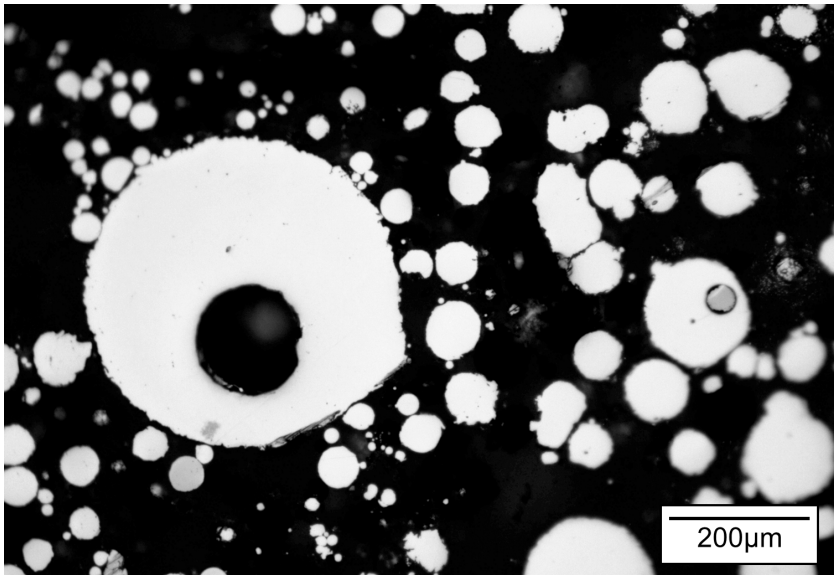

Figure 3.6: Light micrograph showing an example of internal powder porosity in the feedstock 131072 powder.

3.4 Hot Isostatic Pressing of the 13072 Powder

The powder was used to produce material using two different production routes, the first being the more traditional hot isostatic pressing technique, the second being the field assisted sintering technique discussed in Chapter 4. The HIP technique was chosen as a production route to produce test material for machining trials due to its established use in industry.

Before the HIP could be performed, a can was first needed to be produced into which the powder could be filled. Knowing that the HIPed material would be used for industry scale forging trials, a series of finite element models were used to determine the load requirement for forging nickel superalloy billets of different sizes. The available press was limited to a maximum of 500 tonnes. Rudimentary finite element models produced using the DEFORM software package determined that the press could successfully forge billets 73mm in diameter. Using this information, the HIP can was sized to be able to produce 7 billets of 73 mm diameter as well as 6 rods with a diameter of 11 mm which would be sectioned into sub scale compression test pieces to first simulate the forging on a small scale. The length of the HIP can was determined using the mass of powder available and an estimated final billet density, these dimensions were used to produce the HIP steel can. A

schematic for the HIP steel can produced is shown in Figure 3.7.

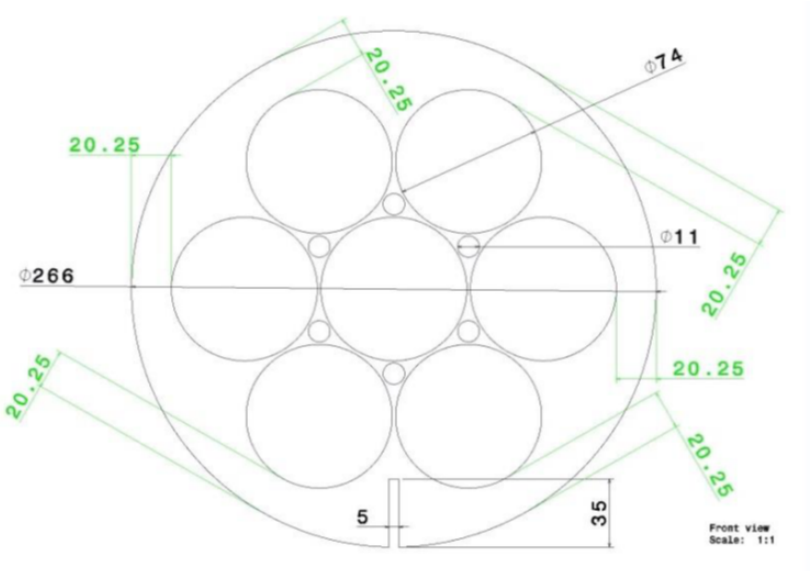

Figure 3.7: Steel can design produced to conduct the hot isostatic pressing of nickel superalloy 131072. showing the position of bars extracted from the HIP can post sintering.

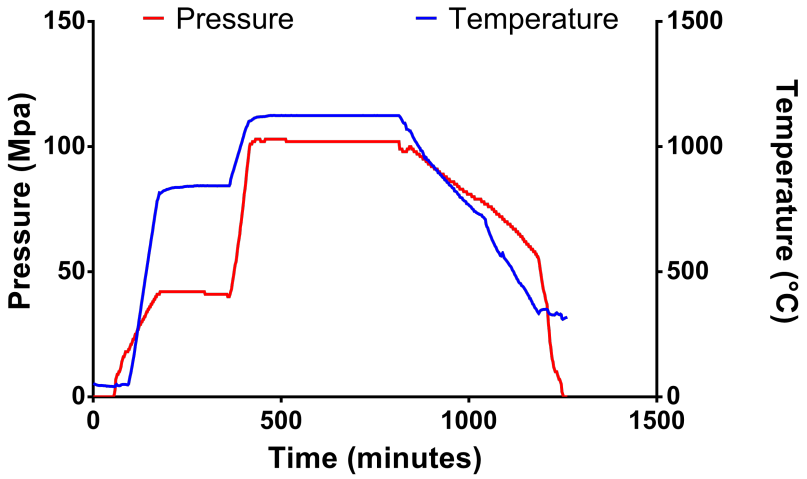

Figure 3.8: Temperature and pressure profile used during the HIP cycle to consolidate the 131072 billet.

The HIP can was manufactured using stainless steel alloy SS304. The can was filled with the 131072 powder before being degassed with Argon

gas. The billet was then transported to Bodycote limited. The material was then hot isostatically pressed using a cycle based on recommendations from Rolls-Royce. The HIP cycle can be seen in Figure 3.8. The billet is exposed to temperatures above 400°C for 17 hours and was exposed to the dwell temperature of 1125°C for a total of 350 minutes (5.83 hours). This dwell temperature was chosen in order to stay close to, but below the solvus temperature of the material. This ensures that the γ' did not go into solution; thereby removing the pinning effect the precipitates provide allowing grain coarsening. It is therefore preferable to maximise the HIP temperature without reaching the solvus temperature, thereby maximising the thermal driving force for consolidation without the production of a coarse grain microstructure. As demonstrated by Qiu [81], a sub-solvus HIP temperature maximises the yield strength and ultimate tensile strength and minimises the elongation at failure when the material is exposed to tensile loads at room temperature.

3.5 Determination of the Depth of Diffusion Between the HIP Can and Consolidated 131072 Material

Qiu [2] conducted extensive work looking at the effects of diffusion from the steel can material to the nickel superalloy region during HIP consolidation. It stands to reason that the high temperatures and pressure utilised during HIP to drive the consolidation mechanisms between nickel superalloy powder particles also result in diffusional transfer between the HIP can and the nickel powder to be consolidated. In the presented work, electro-discharge machining (EDM) was chosen to extract samples from the central region of the billet, as illustrated in Figure 3.7. Before this could be completed, it was necessary to first determine the thickness of the diffusion layer between the two materials to ensure the extracted billets are purely representative of the chemistry outlined in Table 3.1. To do this, a slot sample was extracted from the external diameter of the billet with a thickness of 35 mm extending towards the billet centre. Images of the slot sample and the location from which the sample was extracted are shown in Figure 3.9.

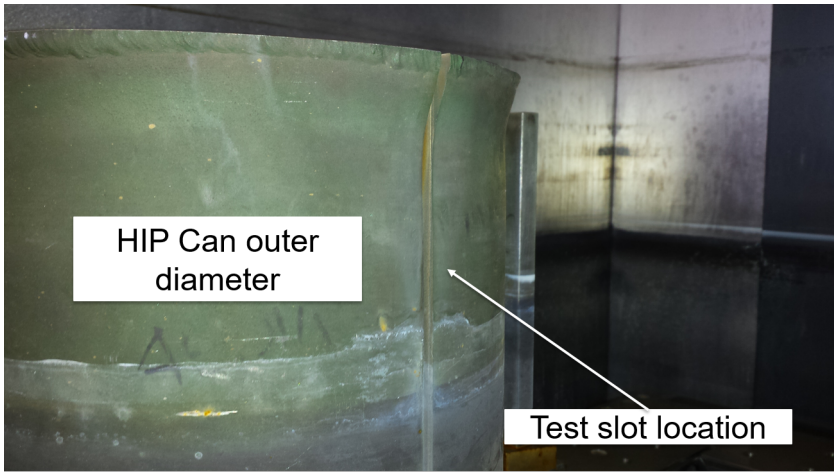

(a) Slot sample extraction location relative to the outer diameter of the HIP can.

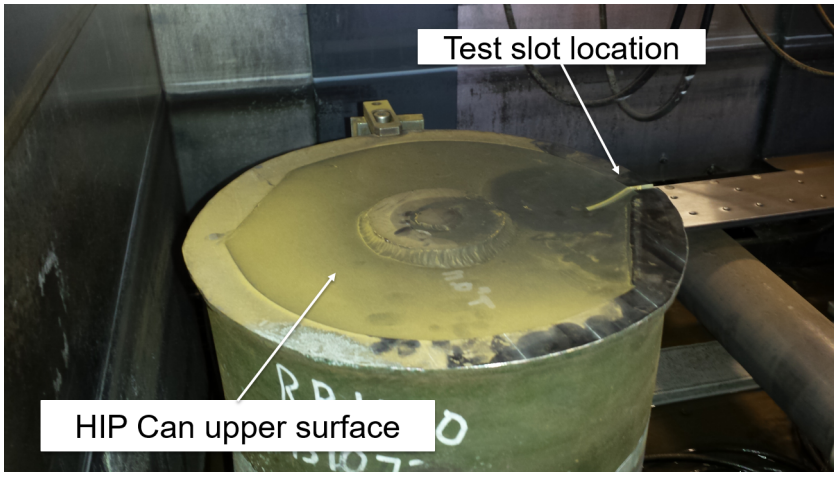

(b) Slot sample extraction position relative to the upper surface of the billet.

Figure 3.9: Photographs of the as HIP billet showing the position at which the slot sample was extracted.

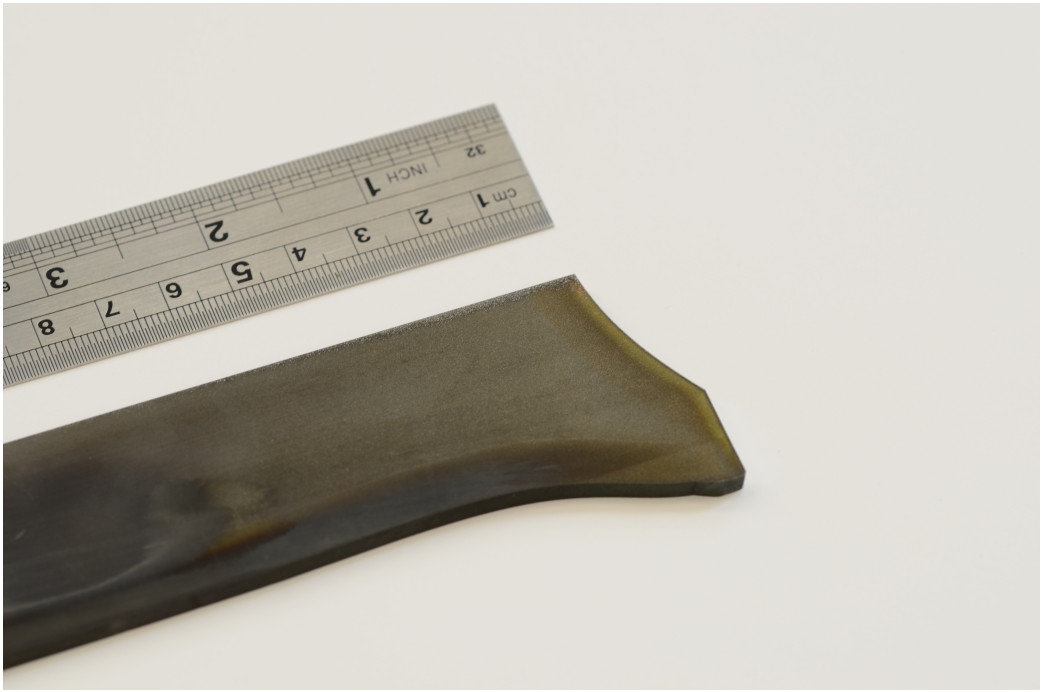

Figure 3.10: Photograph of the extracted slot sample, extracted from the HIP billet at the position shown in Figure 3.9.

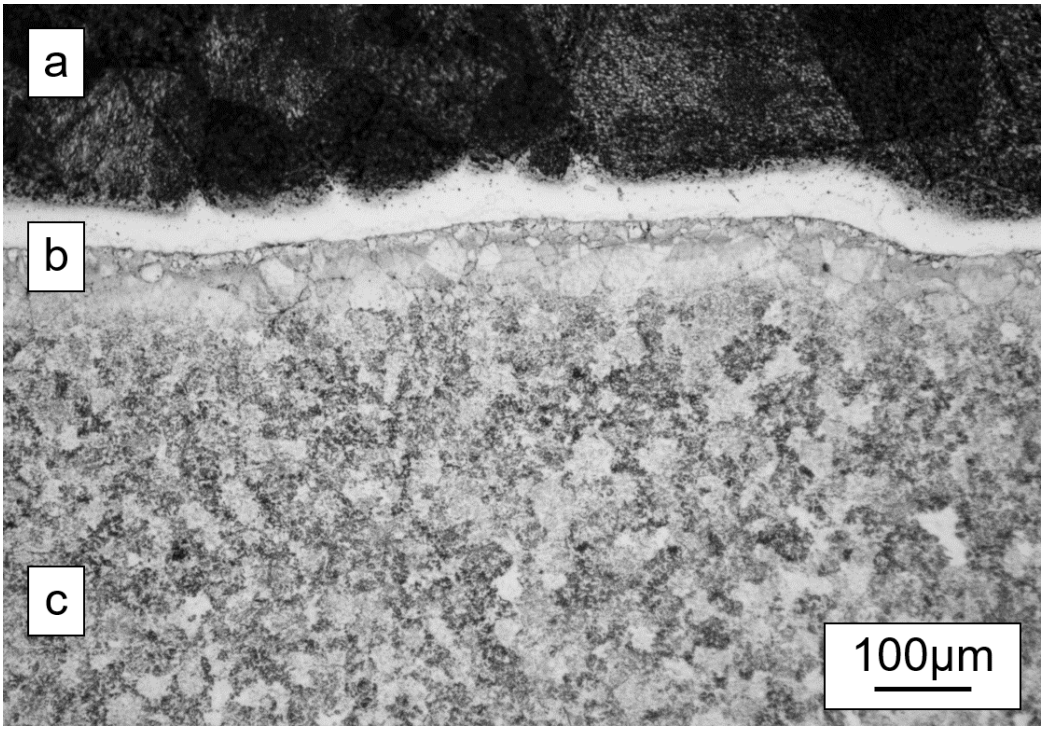

Figure 3.11: Slot sample light micrograph, showing the steel/nickel interface after the application of a Kalling's waterless reagent. Showing (a) the steel can material (b) the interface region and (c) and the nickel superalloy material.

As can be seen in Figure 3.10 it is possible to see that a band of material exists at the exterior perimeter of the slot sample. This material has a markedly different appearance than the inner region which is indicative of the stainless steel and nickel superalloy billet. A metallographic sample was produced and etched using Kalling's waterless reagent to reveal the nature of the boundary between the two materials, as shown in Figure 3.11. There is a clear diffusion region between the steel and nickel material, this interface represents the region of diffusion of several species between the two materials. The thickness of the region is approximately 100-150 μm. The interface region was also examined using backscattered electron imaging, see Figure 3.12 which reveals the transitional region between the two materials in greater detail. There is a larger grain structure followed by a sudden decrease in grain size, this is a clear indication that the composition of the material changes suddenly. The presence of PPBs was found to increase in the interface region between the can and the 131072 material, as shown in Figure 3.13. This carbide based PPB enriched region was reported by Qiu [2] who found that

the thickness of this PPB enriched region was strongly related to carbon content of the can material selected. Considering Figures 3.11, 3.12 and 3.13 it can be seen that the visible diffusion layer extends approximately 50-100 μm below the visible can/billet interface. This gives an indication that the chosen distance between the edge of the larger forger billets (as shown in Figure 3.7) would be sufficiently large enough to ensure that the billets are representative of the chosen 131072 chemistry.

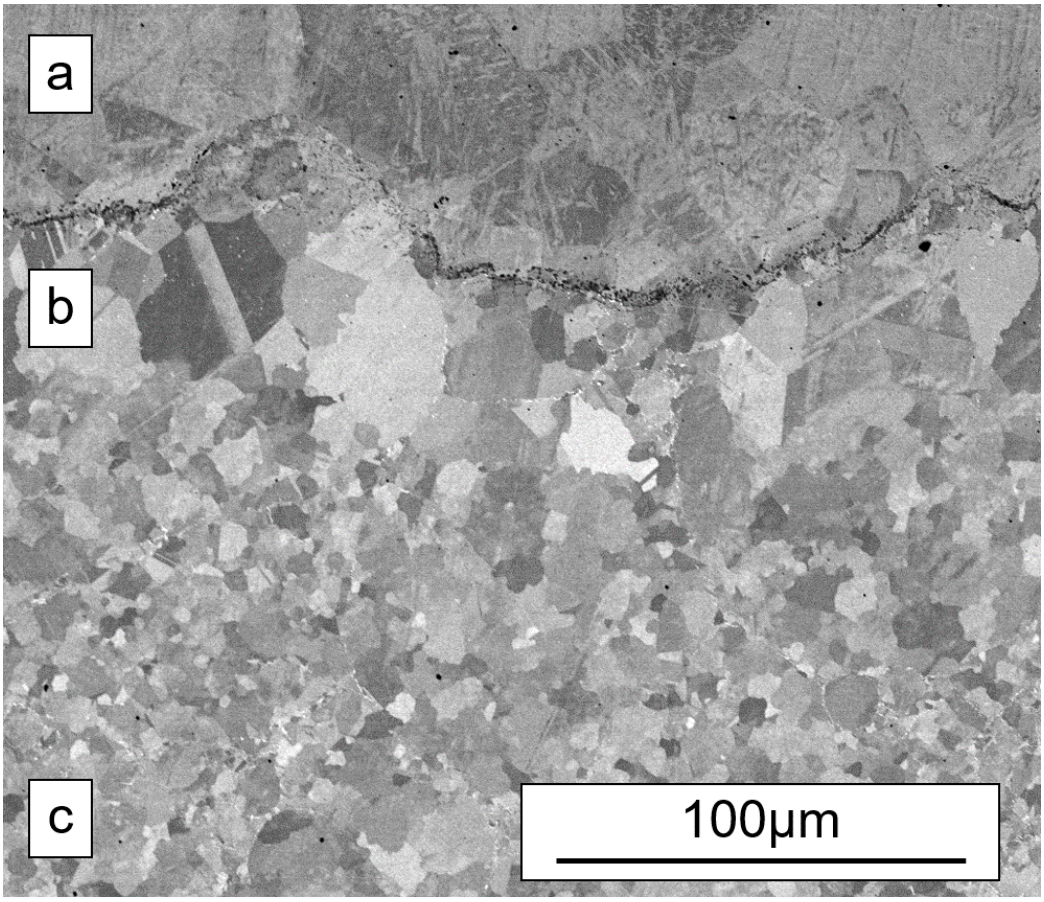

Figure 3.12: Backscatter electron micrograph of the slot sample diffusion region. Showing (a) the steel can material (b) the interface region and (c) and the underlying nickel superalloy material.

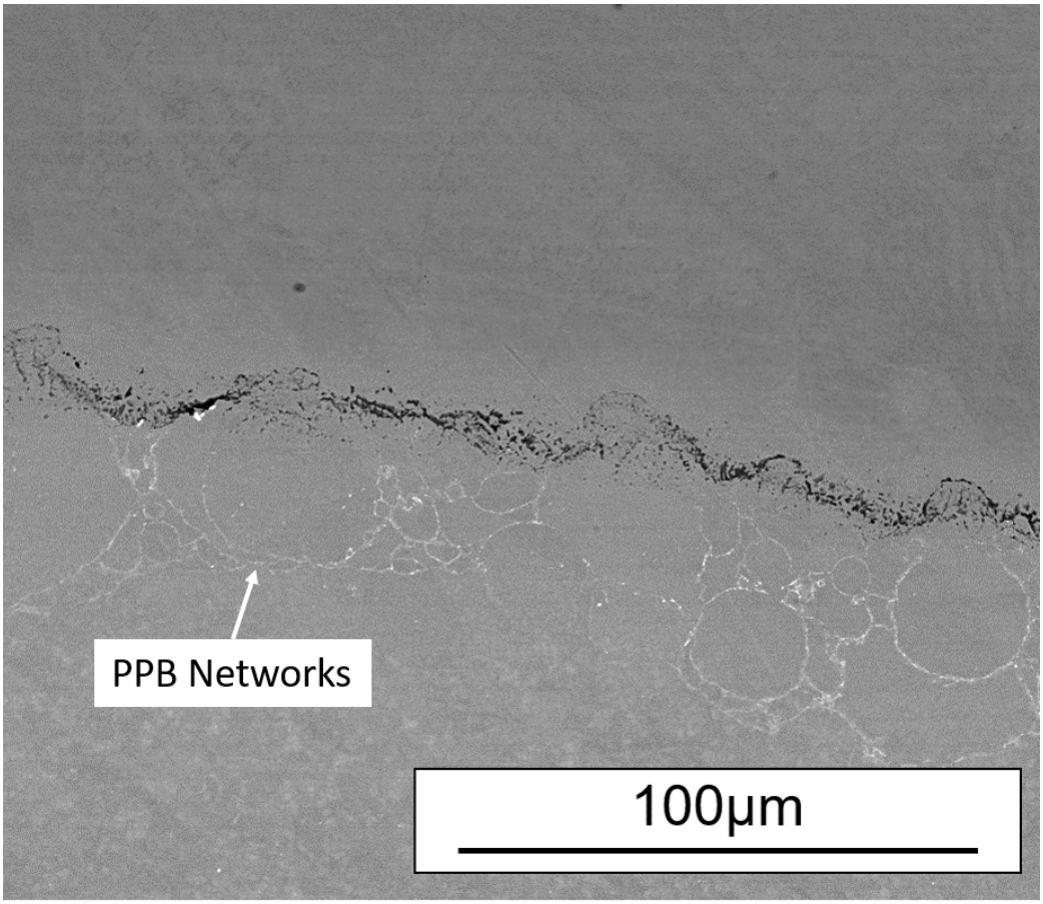

Figure 3.13: Backscattered electron micrograph showing the increased presence of the PPBs at the steel/nickel interface in the slot sample.

3.6 Characterisation of the as-HIP 131072 Billet

3.6.1 Grain Structure and Homogeneity

Characterisation of the as HIP material was important for two reasons. First to ensure that the material within the large billet is homogeneous and secondly to allow a comparison with material produced through the alternative Field assisted sintering (FAST) route.

In order to characterise the HIP billet, two samples were taken at different radial and axial positions across the billet as illustrated in Figure 3.14, these samples were subjected to standard metallographic processing. The samples produced were compared using a combination of hardness testing and grain

size measurement. Micrographs were taken at two regions as shown in Figure 3.15, supplementary micro-hardness data is shown in Table 3.3.

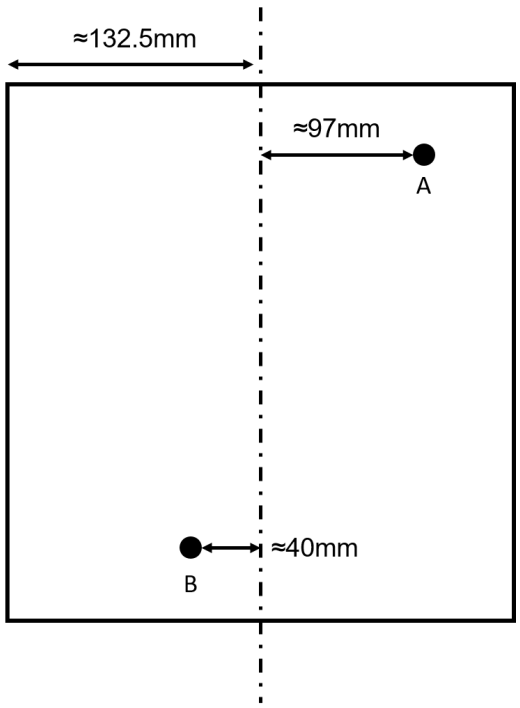

Figure 3.14: The as HIP billet characterisation sample extraction positions. Specimens A and B were subsequently imaged as shown in Figure 3.15 and hardness testing was also conducted, detailed in Table 3.3.

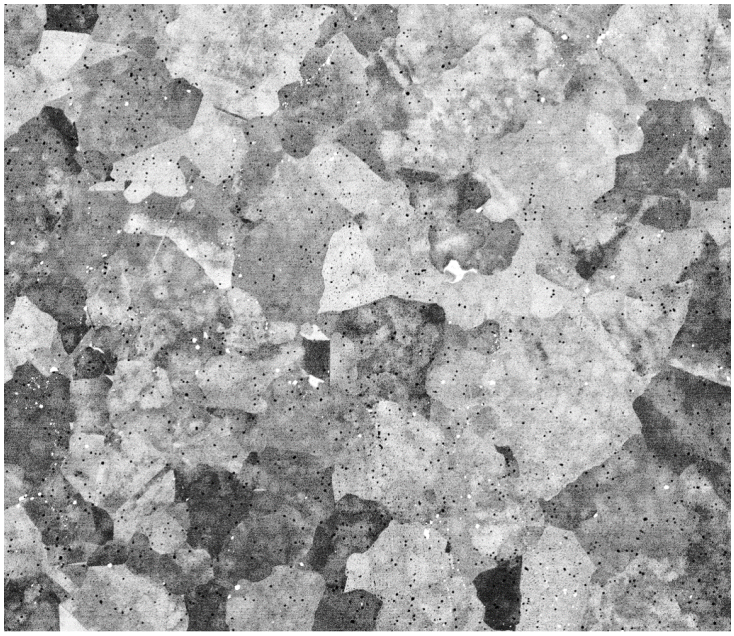

(a) Backscattered electron micrograph of the HIP billet sample extracted from position A in Figure 3.14.

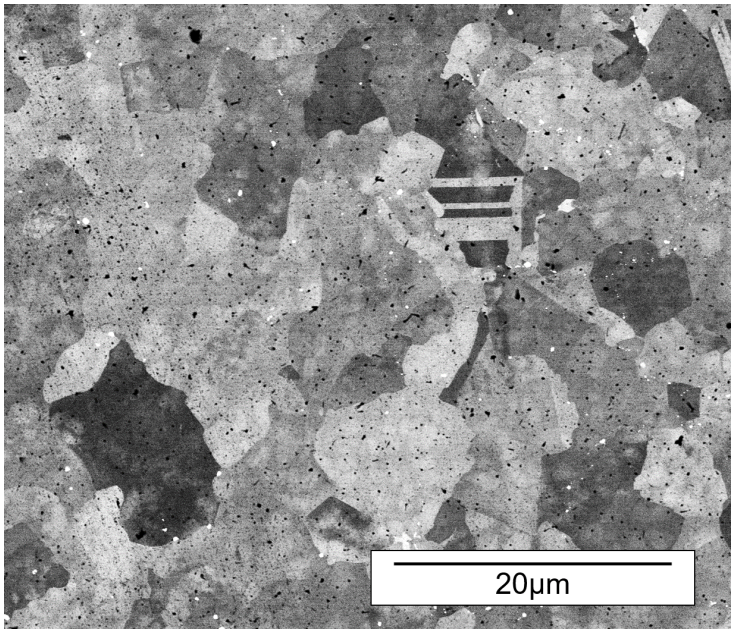

(b) Backscattered electron micrograph of the HIP billet sample extracted from position B in Figure 3.14.

Figure 3.15: Backscattered electron micrographs of the as HIP material showing the grain structure for two samples extracted from different locations within the as HIP billet. The scale bar is valid for both micrographs.

Table 3.3: $Hv_{0.5}$ Vickers Hardness measurements conducted on specimens extracted from the HIP material as illustrated in Figure 3.14.

Measurement Number	Sample B	Sample A
1	369	389
2	366	368
3	369	377
4	373	387
5	379	392
6	385	377
7	389	381
8	381	385
9	373	383
10	387	391
Average	377.1	383
Standard deviation	7.803	7.085

3.6.2 Characterisation of the As-HIP Precipitate Morphology

The samples used to produce the micrographs in Figure 3.15 were subjected to a waterless Kalling's reagent etch in order to reveal the γ' precipitate morphologies. The resultant samples were then subjected to scanning electron microscopy in order to reveal the nature of the precipitates. Figure 3.16 reveals that the as HIP microstructure contains a large volume fraction of γ' precipitates, which is expected with the large amount of γ' forming additions present in the alloy composition. Reed [1] states that RR1000, on which the chemistry of 131072 is based, has close to 45% volume fraction of γ'. It can be seen that multiple sizes of γ' precipitates exist in the structure, with the larger γ' being 2-5 μm in size and a distribution of finer γ' precipitates with sizes below 1 μm. This is typical of Nickel superalloys and the morphologies seen in Figure 3.16 are similar to those seen by Qiu [2] whereby blocky morphologies are present in different size fractions.

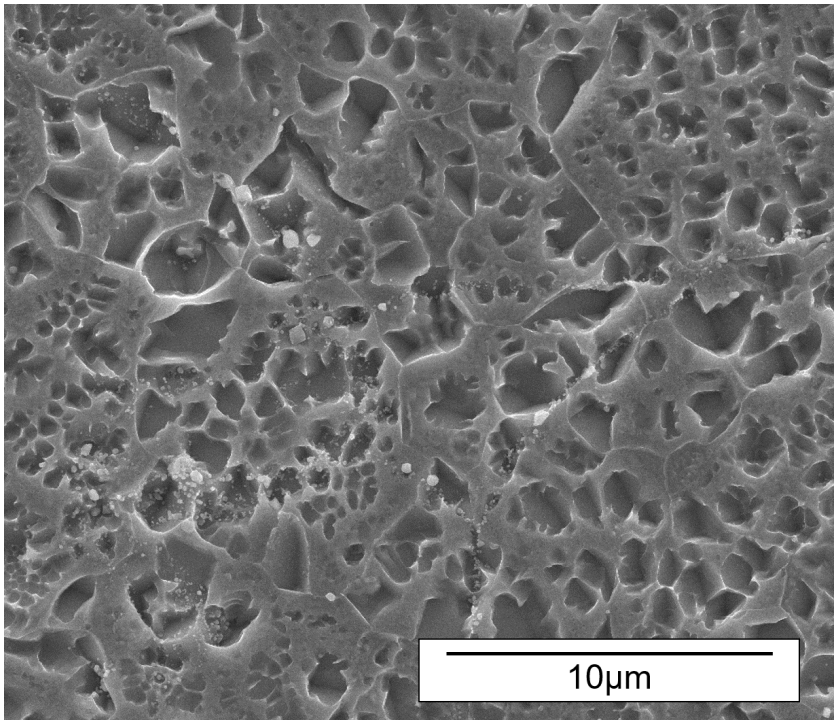

Figure 3.16: Secondary electron micrograph showing the γ' precipitates in the as-HIP material. The HIP cycle employed involved thermal exposure at the dwell temperature of 1125°C for 350 minutes.

3.6.3 Texture Analysis of as HIP 131072 Material

Figure 3.17 shows the electron backscatter diffraction data collected for a sample of as HIP alloy 131072 material. As can be seen, there are no macrozones (areas of common texture) material and the grain size is approximately uniform. The pole figure plot shown in Figure 3.18 also confirms that no significant texture is present in the material, with multiples of uniform density (MUD numbers) of 0.77 to 1.22. An untextured material is expected in the as-HIP condition due to the isostatic application of pressurised argon during the HIP process, which provides a uniform sintering driving force during consolidation.

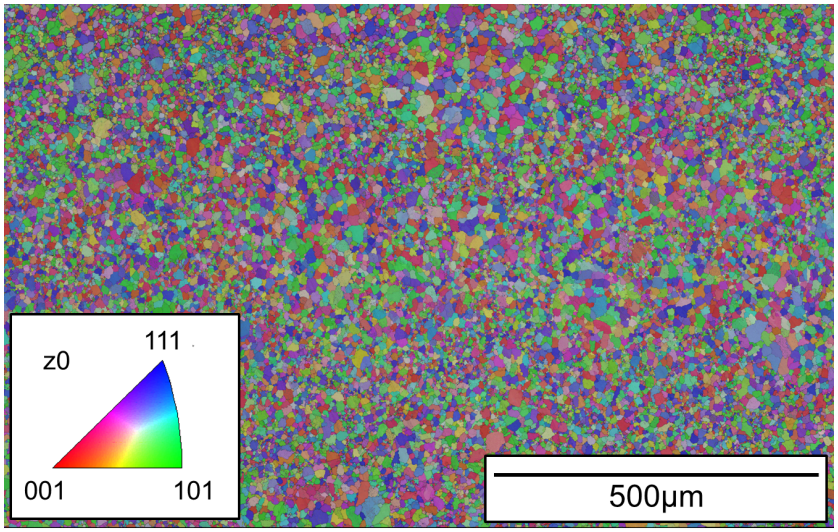

Figure 3.17: Electron backscatter diffraction micrograph of as-HIP material showing the orientation of grain across the samples using standard IPF (Inverse pole figure) colourings.

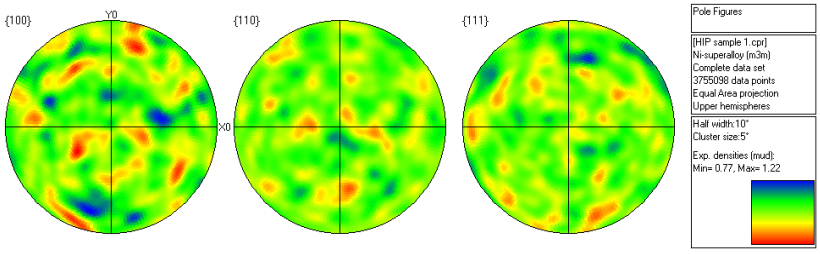

Figure 3.18: Pole figure plot extracted from the EBSD map shown in Figure 3.17, showing multiple of uniform density values ranging from 0.77 to 1.22.

3.7 Summary

The HIP processing of the feedstock 131072 powder resulted in a billet of fully dense material with a highly uniform grain size and precipitate morphology. The produced billet was therefore suitable for use in small scale to determine the effect of varying processing parameters on the microstructure. This would then allow the forging to be up-scaled to a suitable size in order to produce forged billet suitable for machining trials.

The schematic shown in Figure 3.7 shows that although 7 large billets and 6 smaller billets were able to be extracted from the as HIP billet, a large amount of material surrounding the extracted material remained leading to

a large amount of wastage. This practice is undesirable given the cost of processing which scale with the dimensions of the HIP can as well as the cost of the powder. However, due to the nature of the diffusion of the can material as well as the non uniform shrinkage during consolidation, multiple processing steps are required before subsequent processes can be performed. Considering that reducing the cost of machining trials was a key industrial driver for the work, an alternative way of producing consolidating metal powder was considered. Chapter 4 introduces the technique and its application to produce material for machinability trials via an alternative production route.

Chapter 4

Exploration of Field Assisted Sintering for Nickel Superalloys

4.1 Introduction to the FAST Technique

Field assisted sintering technology (FAST) is capable of producing solid billet materials from an input powder feedstock by using electrical current and mechanical load to drive a solid state sintering process. A typical FAST furnace is shown in Figure 4.1. The powder to be sintered is loaded into a graphite die set which is lined with graphite foil to prevent bonding between the powder and the die set during sintering. The die set is then placed between two graphite punches and loaded into a pressure vessel. The pressure vessel is evacuated and a hydraulic ram is used to apply a uni-axial load which is transferred to the powder within the die set. Pulsed DC current is then applied to heat the powder feedstock via resistive heating mechanisms. An infra-red pyrometer is used to measure the temperature close to the powder feedstock during sintering and the input electrical powder is modulated to achieve a fixed temperature profile during sintering. A graphite insulating jacket is used to reduce radiative heat loses from the exterior of the die set. Once the prescribed sintering cycle has been performed, typically involving a dwell at a fixed temperature and load, the graphite die is removed from the pressure vessel and the sintered material is removed from the die set. The FAST process offers several advantages over the HIP technique, including higher achievable heating rates and uni-axial shrinkage due to the constrained diameter of the graphite die set. Compared with the indirect heating method used in the HIP process, the resistive heating mechanism used in the FAST process offers cost savings due to higher efficiencies. The use of the FAST process for the sintering of nickel superalloy powders is relatively unexplored

in literature and may offer a method to produce such materials with lower lead times and costs. The FAST process was therefore employed as a tool for producing material for machining trials in parallel with the HIP+forge route.

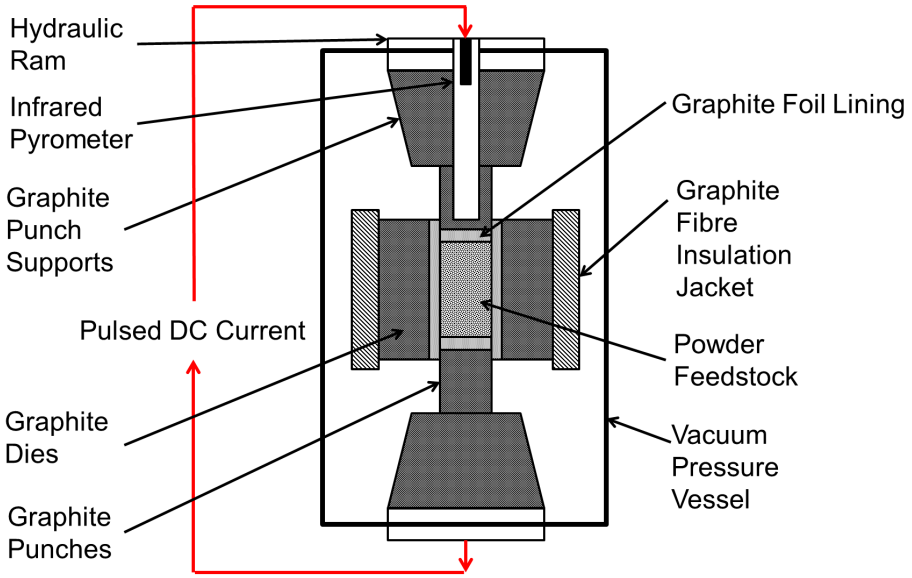

Figure 4.1: Diagram showing the typical layout of a field assisted sintering (FAST) furnace.

A range of terms are used to describe Field Assisted Sintering Technology (FAST) in the literature. In a review of the technology by Orrú et al [82], terminology such as spark plasma sintering (SPS), pulsed electric current sintering (PECS), pulse discharge sintering (PDS) are commonly used for the technique. Orrú et al [82] summarises all these process terms as resistive sintering techniques, however the name field assisted sintering technology or FAST is used by many of the machine manufacturers and is the authors preferred description of the technique.

The temperature distributions seen during field assisted sintering have been found to be related to the conductivity of the powder charge. The modelling techniques used by Munoz et al [83] show that the temperature profile is more uniform if the powder charge is conductive, compared to non-conductive powder feedstock. This is likely to be due to a greater level of homogeneity in the current density, between the powder charge and conductive die arrangement, leading to an even distribution of resistive heating. It has been found by Minier [84], that the electrical power required for constant sintering conditions depended on the dimensions of the die and sample ar-

rangement. It was found that for conductive powders the die volume must remain constant in order to achieve a repeatable microstructure. The ratio of the volume of die to powder was required to be constant to produce microstructures for insulating powders. In the modelling work of Vanmeensel et al [85] the temperature distribution is more homogeneous during the field assisted sintering of non-conductive ZrO_2 material, as all the current flows through the die materials, resulting in a reduction in the radiative heat loses from the die surfaces. This means more heat is transferred to the outer radius of the powder charge, leading to a more homogeneous temperature distribution, when compared to a conductive TiN powder charge. In similar work by Rathel [86], conductive tungsten carbide powder was sintered alongside non-conductive silicon nitride powder. The conductive material was found to be cooler in the exterior region of the die than the central region during sintering. The opposite was found to be true for the non-conductive material. This behaviour is in agreement the work of Vanmeensel et al [85], however the conclusions by Rathel [86] are contradictory in the sense that the conductive material exhibited a more homogeneous temperature distribution during sintering. Both studies agree that the electrical and thermal properties of the material being sintered have a profound effect on the temperature distribution. In the work of Rathel [86], idealised modelling techniques were used to further conclude that the conductive tungsten carbide is subjected to a more homogeneous temperature distribution during sintering, than the non-conductive silicon nitride powder. It is also stated that the use of a thermal shield, such as graphite felt, is essential to reduce radiative heat loses from the exterior of the mould, exacerbating thermal gradients across the powder charge. Voisin et al [87] examined the consolidation of a TiAl alloy applying FAST, using three separate FAST furnaces. The temperature control during the process was evaluated by exploiting the phase transformation. It was also demonstrated that a complex shape could be produced without porosity through the varying thicknesses, with adequate control of the temperature during sintering.

The applicability of the FAST method for producing more complex shapes, faces challenges due to the uni-axial nature of the applied load, which increases the densification of the powder charge. Two recent publications highlight the issues surrounding the production of complex shapes, presented in [88] and [89]. Maniére et al [88] examined FAST in order to provide the input data required for the implementation of the model of sintering proposed by Olevsky [90]. It was demonstrated that the non-uniform thickness can inhibit punch motion in thicker sections, leading to a lower density in those regions. In order to counteract this effect, a follow up study demonstrated that a sacrificial powder ring could be used to promote equal shrinkage in the

thinner sections, leading to uniform densification through all thickness of the complex part [8]. This effort lead to high uniform density throughout the alumina part, with a homogeneous microstructure. Maniére et al [89] are honest in their assessment of this method with regard to material wastage through the sacrificial powder ring. However, such work demonstrates the appetite to develop the technique to a point at which it can be used to produce near net shape components for production purposes.

The application of FAST to aerospace nickel superalloys has received little attention; however, work regarding the sintering of elemental nickel powders has been produced. Minier et al [84] proved that elemental nickel powder can be used to produce high density nickel compacts with relatively homogeneous microstructures. In the work of Tingaud et al [91], a bimodal nickel powder was sintered using FAST. A nano-scale powder was mixed with a micro scale powder in the ratio of 45:55 by percentage volume. Examination of the post consolidated material revealed a retainment of the bimodal grain structure. It was found that the regions with a large volume of ultra-fine grains contained porosity, which Tingaud et al [91] relate to the presence of NiO on the surface of the nanoscale powder, preventing incomplete bonding in these regions.

High performance nickel superalloys are commonly produced via powder metallurgy processing routes, where controlled pre-alloyed powder is consolidated. Hot isostatic pressing (HIP) followed by extensive forging, extrusion and heat treatment is typically used in order to produce favourable microstructures in the post consolidated material. Powder metallurgy processing of nickel superalloys is beneficial, as it reduces the risk of microsegregation and can produce a fine grain structure, using fewer processing steps. In this work the use of FAST, is explored as an alternative solid-state process for consolidating aerospace grade nickel superalloy powder.

4.2 Methodology

4.2.1 Consolidation of 131072 powder via Field Assisted Sintering

Powder pre-compacts were produced by filling a graphite die arrangement with 26 g of the 131072 powder described in section 3.3. The mass of powder was selected in order to produce samples 20 mm in diameter and 10 mm in thickness. All surfaces of the graphite die were lined with graphite foil to aid conduction and to prevent powder from bonding to the tooling. Once assembled, all preforms were subjected to a cold compaction pressure of approximately 20 MPa, before being loaded into the FAST furnace. FAST

consolidation was performed using a FCT Systeme Type HP D 25 field assisted sintering platform at the University of Sheffield. A parametric study was conducted to determine the effect of sintering load, dwell time and dwell temperature, with a full list of parameters used for consolidation listed in Table 4.1. The sintering dwell time at temperature, sintering temperature and applied load were varied in order to assess the impact on the microstructure of the consolidated material. The typical FAST cycle used in this study consists of the following stages;

1. Application of unmodulated high electrical power to increase the temperature of the sample to 400°C, at which point the pyrometer starts to register the temperature of the material. A load of 5 kN (15.9 MPa) is applied during this time. The pulsed DC current is applied with pulse timings of 15 ms on, 5ms off using a square waveform.

2. Once the pyrometer registers a temperature above 400°C, the electrical power output is moderated to achieve a heating rate of approximately 300°C.min^{-1}.

3. Once the temperature reaches approximately 600°C, the load is increased at a rate of approximately 8 kN.s^{-1} (25.5 MPa.min^{-1}), until the set-point load is reached.

4. Once the temperature reaches 100°C below the setpoint temperature, the power output is again modulated to reduce the heating rate to approximately 90°C.min^{-1}. This is chosen to reduce the overshoot above the set-point temperature, and was measured to be 7°C in the worst case scenario.

5. The sample is then dwelled with the prescribed load and temperature for the chosen time, again power is modulated to maintain the set point temperature.

6. Once the dwell time has ended, the sample is cooled by flooding the furnace with room temperature argon gas, which results in an average cooling rate of approximately 425°C.min^{-1}.

7. Once the temperature of the sample drops below 600°C, the load is reduced at a rate of 1 kN.s^{-1} (3.2 MPa.min^{-1}), until only a load of 5 kN remains. During this time the sample cools to room temperature.

8. The furnace is then opened, the 5 kN load removed, and the sample is extracted and the remains of the graphite spacers are remove using abrasive grit blasting.

Table 4.1: List of FAST runs performed using nickel-based superalloy 131072 powder.

Run	Dwell Temperature (°C)	Dwell Time (mins)	Sintering pressure (MPa)
1	1100	60	50.9
2	1100	10	50.9
3	1100	240	41.4
4	1100	120	41.4
5	1100	60	41.4
6	1100	10	41.4
7	1150	10	41.4
8	1150	60	41.4

4.2.2 Characterisation of as-FAST 131072 Material

The vickers micro-hardness of all samples was measured using a Struers Durascan automatic hardness indentation unit using a load of 0.5kg. Ten distributed hardness measurements were collected per sample. The densities of all samples were measured using the Archimedes technique using a Mettler-Toledo MS-DNY-54 Density balance. Ten measurements of density were taken for each sample. All samples were sectioned axially to reveal the microstructure in the centre of the sample to verify the homogeneity of the sample in the direction of the applied current and load. All samples were prepared using standard metallographic techniques for light and scanning electron microscopy. Two etchants were employed to reveal the various microstructural features present in nickel superalloys. The first etchant selected was Kallings waterless reagent which is comprised of 50 ml HCl, 50 ml ethanol and 2.5 g of copper (II) chloride, which is used the reveal the grain boundaries and γ' precipitates. The second etchant used was 10% phosphoric acid, which was used under electrolytic conditions with a 5 V potential difference; this etchant embosses γ' precipitates by removing the γ matrix to allow high resolution imaging of precipitates. Micrographs were collected using a Nikon light microscope and electron micrographs were collected using a FEI inspect F scanning electron microscope.

4.2.3 Comparisons with as-HIP Material

The characterisation performed on the as FAST consolidated material was compared directly with the material produced in Chapter 3. The characterisation performed in section 4.2.2 was performed equally from material from the as HIP billet including EBSD, microscopy, hardness and density

measurements. Direct comparisons were made with regards to the material properties, grain structure and precipitate characteristics.

4.3 Results

An example of the sintering temperature and load applied profile is shown in Figure 4.3, the data shown is for a sub-solvus dwell temperature and is listed as run 2 in Table 2. The temperature ramp profile can be seen to include the high heating rate of 300°C.min^{-1} followed by a decrease in temperature ramp rate to the slower 90°C.min^{-1}. Figure 4.3 shows the temperature exceeds the pre-programmed dwell temperature by approximately 7°C, this was deemed to be acceptable given the γ' solvus temperature is not exceeded for the sub-solvus dwell runs.

An example of a sample produced post FAST is shown in Figure 4.2, the bonded graphite foils were removed prior to sectioning and metallographic preparation. The samples produced exhibited a perfect cylindrical shape, with complete die filling and no surface breaking porosity visible on the surface of the material. No loose powder was observed when the sintered material was removed from the die chamber. Light micrographs of the near surface regions of a typical sample after metallographic preparation and etching are shown in Figure 4.4. In Figure 4.4a, a near surface diffusion region was observed for all samples where the powder is in contact with the graphite foils, as indicated by arrow 1. Arrow 2 indicates a residual porosity post sintering. In both Figure 4.4a and 4.4b, circular regions can be seen which corresponds to prior particle grain morphologies.

Figure 4.2: Photograph of a 20mm FAST specimen produced nickel-based superalloy billet post sintering.

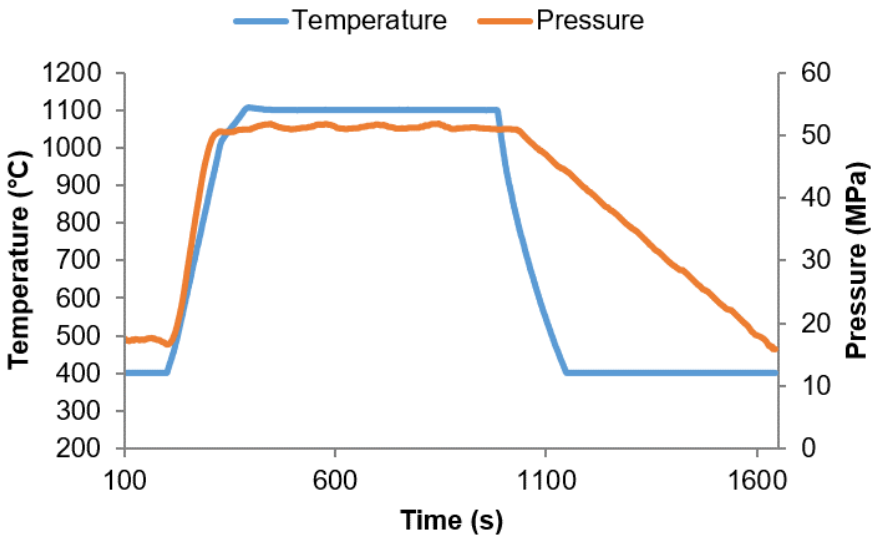

Figure 4.3: The FAST temperature and applied pressure profiles vs time, captured during run 2 as described in Table 4.1.

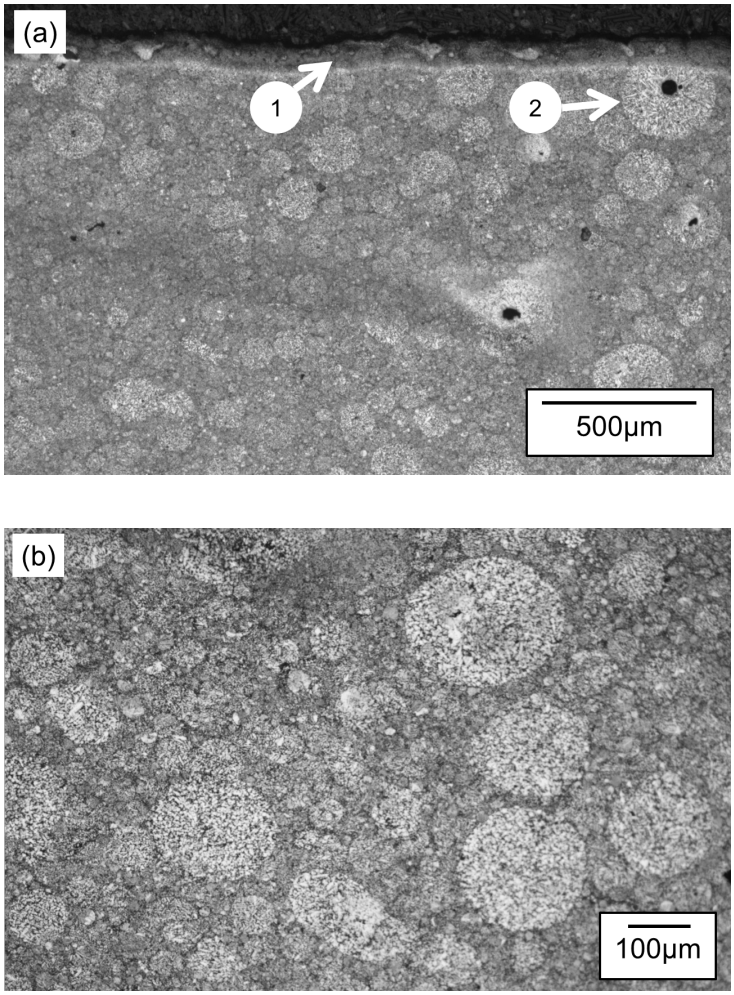

Figure 4.4: Light micrographs of the post FAST microstructure of run 6, etched using Kalling's reagent. Demonstrating the (a) carbon diffusion, see arrow 1 and retained prior particle microstructure and internal powder porosity, see arrow 2. Retained prior particle microstructure can be seen in (b).

As is apparent in Figure 4.4, the microstructure consists of very fine grains and precipitates, and therefore, the use of scanning electron microscopy was required to fully characterize the post sintered microstructure. Backscattered electron micrographs showing the change in grain morphology for a 60 min (Figure 4.5a) and a 10 min dwell time (Figure 4.5b) are shown for a sintering pressure of 41.4 MPa. Figure 4.5 reveals that irrespective of the sintering time used, a fine grain size is produced with some local inhomogeneity in grain size visible in the microstructure.

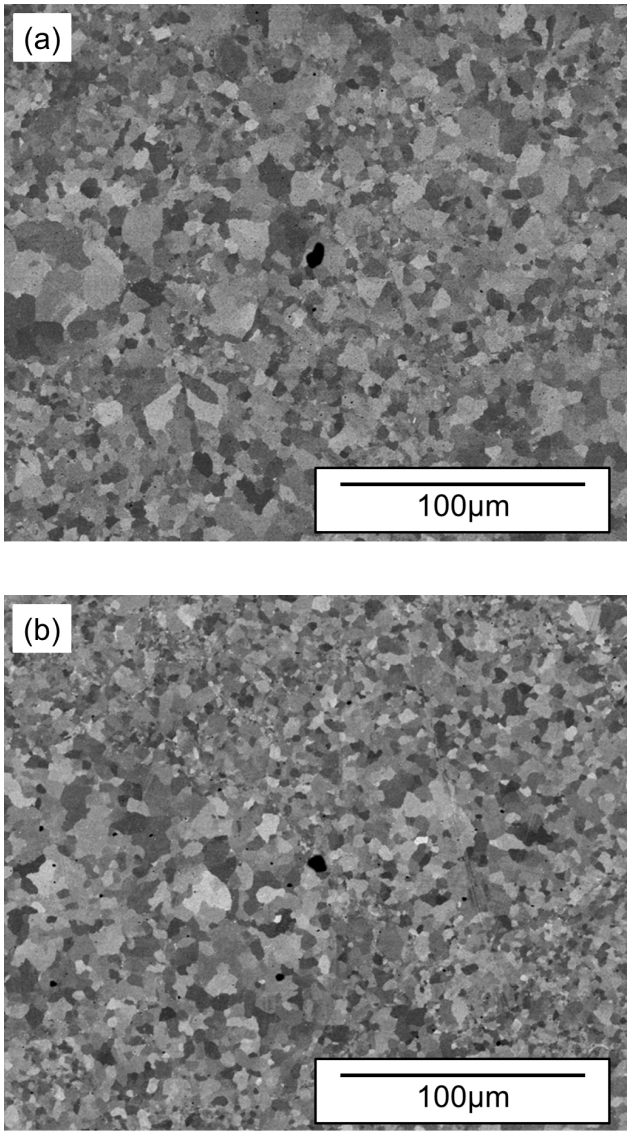

Figure 4.5: Backscattered electron micrographs showing the microstructure produced using 1100°C sub solvus dwell temperature for (a) 60 minute dwell time (run 5) and (b) 10 minute dwell time (run 6).

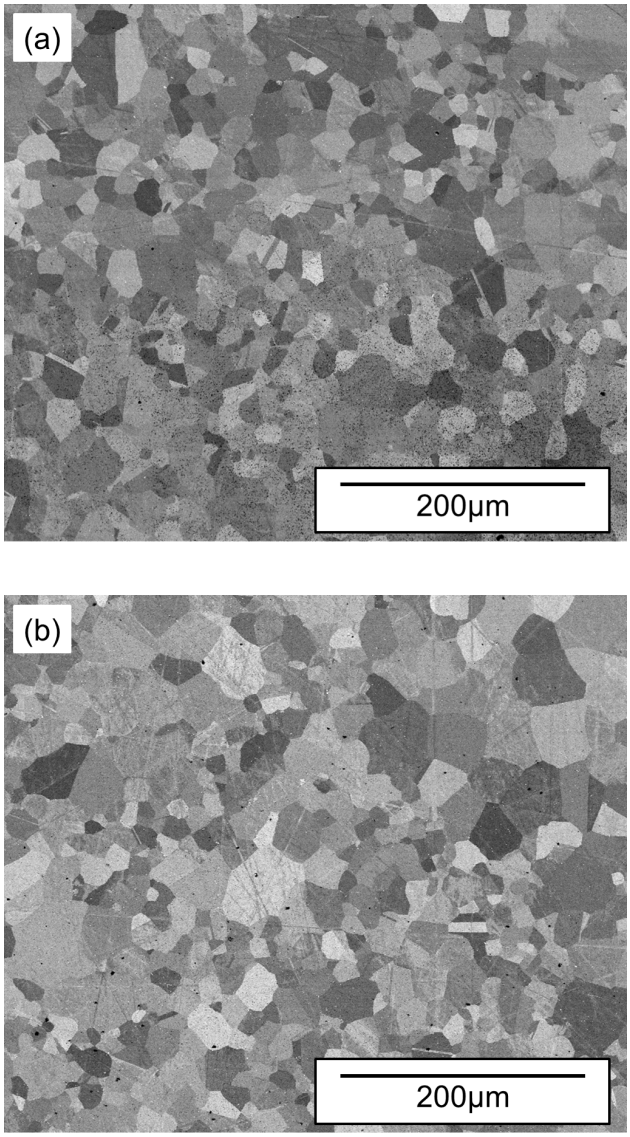

Figure 4.6: Backscattered electron micrographs showing the microstructure produced using 1150°C super solvus dwell temperature for (a) 10 minute dwell time (run 7) and (b) 60 minute dwell time (run 8).

The effect of an increase in dwell temperature beyond the γ' solvus is shown in Figure 4.6. As can be seen for both a 10 min (Figure 4.6a) and a 60 min (Figure 4.6b) dwell time the increase in dwell temperature results in an increased grain size compared to the sub-solvus dwell microstructures shown in Figure 4.5. Examples of γ' morphologies produced after 10 and 60 min

dwell times using a sintering pressure of 41.4 MPa are displayed in Figure 4.7. Visually, It can be seen that both a dwell time of 10 to 60 min results in a multi-modal distribution of γ' precipitates with secondary γ' existing within arrays of fine tertiary γ'. It can be observed that increasing the dwell time from 10 min (Figure 4.7a) to 60 min (Figure 4.7b), appears to result in the increase in the number of secondary γ' precipitates, some evidence of coalescence of precipitates is observed. The samples produced during two dwell times are displayed in Figure 4.8. It can be seen that that the material produced using the longest dwell time of 240 min (Figure 4.8b) still exhibits multi-modal precipitate morphologies. It can be observed that both the 240 min (Figure 4.8b) and 120 min dwell (Figure 4.8a) little change occurs in the general precipitate morphology with respect to dwell time.

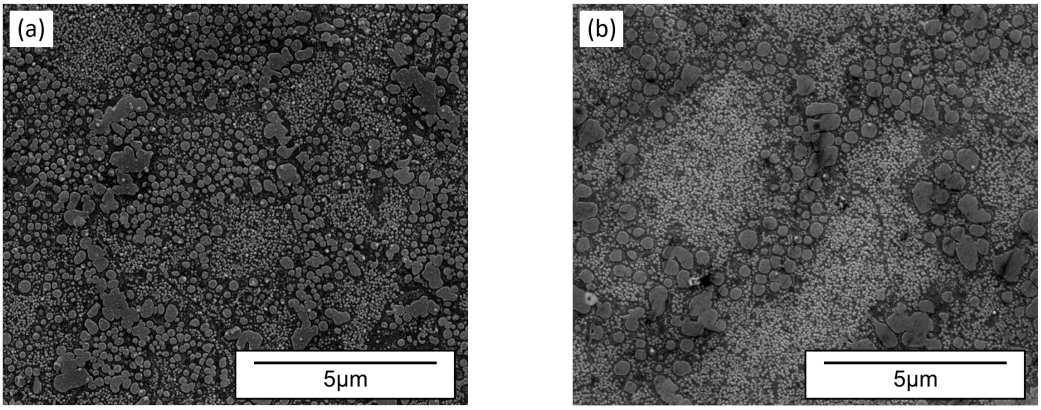

Figure 4.7: Secondary electron micrographs showing the γ' morphologies produced during (a) run 6 with a 10 minute dwell time and (b) run 5 with a 60 minute dwell time. Both samples were produced using sub solvus (1100°C) dwell temperatures and the γ' precipitates were revealed using phosphoric acid etching.

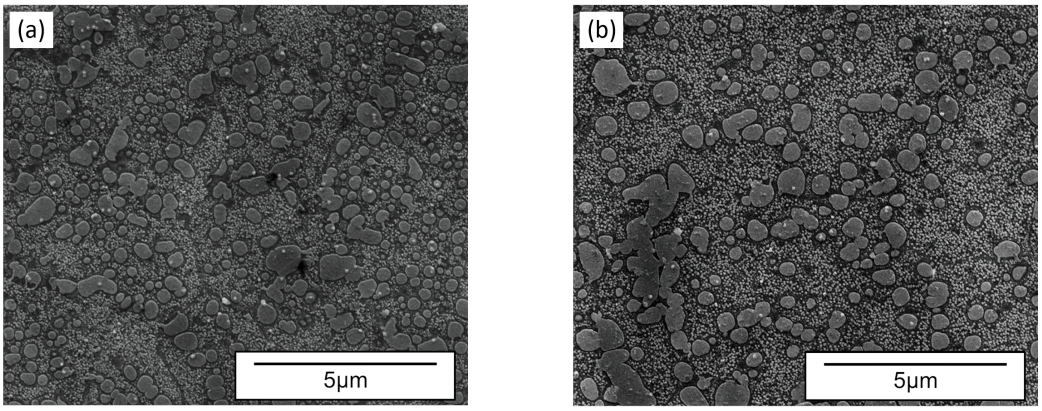

Figure 4.8: Secondary electron micrographs showing the γ' morphologies produced during; (a) run 4 with a 120 minute dwell time and (b) run 3 with a 240 minute dwell time. Both samples were produced using sub solvus (1100°C) dwell temperatures and the γ' precipitates were revealed using phosphoric acid etching.

A comparison between the FAST material produced using a dwell time of 60 min with a 1100°C dwell temperature using a pressure of 41.4 kN (Run 5) with the HIP sample is shown in Figure 4.9. The similarities in grain size can be observed between the two materials, indicating that the FAST method results in similar structures post consolidation.

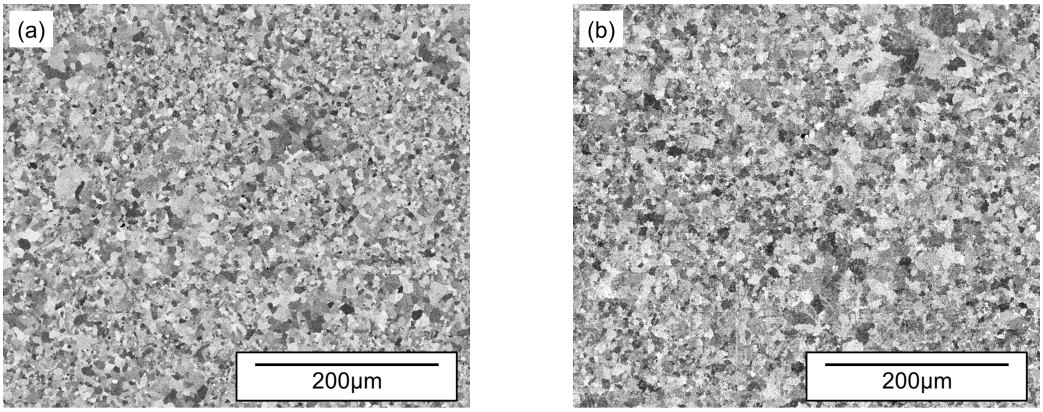

Figure 4.9: Backscattered electron micrographs showing (a) FAST material produced during run 5 using a dwell time of 60 minutes, sintering temperature of 1100°C, sintering pressure of 41.4 MPa and (b) Material produced during sub-solvus (1125°C) HIP consolidation using a dwell time of 350 minutes.

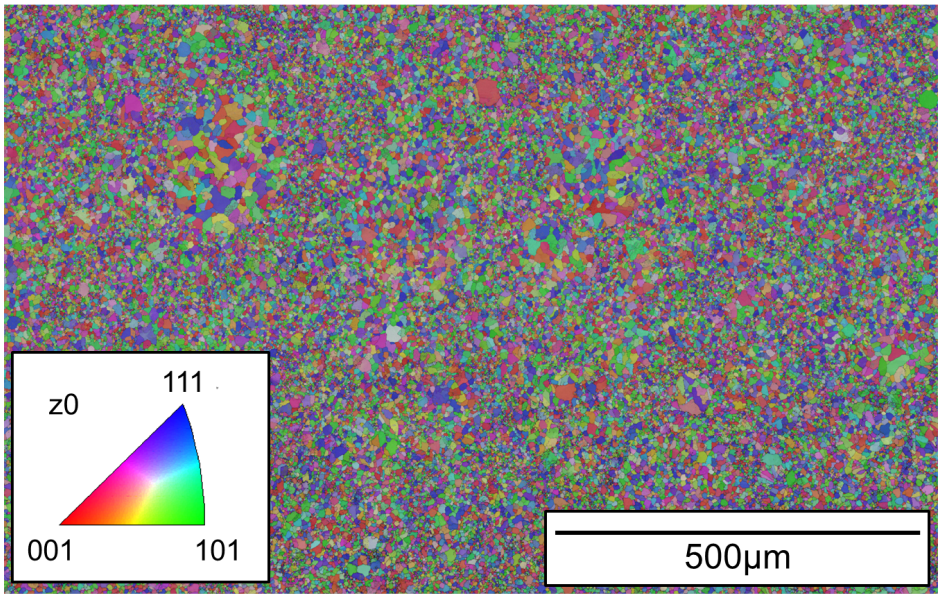

Figure 4.10: EBSD map of FAST produced material produced during run 1, using a dwell time of 60 minutes, a dwell temperature of 1100°C and an applied pressure of 50.9 MPa.

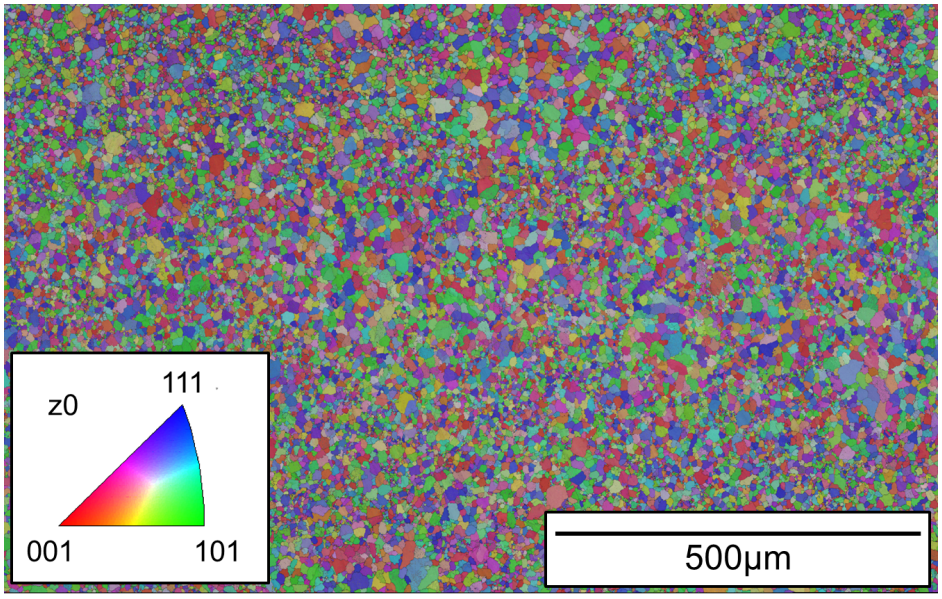

Figure 4.11: EBSD map of HIP produced material produced using GA alloy 131072 powder using a sub-solvus dwell temperature (1125°C) and a dwell time of 350 minutes.

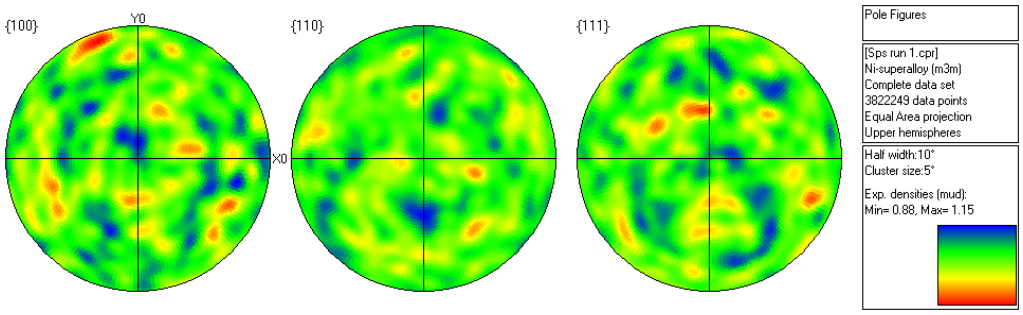

Figure 4.12: Pole density figure for as-FAST 131072 material produced using a dwell temperature of 1100°C and an applied pressure of 50.9 MPa (run 1). Showing multiple of uniform densities values ranging from 0.88-1.15.

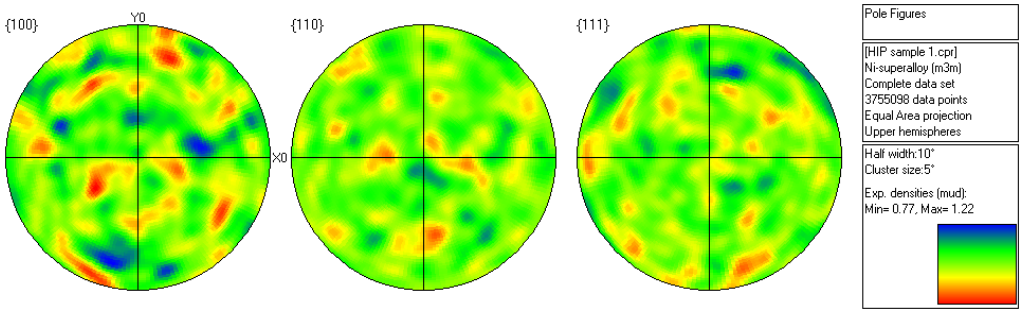

Figure 4.13: Pole density figure of HIP produced material produced using GA alloy 131072 powder using a sub-solvus dwell temperature (1125°C) and a dwell time of 350 minutes.Showing multiple of uniform densities values ranging from 0.77-1.22.

An EBSD map of FAST material produced using a sub-solvus dwell at 1100°C and 41.4 MPa and 60 min dwell time is shown in Figure 4.10, a comparative map for the HIP material is shown in Figure 4.11. The ESBD map for the FAST material (Figure 4.10) reveals some inhomogeneity in grain size, Figure 4.10 also reveals the presence of a circular regions with increased grain size which is indicative of a retainment of the grain structure within particles prior to sintering. This effect is not visible in the HIP material (Figure 4.11). Comparing Figure 4.10 and Figure 4.11, it can be seen that the HIP material possesses a larger grain size in comparison with as FAST, a greater degree of homogeneity is also visible in the HIP material.

From the EBSD maps shown in Figure 4.10 and Figure 4.11, texture was evaluated through the production of pole figures using the multiple of uniform density to highlight dominant crystallographic orientations present in the material. Comparing the texture in the as FAST material (Figure

4.12) and as HIP material (Figure 4.13), it can be seen that neither material possesses strong texture with MUD numbers close to 1 across all orientations.

The precipitate morphologies of FAST material produced using parameters of 60 min at 1100°C using a load of 13 kN (Run 5) and the HIP material is shown in Figure 4.14. As can be seen the FAST material contains a range of precipitates sizes (Figure 4.14a) while the HIP material (Figure 4.14b) has a large density of larger precipitates decorating both the interior of grain and grain boundaries.

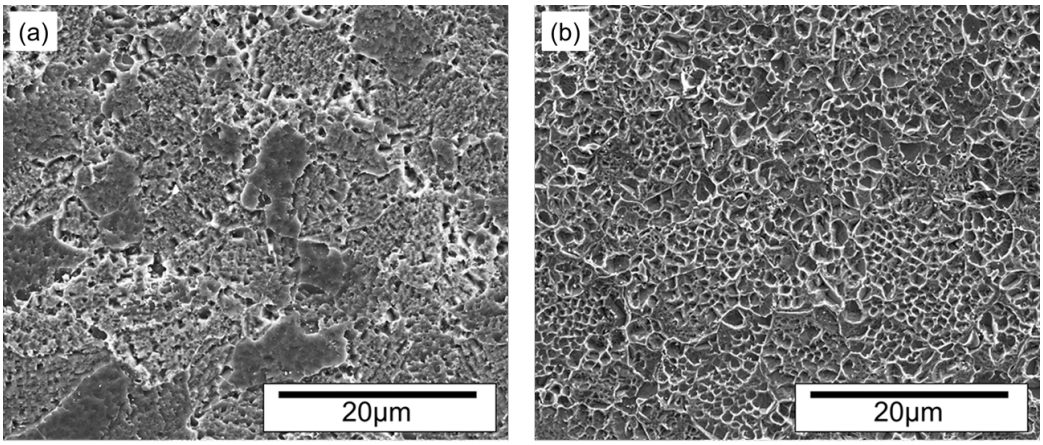

Figure 4.14: Secondary electron micrographs showing a comparison between precipitate morphologies in (a) the as-FAST material produced using a dwell time of 60 minutes, a dwell temperature of 1100°C and a load of 41.4 MPa. Compared with (b) the as-HIP material.

4.3.1 Hardness and Density Measurements

The density measurements captured for change in dwell time and sintering load are shown in Table 4.2. An increase in density was observed when the dwell time was increased from 10 to 60 min, for both the 41.4 MPa and 50.9 MPa sintering pressures. A further increase was observed when the dwell time was increased from 60 to 120 min, for a 41.4 MPa sintering pressure. A further increase in dwell time from 120 to 240 min results in a large drop in density compared to the 120 min dwell time. For a dwell time of 10 minutes, an increase in sintering pressure from 41.4 MPa to 50.9 MPa results in a positive increase in the measured density. Table 4.3 displays the measured density and hardness values for the as HIP material which is nominally considered to be 100% dense after the applied cycle. Using this data as a comparison it can be seen that the minimum relatively density achieved with the FAST process is 98.64% which was produced using a dwell

time of 240 min with a dwell temperature of 1100°C and a sintering pressure of 41.4 MPa. The maximum relative density achieved was 99.4% which was achieved using a dwell time of 120 min using a dwell temperature of 1100°C and a sintering pressure of 41.4 MPa.

Table 4.2: Density Measurements post FAST consolidation with respect to sintering dwell time and applied load, measured using the Archimedes method in water.

	41.4 MPa				50.9 MPa			
	Density ($g.cm^{-3}$)				Density ($g.cm^{-3}$)			
Dwell time (minutes)	Mean	Max.	Min.	Std. Deviation	Mean	Max.	Min.	Std. Deviation
10	8.093	8.101	8.083	0.006	8.130	8.152	8.117	0.012
60	8.126	8.132	8.117	0.005	8.128	8.142	8.106	0.014
120	8.131	8.159	8.091	0.021				
240	8.065	8.079	8.053	0.009				

Table 4.3: Density and Hardness measurements of material produced via the conventional HIP processing of GA alloy RR1000 powder.

HIP material data				
	Mean	Max.	Min.	Std. Deviation
Density ($g.cm^3$)	8.176	8.184	8.156	0.028
Hardness $Hv_{0.5}$	377.1	389	366	7.8

Table 4.4 and Table 4.5 detail the hardness measurements made for the material produced using sub-solvus and super-solvus fast dwell temperatures, respectively. For the samples produced using the sub solvus dwell temperature (Table 4.4) and for a sintering pressure of 41.4 MPa, the hardness value experiences very little change with increasing dwell time. The peak mean value is achieved when a 60 min dwell time is employed, however the experimental scatter prevents any positive correlation between the dwell time and the measured hardness from being achieved. In general for both the 41.4 MPa and 50.9 MPa applied sintering pressures, Table 4.4 shows that reduced dwell times produce higher hardness values. Table 4.5 shows that the hardness values produced when a super-solvus dwell temperature is employed, the hardness is reduced for the two dwell times compared to the sub-solvus data. Comparing with the HIP material hardness data shown in Table 4.5 it can be seen that all samples produced using the FAST process registered a higher hardness than the HIP process for the same powder feedstock.

Table 4.4: Vickers Hardness measurements post FAST consolidation for samples produced using a dwell temperature of 1100°C, captured as a function of load and sintering dwell time.

	41.4 MPa				50.9 MPa			
	$Hv_{0.5}$				$Hv_{0.5}$			
Dwell time (minutes)	Mean	Max.	Min.	Std. Deviation	Mean	Max.	Min.	Std. Deviation
10	448	466	420	12.5	455	463	440	6.35
60	451	460	442	5.46	448	458	432	7.17
120	444	452	435	5.54				
240	434	442	427	5.31				

Table 4.5: Vickers Hardness measurements post FAST consolidation for samples produced using a dwell temperature of 1150°C, captured as a function of load and sintering dwell time.

	41.4 MPa			
	$Hv_{0.5}$			
Dwell time (minutes)	Mean	Max.	Min.	Std. Deviation
10	429.9	445	418	8.13
60	430.9	440	420	6.66

4.4 Discussion

4.4.1 Microstructural Response to FAST Sintering

The visual characteristics of a post FAST sample shown in Figure 4.2 corroborate with the density data displayed in Table 4.2, demonstrating that the FAST process is capable of producing highly dense compacts using the nickel superalloy powder feedstock. The microstructure in Figure 4.4 reveals that the post sintered material possesses two characteristics; Figure 4.4a shows that the perimeter of the sample contains a prevalent diffusion region, in which carbon from the graphite foil die lining ingresses into the consolidated nickel superalloy material. This is unsurprising given the relatively high diffusion rate of carbon in nickel and the extended dwell periods shown. This carbon diffusion leads to the formation of carbides with some of the alloy constituents of the powder feedstock, in particular titanium, tantalum and hafnium. Although these carbides are likely to have an effect on the material properties within this diffusion region, the depth of the diffusion region does

not extend above 150-200 μm for all samples produced. Aerospace nickel superalloy components generally have greater than 500 μm removed from the surface of the forged as-HIP product via machining processes. Both Figure 4.4a and Figure 4.4b reveal the presence of circular regions within the microstructure with similar grain sizes. This is likely a retainment of the prior particle grain morphologies, given that these circular regions are within the length scales of the input powder particle size. This effect has been noted in the work of Tingaud et al [91]. Another feature notable in Figure 4.4b is the presence of porosity within the prior particle grain substructures, this is unsurprising given the level of porosity within the feedstock powder visible in Figure 3.6. During the FAST sintering process, the diffusion mechanisms driven by the elevated temperature and uni-axial load, drive the reduction in porosity within the powder feedstock. However the uni-axial load used in this study is likely to be insufficient to drive the closure of internal gas pores within the feedstock powder. The limiting factor regarding the application of uni-axial load is the strength of the graphite die set. If an alternative die set material is used, such as steel, the uni-axial load may be increased however the resistive heating characteristics are likely to change. This inability to close large internal powder porosity is likely to be the cause of the disparity in density between the FAST material (Table 4.2) and the HIP material (Table 4.3) as the isostatic load used in the HIP process (102 MPa) is much higher than the uni-axial 41.4 MPa-50.9 MPa used in the FAST process.

The grain structure of the material produced using sub-solvus dwell temperatures for a 10 min and 60 min dwell time are displayed in Figure 4.5. It can be seen that the grain size does not change dramatically when the dwell time is increased from 10 min (Figure 4.5a) to 60 min (Figure 4.5b). This is to be expected as the γ' solvus of the material is not exceeded and the γ' precipitates as well as the carbide phases will effectively pin the grain boundaries preventing significant grain growth. For both the 10 min and 60 min dwell time, the grain size is heterogeneous, which is thought to be due to the retainment of the heterogeneous prior particle grain morphologies. When the dwell temperature is increased to 1150°C, the grain size increases for both the 10 min (Figure 4.6a) and 60 min dwell time (Figure 4.6b). At 1150°C the γ' precipitates go into solution during the heat up and dwell period, eliminating the grain pinning effect and enabling grain growth. The occurrence of this grain growth when the dwell temperature is 1150°C and lack thereof when at 1100°C provides evidence of excellent temperature control during the FAST process. The precipitate morphologies of materials produced using a range of dwell times are shown in Figure 4.7 and Figure 4.8. Comparing the precipitate morphologies produced using shorter dwell times of 10 minutes (Figure 4.7a) and 60 minutes (Figure 4.7b) it can be seen

that both materials possess multi-modal precipitate size distributions that are mostly spherical in nature. According to Jackson and Reed [24], these precipitates can be classified as secondary and tertiary due to their size distributions and intra-granular nature. The cooling rates measured using the pyrometer post FAST recorded an average cooling rate of 276.42 $K.min^{-1}$, by way of comparison, this cooling rate is beyond that quoted for an industrial oil quench . Jackson and Reed [24] found that higher cooling rates resulted in low coarsening of the secondary γ', this can also be seen in Figure 4.7a and Figure 4.7b. With regards to the material produced with increased dwell times of 120 and 240 min (Figure 4.8a and Figure 4.8b, respectively) it can be seen that only subtle changes in precipitates morphologies are visible. The application of extended dwell times during solution heat treatments, results in coarsening in the tertiary γ' precipitates while no such coarsening occurs in secondary precipitates as discussed by Jackson and Reed [24]. No such coarsening of tertiary precipitates can be observed between Figure 4.7 and Figure 4.8, however higher resolution TEM in further work would provide a full quantitative analysis of the secondary and tertiary precipitates and the small variations that may occur due to increased dwell time.

4.4.2 Comparison of FAST and HIP Processing

The grain size of the FAST material is comparable to the HIP material, as shown in Figure 4.9, this confirms that both the HIP and FAST materials were consolidated below the solvus temperature, as indicated by the relatively fine grain size. The comparison is further reinforced by EBSD maps produced for the FAST and HIP samples shown in Figures 4.10 and 4.11, respectively. It can be seen that the grain size in both materials is comparable but with a slightly larger grain size observed in the HIP material. This is hypothesized to be related to the extended dwell period and slightly higher processing temperature seen during consolidation of the HIP material. Figure 3.4 shows that the rapid onset of γ' dissolution starts to occur at approximately 1050-1075°C. Therefore, when the temperature of the material increases from 1100-1125°C reduction in γ' volume fraction occurs, enabling grain boundary migration. The EBSD data shown in Figure 4.10 also confirms the presence of circular grain clusters with similar sizes as shown during light microscopy in Figure 4.4. It is highly likely that these clusters are retained prior particle grain morphologies. The Carpenter nickel superalloy 131072 powder used in this study had a very large size distribution. It can be inferred that the larger particles will have experienced slower cooling rates due to a smaller surface area to volume ratio as the powder droplet solidifies. This is likely to result in larger particles with larger grain sizes. It is also

likely that this distribution of grain sizes is retained during FAST consolidation due to the pinning effect provided by both γ' and carbide precipitates. The texture comparison via MUD numbers shown in Figures 4.12 and 4.13 reveals very little evidence of strong texture in the material, which is to be expected in the HIP material due to the isostatic conditions. During FAST processing the load is applied uni-axially however this does not generate a strong texture component when the material is viewed normal to the principle loading direction. This suggests that the FAST is neither imparting deformation nor grain growth in a particular direction. This apparent lack of strong texture in the HIP material is beneficial in terms of the use of FAST material in service. A comparison of the precipitate morphologies between the FAST and HIP material (Figure 4.14) reveals both larger and more dense regions of larger secondary and primary precipitates in the HIP material compared to the FAST material. The precipitates in the HIP material also appear to be more angular than those observed in the FAST material (shown in more detail in Figures 4.7 and 4.8). This is a consequence of both the time at elevated temperature and the cooling rate employed, as longer cooling times facilitate the coarsening of precipitates. The average cooling rate of the HIP material was measured to be two orders of magnitudes lower than that of the FAST material as shown in Figure 3.8.

4.4.3 The Effect of FAST Processing on Density and Hardness

Table 4.2 shows that for a fixed sintering load of 41.4 MPa, the density is improved with increasing dwell time, with the peak density being produced using a dwell time of 120 min with a relative density of 99.45% when compared with the HIP material (Table 4.3). The minimum relative density was produced when the dwell time was increased to 240 minutes, with a value of 98.64%. The reason for this result is not fully understood but may be attributed to the expansion of entrapped gas from the original powder porosity seen in Figure 3.6. At the higher temperature, the partial pressure of the gas will increase. If the sintering load applied is insufficient, the gas pore will expand. This is the advantage of the conventional HIP process, where higher isostatic pressures are able to close gas pores and hence why the density measured for the HIP material (Table 4.2) is higher than that produced for all FAST conditions. Increasing the sintering pressure to 50.9 MPa, leads to an increase in density for shorter dwell times, particularly when a 10 minute dwell time is employed. When a 60 minute dwell time is employed the benefit is more modest. The increase in sintering load will produce enhanced particle

rearrangement during the early stages of sintering, which will manifest in an increase in densification rates, pore closure will also be improved. For the sub-solvus processing conditions, increased dwell times were found to have a negligible effect on the hardness, the peak hardness was produced using a dwell time of 60 min for a sintering load 41.4 MPa. Shorter dwell times resulted in higher hardness values as a result of γ' coarsening at longer dwell times. Increasing the sintering load to 50.9 MPa resulted in little change in the measured hardness for a 10 and 60 min dwell. The sample produced using the 240 min dwell time, also exhibited the lowest density. Increased porosity will result in lower hardness values. All hardness values measured for the FAST material exceeded those for the HIP material. Comparison of EBSD maps from samples from the two processes shows that the FAST process produces a smaller grain size, which according to the Hall-Petch relationship will produce higher hardness values. However, the comparison of γ' structures shown in Figure 4.14 shows that the γ' precipitates are coarser in the HIP processed material. Mitchell et al [92] demonstrated that coarser precipitates result in lower hardness values. The hardness data measured for the FAST and HIP material is hypothesized to be an example of this effect. Hardness measurements for the material produced using super-solvus FAST processing conditions (Table 4.5) shows a modest decrease compared with those for materials produced sub-solvus (Table 4.4), despite the large increase in grain size (comparing Figures 4.5 and 4.6). The (γ') precipitate structure is likely to play a dominant role as they are fully dissolved during FAST consolidation and re-precipitate during cooling, providing a fine network of tertiary precipitates at faster cooling rates. In the work of Radis et al [93] the precipitate mechanism is described and it is shown that faster cooling rates provide finer precipitates when cooling from above the solvus temperature. This correlates with the work of Mitchell et al [92] who suggested that faster cooling rates result in higher strengthening effects from the precipitates. In the sub-solvus condition, larger precipitates will remain and coarsen during the dwell period, providing less of a strength benefit in the final product. From the study in this paper, the dominant (γ') precipitate strengthening effects clearly offset the reduction in hardness associated with grain growth, leading to the modest reduction seen between the sub-solvus and super-solvus conditions.

4.4.4 Summary of Findings From Small Scale FAST Trials

- Field-assisted sintering technology (FAST) has been demonstrated to be a competitive process to HIP for consolidating advanced nickel superalloy powders. The key advantages being the reduction in processing time and no can being required.
- Density and hardness measurements have confirmed that highly dense material (with densities of 99.45% relative to a HIP baseline material) can be produced using a dwell time of 60 min and a sintering load of 13 kN (41 MPa) for a sub-solvus sintering dwell temperature of 1100°C.
- Microstructural examination revealed circular regions with differing grain sizes post FAST consolidation, which were observed both with light microscopy and EBSD. This strongly indicates that the prior powder particle grain morphologies were retained.
- Super-solvus dwell conditions during FAST sintering resulted in a large increase in grain size compared to sub-solvus conditions consistent with the removal of the pinning effect provided by the γ' precipitates.
- FAST processing produces materials with higher hardness values compared to HIP process materials. This is likely due to the fine network of γ' precipitates generated during the faster cooling rates after the FAST process.

4.5 Up-scaling of the FAST Technique to Large Scale Billets

The small scale FAST trials performed revealed that the FAST process is capable of producing highly dense material with microstructures comparable with the HIP process, with a network of γ' precipitates. This description alone "defines" the FAST produced material as a modern nickel superalloy. The technique was therefore employed to produce material for machining trials to examine the relationship between the microstructure and induced subsurface damage. To produce this material the FAST process was up-scaled to produce billets with a diameter of 125 mm prior to consolidation with a thickness of approximately 25 mm. For these up-scaled trials, a secondary powder source was available. This powder represented the proprietary alloy RR1000 the chemistry of which is shown in Table 3.2. In comparison with the

131072 powder, the RR1000 powder is more spherical in morphology and is sieved to a maximum powder size of 53 μm. At this powder size the frequency of internal powder porosity is considerably lower than that observed in the 131072 powder.

Two temperatures were chosen for the consolidation, these were 1100°C and 1150°C which represent sub-solvus and super-solvus consolidation temperatures, as described previously. Each of these temperatures were used to consolidate both of the chosen powders in order to produce a finer grain and coarser grain billet from the two powders through varying the consolidation temperature. An understanding could therefore be gained regarding the effect on the resultant grain size and also the effect on varying powder feedstock both in terms of the post consolidated microstructure and also the response of the billets to machining.

To produce the billets, a large scale FAST furnace based at Kennametal in Newport South Wales was used. The furnace has sufficient electrical power and uni-axial pressure to sinter powders in dies up to 250 mm. For this comparison a 125 mm die set was chosen in order to produce billet suitable for machining trials while minimising the usage of the limited powder available.

The process of sintering is as described previous for the small scale trials, the only exception is the inclusion of a carbon fibre support ring which fits around the outer diameter of the outer cylindrical die set. The purpose of this ring is to minimise radiative heat losses during sintering and also provide additional strength to the die while maintaining conductivity. Approximately 2.5 kg of powder is loaded into the die and a uni-axial cold compaction load equating to 20 MPa is applied for approximately 5 mins. After this process the pre-compact is transferred to the FAST furnace and sintering begins.

Similar to the method used in the small scale trials, the powder compacts were first heated rapidly until the pyrometer started recording the temperature at 449°C. For the billets sintered at 1100°C the billet was heated rapidly until the temperature of 1050°C was reached at which the heating rate was reduced, see Table 4.6. This approach was taken to minimise temperature overshoot to prevent the material exceeding the γ' solvus leading to rapid grain growth. This was particularly important considering that limited powder was available for sintering, it is possible that the heating rate could have been maintained at the highest setting however insufficient material was available to test this approach. For the material sintered at 1150°C, the heating rate was reduced to a lesser degree once the material reached 1100°C as the desire was to achieve super-solvus conditions. All larger billets were processed using a dwell time of 2 hours, the small scale trials showed that the billet was fully consolidated after a dwell time of 1 hour but the effect of up scaling on the process could not be determined so a conservative dwell

time of 2 hours was chosen. A sintering pressure of approximately 35 MPa was applied during sintering. Initially sintering loads of 50kN were applied however it was found the expensive die set was prone to cracking, so this was reduced. This is another justification for increasing the sintering dwell time in order to counteract the expected increase in porosity associated with decreased sintering pressure. Once the sintering cycle was complete, the FAST chamber was purged with Argon and the billet allowed to cool, due the larger diameter of the billet, the cooling rate employed was much slower compare to the small scale cycles. A full list of the billets produced and the pyrometer measured heating and cooling rates when the temperature was above 449°C are shown in Table 4.6. An example of the temperature and load cycles for the sub-solvus and super-solvus consolidations are shown in Figure 4.15 and Figure 4.16.

Table 4.6: Average heating and cooling rates of the FAST produced intermediate scale billets.

Billet	Initial heating rate (°C.min^{-1})	Slow heating rate (°C.min^{-1})	Cooling rate (°C.min^{-1})
RR1000/1100°C	25.08	9.10	8.81
RR1000/1150°C	25.11	19.75	9.23
131072/1100°C	25.10	9.45	9.35
131072/1150°C	25.07	19.74	9.56

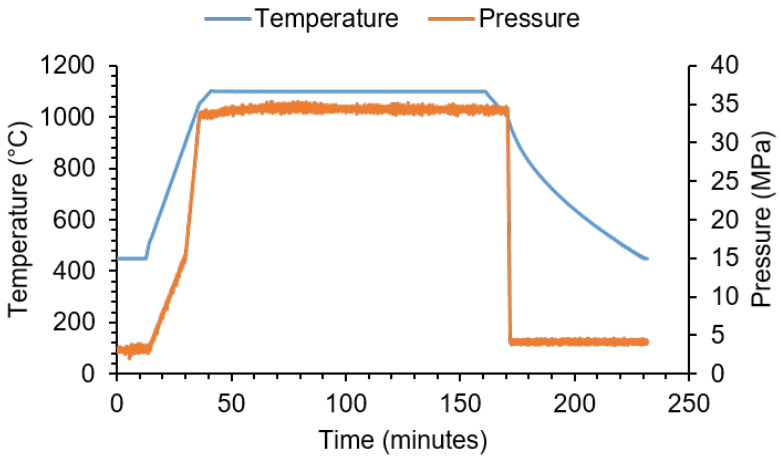

Figure 4.15: Sub-solvus dwell cycle used in the production of the 125mm diameter FAST billets, cycle shown was used to produce the billet from the Carpenter 131072 powder.

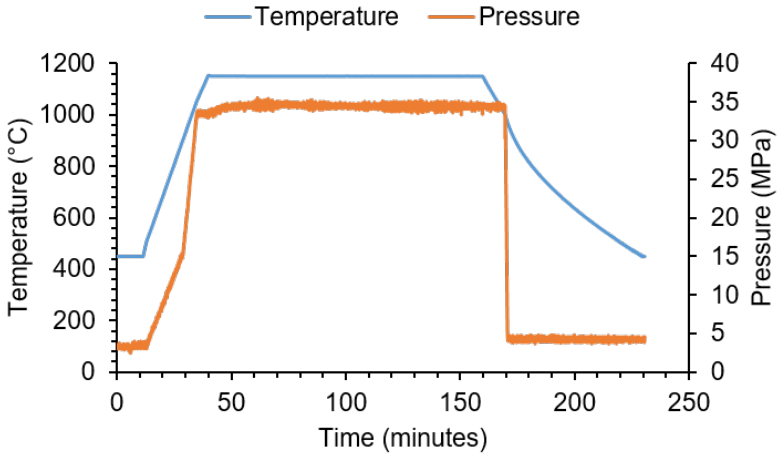

Figure 4.16: Super-solvus dwell cycle used in the production of the 125mm diameter FAST billets, cycle shown was used to produce the billet from the Carpenter 131072 powder.

The billets were left to cool in the FAST chamber overnight before being removed and grit blasted to remove loosely adhered graphite foil. The final thickness of the billets were approximately 25 mm. To remove the diffused carbon layer from the exterior of the produced billets, approximately 2 mm of material was machined from each face. This left billets with a circularity to a high tolerance and a good quality surface finish ready for the machining trials detailed in Section 6.

Chapter 5

Investigation into the Forging of as-HIP 131072 Superalloy

5.1 Introduction

In order to produce the properties required for structural components, HIP produced nickel superalloys are subjected to subsequent hot working processes. These include but are not limited to; extrusion, forging, heat treatment. These processes typically lead to refinement of the microstructure to increase the strength of the material but in PM nickel superalloys hot working serves an additional function. The PPBs that are contained within the microstructure have been demonstrated to reduce the hot ductility of the material by providing a brittle pathway through which cracks can propagate through the material during hot working and during in service usage. As previously demonstrated, the processing temperature used greatly affects the grain size and precipitate morphology of the material. By extension, the processing conditions used during forging will also affect the in service performance of these alloys and more relevant to this work, the machinability.

In order to investigate how the microstructure of the material influences the machining process, first it is necessary to determine the range of microstructures which can be produced through a single open die uni-axial forging. Uni-axial compression provides a differential strain profile within as forged material which allows the examination of how the local strain produces differential microstructures and can be easily simulated on a small scale before up-scaling to industrial equipment. Another advantage to using a uni-axial forging process is that cylindrical billets can be readily produced for machining trials. A uni-axial forging process is also lower cost as only plain flat dies are required.

A small scale forging study was conducted using the as HIP material described in the chapter 3, to understand the influence of forging parameters on the flow stress behaviour and resultant microstructure. This information was then used to inform larger scale forgings trials to produce material for machinability testing. The small scale testing allowed the post forged microstructure to be examined on a manageable scale for varying forging input variables. Flow stress curves were produced which allowed inferences to be made regarding the material's response to deformation and how the microstructure changes as the deformation proceeds, these flow stress curves could then be used by the industrial partners for modelling purposes. The small scale testing allowed a large number of trials to be produced using the material removed from the HIP billet, this allowed the determination of the range of parameters at which successful forgings would be produced without cracking of the billet, and also explore multiple step deformation trials to try and increase the amount of upset (reduction in height) that could be achieved on the final billet.

5.2 Literature review

5.2.1 Fundamentals of Hot Forging

Hot working is used to convert simple shaped billets into shapes that are close to that of the finished component which can then be machined. Forging is the most common form of hot working process and consists of compressive deformation at high temperature, either in single or sequential steps using dies with varying levels of complexity depending on the operation and component. Forging offers numerous advantages, particularly in difficult to produce material, however the main advantage is the ability to simultaneous modify the shape and the microstructure to give a shape close to the finished component while simultaneously improving properties.

An industrial scale hot forging process relies on the increase in ductility and reduction in yield stress associated with increased temperature, which occurs readily for most metals, although nickel alloys in particular resist this reduction in strength up to very high temperatures. Once a material is heated up to a certain temperature in a furnace, it is placed between two dies and compressed. The geometry and material of the dies can vary greatly. The dies are pushed together via hydraulic or pneumatic actuation or in some cases via gravity in the case of hammer forging. The dies compress the heated material in order to achieve a certain reduction in height and spread in the case of open die forging, or until the material conforms to the die shape in the case of close

die forging. Forging normally takes place in numerous steps due to material cooling due to contact with the surrounding air and relatively cool die set. Heat treatment steps are often interwoven with the numerous forging steps to optimise workability and manage microstructural change. This approach is particularly effective in the case of nickel superalloys [94]. There are often high frictional forces to consider that exist between the die and work piece material so glass based lubrication is often applied as well as insulation to manage heat transfer at the interface and ensure that the material freely flows across the face of the dies. One alternative to overcoming heat loss issues is to employ isothermal conditions in which the dies and surrounding environment are maintained at the target forging temperature. This is readily employed in superalloys but the number of facilities which are capable of isothermal forging on a suitable scale for aerospace parts are limited.

The response of the material to forging is dependant on the diligent design of the forging process that relies on an understanding of how the material responds to changes in the key variables involved. The next sections aim to describe some of the key process variables and how these subsequently affect the material during forging.

Strain

Strain is a measure of the level of deformation and can be defined as either engineering or true strain. The amount of strain has implications regarding resultant material properties as a minimum strain is required to achieve beneficial microstructural change. Too much strain can result in cracking due to the workability limits of the material being reached. The true strain varies throughout the cross section of a forging and is dependent on the die shape and workpiece geometry. Areas close to the die surface typically experience the lowest level of strain and are termed dead zones due to the low level of deformation. Friction between the die and the work piece also determines the level of strain as the material flow is influenced.

Forging Temperature

The forging temperature determines both the workability of the material and the level of microstructural change which will occur during the process. Higher temperatures generally allow higher final strain to be achieved without material failure due to the increase in ductility associated with higher temperatures. Higher temperatures speed up microstructural change and may dissolve strengthening precipitates which further increases workability. Although higher temperatures are generally favourable, the temperature may

be chosen to achieve specific structures as is the case with α and β phase field forging in titanium alloys and below the γ' solvus of the material in nickel alloys. Higher forgings temperature however are more difficult to achieve and maintain during forging and the limitations of the die strength and safety of surrounding workers should be considered. The die temperature may also be strategically selected to optimise heat transfer preventing rapid cooling at the interface.

Rate of Deformation or Strain Rate

The rate of deformation has implications regarding workability. In strain rate sensitive alloys such as nickel based superalloys, the rate of deformation can limit workability as the ductility limit is reached quickly and the material fails during forging. Strain rate also affects the level of adiabatic heating which is heat generated internally in the material as a result of the plastic deformation occurring during forging. High strain rates lead to high levels of adiabatic heating which needs to be avoided when the forging temperature is critical, for example, when phase changes are to be avoided. It is for this reason that low strain rates are employed when forging under isothermal conditions. Low strain rate forging is achievable on hydraulically actuated presses, traditional techniques such as hammer forging typically exhibit higher strain rates. The strain rate is not constant during most industrial forgings, as the speed of deformation is controlled via press velocity rather than strain rate. The strain rate will not be constant through the workpiece, even in the case of simple uni-axial upsetting.

Forging Load - Applied Force During Forging

The load applied during forging is often uncontrolled and is instead a consequence of the forging strain, strain rate and temperature. The load applied by the forging press is generated through the material's resistance to deformation, also known as flow stress. The flow stress of a material is characterised via flow curves which plot the stress vs strain at a fixed strain rate and deformation temperature. This is captured through hot compression tests for which various international standards exist for collecting the strain vs strain behaviour. This behaviour can be then used to simulate larger forging processes using finite element methods. The forging load is normally relevant when choosing the appropriate press for a particular forging. The effects of friction increase the forging load particularly for high levels of displacement.

To be a true representation of the materials behaviour, the flow stress

must be corrected for changes in temperature, strain rate and the friction between the die and the workpiece which will artificially increase the flow stress. These factors can prevent the microstructural changes which occur during compression from being inferred and empirical relationships to correct for these factors are introduced later in this chapter.

5.2.2 Stress vs Strain Behaviour During Hot Working

A typical stress vs strain curve for hot compression can be characterised by 3 distinct regions [95–102], this is shown schematically in Figure 5.1.

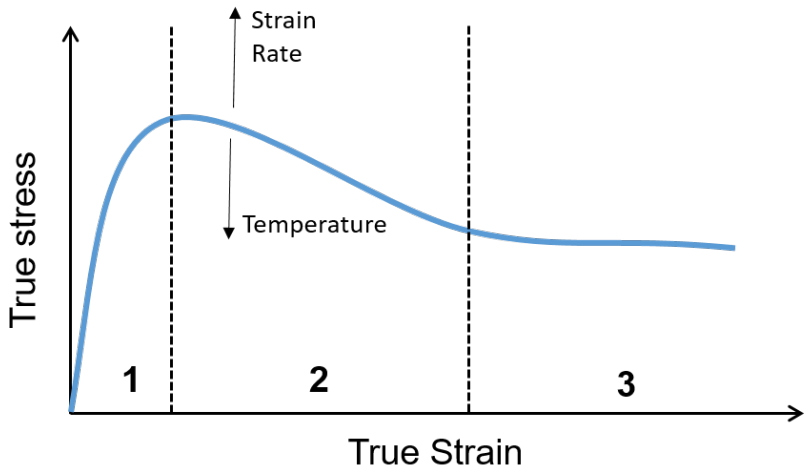

Figure 5.1: Schematic showing a typical true stress vs true strain curve exhibited during a hot compression test, showing the 3 distinct stages during hot compression [95–102]. The effect of the applied strain rate and temperature on the flow stress is also shown.

The three distinct regions in Figure 5.1 can be described as follows:

1. The first stage consists of rapid work hardening as the strain increases from zero. In this region the dislocation density in the material increases rapidly as dislocation motion and pileup occur, the work hardening rate has been stated to be proportional to the square root of the dislocation density [103].

2. The second stage is characterised by the reaching of a peak stress value at a critical strain. At this point the dislocation density is reduced by mechanisms such as dynamic recrystallisation and dynamic recovery

which act to reduce the flow stress during subsequent deformation. The flow softening rate provided by dynamic recovery is said to scale linearly with dislocation density [103].

3. The third stage is reached during further deformation whereby the recovery mechanisms and work hardening behaviour reach equilibrium which produces a steady state flow stress during subsequent strain. This stage is not always reached the behaviours described can occur cyclically depending on the material and deformation parameters. Continuous flow softening can occur at higher strain rates [96].

As the flow stress is heavily influenced by the deformation temperature and strain rate, adiabatic heating can distort the analysis of a flow curve. Adiabatic heating is predominantly caused by the generation of heat due to energy generated through plastic deformation in the material. This effect can lead to further softening in a material and requires correction to determine the true stress vs strain behaviour without its influence. It has been noted in previous works that adiabatic heating can prevent the determination of the point at which a steady state flow stress is achieved [95].

The phenomenon of flow instability can be severely detrimental to thermomechanical processing as it generally leads to gross material cracking and renders the product unusable and must therefore be avoided at all costs. Flow instability can be identified using processing maps which describe the processing windows (i.e. combination of strain, strain rate and temperature) which can result in the occurrence of flow instability. This technique has previously been used for a range of nickel superalloys [95, 96] and in general it has been shown that a combinations of high strain rates and low processing temperatures produce conditions where flow instability is likely to occur. In combination with the instability map, a power dissipation efficiency map can also be produced. The energy input into a material as a result of hot deformation can either be dissipated via plastic deformation of the material which is predominantly converted to heat and leads to adiabatic heating, or energy is consumed through microstructural change [96]. The power dissipation energy therefore communicates the percentage of the energy which goes towards the desirable outcome of microstructural change, with high efficiencies being indicative of dynamic recrystallisation.

5.2.3 Recovery Mechanisms During Hot Working

Dynamic Recovery

Dynamic recovery (DRV) proceeds through the rearrangement/realignment of dislocations, thus reducing the resistance to deformation and counteracting work hardening. This continues until the critical dislocation density for the onset of dynamic recrystallisation is achieved [102]. Dynamic recovery can be characterised as the climb and cross slip of dislocations leading to their annihilation and the formation of sub-grain networks. Dynamic recovery is accelerated by increasing the deformation temperature, which facilitates diffusional mechanisms. The level of dynamic recovery is also dependent on strain and strain rate, sufficient strain is required to produce the required critical mass of dislocations. The process is time dependent, therefore increasing strain rates reduces the opportunity for dynamic recovery.

Dynamic Recrystallisation

Dynamic recrsytallisation (DRX) is the process which refines grain sizes in materials during hot deformation [94] and its onset is one of the mechanisms which leads to a reduction in work hardening rates with increasing hot deformation [102]. In essence, dynamic recrystallisation is the process of the formation of nuclei which grow into new, deformation free grains. These nuclei form at locations where there is sufficient dislocation density. For certain conditions dynamic recrystallisation produces new dislocations faster than the annihilation of dislocations via work hardening leading to rapid flow softening. It has been seen that when the rate of DRX cannot counteract the level of work hardening, substructures within grains form due to the internal dislocation structure within grains. These substructures can then lead to DRX onset within grains in order to reduce the stored energy captured within the sub-grain boundaries [94]. The occurrence of DRX produces a finer grain size which often leads to a lower resistance to hot deformation [102]. High strain rates can effect the level of dynamic recrystallisation due to not enough time being available for DRX grains to form and develop however this may be offset by the level of additional adiabatic heating which rises the materials temperature providing more energy for DRX [95].

Two dynamic recrystallisation processes are often commented upon in previous works, these are continuous dynamic recrystallisation (CDRX) and discontinuous dynamic recrystallisation (DDRX). DDRX is indicated by the presence of bulged grain boundaries [95] where local variations in dislocation density lead to a stress distribution along a grain boundary causing a bulging effect. Necklace structures can be seen around bulged grain boundaries in-

dicating these deformed boundaries act as nucleation sites for DRX [96]. In materials which undergo recrystallisation through DDRX, serrations can often be seen around the peak stress value on a stress vs strain curve [104]. In materials with low stacking fault energies, DRV is retarded which leads to rapid recrystallisation through DDRX [104]. When DDRX is the mechanism for recrystallisation, new grains nucleate on grain boundaries and therefore smaller grain sizes accelerate recrystallisation through DDRX. CDRX takes place through the formation of dislocation networks within grains which eventually form sub-grain networks, these networks then absorb lattice dislocations to form high angle boundaries and new grains [95]. It has been shown that the presence of intermetallic precipitates can inhibit DRX [94]. Provided they are sufficiently pinned, the newly formed grains are smaller than the original un-deformed grains prior to forging. This is a principle justification for performing a forging operation in order to produce finer grain sizes as the grain size in Ni based superalloys cannot be tailored through heat treatment alone [94]. This is in contrast with titanium alloys where the α and β phase field transitions can be exploited to change the microstructure significantly. It should therefore be apparent that the onset of DRX is beneficial and forging operations are specifically designed to induce DRX.

Static Recrystallisation (SRX) and Static Recovery

Recovery can also take place during inter-pass heat treatments or sample cooling after hot deformation. These recovery mechanisms are normally driven by energy stored in the material due to the hot deformation. These recovery mechanisms are known as static, as they do not occur during the hot deformation. These recovery mechanisms operate in the same manner as dynamic recovery and dynamic recrystallisation, lowering the dislocation density via diffusional mechanisms and the nucleation of new grains respectively. An additional mechanism known as meta-dynamic recrystallisation can also occur which is associated with the hold times between forging steps. These recovery mechanisms can have significant effects on subsequent hot deformation steps [105]. Lin et al [105] provide a description for the mechanisms of SRX for a hot deformed sample. It is proposed that sub-grain boundaries formed during deformation grow near primary grain boundaries due to the driving force of the grain boundary energy, once these sub-grain boundaries achieve a critical size, they form a SRX nucleus. These nuclei grow to reduce the grain boundary energy stored as a consequence of the deformation. Static recovery and static recrystallisation are also active during post forging heat treatments.

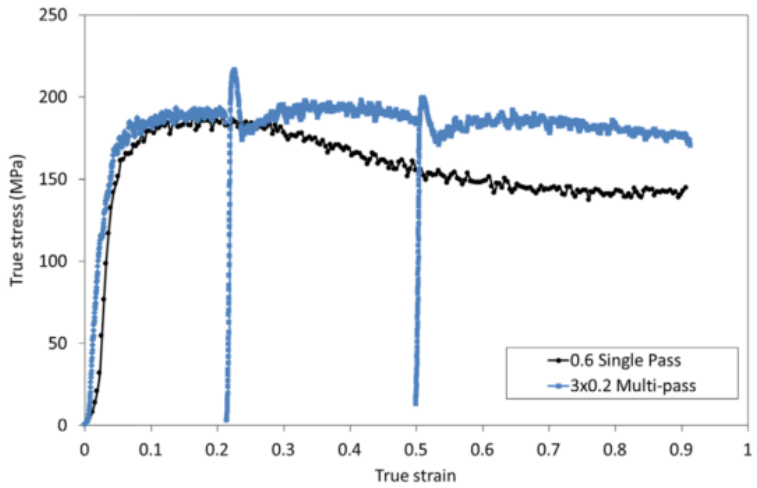

Figure 5.2: Flow stress curves produced using single pass and multi-pass deformation strategies for Haynes 282, presented in the work of Gardner et al [106].

In the work of Gardner et al [106] the hot deformation behaviour of Haynes 282 cast nickel superalloy billet was examined via single pass and multi-pass compression tests. Single pass deformations were performed to engineering strains of 0.6, while multi-pass tests were performed to a final engineering strain of 0.6 in three equal intervals with an anneal at 1100°C for a 1 hour period post deformation. Similar comparisons of single and multi-pass intervals were performed using engineering strains of 0.8 and 0.7+0.1, respectively, with the same inter-pass anneal conditions for the two pass test. Empirical analysis of the flow stress data, at the processing temperature of 1100°C and a strain rate of $0.2s^{-1}$ found that the critical strain required for recrystallisation was 0.09. True stress vs true strain flow curves for both single and multi-pass deformations are shown in Figure 5.2. It can be seen that the flow stress curves for the single hit test display the expected behaviour during hot deformation. Rapid work hardening was observed up to a peak flow stress, after which softening mechanisms occur and the flow stress decreases until hardening and softening mechanisms balance at higher strain leading to a steady state flow stress. When comparing this to an interrupted strain rate test, it was found that the flow stress is higher for the interrupted tests compared with the single pass deformation at equivalent strains (as shown in Figure 5.2). Gardner et al relate this to grain growth and static recrystallisation occurring between passes when the samples are held at temperature

of 1100°C for one hour, whereby grains grow and limit the grain boundary sliding during deformation leading to a lack of flow softening seen during testing. Figure 5.2 also reveals the presence of prominent yield peaks during the start of each deformation pass. The authors suggest that this could be either related to stress release as the dislocations overcome certain microstructural features, or due to lubricant burn off between passes, however no evidence was given for this hypothesis.

In the work of Zhang et al [107] the hot deformation behaviour of a nickel superalloy was examined in terms of the competing recrystallisation behaviours for a range of deformation temperatures (1010°C - 1210°C). Zhang et al [107] examined the shape of flow curves during the hot deformation of cast Inconel 718 material to infer the characteristics of recrystallisation occurring during the deformation for both single pass and double pass hot compression. It was demonstrated that some level of material recovery occurred between deformation steps due to an increase in the flow stress upon the application of the second deformation pass. This was attributed to static and meta-dynamic recrystallisation. Zhang et al concluded that the higher the strain during the second deformation step, the greater the level of recrystallisation post deformation.

In the work of Chen et al [99], the superalloy GH4169 was subjected to hot compression testing in order to understand the nature of recrystallisation with varying processing parameters. Wrought material was first subjected to a solution treatment before being compressed using temperatures ranging from 920-1040°C and strain rates from 0.001-1s^{-1}. Transmission electron microscopy (TEM) demonstrated that when the input strain was low, high dislocation densities in the material could be seen due to rapid work hardening. Higher strain input resulted in the formation of dislocation networks and sub-grain boundaries, Chen et al attributed the formation of dislocation networks is due to a shift in dislocation behaviour from slip to climb. The formation of these networks was related to the development of serrated grain boundaries which acted as nucleation points for DRX to occur. This process matches the description of DDRX. It was found that increasing levels of input strain sees the development of necklace microstructures followed by complete DRX and grain growth in DRX grains leading to equiaxed structures. Overall it was found that increased deformation temperature and lower strain rates resulted in high area fractions of DRX grains within the structure. Chen et al used a contour plot to summarise the effect of deformation parameters on the resultant level of DRX within the processing window.

Tan et al [101] studied the hot deformation behaviour of fine grain Inconel 718. Deformation temperatures of 950-1150°C and varying strain rates were employed to deform solution treated equiaxed material to a strain of 0.7.

Typical flow stress curves were produced and it was found that higher deformation and higher strain rates resulted in a greater amount of flow softening. Tan et al concluded that finer grain alloys require less energy input to initiate deformation. Processing maps were produced to indicate the optimum processing conditions for hot deformation at 1100°C and a strain rate of $0.1s^{-1}$. Table 5.1 shows the activation energy for hot deformation of different alloys and processing conditions.

Table 5.1: Example activation energies for hot deformation for varying nickel superalloy systems from literature.

Alloy	Activation energy (kJ/mol)	Temperature range (°C)	Strain rate (s^{-1})	Strain	ref.
UNS10276	480	950-1200	0.01-10	0.9	[96]
GH696	410	880-1120	0.01-10	0.20-0.60	[108]
FGH4096	376	1100-1200	0.01-10	0.5	[100]
Inconel 718	406.5	950-1150	0.1-10	0.7	[101]
VM207M PM	407	1000-1100	0.001-0.01	0.7	[54]

Recrystallisation during Hot Deformation in Nickel Superalloys

In the early work of Winberg and Dahlen [109], the role of carbides on the recrystallisation dynamics of extruded Astraloy material were studied. By using small deformations of 10% in combination with heat treatments designed to produce minimal recrystallisation, TEM analysis revealed an increase in dislocation density in the region of TiC (MC) carbides in post plane strain deformation. Subsequent recovery led to increased gradient of dislocation density between the regions which were rich and lean in carbides which originated from PPB networks. It was found that these regions were nucleation sites for recrystallisation upon the application of heat treatments. Isothermal recrystallisation treatments revealed a positive correlation between the temperature and duration chosen for heat treatments and the level of recrystallisation. Bimodal structures post recrystallisation were observed with recrystallisation occurring primarily in the region of carbide precipitates. It was found that the critical size of precipitates required to initiate recrystalli-

sation was smaller compared with other alloy systems. This was rationalised through the effects of γ' precipitates which impede dislocation motion due to their ordered nature, which means smaller precipitates are able to capture a greater number of edge dislocations, which in turn generates the required dislocation density for nucleation of new grains. It was found that no coarse γ' precipitates could be observed in newly formed grains, Winberg and Dahlen described this as being due to the coherent nature of the precipitate whereby the orientation of a newly formed grain leads to a large increase in surface energy at the precipitate interface, this would make the precipitate more unstable and therefore reduce its dissolution temperature. Cooling after the recrystallisation treatments resulted in the formation of fine γ' precipitates with an absence of coarse γ'.

In the work of He et al [110], the deformation behaviour and resultant microstructure produced via a two step deformation procedure was investigated. Using a novel nickel superalloy chemistry, HIP consolidated material which had been extruded was subjected to two step isothermal compression testing. The test samples were first subjected to a first compression followed by a dwell at a high temperature, a second compression was then performed before quenching to preserve the microstructure. The strain and strain rate of the two compressions were varied to examine the resultant levels of recrystallisation via EBSD. The inter-pass dwell time and temperature were also varied to study the contribution of each parameter on microstructural development through static recrystallisation processes. It was demonstrated that the single pass and multi-pass deformations led to different flow stress behaviours with a decrease in the flow stress observed between passes compared to the single pass at equivalent strain levels. He et al rationalised this result as being due to the balance between static and dynamic recrystallisation with higher levels of SDX occurring for the lower strain input after during first deformation, leading to a greater level of softening between steps as evident by a drop in the measured flow stress. EBSD analysis revealed that grain sizes after the second deformation were finer for greater levels of strain input during the first deformation step. EBSD micrographs confirmed that finer microstructures could be produced via the use of higher strain rates and higher temperatures during the second deformation step, combined with longer inter-pass dwell times. The work of He et al demonstrated that SDX plays a significant role during the inter-pass dwell in allowing the production of fine microstructures and the reduction in forging induced cracking. The role of adiabatic temperature rise was not considered which could further contribute to the findings of the work.

In the work of Wu et al [95] hot compressions tests were conducted on a new nickel superalloy with the addition of solute strengtheners such as

tungsten, chromium and cobalt etc. Hot compression tests were performed at temperatures ranging from 1000-1200°C, it was found that both CDRX and DDRX mechanisms played a role during deformation. It was found that low strain favoured the DDRX mechanisms (although CDRX mechanisms were still evident) as grain boundary bulging could be seen. At high strain rates, TEM confirmed that dislocation cells were present which suggested CDRX is favoured.

Liu et al [94] examined the recrystallisation behaviour for three variants of Udimet 720. Coarse grain, fine grain and mixed grain size microstructures were subjected to hot compression testing both below and above the γ' solvus temperature. DRX was found to initiate along the grain boundaries for the uni-modal grain size materials, however the nucleation of DRX grain was found to be accelerated in the fine grain material. Flow stress curves for the three materials showed the a prominent yield drop phenomenon after peak stress for the coarse grain variant which was not seen in the fine grain material. The flow stresses for both the fine and coarse grain materials were similar for deformation temperatures above the γ' solvus. Continuous flow softening could be seen for the mixed grain material and no steady state flow stress was reached for strains up to 0.7, unlike the uni-modal varieties of the material. In the coarse grain material, the deformation above a given strain resulted in nucleation of DRX grains along serrated grain boundaries and also within grains, which showed evidence of internal misorientation being points for the nucleation of DRX grains. For the mixed grain material, deformation could be seen in the coarser grains but not in the fine grains. Liu et al suggested that this was due to the preferential deformation and recrystallisation in the coarser grains due to similar mechanisms presented for the uni-modal coarse grain material. Liu et al also discussed in detail the role of γ' precipitates on recrystallisation. It was suggested that for the coarser grain materials, the newly formed boundaries of the DRX grains are pinned by secondary precipitates which coarsen during deformation. For the fine grain material, Liu et al proposed that incoherent primary γ' precipitates provide a grain boundary pinning effect and can deform independently. It was also found that the grain boundaries of finer grains could migrate revealing a reduced pinning effect provided by these precipitates during deformation. It was proposed that the reduction in pinning effect was due to a combination of strain induced grain boundary migration and low densities of pinning precipitates locally within the structure. Liu et al suggested that during deformation, high dislocation densities can accumulate in these precipitates as they deform independently, dynamic recovery then takes place reducing dislocation densities in these precipitates.

In a later work by Liu et al [100], hot deformation of the nickel superalloy

FGH4096 was performed to determine the effect of strain rate and temperature on both the as deformed grain size and the grain size distribution. Testing was conducted between 1110-1200°C and strain rates of 0.01-10 s^{-1}. The flow stress showed that the material exhibited the normal flow curve described previously (Figure 5.1). It was found that higher strain rates and lower deformation temperatures promoted finer grain sizes in the post deformed material. Higher temperatures and slower strain rates were found to promote grain growth over DRX. EBSD showed that the new grains formed in the interior of deformed grains indicating the occurrence of continuous dynamic recrystallisations. It was also found that the recrystallised grain size could be related to the normalised flow stress via a power law relationship.

Azarbarmas et al [98] found that dynamic recrystallisation was the dominant restorative mechanism during the hot deformation of wrought Inconel 718. Hot compression tests were performed on material with a starting microstructure with an average grain size of 45 μm and an abundance of annealing twins due to the prior processing. Deformation was performed to a final true strain of 0.7 using temperatures ranging from 950-1100°C and strain rate from 0.001-10s^{-1}. Flow curves identified continuous flow softening in high strain rate tests that was shown to be due to adiabatic heating, below 1s^{-1} deformation heating was found to be negligible and steady state flow stresses were achieved. The single peak flow curves suggested that the DDRX was the dominant recrystallisation and this was shown to be the case through microstructural examination. Post deformation microstructures demonstrated that in general, high temperatures and lower strain rates increased the volume fraction and grain size of the recrystallised grains which is due to the increased time and energy available for DRX. The exception to this was found when the highest strain rate was employed which produced high levels of recrsytallisation attributed again to adiabatic heating. Azarbarmas et al also refer to work in [111, 112] about the two types of annealing twins present in the material, one being a coherent straight twin and the other being a curved twin which effectively acted as nucleation points due to high levels of stored energy at these features.

Li and Tin [113] studied the effect of hot working and annealing on the formation of twin boundaries was investigated in alloy IN600. The material was subjected to a strain rate of 0.003 s^{-1} during deformations to varying strain levels and deformation temperatures between 25-982°C. The flow curves showed that peak stresses and the level of strain hardening decreased with increasing deformation temperature owing to the activation of recovery mechanisms at higher temperatures, with DRX predominantly occurring for intermediate to high temperatures and dynamic recovery being more dominant at the highest temperatures examined. EBSD maps revealed no evi-

dence of DRX in samples deformed to strains below 11% regardless of temperature and this resulted in higher fraction of twin boundaries produced during post deformation annealing treatments. In general it was found that the formation of twin boundaries occurred during annealing solely. It was concluded that processing parameters leading to dominant recovery through DRV resulted in enhanced twin boundary formation.

Liu et al [103] used the hot deformation of a commercial nickel alloy (52.82Ni-18.96Cr-5.23Nb-3.01Mo-1.00Ti-0.59Al-0.01Co-0.03C-(bal.)Fe) to produce a cellular automaton (CA) model for describing the dynamic recrystallisation process in the alloy. Similar to previous works, it was found that increasing deformation temperatures and decreasing strain rates result in a large grain size post dynamic recrystallisation. This behaviour was explained by the enhanced grain boundary mobility provided by increased available thermal energy while the low strain rates resulted in increased deformation time for grain boundary mobility to occur. Using the results of hot deformation tests conducted using strain rates of 0.001-1.0 s^{-1} and temperatures ranging from 920-1040°C, it was shown that the post DRX recrystallised grain size could be related to the steady state flow stress (characterised via the point of work hardening and recovery equilibrium) via an inverse power law. This was stated to be a feature of alloys with low stacking fault energy which also results in low rates of dynamic recovery. The produced CA model matched well with experimental data and interrogation of the predicted DRX grain size showed that initially DRX is inhomogeneous but becomes more homogeneous with increasing volume fractions of DRX grains.

In the work of Kumar et al [102], the work hardening rates were used to determine the critical stress σ_c and critical strain ε_c required for the onset of DRX for an experimental HIP produced nickel superalloy, using a range of deformation parameters. Using the approach of Meckings and Kocks [114], the flow curves produced were converted to work hardening rates $\theta = d\sigma/d\varepsilon$ vs true strain. Kumar et al noted that these curves consisted of 3 stages, the first being the rapid reduction in work hardening rates with increasing true stress which represents the stage of deformation where recovery mechanisms are active, reducing the work hardening rate. The second stage was characterised by two inflection points, the first being in the onset of sub-grain formation and the second being the onset of DRX which corresponds to σ_c. Using this approach Kumar et al were able to determine σ_c and therefore ε_c for a range of deformation conditions. They found that increasing deformation temperature reduces the ε_c value owed to increased available dislocation and grain boundary mobility associated with higher thermal energy. A reduction in strain rate was also found to affect the ε_c value. Kumar et al related this to the increased deformation time which aids the formation of

sub-grain boundaries. It was found that the critical stresses and strains required for DRX onset could be related to the Zener-Holloman parameter (Z) via a power law curve for the studied alloy. Supplementary microstructural examination performed on samples compressed to a 50% height reduction using moderate strain rates of 0.01-0.1 s^{-1} and temperatures ranging from 1000-1150°C showed that lower deformation temperatures lead to lower levels of DRX. At lower deformation temperatures, the microstructure was characterised as large deformed grains with high relative internal misorientation, bulged grain boundaries and necklace type structures, indicating DDRX as the primary DRX mechanism. Higher deformation temperatures resulted in more complete DRX owing to lower critical strains required for DRX onset and increased available thermal energy.

The interaction between recrystallisation effects and γ' precipitates was examined by Porter and Ralph [115] who used deformation and subsequent sub-solvus annealing treatments to investigate recrystallisation effects in 4 different nickel superalloys with different volume fraction and size distribution of γ' precipitates. Nimonic PE16, Nimonic 80a, Nimonic 115 and Udimet 720 with γ' volume fractions of 8%, 15%, 50% and 60% respectively, were first given commercially representative heat treatments for each alloy before all being deformed by rolling and subjected to an annealing treatment below solvus, designed to induce partial recrystallisation. It was found that in alloys with low levels of γ', the advancing recrystallisation front resulted in the dissolution of γ' followed by re-precipitation after the recrystallised boundary had past. The level of re-precipitation was found to increase with increasing levels of γ' formers in the alloy. In Udimet 720 which had the highest equilibrium γ' volume fraction was observed, some enlargement and discontinuous re-precipitation of γ' was found. Dislocations could be seen to have accumulated along the γ/γ' interfaces. Porter and Ralph proposed that sub-grains formed during deformation rotate until the orientation of interconnected sub-grains align leading to coalescence and a resultant recrystallisation front. Porter and Ralph proposed that the γ/γ' interfaces acted as sinks for dislocations allowing the rotation of these sub-grains. Once formed the recrsytallisation front advances via strain induce grain boundary migration which drives re-precipitation of γ' in a discontinuous manner.

Static Recrystallisation (SRX) in Nickel Superalloys

In the work of Lin et al [105], A cellular automatom modelling technique was developed in conjunction with hot deformation testing of a commercial nickel superalloy. This study proposed that the completeness of SRX is greatly effected by the grain boundary mobility and nucleation rate of SRX grains.

The model showed that grain boundary mobility is retarded by the presence of solute atoms. It was found that the fraction and size of SRX grains is influenced by the level of strain input, strain rate and deformation temperature due to the effect of processing parameters on grain boundary mobility and nucleation rates. Grain boundary mobility is enhanced by higher deformation temperatures, strain and strain rate. SRX grain sizes were found to decrease with increasing strain rate and strain input. The grain size inhomogeneity between SRX grains and primary grains was also studied. It was shown that with increasing SRX fraction the overall grain size inhomogeneity first increases as SRX nuclei are formed however further increase in SRX fraction leads to a more homogeneous grain size due to the development of both primary and SRX grains simultaneously.

Microstructure of Nickel Superalloys Post Hot Deformation

In the work of Gardner et al [106] a slight increase in grain size was found when comparing samples produced using a single forging step to an engineering strain of 0.8 compared with material produced using a multi-pass deformation strategy with annealing at 1100°C for 1 hour between the steps. This was attributed to grain growth occurring between forging steps during annealing. It was found that both single hit and multi-hit deformations led to a reduction in grain size compared to the undeformed Haynes 282 superalloy material prior to deformation. It was concluded that the single step and multi step hot compression produces similar microstructures provided that the total strain imparted produces sufficient DRX.

The concept of grain boundary engineering has been discussed by several researchers including McCarley and Tin [116] who used an experimental Ni based superalloy which was designed to have a low stacking fault energy via high cobalt concentration. By lowering the stacking fault energy of the material, the recrystallisation behaviour is altered due to restriction of dislocation motion via climb or cross slip. The study demonstrated that the retainment of intra-granular strain energy after deformation is key for the formation of the coherent $\Sigma 3$ twin boundary during post deformation annealing. The onset of recrystallisation was found to reduce the level of intra-granular misorientation which corresponds to a reduction in strain energy and ultimately a reduction in the amount of $\Sigma 3$ boundaries post super-solvus annealing. It was determined that the critical strain required for the onset of DRX was 0.15 for a range of deformation parameters, this is indicated through the lack of work hardening up to a peak stress and subsequent flow softening up to strains of 0.15 in contrast with material deformed to a final strain of 0.5. It was found that the application of a super-solvus annealing treatment

produced larger amounts of $\Sigma 3$ boundaries in samples that were deformed to a strain of 0.15. McCarley and Tin attributed this to larger levels of strain energy captured in deformed grains which leads to the formation of $\Sigma 3$ boundaries via strain induced grain boundary migration. This was indicated via EBSD maps of the as deformed material which show larger levels of internal grain misorientation, within samples which show an absence of recrystallisation. McCarley and Tin concluded that grain boundary engineering, which was shown in other studies to improve mechanical properties, requires stored strain energy in the material that is dependant upon the deformation parameters used, which can either be used up in the form of recrystallisation or strain induced grain boundary migration.

Lindsley and Pierron [117] summarised other works and concluded that the secondary precipitates commonly found in nickel superalloys commonly interact with grain boundaries in 3 distinct ways, these are as follows;

- A coherent γ' precipitate can dissolve upon contact with a migrating boundary, γ' precipitates then can re-precipitate coherently either at the boundary or within a grain either side of the boundary.
- Coherent γ' can coarsen on grain boundaries leading to a pinning effect, the nucleation of new grains forms a necklace structure around the pinned boundary.
- A mobile grain boundary of a newly formed grain can shear a γ' precipitate which is then reorientated to be coherent with the newly formed grain.

The formation of abnormally large grains (ALGs), also known as abnormal grain growth (AGG), has been reported frequently in literature and has been related to issues such as solute drag effects [118]. He et al [15] examined the formation of ALGs after hot compression and subsequent near solvus heat treatment. Examination of grain morphologies and orientations via EBSD and a study of precipitate morphologies revealed that areas exposed to high strains experienced DRX and showed no evidence of abnormal grain growth. In the dead zone region no abnormal grain growth was seen. ALGs were prevalent in areas of intermediate strain input and precipitate examination revealed γ' particles were equal in size both within grains and on grain boundaries. Using these results, He et al stated that AGG occurs due to grain boundary migration enhanced by stored energy which is large enough to cause AGG but not enough to result in recrystallisation. The migration of grain boundaries is permitted via the dissolution of large γ' which

normally provide a pinning effect. In the work of Cho [119] it was demonstrated that the dissolution of primary γ' precipitates was not the route cause of AGG in Rene 88. It was demonstrated instead that serrated/faceted grain boundaries rapidly increased the formation time for AGG owing to the preferential grain boundary migration in certain grains caused by local dislocation substructures.

Mignanelli et al [54] studied the effect of delta precipitates and their influence during isothermal forging of the VM207M nickel superalloy. Using deformation temperatures ranging from 1000-1100°C to alter the volume fraction of δ and γ' precipitates and strain rates of 0.001-0.01s^{-1}, flow curves were produced. It was found that at 1000°C (below the solvus temperature for the δ phase) significant flow softening occurred after the peak stress value was achieved at strains of approximately 0.05. When the deformation was above the δ phase solvus no peak stress was seen and the flow stress almost immediately reached steady state. Micrographs presented by the authors indicate that no recrsytallisation occurred during deformation irrespectively of the deformation temperature, nor was any δ fragmentation observed when deformed at 1000°C. The authors concluded that the recovery mechanism allowing steady state flow stress to be achieved was dynamic recovery in the γ phase. The authors also demonstrated that in the sample deformed below the δ phase solvus, the δ phase reorientated normal to the direction of loading and suggested that this could be the mechanisms resulting in the softening observed in the flow curves.

The Limited Hot Workability of Nickel Superalloys

In the work of Ola et al [120], the hot ductility of the alloy IN 738LC after non equilibrium heating to the testing temperature was examined. It was found that although the material could experience plastic deformation when deformed in compression at temperatures above 1060°C after rapid heating at 111-150°C.s^{-1}, the material exhibited zero hot ductility in tension at the same testing conditions. Microstructural examination aimed to examine the disparity in hot ductilities found that γ' precipitates could survive beyond the equilibrium solvus temperature when subjected to non-equilibrium rapid heating. This led to the dissolution of these precipitates leading to intergranular liquation. The resultant solidified phase between grains was found to be metastable. This was attributed to incoherency strains, which lead to local variations in equilibrium compositions either side of the liquid phase allowing the re-solidified intergranular eutectic products to be metastable. The authors attributed the differences in ductility between compression and tension deformation modes to be due to this phase. By comparing samples

which had just been subjected to non-equilibrium heating and compression with samples just subjected to non-equilibrium heating followed by a temperature hold matching the compression time in duration, the intergranular eutectic had dissolved in the case of the compression samples. The authors attributed the dissolution of these eutectic phases to the improvement in ductility when in compression alongside the ductility increases provided by DRX which were not seen in compression. Essentially, it was found that compressive strains help to drive a non-equilibrium state microstructure towards stable equilibrium. Lindsley and Pierron [117] stated that above the γ' solvus temperature, grains grew rapidly leading to a drop in hot workability in Udimet 720Li.

According to Kane et al [121] quench cracking is a common occurrence in high strength nickel alloys with large fractions of γ' precipitates. Kane et al studied the origin of quench cracking in the Superalloy Rene 95. Tensile stresses were induced in notched tensile samples via halogen lamp heating to beyond the γ' solvus temperature of the alloy after which the sample was held between fixed grips during cooling which led to sample fracture. Samples were tested firstly in air, then under vacuum and then in air after coating with nickel plating. It was found that the sample tested in air (in the uncoated condition) exhibited intergranular fracture behaviour, while the samples tested in the vacuum and coated condition exhibited pure rupture behaviour. Kane et al attributed this to oxygen induced dynamic embrittlement which was proposed to be the reason for the quench cracking behaviour. They also noted that in high γ' volume fraction alloys, rapid quenching and inhomogeneous cooling led to the rapid formation of γ' homogeneously throughout the material. The γ' increases a materials resistance to deformation and its rapid formation can provide the tensile internal stresses required for quench cracking.

In Singh et al [122] the issue of hot workability limits of Udimet 720 was explored during hot compression testing. It was demonstrated that cracking was more predominant in the bulged regions of the samples which according to them experienced a higher level of tensile stresses than the centre regions of the as deformed material. The level of cracking increased with increasing strain rates for lower deformation temperatures (below the γ' solvus temperature) and the cracking was found to occur along prior particle boundary networks. At higher deformation temperatures, significant grain growth occurred owing to the dissolution of the grain boundary γ' precipitates. Singh et al proposed that these combined effects led to grain boundary sliding which led to intergranular cracking, which was consistent with microstructural examination. Singh et al linked the crack formation with a lack of super-plastic flow deformation window. The increased cracking propensity for lower de-

formation temperatures and higher strain rates was found by Blackenship Jr et al [123] during the semi-industrial scale forging of Rene 88DT powder metallurgy superalloy.

5.3 Small Scale Forgeability Testing Methodology

5.3.1 Samples Used for Open Die Forging Physical Simulations

The as HIP material described in Chapter 3 was sectioned using electron discharge machining to produce 11 mm bars from the positions described in Figure 3.7. Each bar had an approximate length of 230 mm. 15 mm was removed from the top and bottom of the bars before they were machined into compression test pieces with a 10 mm diameter and a length of 15mm to a high tolerance surface finish and parallelism of the axial ends of the samples. This sample size was selected to allow sufficient total strain to be achieved without the possibility of buckling due to the aspect ratio of the cylinder being too high. The microstructure of the post HIP alloy 131072 material before the application of hot deformation is shown in Figure 5.3, the average grain size prior to deformation was calculated to be 15 μm using the linear intercept method. An N type thermocouple was then attached via spot welding to the external diameter of the sample to read its temperature during testing.

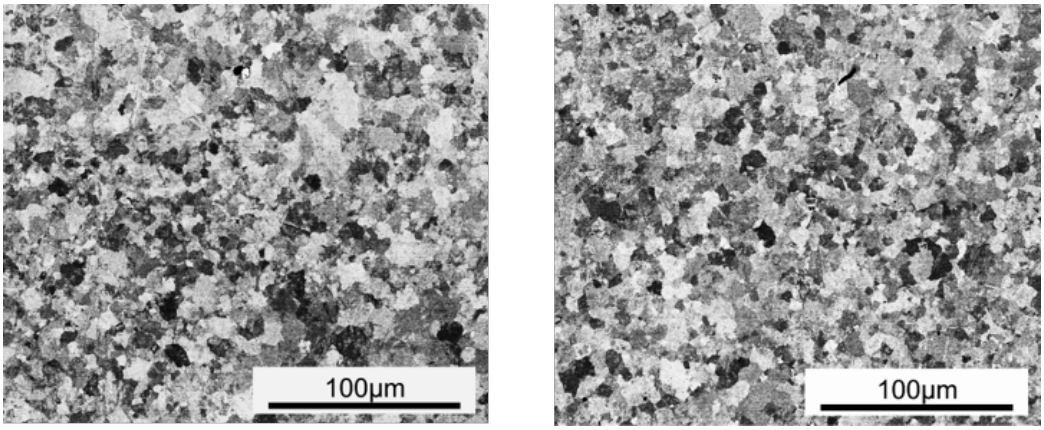

Figure 5.3: Backscatter electron micrographs of the as-HIP 131072 material prior to forging trials.

5.3.2 Forging Simulation Apparatus

Thermomechanical Compression Test Rig

In order to examine the hot forgeability of the material and ensure that the results were independent of the testing method used, two different pieces of equipment, both designed to simulate uni-axial forging, were employed. The first piece of equipment is located at the University of Sheffield and is known as the thermomechanical compression test (TMC) rig (shown in Figure 5.4), the second was a Gleeble 3800 thermomechanical simulator. The TMC is designed to simulate either a uni-axial compression test or simulate a rolling process through plane strain compression. The TMC has a maximum operating temperature of 1050°C and therefore the Gleeble was used to simulate forging temperatures above this. The operation of the TMC can be described as follows;

- A clamshell furnace, which houses the forgings dies, is heated to the required test temperature in order to achieve near isothermal conditions during forging. The dies are dwelled at the forging temperature for a fixed time for all areas of the dies and tool posts to reach a stable temperature. This is important in order to achieve isothermal forging and to ensure that the dies have achieved a steady state of thermal expansion which ensures that the correct deformation geometry is achieved.

- The deformation parameters are programmed into the test rig including the strain and strain rate required as well as the heating and cooling procedure before and after the test respectively. Before deformation, the temperature ramp rate is defined, as well as the hold time, once the test temperature has been achieved. Prior to deformation the strain and strain rate are also defined. After deformation has occurred the method of cooling is also defined. Air or forced cooling can be applied, using either air blown onto the sample or via a water spray to simulate a quench process.

- A calibration procedure is then conducted in order to ensure that the correct distance is read between the dies, to ensure the correct amount of deformation is performed during testing. First, the hydraulic ram which actuates the upper die is used to bring the upper and lower dies together and applying a small pre-load while the dies are at temperature. The distance between the dies is then programmed to read zero. A mechanical stop is then set to ensure the programmed deformation amount is not exceeded, which prevents the dies from impacting and damaging the equipment.

- The sample is placed between the spring loaded gripper arms on the computer controlled hydraulic manipulator. The welded thermocouple on the sample is then connected to the control unit which measures temperature. Boron nitride spray is liberally applied to the sample which acts as a lubricant during forging.

- Once the test is started, the manipulator moves the sample into the centre of a induction furnace in front of the clamshell furnace which heats up the sample according to the required temperature ramp rate via proportional integral derivative control (PID). Once the sample reaches the desired test temperature, the induction furnace power is modulated to maintain the temperature of the sample for a prescribed dwell time.

- Once the dwell time in the induction furnace has expired, the clamshell furnace door is opened and the sample is moved between the dies and the deformation is performed. The spring loaded gripper arms open to accommodate the increasing sample diameter as its height is reduced.

- Once the deformation has been completed, the dies retract and the manipulator removes the sample and the cooling regime is applied until the thermocouple attached to the sample reads a temperature which allows safe sample retrieval.

- During the test, the force, displacement and velocity data of the hydraulic actuator controlling the upper die are recorded and can be retrieved for flow stress analysis. The temperatures of both the dies and sample are also measured throughout.

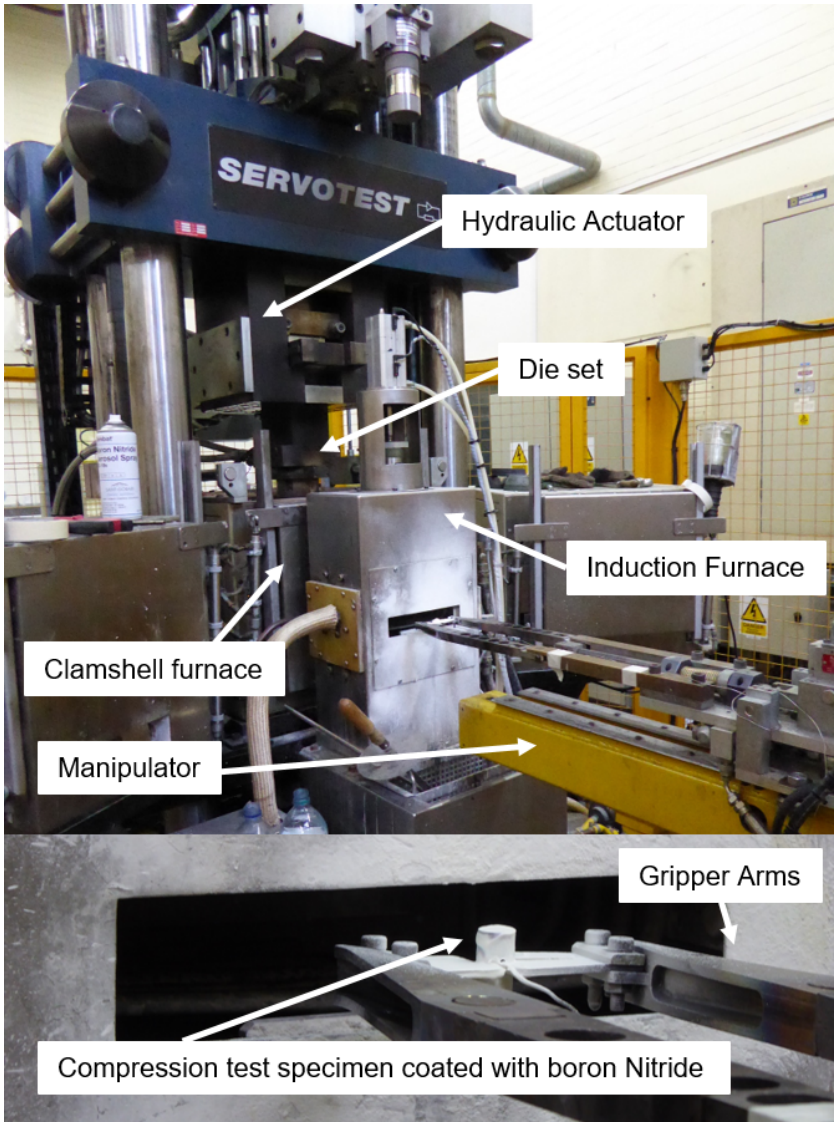

Figure 5.4: The Thermo-mechanical compression (TMC) test apparatus showing the external induction furnace used to heat the sample, the hydraulic manipulator arms, clamshell furnace and position of the die set. Image courtesy of Dr N Weston, the University of Sheffield.

The Gleeble 3800 Thermomechanical Simulator

The second piece of apparatus used for uni-axial compression test was the Gleeble 3800, a photograph of which is shown in Figure 5.5. The Gleeble system differs greatly from the TMC in that both the heating and deformation occur within a vacuum chamber with no need to move the sample between

chambers. The Gleeble heats the sample via direct electrical current instead of via an induction coil. The Gleeble operates using the following procedure.

- The sample is loaded horizontally into the Gleeble test chamber between the tool die posts. One of the post is driven by a hydraulic ram to provide the deformation. A piece of tantalum foil is placed between each end of the cylinder and the dies and this acts a lubricant between the sample and the die posts. A small clamping load of the order of hundreds of newtons is applied to keep the specimen held between the dies. A photograph showing an example of a specimen held between the die posts is shown in Figure 5.6.

- The chamber is then closed and evacuated and electrical current is used to heat the sample. The input power is modulated to produce a pre-programmed temperature ramp rate as measured by the thermocouple attached to the sample.

- Once the temperature of the thermocouple reads the required test temperature, the sample is dwelled for a time sufficient to ensure that the sample temperature is homogeneous. For this test a heating rate of $5°C.s^{-1}$ was chosen and a dwell time of 5 minutes was applied, this is in line with other work [100, 101, 103, 105, 108, 124].

- Once the dwell time had expired, the desired deformation was applied. The Gleeble control system automatically computes the stress vs strain profile by calculating an estimated sample surface area using the initial sample geometry and the constancy of the sample volume during the test.

- Once the test was completed the chamber was recharged with argon to remove the vacuum while the sample cools. The argon was then extracted and displaced with air. The chamber was then opened and the sample was removed.

Both pieces of apparatus have disadvantages and advantages which were examined during testing. It was decided that both would be used to evaluate the performance of each method and to allow data to be compared between the two pieces of equipment.

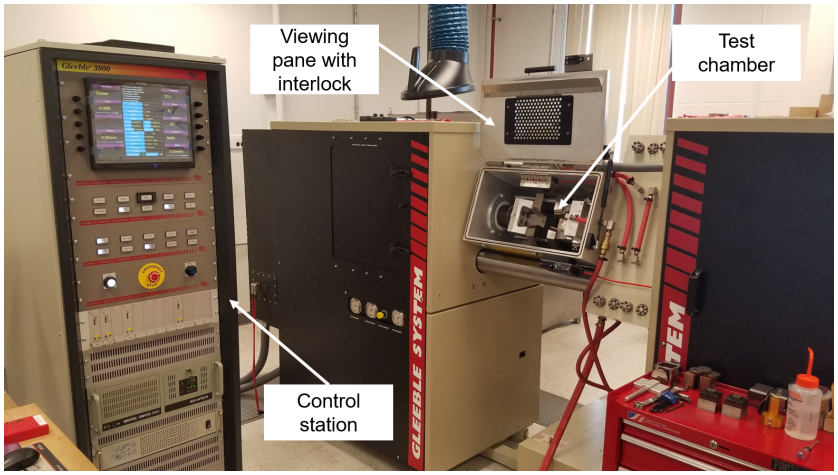

Figure 5.5: Photograph of the Gleeble 3800 showing the layout of the apparatus and key components. Image courtesy of Carpenter Technology.

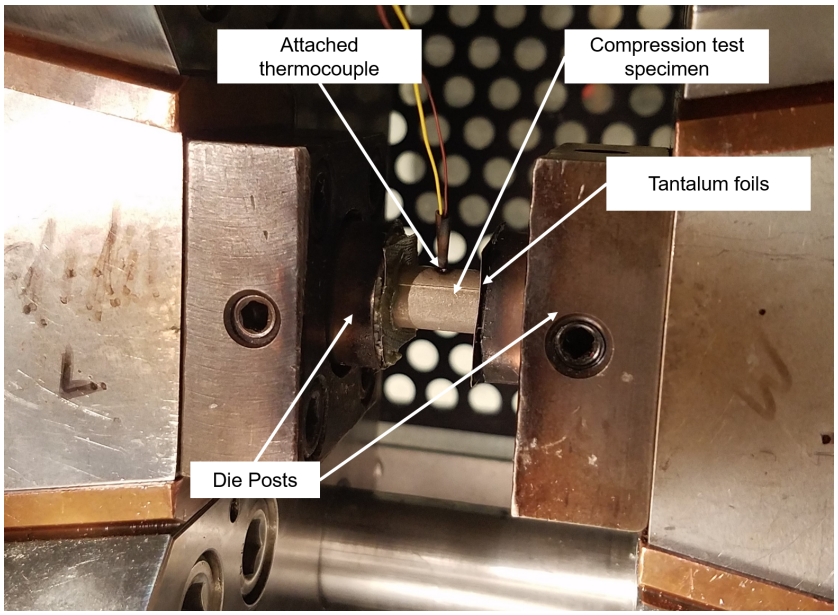

Figure 5.6: Photograph of the Gleeble 3800 test chamber showing the experiment set-up prior to a compression test. Image courtesy of Carpenter Technology.

5.3.3 TMC Output Data Processing

Raw Output Data

Following the completion of a successful TMC flow stress test, the five output variables are time, die displacement, die velocity, measured die load and the temperature read by the thermocouple affixed to the sample. Typical examples of these output data files are shown in Figures 5.7-5.10. It is with this data that the stress vs strain behaviour can be determined.

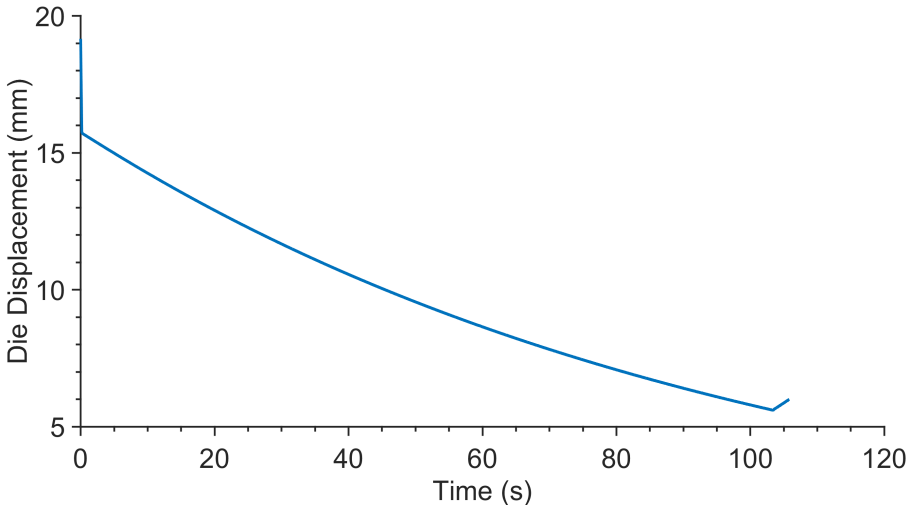

Figure 5.7: Example displacement data recorded as a function of time for a hot compression test performed using a 131027 post HIP sample at 1000°C at a strain rate of 0.01 s^{-1}. The test was performed using the TMC apparatus.

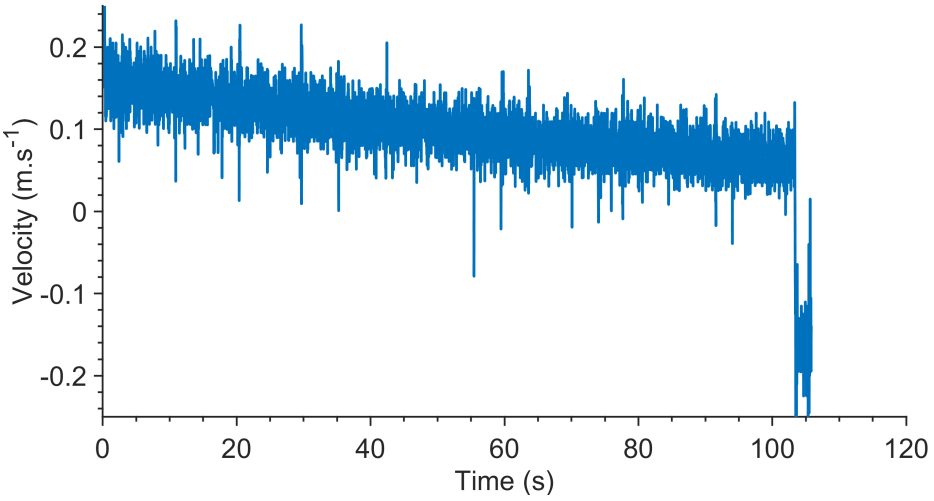

Figure 5.8: Example velocity data recorded as a function of time for a hot compression test performed using a 131027 post HIP sample at 1000°C at a strain rate of 0.01 s^{-1}. The test was performed using the TMC apparatus.

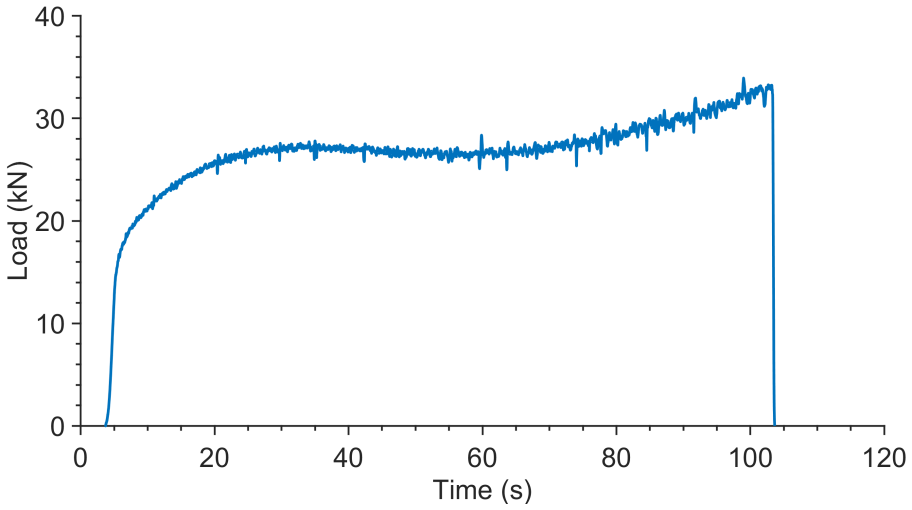

Figure 5.9: Example load data recorded as a function of time for a hot compression test performed using a 131027 post HIP sample at 1000°C at a strain rate of 0.01 s^{-1}. The test was performed using the TMC apparatus.

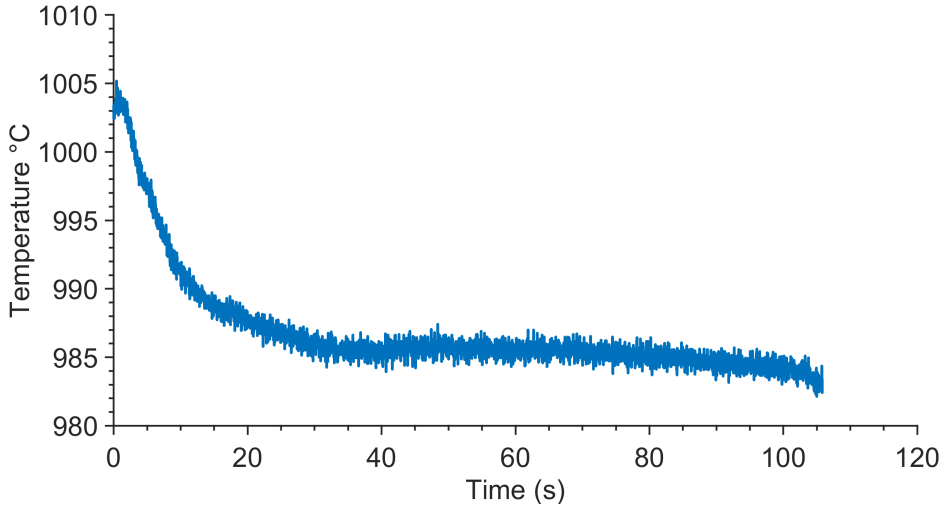

Figure 5.10: Example thermocouple temperature data recorded as a function of time for a hot compression test performed using a 131027 post HIP sample at 1000°C at a strain rate of 0.01 s^{-1}. The test was performed using the TMC apparatus.

Flow Stress Curve Production

An example of the raw load vs displacement data captured by the TMC is given in Figure 5.11. The load measured during the forging is comprised of two components, the first being the resistance of the material to the deformation imposed by the ram and the second being friction due to the interaction between the sample and the dies. In order to remove the friction component, the load vs stroke data must be corrected by first using the constancy of volume to calculate the instantaneous radius of the sample through knowledge of the instantaneous sample height (h_i). The instantaneous sample height can be found by subtracting the instantaneous top die displacement from the original sample height, the instantaneous sample radius can then be calculated using Equation 5.2. Once the instantaneous radius has been computed the load data can be corrected to remove the effect of friction using Equation 5.3. Figure 5.11 shows the effect of the friction correction of a typical load vs stroke curve. As can be seen the friction "tail" usually viewed towards the end of the compression test has the largest correction due to the increasing surface area. Once the load vs stroke curve has been corrected it can then be converted into a stress vs strain flow curve. The strain is calculated by first converting the displacement value of the die to a instantaneous sample height using Equation 5.1 and then by using Equation

5.4. The load is converted into a true stress by dividing the measured load by the estimated sample area, estimated using the instantaneous radius of the sample, calculated previously in Equation 5.2, as described in Equation 5.5. An example flow curve, shown with varying degrees of friction correction is shown in Figure 5.12. In order to ensure that the desired strain rate has been achieved, the true strain can be plotted as a function of time during the test, as shown in Figure 5.13. As seen in the figure, the calculated strain rate closely matches the target strain rate which is typical for the TMC for the range of strain rates tested.

$$h_i = h_o - d_i \tag{5.1}$$

Where;
h_i = Instantaneous flow stress sample height (mm)
h_o = Initial flow stress sample height (mm)
d_i = Instantaneous die displacement (mm)

$$r_i = \sqrt{\frac{V}{\pi.h_i}} \tag{5.2}$$

Where;
r_i = Instantaneous flow stress sample radius (mm)
V = Flow stress sample volume (mm^3)

$$F_{corrected} = \frac{F_i}{1 + \frac{2.\mu.r_i}{3\sqrt{3}.h_i}} \tag{5.3}$$

Where;
$F_{corrected}$ = Friction corrected forging load (N)
F_i = Instantaneous measured forging load (N)
μ = Coefficient of friction between the die and flow stress sample

$$\varepsilon_{true} = \ln\left(\frac{h_o}{h_i}\right) \tag{5.4}$$

Where;
ε_{true} = True Strain

$$\sigma_{corrected} = \frac{F_{corrected}}{\pi r_i^2} \tag{5.5}$$

Where;
$\sigma_{corrected}$ = Friction corrected true flow stress (MPa)

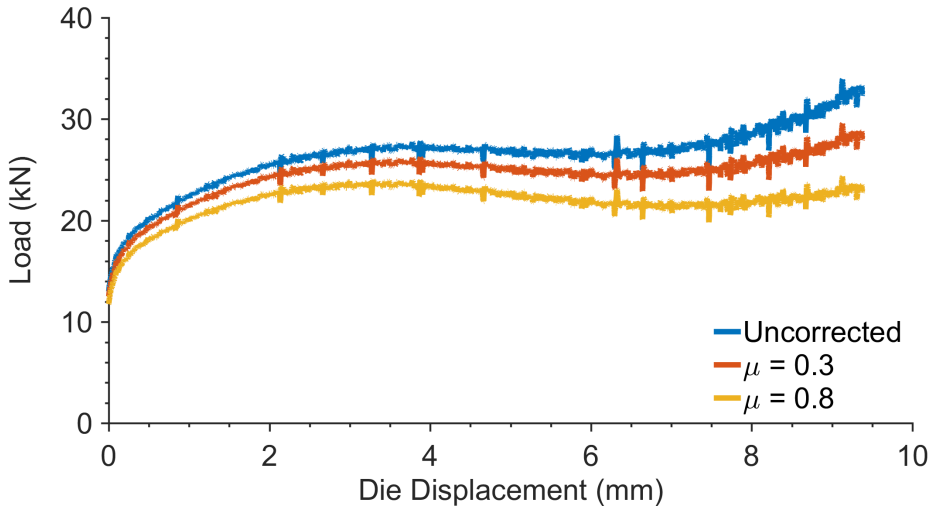

Figure 5.11: Example load vs stroke curves with varying degrees of friction correction for a hot compression test performed using a 131027 post HIP sample at 1000°C at a strain rate of 0.01s.$^{-1}$. The test was performed using the TMC apparatus.

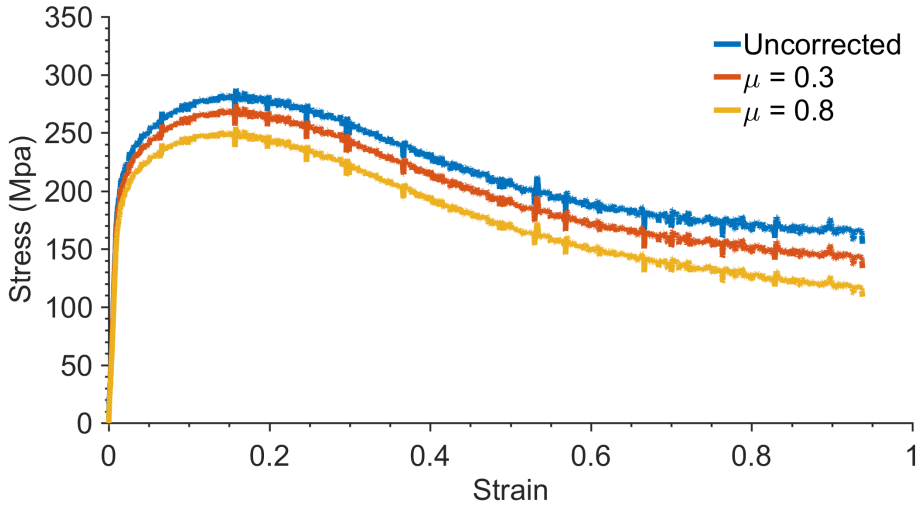

Figure 5.12: Example flow curves with varying degrees of friction correction for a hot compression test performed using a 131027 post HIP sample at 1000°C at a strain rate of $0.01s^{-1}$.

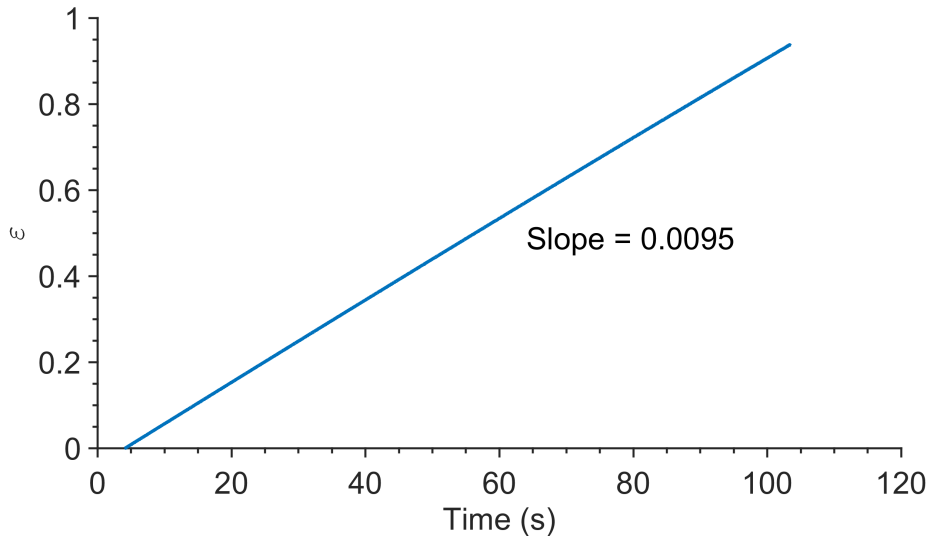

Figure 5.13: Strain rate vs time plot for a compression test conducted on the TMC apparatus at a target strain rate of $0.01s.^{-1}$, the test was performed at 1000°C. The slope calculation reveals that the actual strain rate for the test was $0.0095s^{-1}$, which closely matches the target strain rate of $0.01s^{-1}$.

5.3.4 Gleeble Output Data and Flow Curve Production

Similar to the TMC, the Gleeble 3800 can output time, load, die displacement and sample temperature data. No die velocity data is available from the Gleeble directly and must be calculated. An example of the data outputted by the Gleeble for a typical test are shown in Figures 5.14 to 5.16.

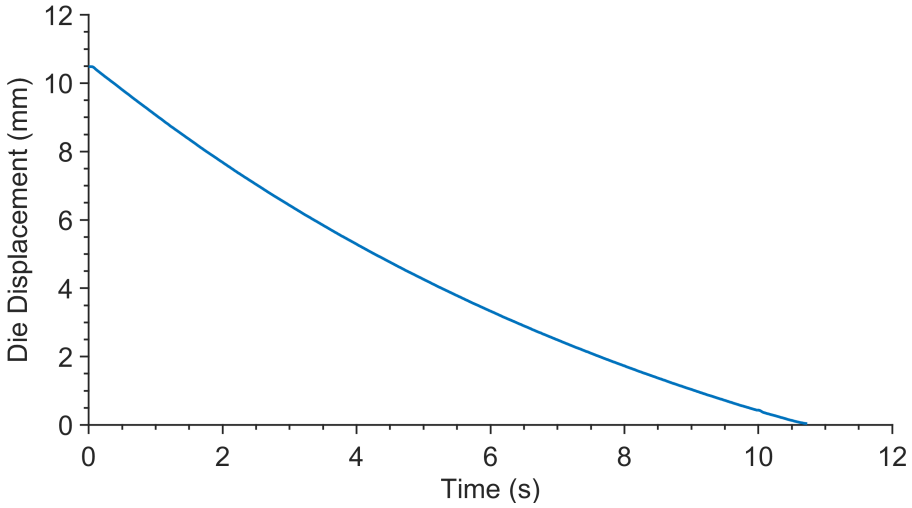

Figure 5.14: Example displacement vs time data produced by the Gleeble 3800. The test used for comparison was performed on the Gleeble 3800 at a temperature of 1100°C and a strain rate of $0.1s^{-1}$.

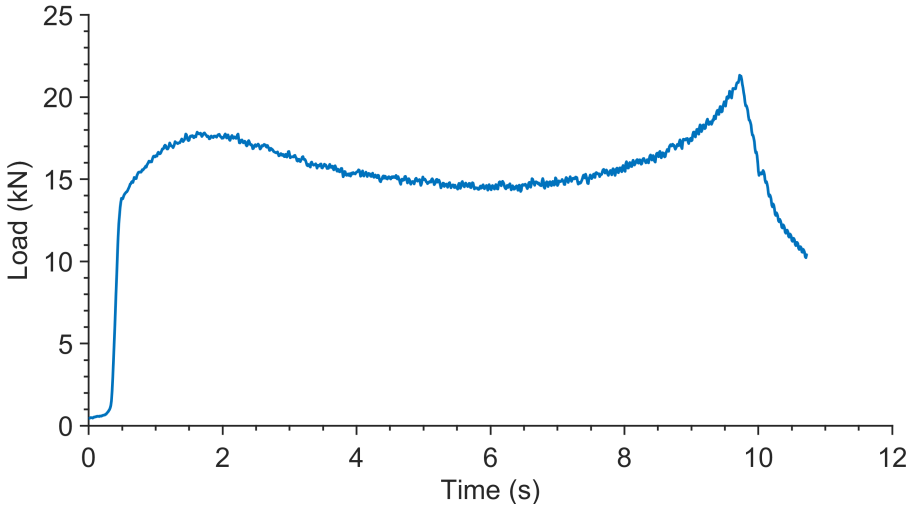

Figure 5.15: Example Load vs time data produced by the Gleeble 3800. The test used for comparison was performed on the Gleeble 3800 at a temperature of 1100°C and a strain rate of $0.1s^{-1}$.

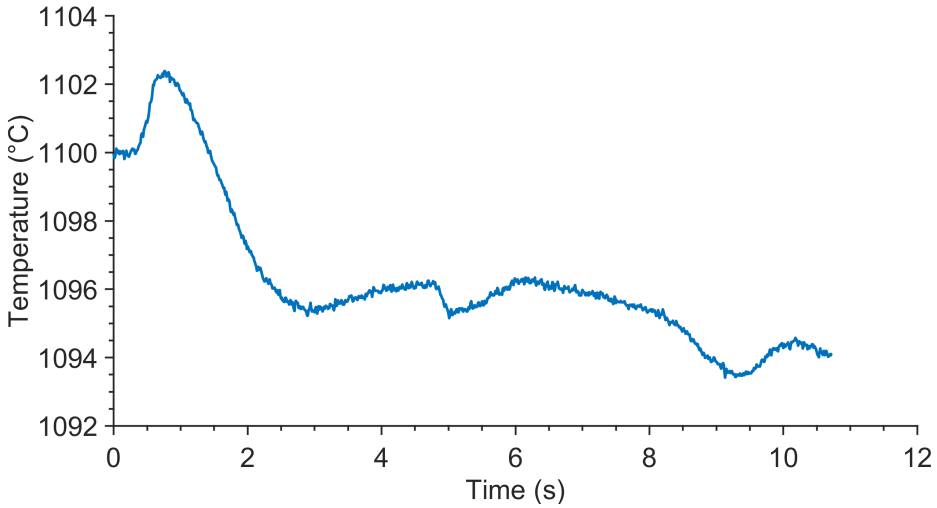

Figure 5.16: Example temperature vs time data produced by the Gleeble 3800. The test used for comparison was performed on the Gleeble 3800 at a temperature of 1100°C and a strain rate of $0.1s^{-1}$.

In contrast to the data collected via the TMC, the Gleeble 3800 control unit directly converts the physically measured load and stroke variables into stress vs strain curves. The Gleeble control unit computes the stress and

strain using the sample starting dimensions and the constancy of volume relationship to estimate the sample diameter during the forging operation at each time step. This is then used to convert the measured load into stress. The strain is calculated using the measured specimen height via die displacement. In order to ensure that the outputted stress vs strain data from the Gleeble is reliable enough to be used directly, the outputted flow curve was compared to a curve post processed from loads vs displacement data using Equations 5.1 to 5.5. It can be observed that the curves match with slight differences in the stress and strain apparent in Figure 5.17. The Gleeble output flow curve is calculated based on the hot dimensions of the specimens while the calculated flow curve relies on empirical determination of the hot dimensions. The errors in the thermally expanded dimensions of the specimen likely give rise the error in the calculation of the completed strain. This error is only noteworthy at high strains, after which it is assumed little microstructural change will have taken place. The error was therefore accepted and not investigated further.

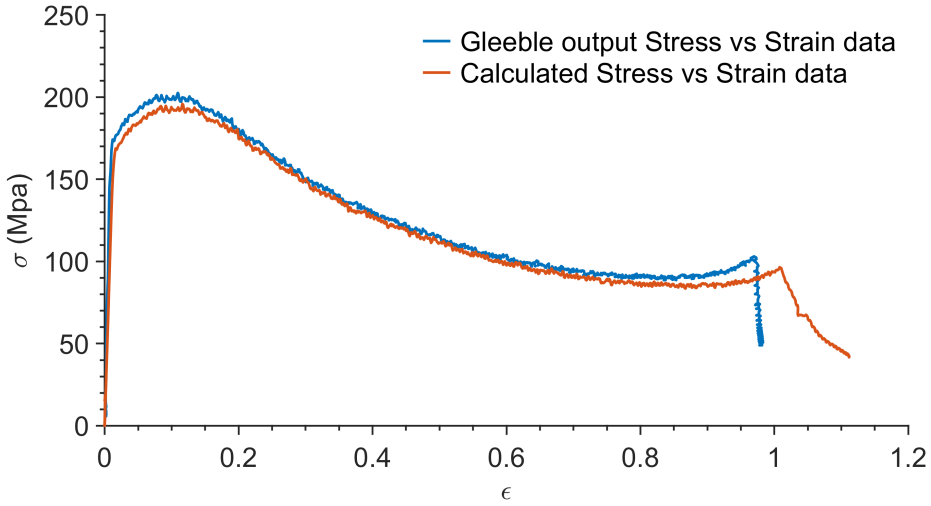

Figure 5.17: Comparison of flow curves produced directly from the Gleeble 3800 and a curve produced in post processing from the raw load vs stroke data (using the same method as that used to produce flow curves from TMC data). The test used for comparison was performed on the Gleeble 3800 at a temperature of 1100°C and a strain rate of $0.1s^{-1}$.

The strain rate can also be examined by using the technique of plotting strain vs time as discussed previously. The strain rate behaviour of the Gleeble is discussed at length in section 5.4.2.

5.3.5 Isothermal Correction

Analysis of the captured flow stress curves during forging infers dynamic restoration processes and microstructural evolution during the compression tests. However, it is first necessary to correct for temperature change during the forging to have a true understanding of a materials deformation behaviour at a given temperature. Due to competing sample cooling and heat generation caused by the deformation and friction, the sample temperature will change throughout the compression test. This means that the friction corrected flow curves displayed in Figure 5.12 are not truly representative of an isothermal compression test. The shape of the flow stress curve can provide information regarding the microstructural change that occurs during hot compression, and therefore it is important to view the true flow stress curve at constant temperature and strain rate in order to isolate the effect of microstructural change on flow stress. Two correction techniques for correcting fluctuations in temperature were explored during this work as presented in the following sections.

Activation Energy Based Approach to Isothermal Correction

According to the work of Thomas [125], One way to account for the change in material temperature during forging is to calculate the activation energy for hot deformation for the material which then aids the production of constitutive equations to describe the flow stress of the material for given conditions. These equations can then be used to adjust the flow stress according to instantaneous changes in temperature due to deformation heating and sample cooling during testing. In order to perform this correction, Equation 5.6 can be employed as presented by Thomas [125]. The use of this equation required the calculation of the parameters Q_{def} (the activation energy for hot deformation) and β (a fitting parameter) must first be determined.

In order to simplify the process of isothermal correction, the raw flow stress curves were discretised by extracting the flow stress values at specific strain points during the test, the stress values at chosen strain levels were calculated by linear interpolation between the data points closest to the chosen strain. This approximation was deemed to have very little effect on the accuracy of the analysis due to the sufficiently high sampling rate of the testing performed which was above a minimum of 1000Hz for both compression test apparatus used. An example of discretised flow curves can be seen in Figure 5.18.

$$\sigma_{iso} = \sigma + \frac{Q_{def}}{\beta R}\left(\frac{1}{T_i} - \frac{1}{T_{iso}}\right) \tag{5.6}$$

Where;
σ_{iso} = Isothermal flow stress (MPa)
σ = Measured flow stress (MPa)
Q_{def} = Activation energy for hot deformation (J/mol)
β = Isothermal correction fitting coefficient
R = Universal gas constant (8.314 J/mol)
T_i = Instantaneous flow stress sample temperature (K)
T_{iso} = Desired isothermal flow stress temperature (K)

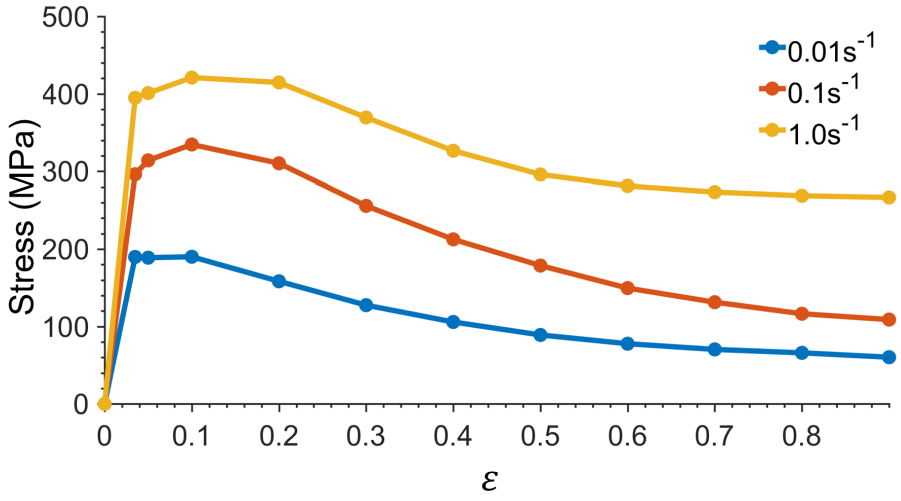

Figure 5.18: Example raw stress vs strain curves captured for a range of strain rates at a deformation temperature of 1050°C using the Gleeble 3800.

To determine the activation energy of hot deformation for the alloy 131072, the Zener-Holloman parameter is first determined. The flow stress is proportional to some function of the Zener-Holloman parameter, as described in Equation 5.7. The Zener-Holloman parameter can be equated to the strain rate $\dot{\varepsilon}$, the activation energy for hot deformation Q_{def}, the temperature T and the universal gas constant R. This relationship can be manipulated by fixing the flow stress, for a fixed strain σ_ε and the strain rate $\dot{\varepsilon}$ such that Equation 5.8 is true and allows the calculation of Q_{def} by plotting $\ln(\dot{\varepsilon})$ against $1/T$

and determining the gradient. In order to plot the required graph to calculate the activation energy, the $ln(\dot{\varepsilon})$ value must first be calculated for a fixed flow stress value for each temperature. This is achieved by plotting $ln(\dot{\varepsilon})$ against σ for a fixed strain value as shown in Figure 5.19. The slope and intercepts calculated in Table 5.2 can be used to build a matrix of σ vs $\ln(\dot{\varepsilon})$ for all temperatures tested as shown in Table 5.3. Plotting $\ln(\dot{\varepsilon})$ vs $1/T$ (Figure 5.20) allows the slope and intercept of $\ln(\dot{\varepsilon})$ vs $1/T$ to be determined, which can be used in Equation 5.8 to determine the activation energy (Q_{def}) for each chosen strain value. The Q_{def} values for a fixed strain of 0.8 and a range of stresses are shown in Table 5.4. Table 5.4 reveals that the activation energy changes as a function of stress which can be expected as higher stress levels implying a greater resistance to deformation and therefore higher energy is required to initiate deformation. The process described can be repeated for different fixed strain values and it can be observed that increasing the strain value results in decreased activation energy. This is to be expected as the flow curves generally peak at lower strains before decaying towards steady state values at higher strains. For this study the value was averaged over a strain range of 0.1-0.8 to give an activation energy of 706,813.48 J/mol, this value was used in all subsequent isothermal correction calculations.

$$\sigma_{\varepsilon} = B_{\varepsilon} f\left(Z\right) = B_{\varepsilon} f\left(\dot{\varepsilon} \exp\left(\frac{Q_{def}}{RT}\right)\right) \tag{5.7}$$

Where;
σ_{ε} = Flow stress for a fixed strain value (MPa)
B_{ε} = Fitting parameter for a fixed strain value
Z = Zener-Holloman parameter
$\dot{\varepsilon}$ = strain rate (s^{-1})
T = Deformation temperature (K)

$$\ln \dot{\varepsilon} = \ln \sigma - \frac{Q_{def}}{RT} \tag{5.8}$$

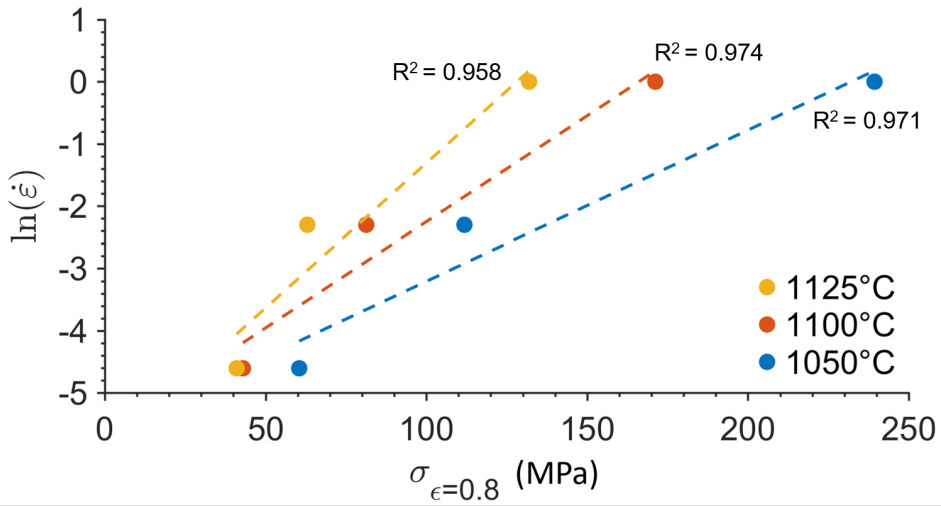

Figure 5.19: Graph of $\ln(\dot{\varepsilon})$ vs σ at for a strain of $\varepsilon = 0.8$, used to determine required strain rate to produce a given flow stress value at a particular temperature at the given strain value.

Table 5.2: Calculated slope and intercept from the data in Figure 5.19, used to determine the strain rate required to produced a given flow stress for a fixed strain and temperature.

Temperature (K)	Slope of $\ln(\dot{\varepsilon})$ vs σ	Intercept of $\ln(\dot{\varepsilon})$ vs σ
1323	0.024274321	-5.63347951
1373	0.034074574	-5.658680983
1393	0.046504467	-5.959989746

Table 5.3: Interpolated $\ln(\dot{\varepsilon})$ values for fixed stress values at a fixed strain for a range of 1/T values, using the slope and intercept value calculated in Table 5.2

	Interpolated $\ln(\dot{\varepsilon})$ values		
	$1/T$ (K^{-1})		
Stress (Mpa)	0.000755858	0.000728332	0.000715308
125	-2.599189352	-1.399359253	-0.146931344
140	-2.235074533	-0.888240646	0.550635665
155	-1.870959714	-0.377122038	1.248202673
170	-1.506844895	0.133996569	1.945769681
185	-1.142730076	0.645115177	2.643336689
200	-0.778615257	1.156233785	3.340903698

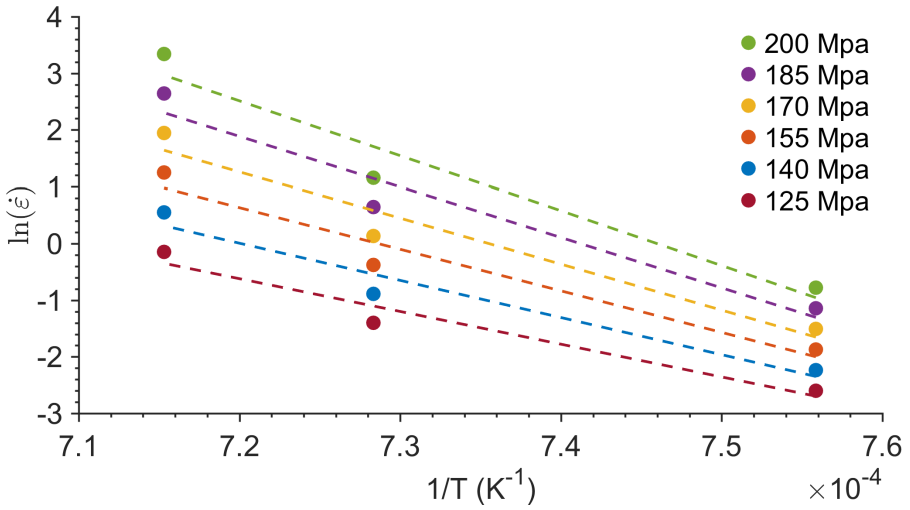

Figure 5.20: Graph of $\ln(\dot{\varepsilon})$ vs $1/T$ for a range of flow stress values using data extracted from Table 5.3. The slope of each line of best fit can be used to determine the activation energy as per Equation 5.8.

Table 5.4: Calculated slope and Q_{def} values fora fixed strain of 0.8 and a range of fixed stress values using the curves calculated curves in Figure 5.20.

Stress value (Mpa)	Slope	Q_{def} (J/mol)
125	-57,853.612	480,994.93
140	-65,629.361	545,642.51
155	-73,405.110	610,290.08
170	-81,180.859	674,937.66
185	-88,956.608	739,585.23
200	-96,732.356	804,232.81
Average Q_{def} (J/mol)		642,613.87

Table 5.5: Calculated Q_{def} values for a range of fixed strain values, averaged over a range of stress values.

ε	Q_{def} (J/mol)
0.1	771,993.28
0.2	768,005.49
0.4	710,573.82
0.6	640,880.90
0.8	642,613.87
Average	706,813.48

Once the activation energy has been determined, constitutive equations presented in [125] can be used to determine the β coefficient. The flow stress can be related to the Zener-Holloman parameter using Equations 5.9, 5.10 and 5.11. Equation 5.9 is valid when ε values are low and Equation 5.10 is more applicable when ε values are high. Equation 5.11 is applicable over a large range of strain values.

$$Z = \dot{\varepsilon} \exp\left(\frac{Q_{def}}{RT}\right) = a_1 \sigma^n \tag{5.9}$$

$$Z = \dot{\varepsilon} \exp\left(\frac{Q_{def}}{RT}\right) = a_2 e^{(\beta\sigma)} \tag{5.10}$$

$$Z = \dot{\varepsilon} \exp\left(\frac{Q_{def}}{RT}\right) = a(\sinh \alpha\sigma)^n \tag{5.11}$$

Where;
a_1, n, a_2, β, a and α are fitting parameters

Manipulation of Equation 5.10 to form Equation 5.12 allows the determination of the β coefficient. This involves calculating the Zener-Holloman parameter via the activation for all strain rates and finding the gradient of the linear relationship between $\ln(Z)$ and σ as shown in Figure 5.22, for a low strain value which allows the determination of the n and a_1 coefficients. Subsequently plotting $\ln(Z)$ against σ, for a high strain value allows the α_2 and β coefficients to be determined. The β coefficient can then be used to correct the flow stress curves for changes in temperature as per equation 5.6. The β coefficient was determined to be equal to 0.0347 which was used in all isothermal correction calculations. It is expected that the β value will change with changing strain, however for the simplicity of analysis a constant value will be employed which prevents the need for holistic determination of the variables required to calculate the isothermally corrected stress at all stress points. The calculated Q_{def} value was used to correct the flow curves for temperature fluctuations using Equation 5.6.

$$\ln(Z) = \beta\sigma + \ln(a_2) \tag{5.12}$$

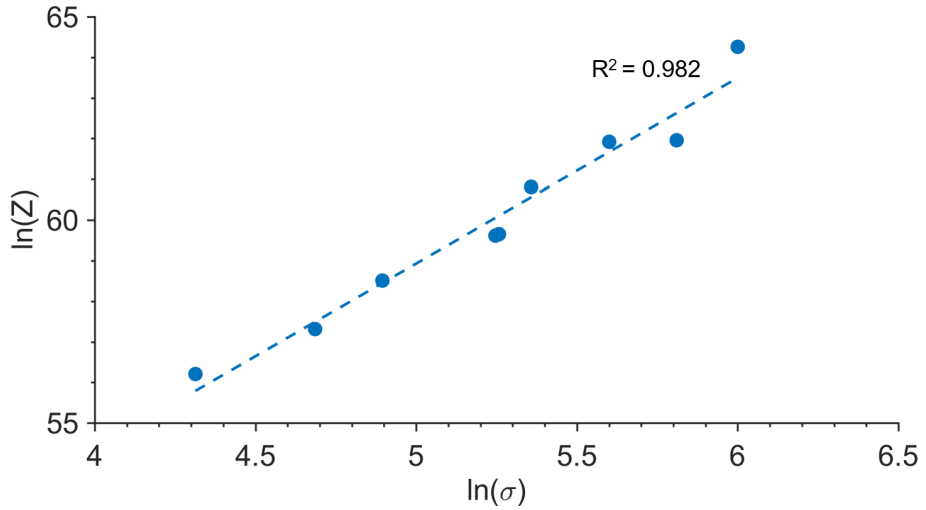

Figure 5.21: Plot of $\ln(Z)$ vs $\ln(\sigma)$ for a low strain value of $\varepsilon = 0.1$. The slope and intercept of this graph can be used to determine the coefficients n and a_1 as per Equation 5.9.

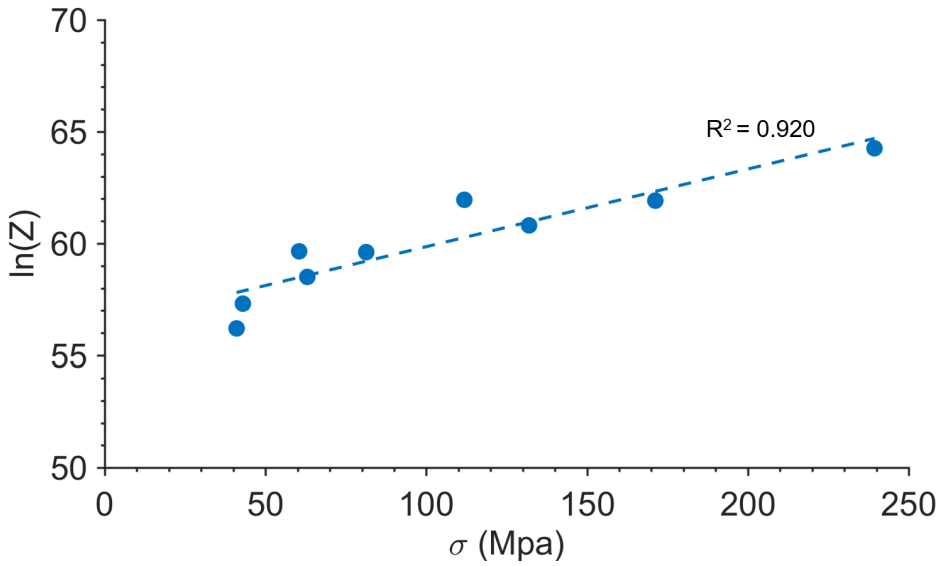

Figure 5.22: Plot of $\ln(Z)$ vs σ for a high strain value of $\varepsilon = 0.8$. The slope and intercept are used to determine the coefficients β and a_2 as per Equation 5.10.

Linear Interpolation Approach

An alternative method for isothermal correction was presented by Dieter et al [126]. According to this method, the change in flow stress with temperature for a fixed strain and strain rate can be reasonably approximated by assuming that a linear relationship exists between stress and temperature. Determining this relationship for all strains and strain rates covered, the isothermal correction is performed according to Equation 5.13.

$$\sigma_{iso} = \sigma + dT_{iso}.\left.\frac{d\sigma}{dT}\right|_{\dot{\varepsilon},\varepsilon} \tag{5.13}$$

Where;
σ_{iso} = Isothermally correction flow stress (MPa)
σ = Uncorrected, measured flow stress (MPa)
dT_{iso} = T_{iso} - T
T_{iso} = Isothermal deformation temperature
T = Instantaneous measured temperature
$\dot{\varepsilon}$ = Strain rate (s^{-1})
ε = True strain

In order to determine the $d\sigma/dT$ operator in Equation 5.13 it is necessary to first produce a database of friction corrected flow stress values at specific strain points, as shown in Table 5.6. Once this has been performed a linear relation can be formed between stress and temperature for each strain rate and strain value, an example of which is given in Figure 5.23. This allows the formation of a database of $d\sigma/dT$ values to be used in Equation 5.13. Equation 5.13 can then be applied for each data point in the uncorrected flow stress database.

Table 5.6: Friction corrected flow stress values (given in MPa) as a function of strain, strain rate and temperature for the range of conditions tested using the Gleeble 3800.

	Strain rate $\dot{\varepsilon}$								
	$0.01s^{-1}$			$0.1s^{-1}$			$1s^{-1}$		
	Temperature °C			Temperature °C			Temperature °C		
Strain	1050	1100	1125	1050	1100	1125	1050	1100	1125
0.000	0.00	0.00	0.00	0.00	0.00	0.00	0.00	0.00	0.00
0.035	186.73	115.43	76.10	292.01	179.83	131.37	391.94	265.56	208.84
0.050	195.43	110.23	76.83	309.18	184.58	133.27	394.21	269.38	209.81
0.1	191.98	108.36	74.68	333.66	189.86	133.59	403.44	270.51	212.20
0.2	158.41	92.31	67.23	321.42	171.63	118.24	380.90	242.74	188.11
0.3	126.18	77.19	58.73	264.63	139.84	106.05	330.36	212.05	171.76
0.4	103.31	64.06	50.24	217.53	121.03	94.41	289.43	192.57	161.06
0.5	85.89	54.57	44.29	181.04	106.61	81.96	262.80	182.62	150.09
0.6	73.65	49.61	39.34	150.80	94.91	73.60	250.76	179.75	142.48
0.7	65.69	45.59	37.58	129.59	86.08	65.87	243.18	176.05	136.22
0.8	60.46	42.96	41.00	111.83	81.32	62.99	239.37	171.21	131.94
0.9	62.51	45.60	45.58	101.63	80.53	74.24	237.30	166.25	139.37

Table 5.7: Actual measured temperatures (given in °C) at varying strain points during deformations for the range of conditions tested on the Gleeble 3800.

	Strain rate $\dot{\varepsilon}$								
	$0.01s^{-1}$			$0.1s^{-1}$			$1s^{-1}$		
	Temperature °C			Temperature °C			Temperature °C		
Strain	1050	1100	1125	1050	1100	1125	1050	1100	1125
0	1049.99	1100.11	1125.13	1050.03	1099.97	1125.74	1049.98	1100.19	1124.92
0.035	1051.71	1101.17	1124.46	1052.46	1102.26	1125.73	1052.35	1101.65	1126.11
0.05	1048.29	1098.92	1124.46	1052.54	1102.16	1125.52	1053.42	1102.44	1127.03
0.1	1049.61	1099.37	1124.60	1050.70	1100.30	1124.24	1056.19	1104.16	1128.58
0.2	1049.69	1099.62	1124.84	1045.62	1096.29	1121.71	1060.93	1106.23	1129.51
0.3	1049.74	1099.72	1124.90	1044.63	1095.71	1121.28	1064.22	1107.50	1129.29
0.4	1049.83	1099.79	1124.88	1044.52	1095.96	1121.72	1064.96	1107.41	1128.19
0.5	1049.82	1099.90	1124.96	1044.33	1095.35	1121.76	1063.50	1106.40	1126.10
0.6	1050.02	1099.99	1124.91	1043.74	1096.22	1120.92	1061.33	1104.84	1123.89
0.7	1049.97	1100.10	1124.95	1044.70	1095.88	1120.80	1059.25	1102.26	1121.42
0.8	1049.99	1099.83	1124.84	1045.62	1095.37	1120.95	1056.18	1099.64	1119.02
0.9	1041.06	1100.07	1124.82	1045.98	1093.81	1120.47	1052.70	1096.77	1116.69

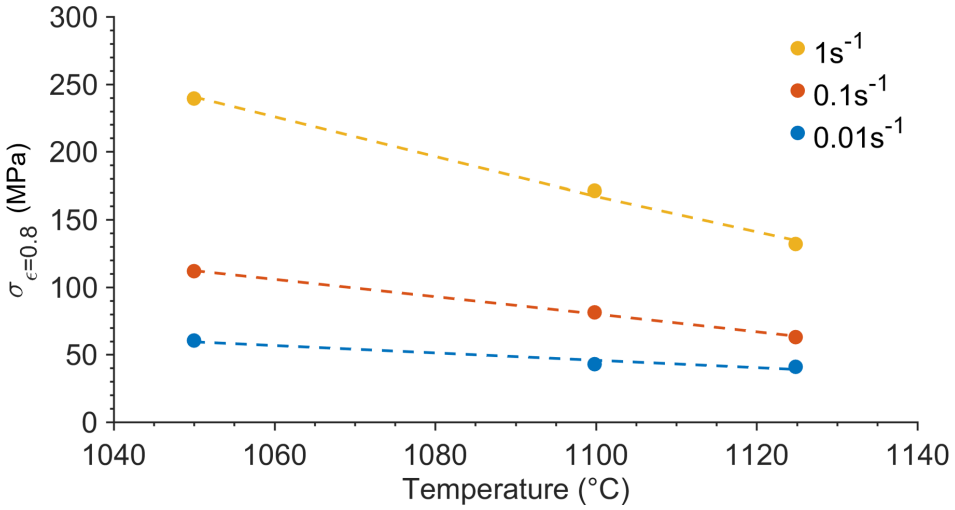

Figure 5.23: Graph of flow stress vs temperature for a fixed strain of 0.8 for all Gleeble tested strain rates. The linear relationship between stress and temperature is used to estimate isothermal flow stress values for each strain rate.

Table 5.8: Calculated $d\sigma/dT$ values for the flow stress data presented in Table 5.6, used to approximate the isothermal flow stress.

	$d\sigma/dT$		
	Strain rate $\dot{\varepsilon}$ (s^{-1})		
Strain	0.01	0.1	1
0	0	0	0
0.035	-1.51	-2.20	-2.49
0.05	-1.57	-2.43	-2.51
0.1	-1.58	-2.75	-2.66
0.2	-1.23	-2.71	-2.84
0.3	-0.91	-2.12	-2.48
0.4	-0.72	-1.63	-2.07
0.5	-0.56	-1.30	-1.81
0.6	-0.46	-1.01	-1.71
0.7	-0.38	-0.84	-1.69
0.8	-0.27	-0.64	-1.69
0.9	-0.22	-0.38	-1.54

Table 5.9: Example application of the linear isothermal correction described in Equation 5.13 for a fixed strain of 0.8 and a strain rate of $0.1s^{-1}$.

ε	$\dot{\varepsilon}$ (s^{-1})	T (°C)	T_{iso} (°C)	σ (MPa)	$d\sigma/dT$	dT_{iso} (°C)	$d\sigma$ (MPa)	σ_{iso} (MPa)
0.8	0.1	1095.37	1100	81.32	-0.64	4.63	-2.98	78.34

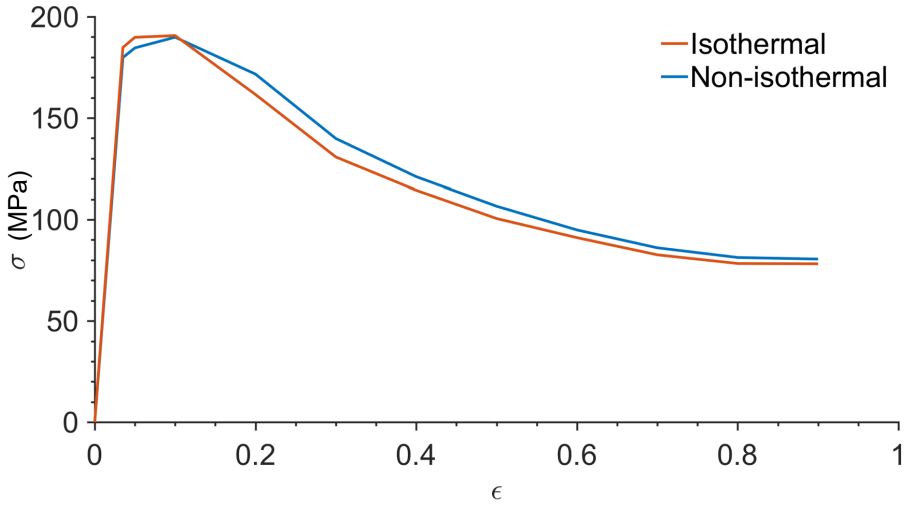

Figure 5.24: Comparison of the isothermally corrected and uncorrected flow stress curve for the test performed at 1100°C and a strain rate of 0.1 s^{-1} using the Gleeble 3800. Isothermal correction was performed using the linear interpolation approach.

An example of the application of Equation 5.13 can be seen in Table 5.9 and an example of how this changes the flow stress curve for a test conducted at 1100°C and a strain rate of $0.1s^{-1}$ is shown in Figure 5.24. The corrected flow stress values are very similar to the original flow data. This is expected as the temperature measured during the tests performed with the Gleeble apparatus closely match the target test temperature due to the heating applied during testing.

Comparison of Isothermal Correction Methods

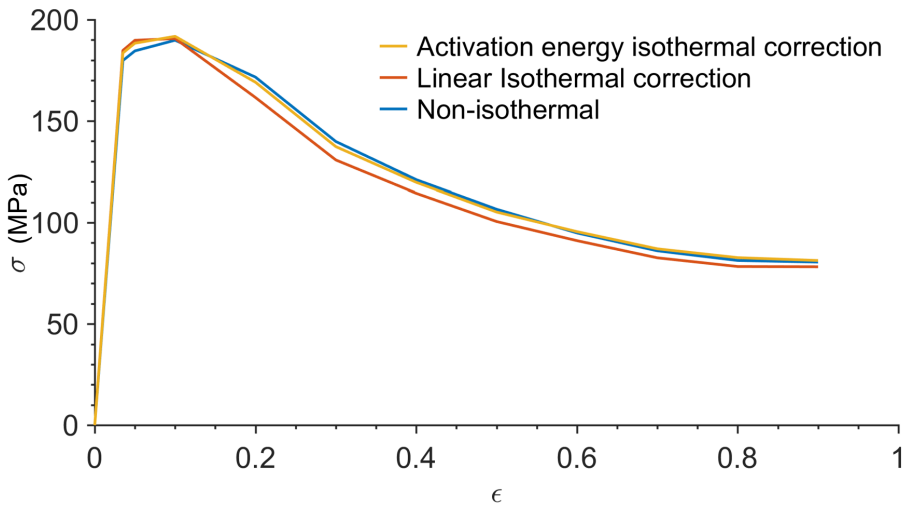

Figure 5.25: Comparison of the two isothermal correction methods examined, compared with the uncorrected flow stress curve for the test performed at 1100°C and a strain rate of 0.1^{-1} using the Gleeble 3800.

5.3.6 Two Step Deformation Tests

Recent work by Bockenstedt et al [127] showed that an increase in hot ductility can be achieved through first reducing the sample height by 30-35% and then reheating the sample to the hot deformation temperature at which the sample is deformed again to higher strain values. The results presented by Bockenstedt et al show that a vast improvement in hot ductility can be achieved using this method resulting in an improvement of forgeability. To investigate this affect, samples identical to those used to first perform a deformation step to a 30% reduction in height equating to a strain of (0.34). The first step of deformation was performed using a fixed temperature of 1100°C and a strain rate of $0.01s^{-1}$. For the second deformation stage, a 3x3 test matrix was examined using temperatures of 1050°C, 1100 °C and 1150°C and strain rates of $0.01s^{-1}$, $0.1s^{-1}$ and $1s^{-1}$. The Gleeble 3800 apparatus was used for these trials as there is a lesser risk of damaging the thermocouple between the two stages of deformation. This first deformation step was performed in an identical manner as described in section 5.3.2 for the Gleeble test procedure up until the compression is performed. For the two step tests the following procedure was followed;

- The sample was heated to and deformed to a strain of 0.34 (which

represents a 30% reduction in height) at 1100°C and a strain rate of $0.01s^{-1}$. As described previously, the process takes place under vacuum.

- Once the deformation was complete, the sample was allowed to cool under vacuum while held between the dies until the attached thermocouple registered a temperature of 200°C or less, which was timed to take approximately 4 minutes.
- The sample was then reheated to the target test temperature and held for five minutes to remove any temperature inhomogeneities in the sample.
- The second deformation was performed at the desired strain rate to the pre-programmed strain value.
- The sample was allowed to cool under vacuum to below 200°C after which the chamber was purged with argon allowing the sample to be removed.

Once the two step test had been performed, the stress vs strain behaviour for each deformation step was extracted. Each sample was photographed to reveal macroscopic features of the samples such as cracking and then sectioned for microstructural examination, as described in section 5.3.7. Alongside these tests, thermal history tests and interrupted compression tests were performed in order to determine the evolution of microstructure as a function of varying degrees of temperature as well as thermal exposures to indicate the changes occurring during heat up. A full list of the interrupted tests performed can be found in Table 5.10.

Table 5.10: List of interrupted hot compression tests performed on the as-HIP 131072 material, NA = Not applicable.

	Deformation conditions (First step/Second step)			
Test ID	Temperature	strain at completion	Strain rate	Cooling method
1	1100/NA	0.02/NA	0.01/NA	Quench/NA
2	1100/NA	0.03/NA	0.01/NA	Quench/NA
3	1100/NA	0.34/NA	0.01/NA	Air/NA
4	1100/NA	0.34/NA	0.01/NA	Quench/NA
5	1100/NA	0.15/NA	0.01/NA	Quench/NA
6	1100/1100	0.34/0.65	0.01/0.01	Air/Air
7	1100/1100	0.34/0.65	0.01/0.01	Air/Quench
8	1100/NA	0/NA	0/NA	Quench/NA
9	1100/NA	0/NA	0/NA	Air/NA

5.3.7 Microstructural Examination of Samples Post Compression Testing

Samples subjected to both the single and two stage compression tests were processed by first measuring the post deformation sample diameter and then using this measurement to determine the mid point of the sample. A Struers Secotom 50 linear traversing sectioning saw was used to cut the sample close to the midpoint of the sample, the thickness of the cut section was then measured. The sectioned sample was then mounted in Conductimet mounting compound. the thickness of the sample after mounting was measured and used to determine the differential between the midpoint of the original sample and the cut thickness. The thickness of the mounted sample was then measured after grinding and polishing to ensure that the revealed microstructure was as representative of the cross section of the sample as closely as practicably possible.

Once ground and polished to a mirror finish the samples were imaged using backscatter electron imaging, using an FEI Inspect F scanning electron microscope. Images were taken at 2 mm intervals horizontally from the left hand edge of the mounted sample to reveal the change in microstructure with the imparted strain profile. Images were also taken at 1 mm vertical intervals to reveal the variation in microstructure from top to bottom. The benefit of using this approach is that the level of symmetry can be assessed which can give indications of any inhomogeneity in sample temperature and differences

in friction etc. at each of the two die interfaces. A schematic showing the positions of the captured micrographs for each compression test sample is shown in Figure 5.26.

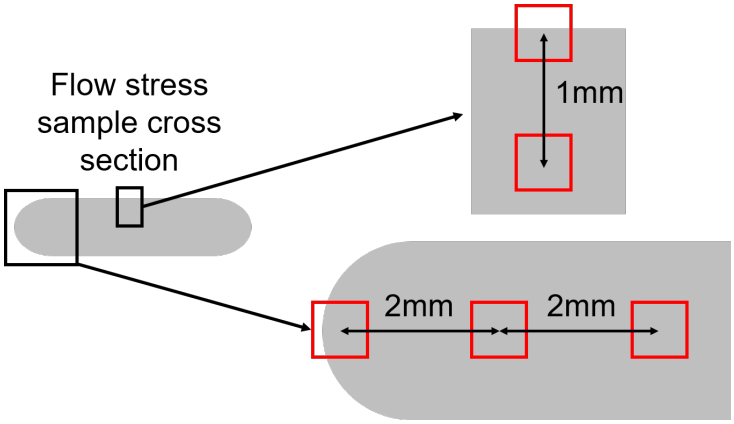

Figure 5.26: Diagram showing the micrograph locations captured for the as prepared flow stress sample cross sections.

To reveal the nature of the γ' precipitates each flow stress sample was subjected to a Kalling's waterless reagent etchant before being imaged using scanning electron microscopy in secondary electron mode.

5.4 Results and discussion

5.4.1 Analysis of Flow Stress Curves

Figures 5.27, 5.28 and 5.29 show the friction corrected and isothermally corrected flow curves for alloy 131072 in the post HIP material condition, collected using the Gleeble 3800. As expected, the flow stress was found to reduce significantly with decreasing strain rates and increasing deformation temperature. The reduction in flow stress is less severe when comparing the flow behaviour at 1100°C and 1125°C compared with the change observed between 1050°C and 1100°C. The reason for this may be due to the change in precipitate volume fraction and morphology as the deformation temperature approaches the γ' dissolution temperature range. This would allow grain growth to occur which would in turn change the deformation mechanisms activated during the compression test.

By analysing the flow curves shown in Figure 5.27 for tests conducted at 1050°C, it can be seen that the stress rapidly raises to a peak value, followed by a gradual decrease in flow stress with increasing strain. This behaviour

was seen for all strain rates and is indicative of recovery mechanisms being active during deformation and increasing strain input. For strain rates of $0.01.s^{-1}$ and $1.s^{-1}$, it can be observed that a steady state flow stress is achieved, whereby the flow stress for the compression performed at a strain rate of $0.1.s^{-1}$ experiences continuous flow softening, with no steady state flow stress achieved. It is likely that this effect is related to the balance between adiabatic heating which will act to decrease the flow stress and the reduced time for recovery to occur. The continuous flow softening is indicative that the balance is shifted towards recovery mechanisms likely enhanced by the increase in adiabatic heating compared with the slower strain rate of $0.01s^{-1}$. For the relatively high strain rate test performed at $1s^{-1}$, it is likely that the rapid increase in dislocation density due to deformation acts to counter the reduction in flow stress due to adiabatic heating. This leads to microstructural recovery cycles which act to produce a steady state flow stress. All strain rates produced a peak stress value at strains between 0.1-0.2 for a deformation temperature of 1050°C, indicating that recovery mechanisms begin at low strain values. It can be inferred that microstructural change will have taken place before the deformation completes.

Figures 5.28 and 5.29 reveal a similar trend, however it can be seen that increasing deformation temperatures reduces the magnitude of the peak stress with respect to steady state flow stress at high strain as temperatures increase. This behaviour clearly demonstrates the material softening at elevated temperatures at all strain rates examined. It can also be observed that the position of the peak stress does not shift with increasing temperature for each of the strain rates, this suggests that the onset of recovery mechanisms is independent of deformation temperature and relies instead on a critical level of strain before recovery commences. This strain value will correspond to the particular dislocation density required to initiate dynamic recovery and dynamic recrystallisation. Considering the flow stress behaviour outlined in Figures 5.27, 5.28 and 5.29, it can be inferred that the material exhibits typical behaviour with regards to flow stress, a prominent peak occurring at low strain, softening at intermediate strain, before reaching steady state at high strain. According to the flow stress data, the material presents the least resistance to deformation when the strain rates are as low as possible and the deformation temperature is as high as possible provided the material does not exceed the γ' solvus. Testing at 1150°C revealed that gross cracking occurs which prevents strains of 1.0 from being reached. This is a clear indication that exceeding the γ' solvus results in a decrease in ductility. Therefore care should be taken to avoid this phase transformation to maximise forgeability.

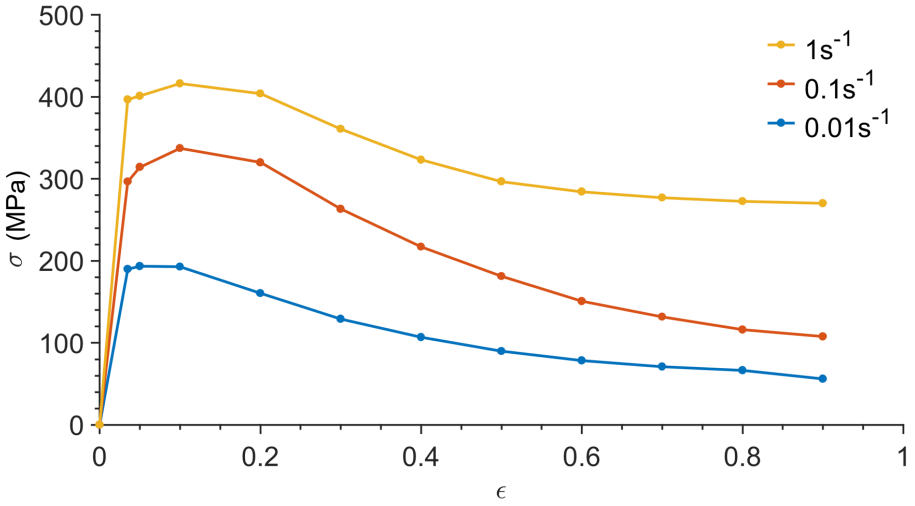

Figure 5.27: Isothermally corrected flow data for the compression tests performed using the Gleeble apparatus at 1050°C.

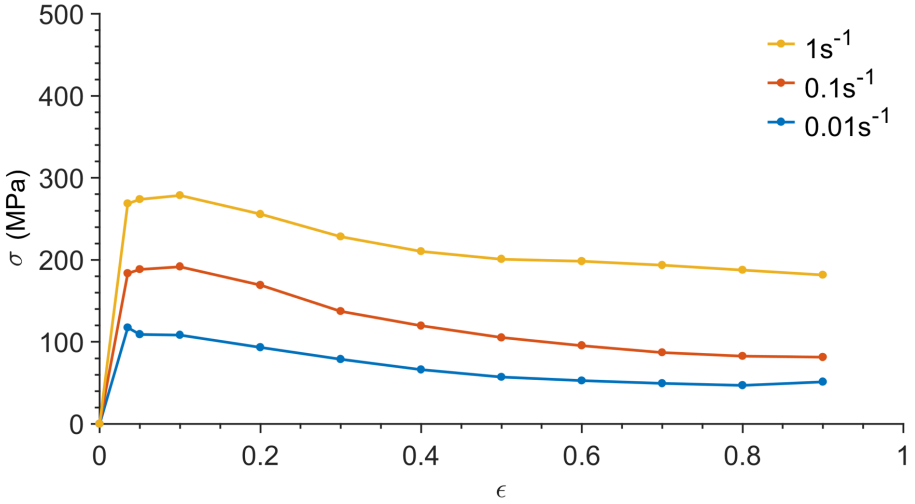

Figure 5.28: Isothermally corrected flow data for the compression tests performed using the Gleeble apparatus at 1100°C.

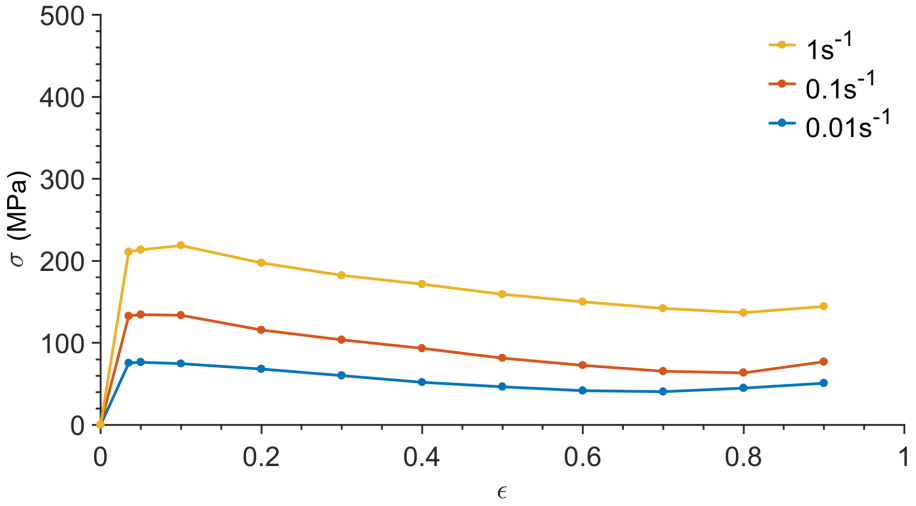

Figure 5.29: Isothermally corrected flow data for the compression tests performed using the Gleeble apparatus at 1125°C.

5.4.2 Observed Stress Spike for Low Strain Rate Gleeble Testing

Upon analysis of the low strain rate tests conducted using the Gleeble apparatus, it was noted that there was a spike in flow stress curves produced from test conducted at $0.01s^{-1}$ at low strain values. The unexpected spike at low strain values for all tests conducted at 0.01 s^{-1} is shown in Figure 5.30. The strain is plotted as a function of time to reveal the strain rates for these tests, as shown in Figure 5.31. It can be seen that at the start of the three 0.01 s^{-1} test displayed in Figure 5.31, the strain rate is much higher than the desired rate and for the tests performed at 1050°C and 1100°C. A shift in strain rate rate can be seen at strain values of approximately 0.034 wherein the strain rate slows to match the target strain rate of $0.01s^{-1}$, as evident by the change in gradient of the strain vs time curves. In Figure 5.30, it can be seen that the stress drops significantly once the strain reaches 0.034, this is clear evidence that the increased strain rate at the start of the test is the cause of the spike in flow stress. The same effect can be seen for the test conducted at 1125°C albeit the transition back to the correct strain rate occurs at a lower strain of approximately 0.016.

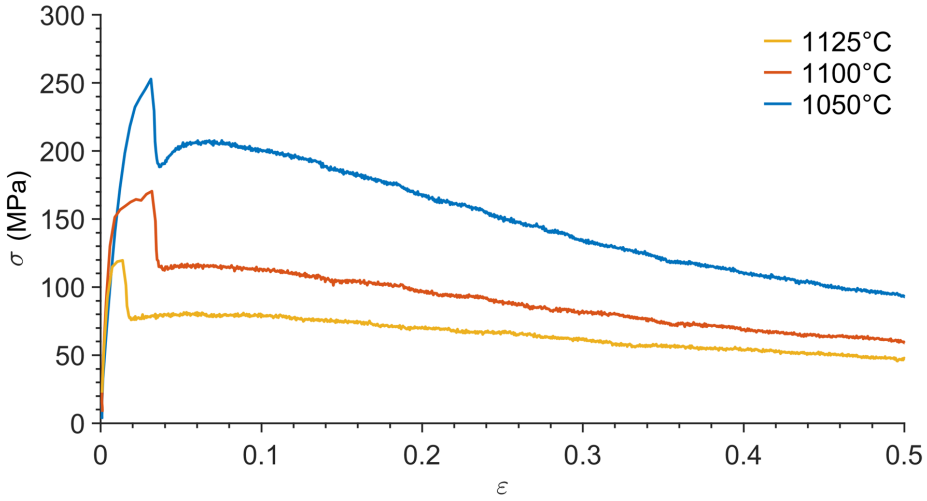

Figure 5.30: Uncorrected flow stress curves from tests conducted on using the Gleeble 3800 for low strain rates ($0.01s^{-1}$). Only data up to strains of 0.5 shown. Graph shows unusual stress spikes at low strain values, only witnessed when performing tests on the Gleeble at low strain rates.

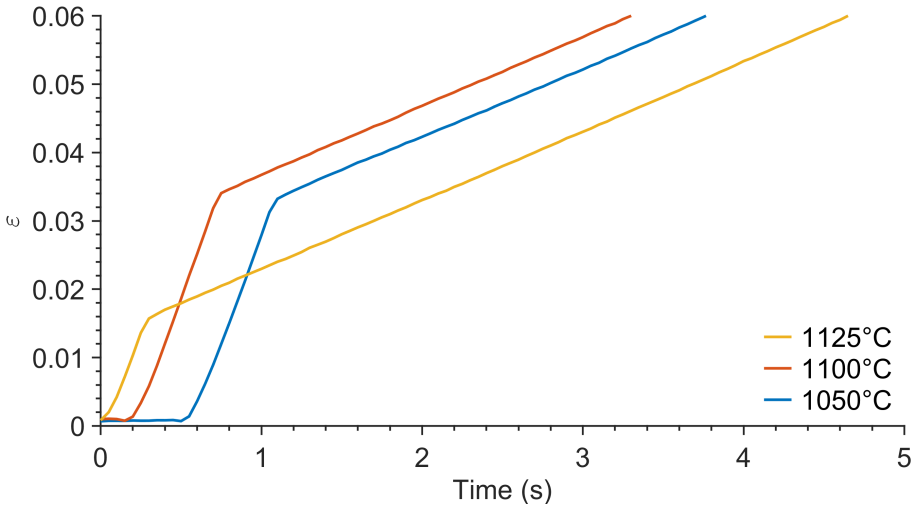

Figure 5.31: Strain vs time plots for tests performed on the Gleeble with target strain rates of $0.01s^{-1}$ for all temperatures tested. Plot shows a shift in strain rate that occurs at strain values concurrent with the stress spikes seen in Figure 5.30.

Although this will inevitably affect the accuracy of the collected flow

stress data, this phenomenon is confined to the start of the test, unlike the load drop seen in the TMC tests further discussed in section 5.4.3. It was therefore decided that the data would be reviewed as planned and data from strains of 0.035 onwards would be considered and data would be interpolated between zero stress and zero strain and flow stress measured at 0.035 strain.

Although this situation prevents complete analysis of the flow curves in this region, it was decided that this approach would be sufficient to make comparisons between the collected flow stress curves and make inferences regarding the resultant as forged microstructure. Initial investigations regarding the Gleeble 3800 concluded that the cause of the error was a mechanical fault with the die actuator linkage at low strain rates. This effect was not seen for higher strain rate tests performed at $0.1s^{-1}$ and $1s^{-1}$. The diagnostic process and retesting of the $0.01.s^{-1}$ tests was not possible within the scope of this work.

5.4.3 Sources of Error with the TMC Testing

In a manner similar to the Gleeble compression tests, the tests that were performed on the TMC were analysed for any potential sources of error which may have produced an erroneous forging in such a way as to potentially affect the as forged microstructure. Examination of the post processed stress vs strain curves for TMC tests conducted at 1000°C to 1050°C revealed that the tests conducted at strain rates at $1s^{-1}$ and above contained a discrepancy at a strain of approximately 0.16 whereby there was a sudden drop in stress, as shown in Figure 5.32 and Figure 5.33. This was apparent for tests conducted in the temperature range of 1000-1050°C. Investigations into this effect did not reveal the route cause of the issue. Plotting of the strain vs time for the strain rates below 1 s^{-1} revealed that the strain rate is well controlled (Figure 5.34). However a noticeable deviation in strain rate can be observed for an example test conducted at 1 s^{-1} (Figure 5.35). Not only does the strain rate deviate but the tool is actually reversed at a strain of 0.16. The consistency of this error pointed to a mechanical issue that could not be identified. This cast doubt on the measurement of tool displacement and therefore strain.

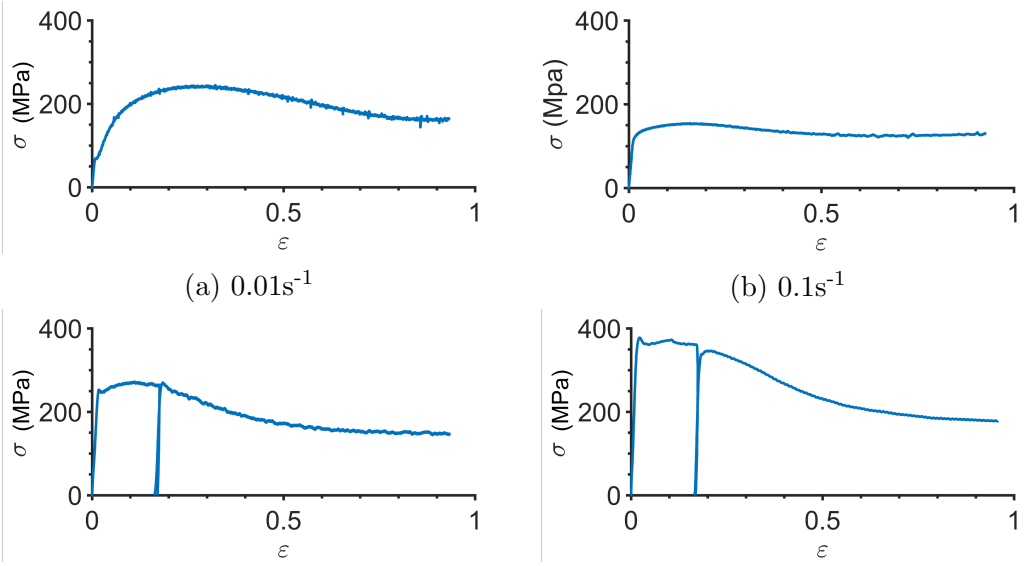

(a) $0.01s^{-1}$ (b) $0.1s^{-1}$

(c) $1s^{-1}$ (d) $5s^{-1}$

Figure 5.32: TMC flow stress curves (with friction correction applied) for tests performed at 1050°C. Graphs shows unusually high stress being produced in the test conducted with a strain rate of 0.01 s^{-1} (a) than when a strain rate of 0.1 s^{-1} is used (b). Unexpected stress drops can be seen in the tests performed at 1 s^{-1} (c) and 5 s^{-1} (d) indicating an error occurred during testing.

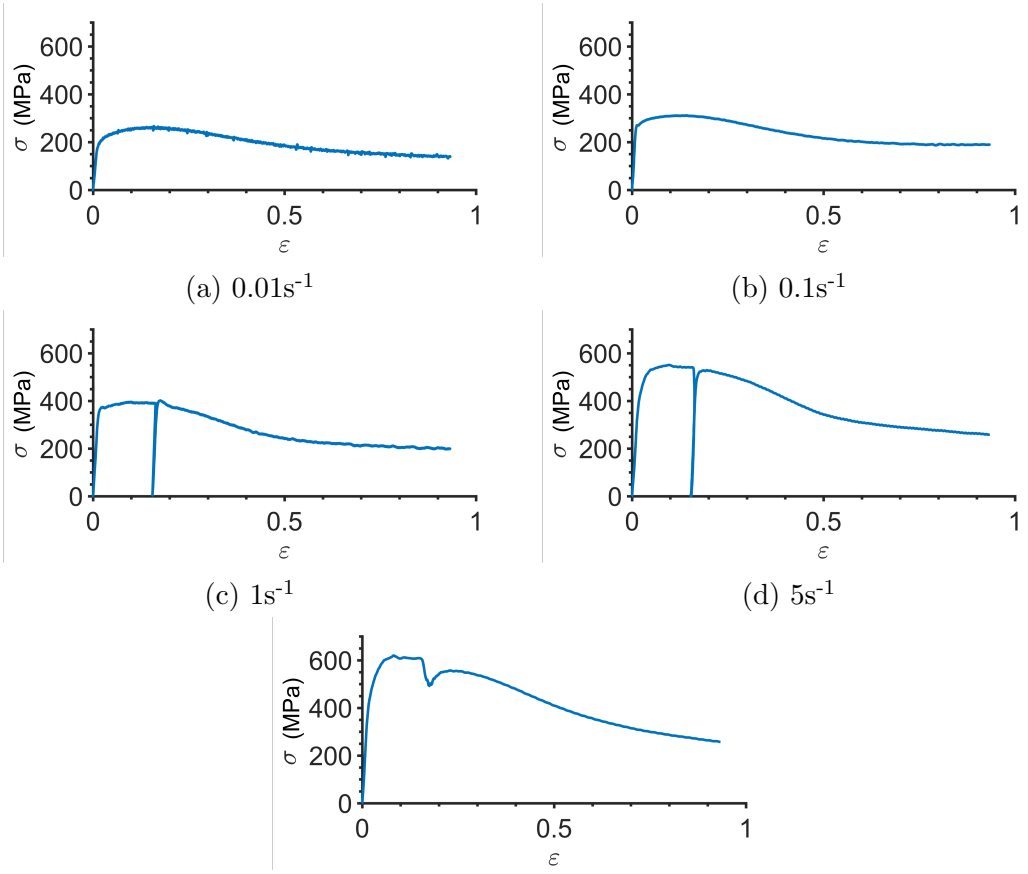

(a) 0.01s^{-1}

(b) 0.1s^{-1}

(c) 1s^{-1}

(d) 5s^{-1}

(e) 10s^{-1}

Figure 5.33: TMC flow stress curves (with friction correction applied) for tests performed at 1000°C. Unexpected stress drops can be seen in the tests performed at 1 s^{-1} (c), 5 s^{-1} (d) and 10 s^{-1} (e) indicating an error occurred during testing.

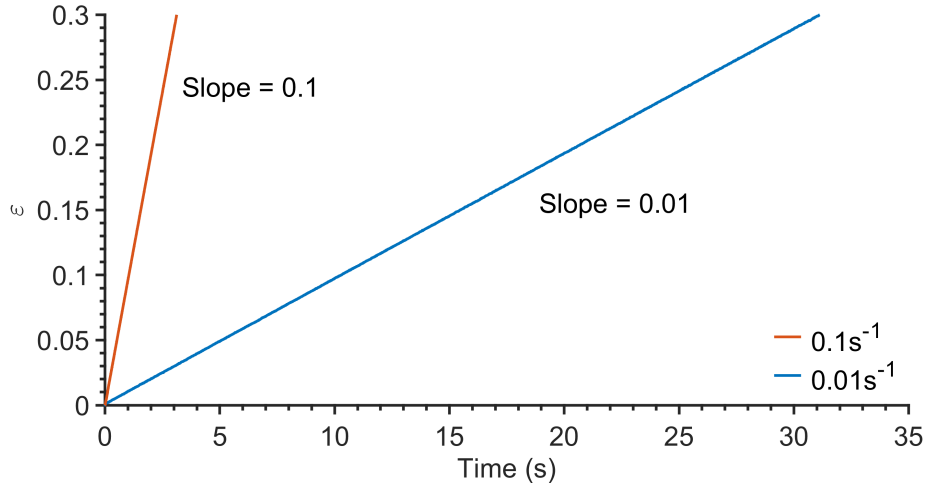

Figure 5.34: Strain vs time plot for the TMC test performed at 1000°C at a target strain rates of 0.01 s^{-1} and 0.1 s^{-1}. The calculated slope of strain vs time match the pre-programmed values for the 0.01 s^{-1} and 0.1s^{-1} tests displayed.

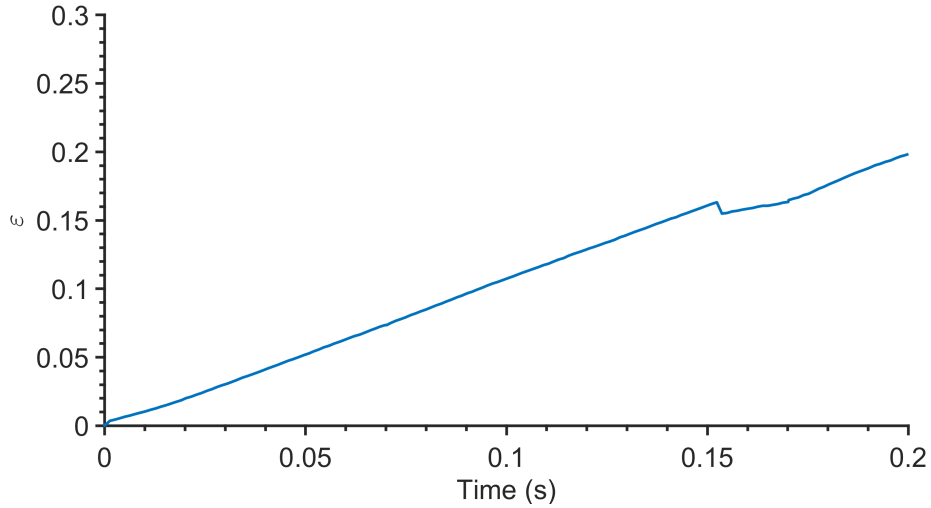

Figure 5.35: Strain vs time plot for the TMC test performed at 1000°C at a target strain rate of 1s^{-1}. It can be seen via the gradient of the graph that the strain rate deviates from the programmed strain rate at approximately at a strain of 0.16. The strain rate momentarily reverses before returning to the pre-programmed strain rate.

Another discrepancy when conducting the tests on the TMC was found

at the lowest temperature tested of 1000°C. The loads, and therefore stresses measured for the test conducted at a strain rate of $0.01s^{-1}$ (see Figure 5.33a), were higher than those measured for a strain rate of $0.1s^{-1}$ (see Figure 5.33b). This is a material impossibility and can therefore only be a consequence of the test and not representative of real flow stress curves for the target conditions. In order to investigate the cause of this error, the calculated strain for each of the two identified tests was plotted against time to determine the strain rate, in order to ensure that the target strain rates are being achieved. Figure 5.34 reveals that the strain rates measured for the tests match the target strain values for the test. This means that the strain rate is not responsible for the higher stresses at lower strain rates. In order to eliminate any error, sample temperatures during testing were examined and are shown in Figure 5.36. As can be seen in Figure 5.36 the test performed at a strain rate of $0.01s^{-1}$ experienced some cooling up to strains of 0.3, before the temperature reached a steady state value. It is reasonable to suggest that this could be attributed to sample cooling when placed in the clamshell furnace of the TMC and was being deformed at a very slow strain rate. At a strain rate of $0.01s^{-1}$ it could be expected that environmental cooling was more dominant than deformation heating. At a strain rate of $0.1s^{-1}$, the sample experienced an initial increase in temperature up to a strain of 0.2 followed by a slow decline in temperature. However, the temperature stayed above the target 1000°C. It can be assumed that the temperature discrepancy between the two tests may be in part the reason why the measured flow stress was higher at the lower strain rate when comparing Figures 5.32a and 5.32b.

These erroneous results show a clear issue with the testing performed on the TMC, with a disparity between the measured flow stress values for the tests shown in Figures 5.32a and 5.32b representing a control issue with the apparatus. As Figure 5.36 shows, during low strain rate testing significant sample cooling can occur. The Gleeble 3800's ability to maintain a more constant test temperature due to the continuous input of resistive heating allows more accurate results to be collected at low strain rates. Another consideration was the consistent thermocouple positioning achievable with the spot welding equipment used with the Gleeble testing. The integrity and placement of the thermocouple would have likely affected the monitoring of temperature. It is assumed that the thermocouple measurement could be responsible for the TMC testing irregularities discussed. Due to the limited hot ductility of nickel superalloys, low strain rates and accurate control of the temperature are required for successful forging and this was more achievable when using the Gleeble.

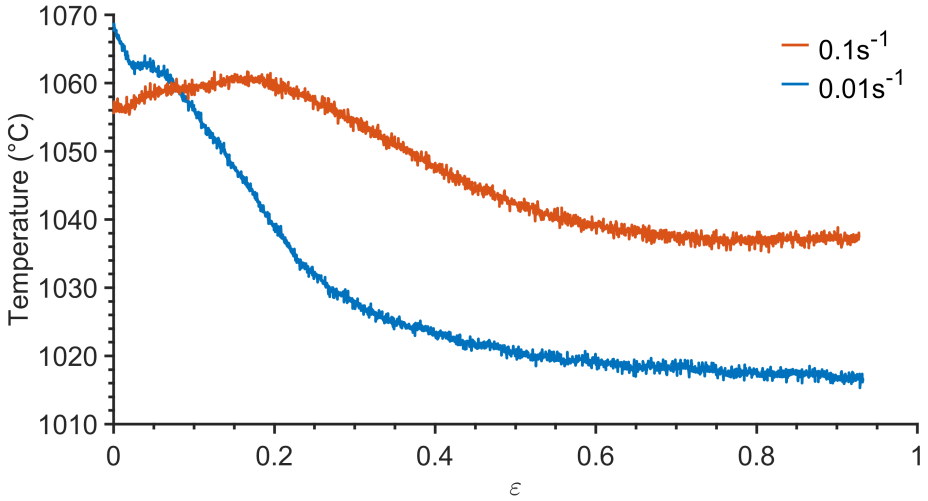

Figure 5.36: Temperature vs strain profiles for the test conducted using the TMC at a target test temperature of 1000°C at for strain rates of $0.01s^{-1}$ and $0.1s^{-1}$. Profiles show significantly cooling in the test performed at a strain rate of $0.01s^{-1}$.

5.4.4 Single Step Forging Sample Macroscopic Examination

Macroscopic images of the samples produced during the single deformation are shown in Figures 5.37, 5.38 and 5.39. By examining the samples produced using a deformation temperature of 1050°C, shown in Figure 5.37, it can be seen that the samples deformed using a strain rate of $0.01s^{-1}$ exhibit no external cracking. This suggests that under these conditions the material has sufficient ductility to deform to a strain value of 1.0. The samples deformed at strain rates of 0.1 s^{-1} and 1 s^{-1} have severe surface cracks on the barrelled surface of the sample. As has been shown previously, the flow stress under these conditions is considerably higher and the external damage to the samples indicate that working limits of deformation have been exceeded. The samples deformed at a temperature of 1100°C, shown in Figure 5.38, have less severe cracks present on the samples deformed at $0.1s^{-1}$ and $1s^{-1}$. Similarly to the sample deformed at 1050°C at a strain rate of $0.01s^{-1}$, the sample produced using the slowest strain rate at a temperature of 1100°C shows no external cracking. The samples deformed at 1125°C (Figure 5.39) show a similar trend, with the samples deformed a slow strain rates of $0.01s^{-1}$ and $0.1s^{-1}$ exhibiting no visual surface cracking. However the sample deformed at the higher strain rate of $1s^{-1}$ had severe surface cracking. In figure 5.39, it

can be seen that the nickel paste coated tantalum foil, used for lubrication, has diffusion bonded to the sample, likely driven by the elevated deformation temperature. This effect was only seen on the sample deformed at a strain rate of $0.01s^{-1}$, again this is understandable, as the sample deformation requires 100 seconds to complete to achieve a strain of 1.0. This extensive deformation time will allow a greater level of diffusion to occur in contrast with the samples deformed at $0.1s^{-1}$ and $1s^{-1}$. This may explain why no bonding of the lubricating foils to the sample can be seen in these tests.

Based on examination of the post deformed samples, several conclusions can be made. Firstly, the forging of nickel superalloys without cracking requires low strain rates. Low strain rates are even more crucial when deforming at higher temperatures. As reported by Bockenstedt et al [127], the hot ductility of the alloy 13072 rapid reduces as the γ' solvus temperature is approached. At higher strain rates, higher levels of adiabatic heating can be observed. This means that if the temperature is close to the solvus temperature at the start of deformation, adiabatic heating may lead to a rapid dissolution of precipitates, leading to a drop off in ductility and the rapid formation of cracks. From these observations it can be seen that temperature should be as high as possible, to reduce the forging loads, without encroaching on the γ' solvus temperature. The strain rates must also be kept as low as possible to minimise deformation heating and maximise material ductility. These findings are particularly important when forging on a larger scale where both the strain rates and temperature distributions are not easily controlled without the employment of isothermal thermal forging techniques.

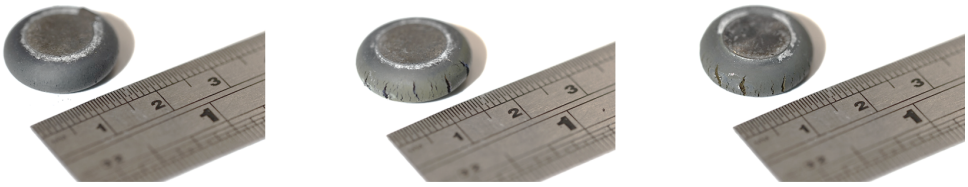

Figure 5.37: Photograph of samples post compression test on the Gleeble 3800 at strain rates of $0.01s^{-1}$ (left), $0.1s^{-1}$ (centre) and $1s^{-1}$ (right). All tests performed at 1050°C.

Figure 5.38: Photograph of samples post compression test on the Gleeble 3800 at strain rates of $0.01s^{-1}$ (left), $0.1s^{-1}$ (centre) and $1s^{-1}$ (right). All tests performed at 1100°C.

Figure 5.39: Photograph of samples post compression test on the Gleeble 3800 at strain rates of $0.01s^{-1}$ (left), $0.1s^{-1}$ (centre) and $1s^{-1}$ (right). All tests performed at 1125°C.

5.4.5 Two Step Deformation Results

Figure 5.41 shows a comparison of a single deformation flow stress curve performed at 1100°C and a strain rate of $0.01s^{-1}$ with a two step deformation, with both steps performed using the same parameters as the aforementioned

single step deformation. It can be seen that during the initial upset to a strain of 0.34, both the single and two step deformation tests exhibit very closely matched stress vs strain curves. The previously mentioned spike in flow stress, due to an accelerated strain rate at the start of the test, can be observed for both tests.

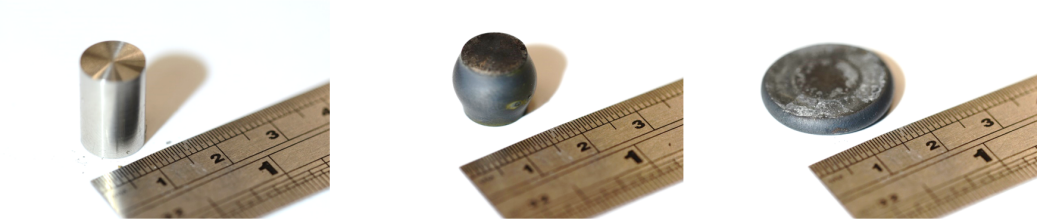

Figure 5.40: Evolution of sample change during the two step deformation procedure showing the sample before deformation (left) after the first 1100°C deformation step to a strain of 0.34 (centre) and after the second 1100°C deformation step to a strain of 1.2 (right).

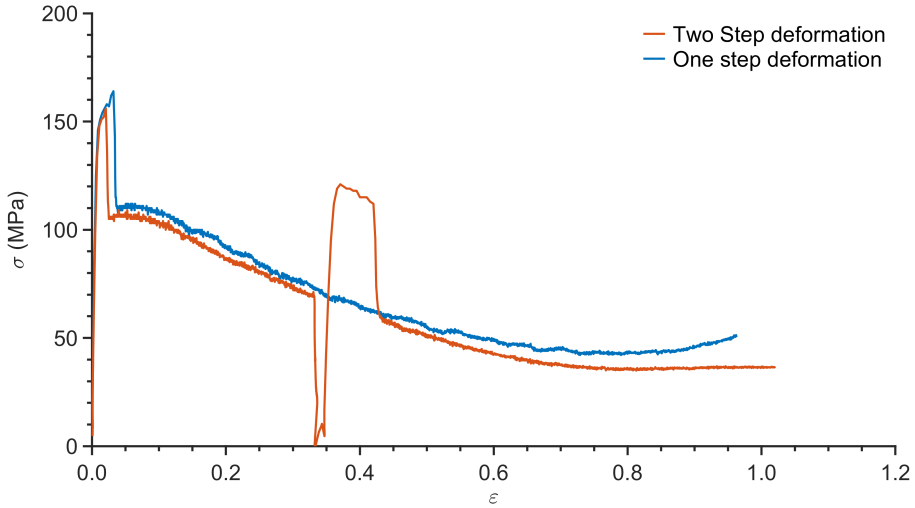

Figure 5.41: Composite flow stress curve showing the resultant stress vs strain behaviour when forging a 131072 sample using the two step forging strategy. The first deformation occurs at a temperature of 1100°C and a strain rate of $0.01s^{-1}$ to a strain of 0.34. The second deformation to a total strain of 1.0 was performed at 1100°C at a strain rate of $0.01s^{-1}$.

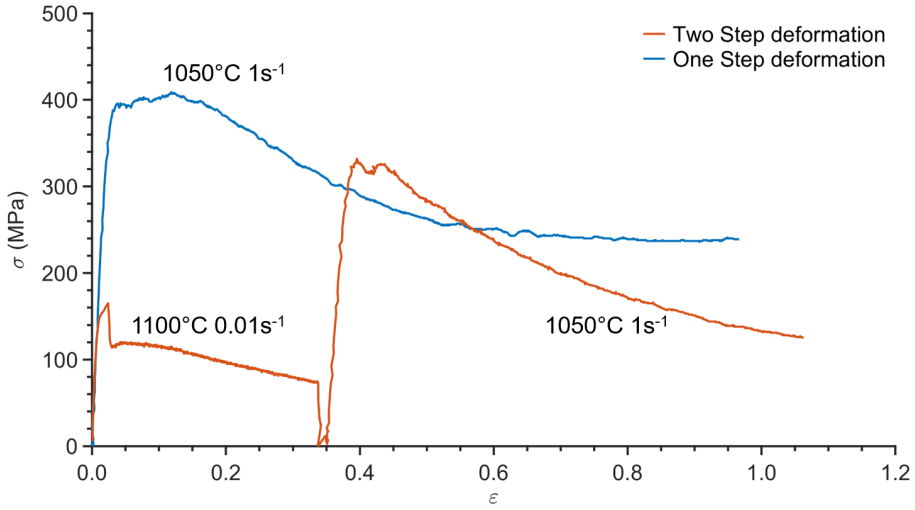

Figure 5.42: Composite flow stress curve showing the resultant stress vs strain behaviour when forging a 131072 sample using the two step forging strategy. The first deformation occurs at a temperature of 1100°C and a strain rate of $0.01s^{-1}$ to a strain of 0.34. The second deformation to a total target strain of 1.0 was performed at 1050°C at a strain rate of $1s^{-1}$.

By comparing the two flow stress curves for the tests shown in Figure 5.41, it can be seen that after 0.34, where the second stage of deformation begins for the two hit test, it can be seen that the two tests display similar flow stress behaviour and magnitudes. For the two step deformation curve, a large peak can be seen from strains of 0.34 to 0.43, the cause of this peak is due to the same issue with the single deformation tests whereby the strain rate is momentarily larger than that programmed. The end of this peak at a strain of 0.43, signifies the point at which the strain rate returns to the programmed value of $0.01s^{-1}$. This feature was only seen for tests where the second deformation step was performed at a strain rate of $0.01s^{-1}$. This is similar to the behaviour noted by Gardner et al [106] whereby a prominent yield peak can be seen at the start of the second deformation step. However it can be demonstrated that the peak at the start of the second deformation is due to the strain rate being too high, leading to an artificial peak. It is unclear whether the strain rate control issue is masking the yield peak effect or whether the peaks seen in the work of Gardner et al [106] are due to a similar issue with strain rate control.

Above strain values of 0.43, the one step and the two step deformation tests produce similar magnitudes of flow stress up to a strain of 0.98-1.0. Both flow curves approach a steady state flow stress value. This indicates

that no significant microstructural change occurs between the first and second deformation steps. Unfortunately, the issue with the accelerated strain rate at the state of the second deformation in the two step test prevents an understanding of any yield peaks present at the start of the second deformation. Figure 5.41 shows results which are in direct contrast with those in Gardner et al [106].

Another example of a comparison between a two hit and single hit test is shown in Figure 5.42, whereby a higher strain rate of $1s^{-1}$ and lower temperature of 1050°C was used for the second stage of deformation. As expected, a larger increase in flow stress occurs between the first stage of deformation and the second stage of deformation in the two hit test, owed to the lower sample temperature and higher strain rate. As previously noted, no peak in stress is seen at the start of second stage of deformation due to the higher strain rate which does not result in a higher strain rate at the start of the test, unlike the first stage of deformation at 0.01 s^{-1}. Figure 5.41 shows that during the second deformation step for the two hit test, the magnitude of the flow stress is initially similar to that of a single step deformation performed with equivalent parameters at equivalent strain values. However after an initial peak in flow stress, the two hit test decays towards a steady state stress, which is below that of the equivalent single step deformation. This gives an indication that the first deformation step at a higher temperature and lower strain rate subsequently leads to microstructural change which facilitates the enhanced flow properties, giving the lower flow stress.

Two Step Deformation - Macroscopic Sample Examination

Figures 5.43, 5.44 and 5.45 show macroscopic images of the two step formation samples after the application of the second deformation. Figure 5.43 shows that when the second deformation step was performed at 1050°C with the lower strain rates chosen ($0.01s^{-1}$ and $0.1s^{-1}$) no cracks were present on the perimeter of the sample unlike the severe cracking seen when a strain rate of $1s^{-1}$ was employed. Comparing these images with those presented in Figure 5.37, it can be seen that the cracking on the single step deformation sample produced using a strain rate of $0.1s^{-1}$ was more severe than the sample produced using a two step deformation where the second stage of deformation was conducted at equivalent parameters used.

Figure 5.44 shows the samples produced using a deformation temperature of 1100°C for the second stage of deformation for a range of strain rates. Samples produced for all strain rates resulted in samples with no severe cracking. These observations are similar to those seen when examining the samples produced using a single deformations step at 1100°C (Figure 5.38).

However for a strain rate of $1s^{-1}$ cracks start to form on the surface for the single hit test as opposed to the sample produced using the two step method.

When the second deformation steps were performed at a temperature of 1150°C, it can be seen that samples failed catastrophically during testing as shown in Figure 5.45. This demonstrates that the two step deformation strategy does little to limit the severe ductility reduction associated with the solvus temperature of the material. It can be seen that even at the lowest strain rate used, severe cracking occurs. The level of cracking seen for all strain rates is a clear indication that 1150°C is not a suitable deformation temperature for the alloy 131072, irrespective of the deformation strategy adopted.

By comparing the samples produced using the two step method, it can be observed that the two step method results in less cracking in two particular test scenarios, those being 1050°C with a strain rate of $0.1s^{-1}$ and 1100°C at a strain rate of $1.0s^{-1}$. This marginal improvement in the reduction of surface cracking, alongside the results presented by Bockenstedt et al [127] provide evidence that applying a small strain and then reheating the samples could provide an alternative processing route in the event of severe cracking during single step deformation in the larger deformation samples.

5.4.6 Microstructural Examination of Flow Stress Compression Test Samples

To examine the microstructure, backscatter SEM micrographs were captured along the horizontal axis aligned along the horizontal centreline of each forging specimen at 2 mm intervals. A 2d axi-symmetric model of the compression test was replicated in the DEFORM software package to estimate the strain at the locations of images. The DEFORM model was programmed to calculate the strain based on geometry only when a 10mm diameter x 15mm specimen is deformed to a strain of 1 using a friction coefficient of 0.3. A diagram showing the position of the captured micrographs and the approximated strain is shown in Figure 5.46. Although images were captured for positions A-E for the majority of the flow stress samples, only positions A and F are shown in order to show the microstructure at the lowest strain and highest strain positions along the horizontal centreline to show the two extremes of the microstructure along horizontal centreline between strain of approximately 0.75 and 1.50. These positions are termed as the sample edge and sample centre respectively.

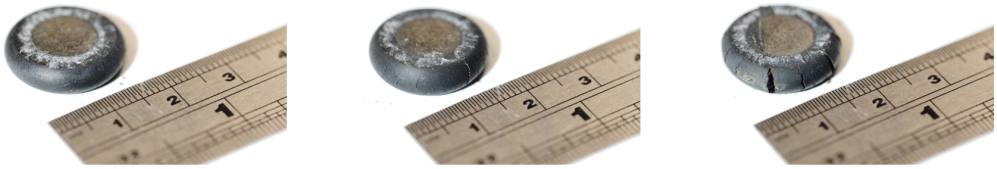

Figure 5.43: Two step deformation compression test samples, the second stage of deformation performed at 1050°C. Performed a strain rates of $0.01s^{-1}$ (left) $0.1s^{-1}$ (centre) $1s^{-1}$ (right)

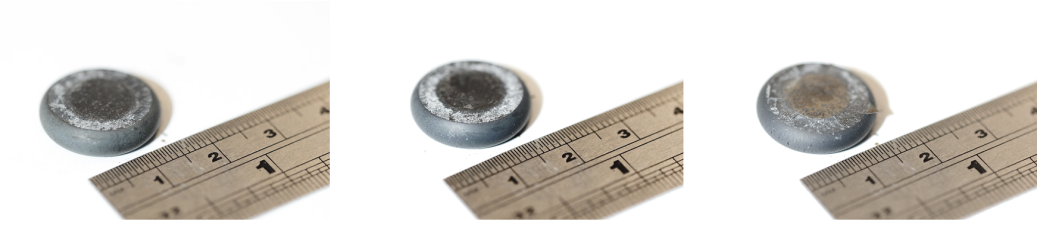

Figure 5.44: Two step deformation compression test samples, the second stage of deformation performed at 1100°C. Performed a strain rates of $0.01s^{-1}$ (left) $0.1s^{-1}$ (centre) $1s^{-1}$ (right)

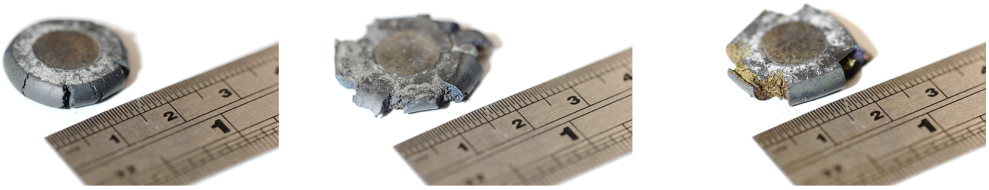

Figure 5.45: Two step deformation compression test samples, the second stage of deformation performed at 1150°C. Performed a strain rates of $0.01s^{-1}$ (left) $0.1s^{-1}$ (centre) $1s^{-1}$ (right).

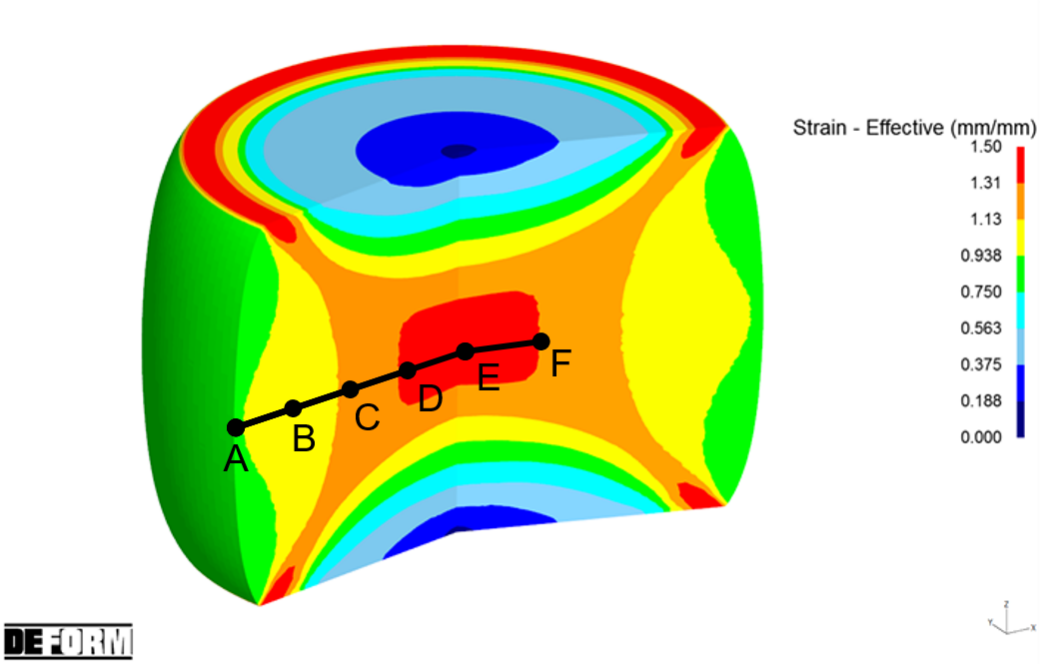

Figure 5.46: Diagram showing the positions of micrographs captured and the corresponding approximate strain locations. Figure was produced using an axi-symmetric finite element model produced in the DEFORM 3D modelling software.

Figure 5.47 shows micrographs captured for the specimen deformed at 1100°C at a strain rate of $0.01.s^{-1}$. These deformation conditions were particularly important as they represent the conditions used to perform the first step in the two step deformation trials. These conditions also appeared to produce a crack free billet in two step deformation, making these conditions suitable for up-scaling to the larger machinability billets. The microstructure of the specimen shows a high level of consistency from the edge region at position A to the centre in positions E and F. Comparing these micrographs with those shown for the un-deformed material in Figure 5.3, it is clear that a marginal level of microstructural refinement has occurred. Coupled with the flow curve in Figure 5.28 suggests that recrystallisation has occurred in regions above strains of 0.75. The level of homogeneity suggests that the deformation conditions were near isothermal across the test piece during deformation, as no abnormal grain growth associated with precipitate dissolution is observed.

In Figure 5.48, the microstructural change associated with precipitate

dissolution is apparent when examining the specimen deformed at a temperature of 1125°C at a strain rate of 0.01 s^{-1}. At this deformation temperature it can be seen that the microstructure drastically changes from the edge at position A to the centre at position E. This change can be associated with adiabatic heating at the centre region of the specimen close to the γ' solvus leading to grain growth. The misorientation contrast associated with deformed substructures can also be seen within grains in positions D and E, this indicates that deformation is retained locally within grains. The microstructure produced when the deformation temperature is increased by 25°C when comparing Figure 5.47 and Figure 5.48, clearly demonstrates the sensitivity of nickel superalloy forging with respect to the chosen deformation temperature.

The effect of strain rate across the sample can be viewed by comparing 5.47 and Figure 5.49 which show samples deformed at strain rate of $0.01s^{-1}$ and $1.0s^{-1}$. Grain size can be seen to differ very little for the two strain rates across all positions. It can be inferred from these results that the increase in strain rate results in little change in the grain size. The strain rate of $1.0.s^{-1}$ was found to result in insufficient adiabatic heating in the higher strain regions to result in grain growth. These findings suggest that the temperature is the dominant parameter affecting microstructure. The increase in the strain rate does little to affect microstructural homogeneity across the sample.

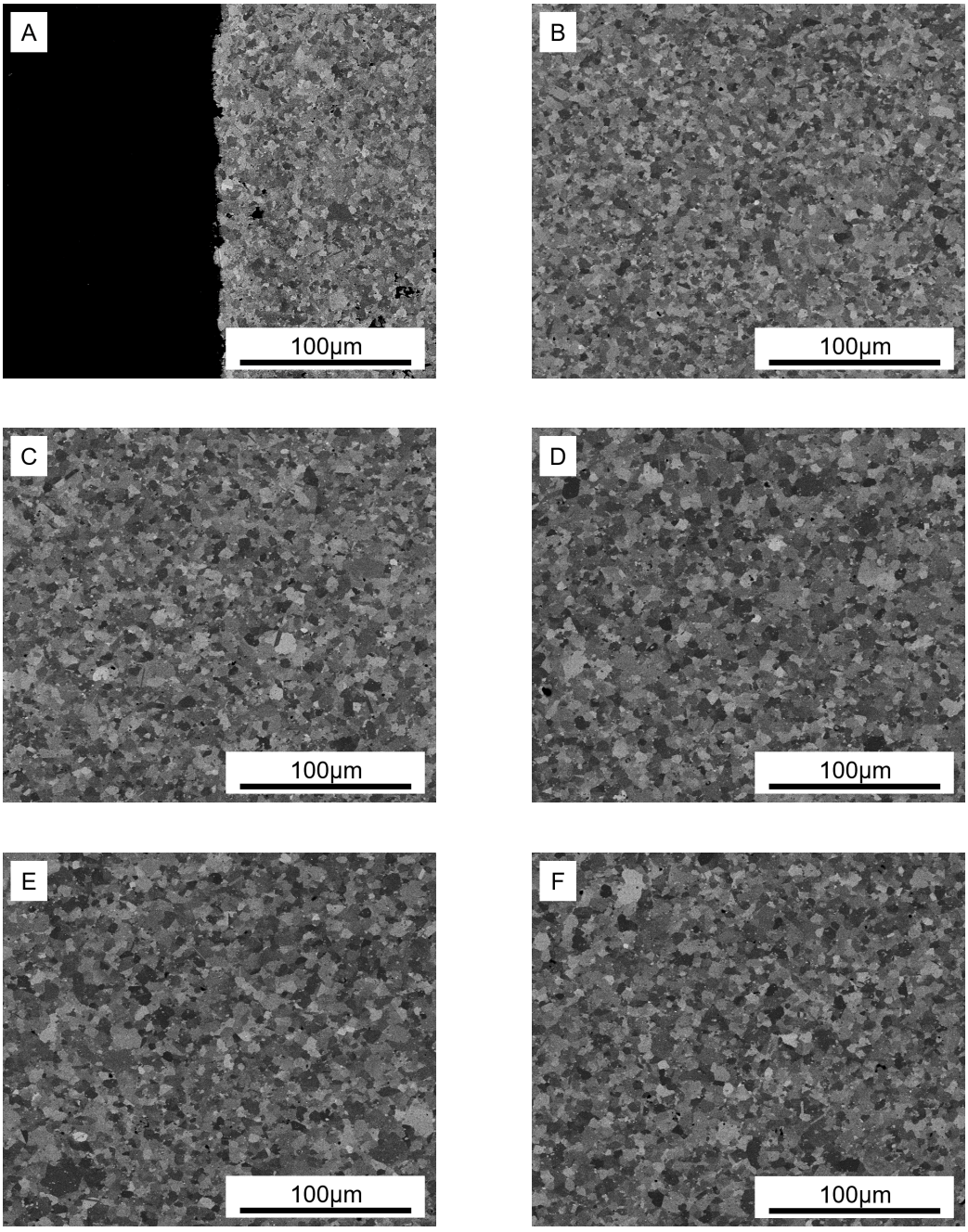

Figure 5.47: Backscatter electron micrographs of the flow stress sample produced using a deformation temperature of 1100°C and a strain rate of $0.01s^{-1}$, showing the change in grain morphology from the edge of the sample in A towards the the centre of the sample in E and F. Letters denote micrograph positions as detailed in Figure 5.46.

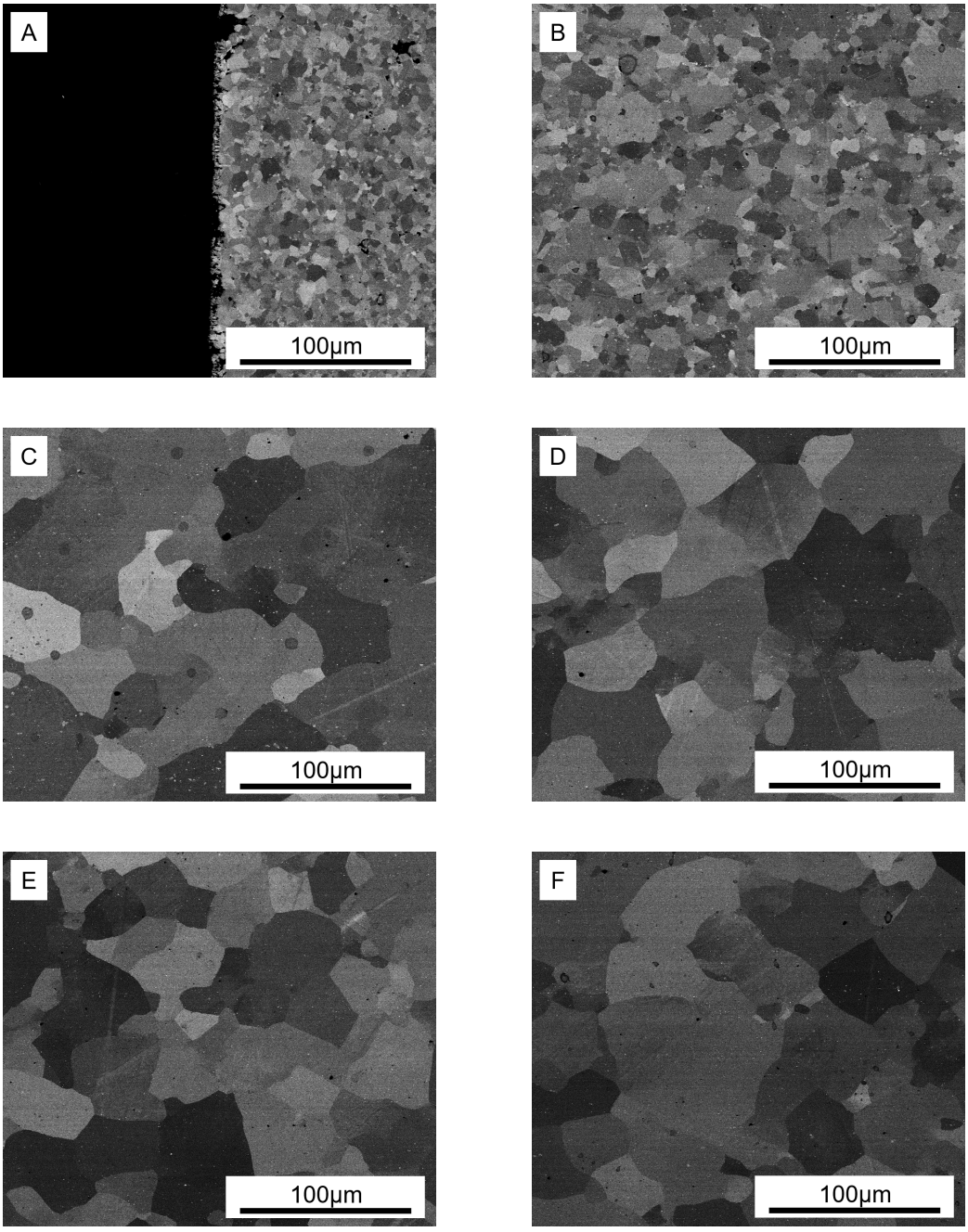

Figure 5.48: Backscatter electron micrographs of the flow stress sample produced using a deformation temperature of 1125°C and a strain rate of $0.01s^{-1}$, showing the change in grain morphology from the edge of the sample in A towards the the centre of the sample in E and F. Letters denote micrograph positions as detailed in Figure 5.46.

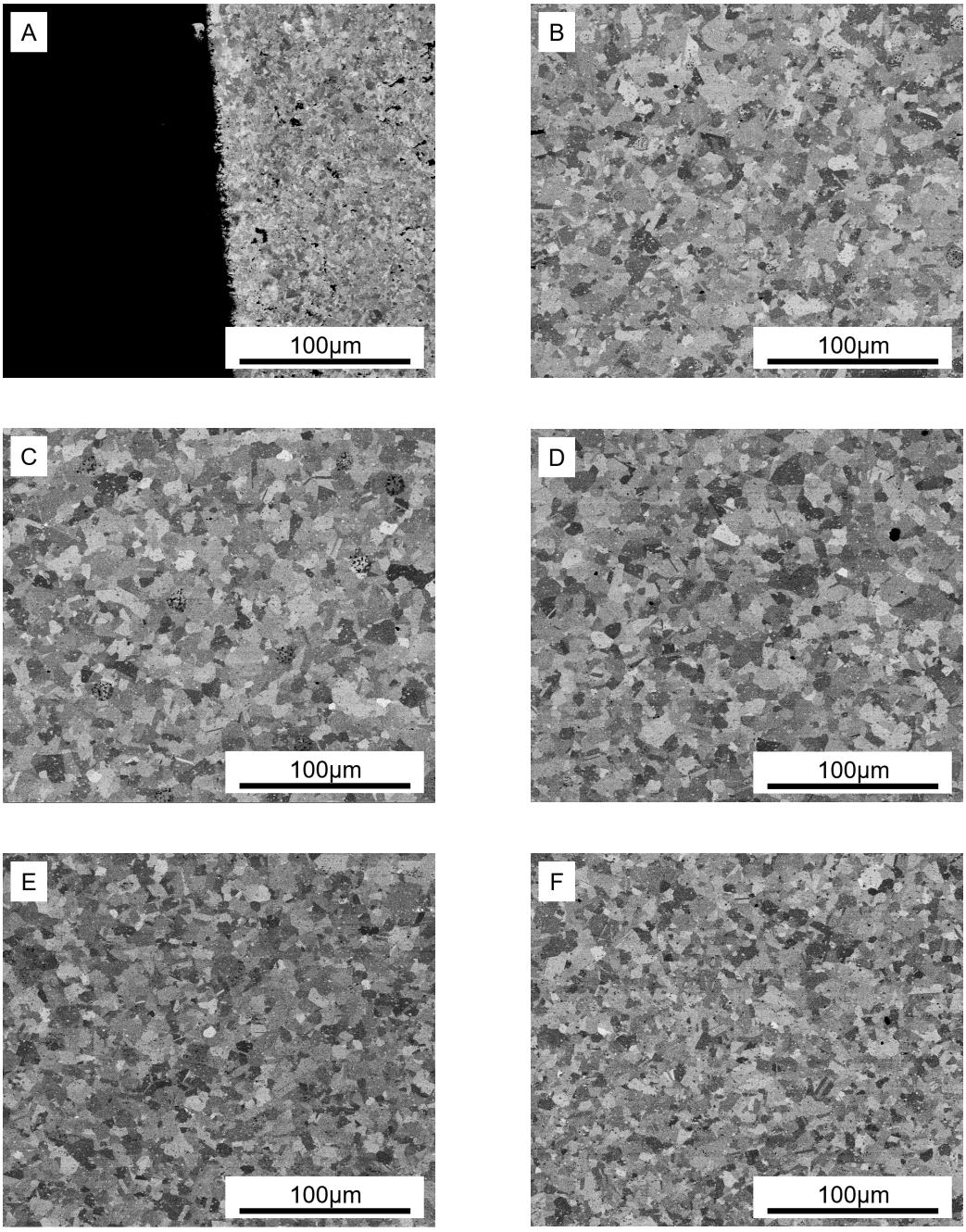

Figure 5.49: Backscatter electron micrographs of the flow stress sample produced using a deformation temperature of 1100°C and a strain rate of $1s^{-1}$, showing the change in grain morphology from the edge of the sample in A towards the the centre of the sample in E and F. Letters denote micrograph positions as detailed in Figure 5.46.

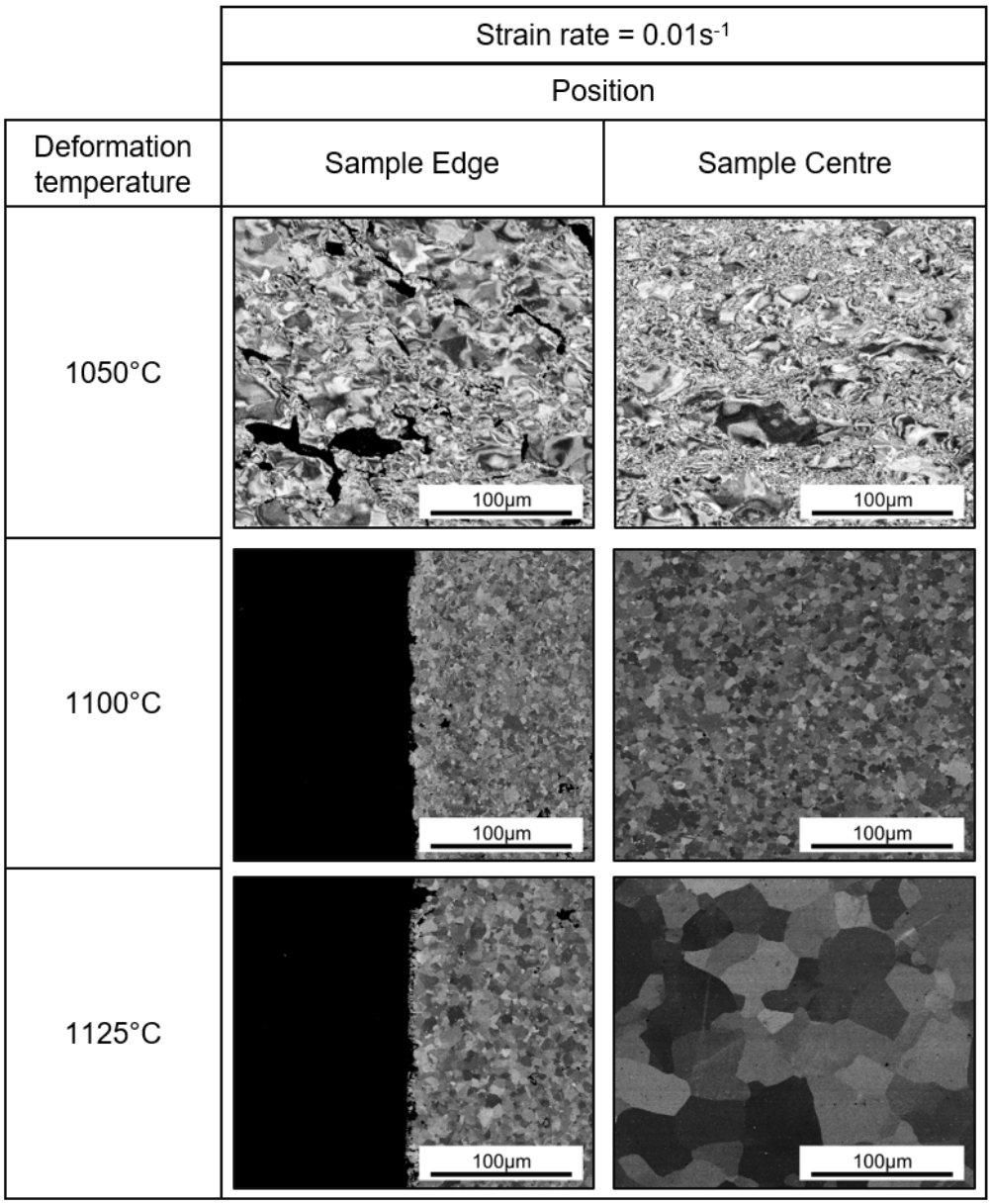

Figure 5.50: Micrographs showing the post deformed microstructure at the edge and centre of samples produced using a strain rate of $0.01s^{-1}$ for temperatures of 1050°C, 1100°C and 1125°C.

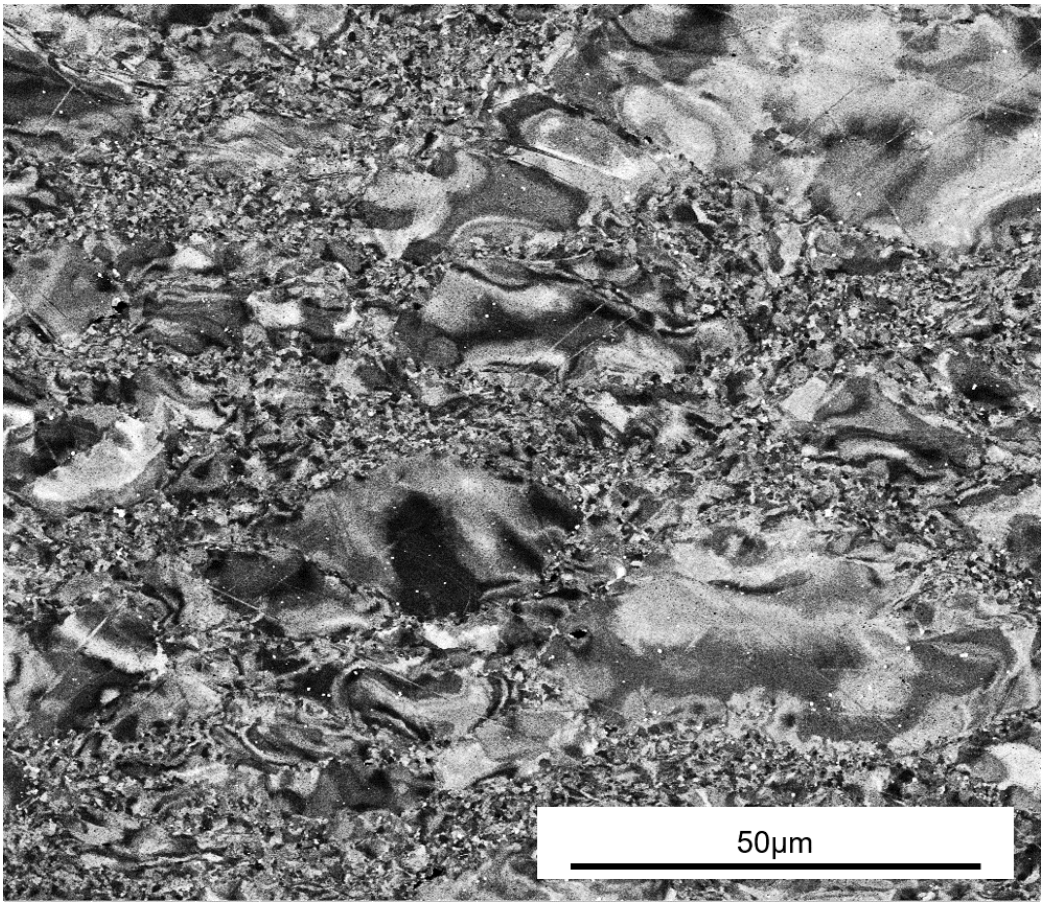

Figure 5.51: Backscatter electron micrograph showing the microstructure of the high strain centre region of a flow stress sample produced using a strain rate of $0.01s^{-1}$ and a deformation temperature of 1050°C.

A comparison of the microstructures at the centre and edge regions (representing approximate strains of 1.5 and 0.75 respectively) for the specimens deformed at a strain rate of $0.01.s^{-1}$, for the range of temperatures tested, is shown in Figure 5.50. As discussed previously, in the samples produced at 1100°C and 1125°C the edge region of the post deformed material both exhibit equiaxed microstructures, with the sample produced using 1125°C possessing significantly larger grains. Comparing the centre regions of the samples it can be seen that large grain growth has occurred in the sample processed at 1125°C. These large grains are approximately 50 - 100 μm which is much larger than the pre-forged grain size of the input HIP material, shown in Figure 5.3, which has a grain size of 10 - 20 μm. This large increase in grain size is more than likely to be due to the local dissolution of γ' precipitates. In the sample produced using a deformation temperature 1100°C at

the lowest strain rate examined, it can be seen that in both the edge and centre of the material, the grain size is smaller than that of the input material, with post forged grain sizes of approximately 5 to 10 μm and 10 to 20 μm in the centre and edge regions, respectively. Therefore the material has undergone recrystallisation as the microstructure in the post deformed material is equiaxed. This is corroborated by the flow curve for the 1100°C $0.01s^{-1}$ deformation shown in Figure 5.28, whereby flow softening can be seen as the strain increases. It is expected that additional static grain growth will have occurred as the sample cooled after deformation. As shown in Figure 5.47, a homogeneous structure is evident across the sample, suggesting that a true strain of approximately 0.9 is sufficient to initiate recrystallisation across the whole of the sample.

The low strain rate sample deformed at 1050°C is by far the most complex to describe from a microstructural perspective. At the edge of the sample, large subsurface cracks are present, which likely lead to the surface breaking cracks if higher strain rates were used. In both the centre and the edge of the sample it can be seen that large elongated regions exist with complex patterns of varying contrast. Surrounding the larger regions are necklace like structures of very fine grains that appear equiaxed in nature, as shown in Figure 5.51. It is assumed that the large elongated regions are un-recrystallised grains, and the varying contrast detected using backscatter electrons within those grains (known as misorientation contrast), are evidence of substructures caused by the deformation. The fine grains are thought to be recrystallised grains formed via dynamic and meta-dynamic recrystallisation.

It is apparent from Figure 5.50 that recrystallisation is very much dependent on temperature at low strain rates. It is assumed that in order to achieve full recrystallisation at a deformation temperature of 1050°C, further strain input would be required, however further strain input will likely lead to sample failure due to cracking due to limited ductility. The temperature of deformation is critical when forging the alloy 131072, particularly with respect to the γ' solvus as an increase in temperature of just 25°C, leads to rapid grain growth which will affect material strength and fatigue resistance. Figure 5.51 informs that at low strain rates (which are required to maximise hot ductility) maximal temperatures should be used without encroaching upon the γ' solvus temperature. Process modelling or other applicable techniques should be utilised to predict the adiabatic heating in order to select the most appropriate temperature for deformation.

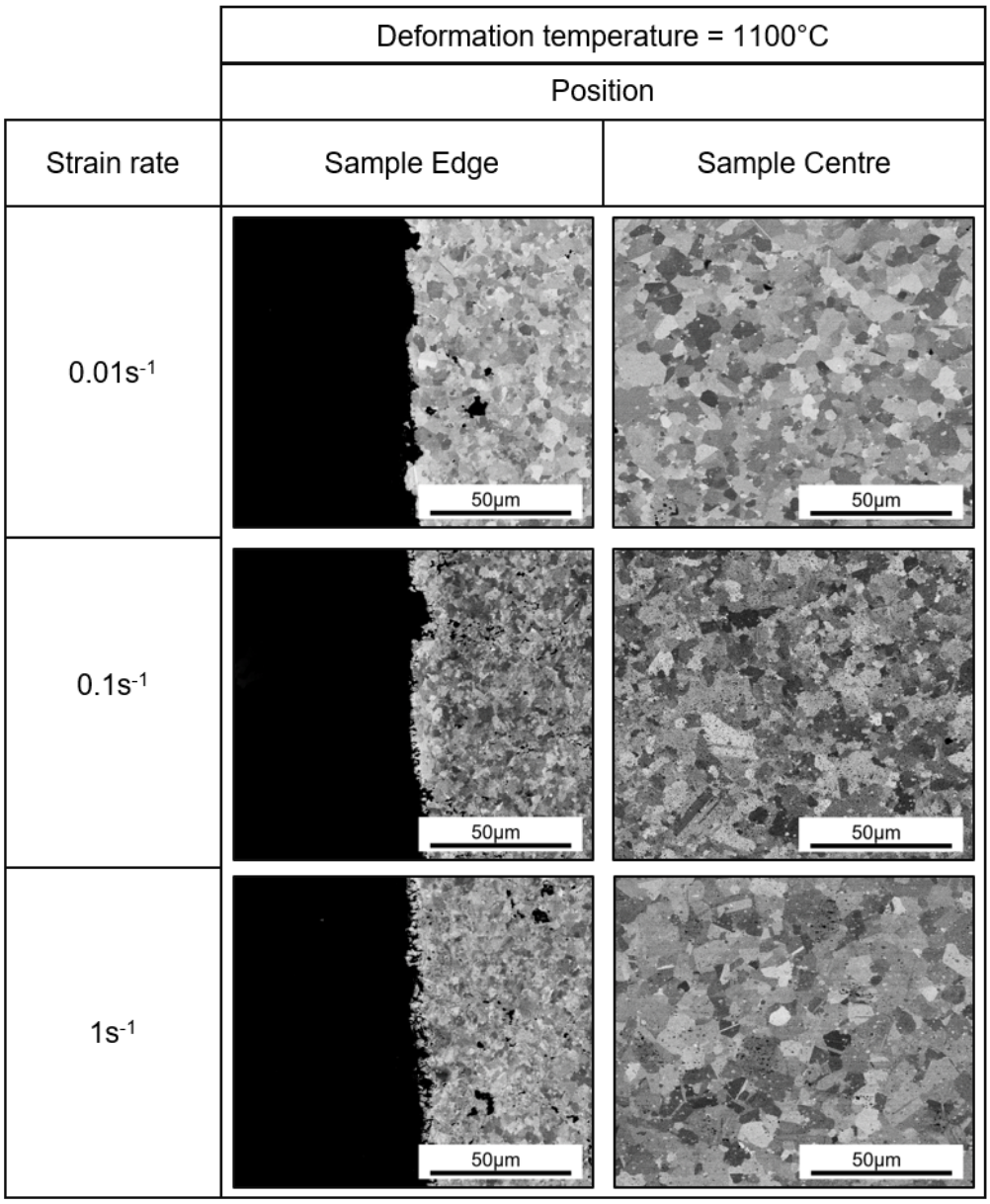

Figure 5.52: Backscatter electron micrographs showing the post deformed microstructure for flow stress samples produced using a deformation temperature of 1100°C for strain rates of $0.01s^{-1}$, $0.1s^{-1}$ and $1s^{-1}$.

The effect of strain rate on material deformed at a temperature of 1100°C is demonstrated in Figure 5.52. It can be seen that all strain rates produce material which has a grain size smaller than that of the as HIP material pre-deformation. It can be seen that the edges of the samples produced

using strain rates of $0.01s^{-1}$ and $1s^{-1}$ have evidence of void formation close to the surface. No voids are visible in the local area studied for the sample produced using a strain rate $0.1s^{-1}$. No voids are visible in the centre regions examined for all strain rates samples. Negligible changes in grain size can be observed for changes in strain rate for the range studied. It can be visually observed that the samples produced using the higher strain rate contain prominent twins in the structure, which have been shown to be $\Sigma 3$ boundaries in previous works. This could be due to a higher degree of stored energy after deformation, which leads to twin boundary formation post deformation. Contrast observable in the micrograph of the edge regions of the samples deformed at strain rates of $0.1s^{-1}$ and $1s^{-1}$ indicate incomplete recrsytallisation as opposed to the samples deformed at $0.01s^{-1}$. This effect is likely due to the shorter deformation times at the higher strains rates which prevents full recrystallisation from occurring within the deformation time frame.

Figure 5.53 shows the variation in microstructure produced with increasing strain rates in samples deformed at 1125°C. The sample deformed at 0.01^{-1} shows a much coarser microstructure when compared with 0.1 s^{-1} and 1 s^{-1}. This is likely due to the elevated deformation time of 100s in the 0.01 s^{-1} sample whereby the grains have significantly more time to grow compared with the samples deformed in a shorter time frame. In samples produced using higher strain rates, recrystallisation mechanisms will offset the growth of pre-deformed grains. Irrespective of strain rate, all samples produced using a deformation temperature of 1125°C can be seen to have a larger grain size than the starting microstructure of the post HIP material prior to any deformation. This may be related to the shape of the flow stress data for 1125°C (Figure 5.29) whereby there is very little flow softening in contrast with the samples produced at 1050°C and 1100°C (shown in Figure 5.27 and Figure 5.28, respectively).

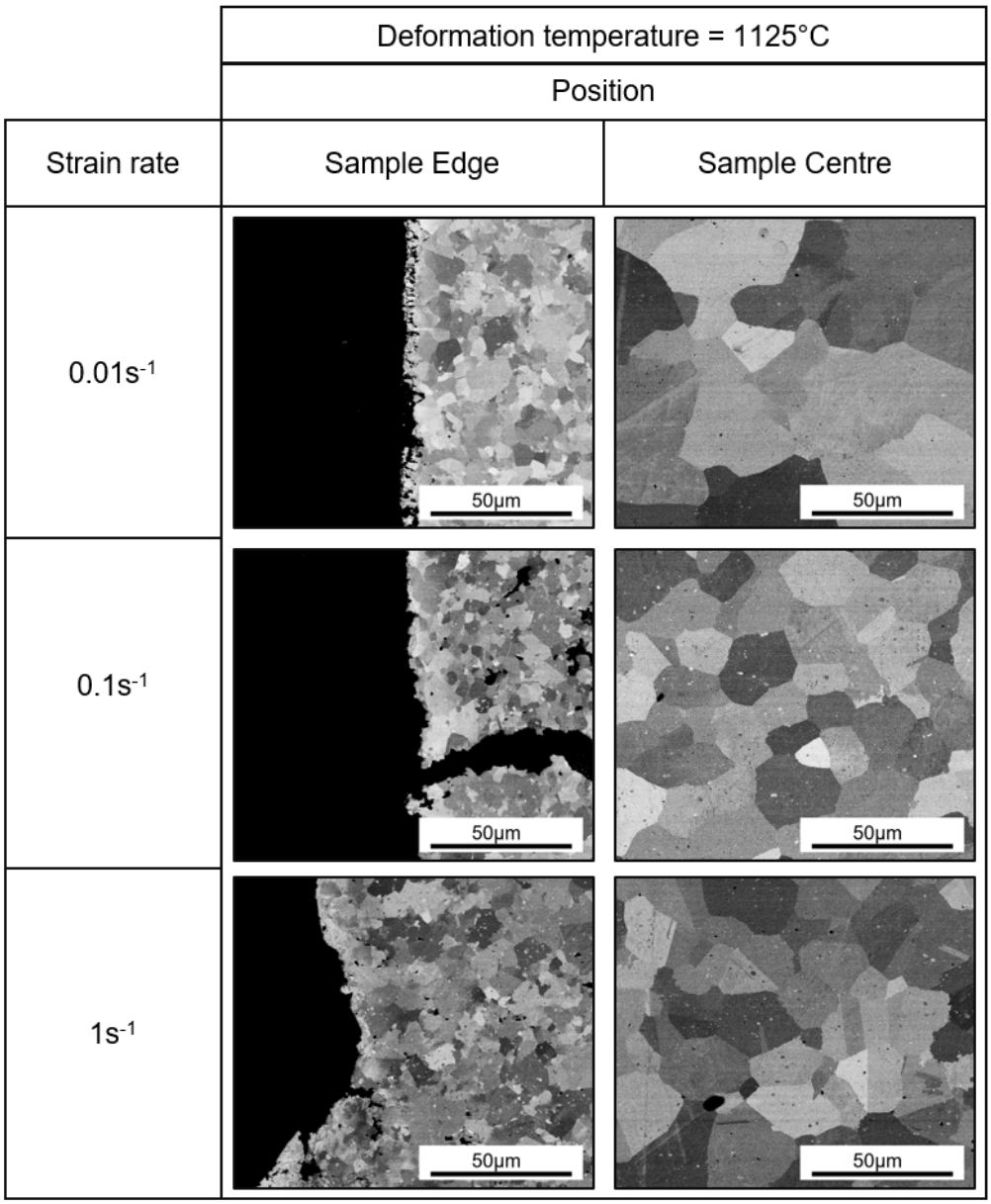

Figure 5.53: Backscatter electron micrographs showing the post deformed microstructure for flow stress samples produced using a deformation temperature of 1125°C for strain rates of $0.01s^{-1}$, $0.1s^{-1}$ and $1s^{-1}$.

5.4.7 Evolution of Microstructures During Two Step Compression Tests

Examination of Microstructures Post the First Deformation Step

The microstructure of the first deformation specimen was examined by deforming to the first strain point of 0.34 before the specimen was allowed to air cool naturally to room temperature. The condition is equivalent to the material condition after the first deformation stage for the two step deformation specimens. In comparison with the material prior to deformation in Figure 5.3, the microstructure after the first deformation step (shown in Figure 5.54) contains much smaller grains than those in the pre deformed material, suggesting that full recrsytallisation has taken place. This is not surprising given that the input strain of 0.34 is beyond that suggested by the flow curves required to trigger recrystallisation effects. It can therefore be assumed that any further deformation after this step would lead to further recovery and hardening cycles, eventually leading to a steady state flow stress.

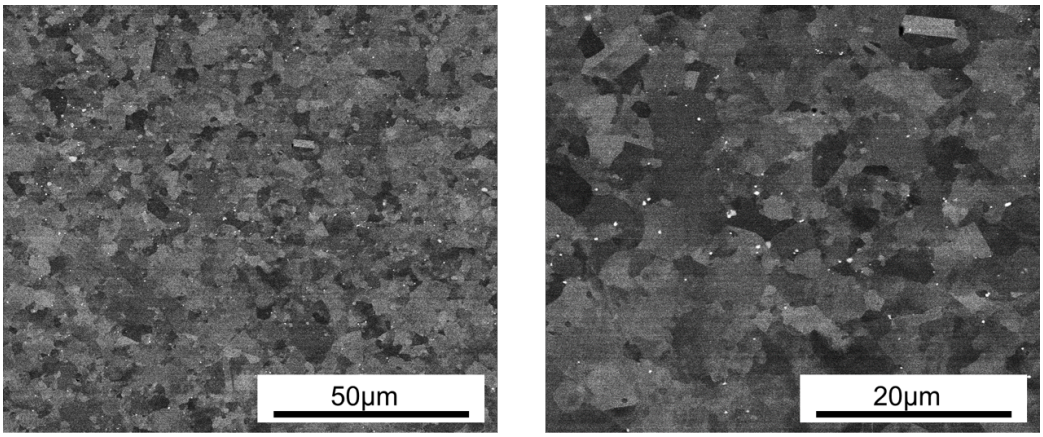

Figure 5.54: Backscatter electron micrographs showing the structure of material produced using the first step in the described two step deformation strategy followed by an air cool to room temperature. Showing the material at 2000x magnification (left) and 5000x magnification (right).

The level of grain refinement evident after the first deformation step potentially gives rise to an explanation why the flow stress increases dramatically as shown in Figure 5.41. A finer grain size results in a large resistance to deformation due to the pinning of dislocations at grain boundaries. Overcoming this initial effect will require a higher flow stress before softening can take place via recovery mechanisms leading to softening at higher strain

levels. Figure 5.54 reveals the presence of additional phases which appear as bright spots within the microstructure. The phases are believed to be prior particle boundaries which are typically hafnium or tantalum carbides hence the bright appearance viewed under backscatter electrons. It is likely that the initial strain to 0.34 followed by cooling and reheating will disperse networks of these phases which are brittle and provide an opportunity for cracks to form and quickly grow. Within Figure 5.54 the bright appearance precipitates can be seen to exist within grains in a dispersed manner. This may prevent the formation of a crack path in the material preventing cracking at high strains, seen in the single hit deformation tests particularly at high strain rates.

Examination of Microstructure After the Second Deformation Step

The flow stress samples used for two step deformation were sectioned as described in Section 5.3.7. Microstructures produced for varying deformation temperatures during the second deformation at the centre and edge regions of the two stage deformed flow stress samples are shown in Figure 5.55. Considering the edge region microstructures, both the samples deformed during the second deformation at temperatures of 1050°C and 1150°C exhibited obvious cracking in the edge regions, indicating a lack of hot ductility in these regions preventing successful deformation to the chosen strain. It can be observed that the sample deformed at 1100°C exhibited no such cracking in this region. In both the samples deformed at 1050°C and 1100°C, grain substructures were present, as previously observed in Figure 5.51. This is indicative of unrecrystallised grains with stored internal strain. These substructure are seen to a lesser extent in the sample deformed at 1150°C within the larger grains. These results are in contrast with those shown in the micrographs for the single hit compressions whereby complete recrystallisation is observed within the edge regions of samples beyond deformation temperatures of 1100°C.

In an attempt to rationalise the variation in recrystallisation the following is proposed. The relative strain imparted on the material during the second deformation step is approximately 0.76. This strain level is beyond the peak of the recrystallisation threshold suggested by the position of the peak in the flow curve data. This suggests that the second deformation step is more than capable of producing recrystallisation in the central regions of the sample. This therefore points to the formation of substructures in newly recrystallised grains produced during the first deformation step. After the first deformation step it is likely that recrystallisation will have occurred, either during cooling period after the first deformation or during the heat up before the secondary

deformation. These grains will likely be finer than the as HIP grains and may resist further recrystallisation during the secondary deformation as suggested in the work of Zhao and Chaudhury [128]. This will lead to the substructures as shown in Figure 5.55. It can be seen when comparing Figure 5.50 and Figure 5.55 that complete recrystallisation is produced when using a two step deformation at 1050°C when compared with a single hit deformation. This indicates that the first deformation step at a temperature of 1100°C either supports or initiates recrystallisation prior to the second deformation at 1050°C.

Besides the mentioned substructures, it can be noted that the two step deformation strategy does little to improve the hot ductility at the super-solvus temperature of 1150°C with strong evidence of cracking in the edge region of the sample. Evidence of abnormal grain growth is evident in the centre region of the sample. This demonstrates further that forging near the γ' solvus temperature should be strictly avoided. Examining the central region microstructures in Figure 5.55, it is clear that the grain size increases with deformation temperature, very fine grains are produced when the second deformation is conducted at 1050°C and this grain size increases with increasing temperature.

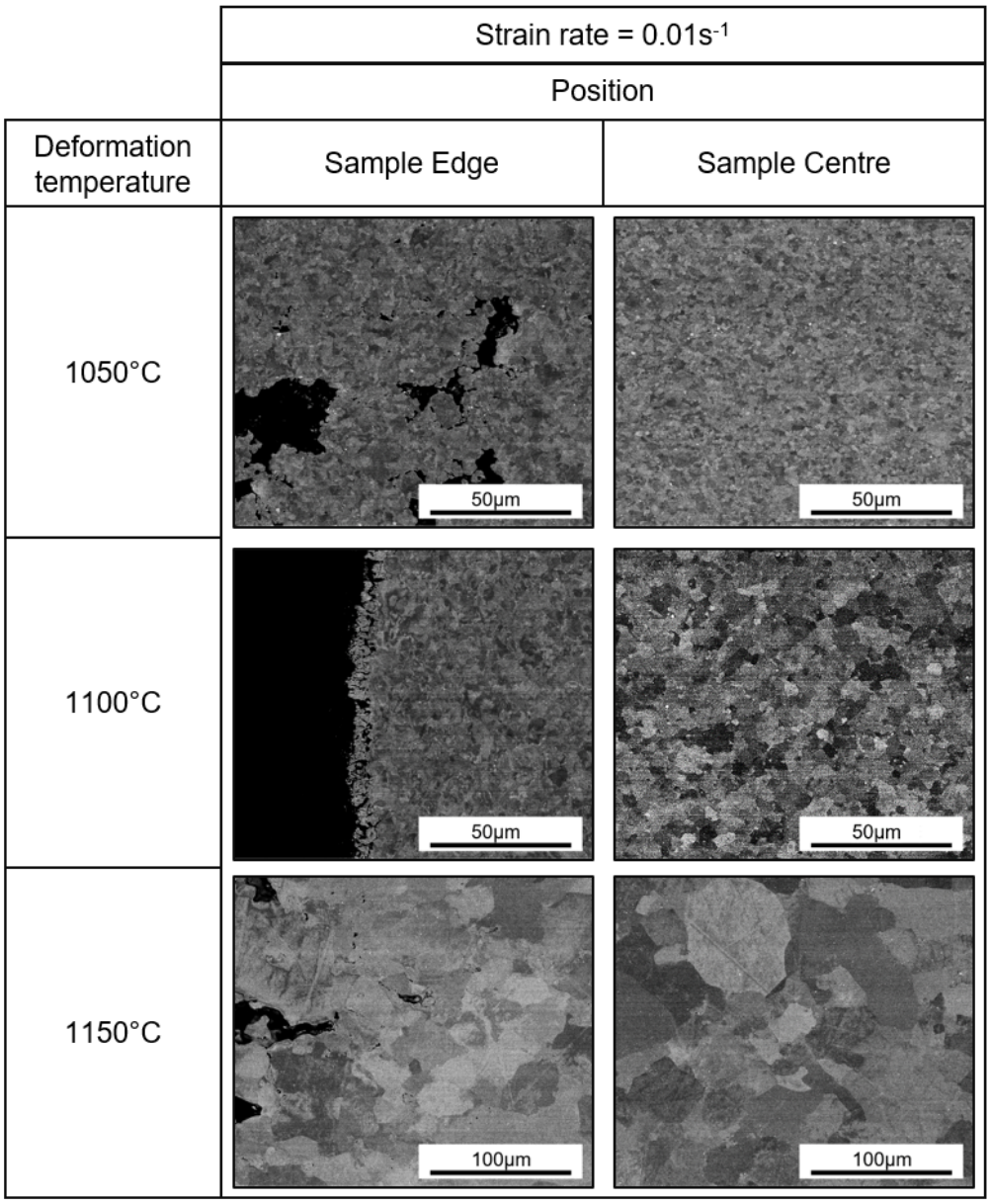

Figure 5.55: Backscatter electron micrographs demonstrating the microstructures produced via two stage deformation for a range of deformation temperatures at a common strain rate of $0.01s^{-1}$ for the second deformation. Microstructures for the edge and central regions of the samples are shown.

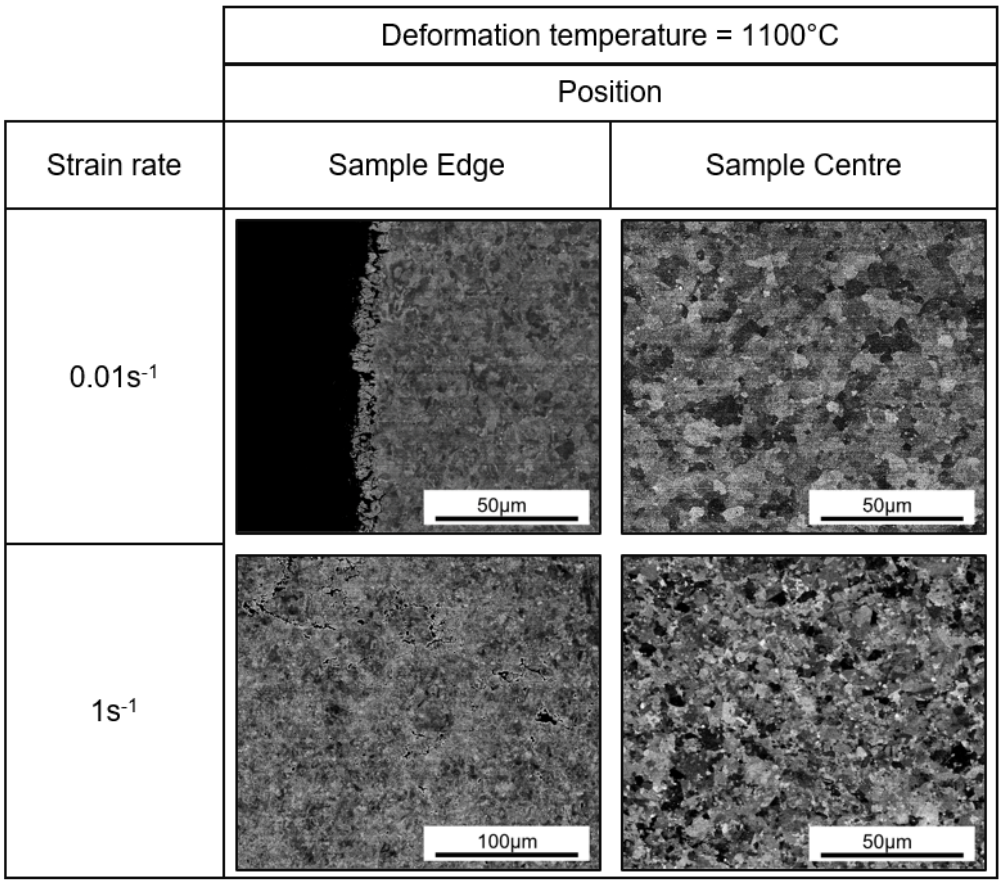

Figure 5.56: Backscatter electron micrographs demonstrating the microstructures produced via two stage deformation strain rates of 0.01^{-1} and 1^{-1} for the second deformation step at a deformation temperature of 1100°C. Microstructures for the edge and centre regions of the samples are shown.

The effect of strain rate during the second deformation step for a deformation temperature of 1100°C was examined as shown in Figure 5.56. As expected, higher strain rates produce smaller grains sizes in the centre regions of the samples owed for a shorter deformation time preventing the growth of as recrystallised grains. Comparing the edge regions of the samples, it can be seen that deformation substructures are present for both test conditions however the higher strain rate produces cracking in the edge of the sample. This is thought to be due to an inability for grain boundary sliding and recrystallisation occurrence for the shorter deformation time associated with a higher strain rate.

The final comparison drawn is between material subjected to a single deformation step compared to a two step compression, with all deformation

steps conducted at 1100°C and a strain rate of $0.01.s^{-1}$. In Figure 5.57 it is clear that both deformation schedules produce similar grain sizes in the centre region of the microstructures, however the difference can be noted in the edge regions with the complete recrystallisation observed for the single hit strategy compared with the two step method. Although this may seem beneficial in the favour of a single hit strategy, cracking is seen in the edge region whereas none is seen for the two hit strategy. It is thought that further deformation can be used to produce complete recrystallisation in the edge region of the sample.

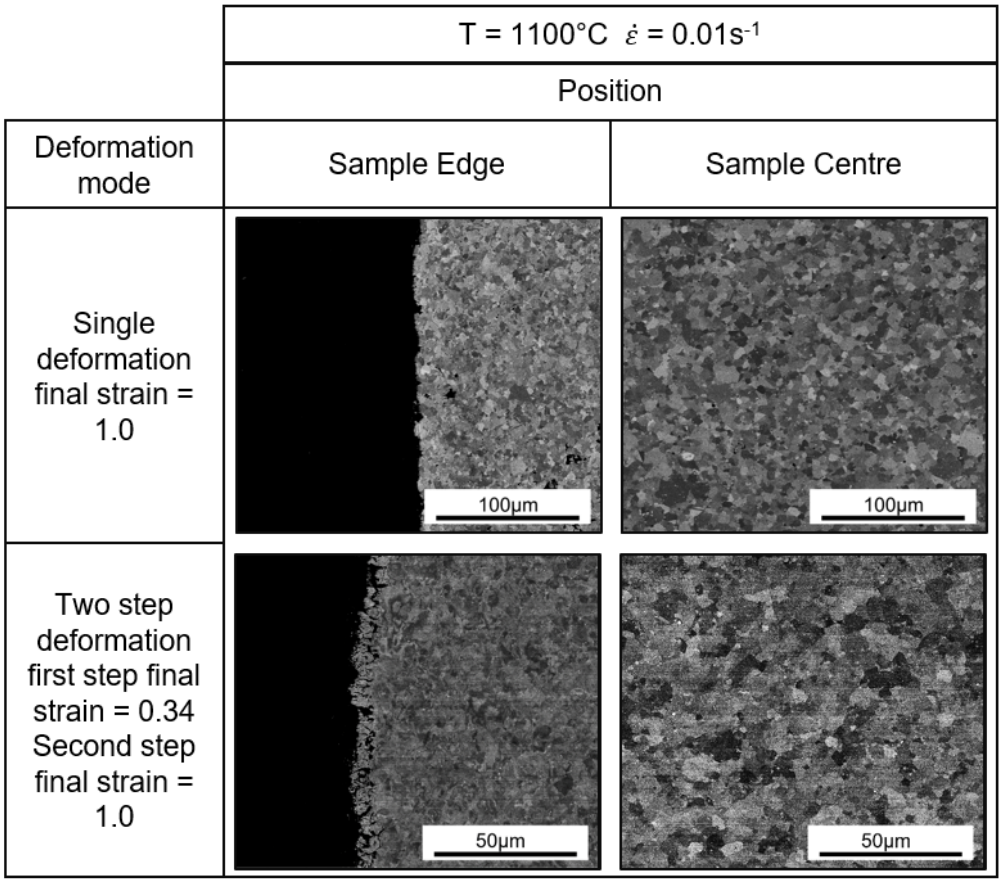

Figure 5.57: Backscatter electron micrographs comparing the centre and edge microstructures produced using single hit and two hit forging strategies, all deformation steps were conducted at a temperature of 1100°C and a strain rate of $0.01s^{-1}$.

Based on these findings, it is not possible to confirm the precise mechanisms that led to the increase in hot ductility with the application of multi-

pass deformations. However the results do offer the following as potential explanations:

- The first deformation step produces a finer microstructure than the starting material when cooled naturally in the presence of argon gas. This may lead to enhanced grain boundary sliding and rotation during the second deformation, akin to an increase in the viability of superplastic flow mechanisms.
- The first deformation step leads to a realignment of PPB networks which otherwise act as crack initiation points due to their brittle nature and provide a pathway for cracks to begin and propagate leading to gross sample cracking.
- γ' precipitates may also be affected in such a way to allow increased material flow, such as a reduction in pinning mechanisms previously preventing grain boundary sliding etc.
- The first deformation is changing the recrystallisation dynamics in the material such the the energy input required for recrystallisation is lower. This means internal strain energy is more readily used in microstructural change as opposed to the formation of cracks.

5.4.8 Thermal History and Interrupted Testing

To extract the effects of the heating and the hold time on the material, a thermal history test was conducted whereby the 10 mm dia x 15 mm samples were placed in the Gleeble, as described previously 5.3.2. Each sample was placed between the dies, the heating was applied in order to produce a heating rate of 5°C.min^{-1}. Once the temperature reached 1100°C the sample was dwelled at constant temperature for five minutes. Upon completion of the dwell, one sample was subjected to an air cool in argon atmosphere, the other sample was quenched using compressed air jets. Due to an error in the programming of the Gleeble system, the cooling curves for both these tests were not captured.

The micrographs displayed in Figure 5.58 and Figure 5.59 show the microstructure in five key positions within the samples for the quenched and air cooled thermal history tests respectively. In Figure 5.58, it can be clearly seen that large grains can be seen in areas B and D of the sample compared to areas A, C and E which have grain sizes similar to the pre-forged microstructures. One may speculate as to why this may occur; Areas B and D are in the corner regions of the sample, which are in direct contact with

the dies which act as the electrodes to provide the electrical power for resistive heating. If the pre-compressed sample is misaligned within the dies, there can be locally high resistance or current density leading to overheating. Based on the considerable grain growth, it can be stated that the material has exceeded the γ' solvus and therefore the temperature would have exceeded at least 1150°C. Intergranular cracking can also be observed in area D which is an indication of local melting or highly focused stresses in the region. Based on previous observations this points to high stresses and local strains possibly as a result of the clamping load. This observation should be noted when considering compression test data via Gleeble testing results, any temperature inhomogeneities may lead to the noted effects and lead to premature cracking thus skewing any forgeability study conducted. Based on these findings it is assumed that all samples that did not feature external cracking were unaffected by these temperature gradients.

Comparing Figures 5.58 and 5.59, the areas identified as A, C and E show comparable microstructures, indicating that the affect of cooling from the hold is not significant in regards to the resultant microstructure. Both samples exhibit similar grain sizes and morphologies as the HIP material presented in Figure 5.3. This suggests that the temperature must not have exceeded the γ' solvus temperature. This is confirmation that the temperature which the sample reaches during heating does not exceed the set point temperature by more than 35°C which would take the specimen beyond the γ' solvus of the material. This suggests that if the sample is aligned correctly within the Gleeble dies, then good temperature control can be achieved. These results prove that a direct comparison can be made between the as HIP material and the post compression test material as the microstructure does not change during the temperature ramp and dwell period.

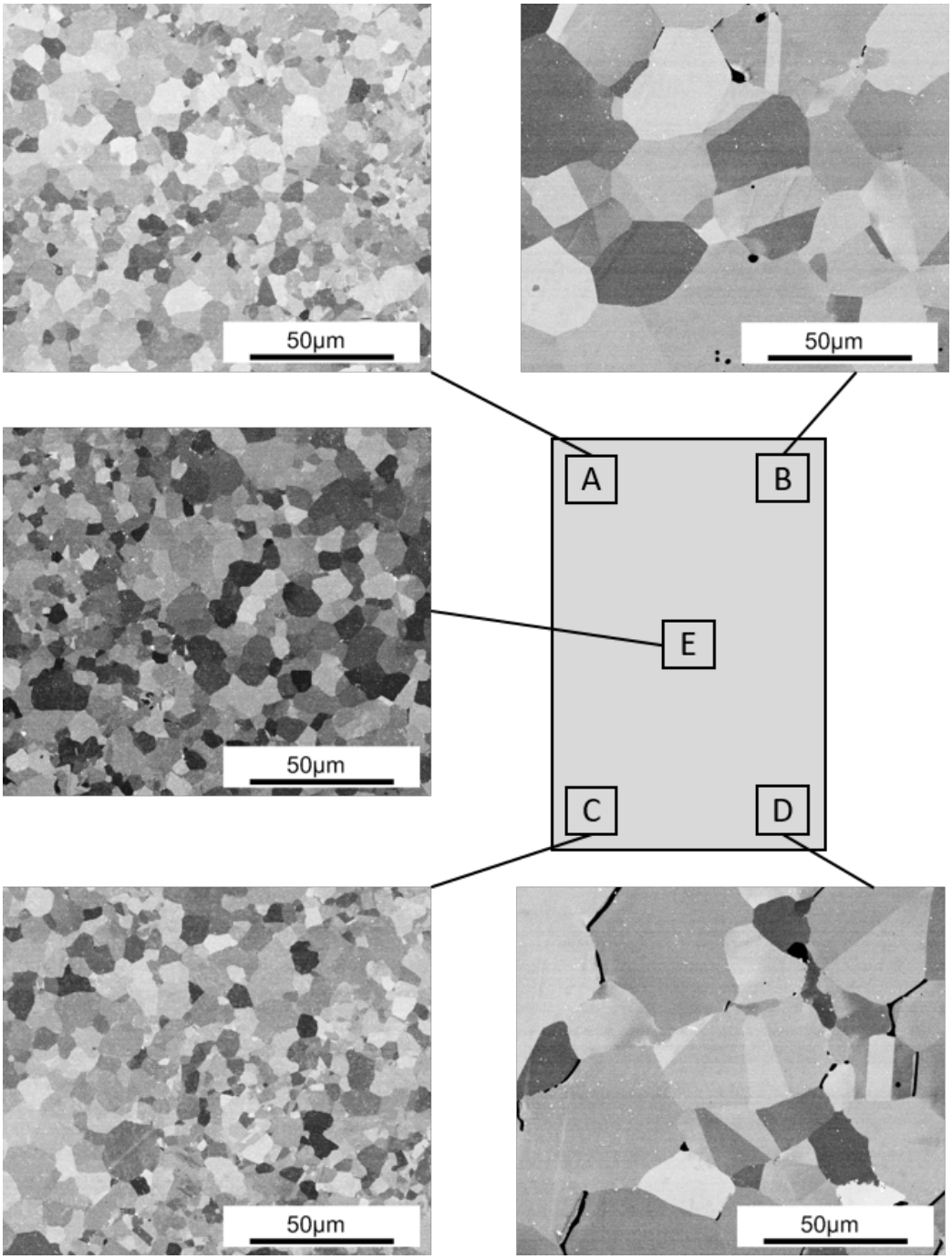

Figure 5.58: Backscatter electron micrographs showing a specimen which was heated to a temperature of 1100°C and held for five minutes before being quenched using high pressure air jets using the Gleeble 3800.

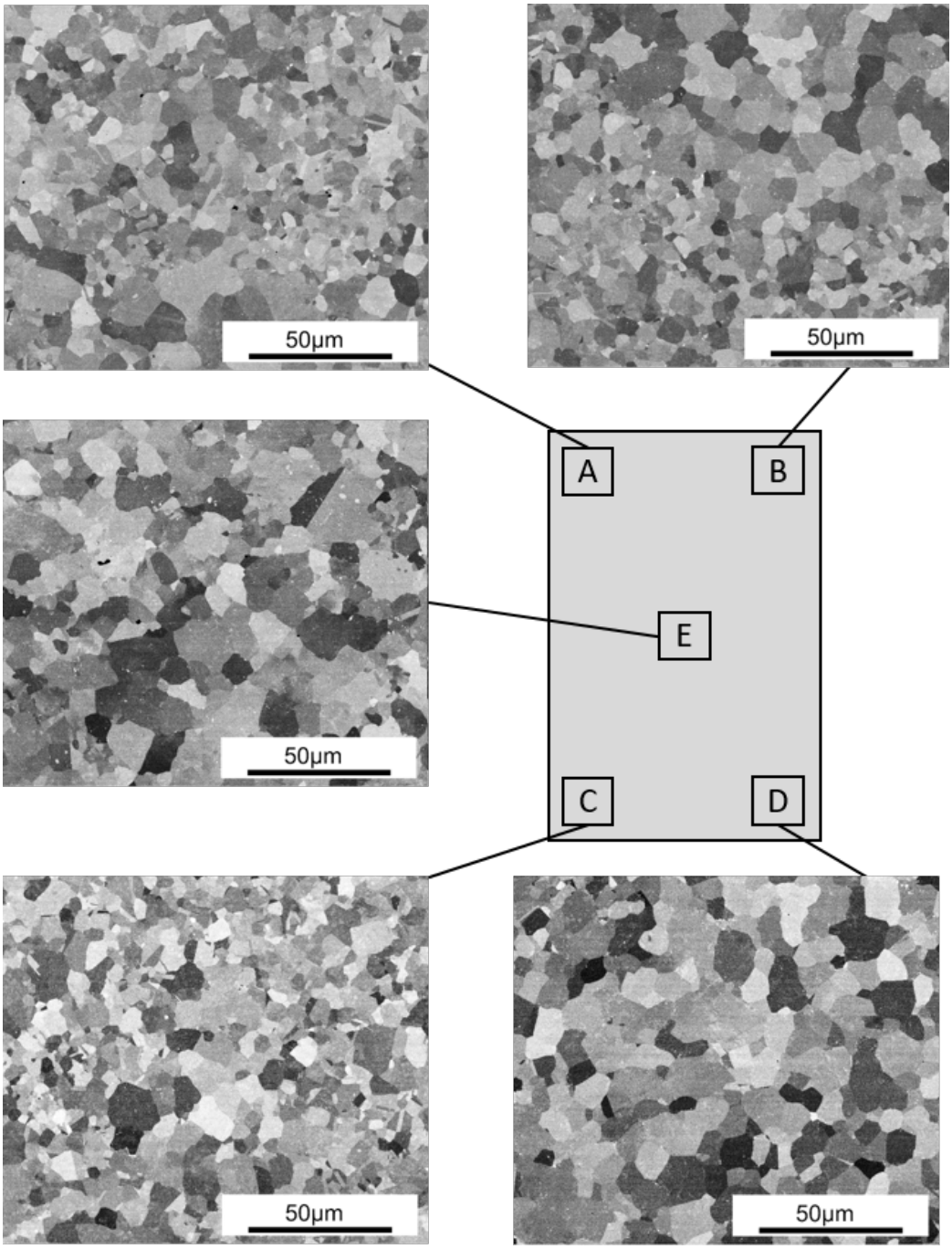

Figure 5.59: Backscatter electron micrographs captured for a specimen which was heated to a temperature of 1100°C and held for five minutes before being allowed to cool naturally using the Gleeble 3800.

Interrupted Deformation Testing

Based on the reduction in cracking observed for some conditions deformed using the two step strategy, it is possible that some microstructural mechanism takes placed which then facilitates further strain without the onset of cracking. Interrupted compression tests were performed using a deformation temperature of 1100°C at $0.01.s^{-1}$ to strains of 0.15 and 0.34. Quenching was used in an attempt to freeze the microstructure to observe features present. After deformation to a strain of 0.15 (Figure 5.60), it can be observed that the sample starts to exhibit non-uniformity. Within the deadzone region where input strain is low (area A), it can be observed that a relatively course microstructure exists. A much finer microstructure present in the centre region (area C). At the edge of the sample, which exhibits moderate strain also had a fine microstructure (area B). This behaviour indicates that recrystallisation occurs even at low strain values. Comparing this sample with the material strained to 0.34 (Figure 5.61) it can be seen that no obvious differences exist between material deformed to the two strain values. This suggests that no grain morphology changes are occurring between the two strain values. Higher magnification micrographs from region C from both Figures 5.60 and 5.61 are presented in Figure 5.62. The clear similarity in grain size and morphology in the centre region of the sample can be clearly seen, the equiaxed structure is clear evidence of the occurrence of recrystallisation occurring at low strain values. Due the samples being quenched after deformation, this recrystallisation must therefore have been dynamic as opposed to static, as the quenching will limit the development of statically recrystallised grain structures.

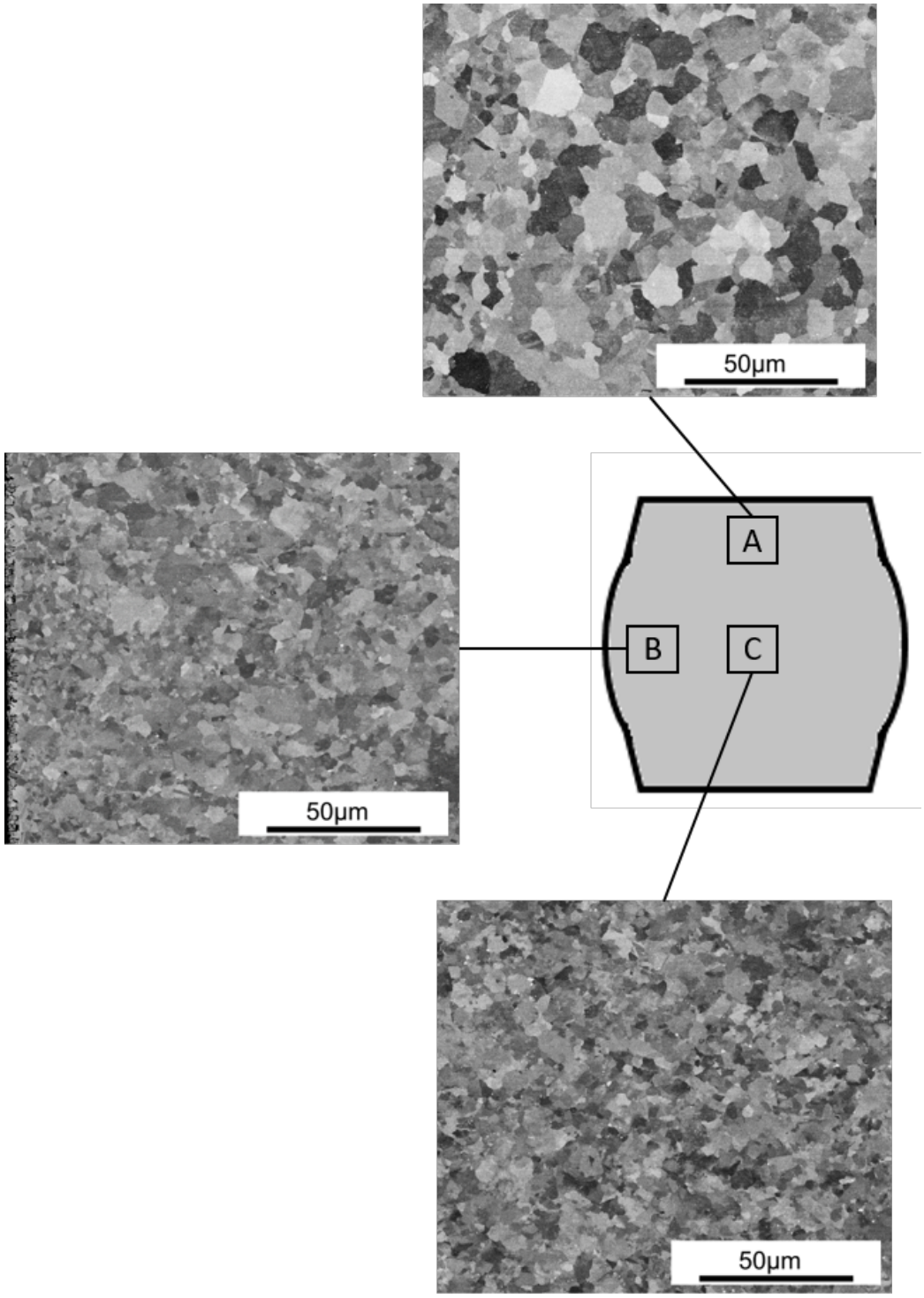

Figure 5.60: Schematic showing the microstructure at various positions in a sample subjected to a compressive strain of 0.15, showing the region near the upper die (A), the edge of the sample (B) and the centre region (C).

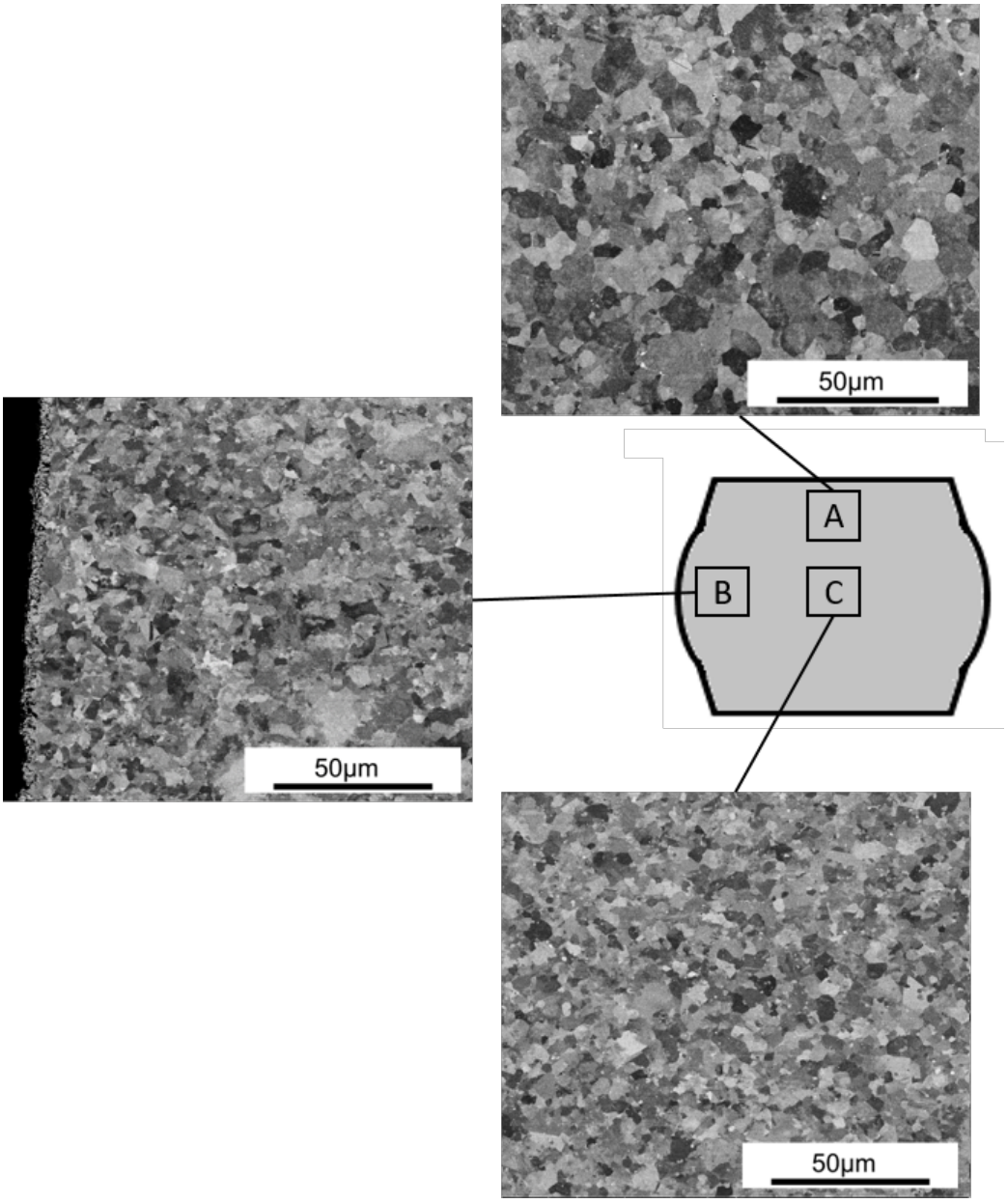

Figure 5.61: Schematic showing the microstructure at various positions in a sample subjected to a compressive strain of 0.34, showing the region near the upper die (A), the edge of the sample (B) and the centre region (C).

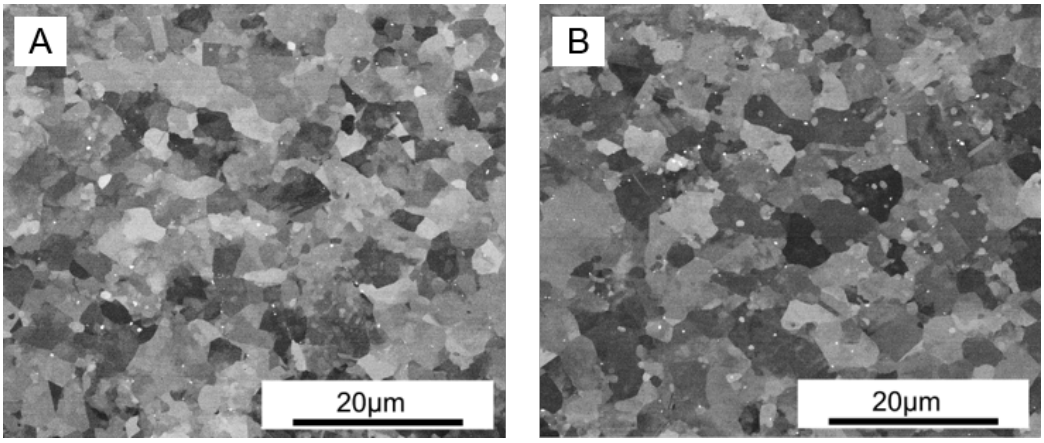

Figure 5.62: Comparisons of the centres of samples produced using compressive strains of 0.15 (A) and 0.34 (B) after compression and rapid cooling via pressurised air jets using the Gleeble 3800.

Over-strain Testing - Deformation to 1.2 Input Strain

Following the successful forging to a strain of 1.0 at 1100°C with a strain rate of $0.01s^{-1}$, it was decided that the final strain would be increased to determine whether a crack free sample could be produced using the two step forging method. One significant reason for increasing the final strain during the final forging is that a larger diameter sample is produced, providing more material for face turning trials. Successful forging on a small scale to higher strains would then give a reason to up-scale higher strain testing to a larger billet.

In order to produce this sample, a 10mm dia x 15 mm sample was first subjected to a strain of 0.34 at 1100°C and a strain rate of $0.01s^{-1}$. After this first upset the sample was air cooled to below 200°C. The sample was then reheated and held at temperature in the manner described for all previous compression tests. The sample was then subjected to an upset strain of 1.2 and was then air cooled. A photograph of the resultant sample is shown in Figure 5.63. Figure 5.65 reveals the microstructural features contained within the sectioned specimen at various positions. No significant cracking except on the exterior diameter of the sample is visible, which shows that the material is capable of withstanding the increased upset. In Figure 5.65 grain size inhomogeneity is clearly apparent with finer grains observed towards the perimeter of the samples and enlarged grains present within the central region, exposed to the highest strain and strain rate. Compared directly with the centre region of a sample deformed under the same conditions to a strain of 1.0 (Figure 5.64) it can be seen that the grains in the centre

region of the 1.2 strain sample are larger in size than the equivalent region in a 1.0 strain sample under equivalent conditions. This grain inhomogeneity can be explained through examination of the γ' precipitates (Figure 5.66), whereby in the centre region (region B) the γ' at the grain boundaries have gone completely into solution, this is in direct contrast with the outer regions (regions A and C) where the primary γ' is still intact. This explains the large inhomogeneity in grain size as the absence of the aforementioned precipitate will have facilitated large grain growth through lack of pinning.

The dissolution of γ' is likely due to an adiabatic temperature increase in the centre region of the sample which will have been subjected to both the highest strain, strain and therefore energy input through adiabatic heating. This energy will drive recovery mechanisms but also lead to temperature rise, particularly for such a small volume of material as is used in the compression test. As no dramatic grain growth occurs in the perimeter of the sample, it can be concluded that incorrect test temperature does not explain the dissolution of γ'.

This result indicates that strains of 1.2 can possibly lead to large grain formation for the given testing conditions. Although this is a concern should the material be processed for industrial application, the inhomogeneity produced could be exploited to produce material suitable for examining the effects of varying grain size and precipitate morphologies on machining effects within a single billet. This testing condition was therefore selected for up scaling to the machinability billet forging trials.

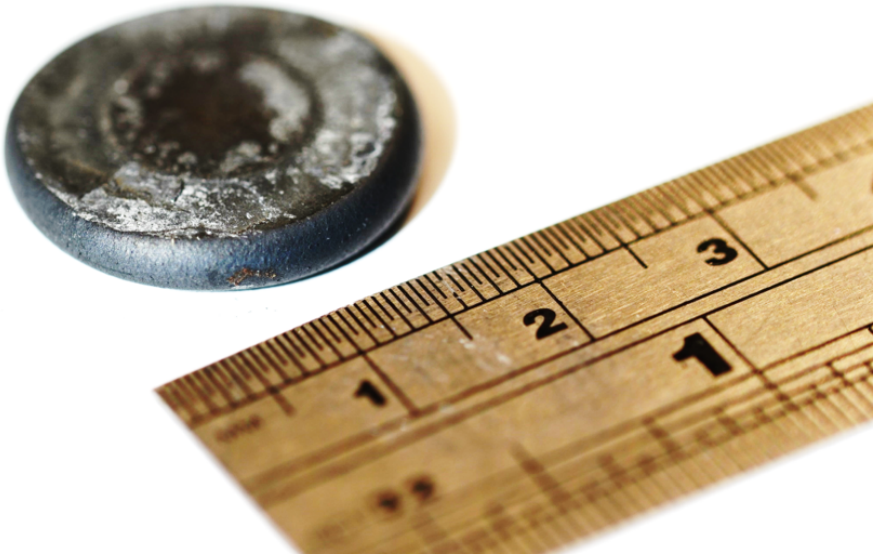

Figure 5.63: Photograph of the compression test sample subjected to an upset to a strain of 1.2 at a strain rate of $0.01s^{-1}$ and at a deformation temperature of 1100°C.

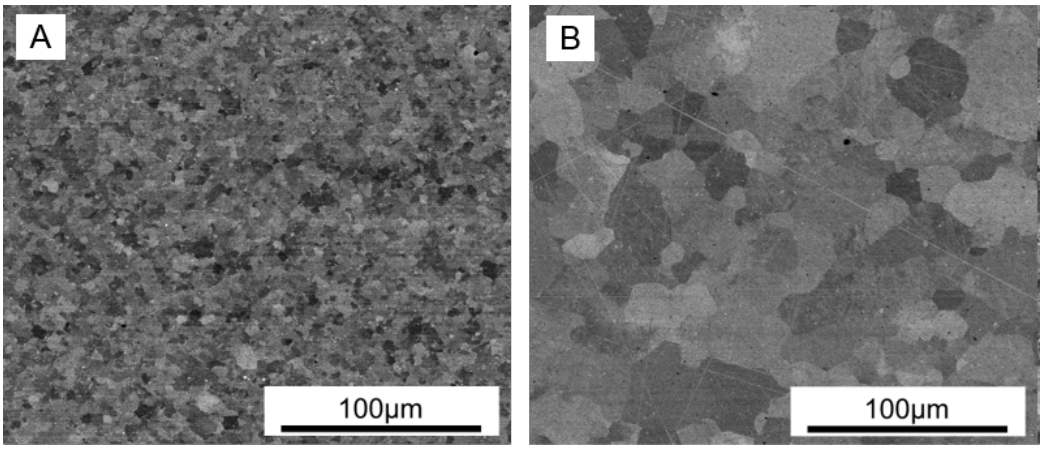

Figure 5.64: Comparison of the γ grain morphology at the central region of specimens subjected to an upset to a strain of 1.0 (A) and 1.2 (B) at a strain rate of $0.01s^{-1}$ and at a deformation temperature of 1100°C.

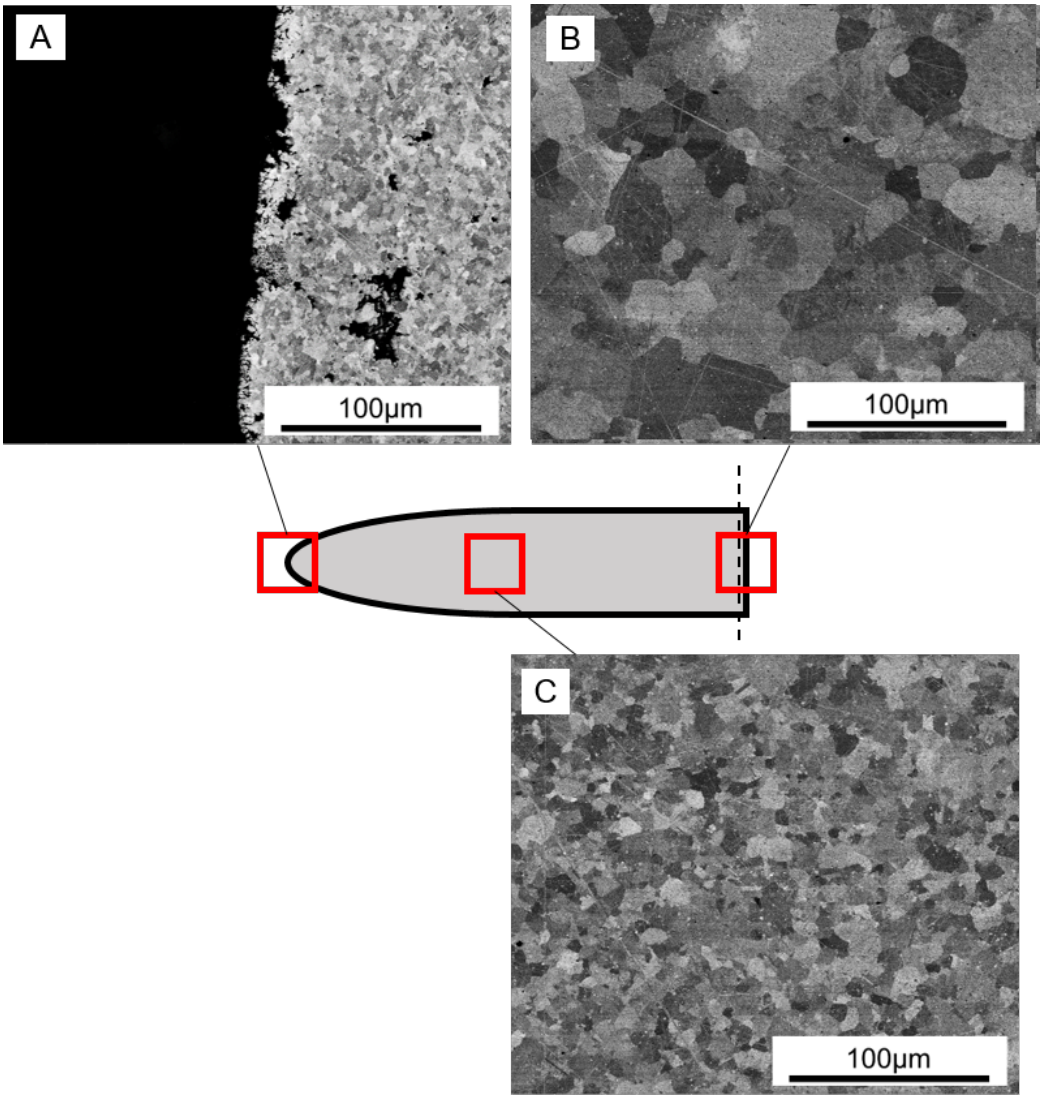

Figure 5.65: Schematic showing the changes in γ grain morphology with changing position within a sample subjected to an upset to a strain of 1.2 at a strain rate of 0.01 s^{-1} and at a deformation temperature of 1100°C. Positions shown cover the edge region (A), the sample centre (B) and a distance equidistant between A and B (C).

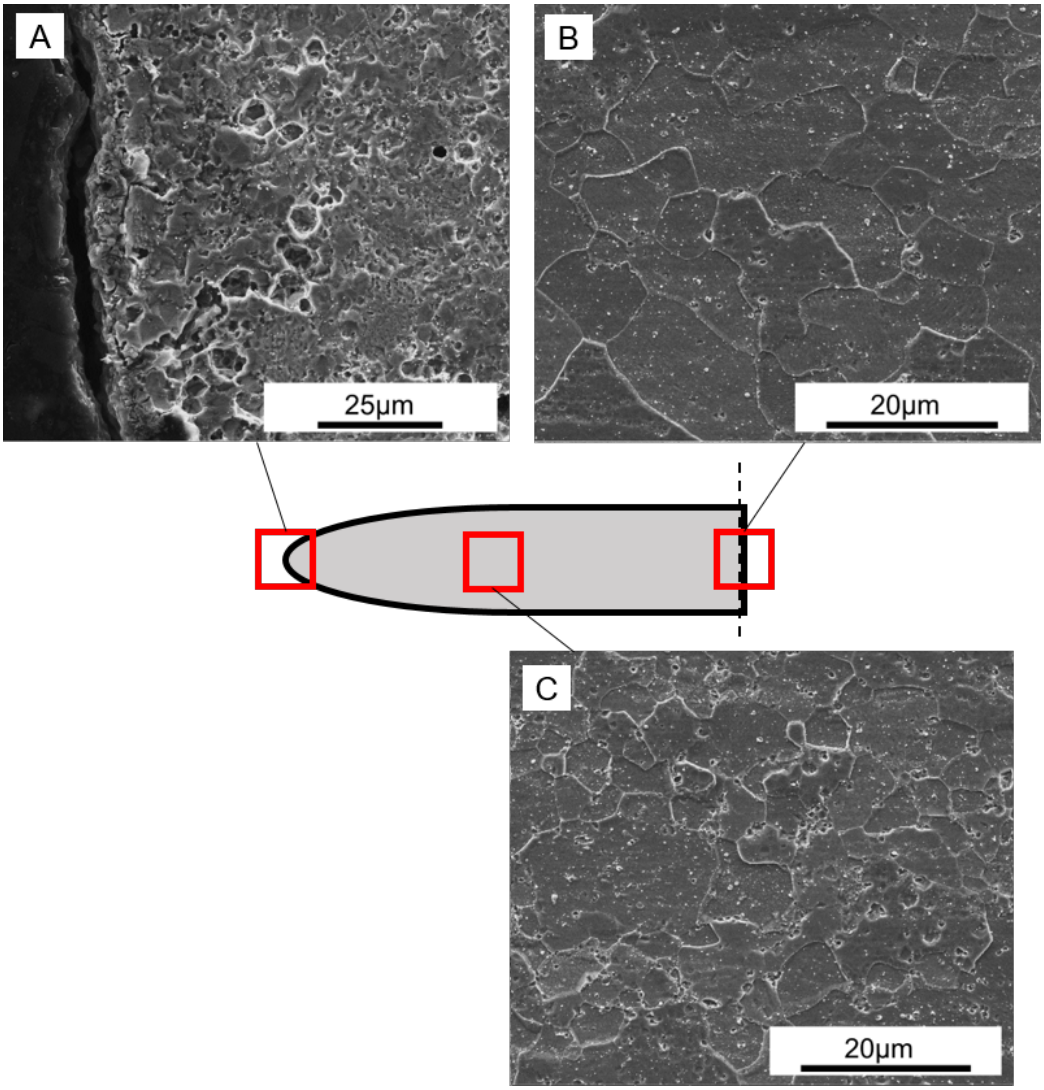

Figure 5.66: Schematic showing the changes in γ' precipitate morphology with changing position within a sample subjected to an upset to a strain of 1.2 at a strain rate of 0.01 s^{-1} and at a deformation temperature of 1100°C.

Intermediate Temperature Deformation Trial

It has been demonstrated that the deformation temperature has significant implications regarding the post deformed microstructure, with lower temperatures giving a finer grain size and higher temperatures reducing the tendency for cracking to occur. To determine whether a compromise could be achieved between the 1050°C and 1100°C, an additional compression test was performed using a deformation temperature of 1100°C to an upset of

0.34 strain, this was then followed by an upset to a strain of 1.0 at a test temperature of 1075°C. The microstructure produced in Figure 5.67 shows when these deformation conditions are used, an unrecrystallised region can be observed in region A, while fully recrystallised structures can be observed in regions B and C. This observation indicates that at a lower deformation temperature, sufficient strain is required in order to induce complete recrystallisation. While the unrecrystallised material is evident in a smaller scale flow stress sample, it can be expected that the slower cooling rate likely produced in the larger billet will increase the time at temperature in the low strain input regions which will produce a greater level of recrystallisation through SRX. These results indicates that the alloy tested is sensitive to chilling effects and therefore care should be taken to maximise die temperature during the conventional forging of the larger billets on the industrial scale.

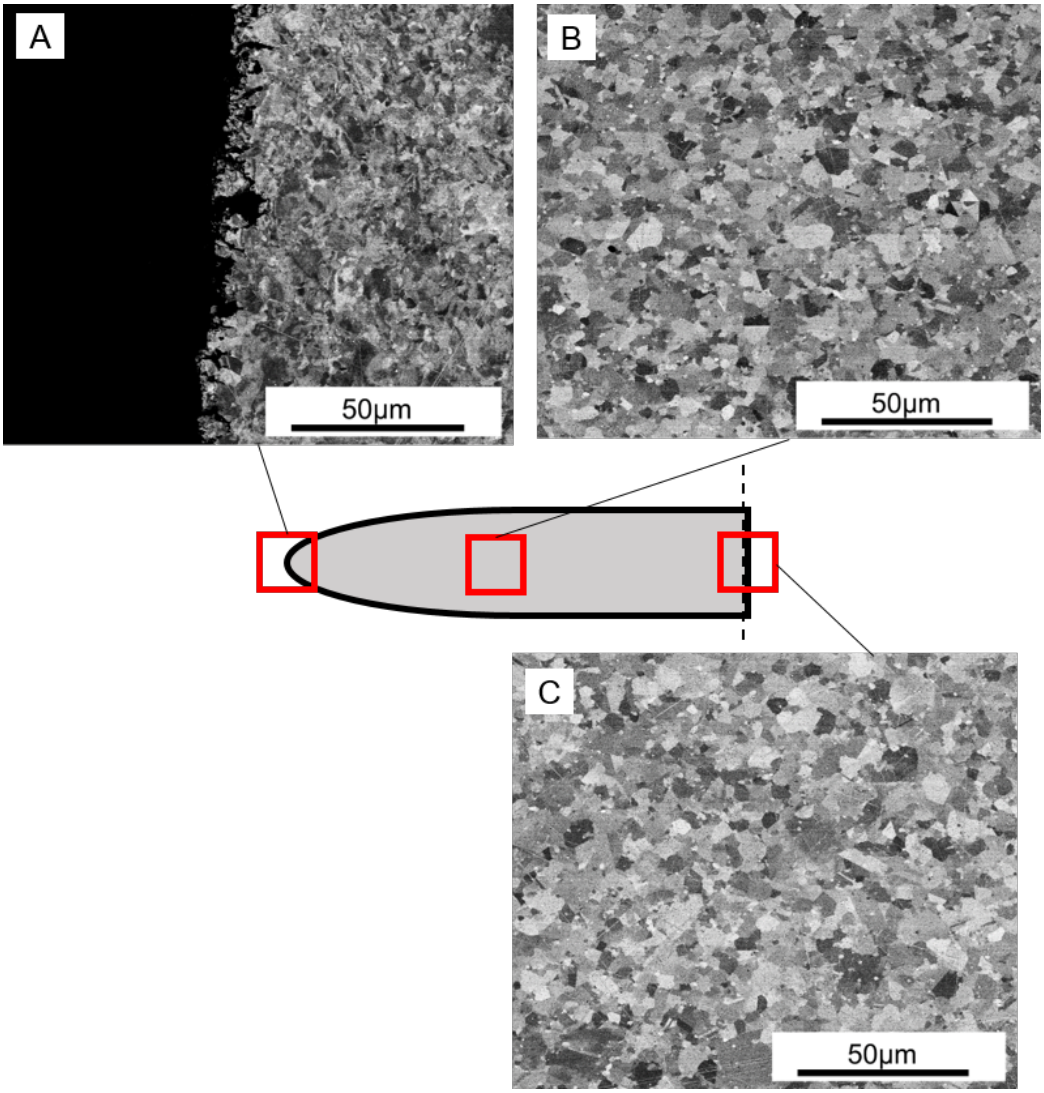

Figure 5.67: Schematic showing the microstructure produced when performing an second upset to a strain of 1.0 at 1075 °C after an initial upset to a strain of 0.34 at 1100°C. Both upsets were performed using a strain rate of $0.01s^{-1}$. Figure shows the edge (A), quarter region (B) and centre (C) of the produced sample.

Microstructural Development During Two Step Forging

Figure 5.68 shows the resultant microstructural development captured through the individual interrupted deformation tests in the centre region of the sample, the area subjected to the highest strain input during hot compression. The microstructures produced after each interrupted test were preserved us-

ing the air quench facility on the Gleeble 3800. It can be observed that the first deformation has clearly the greatest influence over the microstructure in the centre region of the sample. After deformation to a strain of 0.15, recrsytallisation can be clearly observed. By the time the first deformation is ceased at a strain of 0.34 a refined equiaxed structure is observable in the centre region. During the second deformation, at a total strain of 0.65, marginal grain growth can be observed, likely due to temperature effects. Figure 5.41 indicates, although skewed by the strain rate control issue, that the flow stress is close to steady state in this region, further indicating the onset of the balance between deformation and recovery which leads to little change in the microstructure. This is further seen when examining the microstructure at the completed strain of 1.0 in Figure 5.68, as there is negligible microstructural development between strains of 0.65 and 1.0.

Examining the lower strain region on the perimeter of the samples in Figure 5.69, the first deformation leads to microstructural refinement in the perimeter region compared to the pre-deformed structure. However compared to the centre regions after the first deformations (Figure 5.68) it can be noticed that less refinement occurs in these outer regions. It can be seen that the secondary deformation leads further microstructural alteration in the perimeter region. The perimeter regions exhibit fine, equiaxed structures indicating the occurrence of complete recrsytallisation however for the conditions displayed during the second deformation in Figure 5.69 (1100°C at a strain rate of $0.01s^{-1}$), it can be seen that a secondary incomplete recrsytallisation event has taken place. This is evidence that the recrystallisation seen is cyclic in nature. Comparing Figures 5.68 and 5.69 shows that even in the sub-scale samples, large inhomogeneities in structure can occur. Although this is problematic for material to be used in components, it was decided that it would be advantageous to up-scale to billets which could then be machined with a view to determining how the machining process is affected by such changes in microstructure.

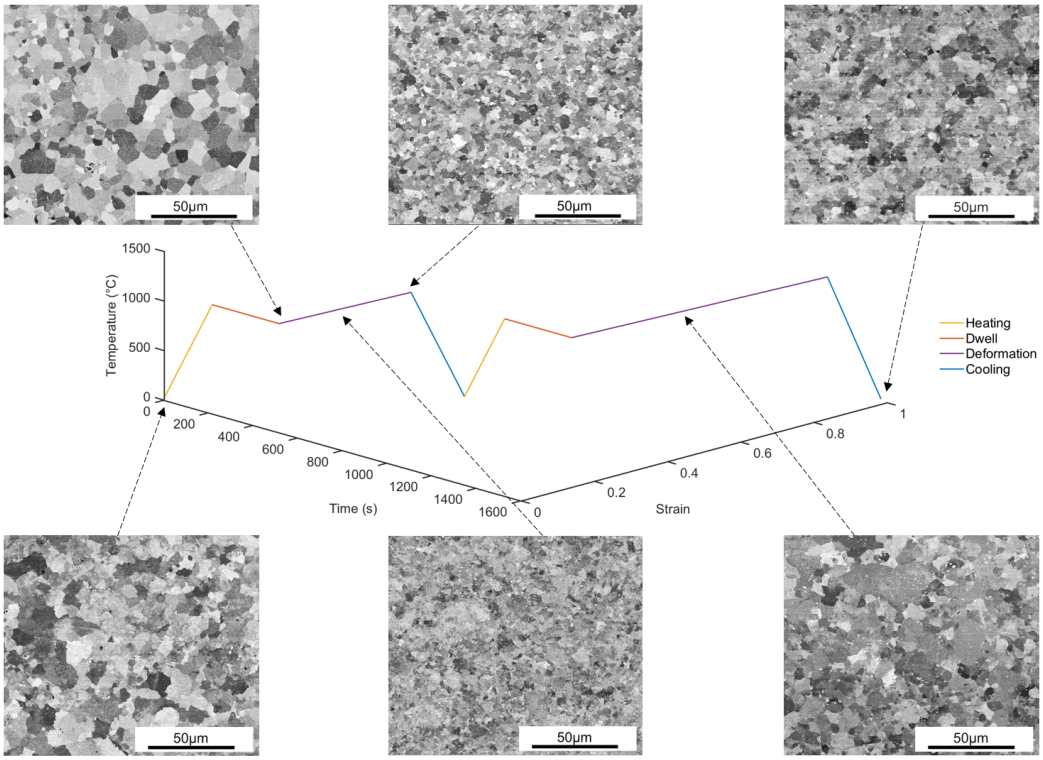

Figure 5.68: Schematic showing the development of microstructure during the two stage deformation strategy as a function of time, temperature and strain. All deformations were performed at a strain rate of $0.01s^{-1}$. All micrographs were captured in the centre region of the forged specimen after quenching.

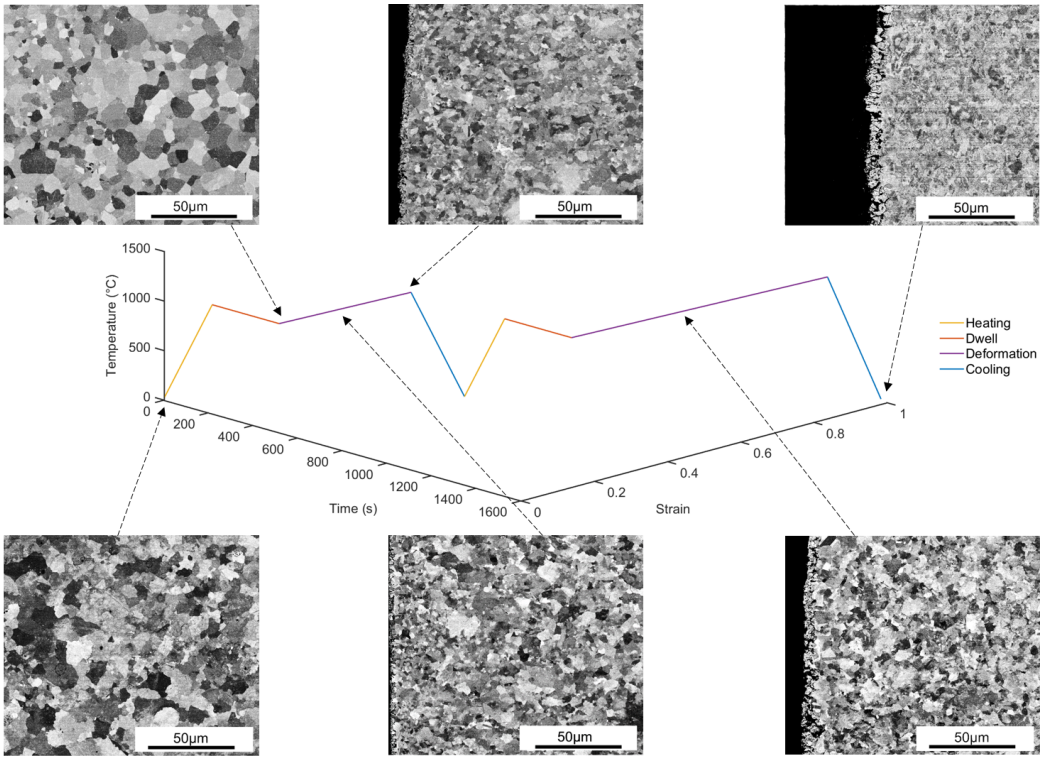

Figure 5.69: Schematic showing the development of microstructure during the two stage deformation strategy as a function of time, temperature and strain. All deformations were performed at a strain rate of $0.01s^{-1}$. All micrographs were captured in the edge region of the forged specimen after quenching.

5.5 Industrial Scale Open Die Forging

Using the knowledge gained from the small scale testing, industrial scale forgings were undertaken using larger billets of the 131072 material in the as-HIP condition. In order to perform such tests, 7 billets were manufactured using two different billet sizes. The first billet size produced was 71 mm in diameter and 106.5mm in length, this represents a scaled up version of the flow stress test samples with the same aspect ratio of 1.5:1. These billets would be used to test some of the conclusions observed during the small scale testing, such as the propensity for crack formation with deformation temperatures close to the γ' solvus of the material and to test the optimum single step deformation parameters using slowest possible strain rate at a temperature of 1100°C. If successful, this parameter set would be up-scaled to a larger billet size. The larger size billets were manufactured to be 71mm

in diameter and 213mm in length (an aspect ratio of 3:1). Once forged, these billets would eventually be used to conduct machining trials.

Industrial Forging Press Specifications

A Photograph of the large industrial scale forging apparatus used to performed the large scale billet forgings is shown in Figure 5.70. An image of the press during a large scale forging is shown in Figure 5.71. The specifications for the forging press are shown in Table 5.11. The forging press is hydraulically actuated and consists of two steel flat plate dies. No in-built die heating was available, however a high power burner can be used to achieve some level of die heating.

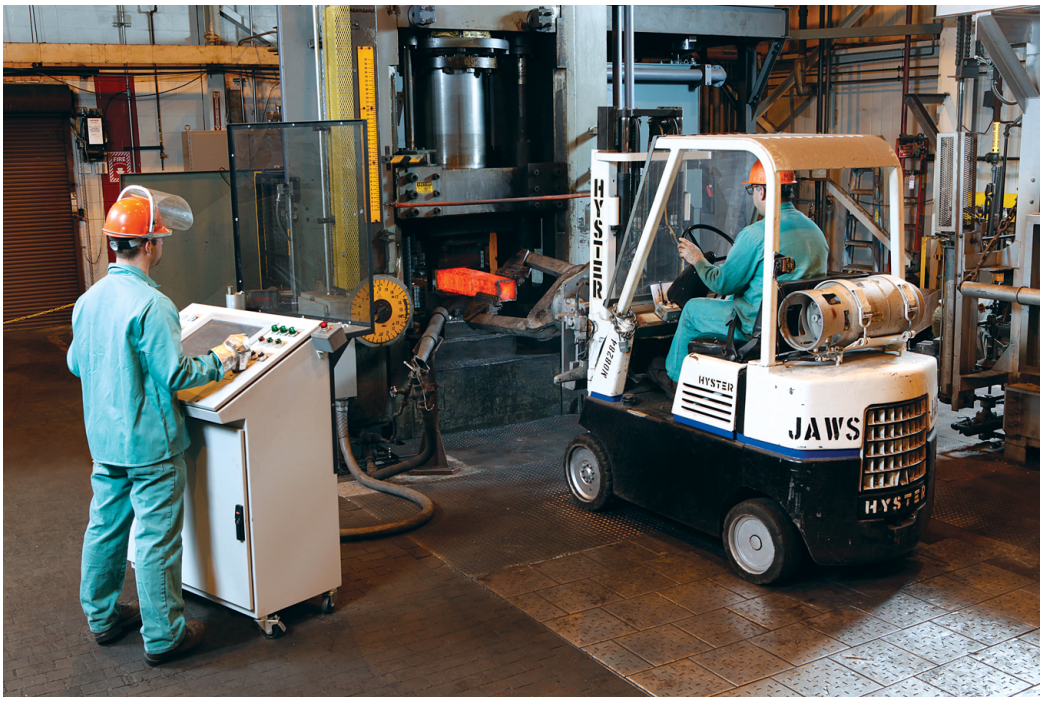

Figure 5.70: Large scale industrial forging press located at Carpenter Technology Corporation Reading PA. Used for forging the large scale billets of the alloy 131072. Image Courtesy of Carpenter technology.

Figure 5.71: Close up image of the dies and work piece using the forging press located at Carpenter Technology Corporation Reading PA. Image Courtesy of Carpenter Technology.

Table 5.11: Large scale forging press specifications

Maximum press force	500 tonnes
Minimum die velocity	4.23 $mm.s^{-1}$ (10 $in.min^{-1}$)

Intermediate Scale Testing - Single Deformation Step Trial

The first test conducted on a industrial scale was the forging of the intermediate scale billet using a deformation temperature of 1100°C. The press operates using a fixed velocity and not fixed strain rate. The maximum velocity used to perform compressions on this press was 63.5 $mm.s^{-1}$ based on measurements from time stamped video stills of each compression.

The sample was heated to the testing temperature over a period of two hours to ensure that the sample temperature was homogenised. Just before the forging commenced the dies were heated using a large gas burner. This was designed to transfer the maximum amount of heat possible in a short period of time. Due to the layout of the furnace it is impossible to accurately

determine the temperature of the dies. This presented two options, either the forging could be performed with the dies at room temperature where the temperature is known, or the dies could be heated as best as possible to minimise the die chill effects. Due to the relationship between temperature and cracking seen in the small scale tests, it was decided that the dies would be heated using the burner to prevent excessive die chill during forging and minimise the probability of cracking.

Once the sample had been held in the furnace for the prescribed time, it was transferred to the furnace with heavy duty tongs and placed on the preheated dies. The forging program was then run which specifies both the velocity of the upper die and the stopping point which equates to the final height of the sample after deformation. Once the sample had been deformed during forging, the sample was left to air cool to room temperature.

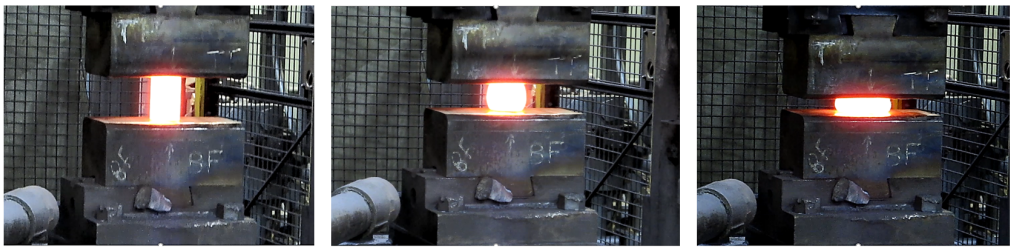

Figure 5.72: Still images extracted from video footage of intermediate size sample being deformed at 1100°C. Showing the start of deformation when the die comes into contact with the billet (left), the middle of the deformation step (centre) and the end of the deformation just before the die retreats from the workpiece (right).

Figure 5.72 shows the evolution of the billet shape during deformation. The billet shows a barrelled geometry indicating the presence of high friction condition, which is expected given the un-lubricated conditions. It can be seen however that geometry is reasonably symmetrical. Although it cannot be seen in Figure 5.72, significant cracking occurred as demonstrated in Figure 5.73.

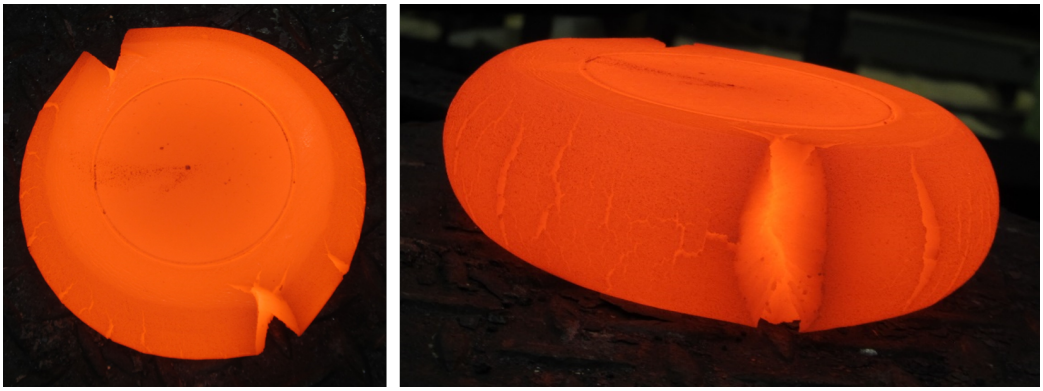

Figure 5.73: Post forged intermediate scale billet. Forged using a single deformation step to a strain of 1.0 at 1100°C, showing severe cracking just after deformation has occurred.

The parameters chosen for the forging shown in Figure 5.72 and 5.73 were representative of the best condition seen in the single step compression tests. However the average strain rate calculated for this test was $0.23s^{-1}$. Comparing the billet morphology in Figure 5.73 and the small scale tests performed at 1100°C shown in Figure 5.38, it can be seen that the level of cracking produced is closer in severity to the sample deformed at a constant strain rate of $1.0s^{-1}$. This gave an indication that the nominal forging conditions chosen for the larger forgings were close to being achieved.

This initial test further highlighted that limited hot ductility is an issue when conventionally forging nickel superalloys and it is why isothermal conditions are currently employed for the forging of turbine discs made of alloys such as RR1000, in order to more tightly control the processing conditions during forging. After this trial test on the intermediate scale billets, it was apparent that the single step forging method would not be suitable for forging the full scale billets. The larger scale billets have an even higher aspect ratio than the intermediate scale billets and are likely to suffer from even higher levels of temperature inhomogeneity than the intermediate scale billets. The longer full scale billets would also be subjected to larger strain rates than the intermediate scale billets which would further increase the propensity for cracking.

Intermediate Scale Testing - Two Step Deformation Trial

The level of cracking on the intermediate scale test suggested that the hot ductility would need to be improved in order to produce a successful forging. The level of cracking seen on the small scale single step tests (Figures 5.38-

5.39) suggested that a change in temperature does nothing to improve hot ductility as external surface cracking is seen unilaterally for all single step deformation tests performed at strain rate of $1s^{-1}$. This observation led to a trial of the two step deformation strategy. It was decided that the worst case scenario would be tested in order to validate the behaviour seen when performing the second step of deformation, a two step strategy was employed on a intermediate size billet matching the previous two hit strategy tested on the Gleeble using the small scale samples.

One of the intermediate size billets was placed in the furnace set to 1100°C for two hours. After the two hour dwell the sample was removed and deformed using the minimum cross head speed to a reduction of 30% in height. The sample was then immediately placed in a separate furnace set to 1150°C and heated for 1 hour. Once the hour had elapsed the sample was then deformed to a final true strain of 1.0. The billet before deformation, after the first step of deformation and after the second step of deformation is shown in Figure 5.74.

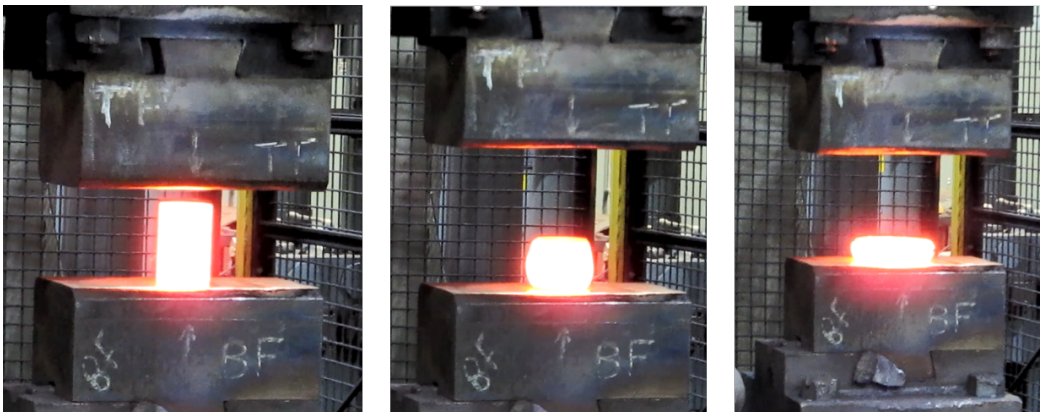

Figure 5.74: Two step deformation forging performed on the industrial scale open die forging press showing an intermediate scale billet before the first deformation step (left) after the first upset to a reduction of 30% height (centre) and after the second upset to a strain of 1.0 (right).

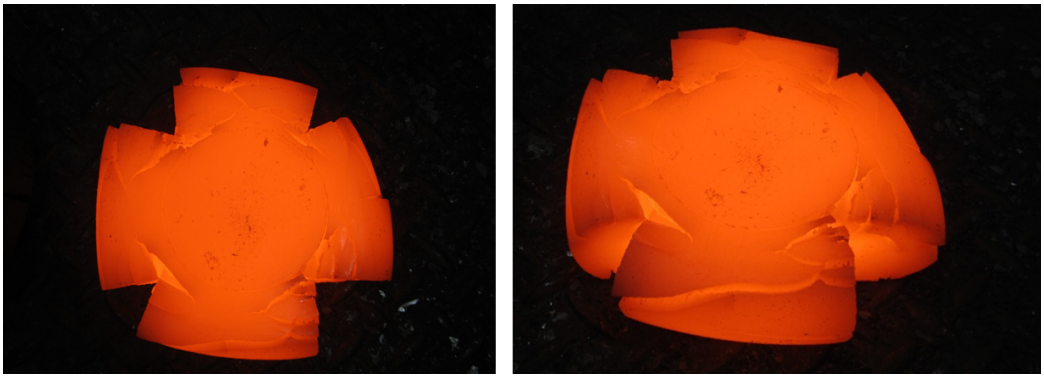

Figure 5.75: Intermediate scale billet post two step deformation, initially upset by 30% at 1100°C and subsequently upset to a strain of 1.0 at 1150°C. Showing gross cracking and sample failure.

Figure 5.74 shows that after the first step of deformation, the sample has no evidence of cracking, however after the second deformation step, catastrophic failure of the sample has occurred, as highlighted in a photograph of the sample after the second deformation at 1150°C, as shown in Figure 5.75. The morphology of this billet after deformation almost matches exactly the sample morphology produced in the small scale two step deformation performed at a strain rate of $1.0s^{-1}$ at 1150°C, as shown in Figure 5.45. This is further evidence that deformation close to the γ' temperature results in a loss of ductility as noted in the work of Bockenstedt et al [127].

This clearly demonstrated that near γ' solvus deformation temperatures should be avoided. However, Visual examination of the billet after the first upset to 30% reduction showed no signs of cracking. This gave confidence that the interrupted deformation strategy would reduce the tendency for cracking and result in a successful forging.

Full Scale Billet Forging Using the Two Step Deformation Approach

A full scale billet (213mm x 71mm diameter) was selected for the two step deformation method at a lower temperature to try and obtain a crack free forging. This larger billet was placed in the furnace at 1100°C for a 2.5 hour dwell time, after which, the billet was removed from the furnace and upset to a 30% height reduction before being placed back in the furnace for approximately 50-60 minutes to allow the sample to return to 1100°C. The second upset was then performed to a strain of 0.8. The final strain was reduced from 1.0 to 0.8 in order to determine whether the 0.8 strain could

be achieved without any cracking. Photographs of the billet during the two step deformation strategy can be seen in Figure 5.76.

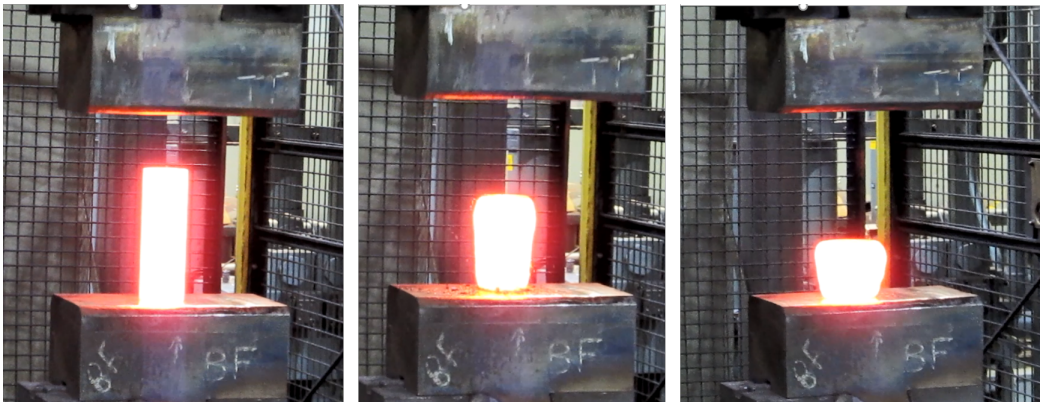

Figure 5.76: Large scale billet during 2 step deformation on the industrial open die forging press, showing the billet just before deformation (left), immediately after the first upset (centre) and finally after the second upset (right).

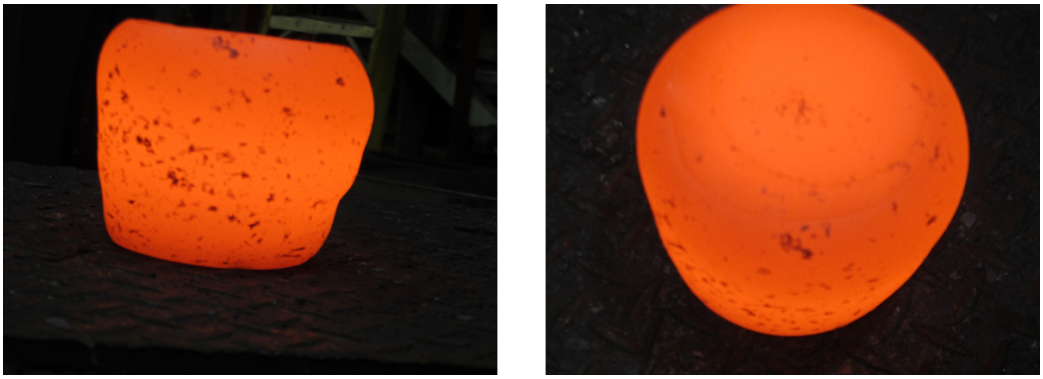

Figure 5.77: Large scale billet after a two hit deformation to a strain of 0.8, performed at 1100°C. Billet showed no cracks after deformation. The billet shown was named 2_1 in Table 5.12.

As can be seen in Figure 5.76, the large aspect ratio billet exhibits some inhomogeneity after the first upset, this is then carried through after the second deformation step. The reason for the inhomogeneity is thought to be due to how the billet was placed in the clamshell furnace used for heating the billet. The billet was placed vertically in the clamshell style furnace during the heat up process, due to the large length of the billet it is suspected that the billet experiences a lower temperature on the end of the billet in contact

with the furnace floor compared to the end of the billet closer to the centre of the furnace. Although it was impossible to determine the temperature of the billet along its length, it is suspected that a sufficient temperature differential existed along the billet to produce an inhomogeneity in the billet. Irrespective of the inhomogeneity in the deformation, it can be seen in Figure 5.77 that no cracks were present after the second deformation stage. This was the first indication that the two step method was capable of producing a forging to a relatively high strain value without failure due to cracking.

Following this forging the same process was repeated, however the target final strain was set to 1.0, this also resulted in a crack free forging as shown in Figure 5.78. This is further evidence that initial upset to 30% is required followed by reheating to produce the required hot ductility to allow higher strains to be achieved without cracking.

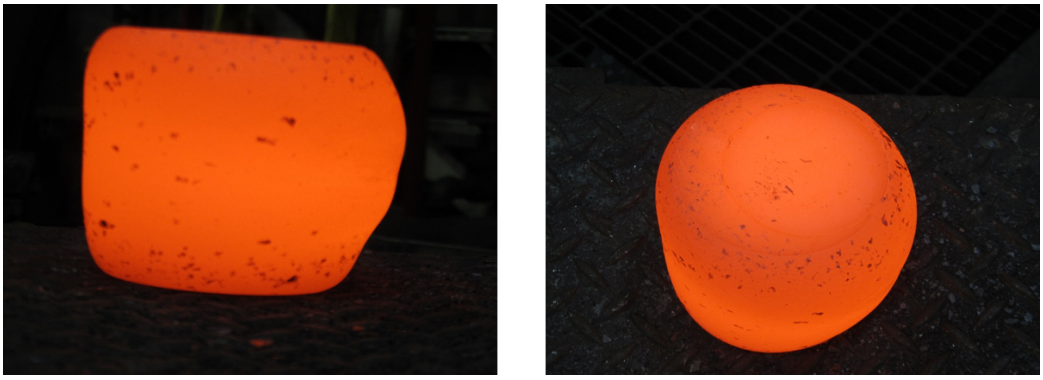

Figure 5.78: Large scale billet after a two hit deformation to a strain of 1.0, performed at 1100°C. Billet showed no cracks after deformation. The billet shown was named 2_2 in Table 5.12.

Figure 5.78 shows that the billet forged to 1.0 strain also has inhomogeneous deformation. The billet was positioned in the same way as the billet shown in Figure 5.77. It is thought that the position resulted in a temperature differential across the billet as described previously. To try and rectify the uneven deformation, one of the large billets was placed horizontally and elevated on furnace bricks in an attempt to reduce any temperature differences across the billet and produce a more uniform deformation profile. The billet shown in Figure 5.79 shows the billet geometry produced by adopting the alternative billet heating setup in the furnace. As can be seen, the deformation is more homogeneous with a constant radius around the billet. The billet shown in Figure 5.79 is free of any external cracks indicating a successful forging had been produced.

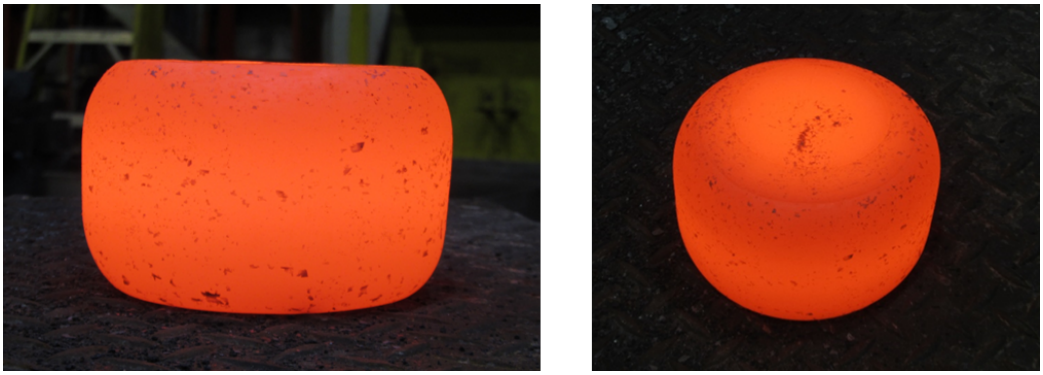

Figure 5.79: Large scale billet after a two hit deformation to a strain of 1.0, performed at 1100°C. Billet showed no cracks after deformation. The billet shown was named 3_2 in Table 5.12.

Once the results of the two step method had been demonstrated to produce crack free forgings, it was decided that the processing window would be explored using the two remaining full scale billets. It was decided that one of the billets would be processed using a reduced temperature of 1075°C during the second upset to a strain of 1.0 as shown in Figure 5.80, the remaining billet was upset at 1100°C to a slightly higher strain of 1.2 as shown in Figure 5.81. It can be seen that both process modifications resulted in successful forgings with no surface cracking apparent on either of the billets and relatively even deformation produced as a result.

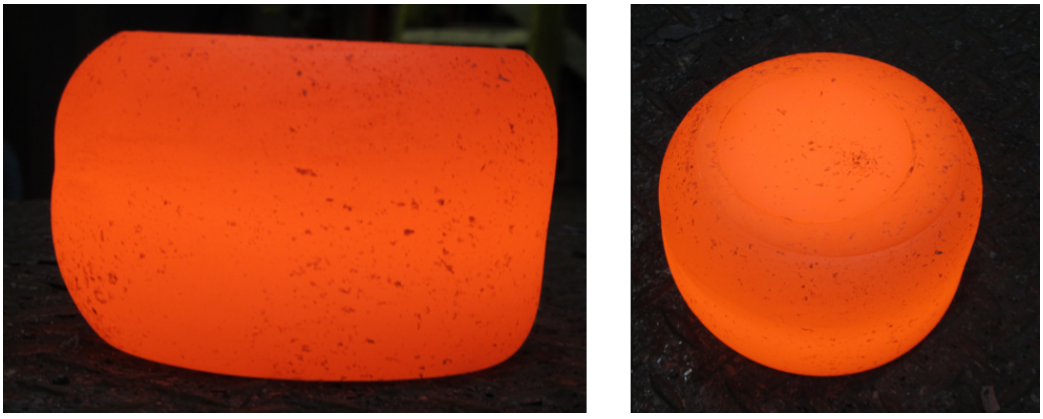

Figure 5.80: Large scale billet after a two hit deformation to a strain of 1.0, performed at 1075°C. Billet showed no cracks after deformation. The billet shown was named 3_1 in Table 5.12.

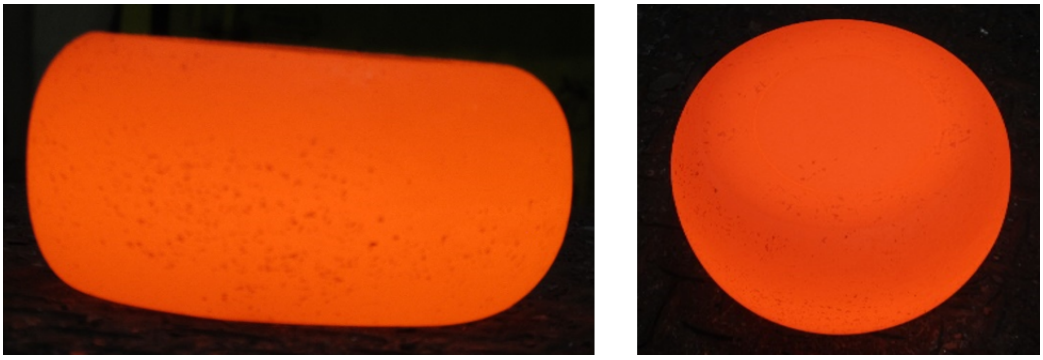

Figure 5.81: Large scale billet after a two hit deformation to a strain of 1.2, performed at 1100°C. Billet showed no cracks after deformation. The Billet shown was named 4_1 in Table 5.12.

Table 5.12: List of intermediate scale (106.5mm length) and full scale (213mm) forgings conducted on the large scale industrial forging press.

			1st upset		2nd upset	
Billet ID	Diameter (mm)	Length (mm)	Strain	Temperature (°C)	Strain	Temperature (°C)
1_1	71	106.5	1.0	1100	NA	NA
1_2	71	106.5	0.34	1100	1.0	1150
2_1	71	213	0.34	1100	0.8	1100
2_2	71	213	0.34	1100	1.0	1100
3_1	71	213	0.34	1100	1.0	1075
3_2	71	213	0.34	1100	1.0	1100
4_1	71	213	0.34	1100	1.2	1100

The results of the full scale forgings validated the two step deformation approach which was simulated successfully using the small scale billets. Based on evaluation of the microstructure, the evidence points to a change in microstructure and break up of PPB networks being responsible for the improvement in hot ductility allowing forgings to a strain of 1.0. The microstructure changes from billet to billet could then be evaluated in terms of the macroscopic machining aspects during cutting trials.

Chapter 6

FAST Billet Machining

6.1 Introduction

Whether production components are produced via the HIP+Forge or FAST approach, final components will always require machining in order to produce shapes, tolerance and surface finishes required for service. Machining is a subtractive process which by its very nature produces microstructural damage within a material, particular in the surface region. This damage can be identified via larger features such as material cracking and lapping, or via mechanisms which indicate microstructural distortion. Regardless of the nature of the damage induced via machining, these defects can result a reduction of the fatigue performance in the material. Components produced using nickel superalloys are used in safety critical components within gas turbine engines, therefore any features that reduce fatigue strength are best avoided. When developing a new material for use in an aerospace rotating assembly, wide reaching machining trials are often required to fully understand how the material responds to material removal. Due to the cost involved, it is difficult to understand how local changes in microstructure affect the response both during machining in terms of cutting forces etc. but also after machining in terms of the deformation produced. In large components, local variations in microstructure are almost inevitable, however it is industry practice to use the same cutting process throughout the component.

The FAST technique employed previously has demonstrated the ability to produce varying microstructures from a powder feedstock without the need of heat treatment. The technique was used to produce 125mm diameter billets which were subjected to machining trials to observe the differing microstructural response to machining in a cost effective manner. This chapter details the results of the trials using the FAST process to quickly generate

varying microstructures on a small scale and subsequent machining trails to determine the response of the differing structures.

6.2 Literature Review

6.2.1 Machining Nickel Superalloys

The Difficulty in the Machining of Nickel Superalloys

Nickel alloys are traditionally termed as difficult to machine materials compared with other alloy systems such as traditional steel and titanium alloys. The reasons for the difficulty in machining are summarised by Persson et al [129] who list the problems associated with the machining of Nickel superalloys; these include the low thermal conductivity, rapid work hardening, abrasive microstructures and tendency for built up edge (BUE) formation where workpiece material bonds to the tool during machining. As a result cutting speeds are usually limited to 50-80 $m.min^{-1}$ in industry.

Ezugwu [130] notes that compared to other systems, aerospace alloys (particularly the nickel based alloys) require a higher degree of energy input during machining which is readily converted to heat. The combination of high heat generation and low thermal conductivity compounds traditional machining issues such as tool wear. Ezugwu also notes that the austenitic structure of nickel based superalloys provides an increased tendency to work harden during machining. Arunachalam and Mannan [131] note that the very properties of nickel alloys which facilitate high strength at temperature are the ones which make them difficult to machine. Arunachalam and Mannan note that in addition to the high shear stresses involved, hard microstructural features lead to rapid tool wear and the reactivity between nickel alloys and common tool materials is also worth consideration. Fan et al [132] reported the presence of both oxidation of the tool and adherence with the workpiece leading to accelerated wear, these processes were found to occur in varying degrees depending on the cutting parameters chosen. Although adherence between the tool and workpiece is considered a negative phenomenon, Zhu et al [133] note that the adherence between the tool and workpiece leads to built up edge (BUE) in nickel alloys which can actually improve the hardness of the tool leading to increased wear resistance. M'Saoubi et al [134] demonstrated that very high residual stresses can be produced at the surface of nickel superalloy parts which increased significantly depending on the condition of the tool. Rapid deterioration of the tool combined with the high residual stresses means constant monitoring of the tool condition is required when machining nickel superalloys. Dudzinski et al [135] provided an exam-

ple of high surface tensile residual stresses as a result of machining which accelerates component failure during service. The discussed difficulties do little to explain the scale of the industrial significance and cost in machining nickel superalloys. When a high volume of parts are being produced, the surface condition after machining requires extensive examination in safety critical parts. These inspections led to increased manufacturing costs. The rapid tool wear also leads to higher consumable costs. The validation of a machining process (including tools and machining parameters) requires substantial costs. Therefore, any techniques which can reduce these costs are of interest to industry.

Tool Wear Considerations When Machining Nickel Superalloys

Zhu et al [133] provided a detailed review of tool wear characteristics in nickel superalloy machining. The required tool properties for machining an alloy such as Inconel 718 are;

- Good thermal stability
- High wear resistance and hardness
- High impact strength and toughness
- Good formability
- High resistance to deformation when exposed to high temperature.

Zhu et al [133] cover the common machining issues when machining nickel alloys including the high material strength and therefore low machinability relative to materials such as steel. Commenting on the use of polycrystalline cubic boron nitride (PCBN) materials for nickel machining, the authors suggest productivity can be improved but the cost of the tooling can be prohibitively expensive compared to some tooling solutions. The authors summarised several works to describe the differing wear mechanisms, of which adhesive and abrasive wear are the most commonly discussed. Devillez et al [136] described the process of adhesive wear which occurs due to the high cutting temperatures, particularly in dry machining. Adhesive wear leads to the bonding of the workpiece material to the tool cutting edge leading to built up edge (BUE) formation. This process can be stable where the adhered material persists during cutting often preventing crater wear from occurring (loss of tool material substrate) [137]. If the BUE edge breaks away during cutting, this can often lead to more extreme tool failures including fracturing and nose breakage. Zhu et al [133] described the abrasive wear

mechanism as the loss of the tool material due to abrasion of the tool due to hard constituents in the workpiece material, this leads to the presence of a wear scar on the tool which appears similar to a ploughed field. Zhu et al [133] also discussed process monitoring strategies to understand tool wear during machining, these typically involve the monitoring of forces whether it be cutting forces or forces generated via vibration. These force signals can be combined with artificial neural networks and training techniques to allow these systems to judge the wear state of the tool without user interaction. The authors stated that while these methods are becoming more technologically possible, they require many experiments to generate the data required for a machine learning approach.

D'Addona et al [138] measured tool wear and surface roughness to examine the machinability of Inconel 718 for cutting speeds ranging from 60 $m.min^{-1}$ and 255 $m.min^{-1}$ for wet cutting conditions. The depth of cut was fixed at 0.5 mm and the feed rate was chosen to be 0.1 $mm.rev^{-1}$, which represents finish turning conditions. Tool wear and surface roughness were measured after machining set lengths using the chosen chemical vapour deposition (CVD) coated cutting tools. It was found that higher surface speeds were found to reduce the surface roughness Ra value. A large increase in surface roughness was found after each 30 m pass for the highest surface speed used (225 $m.min^{-1}$). The increase in roughness between passes was found to be less severe for the lower cutting speeds and almost non-existent for the lowest surface speed used (60 $m.min^{-1}$). Tool wear was found to monotonically increase with cutting speed, this was attributed to the higher cutting temperature with increasing cutting speeds. Heavy notching was noted at the highest surface speeds while only abrasive wear was noted for lower cutting speeds.

6.2.2 Modern Tool Materials in Nickel Alloy Machining

Substrate Materials

Thellaputta et al [139] stated that carbide tools are not applicable when machining nickel superalloys at high speeds due to the elevated cutting temperature produced. In the machining of slots for turbine discs constructed using nickel superalloys, broaching is traditionally employed using high speed steel broaching tools. However Vogtel et al [140] noted that as superalloy development continues these tools exhibit decreasing longevity and are less commonly employed. Vogtel et al compared the traditional tooling with broaching and milling with cemented carbide tooling. Heat treated Inconel

718 material with a fine grain structure was used as a test material for comparing tooling materials. They stated that the requirements for tools in nickel superalloy machining are a combination of high fracture toughness, high bending strength and high abrasion resistance. Trials using an orthogonal broaching rig revealed that there was significant improvements in material removal rates were possible with the use of carbide based tools due to enhanced machining speeds at the cost of higher cutting temperatures. It was noted that a significant decrease in cutting forces when employing carbide tools which was attributed to thermal softening of the material. The authors noted that higher tungsten carbide content in the cobalt binder tools improved their durability but found little improvement was available through the changing of rake angles. The authors calculated that HSS (high speed steel) broaching out-performed carbide tool milling in terms of machining time. However they did not consider other factors in forming the conclusion that insufficient tooling developments have taken place to allow milling to be competitive in slot production operation compared with broaching. It was suggested that ceramic tooling may increase viability for milling.

Lima et al [141] examined the effectiveness of 3 different types of ceramic tooling in the turning of Inconel 751. The effect of coolant conditions, cutting speed and tool holder geometry on the wear mechanisms were considered. The three tools compared included a mixed ceramic tool with Al_2O_3+TiC, a whisker reinforced alumina oxide and a SiAlON (Si_3N_4+Al_2O_3). It was found that the optimal tool wear performance occurred when the SiAlON tool was used in dry conditions. They noted that the resistance to notch wear was related to the toughness of the tool and this was found to be the case as notch wear was most pronounced in the whisker reinforced ceramic tool which had the lowest fracture toughness. It was noted that the application of oxygen and argon atmospheres were ineffective at higher cutting speeds but did provide some benefit at lower cutting speeds. The authors noted that like carbide tools, the predominant wear modes in nickel superalloy machining with ceramic tools are flank wear and notch wear.

Coating Development

The specific problems associated with nickel machining have been used as the development push for new tool coatings in recent times. In the work of Barthelmä et al [142], a holistic approach to tool coating design was adopted, temperatures at the tool, workpiece interface when milling Inconel 718 were estimated via finite element modelling. This data was then used to inform decisions regarding experimental tool coatings. Using this approach, the authors demonstrated an increase in tool life when using cutting speeds as high

as 125 m.min^{-1} by employing a AlTiCrN coating system with nano-composite layering. They recommended that improvements in coating adhesion and strength would yield further improvement.

Although coolant delivery technique development has received a large focus the in literature, tool coating developments have yielded larger benefit for some scenarios. Thakur and Gagnopadhyay [143] compared on the benefit between the application of cooling with cutting fluid (via traditional flood or minimum quantity lubrication) for uncoated carbide tools vs the use of advanced coatings under dry conditions. Inconel 825 was machined using both finishing and roughing conditions and the cutting forces, surface integrity, chip morphologies and tool wear were compared. Given that Inconel 825 is a nickel superalloy with excellent corrosion properties compared to Inconel 718 and contains large grain boundary MC carbides which act as abrasive during machining, it is an ideal candidate alloy for performing such a study. It was found that coated tools produced lower cutting forces compared to uncoated tools combined with the application of coolant. Although built up edge was produced regardless of the tooling insert, machining mode or coolant condition, it was found that coated tooling in dry conditions outperformed coolant applied to uncoated tools. This behaviour was a clear indication of the wear resistance of the TiN used in the coating employed in this study. Although higher cutting temperatures were measured for dry machining conditions, as expected, the surface condition with and without coolant was similar. The authors concluded that advanced coatings offer improved benefits over coolant strategy developments and offer dry conditions with advanced coatings as an alternative to more environmentally damaging strategy of coolant application.

Grzesik et al [144] studied the wear behaviour of inserts varying coating and shape during the turning of Inconel 718 for finish turning conditions for a range of cutting speeds. Tool wear trials performed for varying Ti and Al based physical vapour deposition (PVD) coatings revealed that the A PVD-AlTiN layer provided the greatest resistance to wear compared to PVD-TiAlN+TiN and PVD-(Ti,Al)N_2 coated tools for fixed machining conditions. The authors noted that in their study, the specific cutting energy which was calculated via the measured cutting forces, gave a good indication of wear progression, with rapid increases in specific cutting energy noted for higher wear levels. Using the cutting force to calculate the coefficient of friction between the tool and workpiece, it was found that 3 distinct phases of coating development could be observed. Initially, the coating performs as expected and the coefficient of friction of 0.65 is observed. As wear progresses the coating starts to de-laminate due to, and causing, further built up edge effects, this leads to an increase in the coefficient of friction to 0.75. Finally,

the coating de-laminates completely leading to an increase in the coefficient of friction to 0.85 which is similar to the coefficient of friction for uncoated carbide tooling in Inconel 718 machining presented in the work of Bhatt et al [145].

Bhatt et al [145] described the tool wear development that had taken place allowing machining speeds and productivity to increase as a result. Bhatt et al studied the wear mechanisms in round tools for a PVD derived TiAlN coating vs a triple layer TiCN-Al_2O_3-TiN CVD coating for round cutting inserts. Trials were also performed with uncoated tools for the sake of comparison. Comparing the 3 tools tested, it was found that abrasive and adhesive wear mechanisms were dominant. At high cutting speeds (100 $m.min^{-1}$) and low feed rates, the triple coated CVD tools performed optimally in terms of wear rates. For low cutting speeds tungsten carbide (WC) tools were the most wear resistant (50 $m.min^{-1}$). At intermediate speeds of 75 $m.min^{-1}$ the PVD tool performed the best. The conclusion of this study was that the selection of the optimal tool coating depends very much on the machining parameters chosen, and one tool grade may outperform another depending on the aggressiveness of the selected cutting parameters. The authors did not specify whether coolant was used or not. It is assumed that the cutting was performed without the application of coolant.

In the work of Imram et al [146], micro-scale drilling was used to investigate the influence of coolant application and parameters on the surface integrity and tool wear characteristics when machining Inconel 718. Using TEM and EBSD, it was revealed that both with and without coolant a near surface layer exists which contains high dislocation densities, deformed grains and nano-scale grain formation. Dry conditions for a range of cutting parameters resulted in lower sub-surface deformation which the authors attributed to an annealing effect produced by the higher cutting temperatures. EBSD revealed the presence of a higher density of high angle grain boundaries and the presence of more equiaxed grains which pointed to sub-surface recovery under the effect of higher cutting temperatures. The authors also described a quenching effect provided by the coolant which led to the retainment of deformation structures near surface.

Razak et al [147] used a qualitative approach to examine the development in tool deterioration in Inconel 718 machining. Cutting trials involving the milling of 718 were interrupted to capture SEM images to observe tool wear modes. It was observed that fracture of the uncoated WC tools occurred through deformation and fracture in the Co binder which led to micro then macroscopic fracture. The authors state that a tool coated with TiAlN provides little benefit as the coating is quickly worn away during milling trials.

Exploiting the developing trend for micro-machining strategies, Swain

et al [148] used slot micro-milling to investigate the performance difference between coated and uncoated micro-milling tools when machining Nimonic 75 superalloy. Using wet machining conditions with varying parameters, the authors found that tool wear rates increased with both feed rate and machining speed. A TiAlN sputter coating was applied to micro-mills and compared against their uncoated counter parts. It was found that tool wear reduced by nearly half over a range of machining conditions for the coated tools. It was found that burr formation was also reduced when a coated micro mill was employed. This study provided evidence that the modern coating techniques applied to carbide tools in nickel alloy machining are effective on a multitude of length scales.

Considering the effect of coolant application on tool wear, Imran et al [146] proposed a diagram showing the sequence of tool wear mechanisms for dry and wet machining, see Figure 6.1. Abrasive wear is the start of the tool wear process, whereby the coating (in this case TiN on a WC substrate) is removed revealing the underlying WC substrate. Once this occurs adhesive and diffusion mechanisms take hold, this is where the dry and wet conditions deviate. In the case of dry machining the cutting temperatures are increased accelerating diffusion between the tool and work piece, due to this increase porosity and macro cracking can develop in the tool leading to total failure. In lower temperature conditions, when coolant is applied, this effect is limited to the formation of micro-cracks which blunts the cutting edge. The authors concluded that ultimately, the ability of the tool coating to remain adhered to the underlying substrate is what determines the longevity of the tool in both wet and dry conditions.

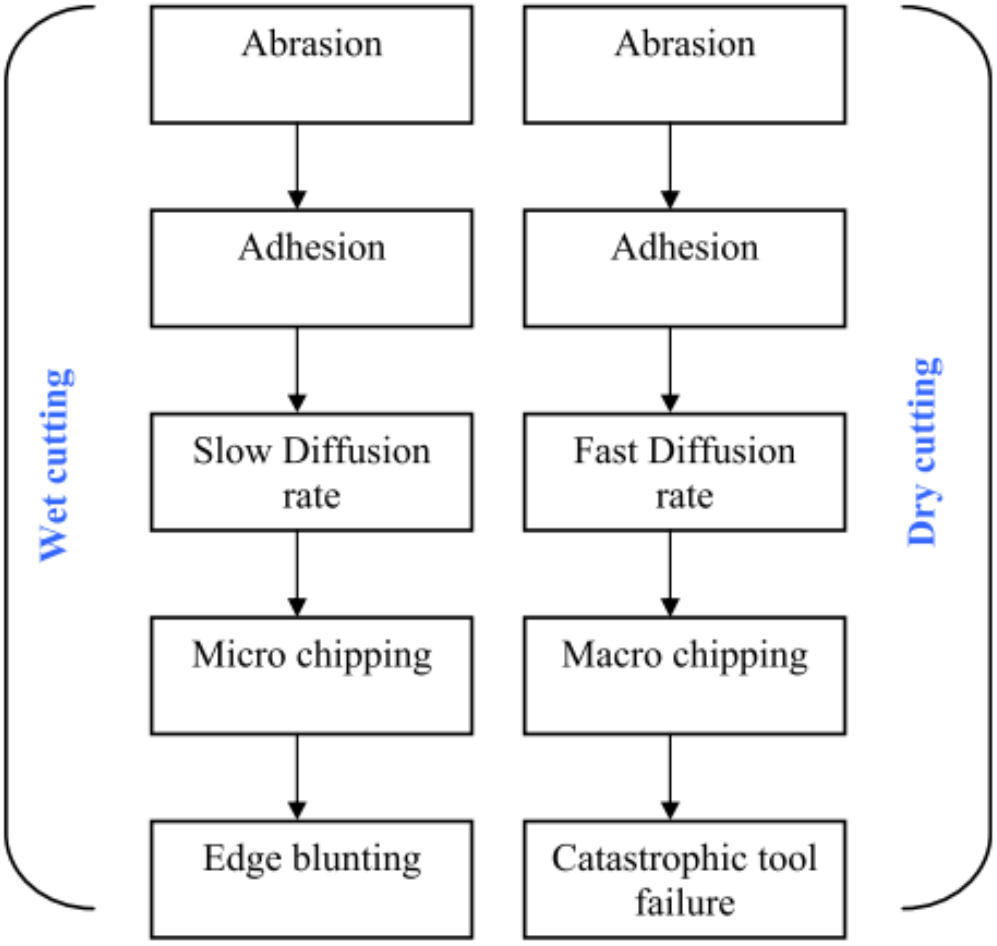

Figure 6.1: Diagram detailing the development of tool wear in wet and dry micro-drilling conditions, according to Imran et al [146].

6.2.3 Novel Machining Techniques for Improving Productivity in Nickel Superalloys

Air jet assisted (AJA) machining is another modern tooling development explored by Obikawa et al [149]. In this study, Inconel 718 was machined using finish turning conditions and AJA was employed. AJA involves the application of compressed air directed through a nozzle towards the cutting edge in combination with traditional coolant delivery. A comparative study revealed that up to 30% improvements in tool life could be made when using AJA instead of traditional coolant delivery systems. Both experimental data and computational fluid dynamics models agreed that AJA provides a reduction

in cooling temperature and enhances the flow of coolant to the cutting edge. The authors stated that this is the main reason for enhancement in tool life. When the air jet was substituted for a nitrogen jet, no further enhancements in tool life were observed, ruling out possible oxidation wear due to the application of high pressure air towards the relatively high temperature cutting edge.

The use of cryogenic coolant in machining of Inconel 718 has been reviewed by Pusavec et al [150]. Surface integrity markers such as residual stresses, surface roughness and micro-hardness profiles below the machined surface were compared with combinations of dry, minimum quantity lubrication (MQL) and cryogenic coolant choices. Residual stress profiles in the feed and cutting directions revealed the presence of high tensile residual stresses at the surface regardless of cooling conditions. Below the sub-surface the tensile residual stress decreases with depth until a peak compressive stress is achieved. The magnitude and depth of penetration of the compressive stress was found to increase with the application of cryogenics with and without simultaneous application of MQL. The depth of work hardening was examined via micro-hardness measurements and it was found that cryogenic coolant led to a harder but shallower deformed sub-surface which was confirmed by SEM images of the machined sub-surface. In a follow up publication by Pusavec et al [151], genetic algorithms were employed to optimise machining properties alongside chip breakability for cryogenic conditions. The study showed that coolant application was required to produce good chip breakability and as found in the previous study the application of cryogenic coolant further enhanced this. The authors related this to the embrittling properties of the cryogenic coolant which allowed for enhanced chip breaking.

Aramesh et al [152] examined the use of a novel pre-processing technique to improve the wear resistance of an uncoated WC tool. In this paper carbide inserts were first used to perform a preparatory machining pass on a Al-Si work piece prior to machining Inconel 718. Using a high cutting speed and low feed rate, the carbide tool was found to receive a thin coating of Al-Si after the preparation treatment. Subsequent machining trials found that the wear rate was reduced compared to uncoated WC tools. The authors relate this to molten Al-Si which fills the pre existing cracks and cavities of the WC tool which prevents them from propagating during machining. All wear mechanisms were found to be reduced after the application of the Al-Si pretreatment compared to the benchmark tool. A large reduction in cutting forces was also observed. Surface integrity was also shown to be improved through measurements of the work hardening.

Ananda-Kumar et al [153] examined the machinability response of additively manufactured IN 625 compared to cast/wrought material. The com-

bination of additive manufacturing with subtractive machining operations is known as hybrid manufacturing and machines are currently being rolled out to exploit this technique to aid rapid prototyping. It was found that both cutting temperature and tool wear were more severe in the additively manufactured material, this is explained by the higher strength and lower ductility in the material produced through additive manufacturing which needs to be considered when moving towards a hybrid manufacturing production route.

Tadavani et al [154] studied the use of a pulsed laser to improve the machinability of Inconel 718 by measuring machinability factors with and without the application of a Nd:YAG pulsed laser. Using an air jet to protect the laser pointed at the machined surface ahead of the tool, turning trials were performed and cutting forces were measured using strain gauges on the tool holder. It was found that increasing the input power of the laser, the specific cutting energy was reduced which was attributed to thermal softening provided by the laser. Surface roughness was also found to decrease with increasing laser power. For laser assisted machining it was found that increased feed rate and cutting speeds improved the surface roughness, contrary to normal machining in dry conditions. Surface investigations revealed that the chemistry of the Inconel 718 was not altered by the laser at the surface. To summarise this study, the application of laser assisted machining seems a promising method of reducing the difficulty in machining nickel superalloys. However, since these materials are used in critical aerospace components, more work needs to be done to verify it as a viable technique.

6.2.4 Surface Integrity in Machining Nickel Superalloys

In the in depth review article published by Thakur et al [155], the reputation of the difficulty in machining nickel alloys was stated. In the review, numerous publications were used to describe the properties of nickel superalloys which hinder machining, these include but are not limited to:

- Hot hardness
- Low thermal conductivity
- The presence of abrasive carbides
- Chemical affinity for the tool materials used in modern machining.

Besides the previous list, the damage induced in the machined sub-surface is considered to be detrimental to the fatigue resistance of these alloys. The

various facets of surface integrity were discussed including surface roughness features including material laps and redeposited material which are both highly detrimental to fatigue life. On the topic of microstructural modification, the authors noted that a machined surface normally consists of two zones. Zone 1 is located closest to the machined surface and contains a highly deformed region of nano scale grain structures, which is produced through mechanical and thermal loading. Zone 2 consists of a layer deformed to a lesser extent in which slip bands and visually deformed grains can be observed. Below these two regions, un-deformed bulk microstructure can be observed. EBSD techniques revealed that the material becomes more deformed towards the machined edge, however TEM is required to gain understanding of the nano-scale structures formed at the machined surface. The authors noted that this surface layer has been called "white layer" in some publications as it appears white in colour when etched and observed under SEM. The white layer region also exhibits much higher hardness than the bulk material. The authors noted that the higher strength nickel superalloys demonstrate a high resistance to sub-surface damage however higher strength alloys also exhibit near surface cracking due to machining effects. The authors concluded that higher cutting speeds led to a reduction in surface roughness due to less built up edge effects and lower cutting forces, however surface roughness tends to increase again with very high surface speeds. With regards to residual stresses, the authors concluded that more abusive cutting parameters promote a shift from beneficial compressive surface residual stresses to detrimental tensile residuals. They also suggested that the optimal cooling conditions should be sought to mitigate white layer formation as a priority.

Umbrello [156] performed orthogonal machining trials using Inconel 718 material under dry conditions for a range of machining parameters. Taking care to minimise the affect of transient machining movements, it was found that surface roughness decreased with increasing cutting speed. Sub-surface investigations revealed a region of grain refinement and amorphous layer near the surface, both of which increased with more aggressive machining conditions, with feed rate in particular having a large effect. XRD revealed that dry cutting conditions led to phase change and microstructural modification consistent with high temperature input. To conclude, Umbrello strongly linked an increase in microstructural modification with increasing heat input provided by more aggressive machining conditions.

The interaction between machining conditions and the fatigue performance in GH4169 nickel superalloy was examined by Sun et al [157]. Varying the machining speed and observing the resultant residual stress profiles, it was revealed that for 15 $m.min^{-1}$, 30 $m.min^{-1}$ and 45 $m.min^{-1}$ machining

speeds, the 30 m.min^{-1} speed results in the best fatigue performance for fixed feed rates and depths of cut. Examining the residual stress profiles it was found that the 30m.min^{-1} condition led to the greatest magnitude of compressive residual stress. All surface speeds chosen resulted in tensile residual stresses near the surface which corresponded with near surface fatigue initiation. Examination of the fatigue striation spacing, found that the 30m.min^{-1} condition resulted in smaller striation spacings than the other conditions examined. This is a clear indication that the greater magnitude of compressive sub-surface stress slows fatigue crack growth. Discussing why an intermediate machining speed resulted in the best performance, the authors proposed that a balance of thermal effects and imparted plastic deformation results in optimise residual stress profiles, but did not elaborate further.

M'Saoubi et al [134] applied high resolution analysis techniques to examine surface integrity aspects in Inconel 718 machining. PCBN TiAlN-TiN cemented carbide inserts were utilised at appropriate cutting speeds for each tool type in turning trials. Surface speeds for the carbide tools were used with cutting speeds ranging from 60-90 m.min^{-1} and the PCBN tools were used with cutting speeds ranging from 200-300 m.min^{-1}. A constant feed rate of 0.15 mm.rev^{-1} and a depth of cut of 0.25 mm were employed. Surface examination revealed that tool wear was found to greatly increase surface waviness in the carbide tooling but the PCBN tool produced less deterioration in surface quality in the worn condition. Tool wear measurements found accelerated wear occurred when the PCBN tool was used in comparison to the carbide tool, which was attributed to the wear mechanisms taking place. Notch wear was observed in the carbide tools while flank and crater wear were observed for the PCBN tool. In the new condition however the surface was comparable, which is expected with the consistent feed rate which determines the initial surface roughness. For both tools, slip bands and nano scale recrystallised grains were observed near the machined surface. Diffraction patterns in TEM revealed the presence of fine grain crystalline material at the surface while underneath highly elongated fine grains were present. XRD produced pole figures revealed that the microstructural texture was slightly increased with the increasing cutting speeds used for the PCBN compared to the carbide tool. However, this effect was found to diminish when the tools were in the worn condition. EBSD data was used to produce strain contouring maps where the misorientation was used to map the level of strain at a machined surface. The strain contouring maps revealed that levels of misorientation were similar for the new tools for the range of cutting speeds examined. In the worn condition, greater misorientation was seen for the carbide tool in the worn condition when the 90m.min^{-1} surface speed was used. When the lower surface speed was used less of an increase in misorientation was

observed. For the PCBN tool, the misorientation was shown to be similar for both the new and worn conditions regardless of surface speed. Residual stress measurements revealed similar levels of tensile stress in the machined surfaces for new tools regardless of tool materials or machining speed. In the worn condition of the PCBN tools a large increase in residual stress was observed. In the carbide tools the change in residual stress was more modest when worn tools were employed. The authors concluded that PCBN tools offer productivity advantages with large increases in surface speed achievable with little penalty observable in surface integrity when the tools are in the new condition, however wear limits must be considered to avoid excess residual stresses when worn PCBN tools are used.

Wang et al [158] examined surface integrity of powder metallurgy superalloy FGH97 when subjected to drilling using carbide cutting tools. Using varying cutting speeds and feed rates, it was found that increasing the cutting speed initially results in an increase in cutting forces however the cutting force decreases again when a cutting speed of 25 $m.min^{-1}$ was used. It was found that the surface roughness decreased with increasing cutting speeds and the magnitude of surface hardening and the depth thereof decreased with increasing cutting speed. Surface roughness and the measured thrust force were found to monotonically increase with feed rate. The surface hardening effect at first decreased when the feed rate was found to decrease when the feed rate was increased from 0.01 $mm.rev^{-1}$-0.03 $mm.rev^{-1}$ however at increased feed rates the surface hardness increased. The authors related these changing cutting forces and surface roughness values to changing cutting temperature and chip thickness, which alter the rate of surface hardening mechanisms.

Residual Stresses When Machining Nickel Superalloys

Gunnberg et al [159] proposed a mechanism for the generation of residual stresses by considering the mechanical and thermal effects that occur during machining. The mechanical effects, generated by the material removal process, generate plastic deformation in the surface and elastic deformation in the sub-surface. The surface plastic deformation leads to compressive residual stresses as the material acts to maintain geometry after the deformation occurs. The thermal effects, which are driven by heat generation in the cutting zone, lead to surface expansion and upon cooling, the material contracts again leading to the development of tensile stresses at the surface. It is the combination and the relative contributions of these two effects that produce the residual stress state in the material which has been machined. It can be inferred that in order to produce beneficial surface compressive stress,

the thermal effects should be limited as much as possible, thus limiting the production of surface tensile stresses.

Xavior et al [160] studied the residual stress and work hardening in the turning of Inconel 718 for a range of cutting tools and coolant conditions (including dry cutting) and with two machining speeds. As has been noted in other studies, the surface stresses are tensile in nature with a compressive sub-surface layer. Although Xavior et al drew conclusions regarding which conditions produce severe residual stresses, the differences in the measured residual stress profiles were only slight given the large changes in cutting conditions. One stand out result was that MQL coolant conditions, combined with ceramic tool material and a machining speed of $100 m.min^{-1}$ produced greater magnitudes of sub-surface compressive stress. Overall this study concluded that residual profiles can be similar for a wide range of machining conditions.

In the work of Ulutan et al [161], turning of IN-100 and face milling of GTD-111 were used as test cases for modelling the machined surface residual stress profile using a sinusoidal decay function. Using X-ray diffraction measurements to validate this approach, the authors used an evolutionary particle swarm optimisation process to optimise the fit between experimental measurements and the model. It was found that the sinusoidal decay function could be used to represent the residual stress profiles produced during both milling and turning trials on two different superalloys. Both experimental measurements and modelling showed purely compressive residual stresses at both the surface and sub-surface, contrary to other publications regardless of machining condition.

Niaki and Mears [162] studied the effect of feed rate and tool condition on the surface integrity produced by turning in Inconel 718. They defined 3 parameters for workpiece to quantify health during a machining trial. These are surface quality, residual stress state and dimensional integrity. The cutting speed and depth of cut was fixed and represented finishing conditions for machining trials with increasing levels of tool wear and varying feed rates. It was observed that dimensional integrity (measured via deviation from the programmed depth of cut) did not increase greatly with low levels of tool wear up to 200 microns, however further wear lead to large deviations. Surface roughness variation vs tool wear was analysed using the analysis of variance (ANOVA) approach and it was found that tool condition did not have a specific correlation with surface roughness. Residual stresses were found to be tensile on the surface and compressive in the sub-surface, regardless of tool condition or machining feed rate. Examination of the tools revealed that adhesion of workpiece material, coating de-lamination and flank wear were all visible via SEM and EDX. The authors explain the poor repeatability of

the experiments with the randomness associated with these wear modes.

Girinon et al [163] studied the residual stresses produced during drilling operations in Inconel 718 and two stainless steel alloys with respect to varying coolant conditions. They noted that the coolant conditions had strong influence over the residual stresses formed during machining. It was noted that for all materials tested, dry coolant conditions led to tensile stresses at the surface. External coolants provided a shift towards tensile stresses and through tool coolant provided the most compressive residual stresses. The authors rationalised this by the change in temperature as chip development occurs. When through tool coolant conditions were used cutting temperatures were kept low and high temperature chips were removed from the cutting zones, the contrary was true in dry conditions. The authors did not however consider frictional effects in their analysis. It was also found that the residual stresses became more tensile as the tool propagated deeper into the hole. The authors related this again to changing cutting temperatures as in general the cutting temperatures increase as drilling progresses. Summarising their results, the authors noted that higher cutting temperatures resulted in more tensile residual stresses and therefore coolant conditions are critical to machining operations.

The feasibility of removing coolant from machining operations for cost reduction purposes was evaluated by Devillez et al [164]. They listed some of the thermal effects activated by high cutting temperature that are associated with dry machining these include: burning/overheating, formation of surface irregularities and phase transformations. Examining cutting forces in coated carbide tool turning of Inconel 718, a reduction in cutting forces was consistently observed with dry machining owing to workpiece softening. For wet and dry conditions, cutting forces were observed to decrease when the cutting speeds increased from 40-80 $m.min^{-1}$. Surface roughness was observed to consistently decrease with higher cutting speeds for dry conditions, but reach of peak value at intermediate cutting speeds for the wet trials. Surface roughness was consistently lower for the dry conditions than the wet machining. Surface examination revealed that this is likely due to the re-deposition of workpiece material and side flow which produces secondary feed marks, thus lowering the measured roughness Ra value. In all cases, regardless of surface speed or coolant condition, measured residual stresses were found to be tensile on the surface with a compressive layer in the sub-surface. In almost all cases, tensile residual stress were found to be higher for the dry conditions, both in the perpendicular and parallel orientations. For the dry conditions, tensile residual stresses reduced with high cutting speeds. Although it is known that higher cutting temperatures produce higher tensile residual stresses through the mechanism explained by Gunnberg et al [159],

Devillez et al proposed that higher cutting speeds may reduce temperatures as chips are being evacuated at a higher rate which take with them thermal energy generated at the cutting edge at a higher rate. Microstructural examination revealed sub-surface deformation in both wet and dry conditions at similar depths in the sub-surface, this was confirmed by micro-hardness measurements for which dry conditions produced a very slight increase in micro-hardness near the surface compared with wet conditions.

He et al [165] examined the effect of cryogenic coolant on the residual stresses in the turning of Inconel 718 using carbide tooling. Combining experimental work and finite element modelling, it was found that cryogenic conditions reduce the tensile nature of surface residual stresses. The authors converted modelled principle stress values to residual stresses and the authors produced residual stress profiles. These were similar to the profile measured through experimentation. The assumption that the yield stress was approximately constant for the cutting temperatures in the dry and cryogenic conditions was used to justify similar deformation mechanisms for both conditions. The authors used this assumption to explain the similarity in cutting forces for dry and cryogenic conditions.

Wang et al [166] examined two different modelling techniques for describing the residual stress profiles after ball end milling of Inconel 718 using carbide tools and wet cutting conditions. A 3D model was chosen to model the cutting process however it was found that factors such as chip formation and tool wear lead to differences between experimental and predicted residual stress profiles. An empirical model was produced which fitted the measured residual stress profiles using a decaying cosine function, this approach performed well in modelling the residual stress profiles for a range of conditions using a particle swarm optimisation to maximise the read across between the model and experimental data. In this study, the residual stresses were compressive throughout the sub-surface. To summarise the authors suggested that 3D FEM models can provide a good prediction of residual stresses, however work is required to include the other variables which were not considered in the study.

The effect of rake angle on the residual stresses and fatigue performance was studied by Choi [167]. Conducting turning trials on AISI 1053 steel using PCBN tools, the rake angle was increased from 5-20°. Micro-hardness tests were performed to analyse the effect of the underlying strain after machining on the underlying material structure. Residual stresses were found to be more compressive when higher rake angles were used, for both in the radial and circumferential directions. The benefits of the enhanced compressive residual stress were noted when fatigue tests were performed and found that increasing rake angle increased both the crack initiation and propagation

lives.

Considering the literature review, it is notable that a large number of variables can greatly influence both the effectiveness of machining operations, in terms of productivity but also the quality of the produced surface. Understanding the influence of said variables can be expensive as each must be varied in turn to fully understand the process. In this chapter, it is thought that the FAST produced material may provide an opportunity to perform the required testing at less cost than full scale HIP+Forged routes from a first principles perspective. To that end, simple turning trials were performed on the as FAST billets employing some of the techniques and recommendations in the literature.

6.3 Methodology

6.3.1 Description of the as-FAST billets Used for Machining Trials

FAST billets were produced using 2 variants of powder based on the chemistry of RR1000, one of these powders was produced by Rolls-Royce plc. and had a powder size below 53μm with a highly spherical morphology. The second powder was produced by Carpenter Technology with a powder size below 425μm and less desirable powder characteristics such as the presence of satellite particles and internal powder porosity. These two powders were used to produce billets using two dwell temperatures of 1100°C and 1150°C. These processing temperatures represent the sub-solvus and the super-solvus conditions discussed in Chapter 4. In Chapter 4 it was demonstrated that the two processing temperatures resulted in varying grain sizes with the super-solvus condition providing a large increase in grain size. The as-FAST billets would therefore provide an opportunity to understand how the machining process is affected by the change in processing temperature for two powder feedstocks of a similar chemistry, with differing morphologies.

A list of the billets produced via FAST for the purpose of machining trials is shown in Table 6.1. Although the billets were sintered to 125mm diameter with a thickness of 28mm, each billet was pre machined to give a constant diameter of 121mm and a thickness of 25mm prior to machining trials. This was to ensure that the carbon diffusion layer noted in chapter 4 was removed prior to the machining trials, as this layer would respond differently to the bulk material.

Table 6.1: List of billets produced via FAST for the purpose of machining trials.

Billet ID	Feedstock powder	Dwell temperature	Dwell time
RR1000/1100°C	RR1000	1100°C	2hrs
RR1000/1150°C	RR1000	1150°C	2hrs
131072/1100°	131072	1100°C	2hrs
131072/1150	131072	1150°C	2hrs

6.3.2 Measurement of Cutting Forces

Cutting forces are an indication of how difficult a particular material is to machine. The cutting forces are therefore a useful measure to compare differing materials. In order to determine how the cutting forces change with regards to changing cutting parameters and billet material, a Kistler (Type 9129a) force Dynamometer was used to measure forces during cutting. The Dynamometer consists of a unit with 3 piezoelectric crystals which measure the forces translated from the cutting inserts in the 3 principle axes to the tool holder and finally to the Dynamometer. The applied force causes the generation of a charge which is detected via an insulated cable at the external charge amplifier (Kistler type 5019). The charge amplifier is pre-set with calibration values that convert the measured charge into a voltage which is then converted to a force value which is registered by the DynoWare software package running on a connected computer. The system is capable of very high sampling rates, for all cuts performed a minimum sampling rate of 2500Hz was employed for all cutting trials performed. The maximum rotation speed available on the MAG Hawk lathe is 3000 RPM. At this maximum speed the minimum sampling rate would allow for 50 samples per billet rotation. This was deemed to be adequate in order to investigate cutting forces for each billet as in reality the maximum speed the billet reached was 1275 RPM, which results in approximately 112 samples per rotation. After the force data was captured, the data was exported from the DynoWare software package and processed in Matlab.

6.3.3 Tooling Used During FAST Billet Machining Trials

The machining trials were conducted on a MAG Hawk CNC lathe. The MAG Hawk lathe uses a C5 Capto tool interface and is capable of providing high pressure coolant through the tool provided by a 72 bar coolant pump. The Kistler force dynamometer previously described was used to mount the chosen tool holder as shown in Figure 6.2. The dynamometer consists of a tool clamp into which a 20x20mm shank style tool holder can be inserted and clamped.

A 20x20mm shank holder compatible with the force dynamometer was selected based on recommendations from Sandvik Coromant. The tool holder is designed to work with a CNGG-120408 geometry insert which was recommended for the semi-finishing/finishing conditions chosen for the machining trials when cutting nickel superalloys. The tool holder is connected to the high pressure cooling supply provided by the lathe's 72 bar coolant pump and directed nozzles project the coolant in jets to the tool/workpiece interface. This ensures that coolant is used to help lift machining chips away from the material, minimise friction and help cool the cutting edge. The insert grade chosen for the trial was the S05F grade produced by Sandvik Coromant. This grade consists of a carbide substrate which is triple coated using chemical vapour deposition. This grade is commonly used in the machining of high temperature materials and is the current grade of choice for the machining of nickel superalloys in aerospace applications. A summary of the tool set-up can be found in Table 6.2. Detailed technical summaries for the tool holder and inserts used can be found in Table 6.3 and Table 6.4 respectively. A photograph of the tooling setup mounted within the jaws of the force dynamometer can be found in Figure 6.2 where the alignment of the 3 measured force directions is indicated.

Table 6.2: List of tooling set-up components used during machining trials.

Tool component	Supplier	Product code	Description
Tool holder	Sandvik	PCLNL-2020K-HP	20mm x 20mm Shank style tool holder with directed, high pressure coolant nozzles
Indexable Inserts	Sandvik	CNGG 120408-SGF SO5F	S05F grade C style finishing inserts, each insert has 4 usable edges

Table 6.3: Technical data for the PCLNL-2020K-HP tool holder used during machining trials.

Feature	Value
Tool holder shank width	20mm
Tool holder shank height	20mm
Tool lead angle	-5°
Orthogonal rake angle	6°
Handedness	Left
Coolant pressure capability	275 bar

Table 6.4: Technical data for the CNGG 120408-SGF SO5F indexable inserts used during machining trials

Feature	Value
Insert shape	C
Inscribed circle diameter	12.7 mm
Corner radius	0.794 mm
Clearance angle	0°
Effective cutting edge length	8.5mm
Coating	CVD Ti(C,N)+Al2O3+TiN

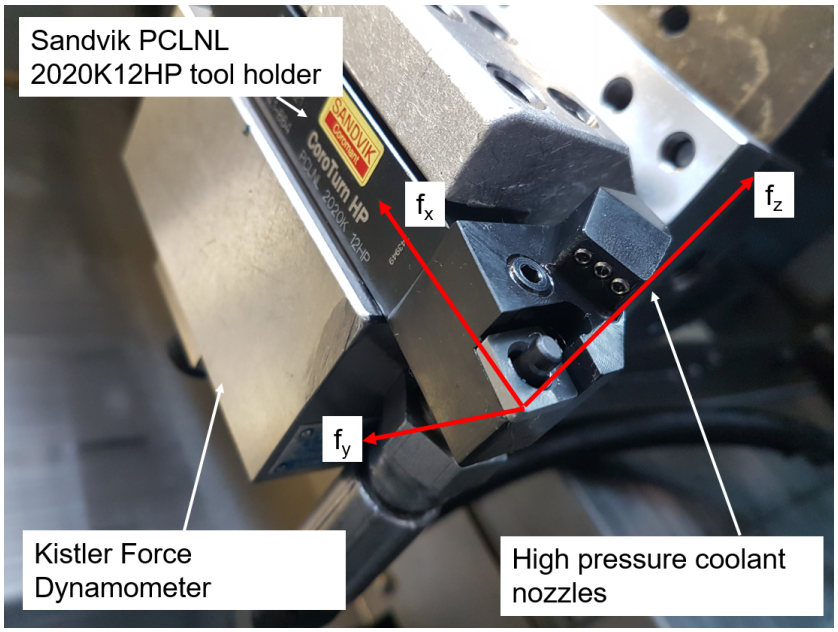

Figure 6.2: Photograph showing the tool holder located in the Kistler 9129a Force dynamometer. The direction and alignment of the measured tool forces are also indicated.

6.3.4 Coolant Delivery and Properties

The coolant employed during trials was Hocut 795-B which is mixed with water to give an emulsion with a concentration of between 6-8%. This coolant contains additives to minimise foaming allowing it to be compatible with high pressure coolant applications. The coolant concentration level was measured using an optical refractometer twice per day during trials, the pH level was monitored using litmus paper twice per trial day, example measurements taken are shown in Figure 6.3. High pressure coolant was chosen for machining trials due to enhanced chip breaking capability provided which minimises random events involving chip entanglement from occurring. An additional benefit of high pressure coolant is enhanced tool wear resistance, which leads to more consistent finishing cuts as the influence of tool wear on the machined surface and subsurface is lessened. High pressure coolant is commonly used in industry and at the time of writing represents part of the state of the art solution for machining nickel superalloys.

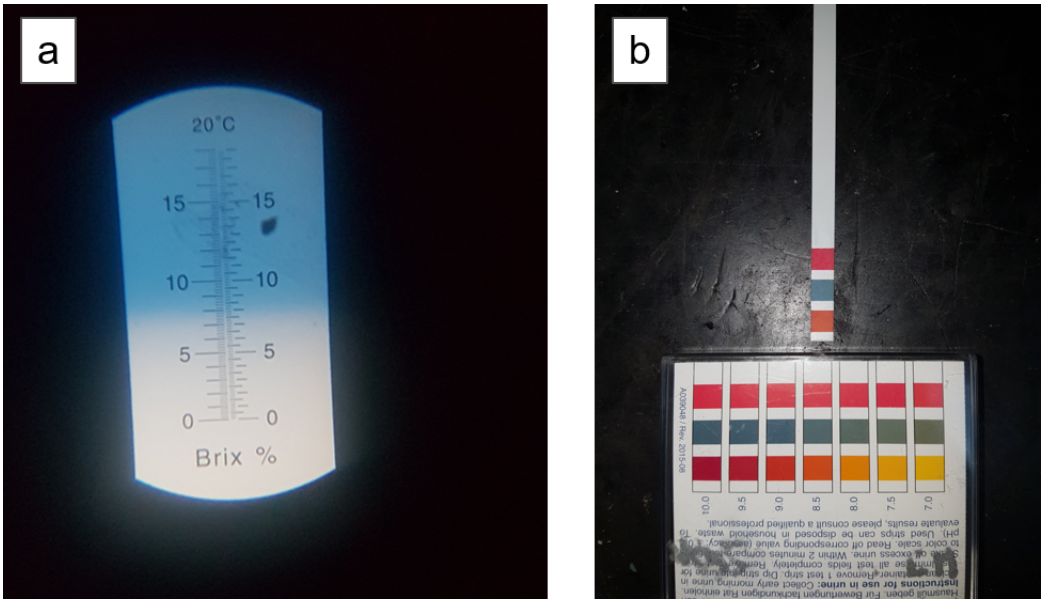

Figure 6.3: Photographs showing (a) an example measurement captured using the refractometer (note the value is corrected using a refractometry index of 1.1 which is recommended by the coolant supplier) and (b) an example pH reading showing a pH of 8.5.

The coolant is delivered to the cutting edge using a high pressure pump from a large reservoir tank, the coolant flow rate was measured by collecting discharged coolant in a large bucket. The coolant was then transferred to a

second bucket which was weighed to determine the mass of coolant discharged within a given time frame. The density of the coolant was determined by measuring out 1 l of coolant and measuring the mass of the coolant taken into account the container used for this process. This method was repeated to give two readings which were then averaged to give the volumetric flow rate of coolant of 18 $l.min^{-1}$. An image showing the coolant mass collected after 30.2 seconds of coolant discharge and the measured coolant flow rate is shown in Figure 6.4. Note that although the bucket exceeds 10 l, the high flow rate and contact with the tube leads to air entrainment which artificially increases the volume of the coolant. The coolant captured in the bucket was noted to have a foamy appearance.

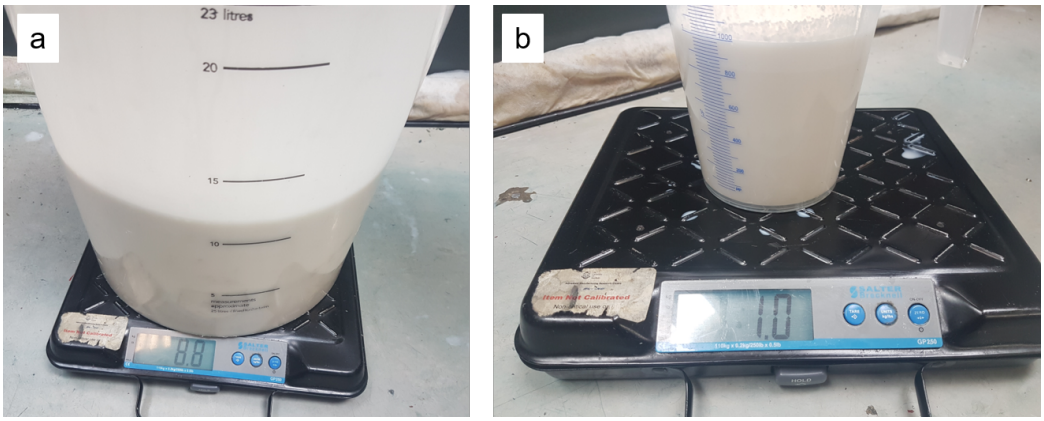

Figure 6.4: Photograph showing (a) the measured coolant volume and mass after a period of 30 s (b) the mass of approximately 1l of coolant.

6.3.5 Measurement of Edge Rounding

Measurements of the cutting edge radius, known as edge rounding or edge sharpness were conducted to ensure that none of the cutting tools used would provide an anomalous result. It was decided that tools which differed from the mean edge rounding value by more than 1 standard deviation would not be used to produce the surfaces used for subsequent damage examination. Variations in cutting force due to edge rounding effects will likely translate to variations in the sub-surface damage imposed in a material. In an attempt to reduce the impact of this variable from the machining trials, it was decided that a large number of cutting inserts would be characterised in terms of edge rounding to understand the statistical distribution in inserts and how likely this is to effect the results of the machining trial. To perform this analysis, an Alicona SL40 microscope was used to capture 3D topography images on

the cutting edge of each tool.

The microscope conducts measurements by using a vertically oscillating lens during scanning at a fixed position. Changes in focus are then used to determine the vertical height of the features in focus relative to each other. These measurements are then repeated over an area to build a topographical map of the cutting edge of a tool mounted at 45°to the horizontal. The Edgemaster software package then analyses a fixed number of 2D profiles of the edge. The profiles are extracted from the 3D scans by extracting 2D profiles which are perpendicular to the radius of curvature of the edge. 50 profiles were used for the measurement of edge rounding, a 4 mm^2 scan area was used the centre of which was focused on the cutting tip. The edge rounding was measured on the corner of the tool, however for higher depths of cut the tool would be engaged beyond the nose radius of the tool meaning areas beyond the scanned tool depth. Given the tight tolerance provided by tooling manufacturers, it was assumed that the area scanned was representative of all cutting regions. A diagram showing the identification system chosen for identifying the scanned edges is shown in Figure 6.5. Inserts were provided in packs of 10, each insert was assigned a number based on the pack number, insert number within that pack and each edge was identified using the aforementioned diagram. This system allowed each particular edge to be correlated with an edge rounding value for all trials.

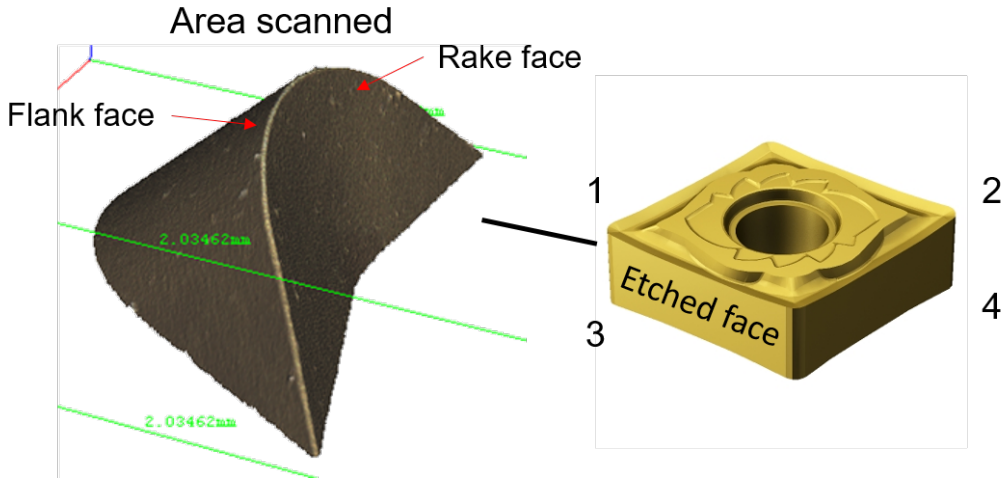

Figure 6.5: Diagrammatic representation of the area during edge rounding measurement and the naming convention used to identify a particular cutting edge.

6.3.6 Post Processing of Cutting Force Data

For the measurement of cutting forces, it was necessary to post process the data files to eliminate issues such as signal drift and extract meaningful average cutting force values at strategic positions during each trial. Example cutting force data without post processing is shown in Figure 6.6. As can be seen, the force feedback is offset from zero due to the charge state of the piezoelectric crystals present in the force dynamometer. This can be mitigated by reinitialising the charge amplifier before each cut, which was adopted for later trials. For trials performed where this large offset was present, the forces were corrected to read zero when the coolant was on and the spindle running but no cut was performed, this eliminates vibrational and push back effects caused by the rotating spindle and high pressure coolant. This was performed by averaging the measured forces during this non-cut period and subtracting from the remaining data therefore eliminating the steady state error for the cutting forces in each of the principle directions. An example of Z direction force data both prior and post zero correction is shown in Figure 6.7.

Figure 6.7 reveals that although correcting the data leads to the correct definition of zero force prior to the beginning of cut, after the tool has disengaged, the forces do not return to zero. The phenomenon is not a physical one, but rather a consequence of the piezo-electrics used to measure the forces. These sensors are extremely sensitive to changes in temperature among other factors, which can lead to signal drift occurring. It is for this reason that the force does not return to zero after the tool is no longer engaged with the work piece. To correct for these effects, the measured forces were averaged over a period of time before and after the cut, where the coolant and spindle are still running, hence by producing equivalent conditions but when no material is being removed. A linear relationship between the cutting force before and after cut and the time elapsed is then determined between the two averages and the gradient found. An inverse linear relationship is used to correct for the drifting signal. A diagram showing this procedure graphically, is shown in Figure 6.8. The importance of measuring data before and after cutting while coolant and spindle are still operation can be seen. The sudden switching off of either the spindle or the coolant results in further modification of the force feedback data which can lead to incorrect drift correction being performed. Once the assumed linear relationship is characterised in terms of gradient and intercept, a correction factor for each time step is calculated using the inverse of the signal drift gradient. An example Z direction force feedback data set before and after drift correction is displayed in Figure 6.9. As can be seen, the proposed drift correction

procedure leads to the corrected scenario, whereby forces in the principle cutting direction (Z) register zero on average both before and after the tool is removing material. This procedure was followed for all force feedback data collected in all of the captured force directions X,Y and Z in order to perform a true comparison between data sets.

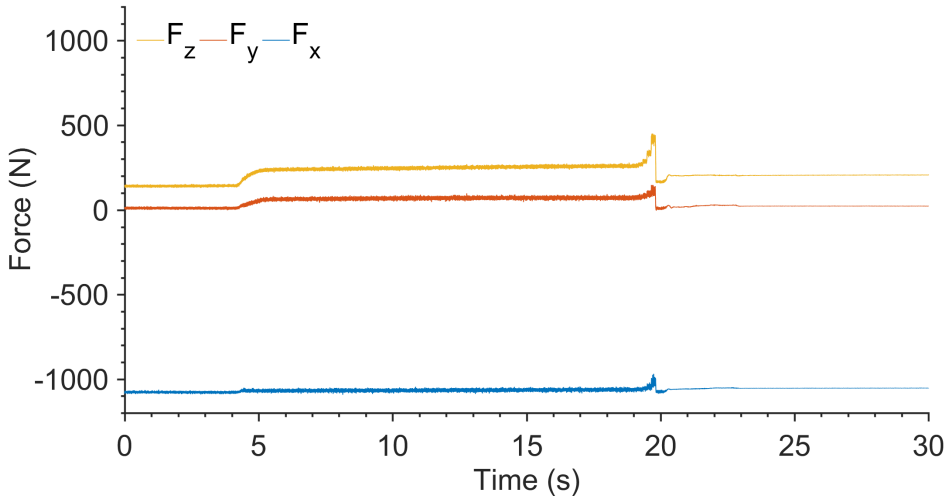

Figure 6.6: Example raw cutting force data for a machining pass during preparation of a FAST billet, showing the non-zero offsets that are required to be removed prior to meaningful analysis of the cutting force data.

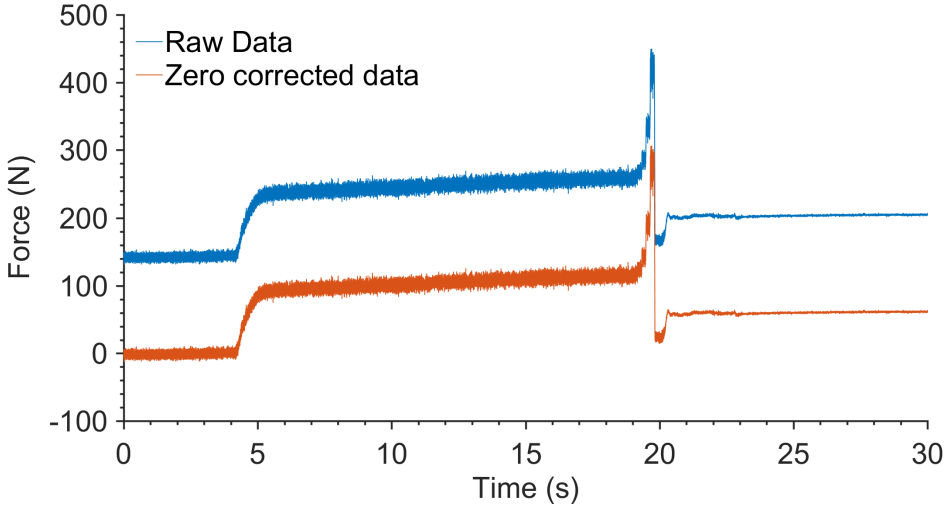

Figure 6.7: Example cutting force data registered in the Z axis during a preparatory machining pass of an as FAST billet. The figure shows the result of zero offset correction.

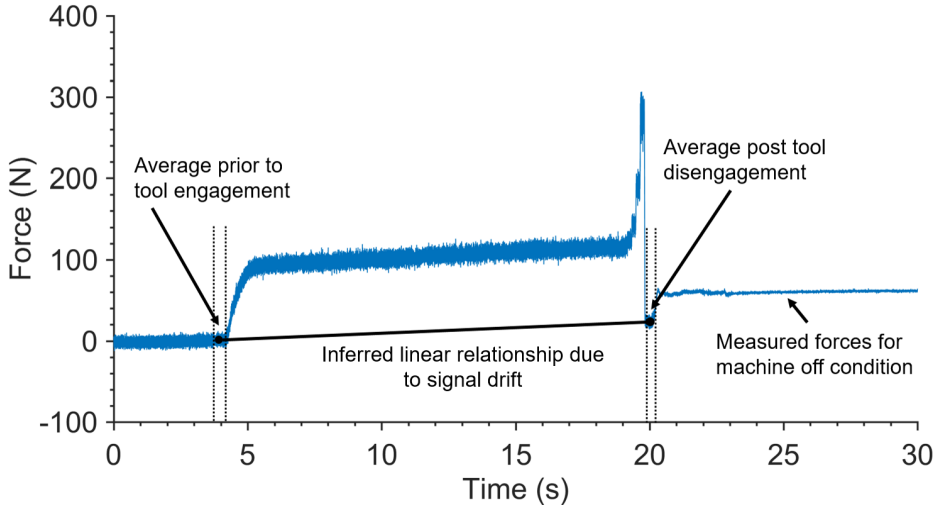

Figure 6.8: Diagrammatic representation of the signal drift correction procedure for the Z (cutting) axis cutting forces. The registered cutting forces before and after cutting are averaged and a linear relationship between the two averages with regards to time is calculated.

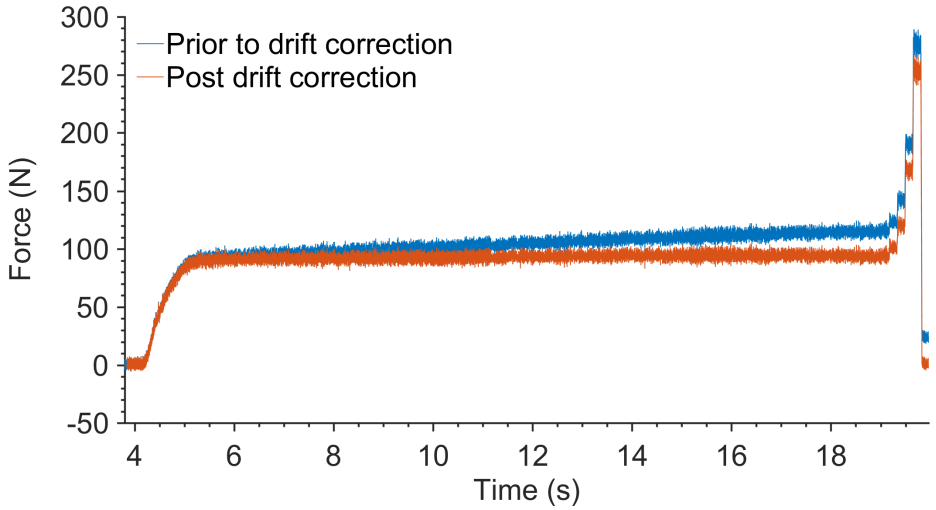

Figure 6.9: Example cutting force data (measured in the Z axis) both before and after signal drift correction. As can be seen, the cutting force returns to zero after tool disengagement.

Once the cutting force data had been corrected as described, the various regions of the cutting force data could be identified with the aid of figure 6.10. With reference to the markers identified in the Figure 6.10, certain key events can be identified from a typical cutting force data set, as detailed in Table 6.5. As explained in Figure 6.11, once the tool reaches an uncut shoulder, there is a large increase in the contact area between the tool and work piece, this results in a momentary increase in the forces experienced by the tool, which is diagrammatically shown in Figure 6.11.

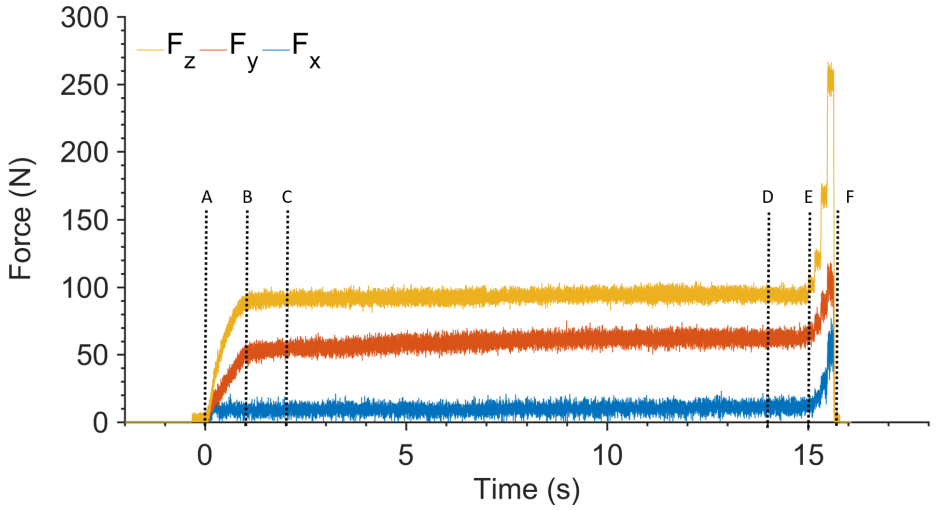

Figure 6.10: Example cutting force data showing key points during a cutting pass. The description of points A-F can be found in Table 6.5.

Table 6.5: Description of events identified during a machining trial.

Event	Description	Prefix
A	Start of tool engagement	STE
B	Tool fully engagement	TFE
C	1 Second after tool engagement	1SAE
D	1 second before corner interaction or tool engagement	1SBD
E	Start of corner interaction and disengagement	SOD
F	Full Tool disengagement	TD

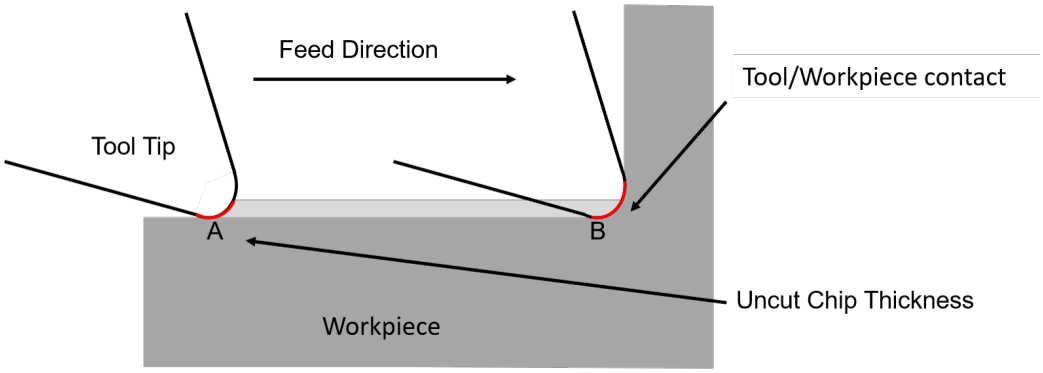

Figure 6.11: Diagrammatic representation of the increase in tool/workpiece contact area when a tool reaches an uncut shoulder.

6.3.7 Machining Strategy and Machining Conditions

Each as-FAST billet was machined from a starting diameter of 121 mm and thickness of 25 mm, sequential machining passes were performed in order to produce a stepped geometry with 3 machined faces with equal surface area. Each face on the stepped geometry was separated by a distance of 1 mm and machining speeds varying from 40-120 $m.min^{-1}$. In order to produce these faces, several machining passes were performed with varying depths of cut from 0.25 mm, 0.75 mm and 1.00 mm. All trials were performed with a constant feed rate of 0.12 $mm.rev^{-1}$, which is within the recommended range for the provided S05F inserts. As the trials performed were facing trials, the rotational speed of the spindle increased to maintain a constant surface speed. In order to prevent the maximum speed of the lathe from being reached, a centre circle of 5 mm diameter was left un-machined. The machining passes performed were designed to give 2 repeats of each machining condition. A diagram showing the machining passes performed for each billet is shown in Figure 6.12. A diagram of the billets post machining showing the location of sub-surface examination locations is shown in Figure 6.13. Table 6.6 displays the start and finishing diameter for each of the locations identified in Figure 6.13, a photograph of the as-FAST billet before and after machining is shown in Figure 6.14. Information regarding the cutting time for the associated passes is shown in Table 6.7.

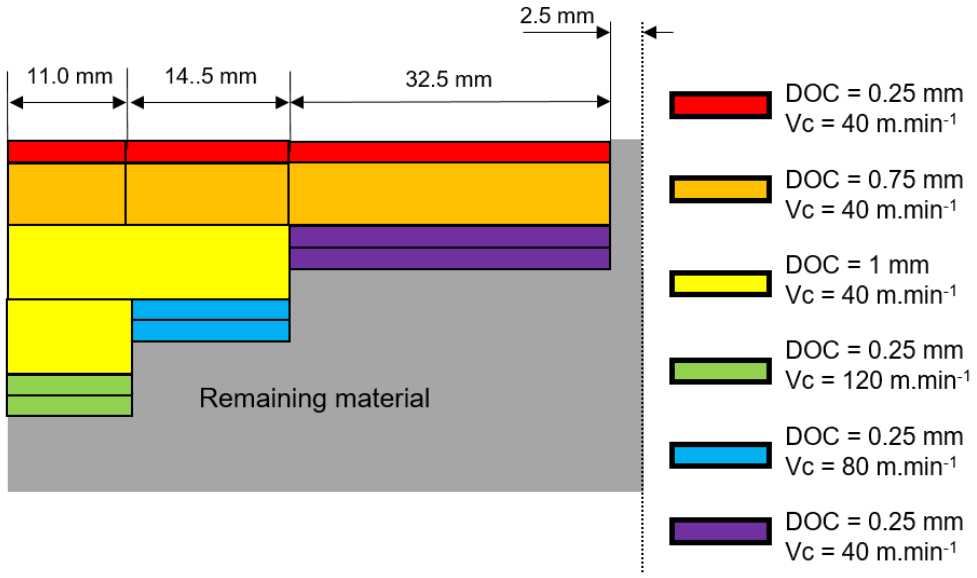

Figure 6.12: Diagrammatic representation of the machining passes performed for each FAST billet. Depths of cut (DOC) and surface speeds (V_c) for each pass are shown.

6.3.8 Examination of Post Machined Sub-Surfaces

Upon completion of the final machining passes consisting of faces turned with decreasing surface speed, from 120 m.min^{-1} to 40 m.min^{-1} the machined billets were sectioned according to the diagram described in Figure 6.13 using wire electron discharge machining (EDM). Once the sectioning had been completed, the strips extracted were sectioned further using an abrasive cut off wheel on a Struers Secotom-50 sectioning unit. The linear traverse speed used during abrasive sectioning was maintained below 0.1 mm.min^{-1} in order to minimise further damage to the material. The surfaces were revealed using this procedure are identified in Figure 6.13.

The revealed cross sections were then mounted in Buehler Conductimet conductive mounting compound designed for SEM use. The standard metallographic preparation procedure was then applied to produce surfaces suitable for etching to be carried out. When viewing the γ' precipitates, etching was conducted using Kalling's waterless reagent (50ml HCl, 50ml methanol, 2.5g $CuCl_2$) and samples were immersed in the etchant for approximately 20 seconds to leave γ' precipitates in relief and also reveal the grain boundaries. Once etched, samples were initially examined using light microscopy, however this was found to be of insufficient resolution to reveal machining induced sub-surface damage. To this end, secondary electron imaging was

employed to provide higher resolutions. SEM examination was conducted using a combination of two SEM systems. Backscatter electron microscopy was also employed using the described SEMs to view the surface in the un-etched condition to reveal the γ grain structure. The details of and parameters used for each system are described in Table 6.8.

Table 6.6: Dimensions used for the machining of the 3 FAST billet locations identified in Figure 6.13, showing the dimensions of the passes performed, the calculated surface area removed by each machining pass and the measured time in cut for a 40m.min^{-1} machining speed, averaged over 3 dummy passes in the locations.

Location	D_s (mm)	D_f (mm)	t_c (s)	A_r (mm^2)
1	121.00	98.84	47.73	3826
2	98.84	69.98	47.68	3826
3	69.98	5.00	47.95	3826

Table 6.7: Measured time in cut for the 3 locations machined using variable surface speed, values were averaged over 3 dummy passes.

Location	V_c (m.min^{-1})	t_c (s)
1	120	14.81
2	80	23.08
3	40	47.51

Table 6.8: SEM parameters used for the imaging of the machined FAST billet microstructure. Both Secondary electron (SE) and Backscatter (BS) electron mode optimal settings are given.

Microscope system	FEI Inspect F	FEI Inspect F50
Working distance (SE/BS)	10 mm/6.5 mm	10 mm/6.5 mm
Spot Size (SE/BS)	4.0/4.0	3.5/3.5
Accelerating voltage (SE/BS)	10 keV/5 keV	20 keV/ 10 keV

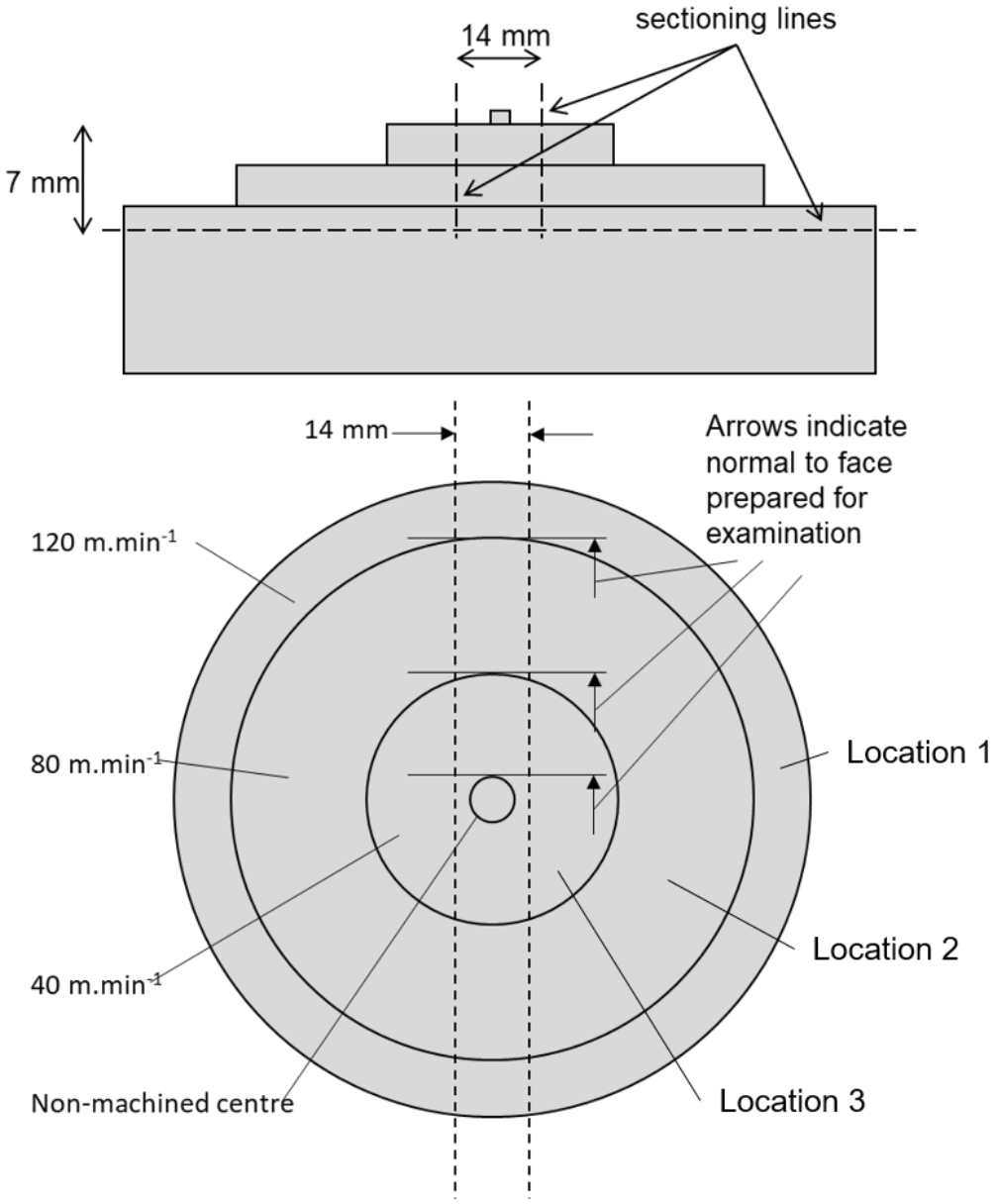

Figure 6.13: Section procedure in order to extract surfaces perpendicular to the machining direction in the FAST billets, the location of the samples used in follow up metallographic preparation are indicated.

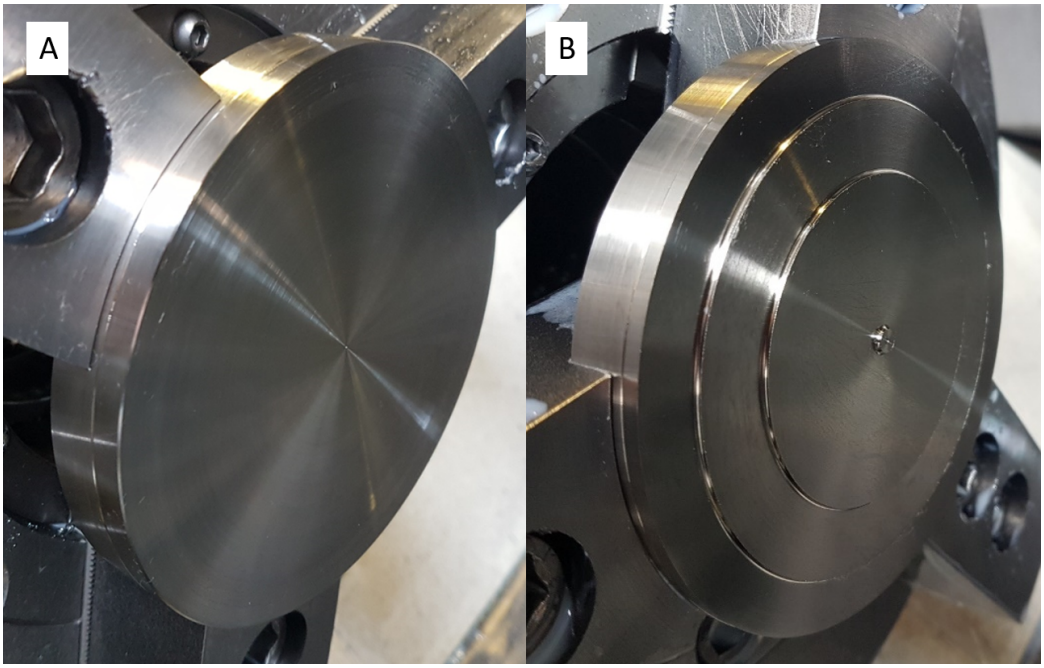

Figure 6.14: Photograph showing an example of an as-FAST billet (A) prior to machining and (B) Post machining.

6.4 Results and Discussion

6.4.1 Edge Rounding Analysis

Figure 6.15 shows the results of the edge radius measurements performed for 80 inserts selected for the cutting trials. As revealed in the figure, although manufactured to high tolerances, the inserts exhibit a range of edge radii values within the scanned inserts. The statistical values associated with the edge rounding data are displayed in Table 6.9. The data concludes that the tool edges display a near symmetrical distribution with a relatively sharp peak as indicated by the near zero for the skewness and the positive value determined for the kurtosis. It can be inferred that the edge rounding has implications with regards to the forces required during cutting and also the sub-surface damage imparted, with a sharper tool and lower edge radius requiring lower cutting forces, for example. The finish surfaces which were examined for microstructural damage were machined using inserts within 1 standard deviation above and below the mean value of 13.678.

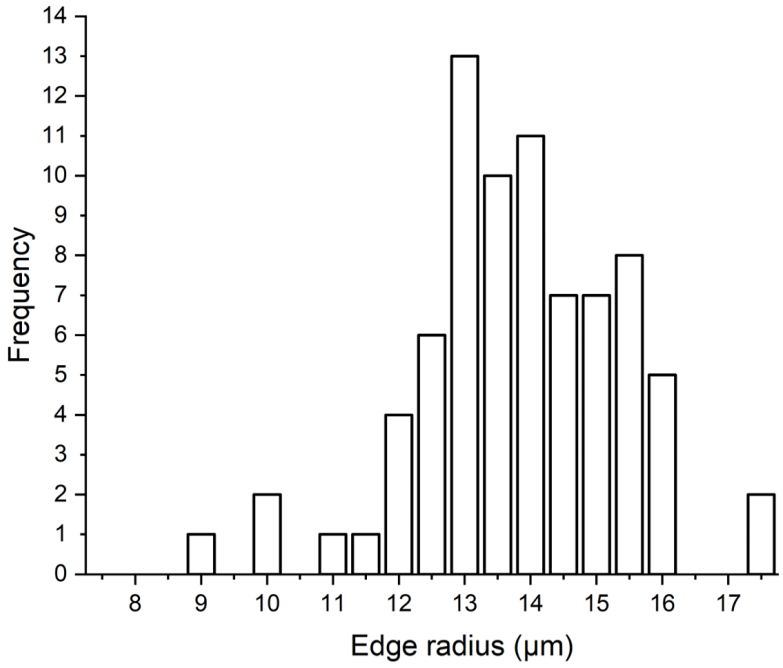

Figure 6.15: Histogram displaying the frequency of edges with specific edge rounding values for 80 S05F cutting edges with a 8mm tool nose radius. No data is available publicly for the expected nominal value.

Table 6.9: Descriptive statistics for edge rounding data collected for the cutting edges used in the FAST machining trials

Mean	13.678 mm
Standard Error	0.190 mm
Mean + 1SD	15.380 mm
Mean + 1SD	11.975 mm
Median	13.527 mm
Standard Deviation	1.702 mm
Sample Variance	2.900 mm
Kurtosis	1.075 mm
Skewness	0.068 mm
Range	9.891 mm
Minimum	8.795 mm
Maximum	18.687 mm

6.4.2 Measured Cutting Forces when Machining As-FAST Material

Figures 6.16, 6.17 and 6.18 show the measured cutting forces for 0.25 mm, 0.75 mm and 1.0 mm depths of cut, respectively, averaged over 1 second after tool engagement. Averaging over the first second of tool engagement allows direct comparison of cutting forces as the tool is in the new condition and was considered to be the most representative comparator for cutting forces across the billets. Comparing Figures 6.16, 6.17 and 6.18, it can be observed that the depth of cut has the largest influence on the measured cutting forces which is as to be expected. This can be seen when the Z direction cutting forces (which are in the cutting direction) are plotted as a function of depth of cut for each billet in Figure 6.19.

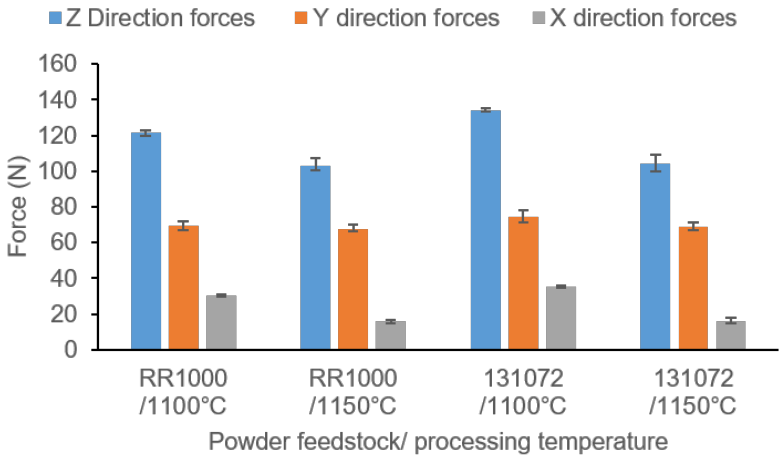

Figure 6.16: Cutting forces measured in the 3 principle directions averaged over the 1st second after tool engagement for the passes performed with a depth of cut 0.25 mm and a surface speed of 40 m.min[1].

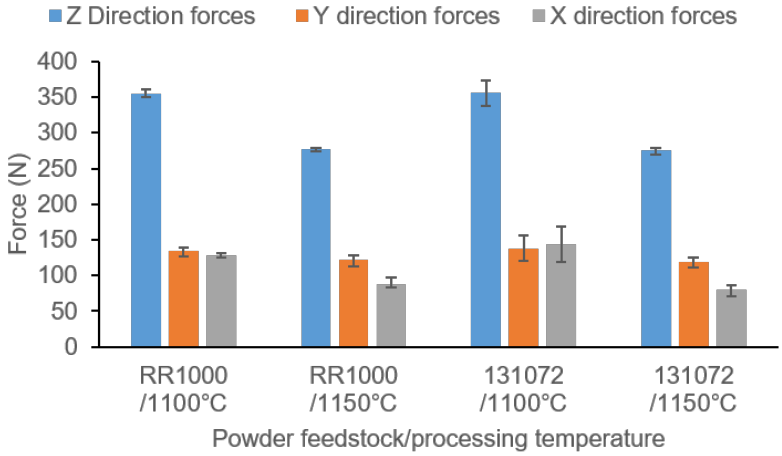

Figure 6.17: Cutting forces measured in the 3 principle directions averaged over the 1st second after tool engagement for the passes performed with a depth of cut 0.75 mm and a surface speed of 40 m.min[1]

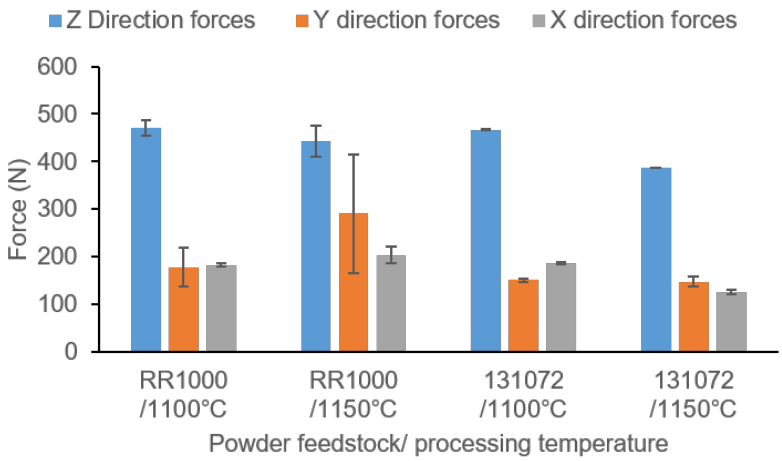

Figure 6.18: Cutting forces measured in the 3 principle directions averaged over the 1st second after tool engagement for the passes performed with a depth of cut 1.0 mm and a surface speed of 40 m.min[1]

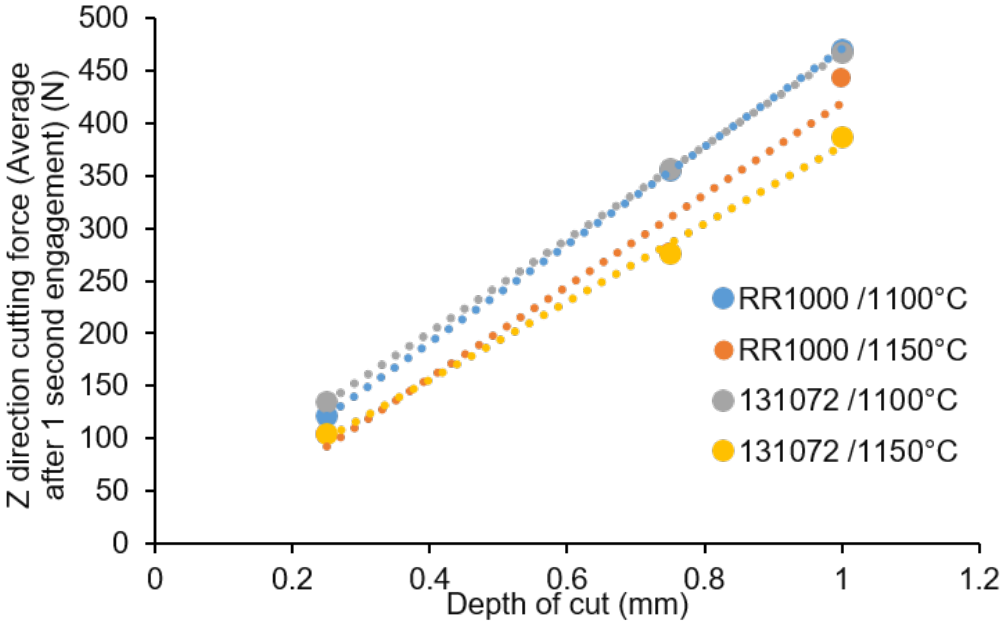

Figure 6.19: Measured Z direction (cutting direction) forces vs depth of cut for all as FAST billets.

In Figure 6.16 it can be seen that the change in powder source does not greatly alter the measured cutting forces in all principle directions for a

fixed FAST processing temperature. Two things can be inferred from this finding, the first being that the differences between the RR1000 powder and the 131072 powder leads to little change in the material properties which would manifest as a change in cutting forces. The second inference is that the FAST process is repeatable given that the resistance to cutting force is very similar for both billets. Figure 6.16 demonstrates that a difference in cutting force can be observed when machining FAST billets processed using a different dwell temperature. The billets produced using the super-solvus dwell temperature of 1150°C display lower cutting forces in the Z and X directions than those measured for the billets produced using the sub-solvus dwell. This trend can be observed in the cutting forces for a 0.75 mm depth of cut in Figure 6.17 and for a 1 mm depth of cut in Figure 6.18. For the 1 mm depth of cut however the difference in cutting force is less pronounced. Examination of the Y direction forces in Figure 6.16 reveals that regardless of the billet processing conditions, the Y direction forces are approximately constant, this can also be seen for the 0.75 mm depth of cut (Figure 6.17). For the 1 mm depth of cut however, an abnormally high average Y direction force is observed for the RR1000 powder billet processed at 1150°C. This is likely due to a tool breakage event which is a result of the 1mm depth of cut being beyond the 0.8 mm nose radius of the tool. At higher depths of cut, particularly for the finishing inserts used, it is proposed that the material base properties will have less influence over the cutting forces than tooling effects.

The effect of cutting speed on the measured cutting forces are shown graphically in Figure 6.20. Figure 6.20 confirms that the cutting force in the principle cutting direction (Z direction) are greater for FAST billets produced using sub-solvus processing conditions across the range of speeds examined. The surfaces produced using the machine passes in Figure 6.20 represent the finish surfaces which were sectioned and examined as described in Figure 6.13. Location 1 was machined at 120 $m.min^{-1}$, location 2 with 80 $m.min^{-1}$ and location 3 with 40 $m.min^{-1}$. It can also be seen that 3 of the 4 billets exhibit increased cutting forces when lower surface speeds are employed. Considering the RR1000 billet produced using a 1150°C, it can be seen that the cutting force measured when a cutting speed of 80 $m.min^{-1}$ is greater than that when 40 $m.min^{-1}$ is used. This result is unexplained and thought to be due to erroneous depth of cut during the first finish machining pass at 80 $m.min^{-1}$.

These results indicate that although the powder feedstock used in the FAST production stage appears to have little effect on the cutting forces observed during machining, the measured forces point to a variation in materials properties with the variation in the FAST processing temperature

used. This is a strong indication that the machining process is being influenced by the variation in grain size which occurs when the γ' solvus temperature is exceeded, as discussed in Chapter 3. The reason for the decrease in cutting forces with increasing machining speed is explained by increased cutting temperatures associated with increased machining speed. No evidence is available however without the repeat of the trials with embedded thermocouples, which cannot be used with the simultaneous application of high pressure coolant.

To examine the uniformity of the cutting forces with respect to billet position, passes with depths of cut of 0.25 mm and 0.75 mm were performed at each of the 3 locations defined in Figure 6.13, as described in Figure 6.12. Figure 6.21 shows the measured forces for each of the 3 locations for each billet captured for the 0.25 mm depth of cut passes. As is clearly visible in the chart, the billets produced using super-solvus dwell conditions display lower Z (cutting direction) forces than those measured for the sub-solvus billets for both powder feedstocks. This observation is consistent across all locations. This provides further evidence that the processing conditions and therefore the underlying material structure has influence over the cutting forces. For each billet, it can be seen that there are marginal differences in cutting forces across locations suggesting that the microstructure is uniform across the billets. The same trend can be observed for the forces measured for the 0.75 mm depth of cut passes detailed in Figure 6.22. This is conclusive evidence that the factor which influences the cutting forces the most is the processing temperature used to produce the billet which, as discussed previously, is heavily linked with microstructure.

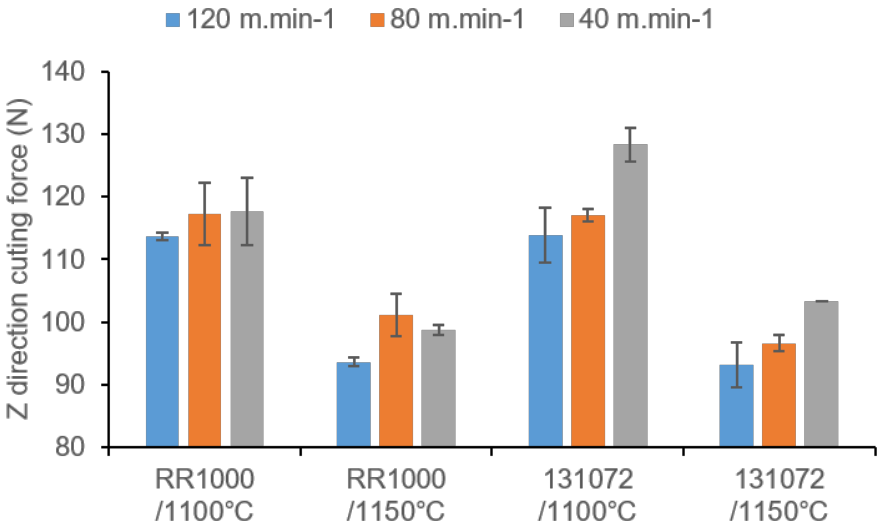

Figure 6.20: Bar chart showing the average cutting forces measured over the 1st second of cutting after tool engagement for the finish surfaces on each FAST billets in locations 1,2 and 3 for differing machining speeds. The data shown is averaged for the 2 passes performed for each condition, the error bars show the resultant range.

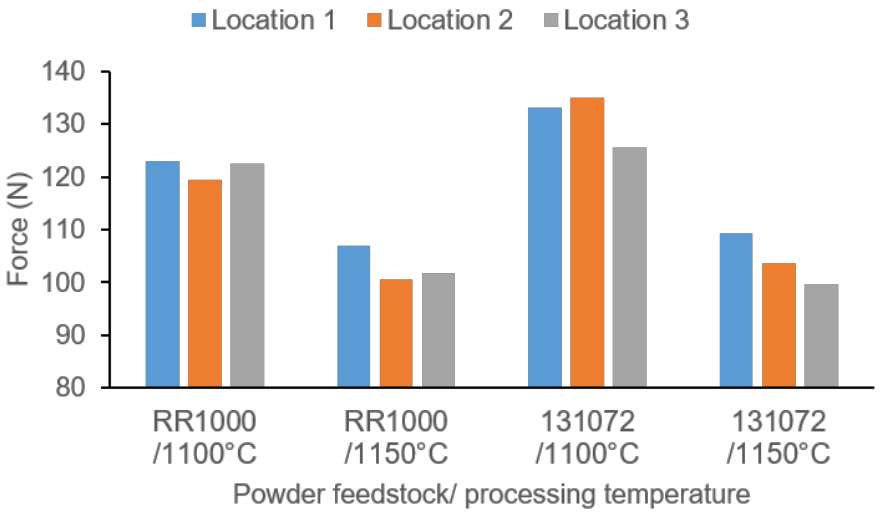

Figure 6.21: Bar chart showing the variation in the Z direction cutting forces for passes performed using a depth of cut of 0.25mm and a surface machining speed of 40 m.min^{-1} at the differing locations defined in Figure 6.13.

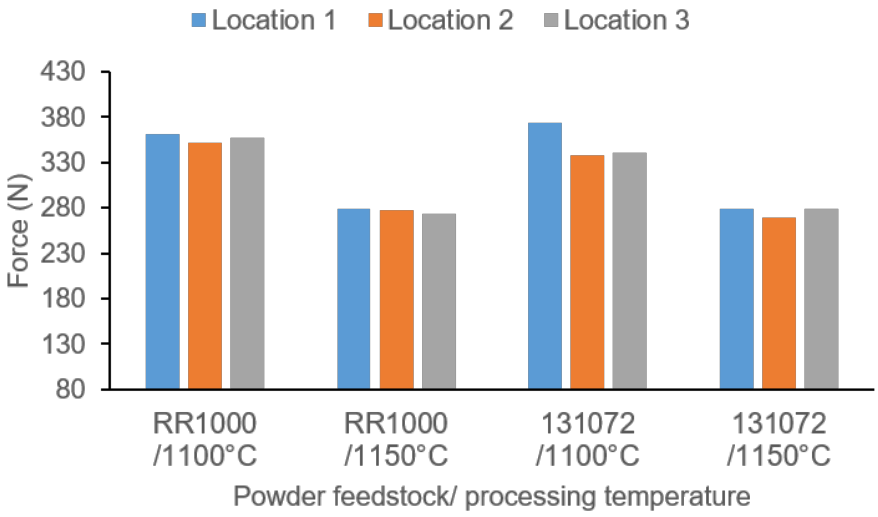

Figure 6.22: Bar chart showing the variation in the Z direction cutting forces for passes performed using a depth of cut of 0. 75mm and a surface machining speed of 40 m.min^{-1} at the differing locations defined in Figure 6.13.

6.4.3 Tool Wear During FAST Billet Machining

The tool wear produced when machining the super-solvus and sub-solvus processed FAST billets (for both powder types) as a function of the surface speed used are shown in Figures 6.23 and 6.24 respectively. By the design of the trial, each tool removed the same volume of material. As can be seen the level of tool wear is exceptionally low, this is primarily due to the short cutting times employed, as shown in Table 6.7. It can also be seen that the level of tool wear is almost indistinguishable across both cutting speeds and the billet machined. It is expected that should longer machining trials be conducted, the tool wear would become more evident when the cutting speed is higher. Across all the billet materials, it can be seen that the tools exhibit very similar flank wear scars with no notching or evidence of built up edge, which is an indication that the material is not significantly affecting tool wear. It can also be said that the cutting force data across billets and cutting speeds is directly comparable as the tools are undergoing similar levels of tool wear across billets. Also, it can be inferred that the observed differences in cutting forces for each of the billets in Figure 6.20 are due to material differences and not due to tool wear effects. It is recommended that if sufficient material is available, tool wear trials are conducted to fully understand the wear behaviour of the tool as a function of the input billet

material and also the cutting speed employed.

Considering the tool wear for varying depths of cut for the super-solvus and sub-solvus FAST billets in Figures 6.25 and 6.26 respectively, it can be observed that the increasing depth of cut for a fixed surface speed has a larger influence on the tool wear than varying machining speeds. Figure 6.25 shows that for the super-solvus processed billets, an increase in the wear scar is observable which is due to an increase in the engagement length for an increased depth of cut. It can be seen that a marginal increase in the depth of wear scar is also observed for the higher depths of cut. For the 1 mm depth of cut this is particularly evident for the billet produced using the RR1000 powder feedstock. It can also be observed that some built up edge features are visible on the tool faces which may indicate an increased tendency for built up edge to occur with increasing depths of cut. Based on these findings, it can be said that the cutting forces at higher depths of cut are more likely to be affected by the tool condition, which may mask the effects of underlying material properties. Furthermore, the S05F inserts used in these trials are unsuitable when machining depths of cut of 1mm for these materials types due to rapid degradation via chipping.

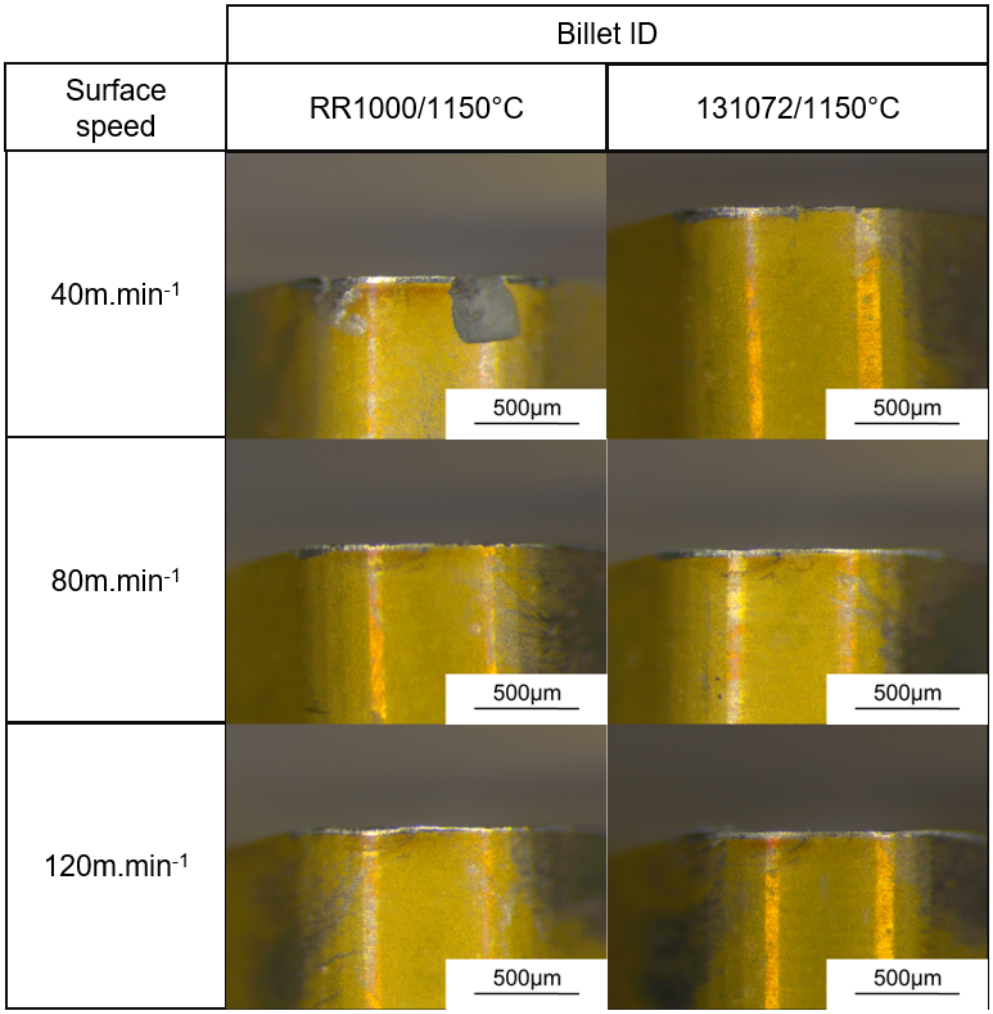

Figure 6.23: Typical tool flank wear characteristics for the machining the FAST billets produced using super-solvus dwell conditions.

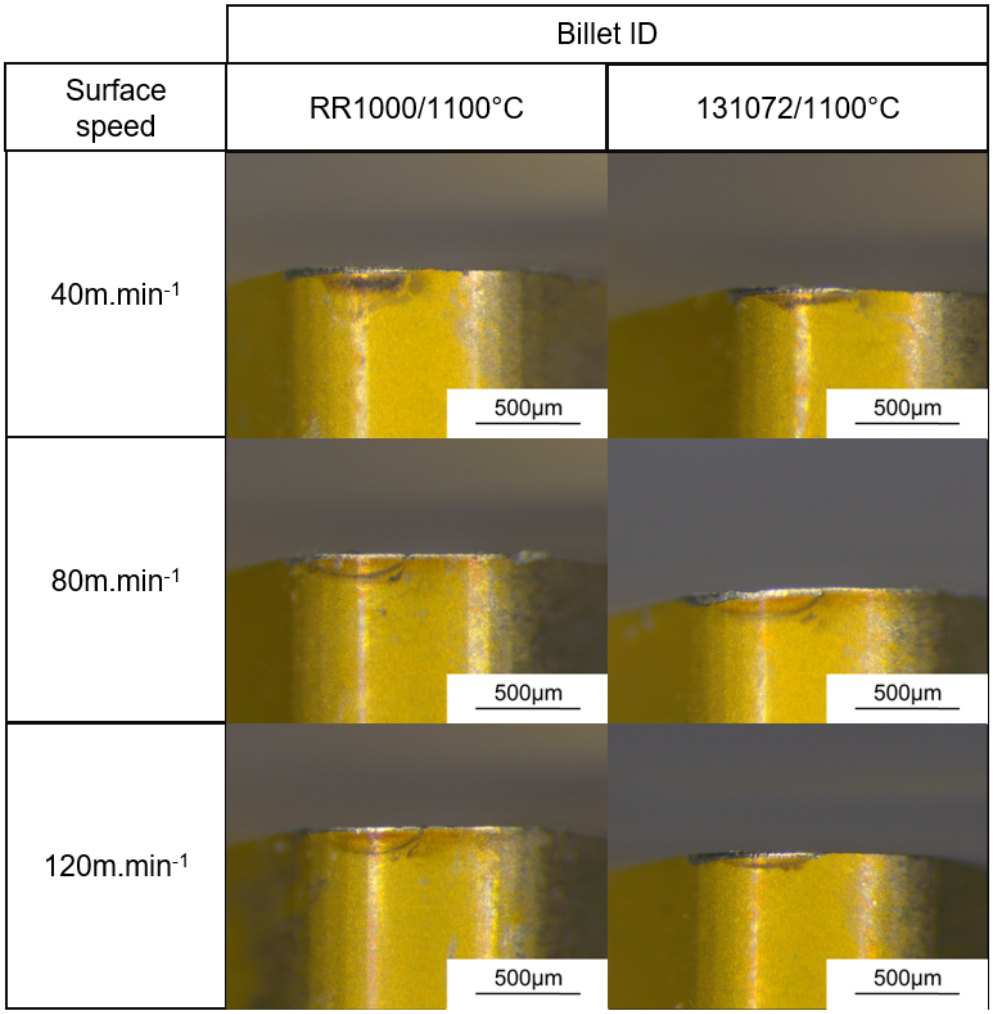

Figure 6.24: Typical tool flank wear characteristics produced during the machining of the sub-solvus FAST billets as a function of depth of machining surface speed

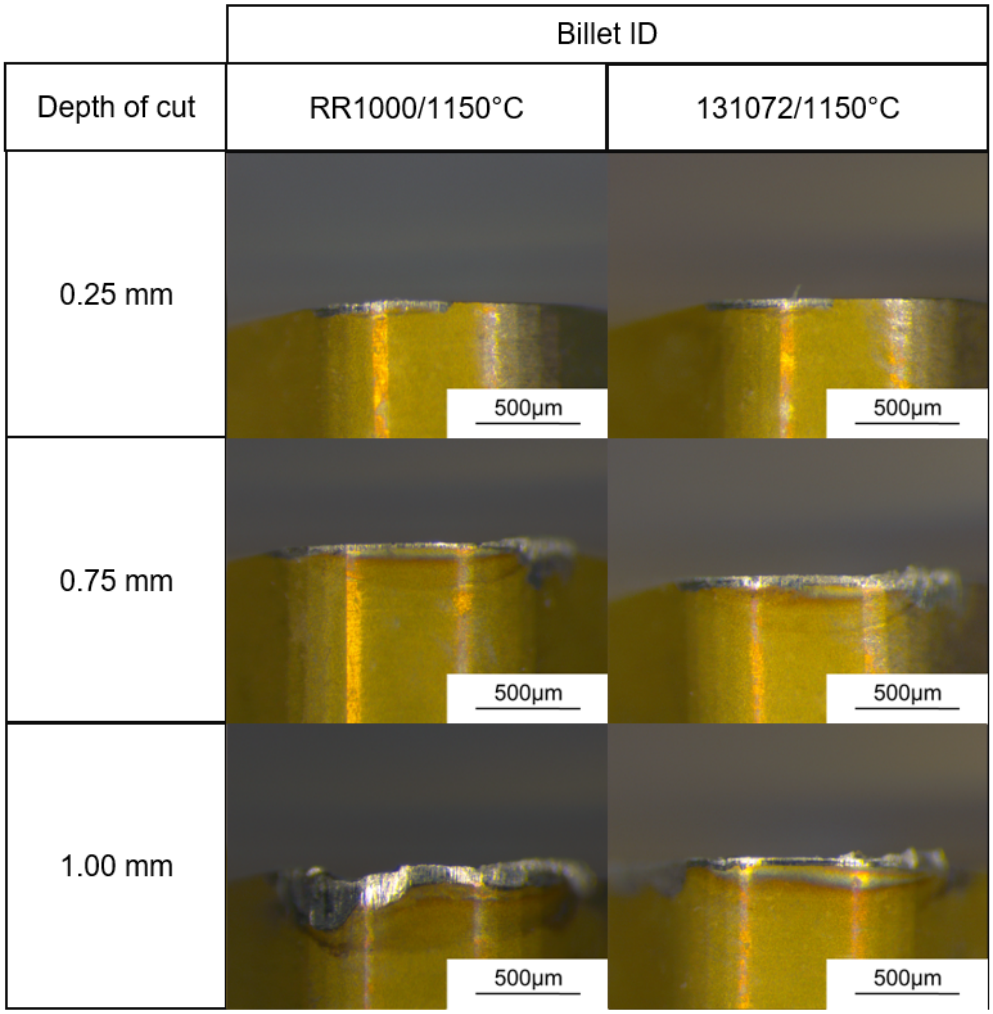

Figure 6.25: Typical tool flank wear characteristics produced during the machining of the super-solvus FAST billets as a function of depth of cut.

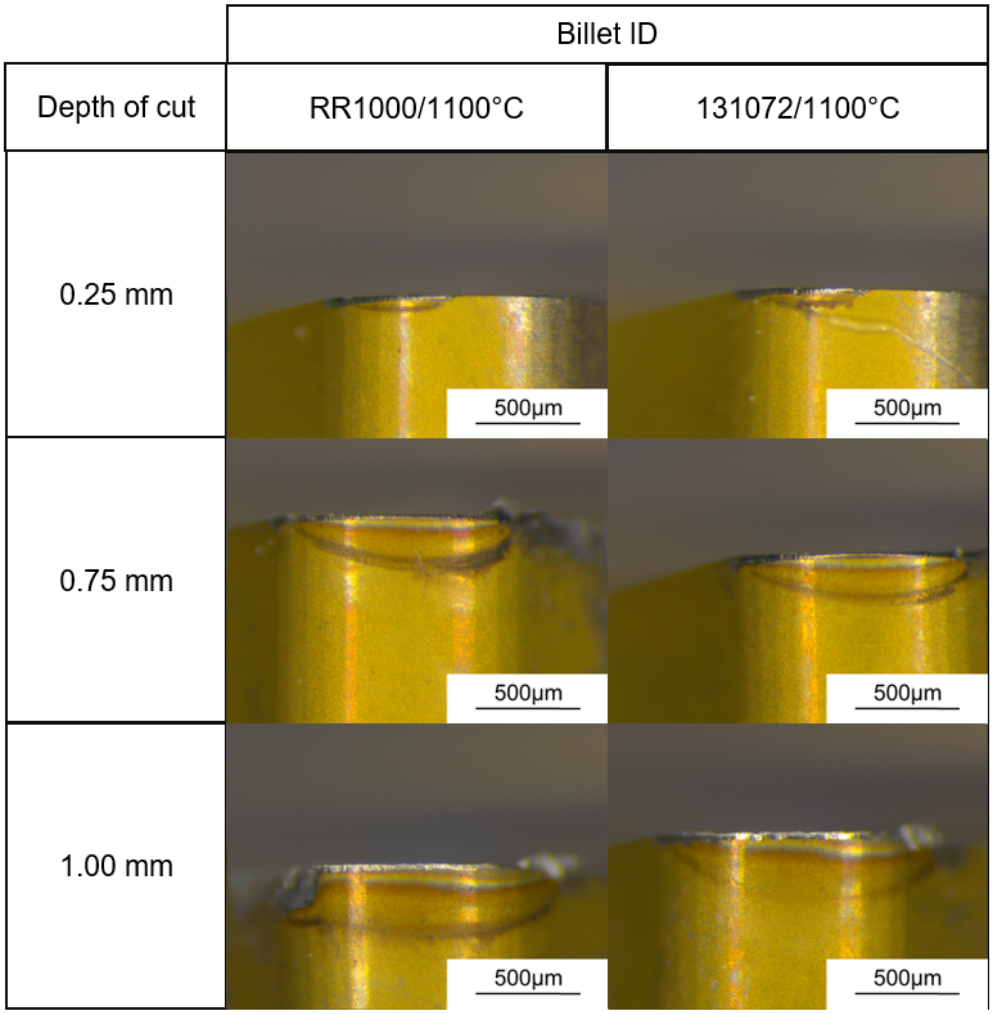

Figure 6.26: Typical tool flank wear characteristics produced during the machining of the sub-solvus FAST billets as a function of depth of cut.

6.5 Microstructural Characterisation of Up-scaled as-FAST Billets

Figures 6.27 and 6.28 show the microstructure at the 3 locations (described as locations 1, 2 and 3 in Figure 6.13) imaged approximately 500 μm away from the machined surface edge. This examination was conducted in order to examine the local microstructure in close proximity to the machining zone, without viewing the microstructure effected by the machining process. For FAST material produced using 131072 powder (Figure 6.27), at the sub-solvus dwell temperature of 1100°C, fine equiaxed grains are observed at each examined location. As noted in Chapter 4, a wide distribution of grain sizes is visible in all locations which is consistent which the small scale FAST study conducted. When a super-solvus (1150°C) dwell is utilised , the grain size is observed to increase significantly in locations 1 and 3 compared to the equivalent positions in the sub-solvus material. This is expected as the pinning γ' precipitates are no longer present. In location 2, however, the grain size is comparable to the material produced using sub-solvus temperature conditions in the equivalent location. This points to a lower temperature during sintering in location 2, or this potentially points to a sampling effect where the image represents an area of finer grains compared with the bulk.

The same observations can be made for the material produced using the RR1000 powder feedstock except at location 2 whereby the grain size in for the super-solvus material greatly exceeds that of the sub-solvus material, indicating that all areas of the billet have exceeded the solvus temperature during processing. The microstructure of the super-solvus dwell appears uniform across all 3 locations with a clear increase in grain size compared to the sub-solvus material. Hardness data measured at location 1 for each of the billet further confirmed a change in grain size, as shown in Figure 6.29. However the measurements contain a large amount of scatter which is unsurprising given the local variations in grain size visible in Figures 6.27 and 6.28. It is also noteworthy that the variation in hardness across billets also correlates with the change in cutting forces, as shown in Figure 6.16, 6.17 and 6.18. The material with marginally higher cutting forces exhibits marginally higher hardness.

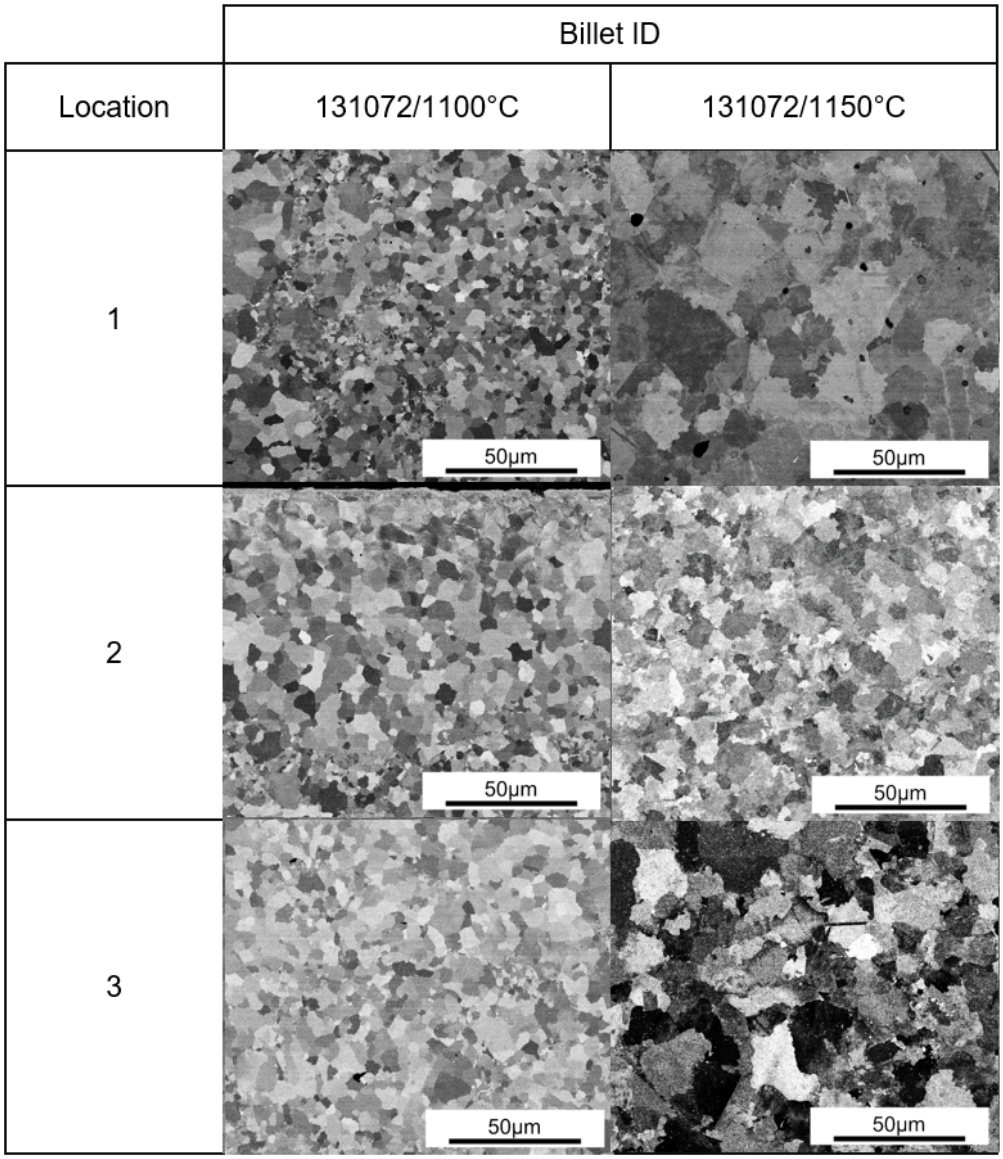

Figure 6.27: Backscattered electron micrographs showing the bulk microstructure grain characteristics of the billets produced using the 131072 powder feedstock for both sub-solvus and super-solvus processing. The locations examined are identified in Figure 6.13.

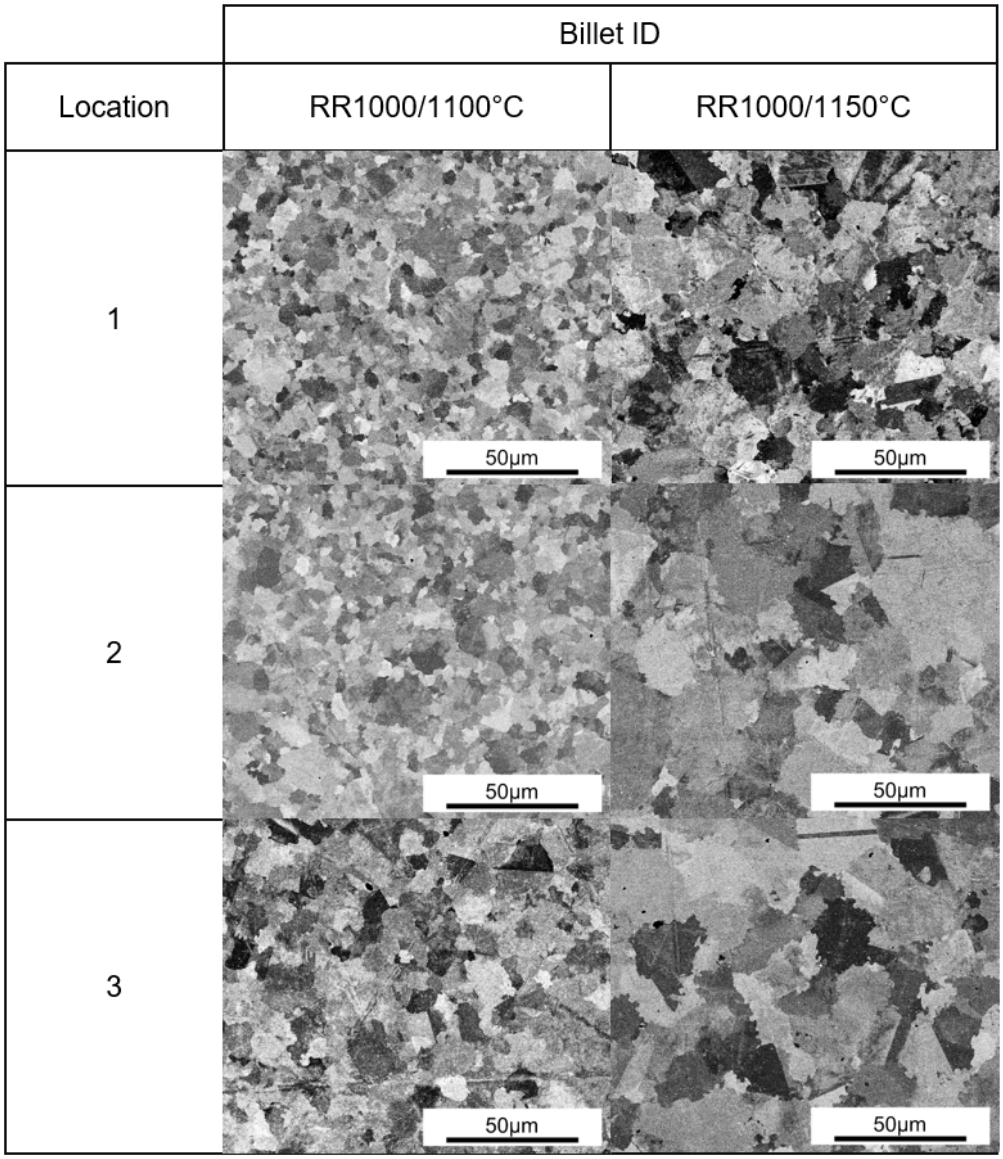

Figure 6.28: Backscattered electron micrographs showing the bulk microstructure grain characteristics of the billets produced using the RR1000 powder feedstock for both sub-solvus and super-solvus processing. The locations examined are identified in Figure 6.13.

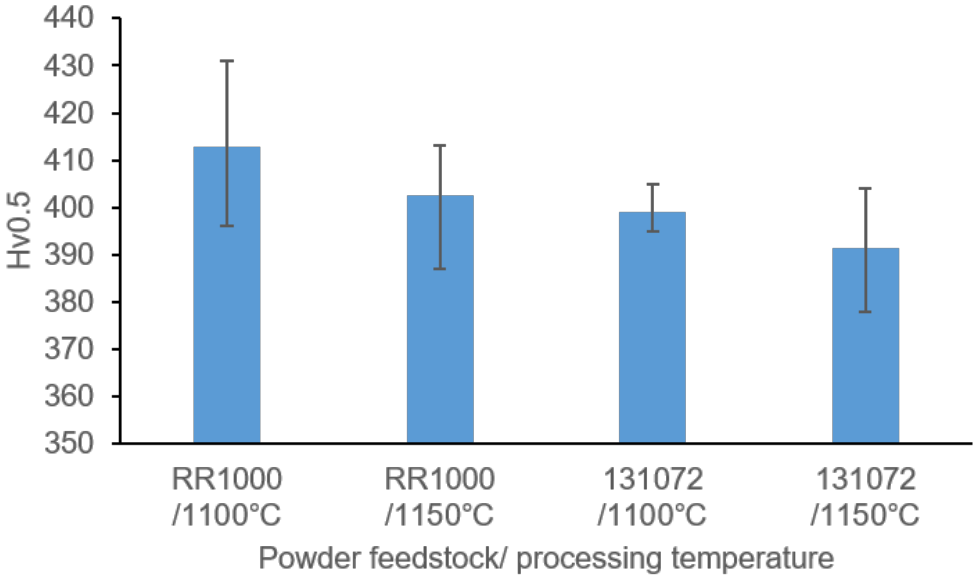

Figure 6.29: Hardness for the FAST produced billet used during machining trials. 10 measurements were taken in the bulk region of location 1 (described in Figure 6.13) from each billet.

6.5.1 Sub-surface Examination of the As-machined FAST Billets

The sub-surface examination performed for the billets produced using the RR1000 powder feedstock in the sub-solvus and super-solvus processing conditions are shown in Figure 6.30 and Figure 6.31. Examining Figure 6.30, it can be observed that regardless of the machining speed, the sub-surface damage observed is not severe whether examined through backscatter electron imaging in the polished condition or secondary electron imaging in the etched condition with deformation only evident within the first 10 μm beneath the machined surface. Comparing the backscatter electron images in Figures 6.30 and 6.31, the grain size difference between the sub-solvus and the super-solvus processing conditions can be observed, with coarser grain visible in the material processed beyond the solvus temperature in Figure 6.31. Backscatter electron imaging reveals an unresolvable deformed surface layer in the γ grains as opposed to the more obvious, distinguishable grains towards the bulk of the material. This is evident in both the RR1000 processed at a sub-solvus and super-solvus temperature. The etched micrographs in Figures 6.30 and 6.31 reveal a region of near surface precipitate deformation,

however no obvious difference between the levels of deformation are present regardless of location, machining speed and processing temperature.

The equivalent sub-surface damage images for the 131072 billets are shown in Figures 6.32 and 6.33. As is visible in the figures, the same findings discussed for the RR1000 material are applicable to the 131072 billets. The backscatter electron imaging reveals the same deformed layer near surface in the both the sub-solvus and super-solvus condition. The bulk grain structure in Figure 6.32 and 6.33 reveals that the super-solvus sintering condition results in grain growth, the precipitates morphologies are also consistent for both processing temperatures as was found for the RR1000 produced material previously discussed.

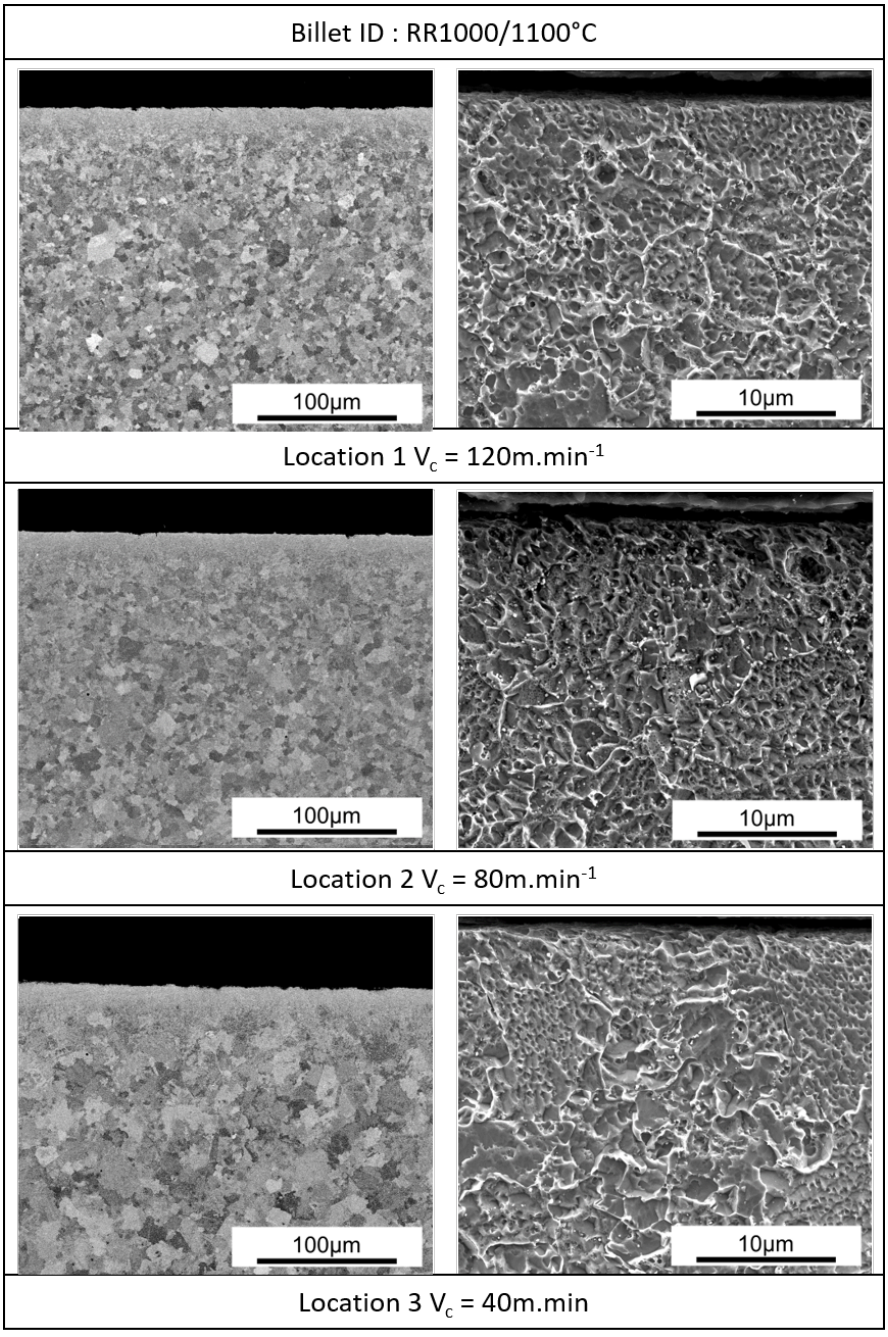

Figure 6.30: Sub-surface damage at various billet locations for the changing machining parameters, for the FAST billet produced using RR1000 feedstock powder using a sub-solvus dwell at 1100°C. Sub-surfaces images were taken using backscatter electron imaging (left) and secondary electron imaging after a Kalling's waterless reagent etch (right).

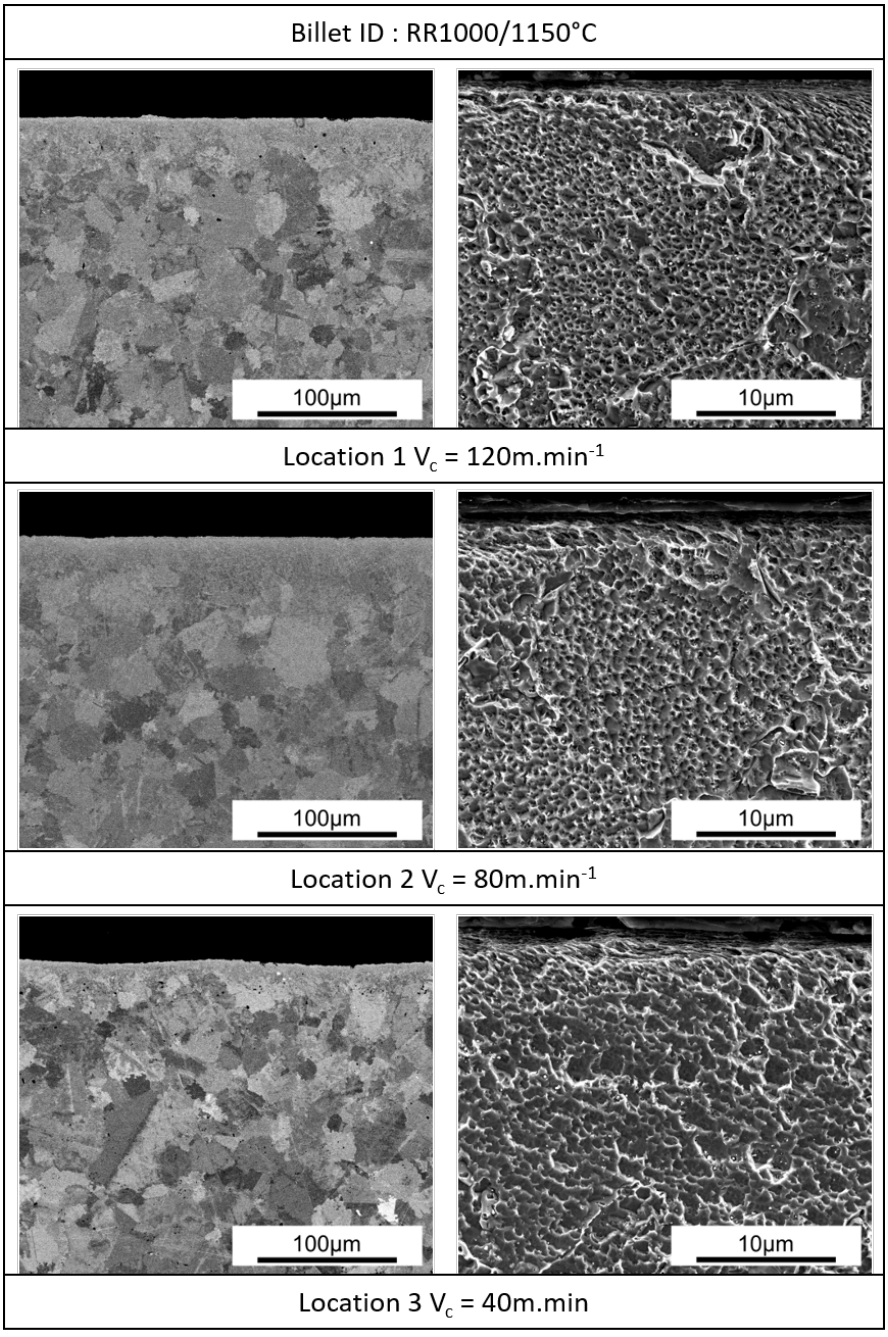

Figure 6.31: Sub-surface damage at various billet locations for the changing machining parameters for the FAST billet produced using RR1000 feedstock powder at a sub-solvus dwell at 1150°C. The sub-surface regions were imaged using backscatter imaging (left) and secondary electron imaging after a Kalling's waterless reagent etch (right).

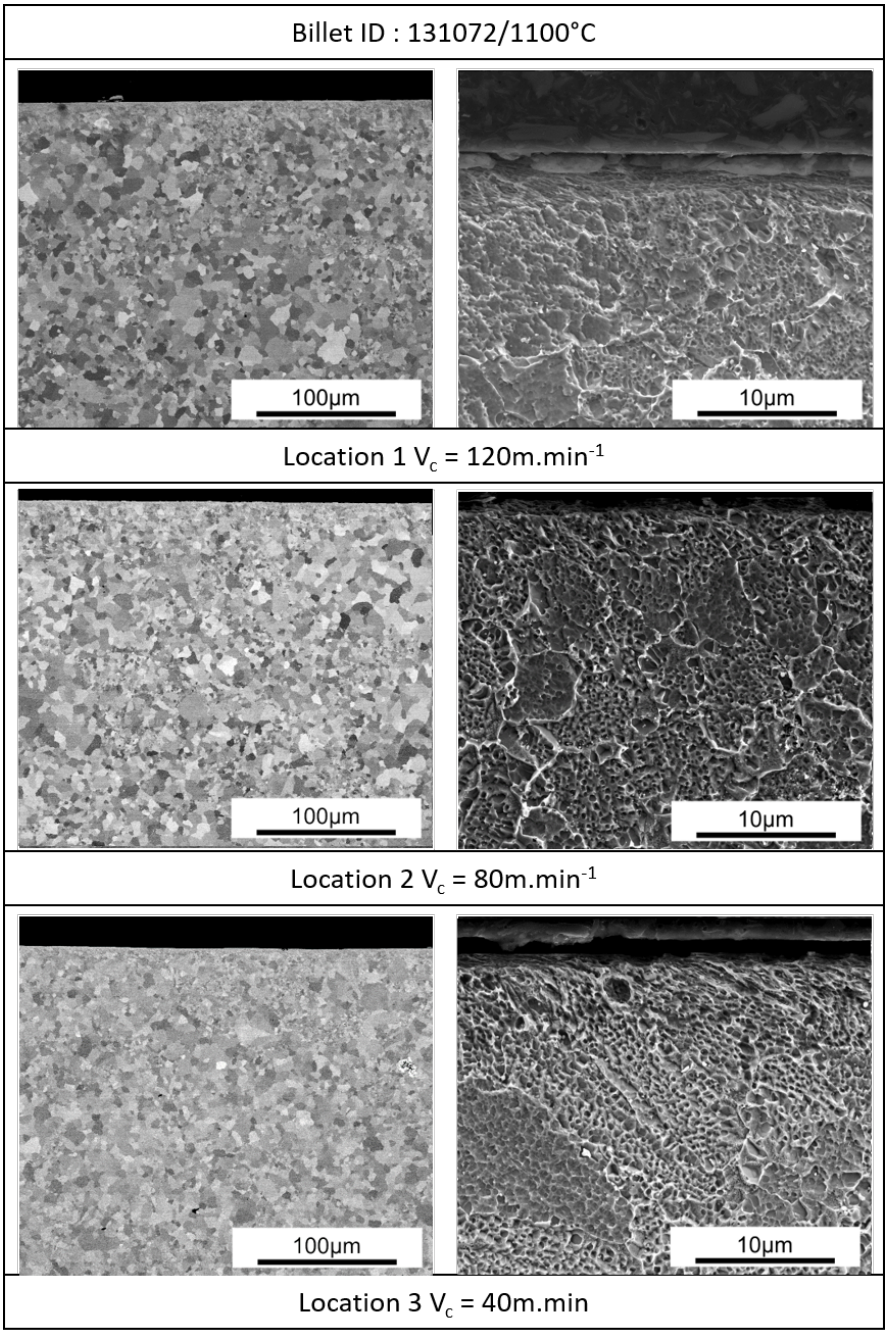

Figure 6.32: Sub-surface damage at various billet locations for the changing machining parameters for the FAST billet produced using 131072 feedstock powder using a sub-solvus dwell at 1100°C. Sub-surfaces were imaged using backscatter electron imaging (left) and secondary electron imaging after a Kalling's waterless reagent etch (right).

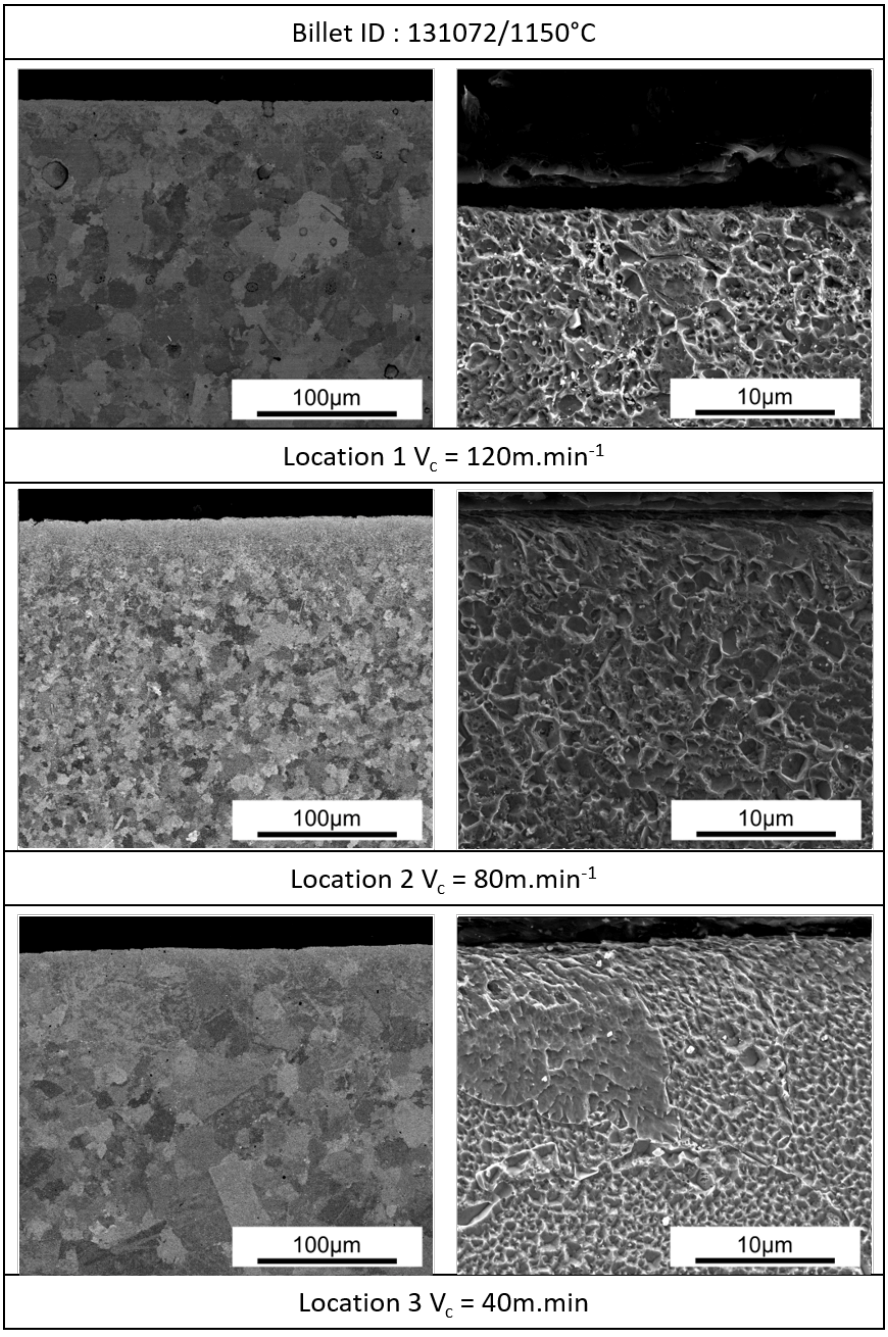

Figure 6.33: Sub-surface damage at various billet locations for the changing machining parameters for the FAST billet produced using 131072 feedstock powder using a sub-solvus dwell at 1100°C. Sub-surfaces were imaged using backscatter electron imaging (left) and secondary electron imaging after a Kalling's waterless reagent etch (right).

6.6 Observations Regarding Sub-surface Damage Mechanisms in the As-FAST Machined Billets

Figure 6.34 shows the sub-surface deformation associated with machining location 1 from the sub-solvus 131072 billet, machined with a surface speed of 40 m.min^{-1}. The figure shows that closest to the machined edge, there is a highly deformed region which contains no observable grain structure when viewed under backscattered electron imaging. It can be observed that the highly deformed layer exists all the way along the surface in regions with both finer and coarser grains, indicating its independence of local grain morphology. Beneath this layer are regions in which the grains can be seen to exhibit misorientation contrast. In Chapter 5 it was discussed that the misorientation contrast is due to local deformation of the crystalline lattice leading to high dislocation densities. It is observable in Figure 6.34 that this layer persists up to approximately 50 μm into the machined sub-surface. The misorientation contrast described appears more prominent in the regions with larger grain structures, this is likely an imaging effect whereby the contrast changes are more defined in the larger grains. This is confirmed in Figure 6.35, which shows the local deformation structure in these fine grain regions of Figure 6.34 which demonstrates that the misorientation contrast artefacts are present in these finer regions. Figure 6.35 also shows slip bands in the near surface layer, which is indicative of severe plastic deformation and work hardening where the amount of strain input into the material is greater.

Within Figure 6.35 a region of prior particle boundaries is visible which appear as bright particle under backscatter electron imaging (due to the heavier element content provided by the Hafnium and/or Tantalum). It can be observed at position 2 in Figure 6.35 that these particles are arranged in a circular structure strongly indicating that they are part of a prior particle boundary network. There appears to be no deformation in these precipitates as the circular structure appears to be undisturbed. This is irrespective of the deformation occurring in neighbouring grains.

Examining the near surface precipitates in the surface of location 3 of the sub-solvus FAST processed 131072 billet (machined at a speed of 120 m.min^{-1}), in Figure 6.36, severe deformation is observed. This deformation is consistent with the heavily deformed region shown in the backscattered electron image in Figure 6.34. The precipitates are clearly deformed in the direction of the machining tool running along the surface. Figure 6.37 displays a higher magnification view of the precipitates away from the machined edge at position 2 in Figure 6.36. It can be seen that although these precipi-

tates show no signs of deformation in Figure 6.36, at the higher magnification in Figure 6.37 evidence of slip bands are present. Evidence of the shearing of precipitates is visible at positions 1 and 2 in Figure 6.37.

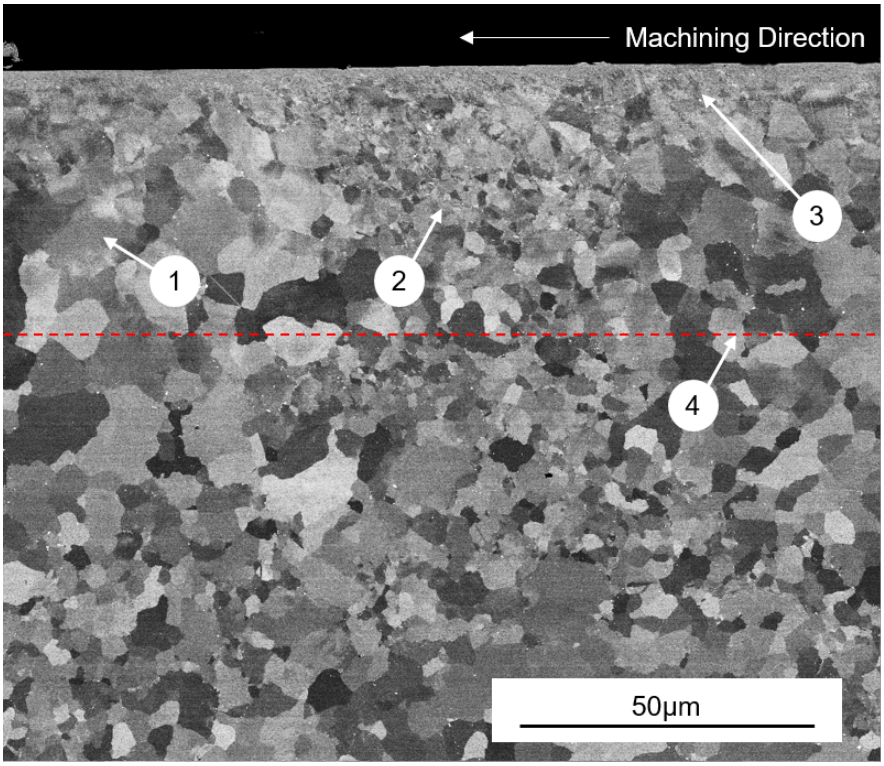

Figure 6.34: Backscattered electron micrograph showing the machined surface examined at location 1 for the billet produced using the 131072 powder using a sub-solvus (1100°C) dwell conditions. Surface shows evidence of (1) misorientation contrast indicating lattice deformation; (2) the presence of near surface fine grains with less evidence of misorientation contrast; (3) the presence of a high deformed layer near the surface and; (4) Evidence of deformation to a depth of 48 μm

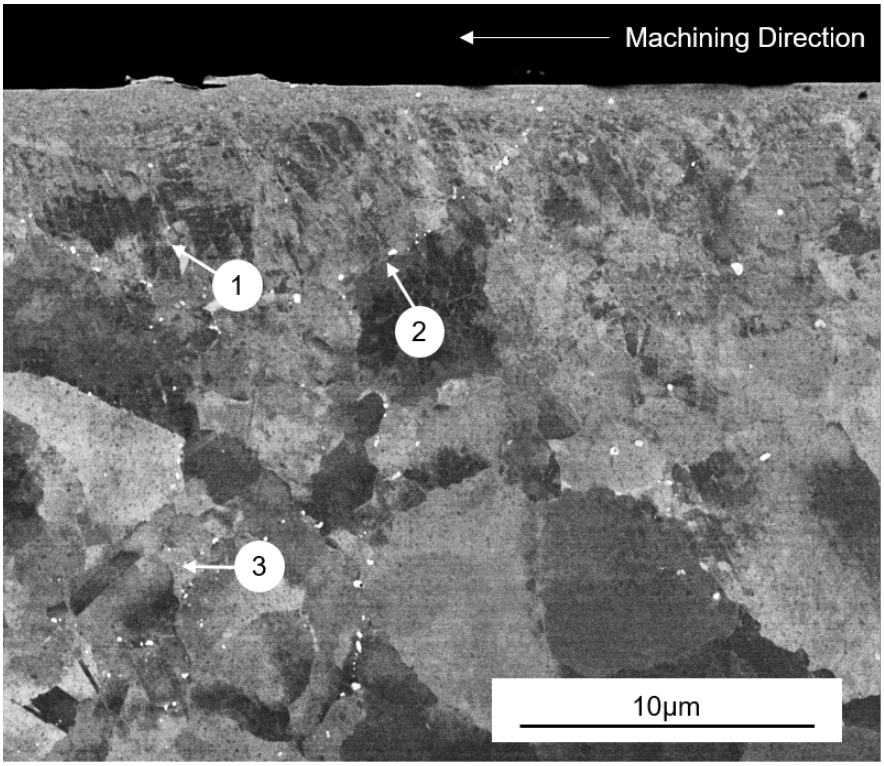

Figure 6.35: Backscatter electron micrograph of the machined surface examined at location 1 for the FAST billet produced using the 131072 powder using a sub-solvus (1100°C) dwell conditions. Surface displays (1) evidence of strain in the proximity of the machined surface, (2) Prior particle boundary networks and (3) Evidence of deformation via misorientation contrast some distance away from the machined surface.

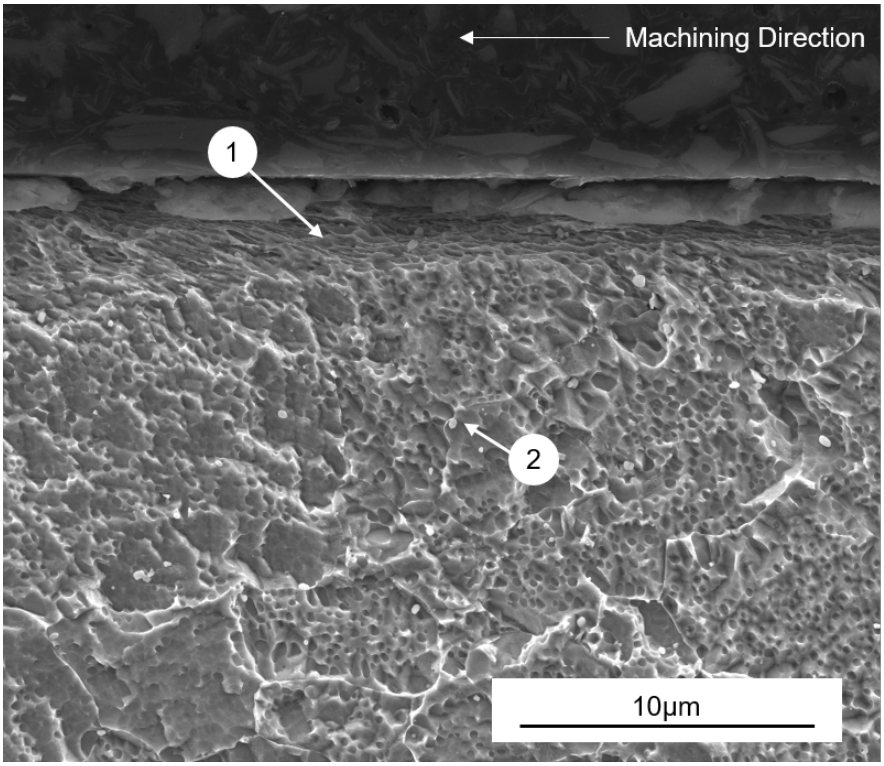

Figure 6.36: Secondary electron image of the machined surface examined at location 1 for the FAST billet produced using the 131072 powder using a sub-solvus (1100°C) dwell conditions viewed after Kalling's reagent etching. Surface displays (1) heavy deformation in near surface γ' precipitates and (2) apparently un-deformed precipitates in the sub-surface.

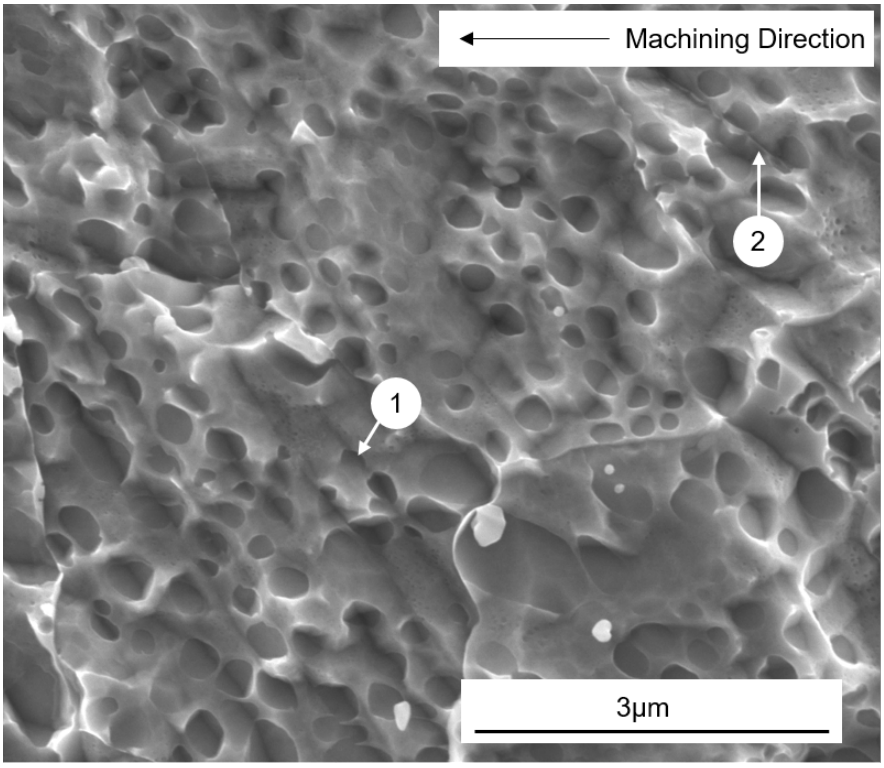

Figure 6.37: Secondary Electron micrograph of the near surface γ' precipitates located at position 2 in Figure 6.36. The micrograph shows the presence of sheared precipitates at positions (1) and (2).

Examining the sub-surface in the same billet feedstock (131072 feedstock using sub-solvus conditions) at location 3, which was machined at 40 m.min^{-1} the same deformation indicators are present as shown in Figure 6.38. Near surface is a region of heavily distorted grain structure with areas showing deformed grains underneath, as indicated by the misorientation contrast. Undisturbed areas of prior particle boundaries can also be observed. These features indicate that the sub-surface damage mechanisms are independent of the machining speed used however, differences in the depths can be observed comparing Figures 6.35 and 6.38 with the 120 m.min^{-1} giving rise to deeper levels of damage. This is expected as the 120 m.min^{-1} results in a greater aggressiveness in the material removal process.

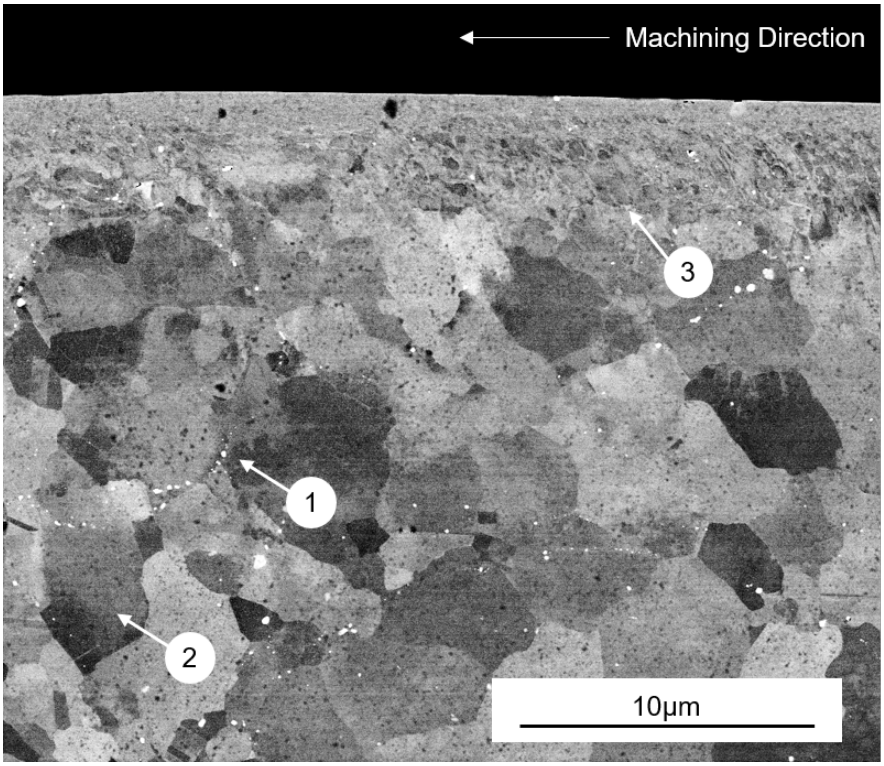

Figure 6.38: Backscatter electron image of the machined surface examined at location 3 for FAST the billet produced using the 131072 powder using a sub-solvus dwell conditions (1100°C). The micrograph shows misorientation contrast at positions (1) and (2) and a heavily deformed surface region (3).

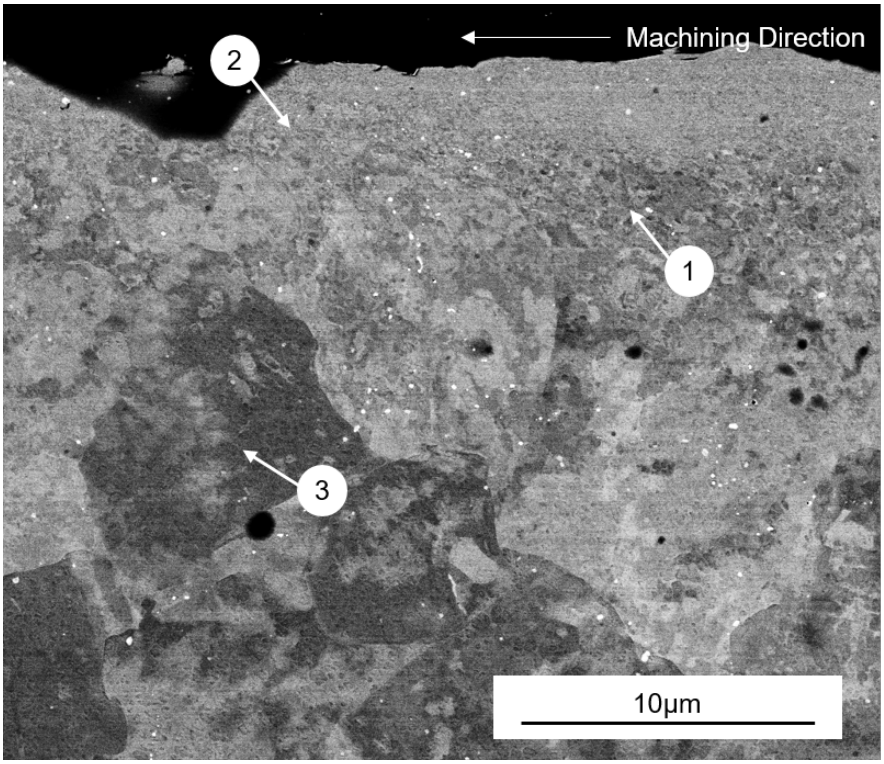

Figure 6.39: Backscatter electron micrograph of the machined surface examined at location 1 for the billet produced using the 131072 powder using a super-solvus (1150°C) dwell conditions. The micrograph shows (1) the typical highly deformed layer, (2) an surface layer with an amorphous appearance and (3) localised misorientation contrast within a near surface γ grain

The deformation in the sub-surface of the 131072 FAST billet processed using a super-solvus dwell temperature is shown in Figure 6.39. The surface shown in the micrograph was taken from location 1 which was machined at a surface speed of 120 $m.min^{-1}$. The micrograph shows a heavily deformed layer near surface at position 1, above which is a layer that appears unresolvable, which is often referred to as amorphous by other researchers (position 2). At a greater distance away from the surface, there is evidence of misorientation contrast within near surface grains. Comparing the appearance of this sub-surface and that of the equivalent surface for the 131072 powder sub-solvus billet in Figure 6.35 it can be seen that no obvious amorphous structure is present. Examining the specimen in the etched condition (shown in Figure 6.40) reveals that no amorphous layer can be seen. It is suggested that the observed layer is a heavily deformed region in which the underlying grain structure is unresolvable when viewed under backscattered electron imaging.

In Figure 6.40, heavy deformation of the near surface precipitates which are in the same region in the apparent amorphous layer in Figure 6.39 is shown. At a distance of approximately 10 μm from the surface however, the deformation of precipitates is minimal. This is consistent with the observation for the equivalent sub-solvus billet in the same location and machined using the same parameters in Figure 6.37.

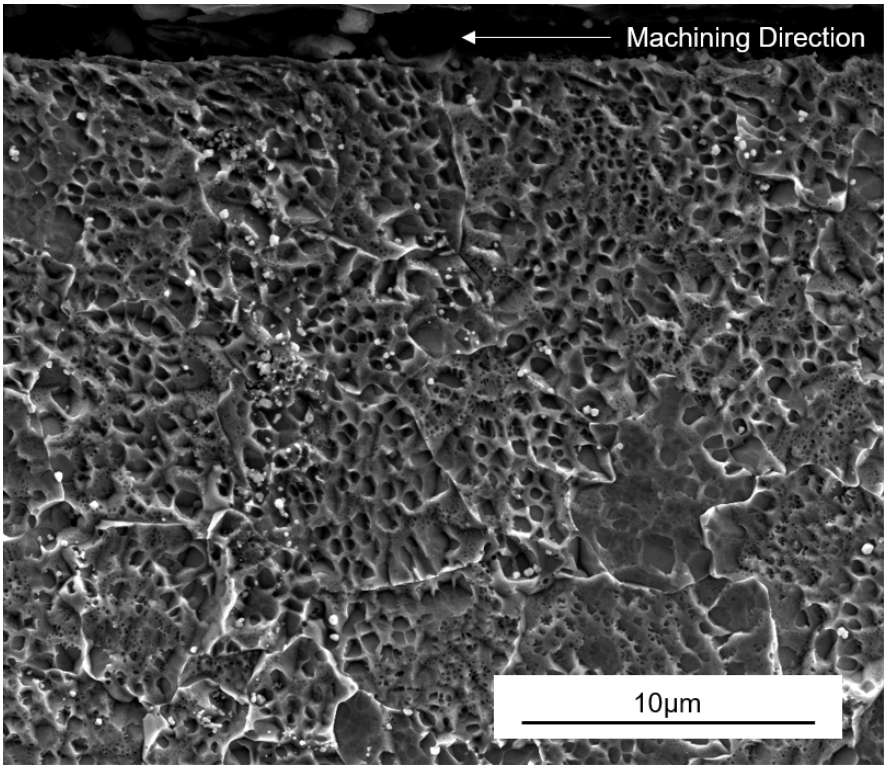

Figure 6.40: Secondary electron imaging of the machined surface examined at location 1 for the FAST billet produced using the 131072 powder using a super-solvus (1150°C) dwell conditions showing no apparent amorphous or highly deformed layer at the machined surface.

To summarise the findings of the sub-surface damage investigation, the following observations can be made:

- Irrespective of the FAST billet processing temperature and location, there is generally a highly deformed layer closest to the machined surface. This layer is so deformed that it can appear amorphous in nature when viewed under backscatter electron imaging.
- In the near surface heavily deformed layer, there is evidence of strain

which is a clear indication of heavy deformation and dislocation motion within the material.

- In both the heavily deformed layer and underlying material, evidence of misorientation contrast is present for all surfaces examined using backscatter electron imaging. misorientation contrast indicates the presence of crystallographic deformation and lattice rotation.

- Near surface γ' precipitates, when viewed in the etched condition, reveal severe deformation. The depths of apparent damage to the underlying precipitates are shallower in comparison to the depth of visible misorientation contrast when the sample is in the polished condition.

- Overall, a true understanding of the level of sub-surface damage can only be obtained by viewing the machined surface using backscattered electron imaging to determine the maximal depth at which misorientation contrast is observable after backscatter electron imaging, which appears to be greater than all other sub-surface damage indicators.

6.7 Summary and Conclusions

Utilising the field assisted sintering process, four billets were manufactured using powder from two different powder sources (131072 and RR1000). Two different processing temperatures were applied in order to give sintering behaviour both below (sub-solvus) and above (super-solvus) the γ' solvus temperature. These billets were then subjected to face turning trials using state of the art coated carbide tool inserts and high pressure cooling. The purpose of the trials was to determine how the cutting forces change as a function of depth of cut, cutting speed, location within the processed billet and the underlying processing conditions used to produce the billet.

It was demonstrated that the super-solvus processing temperatures gave rise to a grain size increase with respect to the sub-solvus processing, in all locations as shown in Figures 6.27 and 6.28. The exception was found at location 2 for the super-solvus 131072 billet, however this was thought to be due to a sampling effect. Micro-hardness measurements captured for the billets at location 1, shown in Figure 6.29, revealed that a small drop in hardness could be observed for the super-solvus processed billets. However significant scatter was present. Precipitate morphologies appeared similar for the sub-solvus and super-solvus conditions for both powder feedstocks however it can be observed that the γ' precipitates in the super-solvus billets were finer in nature, likely due to the re-precipitation during cooling. A finer

precipitate distribution with a higher overall volume fraction may suggest why there is only a small discrepancy in hardness between the two processing conditions for both powder types used.

Finish turning trials performed for depths of cut of 0.25 mm to 1 mm revealed that, for both powder feedstocks, a small but significant reduction in cutting forces in all 3 principle directions can be observed when the billet is processed using super-solvus conditions. The difference in forces noticeable for the 0.25 mm depth of cut trials in Figure 6.16, was most significant for the 0.75 mm depth of cut trials as displayed in Figure 6.17 and is less observable for the 1 mm depth of cut facing trials shown in Figure 6.18. It is suggested that the differences in grain size between the two materials is responsible for the difference in the cutting forces measured. Trials performed with a depth of cut of 0.75mm will remove a larger volume of material than in the 0.25 mm depth of cut trials and therefore a larger number of grains will be removed from the surface within a given time frame. This was thought to be the reason why the differences in cutting forces between the 1100°C (sub-solvus) and 1150°C (super-solvus) conditions are greater for the 0.75 mm depth of cut passes compared to the 0.25 mm depth of cut passes. For the 1 mm depth of cut trials it is suggested that the tool wear effects dominate the measurement of the cutting forces, preventing differences in material from being inferred. This is evident from the tooling condition after the short 1 mm depth of cut passes in Figures 6.25 and 6.26. For the 0.25 mm depth of cut passes and 0.75 mm depth of cut passes, the tool wear is similar with a very small flank wear scar present.

Examination of the cutting forces across 3 locations for each billet for a fixed machining speed of $40.min^{-1}$ and depths of cut of 0.25 mm and 0.75 mm revealed that both the cutting forces are relatively consistent across all 3 locations for all of the 4 billets machined. The reduction in cutting forces previously noted when comparing the sub-solvus and super-solvus condition can be seen for locations 1,2 and 3 for both depths of cut employed as shown in Figure 6.21 and Figure 6.22. This is further evidence that the super-solvus FAST processing condition produced a larger grain structure which reduced the cutting forces.

Considering the effect of cutting speed, it was observed again that the billet processing temperature produced the larger variation in cutting forces, irrespective of the machining speed employed in Figure 6.20. It was observed that an increasing surface machining speed led to a drop in cutting forces with one exception for the super-solvus processed RR1000 billet. However, the scatter in results suggests that this may be an anomalous result.

Overall it was observed that the tool wear were insignificant for the 0.25 mm and 0.75 mm depth of cut passes and the flank wear scars were so small

it proved difficult to quantify. This was applicable across all billets. No significant differences in tool wear was observed across all billets with regards to the billet powder feedstock, processing temperature or the machining speed utilised. It is suggested that the short passes performed during this testing were unlikely to isolate any changes in tool wear with changes in the billet material machined. It is recommended that large scale tool wear trials are required to fully understand how the billet material influences tool wear, which was outside the scope of this study. The tool wear observations made gave confidence that the cutting force effects seen in this study are representative of the effect of material condition rather than tooling related effects.

Examining the sub-surface deformation imparted by the machining passes performed with varying speeds reveals that the level of imparted damage is of a similar depth for all billet materials. This is true when the sub-surface is imaged using both backscatter diffraction techniques and viewing the surface in the etched condition to reveal the γ' precipitates. The level of sub-surface damage does not typically extend beyond 20 μm beneath the machined surface for all billets in all machined locations as revealed in Figures 6.30-6.33.

Higher magnification imaging of the machined surfaces revealed several deformation mechanisms whose severity depends on the technique employed to view the damage. Examination of the sub-surface of the 131072 material machined with a surface speed of 120 m.min^{-1} revealed the presence of a heavily deformed layer at the surface in which the grain structure was difficult to resolve under backscatter electron imaging in Figure 6.34. In general it could be observed that irrespective of the machining speed used, indications of intense slip were present at the sub-surface while misorientation contrast was present in grains further from the machined edge. It was noted that the presence of prior particle boundaries could be observed close to machine edge and these show no apparent signs of deformation even though surrounding grains contain potential slip bands and misorientation contrast. This however may indicate that the techniques used to image such precipitates are inadequate and higher resolution SEM or TEM may be required. For the equivalent position and surface speed in a super-solvus processed 131072 billet, similar deformation indicators were observed. At the surface of the super-solvus 131072 at location 1 (Figure 6.39) it was observed that a surface layer with an amorphous layer was present, below which was a fine grain layer. It is therefore suggested that in the super-solvus material, grain refinement has the potential to occur at the surface, the thickness of this region was larger in the larger grain super-solvus material. Further work is recommended to understand whether larger grains increase the propensity for surface grain refinement to occur.

Overall the study has indicated that a change in input material processing conditions leads to a change in the response during machining for the powders considered. These observations were made by machining billet material produced in a single processing step using the FAST technique after small scale development outlined in Chapter 4. The main outcome of this study is therefore that the FAST process provides a very cost effective technique of producing material for which the microstructure can be varied through the alteration of the processing temperature during FAST production. The material produced through this route has the potential to provide short lead time, low cost testing to fully understand the subsequent processing steps and the microstructural response to machining. It is therefore suggested that FAST is a potentially invaluable tool to help alloy development particular in materials with such a high production cost.

Chapter 7

Forged Billet Machining

7.1 Introduction

During the production of nickel superalloys, once the thermomechanical processing operations have been completed, machining into final component form then commences. This includes machining to rectilinear shape for inspection operations to be performed. Once this machining has been completed, final part shaping is conducted using a large variety of subtractive manufacturing techniques. The prior processing that takes place before this step is stringently designed to produce fixed microstructures which offer the optimum performance in the gas turbine engine. After the investigation performed in Chapter 5, it has been shown that large variations in microstructure can occur for relatively small variations in processing temperatures due to the presence or lack of the γ' precipitates, as well as recrystallisation effects. Currently in the literature, the effects of these microstructural variations on the machining process are relatively unexplored.

In the Chapter 5, it was demonstrated that the forging process can produce differential microstructures within a single billet due to the natural strain variation that occurs during uni-axial upset forging. In this chapter the same billets produced using the industrial two step forging process (detailed in Chapter 5) will be used to perform machining trials to determine how the varying microstructures respond to deformation induced by the machining process.

7.2 Methodology

7.2.1 Input Billet Condition

The forged billets produced in Chapter 5 featured non-uniform deformation and large edge bevels and therefore a combination of traditional and wire EDM machining were used to remove material to produce a uniform external diameter. This approach meant the billets could be safely clamped within a lathe to perform turning trials. Three of the large scale forgings were chosen for trials, these billets captured a change in forging temperature during the second forging and also a change in the final strain imparted on the billet. These billets are identified as 3_2, 3_1 and 4_1 in Table 5.12. Photographs of the billets prior to machining are shown in Figure 7.1, Figure 7.2 and Figure 7.3. As microstructural characterisation prior to machining trials was not possible without cut-ups being performed, the microstructure within the remaining material would therefore be unknown at the time of machining trials. It was postulated that the force feedback data captured could possibly identify differences in microstructure during machining similar to the changes in cutting forces observed during the machining of the FAST billets.

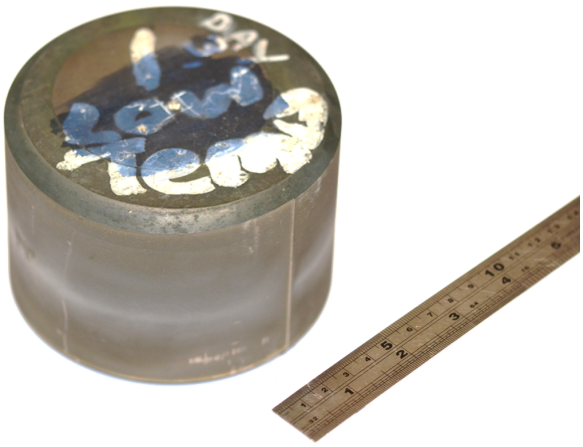

Figure 7.1: Billet 3_1 described in table 5.12, produced using a two step deformation route. The first deformation was performed to a true strain of 0.34 at 1100°C. The second deformation was conducted to a strain of 1.0 at 1075°C. The billet shown had been machined to a cylinder with a constant outer diameter.

Figure 7.2: Billet 3_2 described in table 5.12, produced using a two step deformation. The first deformation was performed to a true strain of 0.34 at 1100°C. The second deformation was conducted to a strain of 1.0 at 1100°C. The billet shown had been machined to a cylinder with a constant outer diameter.

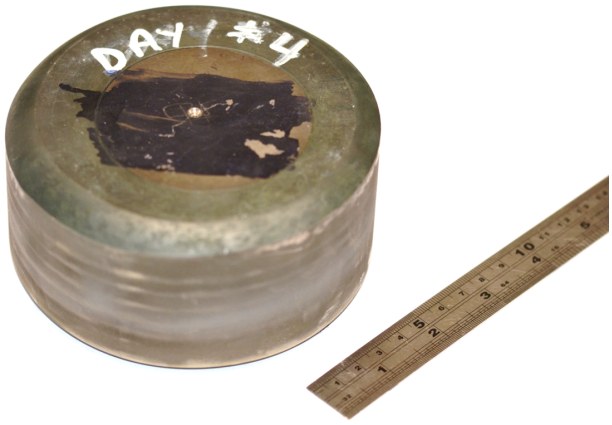

Figure 7.3: Billet 4_1 described in table 5.12, produced using a two step deformation. The first deformation was performed to a true strain of 0.34 at 1100°C. The second deformation was conducted to a strain of 1.2 at 1100°C. The billet shown had been machined to a cylinder with a constant outer diameter.

7.3 Machining Trial Approach

7.3.1 Tool Holder

The same tool holder as used in the machining of the as-FAST billets was employed, details regarding the tool holder can be found in section 6.3.3 in Chapter 6. The tool holder was used for the reasons described previously and was combined with the Kistler force dynamometer arrangement previously described in section 6.3.2.

7.3.2 Cutting Inserts

Two types of cutting inserts were chosen for machining trials based on their suitability to semi-finishing and finish machining. The cutting inserts chosen for the semi-finishing/rough machining were the Sandvik 1105 grade inserts, these inserts consist of a medium grain size tungsten carbide grade with a CVD (chemical vapour deposition) applied (Ti,Al)N coating. For the finishing passes performed, the Sandvik S05F was used which is the industry standard for the machining of nickel superalloys. This grade consists of the same substrate as the 1105 grade but instead features a triple coating of Ti(C,N) + Al_2O_3. Both insert types are suitable for the turning of heat resistant nickel superalloys. Both inserts use the CMGG-120408 geometry, the geometric features of which are shown in Table 7.1.

Table 7.1: Dimensional properties of the CNGG 120408 inserts used during machining trials.

Insert geometry type	C (80°Rhombic)
Inscribed circle diameter	12 mm
Insert thickness	4.763 mm
Corner radius	0.794 mm
Chip breaker type	Cylindrical
Chip breaker angle	15°

Prior to any machining, the edge radii of 60 of each insert type were measured using an Alicona SL40 oscillating microscope, using the method described in section 6.3.5. As can be observed in Figure 7.4 and 7.5, the two insert choices exhibit very different edge profiles, the 1105 grade exhibiting a blunter edge than that of the S05F grade. This is particularly visible

in a 3D replication of the Alicona scan data displayed in Figure 7.6. Although it may lead to more inefficient material removal and greater force input required, the blunter edge of the 1105 grade insert provides greater resistance to chipping when larger depths of cut are used, hence why the tool can be used during semi-finish or rough cutting. Both types of insert exhibit a broadly normal distribution of edge rounding values with large number of measurements falling around the mean value with larger and smaller edge radii occurring with lesser frequency. The standard deviation of the edge rounding was calculated for each insert type and is presented in Table 7.2, inserts with edge rounding values above and below a single standard deviation from the mean were excluded from the machining trial in order to eliminate any extraordinary edges which could interfere with the results of the study. The Alicona scans are also useful for highlighting any pre-existing tool defects which would not normally be identified prior to machining in an industrial environment. An example of such damage is shown in the Alicona scan displayed in Figure 7.7. Inserts displaying such damage were excluded from the machining trials. After machining, all inserts were imaged using a Zeiss Axiozoom light microscope. Micrographs of the rake and flank faces were captured in order to compare the tool appearance after machining.

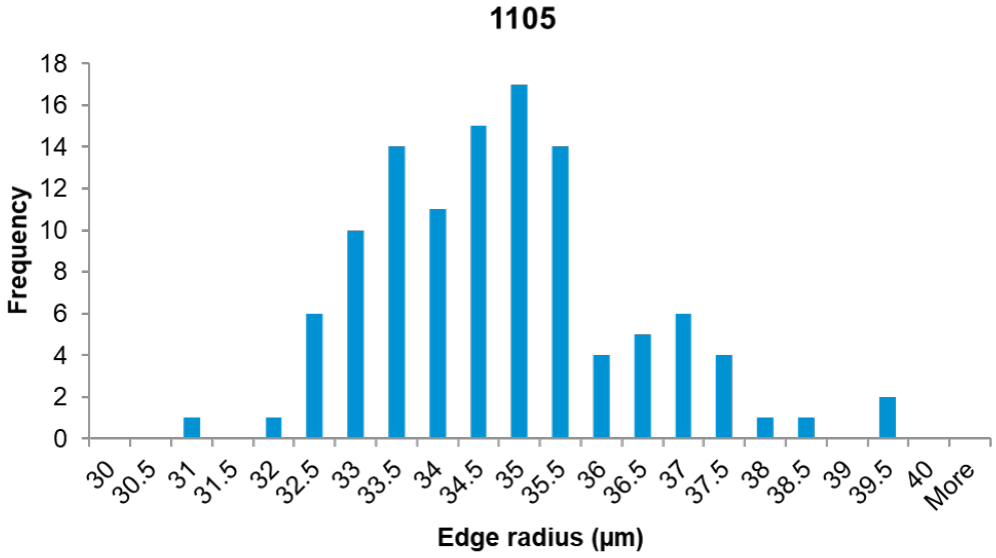

Figure 7.4: Histogram plots showing the edge rounding data for the 1105 inserts used in machining trials

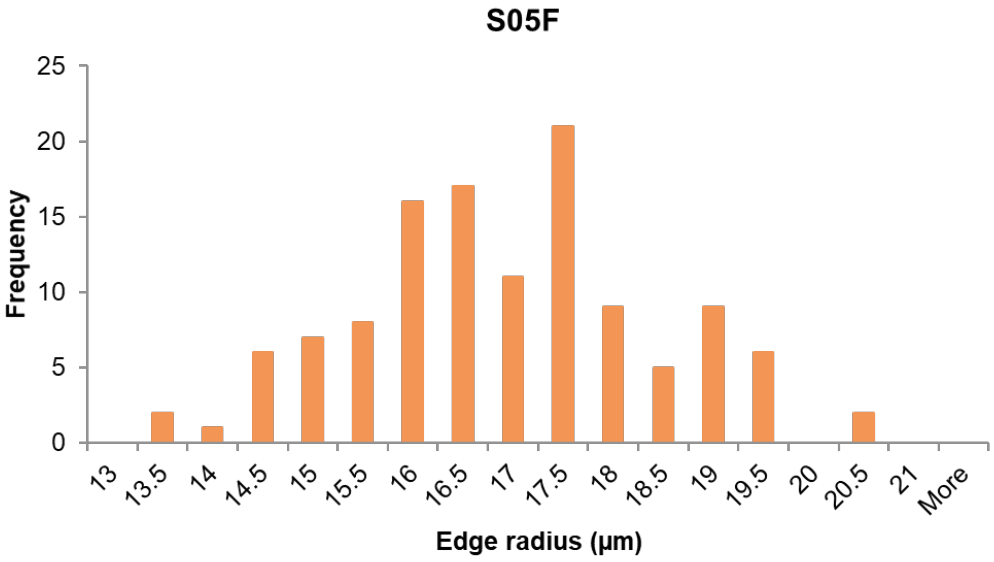

Figure 7.5: Histogram plot showing the edge rounding data for the S05F inserts used in machining trials

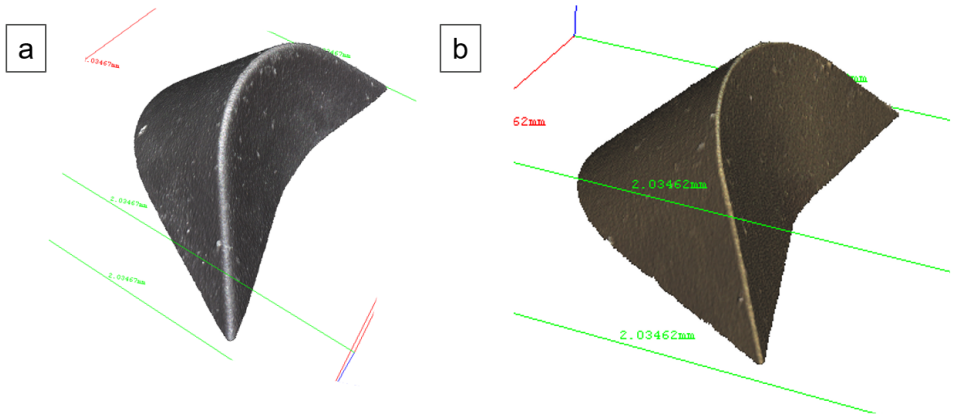

Figure 7.6: 3D recreation of the Alicona scan performed to measure the edge rounding of each insert type showing (a) the 1105 insert edge and (b) the S05F insert edge. Note the difference in sharpness of the cutting edge.

Table 7.2: Edge rounding data collect for the 1105 and S05F inserts.

Insert grade	1105	S05F
Average edge radius (μm)	34.52	16.65
Standard deviation (μm)	1.53	1.43
Minimum measured edge radius (μm)	30.92	13.37
Maximum measured edge radius (μm)	39.22	20.38
Maximum usable edge radius (μm)	36.05	18.09
Minimum usable edge radius (μm)	32.99	15.22

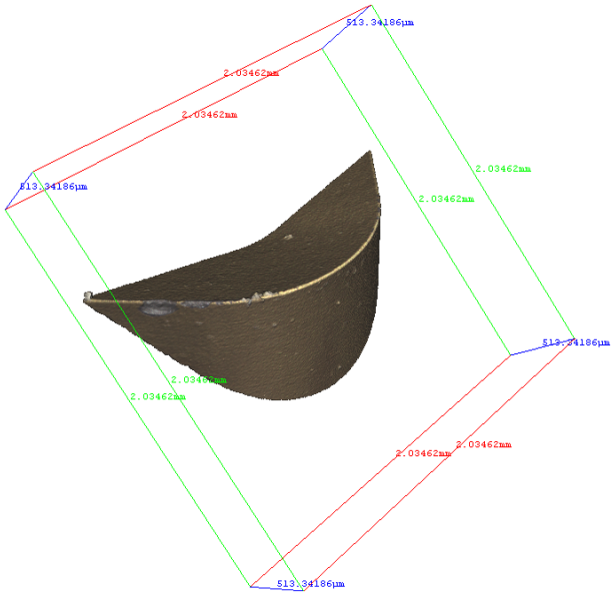

Figure 7.7: Example of a coating defect noted when performing edge radius measurements of an S05F insert, such defects can lead to premature insert failure.

7.3.3 Coolant Properties

The forged billet trials were performed concurrently with the machining of the FAST billets detailed in Chapter 6. Details regarding the properties of the coolant employed can be found in Section 6.3.4.

7.3.4 CNC Lathe Used and Cutting Force Measurements

Details regarding the lathe used and force dynamometer operation and measurement can be found in 6.3.2. The procedure for the post processing of force feedback data files can be found in section 6.3.6.

7.4 Machining strategy

Outer Diameter (OD) Billet turning

In order to expose specific regions of the forged billet for machining, to examine the influence of microstructure on the imparted damage, preparatory machining was required. This also presented an opportunity to examine the cutting forces as a function of position within the as forged billet for semi-finishing machining conditions, as well as conduct trials to understand the wear rates of the S05F tooling employed. The results of the S05F tool wear trials are not reported in this thesis. A three step geometry was produced using outer diameter (OD) turning, providing four faces which were subsequently face turned using finish parameters for the subsurface damage investigation. A schematic showing the steps involved in this approach is displayed in Figure 7.8.

To determine the effect of local microstructure on the force feedback, part of the OD turning step production segments were used for semi finishing passes using a relatively high depth of cut of 1 mm with a new tool insert used for each machining pass. The use of a new insert would allow a direct comparison of the force feedback data with minimal influence from increasing tool wear. This would allow force feedback to be captured as a function of the position within the billet and therefore the local microstructure and material properties. Two tool wear trials were also conducted per step, examining how tool wear changed with respect to relative position within the billet and again microstructure, however these trials are not reported in this thesis. The tool wear trials were conducted either side of the semi-finishing passes as described in Figure 7.9.

A clean-up pass would be performed with a new tool after every trial pass cutting to the same diameter however with a new tool insert, the rationale for this is described diagrammatically in Figure 7.10. When performing a trial pass, increasing tool wear can lead to a gradual or abrupt change in the true depth of cut. This would lead to a deviation from the intended depth of cut during the next pass, which would lead to the measurement of abnormal cutting forces. To prevent this from occurring, a clean-up pass was performed

to ensure that the surface is of a consistent diameter before the subsequent trial pass. The clean-up pass would also remove any redeposited material which may lead to notching of the tool. The length of the clean-up pass was extended by 1 mm with respect to the trial pass, this would prevent the tool in the trial pass from contacting with the shoulder on the work-piece, which would accelerate tool life. This would therefore lead to an improvement in the repeatability of the semi-finishing trials as well as ensure that the tool wear trials would not be dictated by any surface irregularities produced during the previous trial pass. The OD semi-finishing using the 1105 inserts were labelled as 2_Step number_Pass number. The OD tool wear trials using the S05F inserts were labelled similarly, the prefix 1 denoting the first tool wear repeat and the prefix 3 denoting the second repeat.

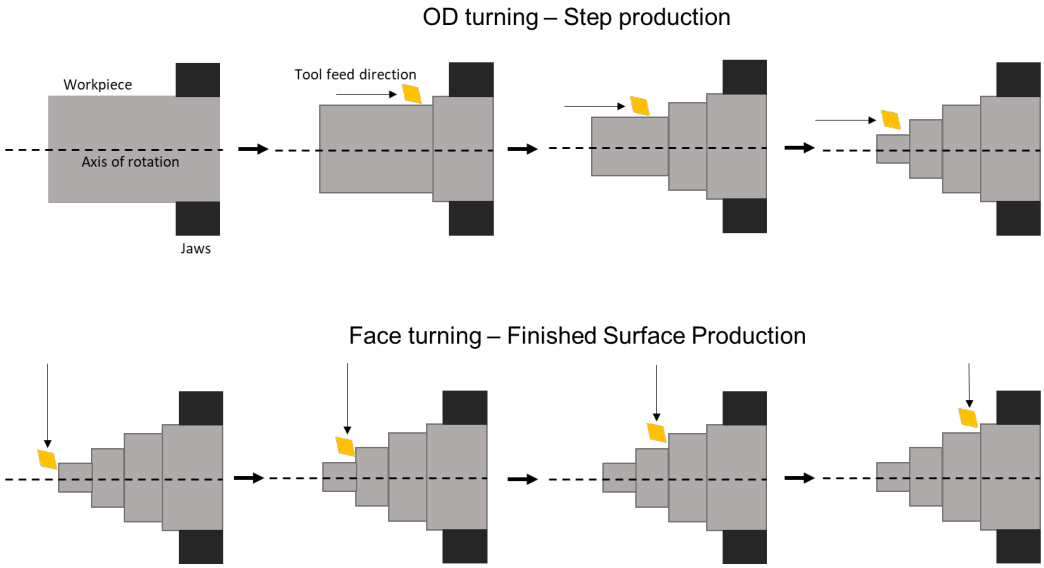

Figure 7.8: Diagram showing the process of producing the stepped geometry on each as forged billet using OD turning, followed by the finish face turning passes.

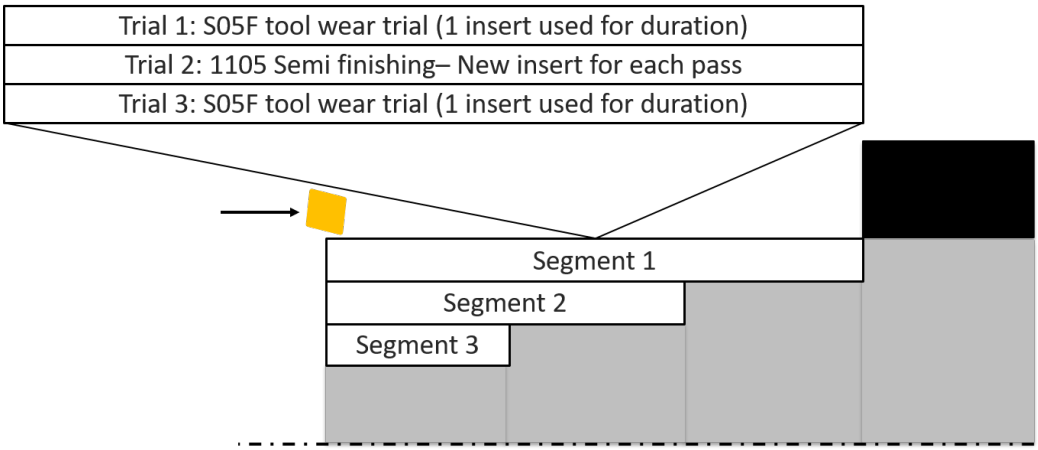

Figure 7.9: Diagram showing the three outer diameter turning segments machined to produce the three step geometry for each billet. Each segment is divided into three trials. Trial 1 is a tool wear trial using a single S05F insert, Trial 2 is a series of semi finishing passes with a new 1105 grade insert used for each pass and Trial 3 is a second tool wear trial using an S05F grade insert.

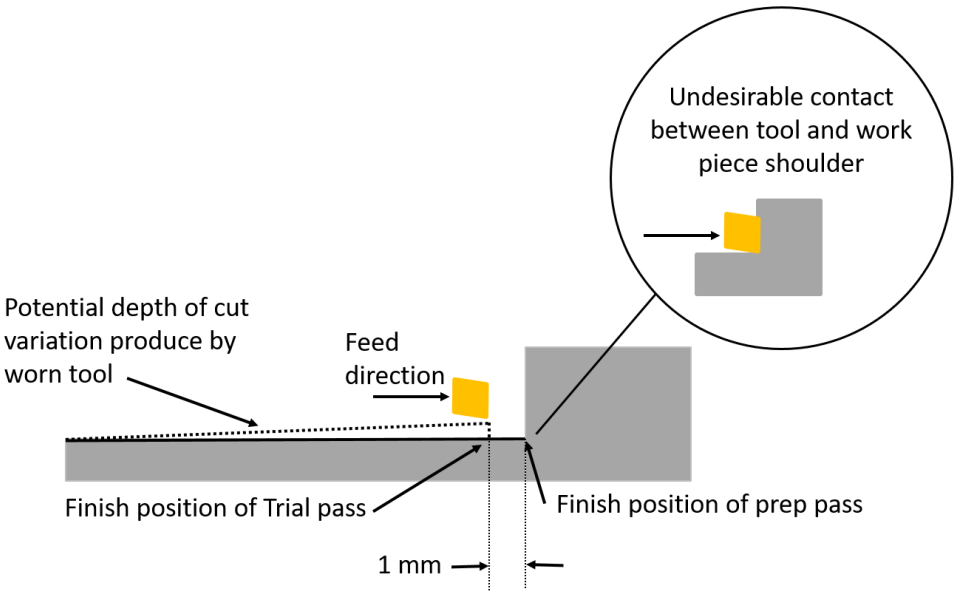

Figure 7.10: Diagram displaying the 1mm extended preparation/cleanup pass. Trials were stopped 1mm before interaction with the billet shoulder to prevent excesses wear of the tools.

Face Turning Trials

Upon the production of the stepped geometry described in Figure 7.8, facing trials were conducted on the four produced surfaces. This was achieved by first performing a cleanup pass which would remove any surface features present after the OD turning process and also allow the machining programme to be tested. The step geometries were chosen to produce equivalent spiral cut lengths (and therefore equivalent material removal volumes) and therefore cutting times using the fixed machining parameters. Once the clean up pass had been performed, a facing cut from the outer to inner diameter of each step was performed with a least 1 repeat for each step. The final surface left on the billet at each step would be used for subsurface microstructural examination. This process was repeated for each step, after which the billet was removed from the spindle jaws and the surfaces were protected prior to cut-ups being performed. A summary of the surfaces left on the billet are described in Figure 7.11. The names given to each of the surfaces will be used in the discussion of results. Note that face 1 of the turning trials does not extend to the axis of rotation, this is due to the RPM (revolutions per minute) limitation of the machine. As the tool moves towards the axis of rotation, the rotational speed of the machine automatically increases to maintain a constant surface speed, until the spindle speed reaches its maximum at which the surface speed will decrease. The minimum diameter of the workpiece at which the surface speed could be maintained was calculated and this was programmed giving the stopping point for the face 1 trial.

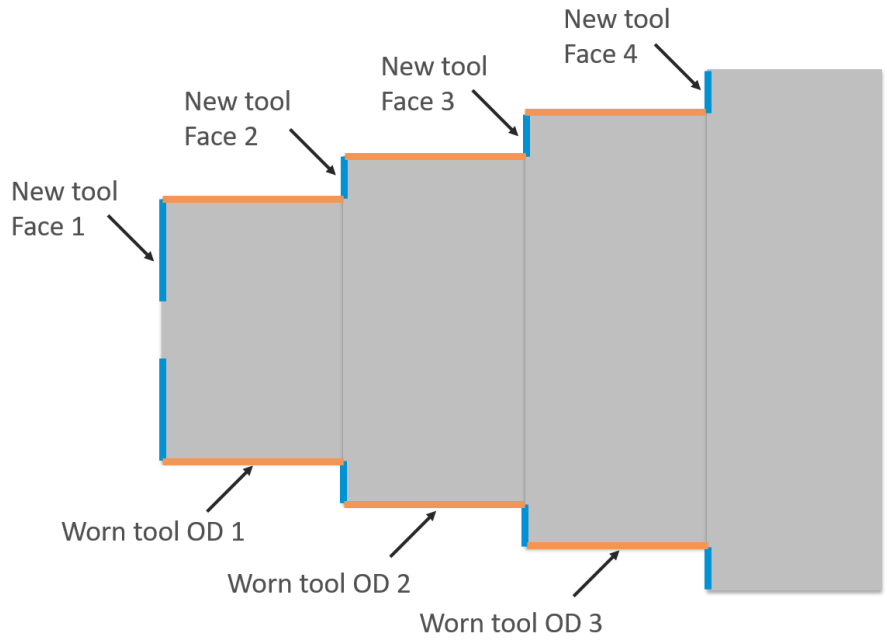

Figure 7.11: Schematic showing the naming convention for machined surface on the as-machined billets, the naming scheme presented is used in the discussion of the results.

The naming convention for trials was as follows. Each pass was denoted using the name of the billet followed by the index segment number_trial number_pass number as described in Figure 7.9. The facing trials were indexed with the following convention 4_Face number_repeat number, with the face number described as per Figure 7.11.

7.4.1 Chosen Machining Parameters

Table 7.3 gives the process parameters used for machining trials. As nickel superalloys are commonly used in gas turbine engines, the surface finish requirements are high, and hence low feed rates and low depths of cut are normally employed. The feed rates and low depths of cut employed for the finishing conditions displayed in Table 7.3 are representative of the processing conditions usually employed in nickel superalloy finishing, as recommended by Rolls-Royce and Sandvik. For the semi-finishing passes, a higher depth of cut of 1 mm was employed which is within the manufacturers recommendation for the chosen 1105 inserts, as well as being within the range expected

during semi-finishing operations during turbine disc manufacture. For all trials, a surface machining speed of 120 m.min^{-1} was employed. This surface speed is higher than what is normally employed for nickel superalloys for producing turbine discs with low levels of subsurface deformation. However, for the purpose of this study, the level of subsurface damage is of great interest. 120 m.min^{-1} was therefore chosen to induce higher levels of subsurface damage. One of the key reasons why slower speeds are employed in industry is to balance metal removal rate with acceptable tool wear, however in this study the cutting times are relatively low and therefore tool wear was not an issue. 120 m.min^{-1} was therefore considered to be the limit of what the S05F and 1105 grade tool are capable of without rapid failure leading to poor machined surfaces.

Table 7.3: Cutting force parameters employed during the semi-finishing and finishing of the as-forged billets using the 1105 and S05F grade inserts.

Cut type	Finishing face turning trials	Semi-finishing OD turning trials
Tool grade	S05F	1105
Depth of cut	0.25 mm	1.00 mm
Surface speed	120 m.min^{-1}	120 m.min^{-1}
Feed rate	0.12 mm.rev^{-1}	0.12 mm.rev^{-1}

7.4.2 Examination of Microstructure Post Machining Trials

Metallographic Preparation

After the completion of machining trials, the billets were removed from the machine and wire electron discharge machining (EDM) was used to remove slots from each billet which were 14 mm in width. One of the slots was sectioned and mounted to reveal the cross sections of faces 1-4 for subsurface microstructural damage investigation. The sectioned samples were mounted in Buehler Conductimet bakelite which is known for its edge retention properties and high conductivity, which enhances resolution upon SEM imaging. The mounted samples were prepared using standard metallographic preparation before imaging. The microstructures were viewed in both the as polished condition and after an etchant had been applied to reveal the nature of the γ' precipitates. Kalling's number 2 waterless etchant was used to reveal γ' microstructures, the samples were immersed in the etchant for 15-30 s.

SEM Microscopy

An FEI insepct F50 and Inspect F FEG-SEM were employed for SEM examination of samples. Both secondary and backscatter electron modes were employed. Secondary electron imaging was used when the samples were in the etched condition to reveal deformation of precipitates. Backscatter electron mode was used when examining the polished samples in order to reveal the γ grain deformation through BSE imaging of the misorientation contrast. When using secondary electron imaging, it was found that a working distance of 10 mm with an accelerating voltage of 10 keV produced the clearest micrographs, which the backscatter imaging produced more optimal results at a shorter working distance of 10 mm and an accelerating voltage of 5-10 keV.

7.5 Results - Semi-finishing passes

7.5.1 Billet 3_1

Measured Cutting Forces

The semi-finishing passes performed on the 3_1 billet are detailed in Table 7.4 and the measured cutting forces in the three measured directions are displayed in Figures 7.12 - 7.14. Reviewing the measured cutting forces averaged over one second, after full tool engagement, Figure 7.12 reveals that the forces measured in the three principle directions are similar irrespective of the changing diameter during subsequent passes despite the change in billet position as detailed in Table 7.4. This suggests that the properties of the billet are similar regardless of location machined within the billet. The forces measured over the first second of tool engagement represent the forces when tool wear will be relatively low and therefore have little influence over the cutting forces. The forces over 1 second of tool engagement therefore represents the condition where the cutting forces are mainly influenced by the machining set-up which is fixed but more importantly the material condition.

When the cutting forces are considered over the final one second of machining (Figure 7.13) it can be seen that the cutting forces deviate considerably in terms of the forces in the y axis direction particularly for passes 1_2_2 to 1_2_5 compared with the 2_2_2 to 3_2_6 passes. Although this could be construed as a change in the billet microstructure and properties, the passes showing increased y direction cutting forces are much longer than the passes performed during step 3. This indicates that tool wear plays a significant role and this is evident comparing Figure 7.15 with Figure 7.19 and Figure 7.20. It can be observed that the tool wear after the passes in the first

OD semi-finishing step was more severe than in the tools after semi-finishing passes during the second and third steps. This confirmed that tool wear was the most significant factor affecting the cutting forces and not underlying microstructure. This also justified the decision to compare the cutting forces by averaging for each pass over a short time after tool engagement, which in this case was chosen to be one second.

Table 7.4: Semi-finishing machining passes performed on billet 3_1, the dimensions are each pass are given, the naming convention used to identify passes is used is referenced in subsequent figures.

Billet	Trial ID	Z_s (mm)	Z_f (mm)	D_s (mm)	D_f (mm)	f_d (mm)	t_c (s)
3_1	1_2_2	0.00	41.00	103.79	101.79	41.00	54.63
3_1	1_2_3	0.00	41.00	101.79	99.79	41.00	53.56
3_1	1_2_4	0.00	41.00	99.79	97.79	41.00	52.48
3_1	1_2_5	0.00	41.00	97.79	95.79	41.00	51.41
3_1	2_2_2	0.00	27.00	87.50	85.50	27.00	30.22
3_1	2_2_3	0.00	27.00	85.50	83.50	27.00	29.51
3_1	2_2_4	0.00	27.00	83.50	81.50	27.00	28.80
3_1	3_2_3	0.00	13.00	69.34	67.34	13.00	11.46
3_1	3_2_4	0.00	13.00	67.34	65.34	13.00	11.12
3_1	3_2_5	0.00	13.00	65.34	63.34	13.00	10.78
3_1	3_2_6	0.00	13.00	63.34	61.34	13.00	10.44

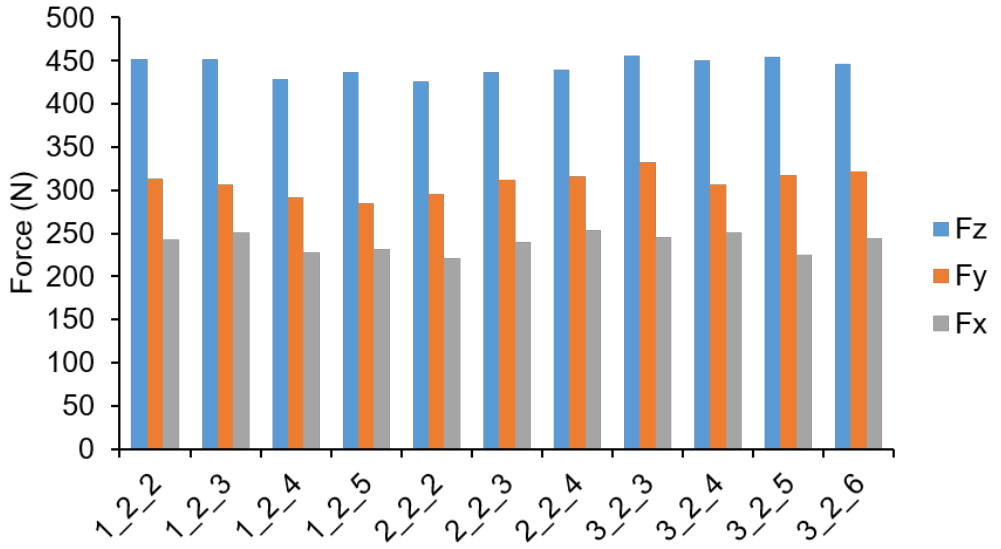

Figure 7.12: Measured cutting forces during the semi-finishing passes performed on the 3_1 billet, the forces shown are averaged over 1 second after tool engagement.

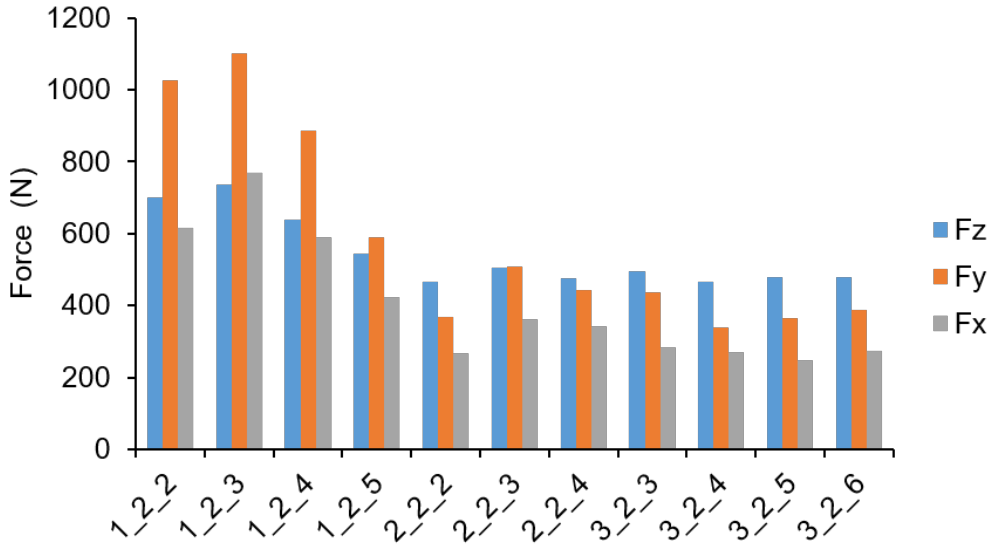

Figure 7.13: Measured cutting forces during the semi-finishing passes performed on the 3_1 billet, the forces shown are averaged over the 1 second of cutting prior to tool disengagement.

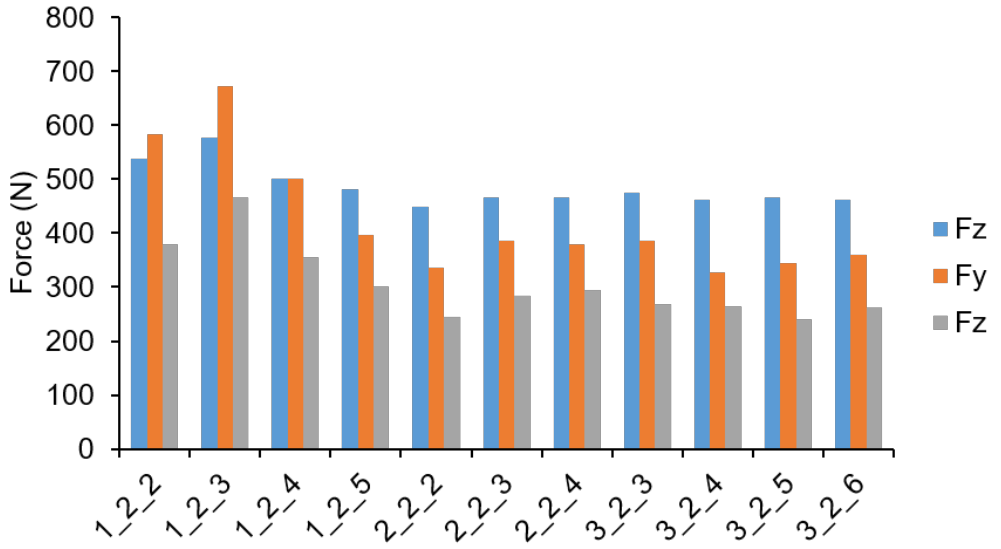

Figure 7.14: Measured cutting forces during the semi-finishing passes performed on the 3_1 billet, the forces shown are averaged over the duration of the machining pass from engagement to disengagement.

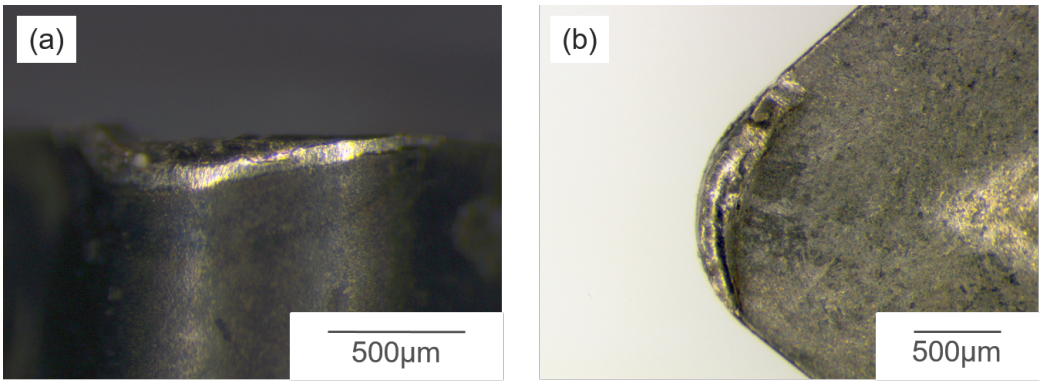

Figure 7.15: Microscope images showing the degree of tool wear after trial 1_2_2 on billet 3_1. Showing (a) the flank face and (b) the rake face.

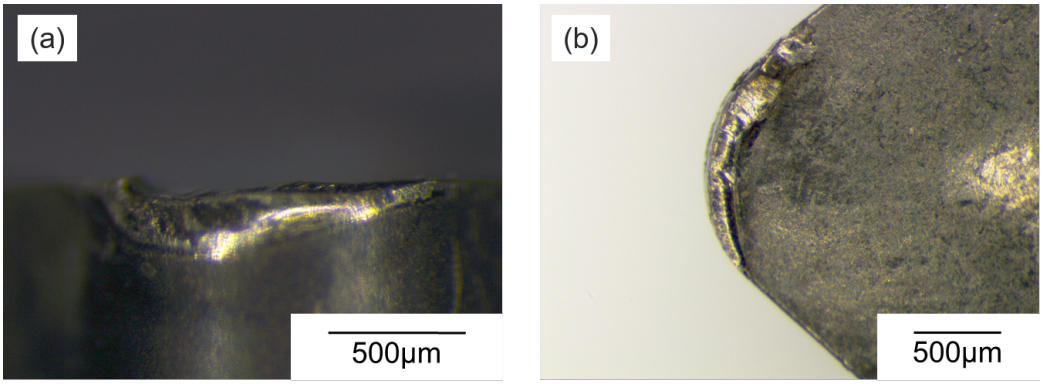

Figure 7.16: Microscope images showing the degree of tool wear after trial 1_2_3 on billet 3_1. Showing (a) the flank face and (b) the rake face.

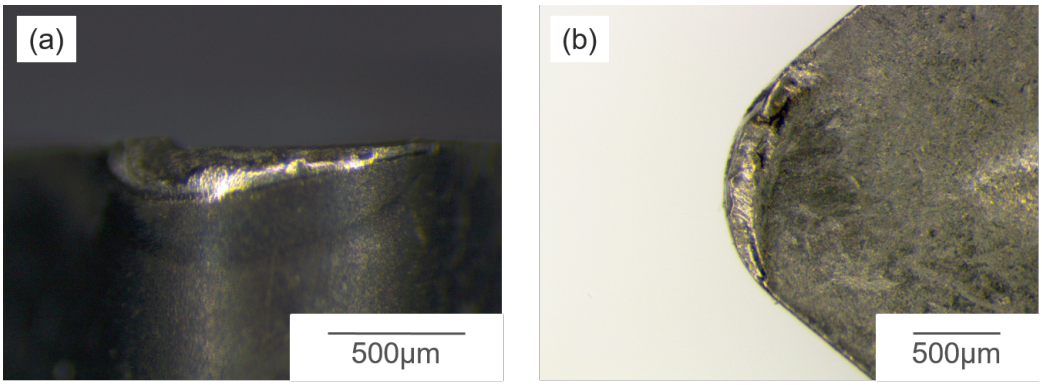

Figure 7.17: Microscope images showing the degree of tool wear after trial 1_2_4 on billet 3_1. Showing (a) the flank face and (b) the rake face.

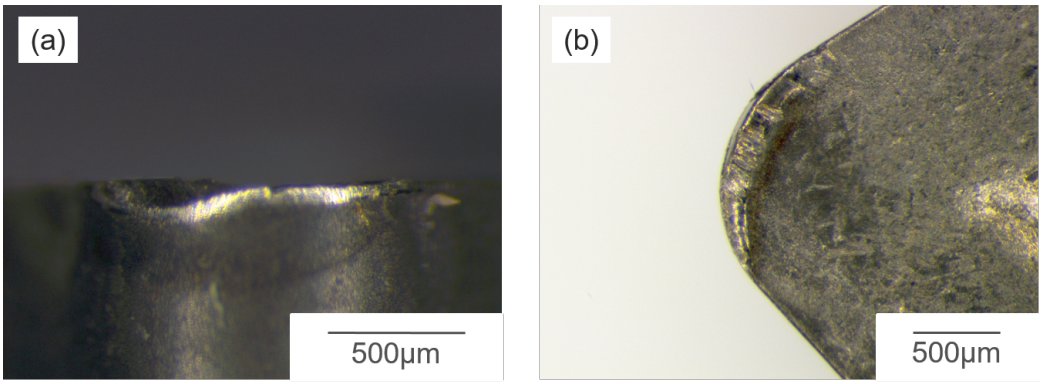

Figure 7.18: Microscope images showing the degree of tool wear after trial 1_2_5 on billet 3_1. Showing (a) the flank face and (b) the rake face.

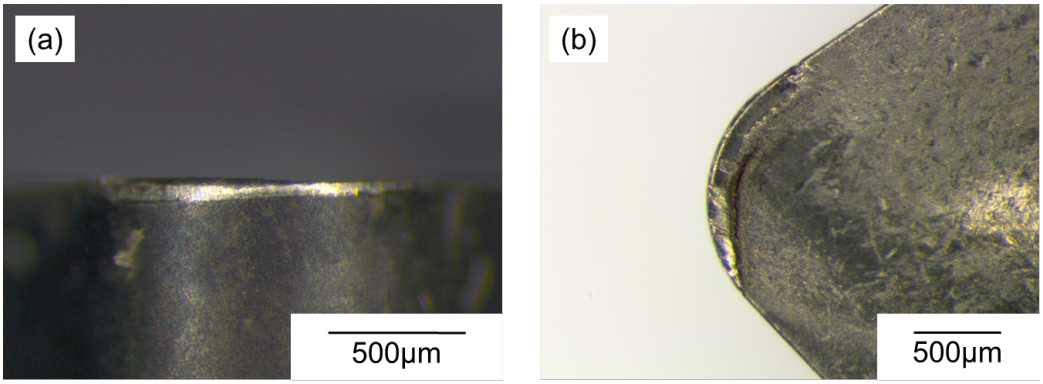

Figure 7.19: Microscope images showing the degree of tool wear after trial 2_2_2 on billet 3_1. Showing (a) the flank face and (b) the rake face.

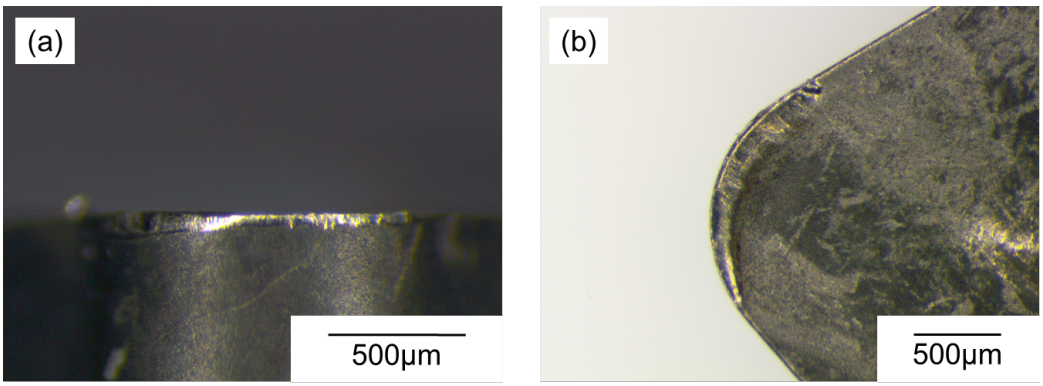

Figure 7.20: Microscope images showing the degree of tool wear after trial 3_2_3 on billet 3_1. Showing (a) the flank face and (b) the rake face.

7.5.2 Billet 4_1

Billet Preparation Passes

Due to the larger diameter of the 4_1 billet, a number of preparation passes were performed using the semi-finishing conditions described previously in Section 7.4.1, using the 1105 grade tool insert. These passes were performed to reduce the billet outer diameter, exposing a more central region with a higher post forging strain. A list of the preparation passes performed as well as the cutting dimensions and cut time are displayed in Table 7.5. The preparation passes consisted of longer cuts with cuts with a duration of approximately 55-50 seconds. The measured cutting forces, averaged over the first second of tool engagement are given in Figure 7.21 and as is obvious, the

cutting forces for each pass are approximately equivalent. The cutting forces measured over the final one second of tool engagement are given in Figure 7.22 and the average cutting forces over the duration of tool engagement are given in Figure 7.23. The cutting forces measured towards the end of tool engagement vary greatly between passes, with prep 1-3 passes producing higher forces. This same trend can be seen reflected in average cutting forces over the cut duration. Examining the tool wear after the completion of the prep passes in Figure 7.24 - 7.30, it can be observed that the tool wear differs greatly between passes, with some tool showing evidence of heavy notch features such as in Figure 7.24, while other tools exhibited heavy flank wear as is shown in Figure 7.25. It is assumed that the relatively long duration of cut for such high machining speeds for a carbide tool greatly wears the tool affecting the cutting forces and hence why the force in the Y direction becomes particularly high in prep passes 1-3. No obvious trend exists between the tool wear noted in Figures 7.24 - 7.30 and the cutting forces average over the final second of tool engagement.

To summarise the results of this study, it can be said that the relatively low changes in cutting forces observed in Figure 7.21 either suggest that there is minimal material change over the depth of the preparation passes or that the cutting forces are independent of any microstructural change. Considering the former explanation, the preparation passes reduced the radius of the billet by 7 mm, from an outer diameter of 122.5 mm to 108.5 mm. This reduction represents a relatively small volume of material and therefore gross material change may not occur. Given that the larger billets were air cooled to room temperature post forging, it could also be suggested that some homogenisation may have occurred leading to a more uniform microstructure compared to that seen on the smaller scale trials in Chapter 5.

Assessing the explanation that the cutting forces are relatively unaffected by microstructural change, the results of the machining trials on the FAST billet suggest otherwise in Chapter 6 where changes in grain size were correlated to changing cutting forces. However, in these trials a much larger depth of cut of 1mm was used, this depth of cut is large compared with the expected grain size and therefore may mask local microstructural change and is more affected by macroscopic changes in the process such as developing tool wear or fluctuating cutting temperatures. Ultimately, without further experimentation, the reasons for the near constant cutting forces are indeterminable. This points to a potential weakness in the method of using a forging process to produce varying microstructures with which to examine the variation in machining response.

Table 7.5: Semi-finishing preparation (prep) passes performed on billet 4_1, the dimensions for each pass are given, the naming convention used to identify passes is referenced in subsequent figures.

Billet	Trial	Z_s (mm)	Z_f (mm)	D_s (mm)	D_f (mm)	f_d (mm)	t_c (s)
4_1	Prep 1	0	35	122.5	120.5	35	55.21
4_1	Prep 2	0	35	120.5	118.5	35	54.29
4_1	Prep 3	0	35	118.5	116.5	35	53.37
4_1	Prep 4	0	35	116.5	114.5	35	52.46
4_1	Prep 5	0	35	114.5	112.5	35	51.54
4_1	Prep 6	0	35	112.5	110.5	35	50.63
4_1	Prep 7	0	35	110.5	108.5	35	49.71

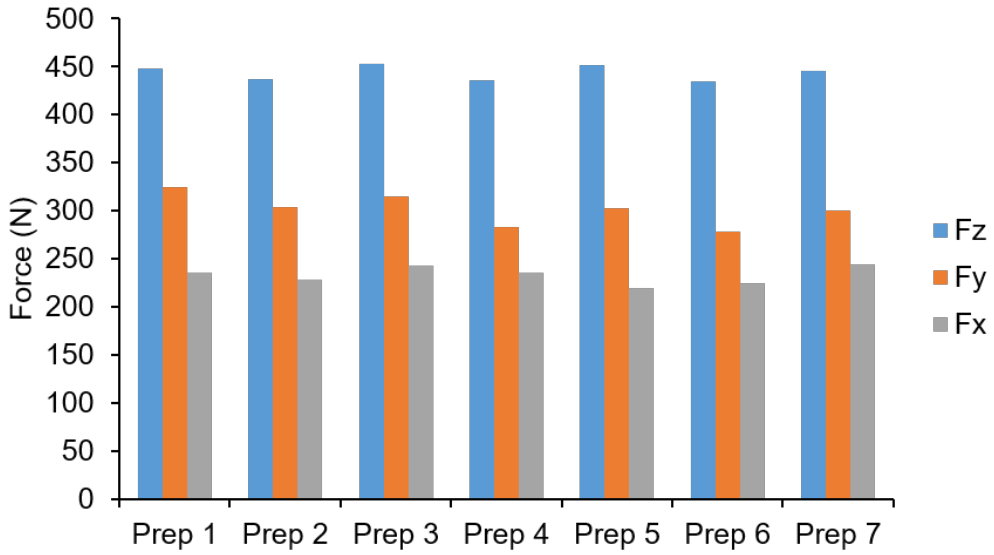

Figure 7.21: Measured cutting forces during the semi-finishing preparation passes performed on the 4_1 billet, the forces shown are averaged over 1 second after tool engagement.

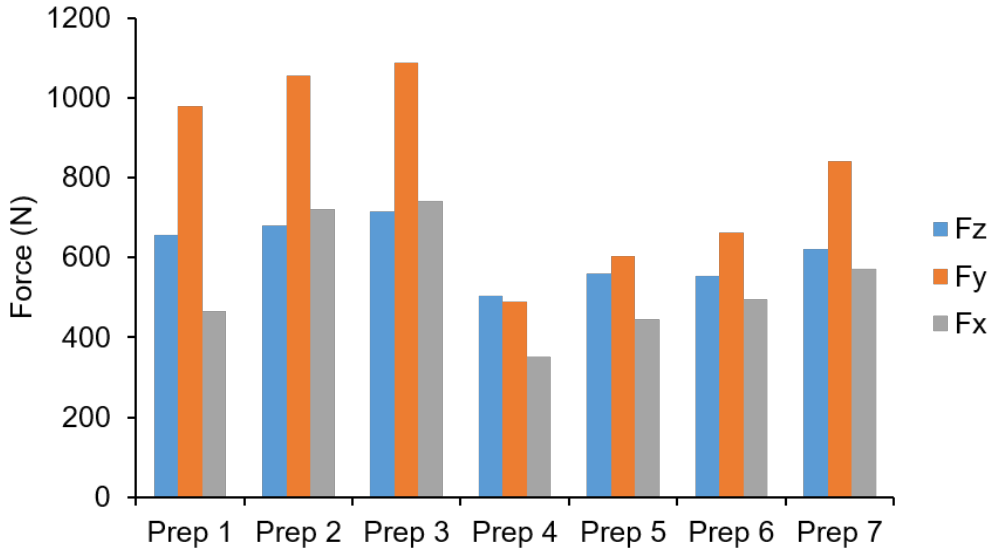

Figure 7.22: Measured cutting forces during the semi-finishing preparation passes performed on the 4_1 billet, the forces shown are averaged over 1 second before tool disengagement.

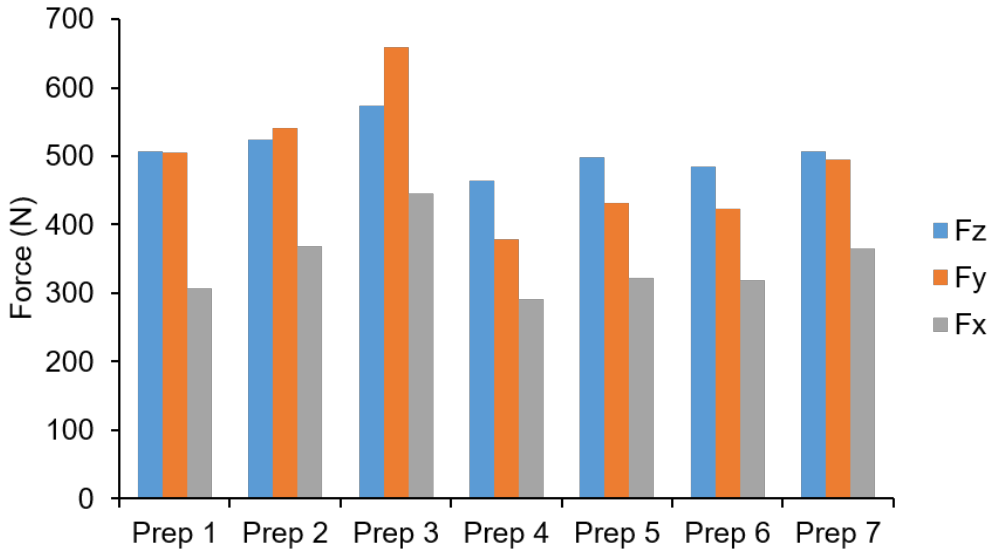

Figure 7.23: Measured cutting forces during the semi-finishing preparation passes performed on the 4_1 billet, the forces shown are averaged over the duration of tool engagement.

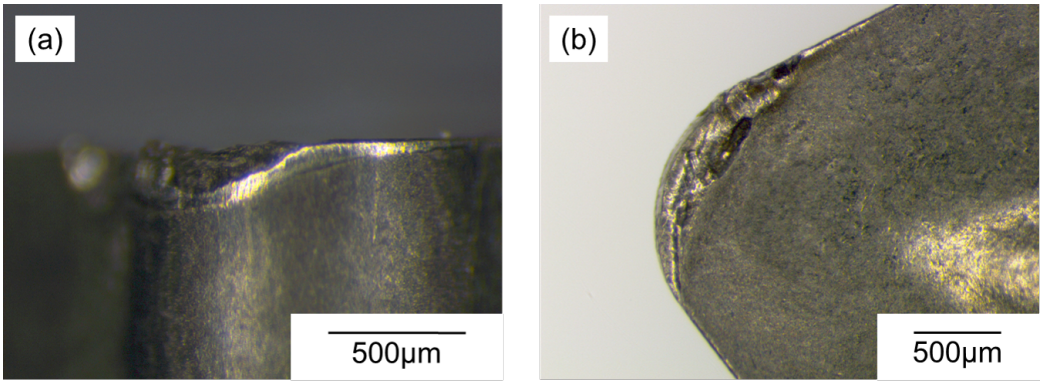

Figure 7.24: Microscope images showing the degree of tool wear after trial prep 1 on billet 4_1. Showing (a) the flank face and (b) the rake face.

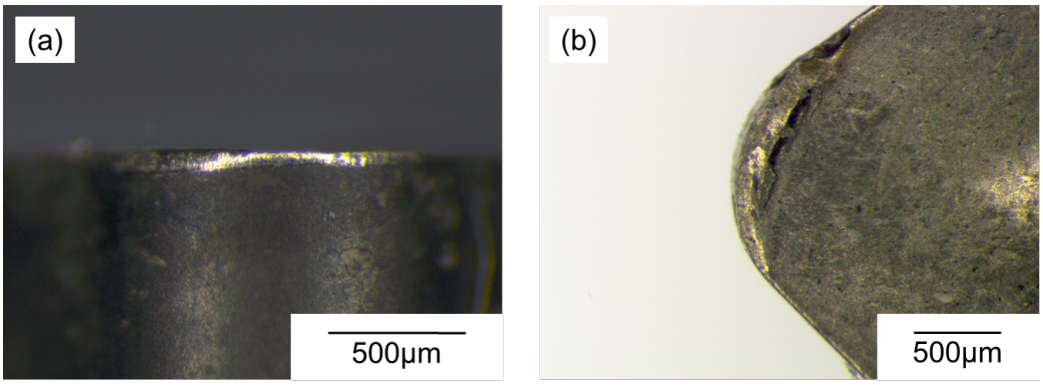

Figure 7.25: Microscope images showing the degree of tool wear after trial prep 2 on billet 4_1. Showing (a) the flank face and (b) the rake face.

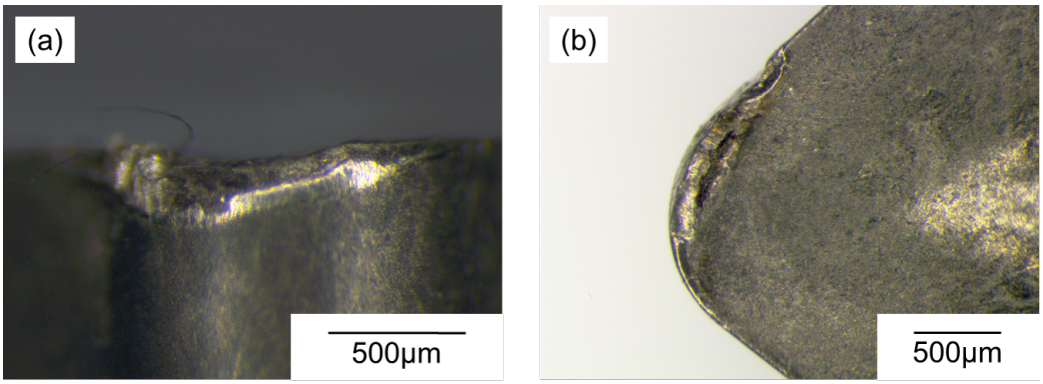

Figure 7.26: Microscope images showing the degree of tool wear after trial prep 3 on billet 4_1. Showing (a) the flank face and (b) the rake face.

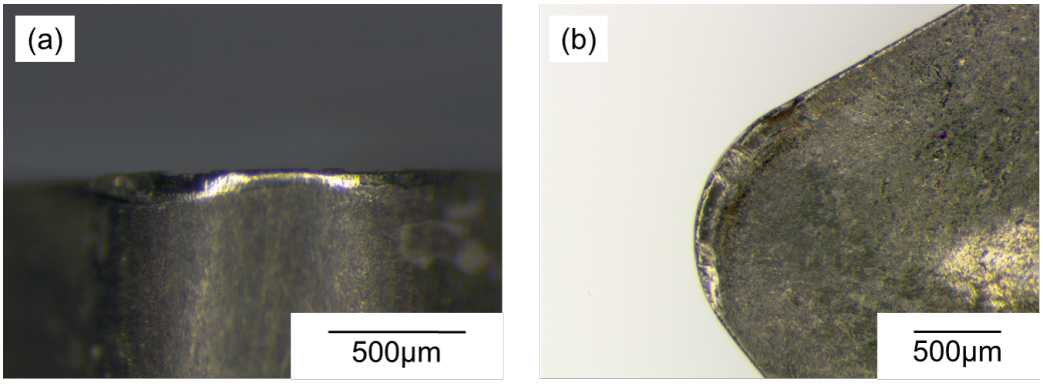

Figure 7.27: Microscope images showing the degree of tool wear after trial prep 4 on billet 4_1. Showing (a) the flank face and (b) the rake face.

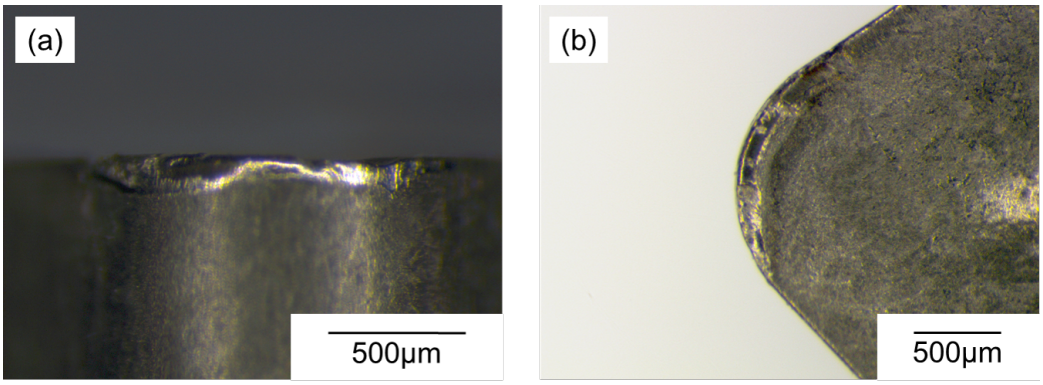

Figure 7.28: Microscope images showing the degree of tool wear after trial prep 5 on billet 4_1. Showing (a) the flank face and (b) the rake face.

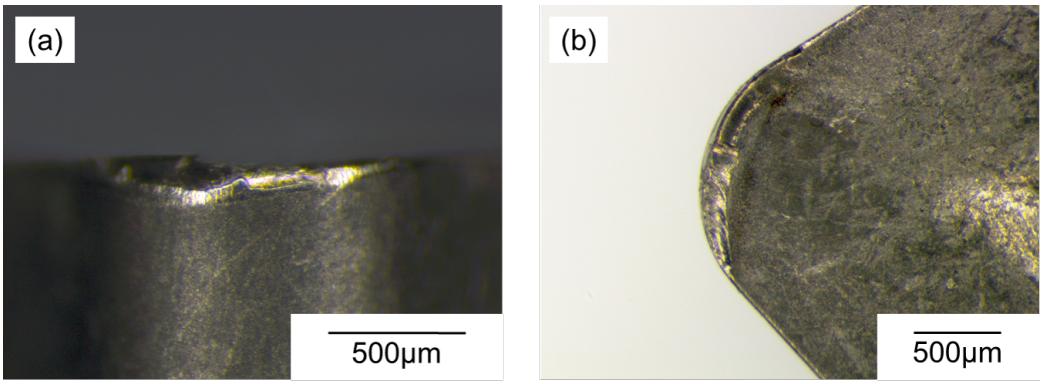

Figure 7.29: Microscope images showing the degree of tool wear after trial prep 6 on billet 4_1. Showing (a) the flank face and (b) the rake face.

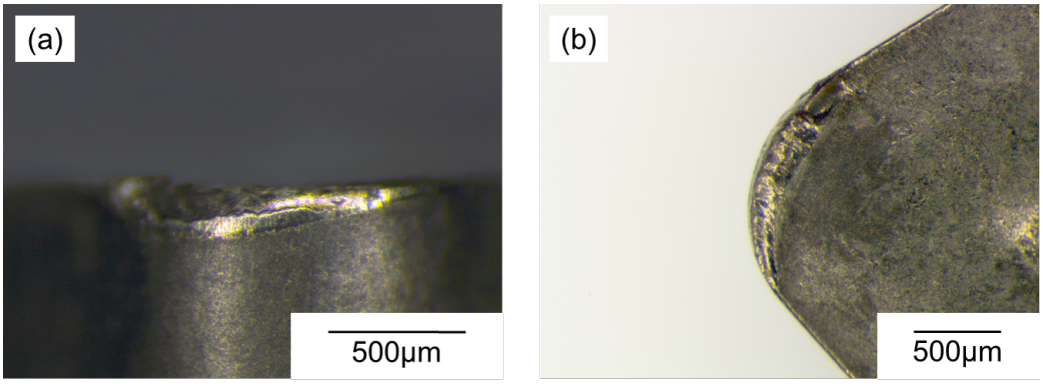

Figure 7.30: Microscope images showing the degree of tool wear after trial prep 7 on billet 4_1. Showing (a) the flank face and (b) the rake face.

Semi-Finishing Passes

Semi-finishing passes were performed on billet 4_1 during the production of the stepped geometry, the dimensions and naming convention of the semi-finishing passes are displayed in Table 7.6. As was the case for billet 3_1, the semi-finishing passes consisted of 3 different steps with 3 different ranges of cutting times ranging from 43 second to 6 seconds. The cutting forces captured over the first second of tool engagement were averaged and are displayed in Figure 7.31. These cutting forces show that the cutting forces over the first second of engagement are approximately equivalent as was the case for billet 3_1 and the preparation passes previously described. When the cutting forces are averaged over the final second of tool engagement it can be observed that the cutting forces are noticeably greater for the longer passes, shown in Figure 7.32. The same is observable for the cutting forces averaged over the duration of the cut (Figure 7.33). Examination of the tools post machining, shown in Figures 7.34-7.45, shows that the tools used for passes 1_2_2 - 1_2_5 exhibited much greater wear, which is the reason for the increased cutting forces observed in Figure 7.32. These observations are thought to be equivalent to the semi-finishing passes on billet 3_1 and the preparation passes performed for billet 4_1.

Table 7.6: Semi-finishing OD turning passes performed on billet 4_1, the dimensions for each pass are given, the naming convention used to identify passes is referenced in subsequent figures.

Billet	Trial	Z_s (mm)	Z_f (mm)	D_s (mm)	D_f (mm)	f_d (mm)	t_c (s)
4_1	1_2_2	0	32	104.72	102.72	32	43.03
4_1	1_2_3	0	32	102.72	100.72	32	42.19
4_1	1_2_4	0	32	100.72	98.72	32	41.35
4_1	1_2_5	0	32	98.72	96.72	32	40.51
4_1	2_2_2	0	21	87.86	85.86	21	23.60
4_1	2_2_3	0	21	85.86	83.86	21	23.05
4_1	2_2_4	0	21	83.86	81.86	21	22.50
4_1	3_2_2	2	11	67.59	65.59	9	7.73
4_1	3_2_3	2	11	65.59	63.59	9	7.49
4_1	3_2_4	2	11	63.59	61.59	9	7.26
4_1	3_2_5	2	11	61.59	59.59	9	7.02
4_1	3_2_6	2	11	59.59	57.59	9	6.78

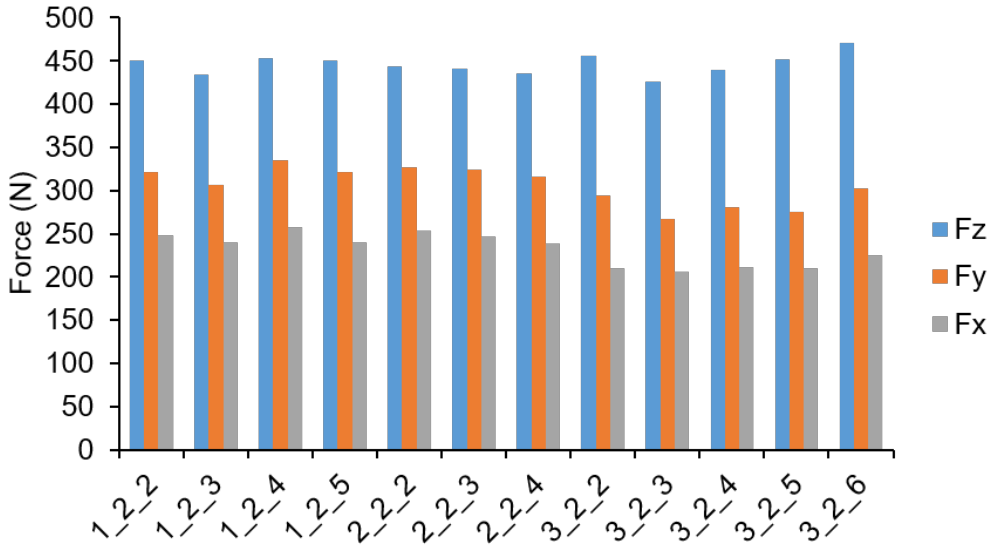

Figure 7.31: Measured cutting forces during the semi-finishing passes performed on the 4_1 billet, the forces shown are averaged over 1 after tool engagement.

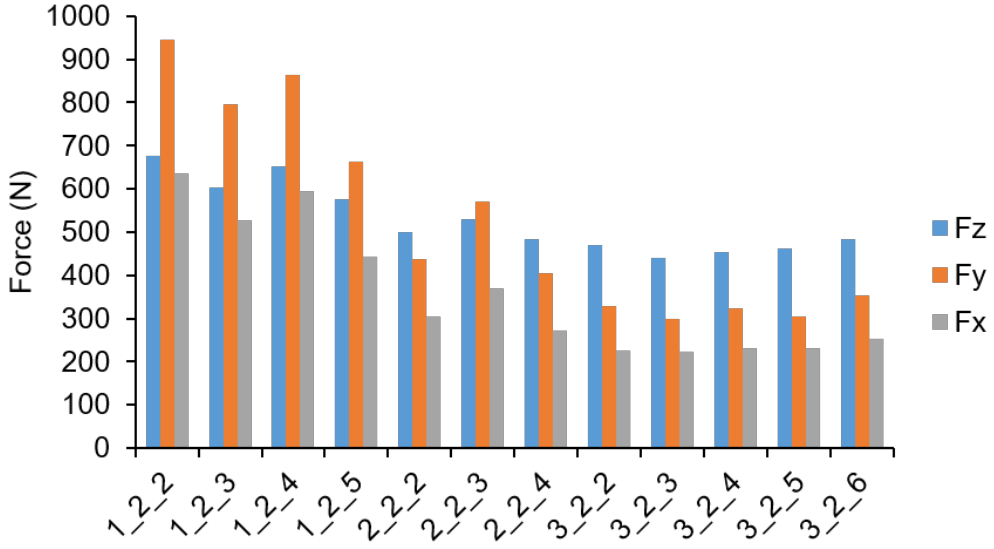

Figure 7.32: Measured cutting forces during the semi-finishing performed on the 4_1 billet, the forces shown are averaged over the 1 second of cutting prior to tool disengagement.

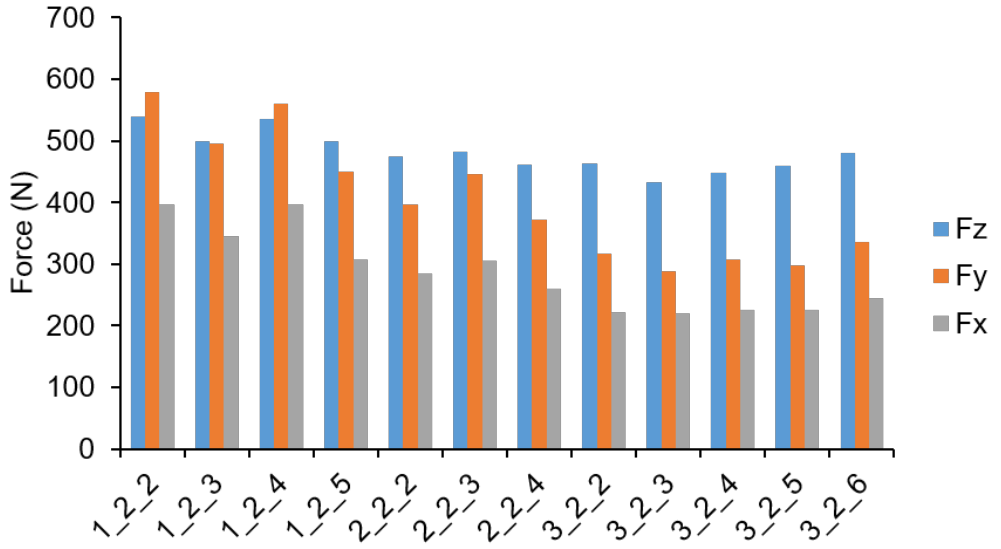

Figure 7.33: Measured cutting forces during the semi-finishing performed on the 4_1 billet, the forces shown are averaged the duration of the machining pass from engagement to disengagement.

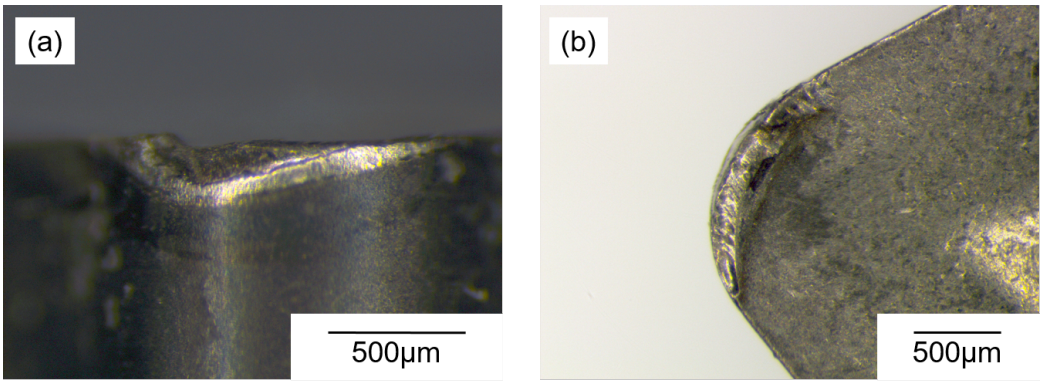

Figure 7.34: Microscope images showing the degree of tool wear after trial 1_2_2 on billet 4_1. Showing (a) the flank face and (b) the rake face.

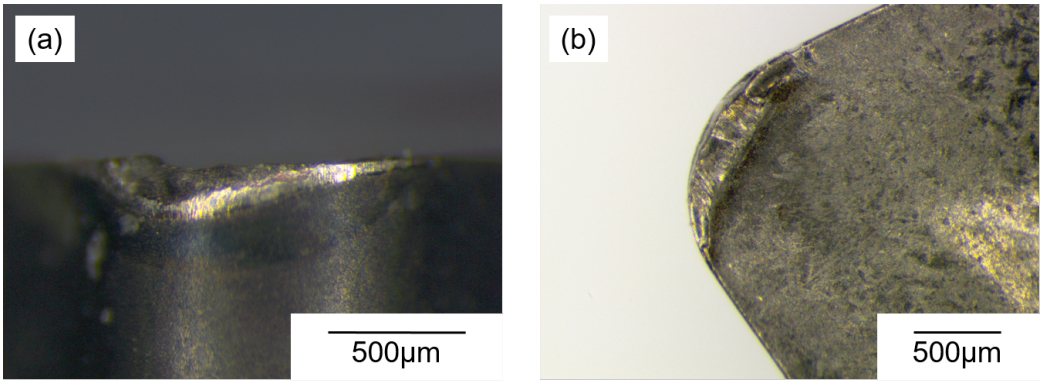

Figure 7.35: Microscope images showing the degree of tool wear after trial 1_2_3 on billet 4_1. Showing (a) the flank face and (b) the rake face.

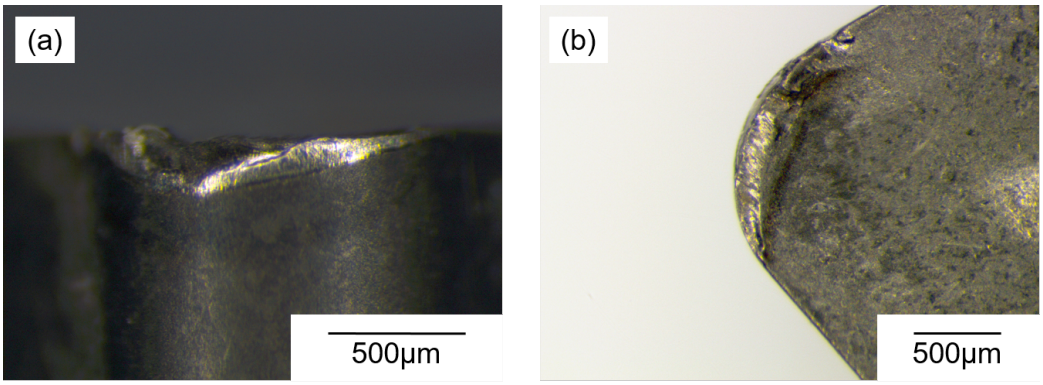

Figure 7.36: Microscope images showing the degree of tool wear after trial 1_2_4 on billet 4_1. Showing (a) the flank face and (b) the rake face.

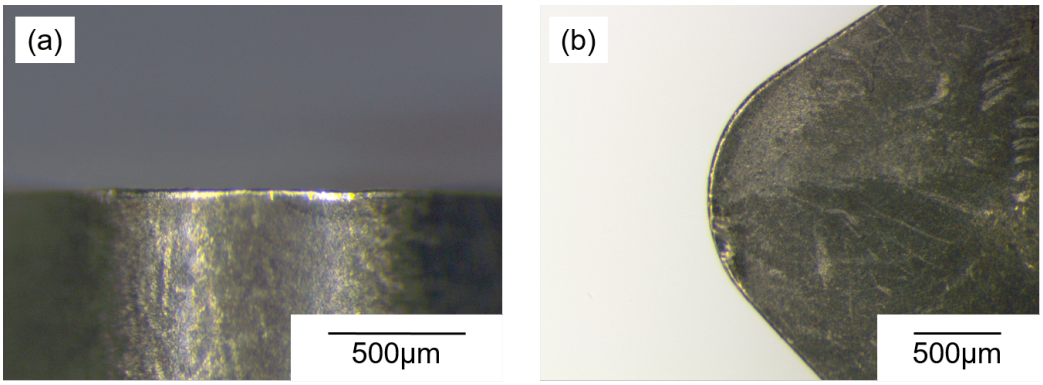

Figure 7.37: Microscope images showing the degree of tool wear after trial 1_2_5 on billet 4_1. Showing (a) the flank face and (b) the rake face.

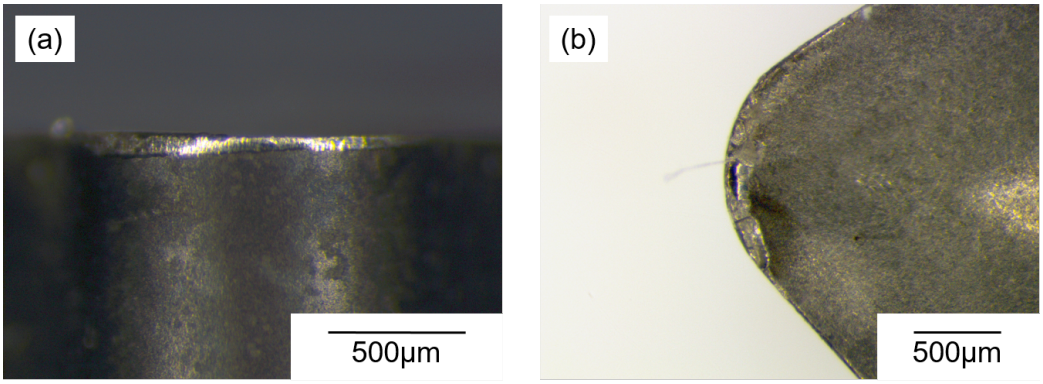

Figure 7.38: Microscope images showing the degree of tool wear after trial 2_2_2 on billet 4_1. Showing (a) the flank face and (b) the rake face.

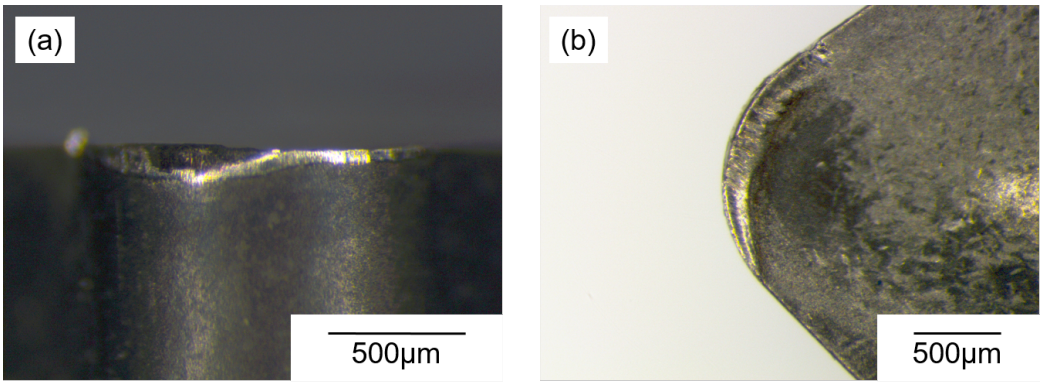

Figure 7.39: Microscope images showing the degree of tool wear after trial 2_2_3 on billet 4_1. Showing (a) the flank face and (b) the rake face.

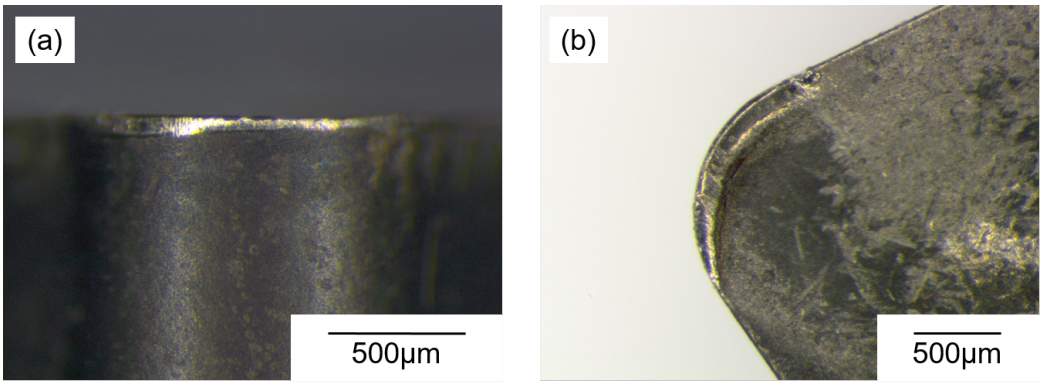

Figure 7.40: Microscope images showing the degree of tool wear after trial 2_2_4 on billet 4_1. Showing (a) the flank face and (b) the rake face.

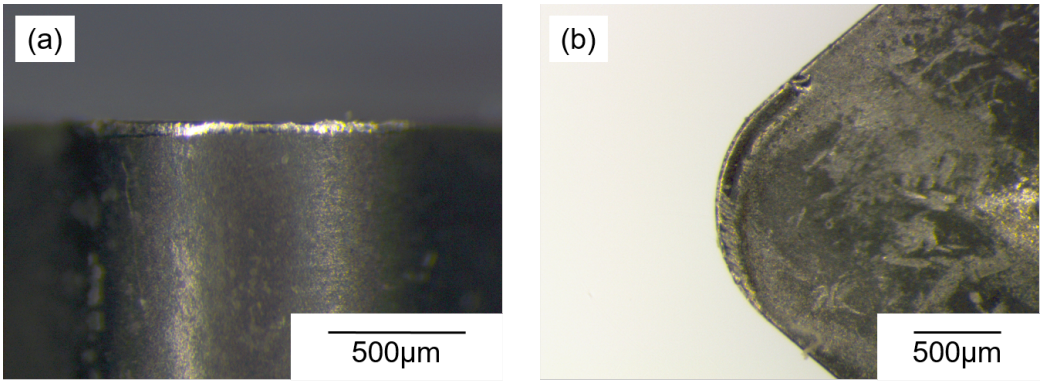

Figure 7.41: Microscope images showing the degree of tool wear after trial 3_2_2 on billet 4_1. Showing (a) the flank face and (b) the rake face.

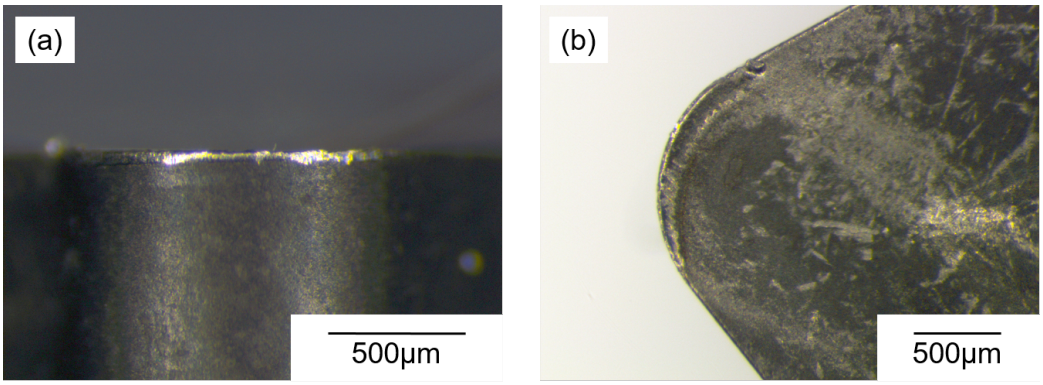

Figure 7.42: Microscope images showing the degree of tool wear after trial 3_2_3 on billet 4_1. Showing (a) the flank face and (b) the rake face.

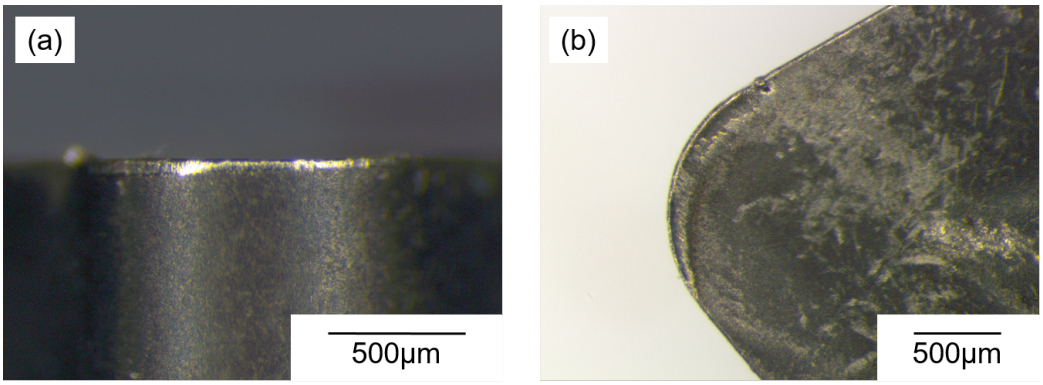

Figure 7.43: Microscope images showing the degree of tool wear after trial 3_2_4 on billet 4_1. Showing (a) the flank face and (b) the rake face.

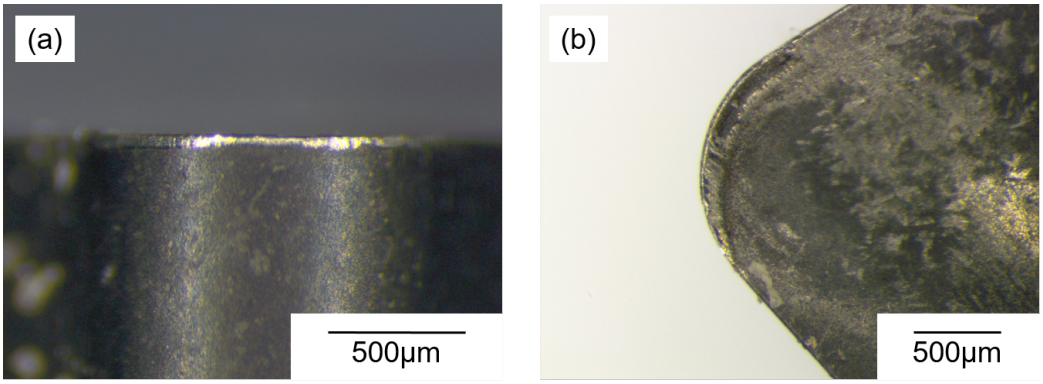

Figure 7.44: Microscope images showing the degree of tool wear after trial 3_2_5 on billet 4_1. Showing (a) the flank face and (b) the rake face.

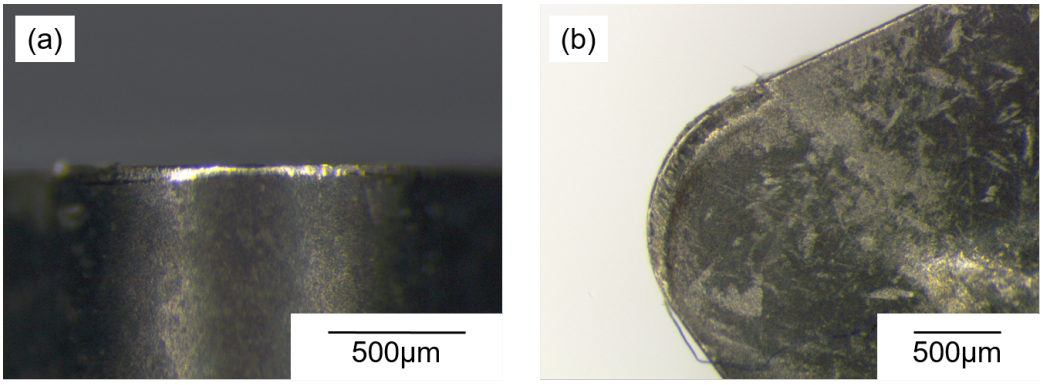

Figure 7.45: Microscope images showing the degree of tool wear after trial 3_2_6 on billet 4_1. Showing (a) the flank face and (b) the rake face.

7.5.3 Billet 3_2

As was the case for billets 3_1 and 4_1, the billet 3_2 was machined to produce the same stepped geometry, the dimensions of the steps are given in Table 7.7. The measured cutting forces over the first second of tool engagement are displayed in Figure 7.46. The observations for this billet are the same as noted for billets 4_1 and 3_1 with the cutting forces across all semi-finishing passes being comparable when compared over the first second of tool engagement. The cutting forces averaged over the final second of cutting (Figures 7.47) and over the duration of the cut (Figures 7.46) show a similar trend with the cutting forces being increased for semi-finishing trials performed to create the first step (prefixed with 1). This is due to the longer cutting times and increased level of tool wear when producing the third step compared

to the second and first. The tools post machining (Figures 7.49 - 7.57) displayed similar traits as noted for billets 4_1 and 3_1 with increased tool wear consistent with an increase in cutting time. An exception to this rule is shown in Figure 7.56, whereby an unusually large wear scar can be observed with a level of built up edge. It is thought that the presence of the built up edge may have acted to effectively sharpen the cutting tool resulting in the lower cutting forces noted for pass 3_2_3 in comparison with 3_2_2 and 3_2_4.

Table 7.7: Semi-finishing passes performed on billet 3_2, the dimensions for each pass are given, the naming convention used to identify passes is referenced in subsequent figures.

Billet	Trial	Z_s (mm)	Z_f (mm)	D_s (mm)	D_f (mm)	f_d (mm)	t_c (s)
3_2	1_2_2	0	46	90.4	88.4	46	53.23
3_2	1_2_3	0	46	88.4	86.4	46	52.02
3_2	1_2_4	0	46	86.4	84.4	46	50.82
3_2	2_2_1	0	30.33	76.4	74.4	30.33	29.54
3_2	2_2_2	0	30.33	74.4	72.4	30.33	28.74
3_2	2_2_3	0	30.33	72.4	70.4	30.33	27.95
3_2	3_2_2	0	15.66	58.5	56.5	15.66	11.58
3_2	3_2_3	0	15.66	56.5	54.5	15.66	11.17
3_2	3_2_4	0	15.66	54.5	52.5	15.66	10.76

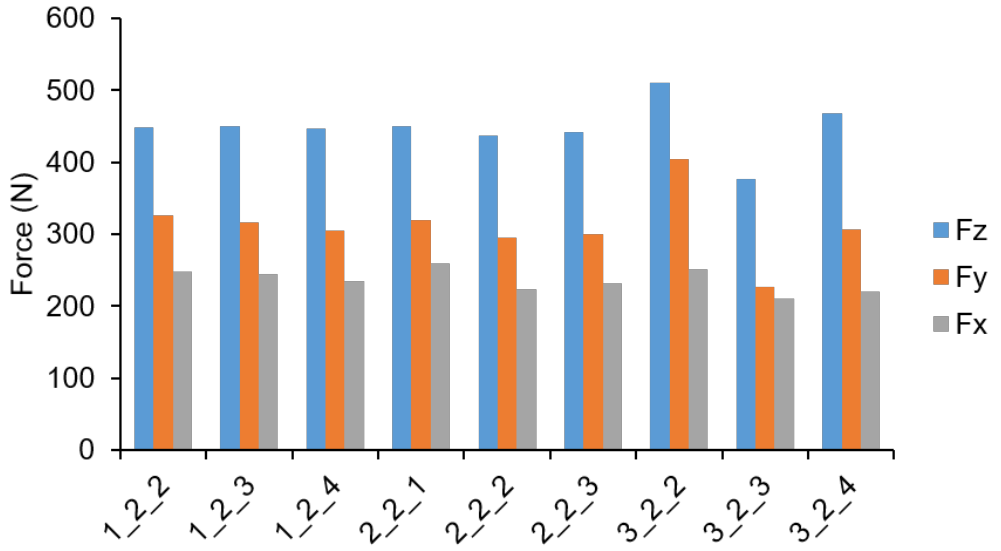

Figure 7.46: Measured cutting forces during the semi-finishing passes performed on the 3_2 billet, the forces shown are averaged over 1 second after tool engagement.

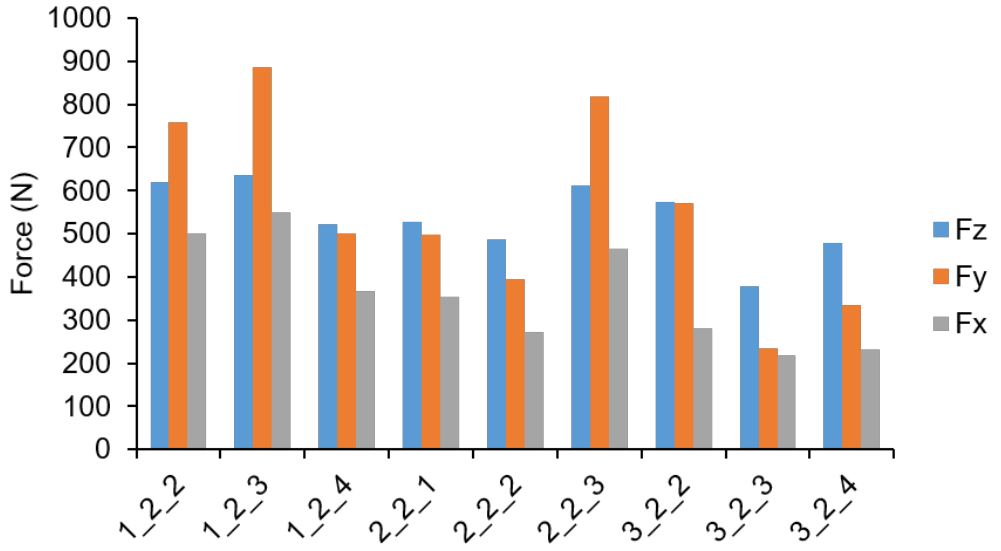

Figure 7.47: Measured cutting forces during the semi-finishing passes performed on the 3_2 billet, the forces shown are averaged over the 1 second of cutting prior to tool disengagement.

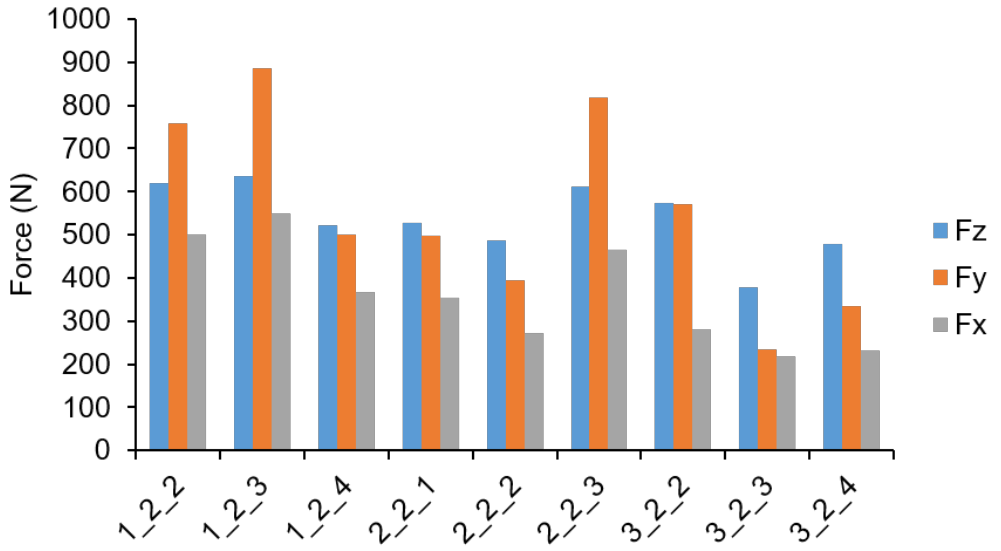

Figure 7.48: Measured cutting forces during the semi-finishing passes performed on the 3_2 billet, the forces shown are averaged the duration of the machining pass from engagement to disengagement.

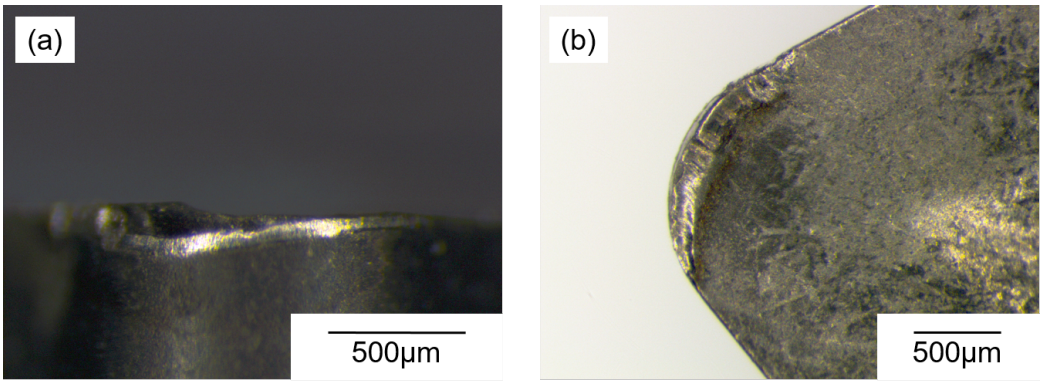

Figure 7.49: Microscope images showing the degree of tool wear after trial 1_2_2 on billet 3_2. Showing (a) the flank face and (b) the rake face.

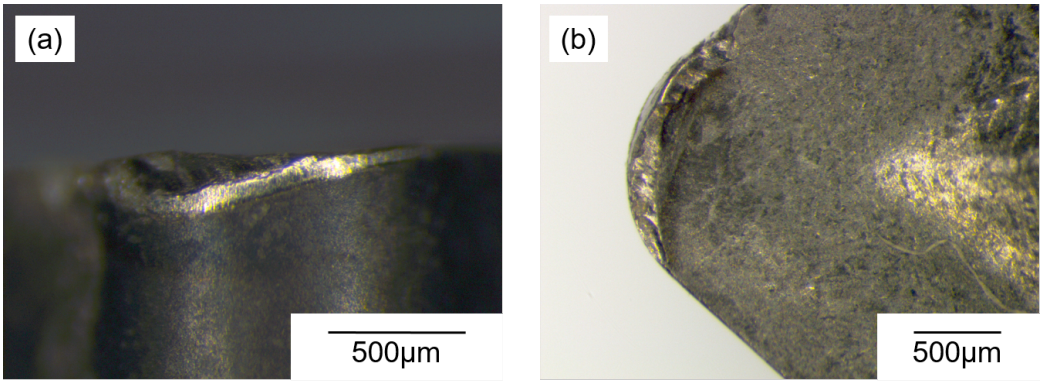

Figure 7.50: Microscope images showing the degree of tool wear after trial 1_2_3 on billet 3_2. Showing (a) the flank face and (b) the rake face.

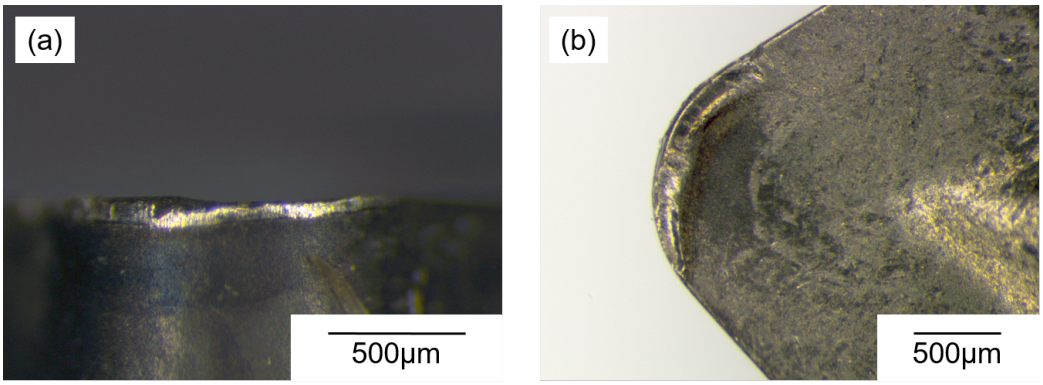

Figure 7.51: Microscope images showing the degree of tool wear after trial 1_2_4 on billet 3_2. Showing (a) the flank face and (b) the rake face.

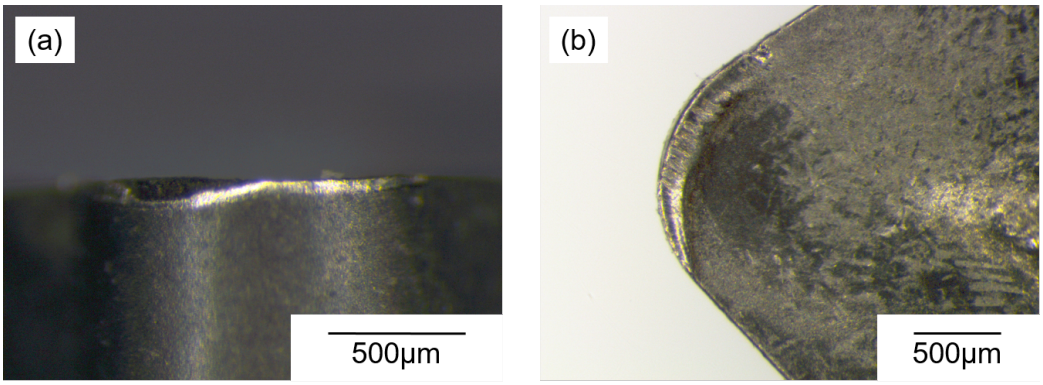

Figure 7.52: Microscope images showing the degree of tool wear after trial 2_2_1 on billet 3_2. Showing (a) the flank face and (b) the rake face.

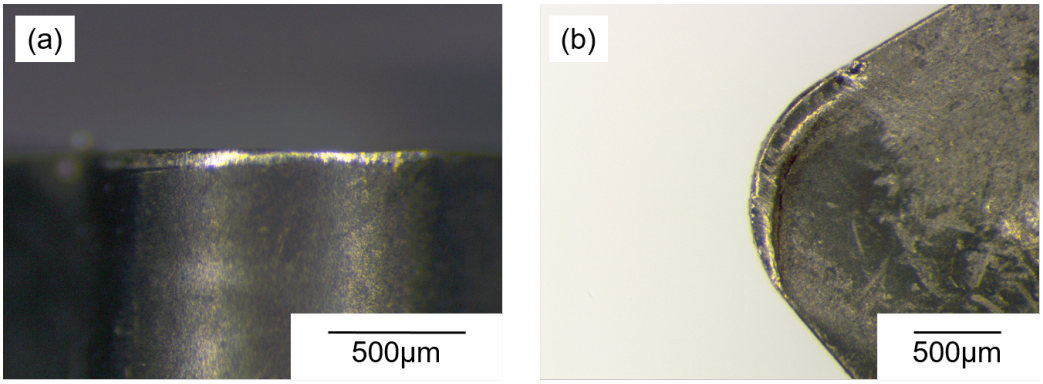

Figure 7.53: Microscope images showing the degree of tool wear after trial 2_2_2 on billet 3_2. Showing (a) the flank face and (b) the rake face.

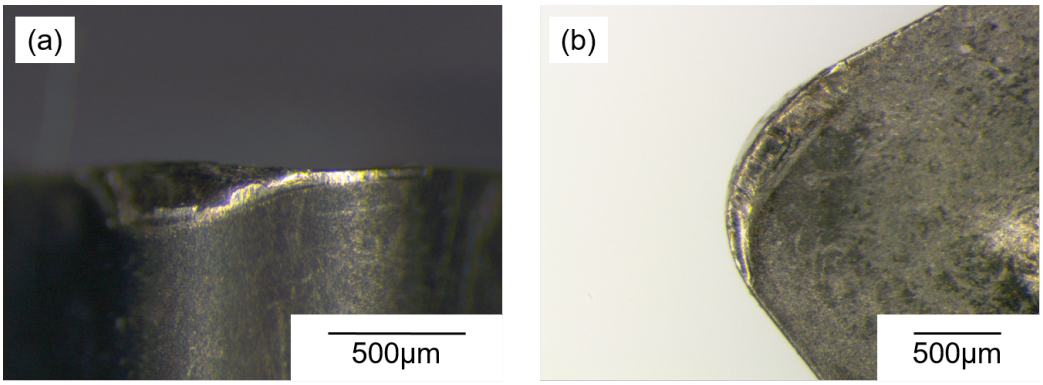

Figure 7.54: Microscope images showing the degree of tool wear after trial 2_2_3 on billet 3_2. Showing (a) the flank face and (b) the rake face.

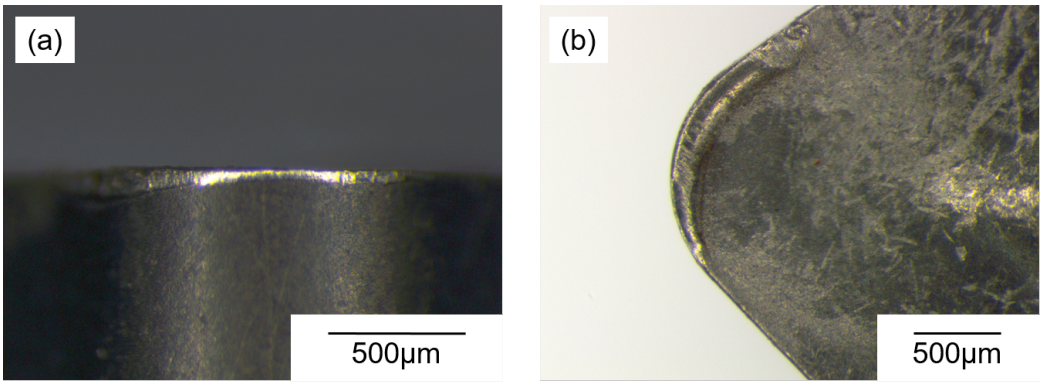

Figure 7.55: Microscope images showing the degree of tool wear after trial 3_2_2 on billet 3_2. Showing (a) the flank face and (b) the rake face.

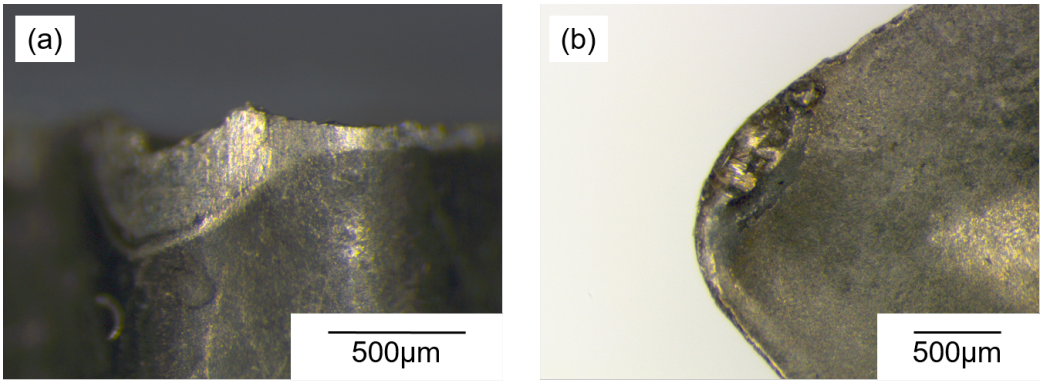

Figure 7.56: Microscope images showing the degree of tool wear after trial 3_2_3 on billet 3_2. Showing (a) the flank face and (b) the rake face.

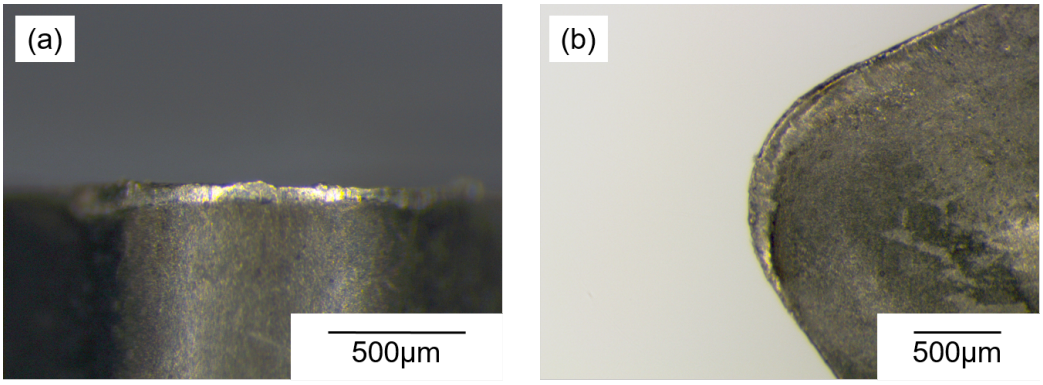

Figure 7.57: Microscope images showing the degree of tool wear after trial 3_2_4 on billet 3_2. Showing (a) the flank face and (b) the rake face.

7.5.4 As-HIP Billet

To provide a comparison with the as-forged billets, semi-finishing passes were performed with equivalent parameters on a billet of as-HIP material. A stepped geometry was not machined on the as HIP billet and the OD turning semi-finishing passes were performed in a sequential manner and cutting forces were measured. The geometry of the performed semi-finishing passes is given in Table 7.8.

The cutting forces measured over the first 1 second of tool engagement are shown in Figure 7.58. The cutting forces are consistent across all the semi-finishing passes in all principle directions. This observation is consistent for cutting forces averaged over the last second of tool engagement (Figure 7.59) and averaged over the entire duration of tool engagement (Figure 7.60). The

tool wear after the trials is shown in Figure 7.61 to 7.63. The tool wear post semi-finishing trials can be seen to show clear similarities and the level of wear is consistent across each pass. The consistency in the tool wear is thought to be the reason for the consistency in cutting forces across all semi-finishing passes on the as HIP billet. The as-HIP billet is assumed to be the most homogeneous of all billets machined and therefore the material properties are expected to be consistent. It is therefore unsurprising that the machining trials produce both consistent cutting forces and consistent levels of tool wear.

Table 7.8: Semi-finishing passes performed on the as HIP billet, the dimensions for each pass are given, the naming convention used to identify passes is referenced in subsequent figures.

Billet	Trial	Z_s (mm)	Z_f (mm)	X_s (mm)	X_f (mm)	F_d (mm)	t (s)
HIP	2_1_1	0	65	66.5	64.5	64.5	54.04
HIP	2_1_2	0	65	64.5	62.5	62.5	52.36
HIP	2_1_3	0	65	62.5	60.5	60.5	50.68

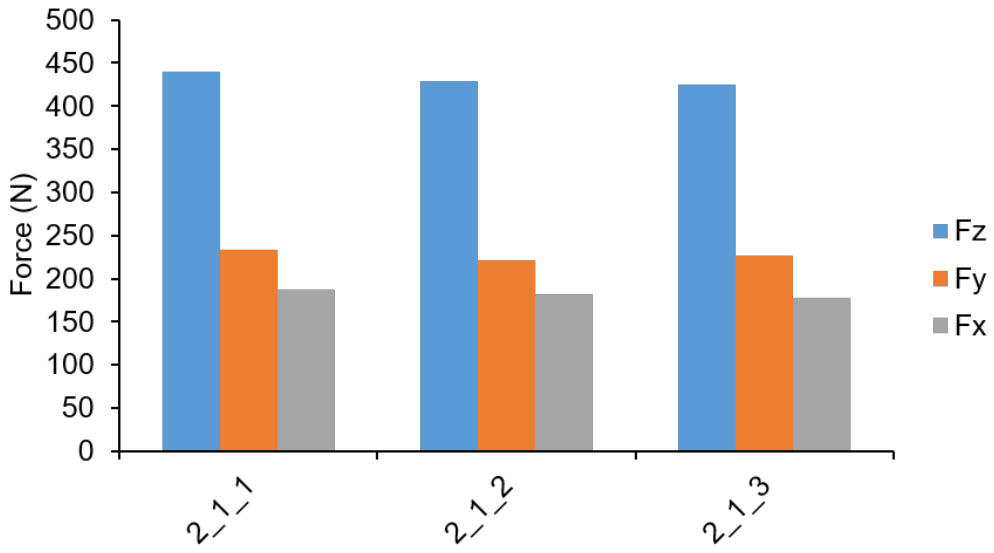

Figure 7.58: Measured cutting forces during the semi-finishing passes performed on the as HIP billet, the forces shown are averaged over the first second of tool engagement.

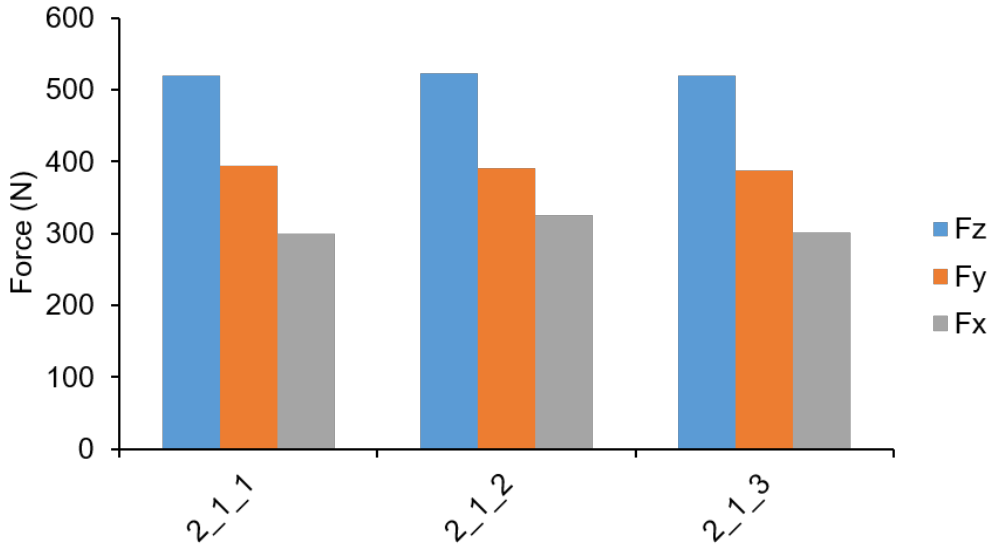

Figure 7.59: Measured cutting forces during the semi-finishing passes performed on the as-HIP billet, the forces shown are averaged over the last second of tool engagement.

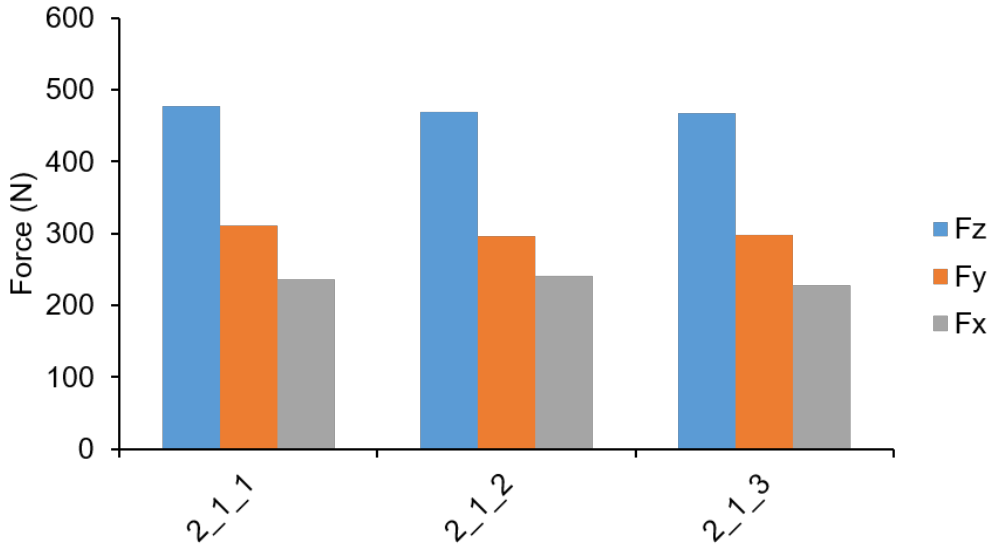

Figure 7.60: Measured cutting forces during the semi-finishing passes performed on the as-HIP billet, the forces shown are averaged over the duration of tool engagement.

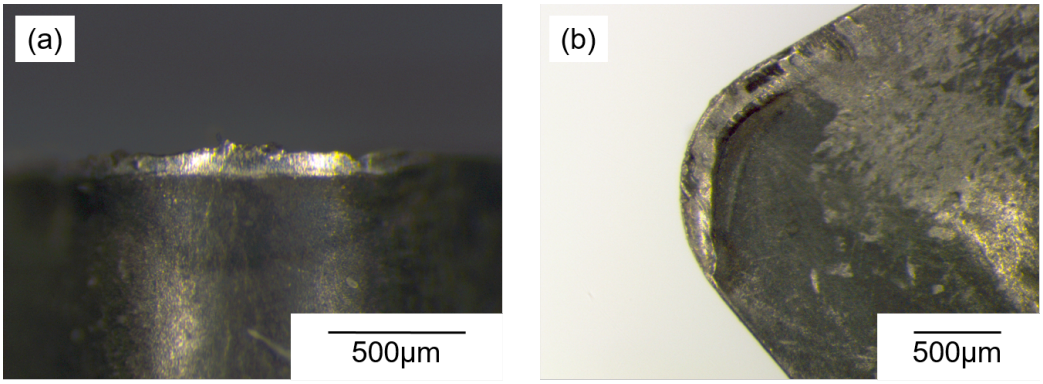

Figure 7.61: Microscope images showing the degree of tool wear after trial 2_1_1 on the as-HIP billet. Showing (a) the flank face and (b) the rake face.

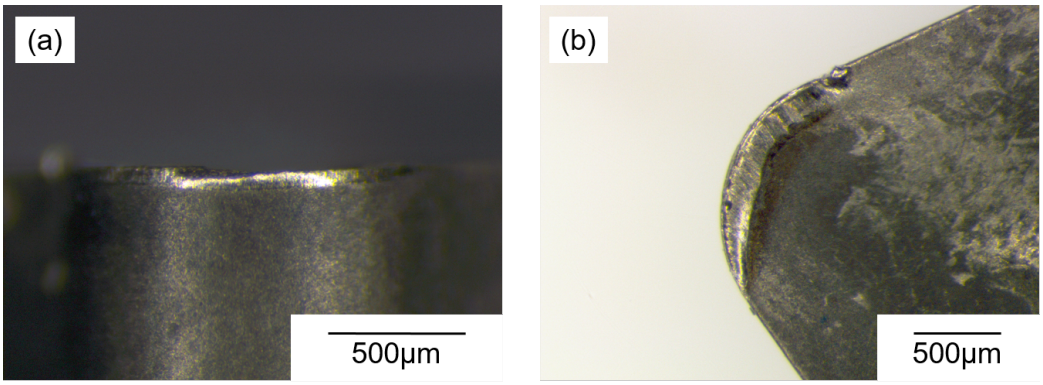

Figure 7.62: Microscope images showing the degree of tool wear after trial 2_1_2 on the as-HIP billet. Showing (a) the flank face and (b) the rake face.

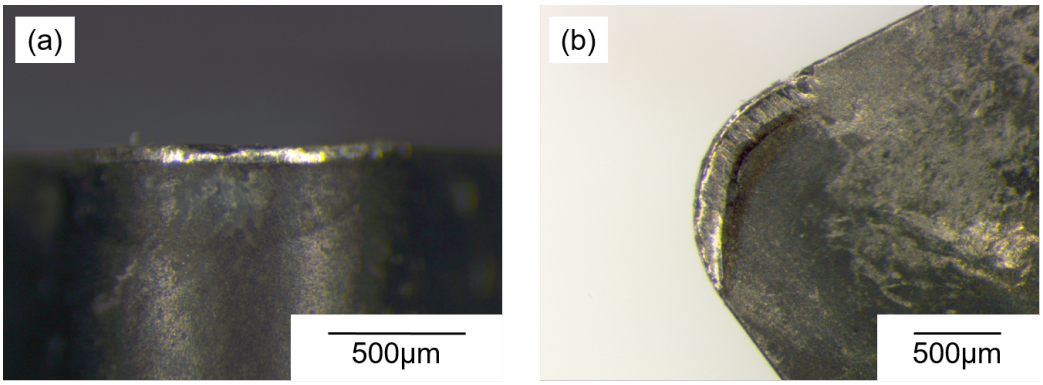

Figure 7.63: Microscope images showing the degree of tool wear after trial 2_1_3 on the as-HIP billet. Showing (a) the flank face and (b) the rake face.

7.5.5 Summary Remarks With Regards to Semi-finishing Pass Results

Cutting forces were measured during all semi-finishing passes performed during the production of the stepped geometry for each billet. The semi-finishing passes performed covered various radial positions across the three as-forged billets and one as-HIP billet. Three semi-finishing passes were performed per billet for each machined step. The cutting forces measured up to 1 second after tool engagement of the work piece were averaged and the results are shown in Figure 7.64. As can be observed in the Figure, the cutting forces shown little deviation across billets, particularly in the Z direction (cutting direction). The HIP material exhibits lower Y and X direction cutting forces. This is due to the smaller starting diameter of the as HIP billet compared to the relatively large diameter of the as forged billets.

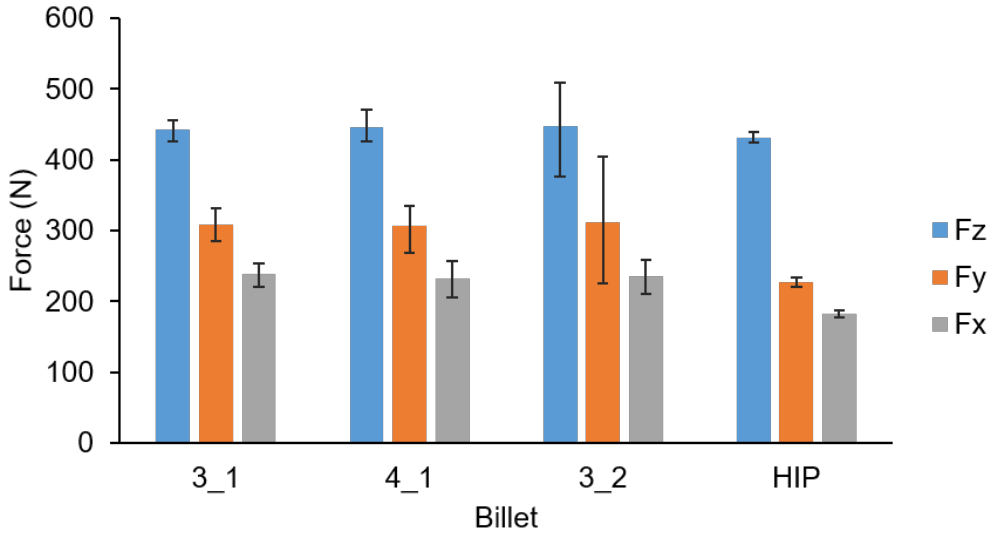

Figure 7.64: Average measured cutting forces in each of the 3 principle directions captured during 1mm depth of cut pass for each of the billets. Forces measured over 1 second after tool engagement were averaged for each pass and the average was then taken of all semi-finishing passes performed.

It can be observed that the scatter in measurements is much higher for the as forged billets than the as HIP billet, this could be interpreted as changing material properties, however this is likely to be due to the varying geometry across billets and steps for the forged billets. On average it can be observed that the cutting forces are approximately equivalent. This suggests that

the varying cumulative strain and temperature differences employed during forging result in very little change in material properties. The alternative hypothesis, as discussed previously, suggests that the machining forces are unaffected by material change due to differing forging parameters. The high level of tool wear observed during machining trials also prevents accurate measurements of cutting force from being captured as the wear state of the tool dictates the forces, as demonstrated. It is therefore recommended that the trials are repeated with depths of cut smaller than 1 mm in order to increase the resolution of cutting force change with microstructural variation.

7.6 Results - Face Turning Trials

7.6.1 Billet 4_1

Measured Cutting Forces

The facing passes performed on the 4_1 billet are detailed in Table 7.9. For this billet, three repeats were performed on each of the 4 faces. Each face was machined to ensure that the same volume of material removal is performed during each pass on the machined face. Due to the short cutting times, the forces were averaged over the duration of engagement to allow comparison in the forces measured across all billets. Considering the cutting forces in the Z direction for all faces in Figure 7.65 it can be seen that face 4 produced consistently lower cutting forces across repeats. It can also be observed that for faces 1-3, the cutting force during the first repeat is significantly higher than that of the 2nd and third repeat. Considering the 2nd and 3rd repeat, it can be observed that the Z direction cutting forces are consistent across all faces.

Face 4 also produced consistently lower cutting forces in the Y direction as shown in Figure 7.66, than faces 1-3. Unlike forces in the Z direction, the first repeat for faces 1-3 did not produce significantly higher forces in the Y direction for all faces. The forces in the X direction (Figure 7.67) show a dramatic reduction when comparing face 4 with faces 1-3. Similar to the forces in the Z direction, the X direction cutting forces show a higher value produced during the first repeat followed by a consistent reduction in the second and third repeat for faces 1-3.

Prior to the first repeat on each face, a preparation pass was performed to check the correct programme of the lathe, these cuts were undertaken within coolant and may have locally work hardened the surface or led to high tensile residual stresses, potentially resulting in the higher forces during

the first measured repeat of each pass. However, no information is available to support this hypothesis.

Table 7.9: Cutting dimensions employed during each facing pass performed on billet 4_1.

Billet	Face	Repeat	Z_s (mm)	Z_f (mm)	D_s (mm)	D_f (mm)
4_1	1	1	2.25	2.5	52.09	14
4_1	1	2	2.5	2.75	52.09	14
4_1	1	3	2.75	3	52.09	14
4_1	2	1	12.25	12.5	73.86	52.2
4_1	2	2	12.5	12.75	73.86	52.2
4_1	2	3	12.75	13	73.86	52.2
4_1	3	1	22.25	22.5	92.72	73.96
4_1	3	2	22.5	22.75	92.72	73.96
4_1	3	3	22.75	23	92.72	73.96
4_1	4	1	34	34.25	108	92.92
4_1	4	2	34.25	34.5	108	92.92
4_1	4	3	34.5	34.75	108	92.92

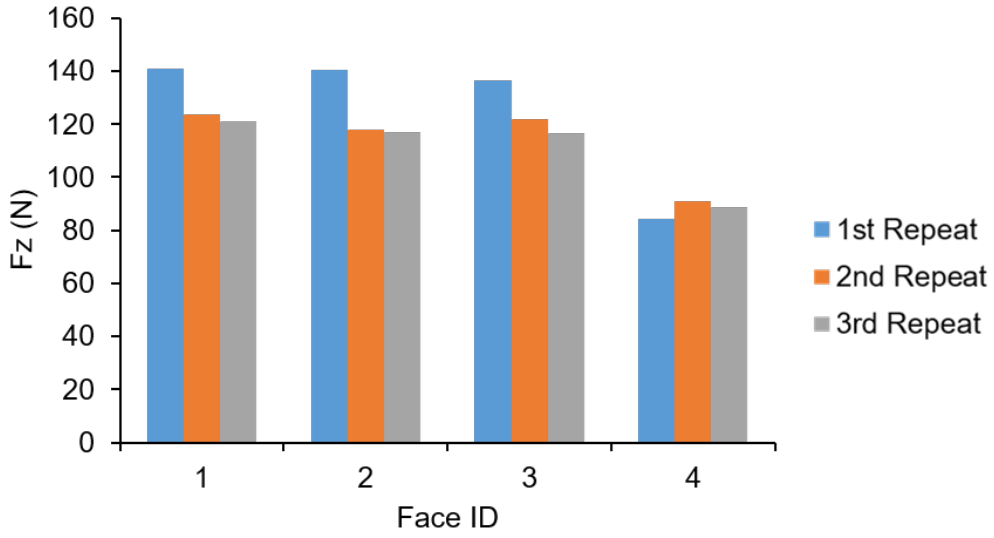

Figure 7.65: Forces in the Z direction measured for repeat passes for each facing pass performed on billet 4_1, the coordinate positions of the tool at the start and end of each pass are displayed in Table 7.9.

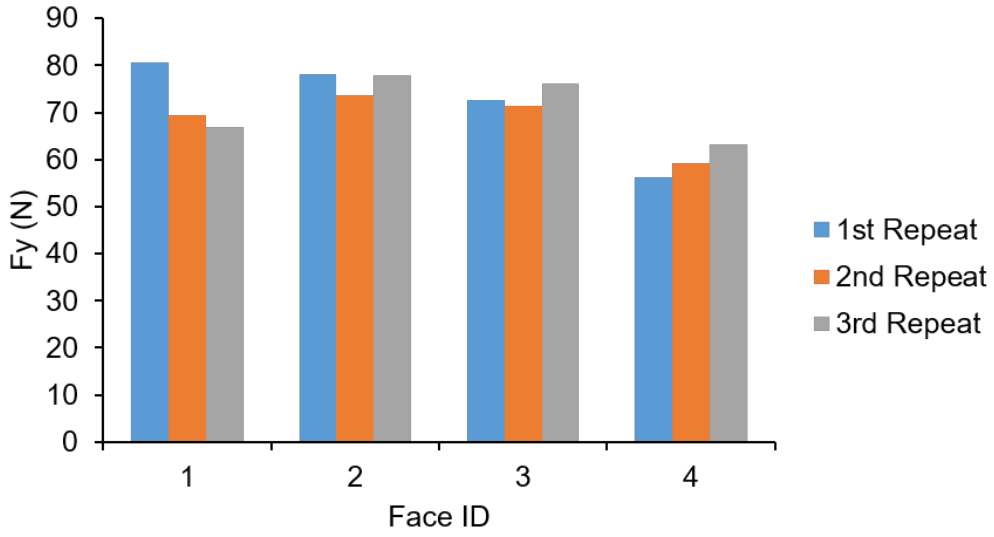

Figure 7.66: Forces in the Y direction measured for repeat passes for each facing pass performed on billet 4_1, the coordinate positions of the tool at the start and end of each pass are displayed in Table 7.9.

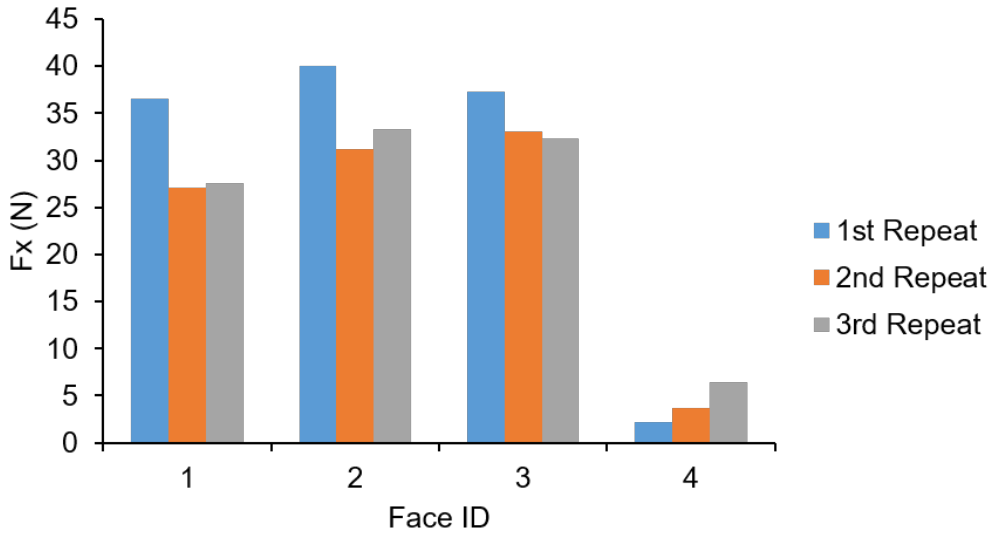

Figure 7.67: Forces in the X direction measured for repeat passes for each facing pass performed on billet 4_1, the coordinate positions of the tool at the start and end of each pass are displayed in Table 7.9.

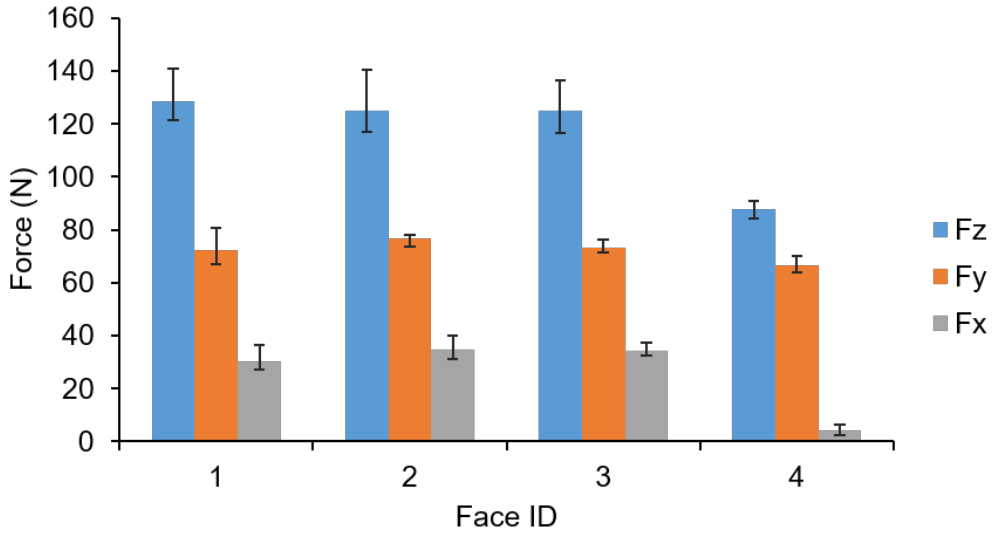

Figure 7.68: Cutting forces in the 3 coordinate direction averaged over the repeats of facing passes performed on billet 4_1, the coordinate positions of the tool at the start and end of each pass are displayed in Table 7.9.

Tool Wear Examination

Figure 7.69 to Figure 7.72 show example of the tools after machining passes on each of the four produced faces. The tool wear images reveal consistently low level of wear for each of the faces. This indicates that both tool engagement and cutting times are consistent across the faces. As tool wear greatly influences the cutting forces as previously demonstrated during the semi-finishing passes, the consistently low wear on the tools means that the cutting forces over the duration of the pass on each face are directly comparable with each other.

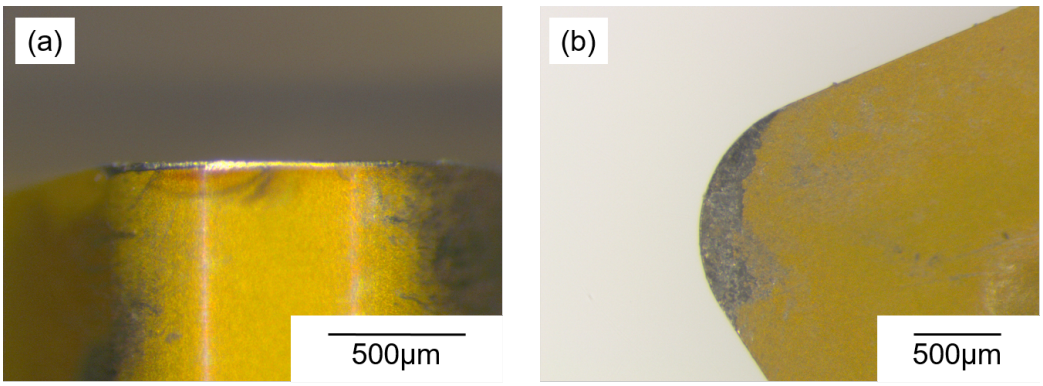

Figure 7.69: Example tool wear produced during face turning of face 1 of billet 4_1. The tool shown was used during the 3rd repeat of face 1. The tool shown is representative of all passes performed on face 1.

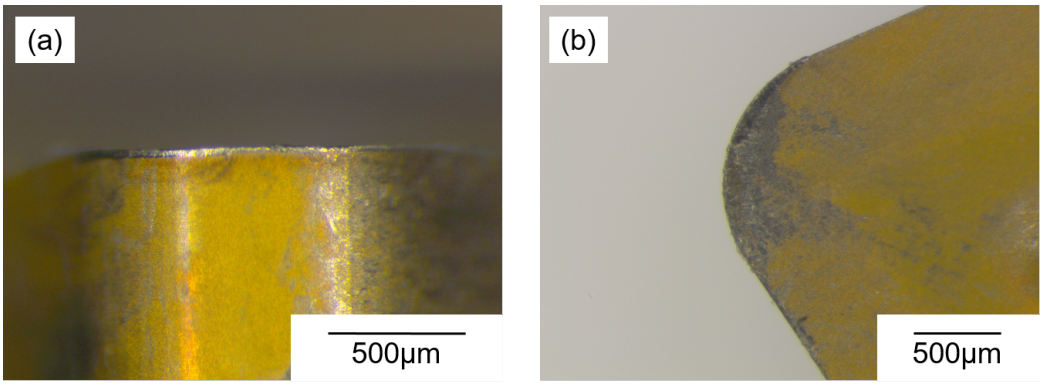

Figure 7.70: Example tool wear produced during face turning of face 2 of billet 4_1. The tool shown was used during the 3rd repeat of face 2. The tool shown is representative of all passes performed on face 2.

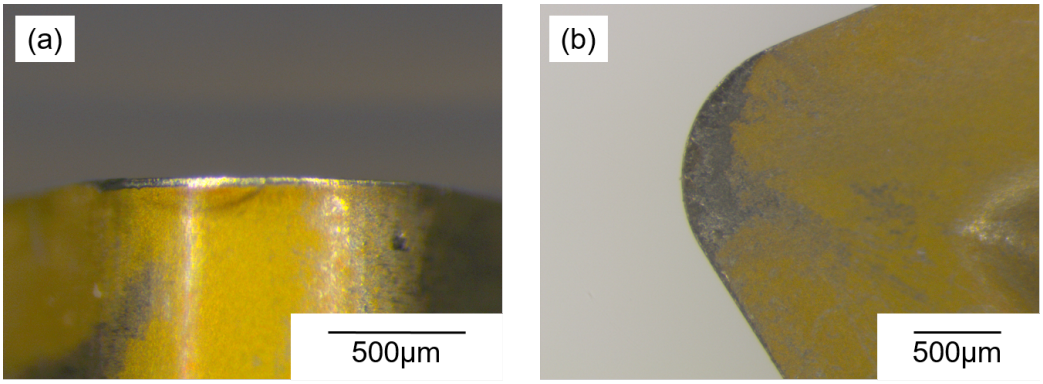

Figure 7.71: Example tool wear produced during face turning of face 3 of billet 4_1. The tool shown was used during the 3rd repeat of face 3. The tool shown is representative of all passes performed on face 3.

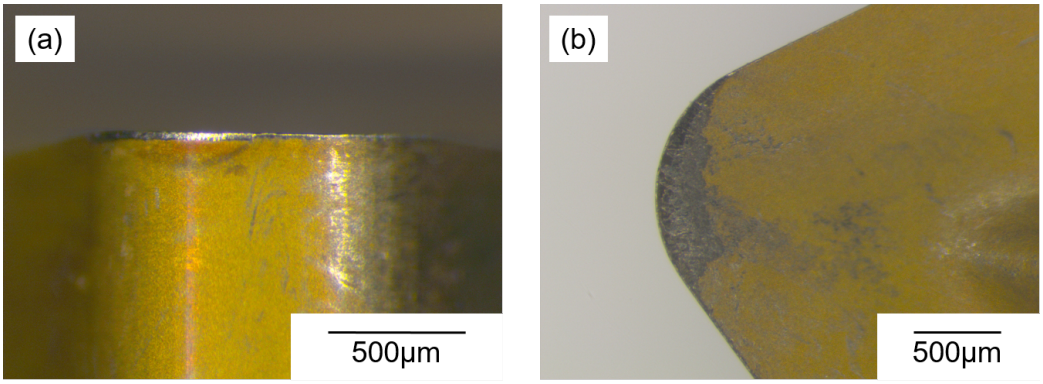

Figure 7.72: Example tool wear produced during face turning of face 4 of billet 4_1. The tool shown was used during the 3rd repeat of face 4. The tool shown is representative of all passes performed on face 4.

Subsurface Damage Examination

Scanning electron micrographs of the subsurface microstructure for each of the four machined faces are displayed in Figure 7.73. The dimensions of facing passes performed are described in Table 7.9 and the naming convention for each face in Figure 7.11. It can be observed that the grain size at face 1 is significantly larger than that at faces 2-4. Face 1 corresponds to the region close to both the exterior surface and the centreline of the billet and will likely be located within the dead-zone of the uni-axial forging. This means the area will have been exposed to relatively low stain and has remained un-recrystallised. This explains the relatively large grain size at the

face 1 subsurface, in comparison with other faces. It can be observed that the grain size appears to be similar at faces 2-4. Comparing these regions with the as HIP material it can be observed that the grain size has been reduced indicating recrystallisation has occurred during forging. It can be seen that all 3 faces present evidence of retained deformation as evident by the misorientation contrast in the backscatter electron micrographs.

Considering the observable subsurface damage, all 4 subsurfaces present a heavily distorted layer at the surface which extends into the subsurface by approximately 3-4 μm when viewed in the backscatter micrographs. In the etched condition secondary electron micrographs however, the highly deformed layer is not observable. This suggests that the heavily deformed layer is not amorphous white layer and is instead a region with highly concentrated strain which leads to areas of misorientation contrast which prevents the underlying grain structure from being observed.

Beneath this heavily deformed layer, the evidence of subsurface deformation varies across the four machined faces. In faces 2-4, very little deformation can be observed with slight evidence of contrast observable in the BSE micrographs. In the SE micrographs, evidence of deformation near surface is observable particularly for face 2 and to a lesser extent in face 1. For face 1 however, subsurface damage is both more obvious and extents deeper into the subsurface compared with faces 2-4. In the BSE micrograph for face 1, clear misorientation contrast is observable to an approximate depth of 25 μm. In the SE micrograph for face 1, clear evidence of strain is seen in near surface grains. Two slip band directions are seen in the subsurface with one orientated at near perpendicular angles to the machined surface and others orientated at angle close to parallel to the machined surface.

It can also be noted that the observable precipitate morphologies can be seen to be visually consistent across all faces with prominent primary γ' placed along grain boundaries and triple points. The presence of the primary γ' indicates that the forging temperature remained below solvus during the forging as these precipitates retained from the as HIP material. Evidence of slip bands extending into the γ' precipitates are observable in face 1. No evidence of near surface precipitate deformation is observable in the SE micrographs for faces 2-4.

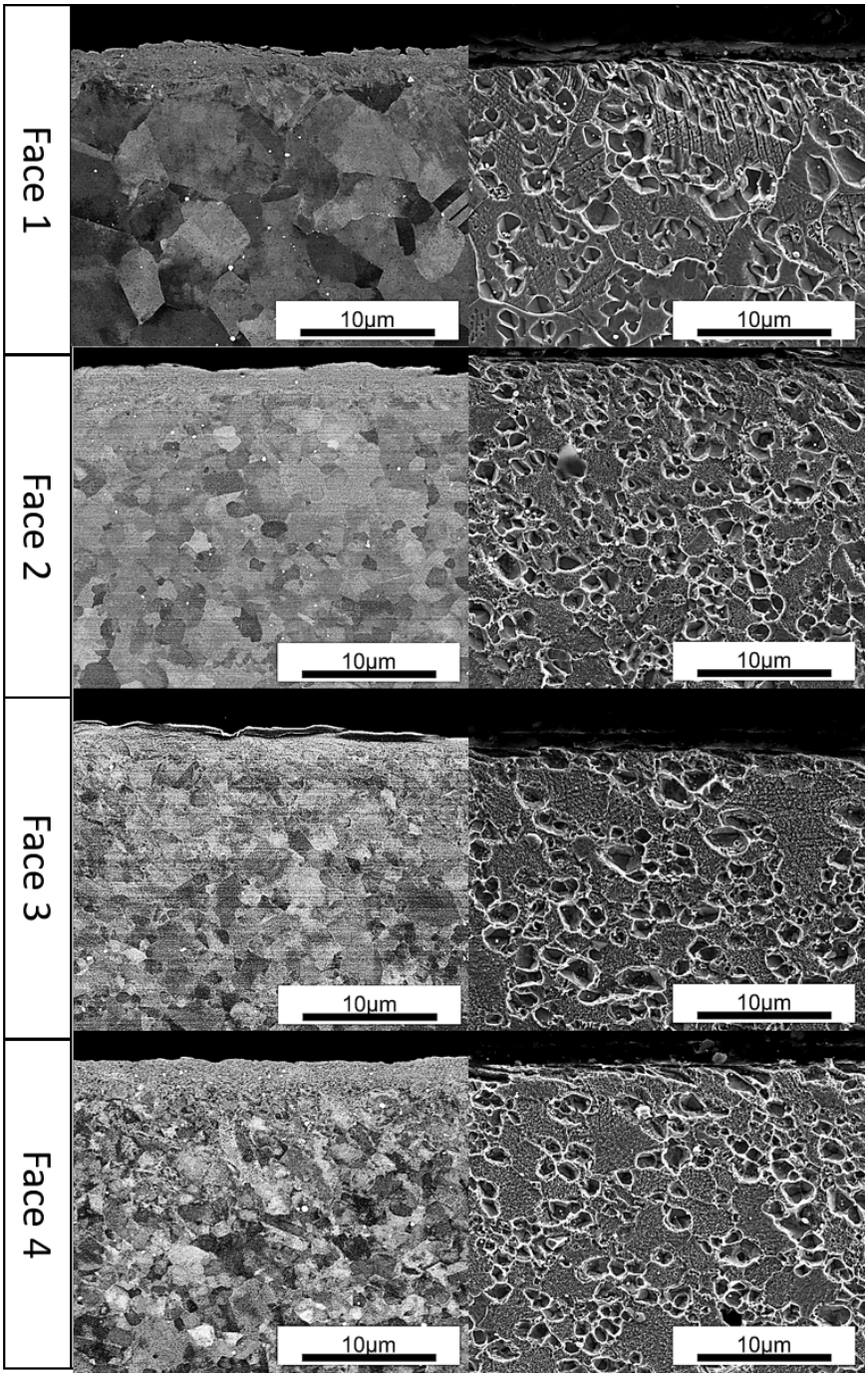

Figure 7.73: Backscatter and secondary electron micrographs showing the subsurface damage observed in the 4 faces machined on billet 4_1. Backscatter electron micrographs were captured with the sample in the polished condition, the secondary electron micrographs were captured with the sample in etched condition.

7.6.2 Billet 3_2

Measured Cutting Forces

A summary of the facing passes performed on the 3_2 billet is shown in Table 7.10. As was the case for the 4_1 billet, 4 faces were machined in varying longitudinal and radial positions across the billet to produce the geometry described in Figure 7.11. Consistent with the 4_1 billet with at least 2 repeats of each facing pass, the cutting forces were averaged for the first second of tool engagement, during the last second of tool engagement and over the duration of tool engagement during each pass.

The cutting forces averaged over the duration of tool engagement for the cutting (Z) direction are shown in Figure 7.74. As can be observed, the cutting forces show a similar trend to those observed in the 4_1 billet. The first repeat demonstrates significantly higher forces (particular for face 4). For the second repeat pass the forces are significantly reduced. This behaviour is consistent across all four faces. Significant scatter in the cutting forces measured for the first pass performed on each surface can be observed. Subsequent passes performed produced more consistent force across the four faces.

Considering the cutting forces in the Y direction, as shown in Figure 7.75, it can be seen that the forces are more inconsistent compared with forces measured in the Z direction. In contrast with the Z direction, the forces in the Y direction for the first repeat pass on each surface are not always higher than subsequent passes but again significant scatter in the measured force can be observed during the first pass with more consistent forces measured after the first pass. The same observations can be made for the X direction cutting forces.

A summary chart of the cutting forces showing the results of averaging the forces in each of the 3 principle directions for all of the repeats performed is shown in Figure 7.77. The chart indicates that according to the average force values, the cutting forces across each of the faces can be considered equivalent in all 3 principle directions. Similar to billet 4_1, it can be therefore inferred that microstructural change across the 4 faces is either non-existent or the changes that are present do not affect the cutting forces.

Table 7.10: Cutting dimensions employed during each facing pass performed on billet 3_2.

Billet	Face	Repeat	Z_s (mm)	Z_f (mm)	D_s (mm)	D_f (mm)
3_2	1	1	0.25	0.5	47	14
3_2	1	2	0.5	0.75	47	14
3_2	2	1	16.91	17.16	65.9	47
3_2	2	2	17.16	17.41	65.9	47
3_2	2	3	17.41	17.66	65.9	47
3_2	3	1	31.83	32.08	81.4	65.9
3_2	3	2	32.08	32.33	81.4	65.9
3_2	4	1	47.5	47.75	94	81.4
3_2	4	2	47.75	48	94	81.4
3_2	4	3	48	48.25	94	81.4

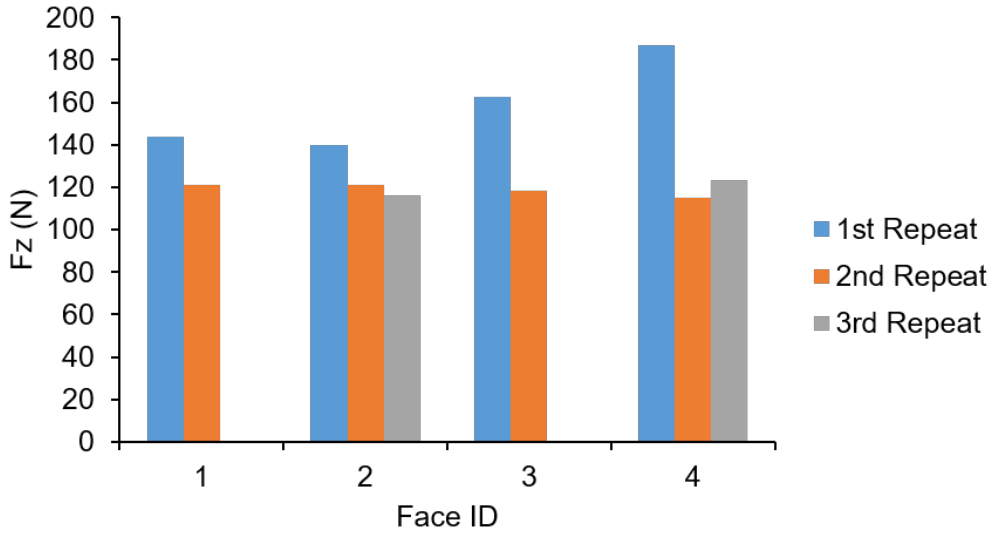

Figure 7.74: Forces in the Z direction measured for repeat passes for each facing pass performed on billet 3_2, the coordinate positions of the tool before and after each cut are displayed in Table 7.10.

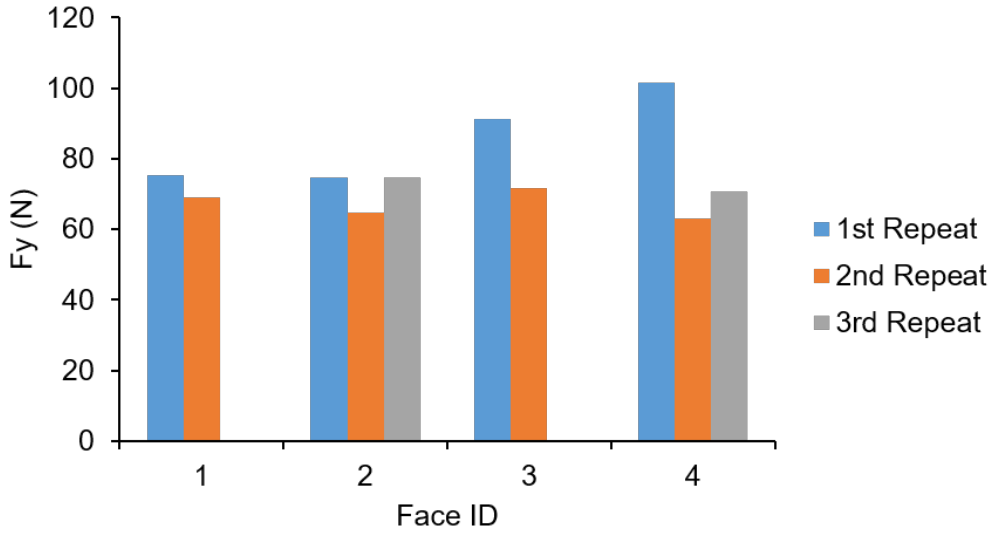

Figure 7.75: Forces in the Y direction measured for repeat passes for each facing pass performed on billet 3_2, the coordinate positions of the tool before and after each cut are displayed in Table 7.10.

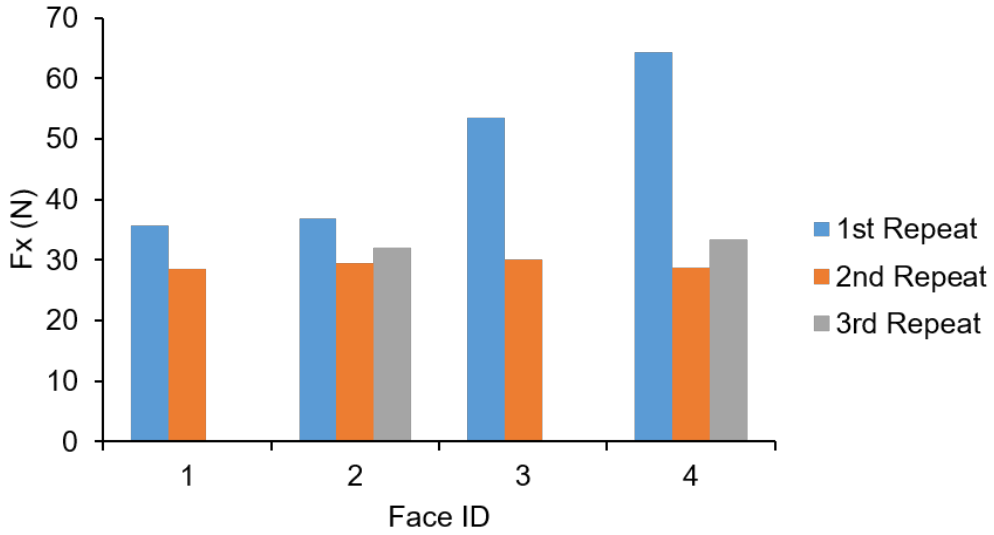

Figure 7.76: Forces in the X direction measured for repeat passes for each facing pass performed on billet 3_2, the coordinate positions of the tool before and after each cut are displayed in Table 7.10.

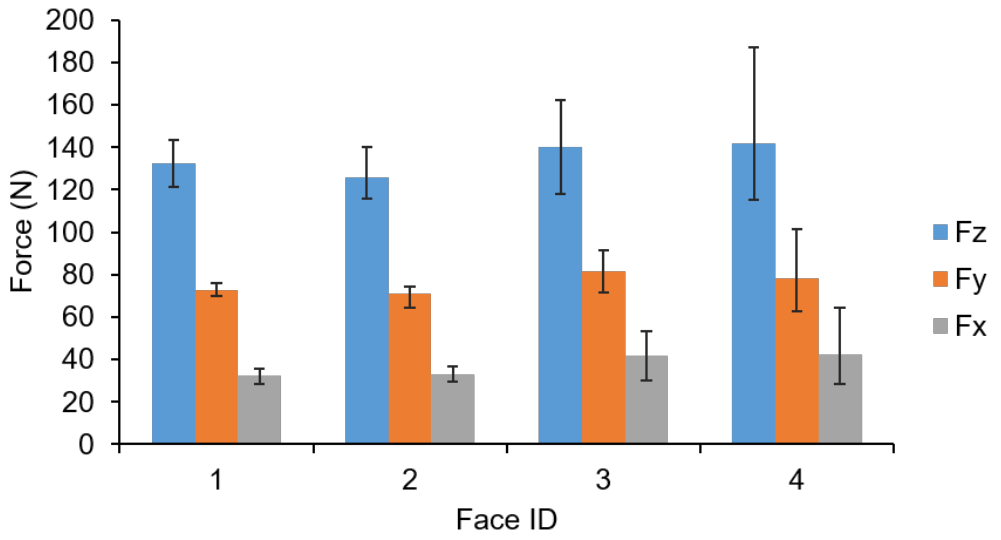

Figure 7.77: Cutting forces in the 3 coordinate direction averaged over the repeats of facing passes performed on billet 3_2, the coordinate positions of the tool before and after each cut are displayed in Table 7.10.

Tool Wear Examination

The images displayed in Figure 7.78 to 7.81 represent typical examples of the tools after completion of the facing passes on each of the four surfaces. As was the case for the 4_1 billet, the tools display a very low level of flank wear of the order of 10μm consistently across all four machined faces. Each of the rake faces present some discolouration but no evidence of notch wear. Small chipping in the tool can be observed in Figure 7.80, which was used to perform the second repeat of the facing pass on face 3. This tool produced no anomalous cutting forces in the preceding figures and therefore will likely have occurred as the tool comes into contact with neighbouring step as described in Figure 6.11. With the low level of tool wear, the forces averaged over the entire cut duration are therefore justified and can be reasonably compared in Figure 7.77.

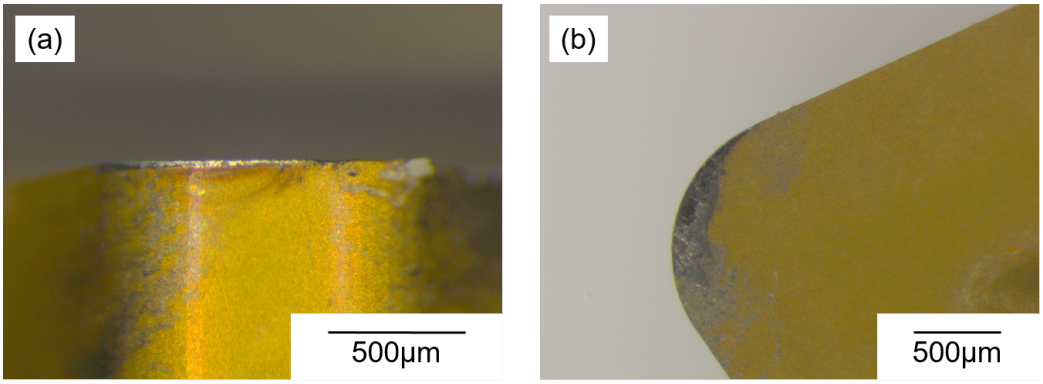

Figure 7.78: Example tool wear produced during face turning of face 1 on billet 3_2. The tool shown was used during the 1st repeat of face 1. The tool shown is representative of all passes performed on face 1.

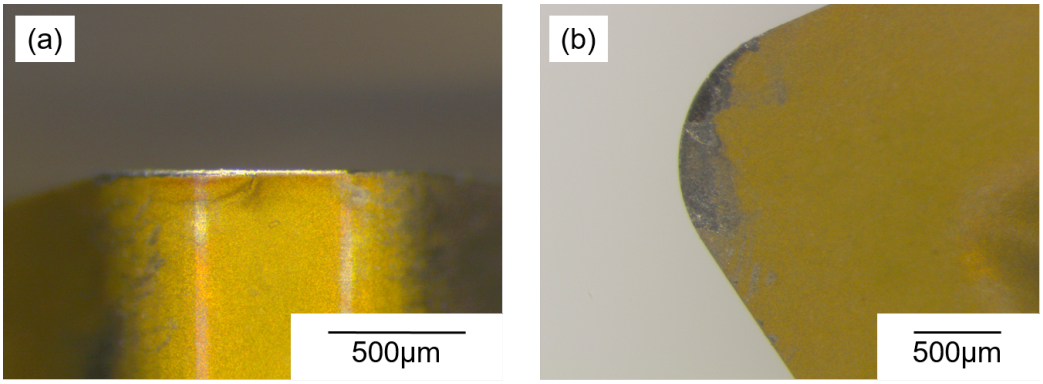

Figure 7.79: Example tool wear produced during face turning of face 2 on billet 3_2. The tool shown was used during the 1st repeat of face 2. The tool shown is representative of all passes performed on face 2.

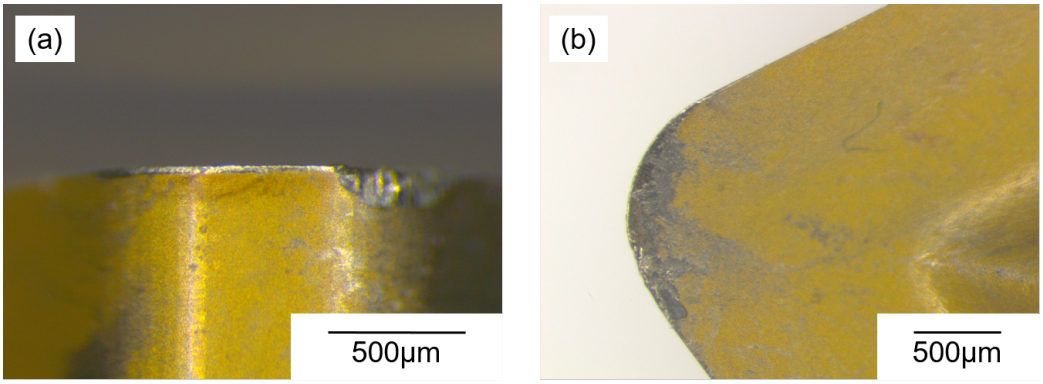

Figure 7.80: Example tool wear produced during face turning of face 3 on billet 3_2. The tool shown was used during the 2rd repeat of face 3. The tool shown is representative of all passes performed on face 3.

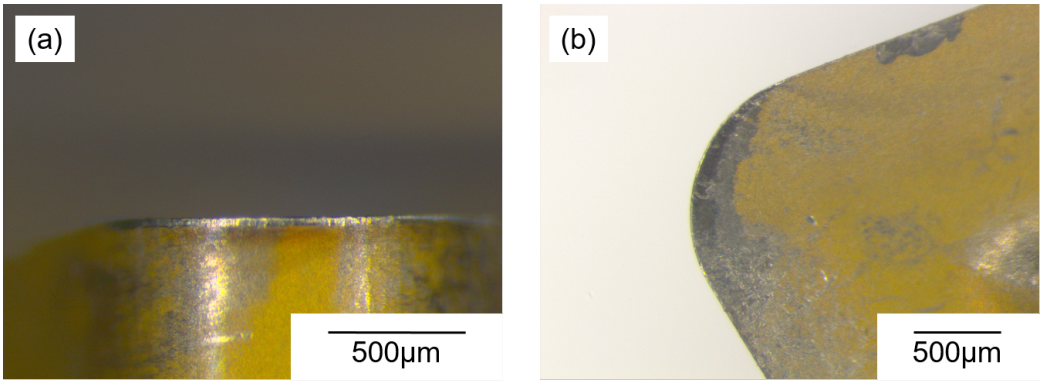

Figure 7.81: Example tool wear produced during face turning of face 4 on billet 3_2. The tool shown was used during the 1st repeat of face 4. The tool shown is representative of all passes performed on face 4.

Subsurface Damage Examination

Images of the subsurface microstructure at each of the 4 machined faces are shown in Figure 7.82 in both the as polished, viewed under backscatter electron imaging and in the etched condition, viewed under secondary electron imaging. As can be observed, all surfaces display evidence of subsurface damage as a result of the facing operation. As was previously noted for billet 4_1 the grain size of the section across face 1 is considerably larger than faces 2-4. As previously noted, the subsurface deformation, consisting of slip bands, is most visible in face 1. slip bands are visible in faces 2-4 however they appear to persist to a shallower depth to those seen in face 1.

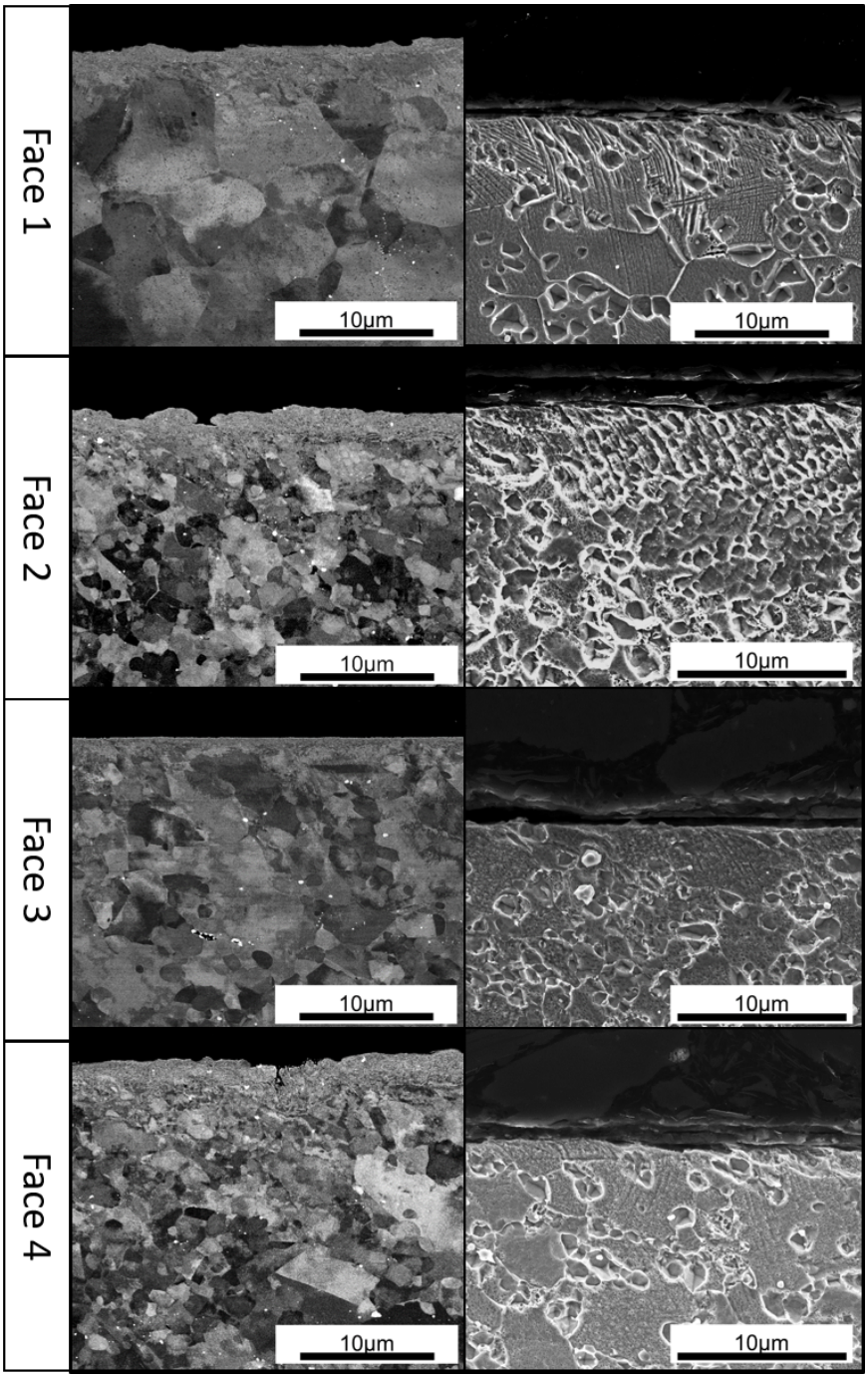

Figure 7.82: Backscatter and secondary electron micrographs showing the subsurface damage observed in the 4 faces machined on billet 3_2. Backscatter electron micrographs were captured with the sample in the polished condition, the secondary electron micrographs were captured with the sample in etched condition.

7.6.3 Billet 3_1

Measured Cutting Forces

The measured cutting forces for the facing passes detailed in Table 7.11 for billet 3_1 are shown in Figures 7.83-7.85. The results for billet 3_1 reveal that the first repeat pass does not consistently exhibit higher Z direction cutting forces than subsequent passes in contrast with billet 3_2. Scatter across repeats is apparent. Comparing a summary of the cutting forces across all faces and repeats performed in Figure 7.86 it can be seen that the cutting forces can be considered consistent across all faces. Billet 3_1 represents the highest level of consistency in terms of cutting forces in all directions across all four machined faces.

Table 7.11: Cutting dimensions employed during each facing pass performed on billet 3_1.

Billet	Face	Repeat	Z_s (mm)	Z_f (mm)	D_s (mm)	D_f (mm)
3_1	1	1	0.25	0.5	55.84	14
3_1	1	2	0.5	0.75	55.84	14
3_1	1	3	0.75	1	55.884	14
3_1	2	1	14.25	14.5	76.5	55.84
3_1	2	2	14.5	14.75	76.5	55.84
3_1	3	1	28.25	28.5	93.29	76.5
3_1	3	2	28.5	28.75	93.29	76.5
3_1	4	1	42.25	42.5	108	93.29
3_1	4	2	42.5	42.75	108	93.29

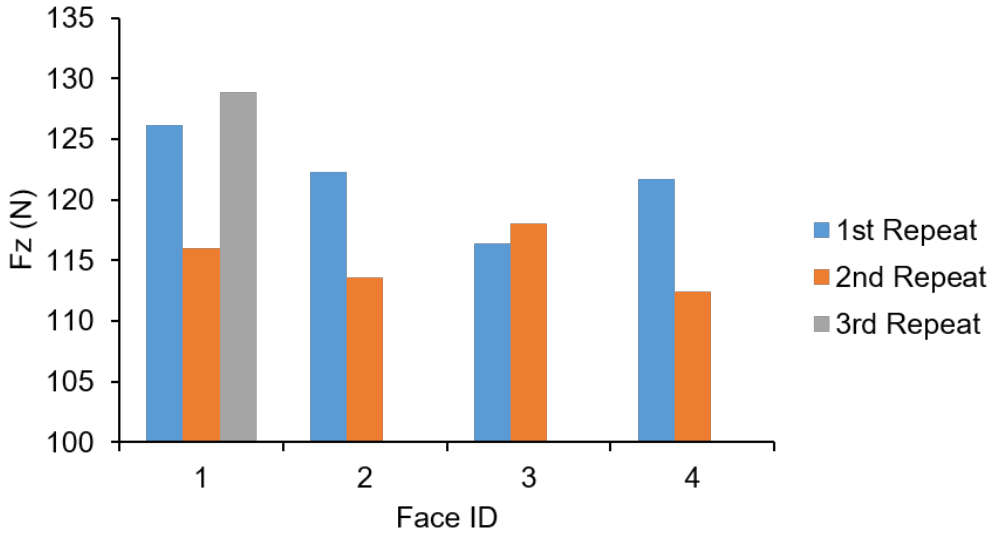

Figure 7.83: Forces in the Z direction measured for repeat passes for each facing pass performed on billet 3_1, the coordinate positions of the tool before and after each cut are displayed in Table 7.11.

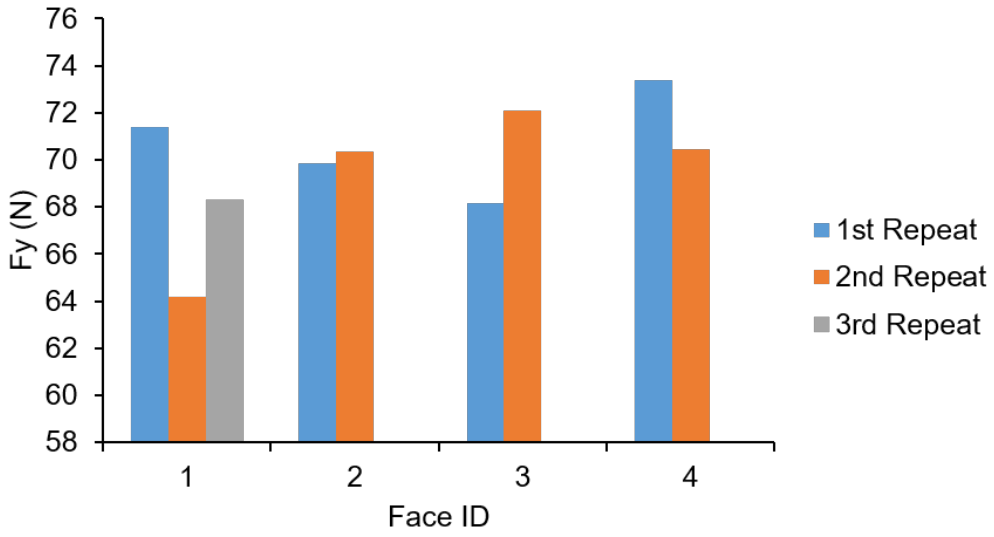

Figure 7.84: Forces in the Y direction measured for repeat passes for each facing pass performed on billet 3_2, the coordinate positions of the tool before and after each cut are displayed in Table 7.11.

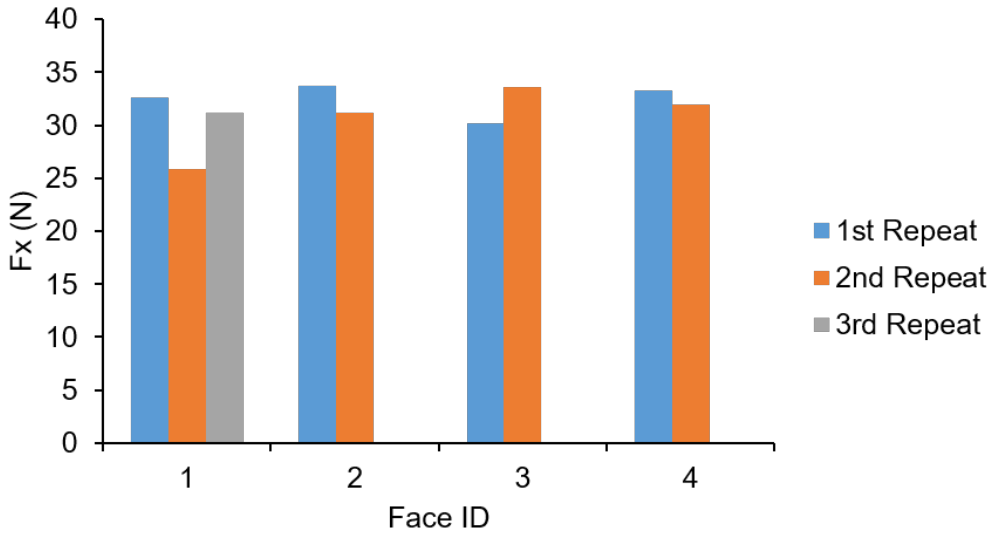

Figure 7.85: Forces in the X direction measured for repeat passes for each facing pass performed on billet 3_1, the coordinate positions of the tool before and after each cut are displayed in Table 7.11.

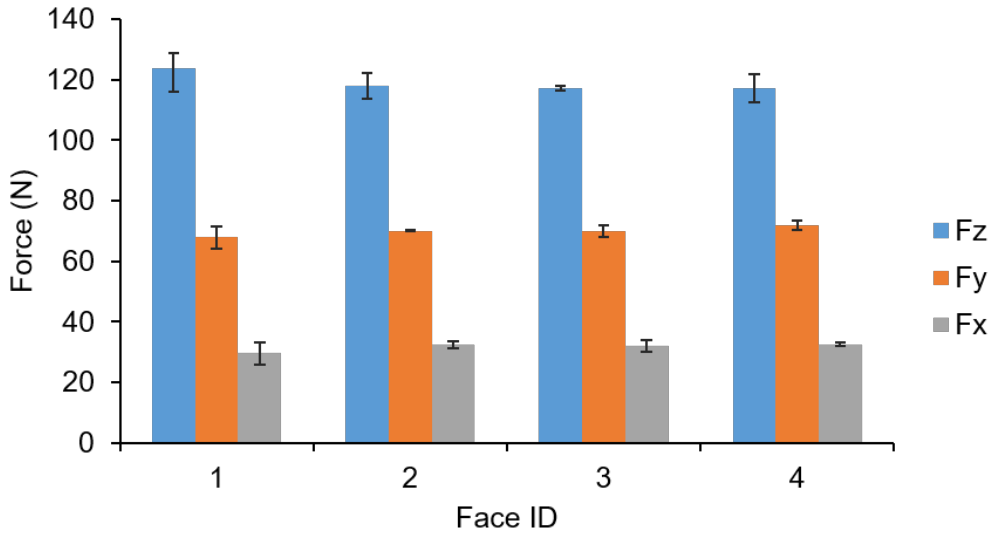

Figure 7.86: Cutting forces in the 3 coordinate direction averaged over the repeats of facing passes performed on billet 3_1, the coordinate positions of the tool before and after each cut is displayed in Table 7.11.

Tool Wear Examination

As found for billets 4_1 and 3_2, the cutting tools used during the facing trials showed consistent levels of tool wear as shown in Figures 7.87 to 7.90.

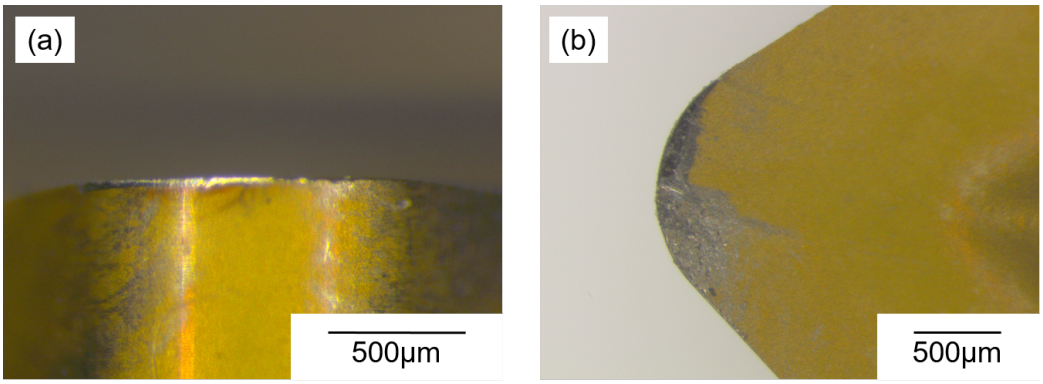

Figure 7.87: Example tool wear produced during face turning of face 1 on billet 3_1. The tool shown was used during the 1st repeat of face 1. The tool shown is representative of all passes performed on face 1.

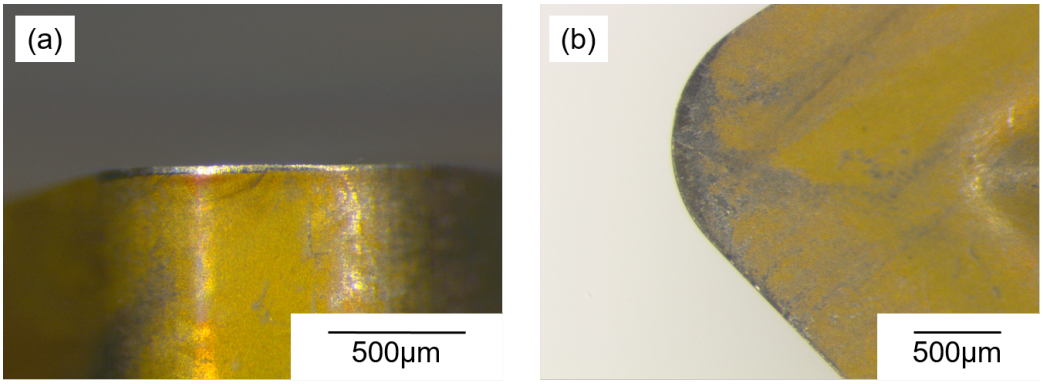

Figure 7.88: Example tool wear produced during face turning of face 2 on billet 3_1. The tool shown was used during the 1st repeat of face 2. The tool shown is representative of all passes performed on face 2.

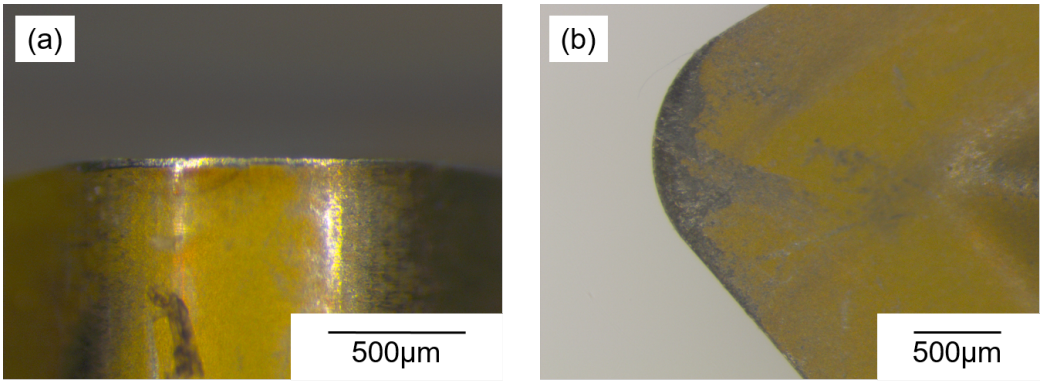

Figure 7.89: Example tool wear produced during face turning of face 3 on billet 3_1. The tool shown was used during the 1st repeat of face 3. The tool shown is representative of all passes performed on face 3.

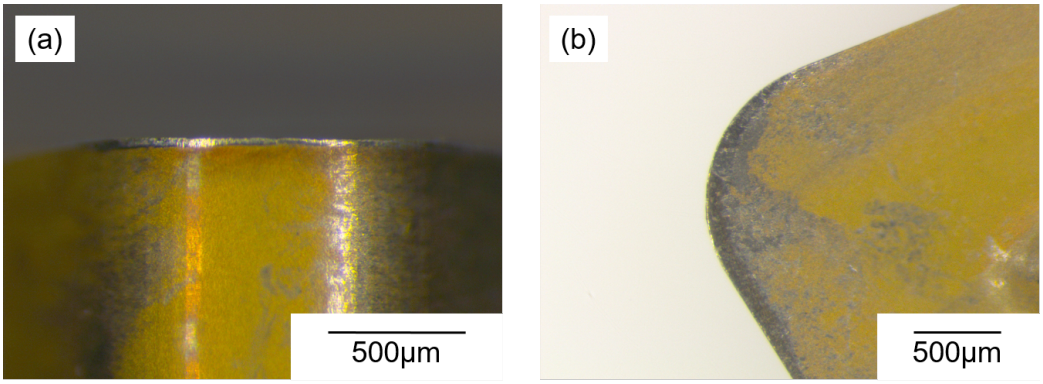

Figure 7.90: Example tool wear produced during face turning of face 4 on billet 3_1. The tool shown was used during the 1st repeat of face 4. The tool shown is representative of all passes performed on face 4

Subsurface Damage Examination

Examination of the subsurface damage across faces 1 to 4 for billet 3_1 showed they were consistent with billets 4_1 and 3_2 with face 1 containing a larger grain structure compared with faces 2-4 and more apparent damage both viewed with BSE and SE imaging, as shown in Figure 7.91. The consistency in cutting forces across all four faces therefore suggests that the underlying microstructure at the face being machined has little impact on the cutting forces in the as forged material.

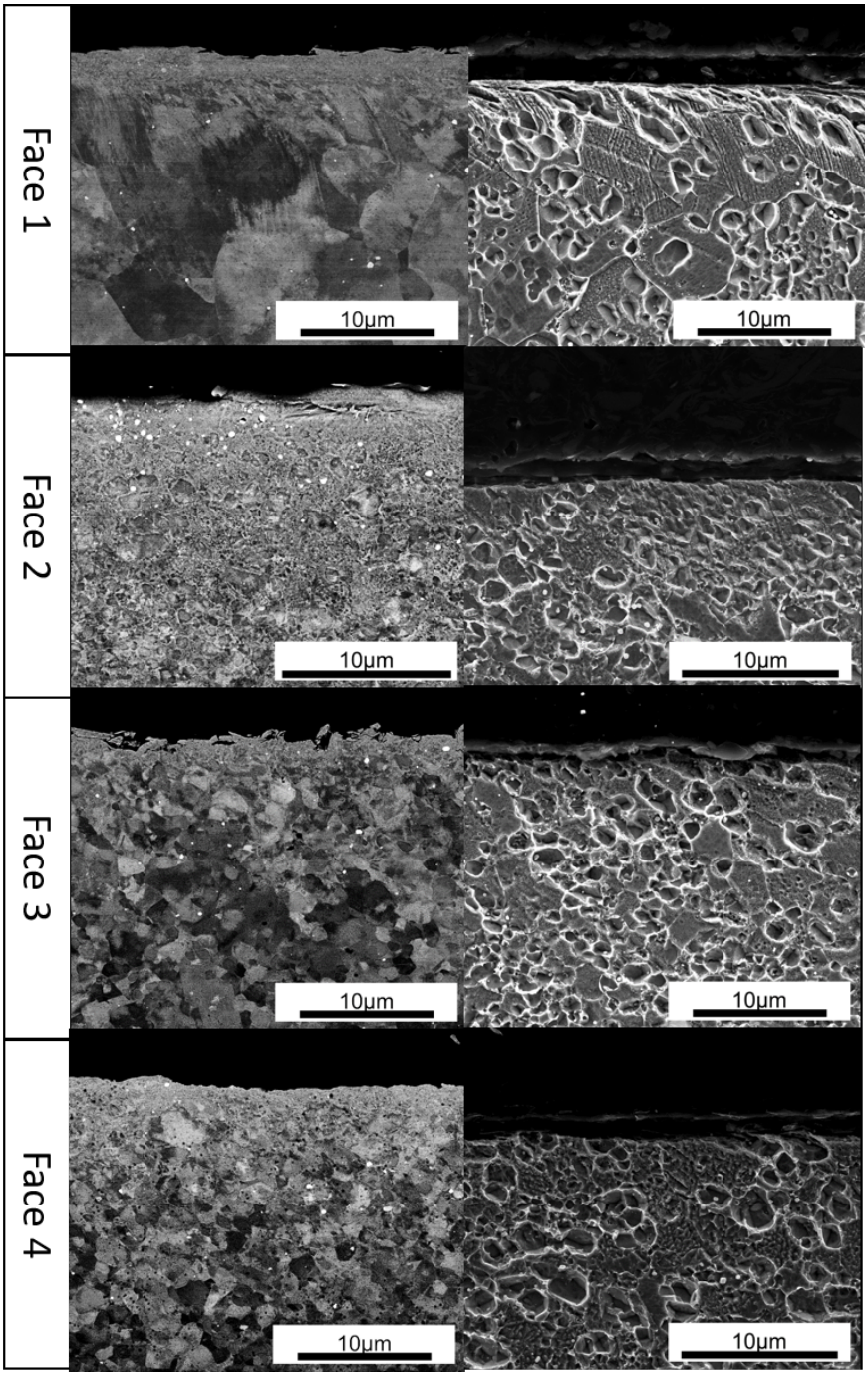

Figure 7.91: Backscatter and secondary electron micrographs showing the subsurface damage observed in the 4 faces machined on billet 3_1. Backscatter electron micrographs were captured with the sample in the polished condition, the secondary electron micrographs were captured with the sample in etched condition.

7.6.4 As-HIP billet

Measured Cutting Forces

The cutting forces measured for facing passes performed on as-HIP material with the finishing parameters outlined in Section 7.4.1 are displayed in Figure 7.92. As can be expected the cutting forces are consistent across the two repeats performed, which is expected for material which is homogeneous.

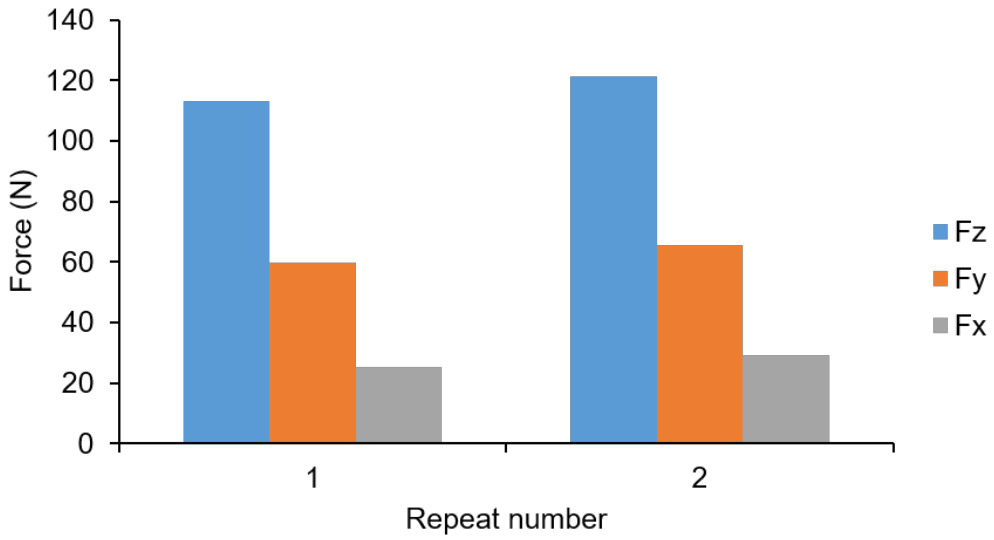

Figure 7.92: Cutting forces in the 3 coordinate direction averaged over the repeats of facing passes performed on billet 3_1, the coordinate positions of the tool before and after each cut are displayed in Table 7.11.

7.6.5 Characterisation of the As-forged Billet Microstructures

Figures 7.93 to 7.95 show the bulk microstructures observed for each of the three machined billets at each of the examined surfaces. It can be observed that at face 1 each of the billets contains a coarser microstructure, likely due to face being within the low strain dead zone of each forging, leading to an unrecrystallised microstructure. It can be observed that faces 2-4 on each of the billets contain a similar microstructure with similar size γ grains present across all three billets.

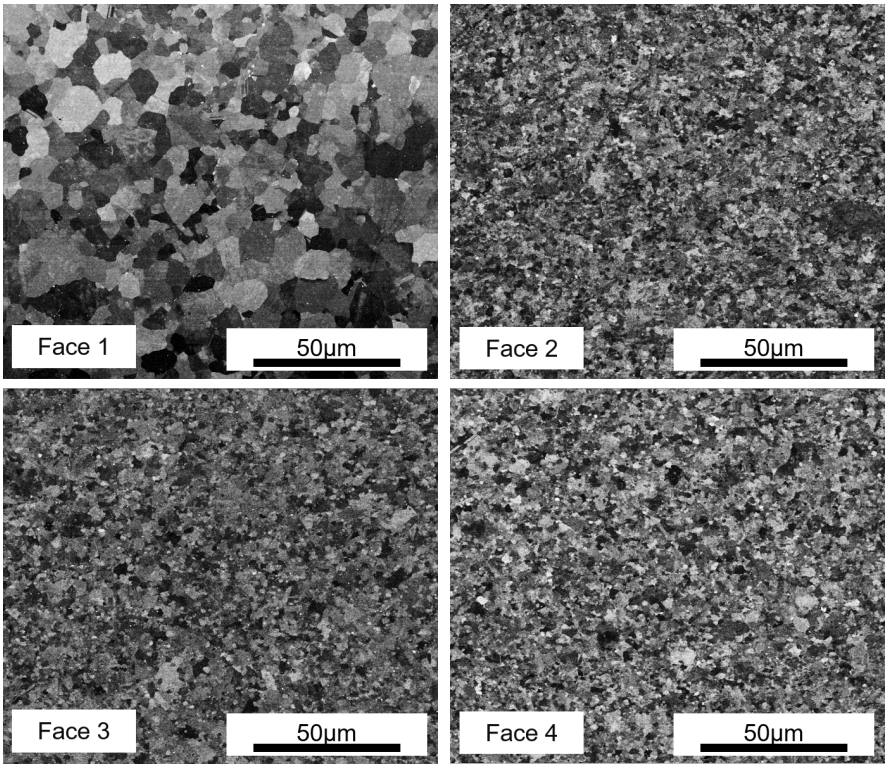

Figure 7.93: Backscatter electron micrographs showing the bulk γ grain microstructure at the four faces examined for billet 4_1.

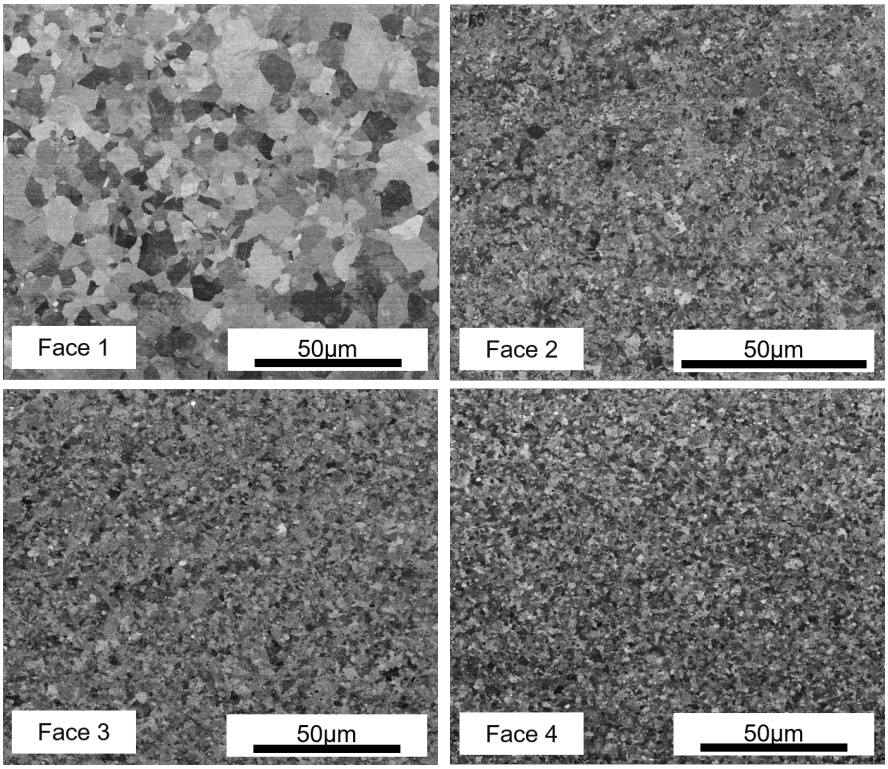

Figure 7.94: Backscatter electron micrographs showing the bulk γ grain microstructure at the four faces examined for billet 3_1.

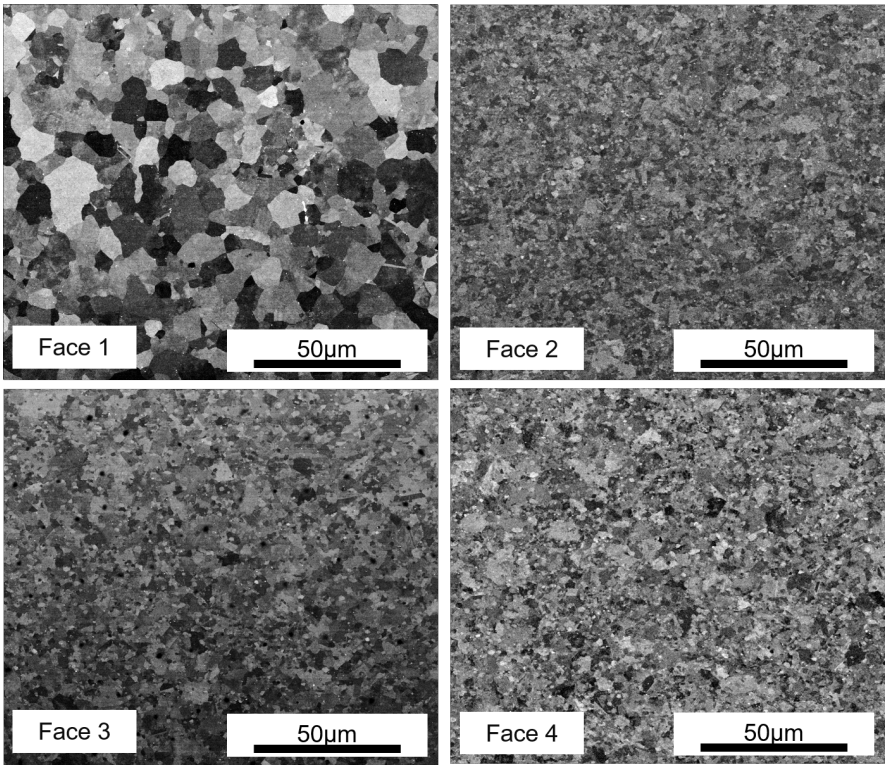

Figure 7.95: Backscatter electron micrographs showing the bulk γ grain microstructure at the four faces examined for billet 3_2.

7.6.6 Observations Regarding Cutting forces and Billet Microstructural Variations

A summary chart of the cutting forces measured in the Z (cutting) direction for the facing trials performed for each billet is shown in Figure 7.96. The values plotted are the average values across repeats for each face and billet. The chart suggests that although there is scatter in the measurements, there is evidence to suggest that the variations in forging across each billet have a negligible impact on the forces during machining with fixed process parameters. This is especially apparent given the forces measured for the as HIP billet are equivalent to those seen for the forged billets. As previously demonstrated, the billets all have considerably larger grains at face 1 than other faces, however this does not produce a consistent variation in cutting forces when comparing face 1 with the other faces for all 3 forged billets. This is in direct contrast with the observations during the machining of the as FAST material in Chapter 6 where the use of a super-solvus dwell temperature resulted in an increased grain size which resulted in a lower cutting

force when machined. The level of scatter in the measured cutting forces for the as-HIP material is comparable to that observed between faces for many of the as-Forged billets. This provides further evidence that the microstructure has little effect on the the measured cutting forces for the machining parameters considered.

Reviewing the microstructures of all billets, it can be observed that the precipitate morphologies are similar regardless of the surrounding microstructure at each of the faces for each billet in Figures 7.73, 7.82 and 7.91. For the as FAST material, super-solvus dwell conditions during consolidation produced a finer precipitate morphology. It is expected that this change in morphology may result in the variation in cutting forces seen. As the as-forged billets underwent no normalisation heat treatment, there are potential residual stress effects that would further influence the cutting forces. Residual stresses are not expected for the as-FAST material due to the limited deformation during consolidation and long cool down times in contrast with the air-cool of the as-forged billets.

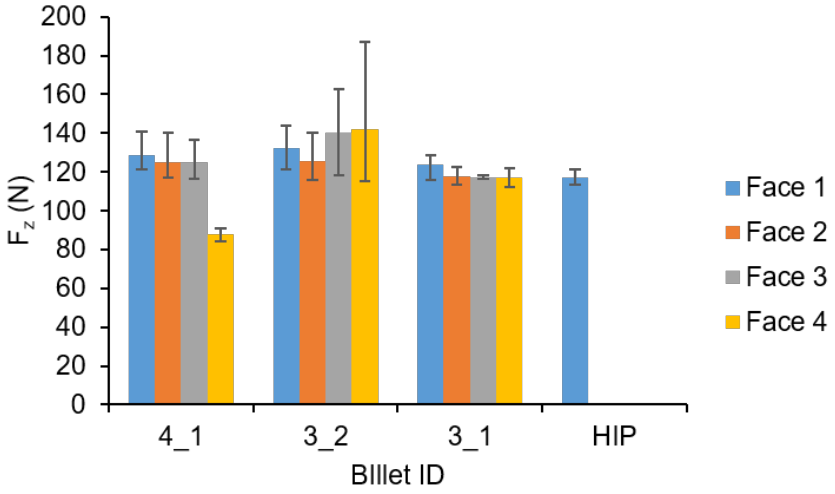

Figure 7.96: Summary of the Z direction cutting forces averaged across repeats on each face of each forged billet, compared with the as HIP material.

7.6.7 Observations Regarding Subsurface Damage

Misorientation Contrast Imaging of Near Surface Deformation

In general the subsurface observed post machining can be seen in Figure 7.97 and Figure 7.98 for a coarser grain structure and finer grain structure respectively. The subsurface consists of 3 distinct layer which can easily

be distinguished. The first layer identified as (a) in Figures 7.97 and 7.98 which is a heavily distorted layer, where the deformation is so severe that the microstructure cannot be easily resolved, and therefore appears amorphous. This description matches what some authors refer to as white layer due to its unresolvable nature. Below this layer we have a subsurface deformed layer identified as (b), the nature of this layer is such that misorientation contrast can be observed within grains which suggests stored strain energy due to deformation taking place in the form of slip and lattice rotation. The final layer (c) is where the microstructure does not contain any obvious deformation and can therefore be considered to be representative of the un-deformed bulk material. For the 3_2 billet the subsurface of face 1 (Figure 7.97) and face 4 (Figure 7.98) show very different grain structures, however the same 3 layers are observable with varying degrees of thickness', even though the machining conditions were the same. This suggests that for the same machining parameters, the observable modes of subsurface damage through misorientation contrast BSE imaging are similar.

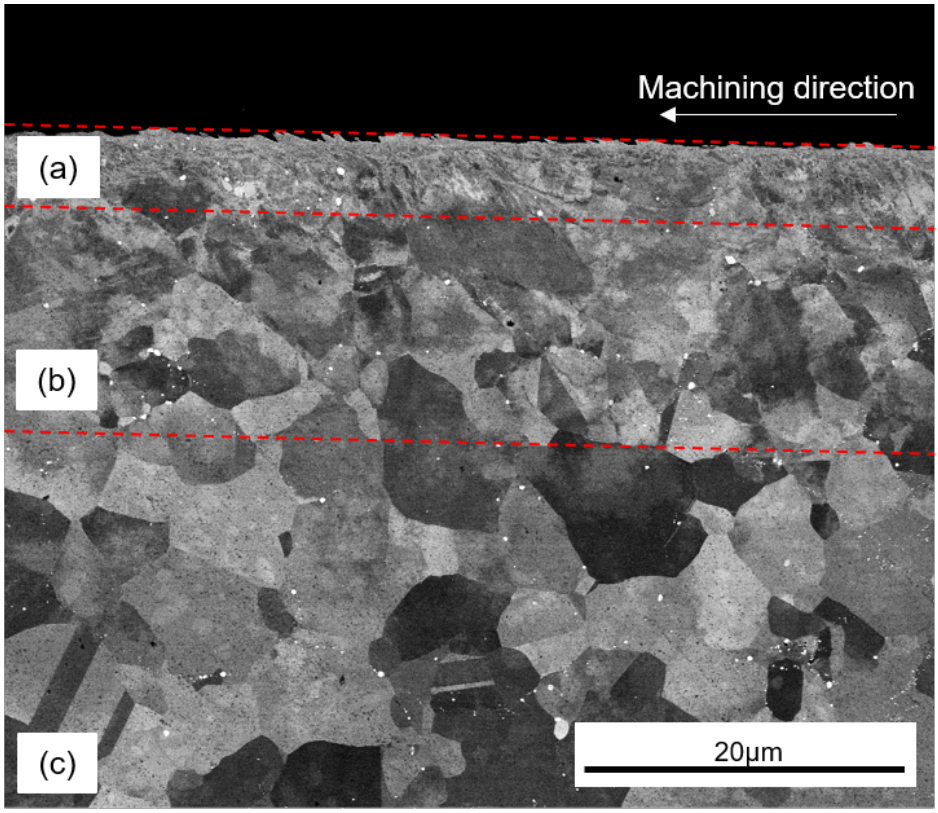

Figure 7.97: General form of the subsurface in a region of coarser grains as observed using backscatter electrons. Imaged from Face 1 of billet 3_2, showing (a) a highly deformed amorphous surface layer, (b) A deformed crystalline subsurface with clear misorientation contrast indicating deformation and (c) the un-deformed subsurface.

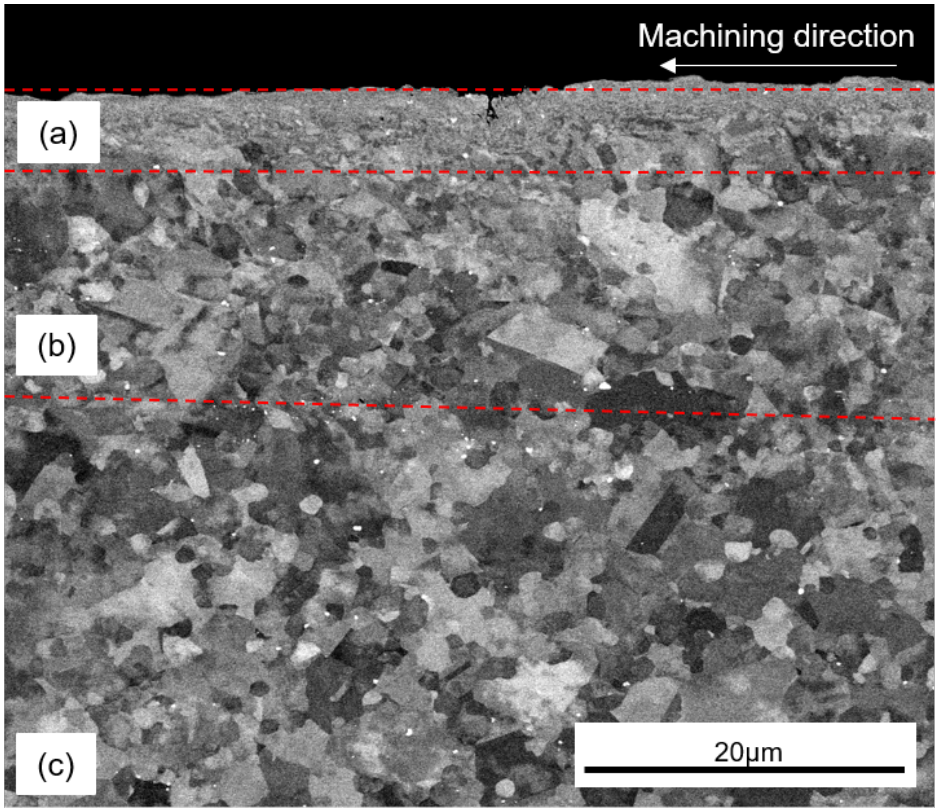

Figure 7.98: General form of the subsurface in a region of finer grain structure as observed using backscatter electron microscopy. Imaged from Face 4 of billet 3_2, showing (a) a highly deformed amorphous surface layer, (b) A deformed crystalline subsurface with clear misorientation contrast indicating deformation and (c) the un-deformed subsurface

High resolution imaging of the subsurface deformed layer reveals the presence of slip bands, as shown in Figure 7.99. The presence of slip bands shows clear signs of inelastic deformation, specifically shear strain due to the material removal process. The formation of slip bands can be seen when the machined subsurface is exposed to an etchant in which the slip bands are greater revealed, as shown in Figure 7.100. The of slip bands in near surface grain can be seen as parallel lines which traverse across the grain. The slip bands orientated perpendicular to the direction of the passing machine tool are identified as primary slip bands. It can be seen that the orientation of the slip bands differ betweens grains which is due to the change in crystallographic orientation from grain to grain. It is also observable that the slip bands are not straight and deflect in the direction of machining (shown as right to left in figure 7.100) This gives a clear indication of crystallographic

reorientation in the machining direction which indicates that the two methods of accommodating deformation are active simultaneously.

Higher resolution imaging of the subsurface reveals the presence of secondary slip bands which are orientated in a different direction with respect to the primary shear planes, in some cases at angles approaching 90°. These secondary slip bands are obvious within the left hand grains in the micrographs shown in Figure 7.100, and are especially visible in Figure 7.101, whereby the interwoven nature of the slip bands is visible. As the crystallographic lattice deforms in one direction due to the deformation induced by machining, a secondary shear deformation is also induced when the input deformation is sufficient. This mechanism leads to the activation of secondary slip systems, when the level of shear deformation is above a threshold value. Close to machined edge the level of deformation is high enough to produce the secondary slip bands, however their presence decreases with increasing distances from the machined edge, as shown in Figure 7.102. The degradation of these slip bands is associated with decreased deformation towards the bulk and can therefore be used to describe the local severity of damage at the machined edge.

Figures 7.100, 7.101 and 7.102 reveal the interaction between the formed slip bands and the γ' precipitates. In Figure 7.100 it can be observed that the strain bands are present either side of the γ' precipitates however no evidence of slip is visible within the cavities left by the precipitates removed during etching. This suggests that the larger primary γ' precipitates are not coherent with the surrounding gamma matrix phase. However it is feasible to suggest that they still may be subjected to crystallographic rotation along with the surrounding gamma grain. However if the interaction between the smaller γ' and deformation is observed in Figure 7.103, smaller precipitates are sheared and distorted by the wake of the formed slip bands. This suggests that a critical size of precipitate exists through which the slip lines do not pass. Contradictory evidence to this theory, however, is present in Figure 7.104, where larger precipitates close to machined edge can be seen to be traversed by the slip lines near surface. This suggests that the mechanism is much more complicated. In order for a slip line to traverse a precipitate the slip planes of the matrix grain must align with the slip planes in the precipitate, to form coherent slip bands. An alternative scenario is that the crystallographic rotation of the precipitate occurs which realigns the precipitate until sufficient alignment exists for slip bands to traverse through the precipitate.

Summarising the findings of the subsurface deformation observed in the γ grains, the deformation induced by machining results in shear planes forming, the presence of which depend on the distance from the machined edge and the level of force applied and the induced deformation. The primary shear planes

which form normally perpendicular to the surface drag are accompanied by secondary slip bands that exist at approximately 60°angles relative to the primary slip bands. The presence of secondary slip bands degrades into the bulk microstructure and is dependant on the crystallographic orientation of the near surface grains, this is evident by grains equidistant from the machined edge both containing and not containing slip lines, as shown in Figure 7.105. In Figure 7.105 it can be seen that the slip planes can be aligned with neighbouring grains in terms of the orientation of the slip bands relative to the surface. However in some instances neighbouring grains can be free from slip bands even though that they are present in nearby grains at the same distance from the machine surface. This that the damage is influenced by crystallographic orientation whereby grains with orientations that are favourable for slip under the shearing action the machine tool at the surface.

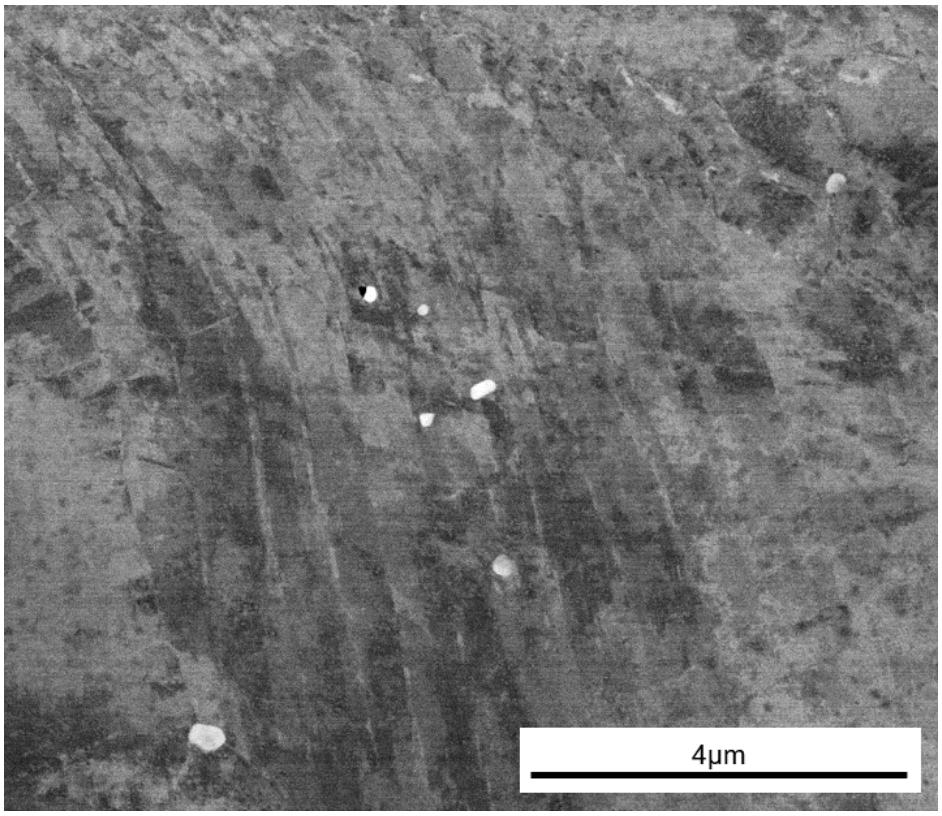

Figure 7.99: Backscatter electron micrograph showing evidence of slip bands in the subsurface layer in Face 1 of billet 3_1.

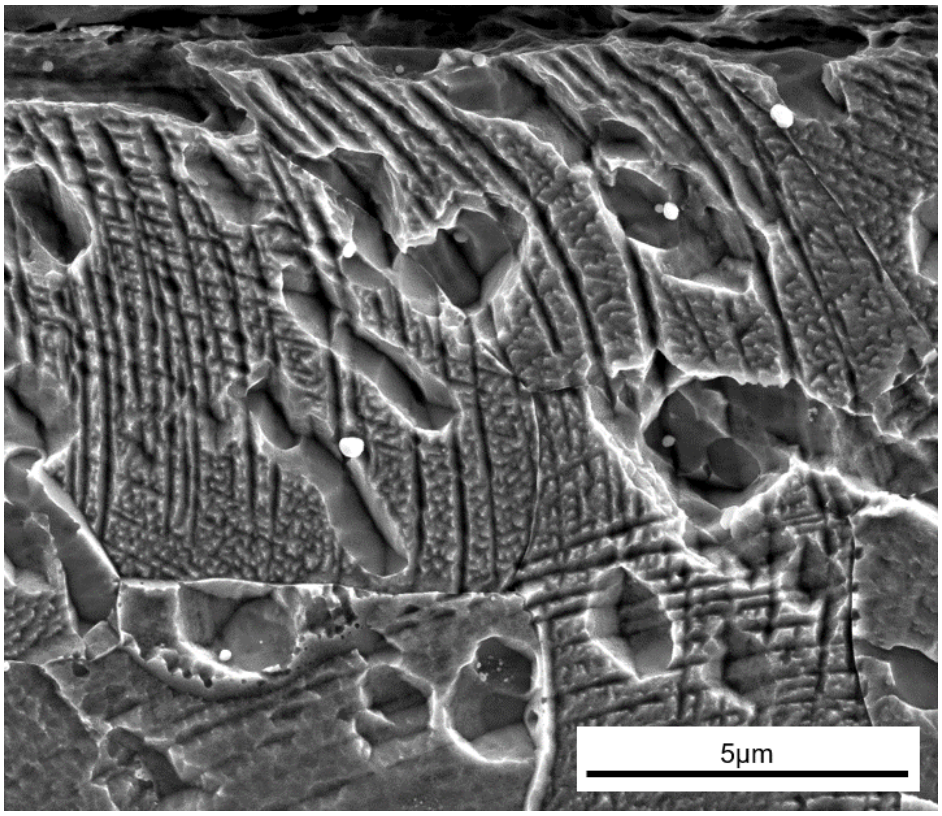

Figure 7.100: Secondary electron micrograph showing evidence of slip bands revealed after the application of an etchant in the machined subsurface layer in Face 1 of billet 3_2.

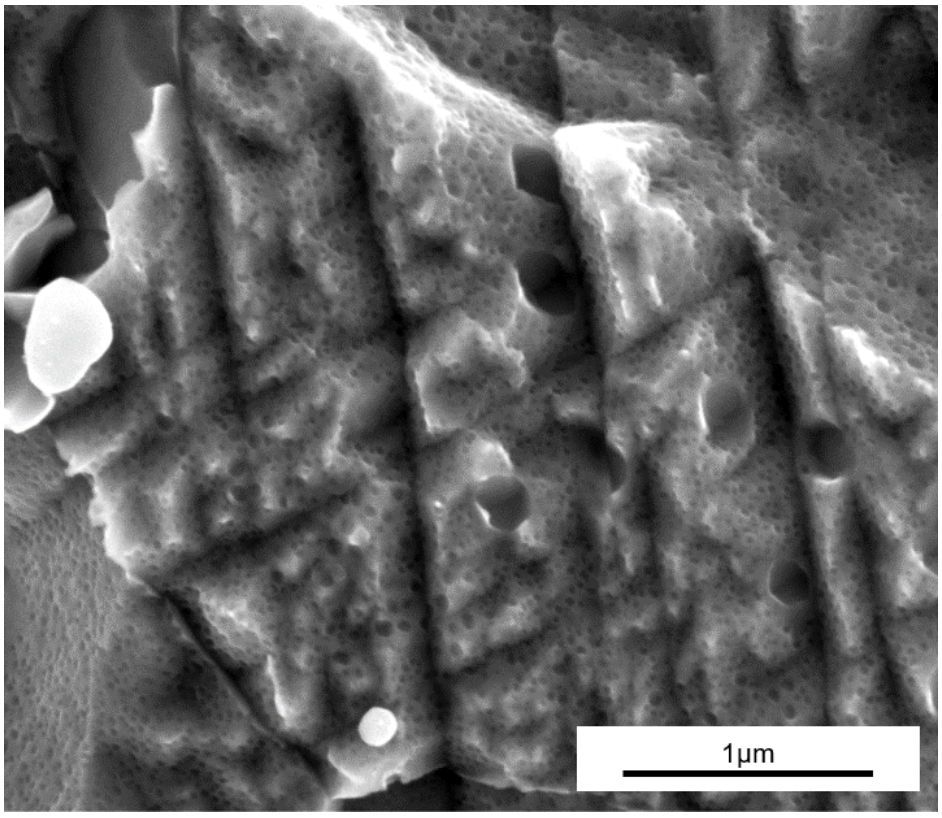

Figure 7.101: Secondary electron micrograph showing evidence of interwoven shear planes in the machined subsurface deformation layer in Face 1 of billet 4_1.

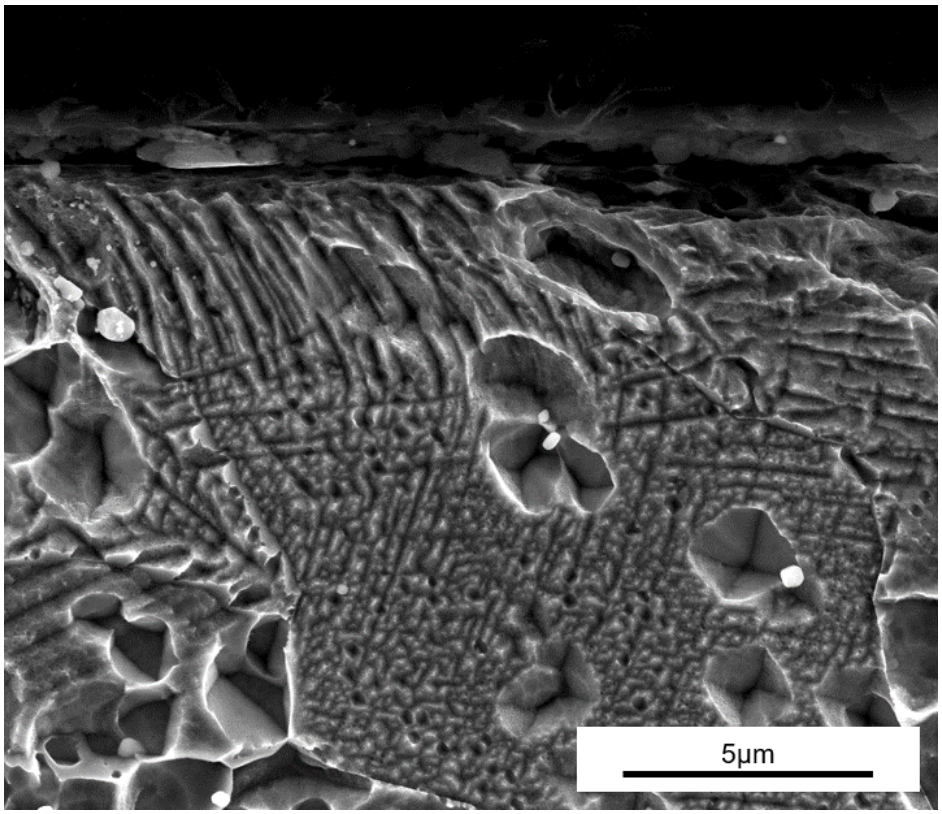

Figure 7.102: Secondary electron micrograph showing slip bands present in the machined subsurface of Face 1 in billet 4_1.

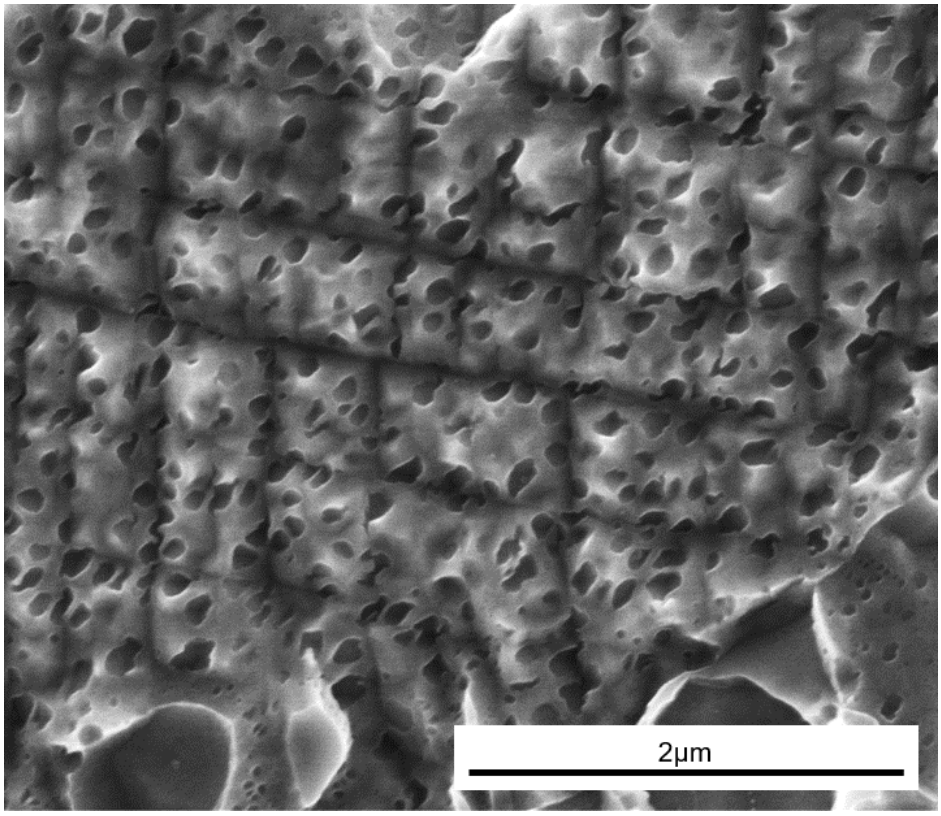

Figure 7.103: Secondary electron micrograph showing the shearing of γ' precipitates in the subsurface deformation layer at Face 1 of billet 4_1.

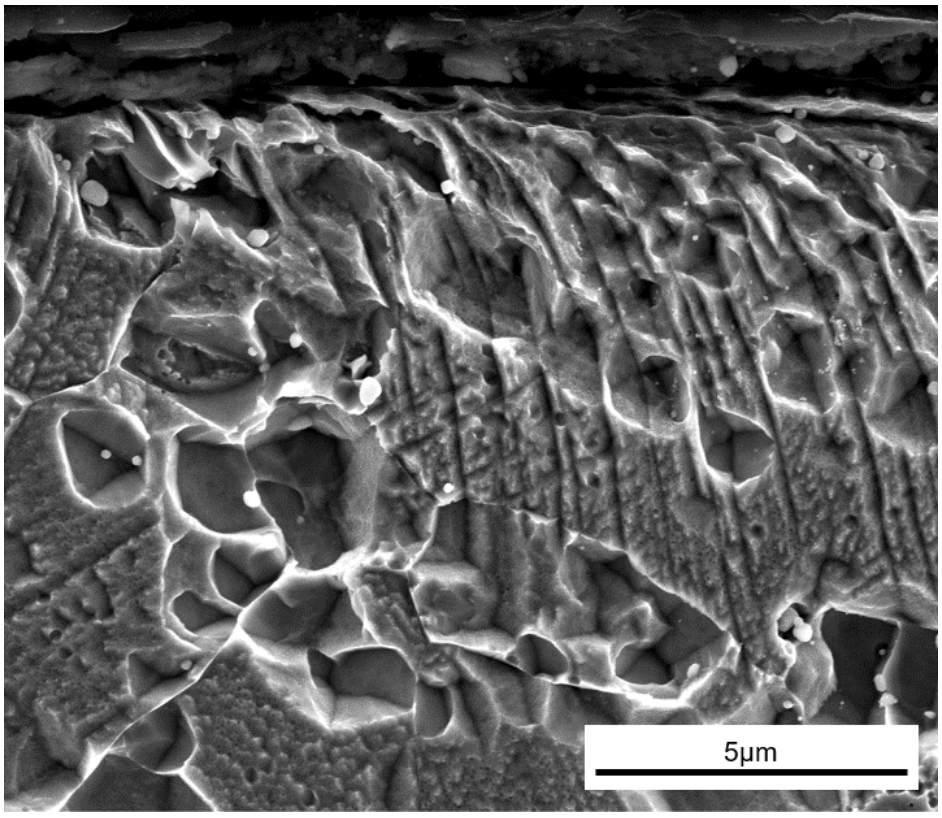

Figure 7.104: Secondary electron micrograph showing the interaction between shear planes and γ' precipitates present in the subsurface deformation layer present in face 1 of billet 4_1.

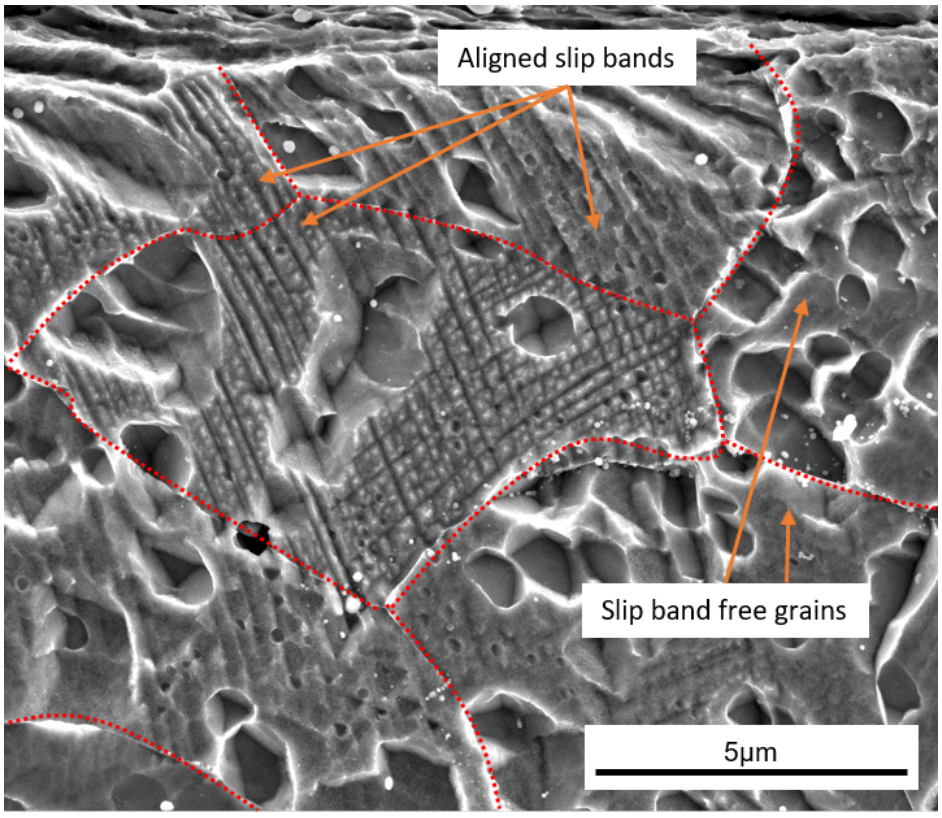

Figure 7.105: Secondary electron micrograph showing the presence of aligned slip bands and shear free grains in the deformed subsurface layer of face 1 for billet 3_1.

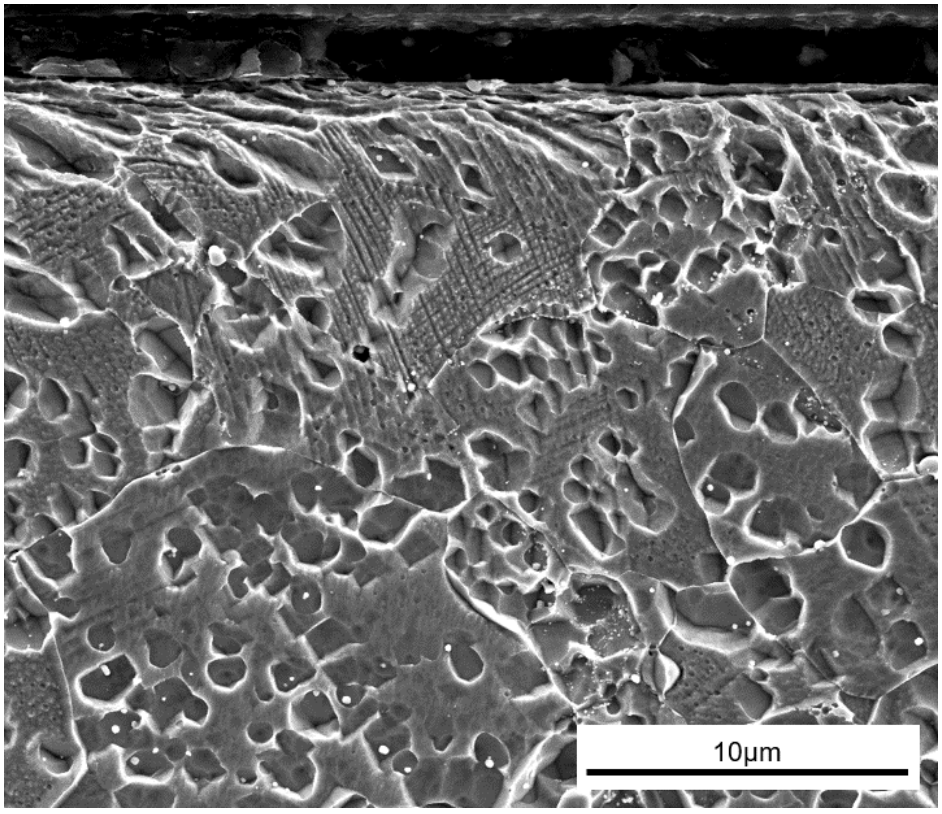

Figure 7.106: Secondary electron micrograph showing the abundance of slip bands in the subsurface of face 1 of billet 3_1. showing an abundance of slip bands which decay towards the subsurface.

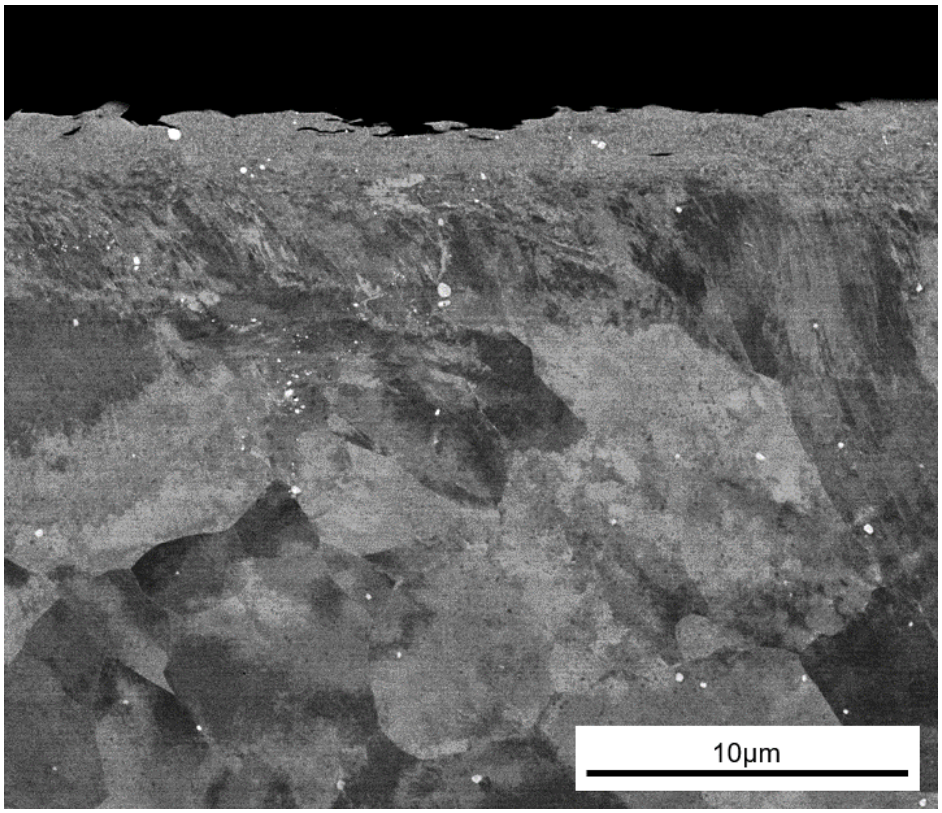

Figure 7.107: Backscatter electron micrograph of the subsurface face 1 of billet 3_1. showing a heavily deformed region at the machined edge, and evidence of slip bands and apparent misorientation contrast indicating deformation.

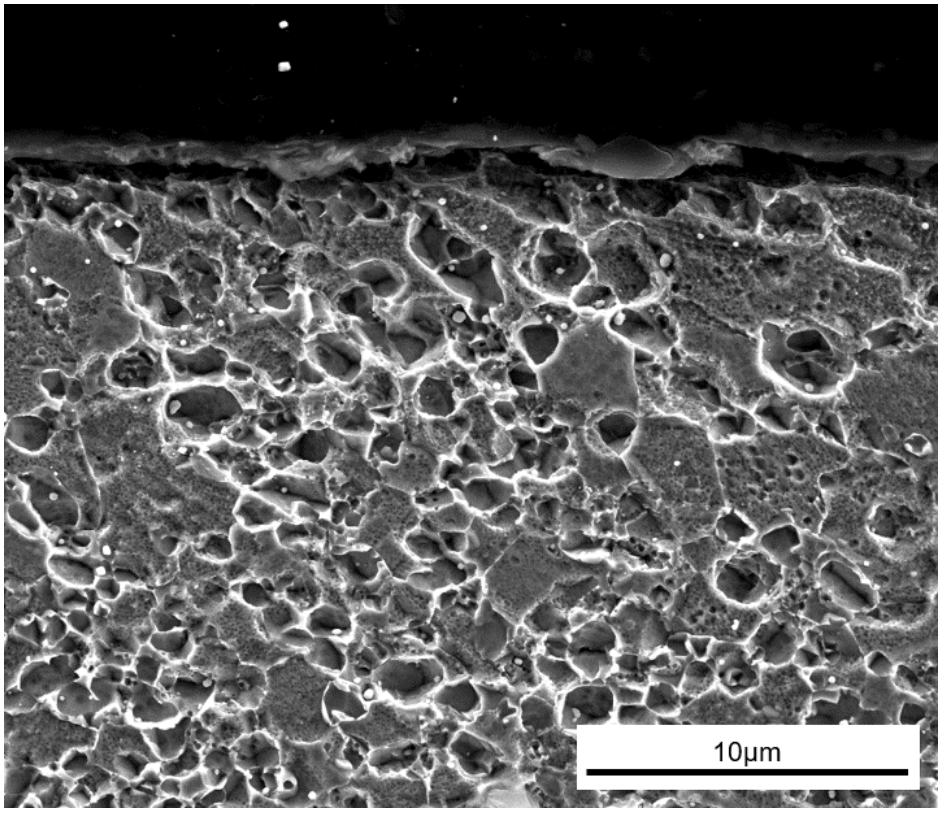

Figure 7.108: Secondary electron micrograph showing the subsurface deformed layer of face 3 on billet 3_1. Deformation can be seen in near surface precipitates but no obvious shear planes are present.

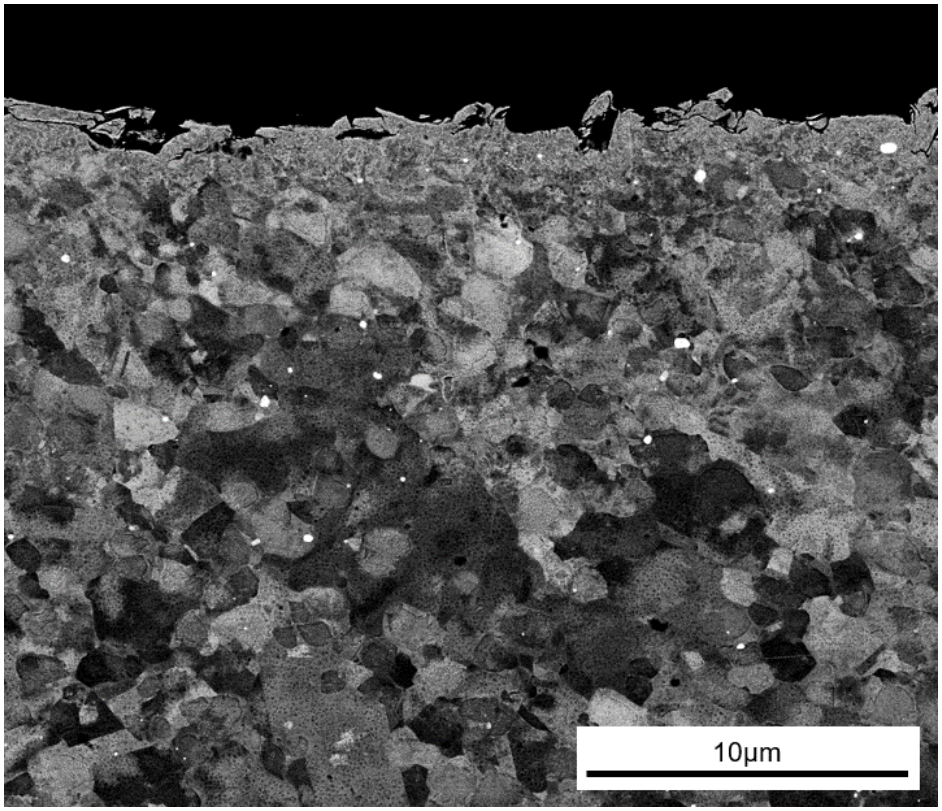

Figure 7.109: Backscatter electron micrograph showing the subsurface deformation present at face 3 of billet 3_1. Misorientation contrast indicating deformation can be observed in the subsurface, however no slip bands are apparent.

The Relationship Between Cutting Forces and subsurface Deformation

Examining Figure 7.86, the cutting forces during the facing trials performed on billet 3_1 are equivalent across the 4 faces. However, the analysis of the subsurface damage indicates that there is a distinct difference in the grain size of the microstructure found local to the four faces. In particular, comparing faces 1 and 3, it can be seen that face 1 contains a coarser microstructure compared to the face 3 which displays a finer structure. This difference in grain morphology would be expected to be observed as a local difference in material properties, however this is not manifested in the measured cutting forces. This scenario can either be explained by the cutting forces being relatively insensitive to grain size or that the local precipitate morphologies in the coarser grain structure make up for the debit in mechan-

ical strength compared to the fine grain structure. With the cutting forces being approximately equal, an opportunity is presented to observe differences in microstructural response in the subsurface, given the same cutting conditions but for different grain sizes.

It can be seen that for the coarser grain structure at face 1 (for billet 3_1), shown in Figures 7.106 and 7.107, near surface slip bands can be seen in abundance as well as strong misorientation contrast indicating high levels of deformation. Comparing this with the finer grain material (at face 3, for billet 3_1) in Figure 7.108 and 7.109, hardly no evidence of slip band formation is visible in the micrograph. However, misorientation contrast is still visible but the depth of which is lesser than that observable in the larger grain material in face 1. From this the following can be proposed. There is a mechanism of deformation that is active in the larger grain material which leads to observable slip band formation and the high occurrence of deformation, as indicated via the misorientation contrast. This mechanism is not active when the parent material has a finer grain structure. To ascertain these effects, high resolution microscopy techniques are required.

7.7 Summary and Conclusions

Using the as-forged billets, the production of which was described in Chapter 5, machining trials were conducted using semi-finishing OD turning and face turning finishing trials to ascertain the variation in cutting forces at varying positions within the billets. Subsequent subsurface deformation investigation on four faces per billet was undertaken. The following conclusions can be made from the study:

- For semi-finishing passes performed on each of the as-forged billets, the cutting forces measured were equivalent for the new tool condition regardless of radial location within the billet. The average cutting forces measured towards the end of machining pass and over the duration of the cutting pass were found to vary predominantly due to tool condition. The cutting forces were therefore found to be not useful for determining changes in microstructure expected with the strain distribution within the uni-axially forged billets.

- Finish face turning passes performed on each of the four billets revealed no significant relationship between cutting forces and the local microstructure when a subsurface damage investigation was performed. Face 1 on each of the billets had a considerably larger grain structure than faces 2-4, however this was not reflected in the measured cutting

forces. Measured cutting forces for the as-HIP material were equivalent to those measured for the three as-forged billets if experimental scatter is considered.

- Investigation of subsurface damage revealed higher levels of visible deformation for faces 1 across all three machined billets due to the larger grain structure. slip bands often traversed through γ' precipitates. Overall it could be observed that local grain structure leads to more visible subsurface damage post machining with fixed conditions when compared to the fine grain structures. Higher resolution microscopy techniques are required to fully understand the interactions between the observed shear planes, micro-texture and size of local γ' precipitates.

Concluding the study, the method of uni-axial forging was demonstrated to be capable of producing non-uniform microstructures in an industrial scale nickel superalloy billets. Machining trials can be designed to understand the influence of varying processing conditions on the machining process and the produced subsurface damage within the material. Supplemented with process modelling to predict the varying grain size, the machining of as forged billets with varying microstructure can provide a powerful tool to understand the link between machining and microstructure during early alloy development. The issue with this process is that conventional forging is difficult to control and costly due to the multitude of processing step. The FAST process may therefore provide an alternative to producing billets with differing, but controlled microstructure, particularly as γ' precipitates can be controlled with higher levels of precision.

Chapter 8

Conclusions and Recommendation for Further Work

8.1 Conclusions

Based upon the work conducted through this EngD project, the following key conclusions can be made:

- Field assisted sintering technology was found to produce highly dense compacts on a small scale. The microstructure of the produced material could be altered by varying the dwell temperature during consolidation, relative to the γ' solvus temperature. The produced material was found to have density values similar to the as HIP material but the measured hardness of the as-FAST material was significantly higher.

- The FAST process was successfully up-scaled to produce material on a semi-industrial scale suitable for machining trials. The FAST processing route was found to offer a new approach to producing material for testing during new alloy development with tailored microstructures possible without the requirement for hot working. The FAST process therefore is a potential processing route for aerospace grade nickel superalloy materials.

- Small scale hot deformation trials, conducted using as-HIP alloy 131072 material, demonstrated that temperatures below the γ' solvus and low strain rates were essential for processing crack free deformation using isothermal forging conditions. A deformation temperature of 1100°C

and a strain rate of 0.01 s^{-1} were the optimal conditions observed during isothermal deformation trials.

- The reduction in hot workability, observed for temperatures above the γ' solvus, can be attributed to grain growth caused by the removal of grain boundary pinning by γ' precipitates. Inhomogeneous microstructures were observed through a cross section of as-deformed specimens owing to the varying levels of recrystallisation and grain growth.

- Adoption of a two step deformation procedure was found to reduce the level of cracking when a uniaxial compression test specimen was deformed to a fixed strain of 1.0. Conventional open-die, non-isothermal forging was found to produce cracking when a single step deformation strategy was adopted for scaled-up billets. However, a two step deformation strategy allowed strains of 1.2 to be reached for a deformation temperature of 1100°C without the occurrence of surface cracking.

- Machining cutting forces were higher for as-FAST 131072 and RR1000 powder consolidated at sub-solvus temperatures compared to super-solvus billets. Post machining examination of the microstructure revealed grain growth in the super-solvus processed billets, compared with those proceed using sub-solvus conditions. Low levels of deformation were observed at the machined surface considering the highest cutting speed (120 $m.min^{-1}$) employed.

- The cutting forces and sub-surface deformation behaviour was consistent across FAST billets produced using two different powders (131072 and RR1000) each with differing size fraction. This suggests changes in the powder size fraction of the powder feedstock used during FAST sintering has little impact on subsequent machining processes.

- Machining trials conducted on large scale as-forged billets produced using conventional, open die two step forging revealed no change in cutting forces with respect to underlying microstructure. One particular face machined on each billet contained a larger grain size than three other machined faces however this was not manifested in cutting forces. This suggests that measurement of cutting forces when face turning is not sufficient to identify changes in underlying microstructure. This conclusion is in direct contradiction of the findings when machining the as-FAST materials.

- Examination of the machined sub-surfaces in both the as-FAST and as-Forged material, revealed that subsurface deformation is more ob-

servable in larger grain size materials. Sub-surface deformation manifested in slip planes within γ grains. These slip planes were observed to deform and pass through γ' precipitates. The interaction of the produced slip planes and γ' precipitates is thought to be dependent on the coherency of the precipitates.

- It has been demonstrated, for the first time, that the FAST processing route is able to produce material with varying microstructures to examine the link between grain size and machining response with less processing steps and complexity than the conventional HIP+forge route.

8.2 Recommendations for Further Work

The following recommendations are given for further work

- A comprehensive review of the effect of as-FAST processing conditions on the microstructure of a modern nickel superalloy such as alloy 131072 or RR1000 is recommended. Within this thesis, only a limited number of processing conditions could be explored. Specifically, full characterisation of the γ' morphologies produced with varying processing conditions is recommended. This requires techniques beyond the scope of this work. It is recommended that full mechanical property testing, especially fatigue response, is examined and compared with traditionally processed materials.

- It is recommended that the mechanism for the apparent improvement in hot ductility with a two step conventional forging route compared to a single step is explored further. In industrial applications it is known that hot extrusion prior to forging improves hot ductility due to the break-up of prior particle boundaries. The degree of analysis required to ascertain the mechanism that improved ductility was beyond the scope of this work and would require high resolution SEM and TEM to understand the effects of changing precipitates, γ grain evolution with the changing levels of microstructural recovery that occurs between the two forging passes.

- Machining of the as-FAST and as-forged billets, revealed a disparity with regards to a reduction in cutting forces in materials with coarser γ grain structures. In super-solvus processed FAST material, a reduction in cutting forces were observed compared with fine grain sub-solvus processed, however this was not observed in the as-forged material. It

is thought that the γ' structures within the material influence over the cutting forces. It is recommended that work is conducted to study the influence of such precipitates on the machining process.

- It is recommended that further characterisation of the effect of grain size and machining damage is performed to capture the effects of local crystallographic texture and γ' precipitates and the observed slip planes. It is reasoned that the coherency of precipitates will determine how they respond to deformation.

8.3 Industrial Significance and Implications

The work presented in this EngD thesis was motivated by a desire to improve the techniques for assessing the machinability of a material, which is a significant factor when selecting a particular alloy for an application in the aerospace industry. A difficult to machine material increases the cost of consumables, reduces the fatigue performance due to retained subsurface damage and may lead to higher levels of part non-conformance. The FAST process introduced in the thesis has the potential to produce material on a scale to perform mechanical property and machinability at lower cost and reduced lead time. By varying the input process parameters the FAST process can simulate material in a range of heat treatment or aged states and allow the impact of thermal exposure and varying microstructure to be evaluated. The FAST process has significant benefits over the HIP process in terms of lead time and cost. The input powder size distribution for HIP produced nickel superalloys is tightly controlled and the FAST process may provide a cost effective method of producing usable components using these powders. The FAST process therefore provides a tool to aid the development and optimisation during the development of nickel superalloy. FAST also has the potential to allow the use of higher specification and more costly nickel superalloy powders in less critical and lower cost aerospace components.

The investigation into the forging response of the 131072 nickel superalloy evaluated in this work revealed the ability of a uni-axial forging process to produce a billet with varying microstructures, both on small and larger scales with both isothermal/non-isothermal conditions, respectively. Subjecting these materials to subsequent machining trials allows the characterisation of the machining response and subsurface damage for varying structures.

Due to the scale of aerospace critical rotating components such as discs, the forging process is likely to produce a varied microstructure due to differential strain and temperature profiles across the components. Understanding

of the variation in machining induced subsurface deformation and associated fatigue debits with local changes in microstructure are key for understanding the performance and life of such critical components. It is foreseen that an understanding of the microstructural change across a component combined with knowledge of how these structures respond to machining will allow the machining process to be intelligently controlled to limit machining induced damage. This is preferential to the current process of machining a component with a set of machining conditions which are selected to produce low levels of damage for a very specific microstructure. It is hoped that the techniques explored and findings gained will contribute towards that process.

Bibliography

[1] R. C. Reed, *The Superalloys, Fundamentals and Applications*. Cambridge: Cambridge University Press, 2006.

[2] C. Qiu, *Net-Shape Hot Isostatic Pressing Of A Nickel-Based Powder Superalloy*. PhD thesis, The University of Birmingham, 2010.

[3] M. C. Hardy, B. Zirbel, G. Shen, and R. Shankar, "Developing damage tolerance and creep resistance in a high strength nickel alloy for disc applications," *Superalloys 2004*, pp. 83–90, 2004.

[4] Y. K. Kim, D. Kim, H. K. Kim, E. Y. Yoon, Y. Lee, C. S. Oh, and B. J. Lee, "A numerical model to predict mechanical properties of Ni-base disk superalloys," *International Journal of Plasticity*, vol. 110, no. June, pp. 123–144, 2018.

[5] C. Nyshadham, C. Oses, J. E. Hansen, I. Takeuchi, S. Curtarolo, and G. L. Hart, "A computational high-throughput search for new ternary superalloys," *Acta Materialia*, vol. 122, pp. 438–447, 2017.

[6] L. Cui, H. Su, J. Yu, J. Liu, T. Jin, and X. Sun, "Temperature dependence of tensile properties and deformation behaviors of nickel-base superalloy M951G," *Materials Science & Engineering A*, vol. 696, no. April, pp. 323–330, 2017.

[7] G.-j. Deng, S.-t. Tu, X.-c. Zhang, Q.-q. Wang, and C.-h. Qin, "Grain size effect on the small fatigue crack initiation and growth mechanisms of nickel-based superalloy GH4169," *Engineering Fracture Mechanics*, vol. 134, pp. 433–450, 2015.

[8] F. Alexandre, S. Deyber, and A. Pineau, "Modelling the optimum grain size on the low cycle fatigue life of a Ni based superalloy in the presence of two possible crack initiation sites," *Scripta Materialia*, vol. 50, pp. 25–30, 2004.

[9] X. Huang, H. Yu, M. Xu, and Y. Zhao, "Experimental investigation on microcrack initiation process in nickel-based superalloy DAGH4169," *International Journal of Fatigue*, vol. 42, pp. 153–164, 2012.

[10] C.-h. Qin, X.-c. Zhang, S. Ye, and S.-t. Tu, "Grain size effect on multi-scale fatigue crack growth mechanism of Nickel-based alloy GH4169," *Engineering Fracture Mechanics*, vol. 142, pp. 140–153, 2015.

[11] L. Liu, D. Hu, D. Li, R. Hu, Y. Gu, and R. Wang, "Effect of Grain Size on Low Cycle Fatigue Life in Compressor Disc Superalloy GH4169 at 600 C," in *3rd International Symposium on Fatigue Design and Material Defects*, pp. 19–22, 2017.

[12] P. Zhang, Q. Zhu, G. Chen, H.-y. Qin, and C.-j. Wang, "Grain size based low cycle fatigue life prediction model for nickel-based superalloy," *Transactions of Nonferrous Metals Society of China*, vol. 28, no. 10, pp. 2102–2106, 2018.

[13] L. Thébaud, P. Villechaise, C. Crozet, A. Devaux, D. Béchet, J.-m. Franchet, A.-l. Rou, M. Mills, and J. Cormier, "Is there an optimal grain size for creep resistance in Ni-based disk superalloys ?," *Materials Science & Engineering A*, vol. 716, no. December 2017, pp. 274–283, 2018.

[14] J. P. Shingledecker, N. D. Evans, and G. M. Pharr, "Influences of composition and grain size on creep rupture behavior of Inconel s alloy 740," *Materials Science & Engineering A*, vol. 578, pp. 277–286, 2013.

[15] G. He, L. Tan, F. Liu, L. Huang, and Z. Huang, "Unraveling the formation mechanism of abnormally large grains in an advanced polycrystalline nickel base superalloy," *Journal of Alloys and Compounds*, vol. 718, pp. 405–413, 2017.

[16] M.-a. Charpagne, J.-m. Franchet, and N. Bozzolo, "Overgrown grains appearing during sub-solvus heat treatment in a polycrystalline γ - γ ' Nickel-based superalloy," *Materials & Design*, vol. 144, pp. 353–360, 2018.

[17] L. Tan, Z. Huang, F. Liu, G. He, X. Wang, L. Huang, Y. Zhang, and L. Jiang, "Effects of strain amount and strain rate on grain structure of a novel high Co nickel-based polycrystalline superalloy," *Materials & Design*, vol. 131, pp. 60–68, oct 2017.

[18] E. Alabort, D. Barba, S. Sulzer, M. Lißner, N. Petrinic, and R. C. Reed, "Grain boundary properties of a nickel-based superalloy: Characterisation and modelling," *Acta Materialia*, vol. 151, pp. 377–394, 2018.

[19] G. Huang, G. Q. Liu, M. Feng, M. Zhang, B. Hu, and H. Wang, "The effect of cooling rates from temperatures above the γ solvus on the microstructure of a new nickel-based powder metallurgy superalloy," *Journal of Alloys and Compounds*, vol. 747, pp. 1062–1072, 2018.

[20] P. Kontis, E. Alabort, D. Barba, D. M. Collins, A. J. Wilkinson, and R. C. Reed, "On the role of boron on improving ductility in a new polycrystalline superalloy," *Acta Materialia*, vol. 124, pp. 489–500, 2017.

[21] C. L. Qiu and P. Andrews, "On the formation of irregular-shaped gamma prime and serrated grain boundaries in a nickel-based superalloy during continuous cooling," *Materials Characterization*, vol. 76, pp. 28–34, 2013.

[22] A. C. Yeh, K. W. Lu, C. M. Kuo, H. Y. Bor, and C. N. Wei, "Effect of serrated grain boundaries on the creep property of Inconel 718 superalloy," *Materials Science and Engineering A*, vol. 530, no. 1, pp. 525–529, 2011.

[23] E. Pu, W. Zheng, Z. Song, K. Zhang, F. Yang, and H. Lu, "Materials Science & Engineering A Evolution of microstructure and tensile properties during solution treatment of nickel-based UNS N10276 alloy," *Materials Science & Engineering A*, vol. 705, pp. 335–347, 2017.

[24] M. P. Jackson and R. C. Reed, "Heat treatment of UDIMET 720Li: The effect of microstructure on properties," *Materials Science and Engineering A*, vol. 259, no. 1, pp. 85–97, 1999.

[25] F. C. Campbell, *Elements of metallurgy and engineering alloys*. ASM International, 2008.

[26] S. A. Hosseini, S. M. Abbasi, and K. Z. Madar, "Materials Science & Engineering A The e ff ect of boron and zirconium on microstructure and tensile properties of the wrought nickel-based superalloy ATI 718Plus," *Materials Science & Engineering A*, vol. 712, pp. 780–789, 2018.

[27] D. Collins, L. Yan, E. Marquis, L. Connor, J. Ciardiello, A. Evans, and H. Stone, "Lattice misfit during ageing of a polycrystalline nickel-base superalloy," *Acta Materialia*, vol. 61, pp. 7791–7804, dec 2013.

[28] R. K. Rai and J. K. Sahu, "Mechanism of serrated flow in a cast nickel base superalloy," *Materials Letters*, vol. 210, pp. 298–300, 2018.

[29] H. Wu, Z. Huang, N. Zhou, J. Chen, P. Zhou, and L. Jiang, "A study of solution cooling rate on γ' precipitate and hardness of a polycrystalline Ni-based superalloy using a high-throughput methodology," *Materials Science and Engineering: A*, vol. 739, pp. 473–479, 2019.

[30] B. Alabbad, L. Li, and S. Tin, "Controlling the grain boundary morphology and secondary γ precipitate size distribution in Ni-base superalloys," *Journal of Alloys and Compounds*, vol. 775, pp. 931–941, 2019.

[31] Z. Wan, L. Hu, Y. Sun, T. Wang, Z. Li, and Y. Zhang, "Effect of solution treatment on microstructure and tensile properties of a U720LI Ni-based superalloy," *Vacuum*, vol. 156, pp. 248–255, 2018.

[32] R. Radis, M. Schaffer, M. Albu, G. Kothleitner, P. Pölt, and E. Kozeschnik, "Multimodal size distributions of γ precipitates during continuous cooling of Udimet 720 Li," *Acta Materialia*, vol. 57, no. 19, pp. 5739–5747, 2009.

[33] L. Whitmore, M. R. Ahmadi, M. Stockinger, E. Povoden-Karadeniz, E. Kozeschnik, and H. Leitner, "Microstructural investigation of thermally aged nickel-based superalloy 718Plus," *Materials Science and Engineering A*, vol. 594, pp. 253–259, 2014.

[34] C. Jia, F. Zhang, K. Wei, and S. Lv, "Effective solution treatment can result in improved creep performance of superalloys," *Journal of Alloys and Compounds*, vol. 770, pp. 166–174, 2019.

[35] Y.-l. Tsai, S.-f. Wang, H.-y. Bor, and Y.-f. Hsu, "Effects of alloy elements on microstructure and creep properties of fine-grained nickel-based superalloys at moderate temperatures," *Materials Science & Engineering A*, vol. 571, pp. 155–160, 2013.

[36] Y. Chen, E. Francis, J. Robson, M. Preuss, and S. Haigh, "Compositional variations for small-scale gamma prime precipitates formed at different cooling rates in an advanced Ni-based superalloy," *Acta Materialia*, vol. 85, pp. 199–206, 2015.

[37] Y. Chen, R. Prasath Babu, T. J. Slater, M. Bai, R. Mitchell, O. Ciuca, M. Preuss, and S. J. Haigh, "An investigation of diffusion-mediated cyclic coarsening and reversal coarsening in an advanced Ni-based superalloy," *Acta Materialia*, vol. 110, pp. 295–305, 2016.

[38] Y. Tang, J. Liu, H. Cheng, H. Yu, Y. Zhang, and J. Zhu, "Effect of hafnium on annealing twin formation in as-hot isostatically pressed nickel-based powder metallurgy superalloy," *Journal of Alloys and Compounds*, vol. 772, pp. 949–954, 2019.

[39] T. Sugui, X. Jun, Z. Xiaoming, Q. Benjiang, L. Jianwei, Y. Lili, and W. Wuxiang, "Microstructure and creep behavior of FGH95 nickel-base superalloy," *Materials Science & Engineering A*, vol. 528, no. 4-5, pp. 2076–2084, 2011.

[40] I. J. Moore, J. I. Taylor, M. W. Tracy, M. G. Burke, and E. J. Palmiere, "Materials Science & Engineering A Grain coarsening behaviour of solution annealed Alloy 625 between 600 800 C," *Materials Science & Engineering A*, vol. 682, no. August 2016, pp. 402–409, 2017.

[41] J. J. Ruan, N. Ueshima, and K. Oikawa, "Phase transformations and grain growth behaviors in superalloy 718," *Journal of Alloys and Compounds*, vol. 737, pp. 83–91, 2018.

[42] Y. Liu, Y. Wu, M. Kang, M. Wang, M. Li, H. Gao, J. Wang, B. Sun, and Y. Ning, "Fracture mechanisms induced by microporosity and precipitates in isothermal fatigue of polycrystalline nickel based superalloy," *Materials Science and Engineering A*, vol. 736, no. 800, pp. 438–452, 2018.

[43] Z. Peng, I. Povstugar, K. Matuszewski, R. Rettig, R. Singer, and A. Kostka, "Effects of Ru on elemental partitioning and precipitation of topologically close-packed phases in Ni-based superalloys," *Scripta Materialia*, vol. 101, pp. 44–47, 2015.

[44] R. Rettig and R. F. Singer, "Numerical modelling of precipitation of topologically close-packed phases in nickel-base superalloys," *Acta Materialia*, vol. 59, no. 1, pp. 317–327, 2011.

[45] J. Belan, "GCP and TCP phases presented in nickel-base superalloys," *Materials Today: Proceedings*, vol. 3, no. 4, pp. 936–941, 2016.

[46] C. Rae, M. S. A. Karunaratne, C. Small, R. W. Broomfield, C. N. Jones, and R. C. Reed, "Topologically close packed phases in an experimental Rhenium-containing single crystal superalloy," in *Superalloys 2000*, pp. 768–776, 2000.

[47] R. C. Reed, M. P. Jackson, and Y. S. Na, "Characterization and Modeling of the Precipitation of the Sigma Phase in UDIMET 720 and UDIMET 720LI," *Metallurgical and Materials Transactions A*, vol. 30, no. March, pp. 521–533, 1999.

[48] F. Long, Y. S. Yoo, C. Y. Jo, S. M. Seo, H. W. Jeong, Y. S. Song, T. Jin, and Z. Q. Hu, "Phase transformation of eta and sigma phases in an experimental nickel-based superalloy," *Journal of Alloys and Compounds*, vol. 478, pp. 181–187, 2009.

[49] M. J. Sohrabi, H. Mirzadeh, and M. Ra, "Solidification behavior and Laves phase dissolution during homogenization heat treatment of Inconel 718 superalloy," *Vacuum*, vol. 154, no. May, pp. 235–243, 2018.

[50] H. Naffakh-Moosavy, "Microstructural investigation and castability anticipation in modern Ti/Al/Nb-containing nickel-based superalloys," *Transactions of Nonferrous Metals Society of China (English Edition)*, vol. 26, no. 6, pp. 1607–1619, 2016.

[51] A. Devaux, L. Nazé, R. Molins, A. Pineau, A. Organista, J. Y. Guédou, J. F. Uginet, and P. Héritier, "Gamma double prime precipitation kinetic in Alloy 718," *Materials Science and Engineering A*, vol. 486, no. 1-2, pp. 117–122, 2008.

[52] P. M. Mignanelli, N. G. Jones, E. J. Pickering, O. M. D. M. Messé, C. M. F. Rae, M. C. Hardy, and H. J. Stone, "Gamma-gamma prime-gamma double prime dual-superlattice superalloys," *Scripta Materialia*, vol. 136, pp. 136–140, 2017.

[53] S. Antonov, J. Huo, Q. Feng, D. Isheim, D. N. Seidman, R. C. Helmink, E. Sun, and S. Tin, "σ and η Phase formation in advanced polycrystalline Ni-base superalloys," *Materials Science and Engineering A*, vol. 687, pp. 232–240, 2017.

[54] P. Mignanelli, N. Jones, K. Perkins, M. Hardy, and H. Stone, "Microstructural evolution of a delta containing nickel-base superalloy during heat treatment and isothermal forging," *Materials Science and Engineering: A*, vol. 621, pp. 265–271, 2015.

[55] P. J. P. Kañetas, L. A. R. Osorio, M. P. G. Mata, and M. D. L. Garza, "Influence of the Delta Phase in the Microstructure of the Inconel 718 subjected to Delta - processing Heat Treatment and Hot Deformed," *Procedia Materials Science*, vol. 8, pp. 1160–1165, 2015.

[56] F. Bois and N. Beaude, "Mechanical delta phase in inconel 718: properties and forging process requirements," *Superalloys 1994*, pp. 281–291, 1994.

[57] Y. Wang, L. Zhen, W. Z. Shao, L. Yang, and X. M. Zhang, "Hot working characteristics and dynamic recrystallization of delta-processed superalloy 718," *Journal of Alloys and Compounds*, vol. 474, pp. 341–346, 2009.

[58] H. Zhang, C. Li, Q. Guo, Z. Ma, Y. Huang, and H. Li, "Delta precipitation in wrought Inconel 718 alloy ; the role of dynamic recrystallization," *Materials Characterization*, vol. 133, no. July, pp. 138–145, 2017.

[59] H. Y. Zhang, S. H. Zhang, M. Cheng, and Z. Zhao, "Microstructure evolution of IN718 alloy during the delta process," *Procedia Engineering*, vol. 207, pp. 1099–1104, 2017.

[60] S. A. Hosseini, S. M. Abbasi, K. Z. Madar, and H. M. K. Yazdi, "The effect of boron and zirconium on wrought structure and gamma-gamma prime lattice misfit characterization in nickel-based superalloy ATI 718Plus," *Materials Chemistry and Physics*, vol. 211, pp. 302–311, 2018.

[61] B. Du, Z. Hu, L. Sheng, C. Cui, J. Yang, Y. Zheng, and X. Sun, "Tensile, creep behavior and microstructure evolution of an as-cast Ni-based K417G polycrystalline superalloy," *Journal of Materials Science and Technology*, vol. 34, no. 10, pp. 1805–1816, 2018.

[62] W. Huther and B. Reppich, "Interaction of Dislocations with Coherent, Stree-Free Ordered Particles," *Zeitschrift fur Metallkunde*, vol. 69, pp. 628–634, 1978.

[63] M. C. Hardy, C. R. J. Herbert, J. Kwong, W. Li, D. a. Axinte, a. R. C. Sharman, a. Encinas-Oropesa, and P. J. Withers, "Characterising the integrity of machined surfaces in a powder nickel alloy used in aircraft engines," *Procedia CIRP*, vol. 13, pp. 411–416, 2014.

[64] N. S. Weston, F. Derguti, A. Tudball, and M. Jackson, "Spark plasma sintering of commercial and development titanium alloy powders," *Journal of Materials Science*, vol. 50, no. 14, pp. 4860–4878, 2015.

[65] J. Zhang, Z. Zhang, Z. Zhao, Q. Zhong, and B. Nie, "Research on the healing behavior of the millimeter-sized cavity defect inside the superalloy by hot isostatic pressing," *Materials Letters*, vol. 235, pp. 57–60, 2019.

[66] X. G. Zheng, Y. N. Shi, and L. H. Lou, "Healing Process of Casting Pores in a Ni-based Superalloy by Hot Isostatic Pressing," *Journal of Materials Science and Technology*, vol. 31, no. 11, pp. 1151–1157, 2015.

[67] L. Mujica Roncery, I. Lopez-Galilea, B. Ruttert, S. Huth, and W. Theisen, "Influence of temperature, pressure, and cooling rate during hot isostatic pressing on the microstructure of an SX Ni-base superalloy," *Materials and Design*, vol. 97, pp. 544–552, 2016.

[68] M. Zhang, Z. Luo, and F. Zeng, "Dynamic behaviour modeling for P/M superalloy during hot isostatic pressing," *Journal of Materials Processing Technology*, vol. 72, pp. 262–266, 1997.

[69] X. Ye, Y. Li, Y. Ai, and Y. Nie, "Novel powder packing theory with bimodal particle size distribution-application in superalloy," *Advanced Powder Technology*, vol. 29, no. 9, pp. 2280–2287, 2018.

[70] E. Bassini, V. Vola, M. Lorusso, R. Ghisleni, M. Lombardi, S. Biamino, D. Ugues, G. Vallillo, and B. Picqué, "Net shape HIPping of Ni-superalloy: Study of the interface between the capsule and the alloy," *Materials Science and Engineering A*, vol. 695, pp. 55–65, 2017.

[71] L. Tan, Y. Li, C. Liu, C. Yang, H. Ding, L. Huang, F. Liu, Z. Qin, and L. Jiang, "The evolution history of superalloy powders during hot consolidation and plastic deformation," *Materials Characterization*, vol. 140, pp. 30–38, 2018.

[72] J. Hou, J. X. Dong, Z. H. Yao, H. Jiang, and M. C. Zhang, "Influences of PPB, PPB affect zone, grain boundary and phase boundary on crack propagation path for a P/M superalloy FGH4096," *Materials Science and Engineering A*, vol. 724, pp. 17–28, 2018.

[73] D. Hu, T. Wang, Q. Ma, X. Liu, L. Shang, D. Li, J. Pan, and R. Wang, "Effect of inclusions on low cycle fatigue lifetime in a powder metallurgy nickel-based superalloy FGH96," *International Journal of Fatigue*, vol. 118, pp. 237–248, 2019.

[74] Y. Ning, C. Zhou, H. Liang, and M. W. Fu, "Abnormal flow behavior and necklace microstructure of powder metallurgy superalloys with previous particle boundaries (PPBs)," *Materials Science and Engineering A*, vol. 652, pp. 84–91, 2016.

[75] L. Chang, W. Sun, Y. Cui, and R. Yang, "Preparation of hot-isostatic-pressed powder metallurgy superalloy Inconel 718 free of prior particle boundaries," *Materials Science and Engineering A*, vol. 682, pp. 341–344, 2017.

[76] Q. Bai, J. Lin, J. Jiang, T. Dean, J. Zou, and G. Tian, "A study of direct forging process for powder superalloys," *Materials Science and Engineering: A*, vol. 621, pp. 68–75, 2015.

[77] Y. Zhou, Z. Zhang, Q. Zhong, and Z. Zhao, "Model for healing of creep cavities in nickel-based superalloys under hot isostatic pressing," *Computational Materials Science*, vol. 65, no. 37, pp. 320–323, 2012.

[78] W. Tillmann, C. Schaak, J. Nellesen, M. Schaper, M. E. Aydinöz, and K. P. Hoyer, "Hot isostatic pressing of IN718 components manufactured by selective laser melting," *Additive Manufacturing*, vol. 13, pp. 93–102, 2017.

[79] M. T. Kim and O. Y. Oh, "Effect of high pressure on the solid-liquid phase change of a nickel base superalloy during hot isostatic pressing," *Journal of Alloys and Compounds*, vol. 477, no. 1-2, pp. 224–232, 2009.

[80] Q. Teng, Q. Wei, P. Xue, C. Cai, H. Chen, H. Chen, and Y. Shi, "Effects of processing temperatures on FGH4097 superalloy fabricated by hot isostatic pressing: microstructure evolution, mechanical properties and fracture mechanism," *Materials Science and Engineering: A*, 2018.

[81] C. Qiu, M. Attallah, X. Wu, and P. Andrews, "Influence of hot isostatic pressing temperature on microstructure and tensile properties of a nickel-based superalloy powder," *Materials Science and Engineering: A*, vol. 564, pp. 176–185, 2013.

[82] R. Orrù, R. Licheri, A. M. Locci, A. Cincotti, and G. Cao, "Consolidation/synthesis of materials by electric current activated/assisted sintering," *Materials Science and Engineering R: Reports*, vol. 63, no. 4-6, pp. 127–287, 2009.

[83] S. Muñoz and U. Anselmi-Tamburini, "Temperature and stress fields evolution during spark plasma sintering processes," *Journal of Materials Science*, vol. 45, no. 23, pp. 6528–6539, 2010.

[84] L. Minier, S. Le Gallet, Y. Grin, and F. Bernard, "A comparative study of nickel and alumina sintering using spark plasma sintering (SPS)," *Materials Chemistry and Physics*, vol. 134, no. 1, pp. 243–253, 2012.

[85] K. Vanmeensel, A. Laptev, J. Hennicke, J. Vleugels, and O. Van Der Biest, "Modelling of the temperature distribution during field assisted sintering," *Acta Materialia*, vol. 53, no. 16, pp. 4379–4388, 2005.

[86] J. Räthel, M. Herrmann, and W. Beckert, "Temperature distribution for electrically conductive and non-conductive materials during Field Assisted Sintering (FAST)," *Journal of the European Ceramic Society*, vol. 29, no. 8, pp. 1419–1425, 2009.

[87] T. Voisin, L. Durand, N. Karnatak, S. Le Gallet, M. Thomas, Y. Le Berre, J. F. Castagné, and A. Couret, "Temperature control during Spark Plasma Sintering and application to up-scaling and complex shaping," *Journal of Materials Processing Technology*, vol. 213, no. 2, pp. 269–278, 2013.

[88] C. Maniére, L. Durand, A. Weibel, and C. Estournés, "Spark-plasma-sintering and finite element method: From the identification of the sintering parameters of a submicronic alpha-alumina powder to the development of complex shapes," *Acta Materialia*, vol. 102, pp. 169–175, 2016.

[89] C. Maniére, L. Durand, A. Weibel, G. Chevallier, and C. Estournès, "A sacrificial material approach for spark plasma sintering of complex shapes," *Scripta Materialia*, vol. 124, pp. 126–128, 2016.

[90] E. A. Olevsky, "Theory of sintering: from discrete to continuum," *Materials Science and Engineering: R: Reports*, vol. 23, no. 2, pp. 41–100, 1998.

[91] D. Tingaud, P. Jenei, A. Krawczynska, F. Mompiou, J. Gubicza, and G. Dirras, "Investigation of deformation micro-mechanisms in nickel consolidated from a bimodal powder by spark plasma sintering," *Materials Characterization*, vol. 99, pp. 118–127, 2015.

[92] R. J. Mitchell, M. C. Hardy, M. Preuss, and S. Tin, "Development Of Y' Morphology In P/M Rotor Disc Alloys During Heat Treatment," *Superalloys 2004 (Tenth International Symposium)*, pp. 361–370, 2004.

[93] R. Radis, M. Schaffer, M. Albu, G. Kothleitner, P. Pölt, and E. Kozeschnike, "Evolution of the size and morphology of precipitates in Udimet 720 Li during continuous cooling," *Superalloys 2008*, pp. 829–836, 2008.

[94] F. Liu, J. Chen, J. Dong, M. Zhang, and Z. Yao, "The hot deformation behaviors of coarse, fine and mixed grain for Udimet 720Li superalloy," *Materials Science and Engineering: A*, vol. 651, pp. 102–115, 2016.

[95] Y. Wu, M. Zhang, X. Xie, J. Dong, and F. Lin, "Hot deformation characteristics and processing map analysis of a new designed nickel-based alloy for 700 C A-USC power plant," *Journal of Alloys and Compounds*, vol. 656, pp. 119–131, 2016.

[96] E. Pu, W. Zheng, Z. Song, H. Feng, and H. Dong, "Hot deformation characterization of nickel-based superalloy UNS10276 through processing map and microstructural studies," *Journal of Alloys and Compounds*, vol. 694, pp. 617–631, 2017.

[97] Y. C. Lin, K.-k. Li, H.-b. Li, J. Chen, X.-m. Chen, and D.-x. Wen, "New constitutive model for high-temperature deformation behavior of inconel 718 superalloy," *Journal of materials and design*, vol. 74, pp. 108–118, 2015.

[98] M. Azarbarmas, M. Aghaie-khafri, J. M. Cabrera, and J. Calvo, "Microstructural evolution and constitutive equations of Inconel 718 alloy under quasi-static and quasi-dynamic conditions," *Materials and Design*, vol. 94, pp. 28–38, 2016.

[99] X.-M. Chen, Y. Lin, M.-S. Chen, H.-B. Li, D.-X. Wen, J.-L. Zhang, and M. He, "Microstructural evolution of a nickel-based superalloy during hot deformation," *Materials & Design*, vol. 77, pp. 41–49, 2015.

[100] Y. Liu, Z. Yao, Y. Ning, and Y. Nan, "Effect of deformation temperature and strain rate on dynamic recrystallized grain size of a powder metallurgical nickel-based superalloy," *Journal of Alloys and Compounds*, vol. 691, pp. 554–563, 2017.

[101] Y. B. Tan, Y. H. Ma, and F. Zhao, "Hot deformation behavior and constitutive modeling of fi ne grained Inconel 718 superalloy," *Journal of Alloys and Compounds*, vol. 741, pp. 85–96, 2018.

[102] S. S. S. Kumar, T. Raghu, P. P. Bhattacharjee, and G. A. Rao, "Work hardening characteristics and microstructural evolution during hot deformation of a nickel superalloy at moderate strain rates," *Journal of Alloys and Compounds*, vol. 709, pp. 394–409, 2017.

[103] Y.-x. Liu, Y. C. Lin, H.-b. Li, and D.-x. Wen, "A Study of dynamic recrystallization in a Ni-based superalloy by experiments and cellular automaton model," *Materials Science & Engineering A*, vol. 626, pp. 432–440, 2015.

[104] K. Huang and R. E. Logé, "A review of dynamic recrystallization phenomena in metallic materials," *JMADE*, vol. 111, pp. 548–574, 2016.

[105] Y. C. Lin, Y.-x. Liu, M.-s. Chen, M.-h. Huang, X. Ma, and Z.-l. Long, "Study of static recrystallization behavior in hot deformed Ni-based superalloy using cellular automaton model," *Journal of materials and design*, vol. 99, pp. 107–114, 2016.

[106] S. Gardner, W. Li, M. Coleman, and R. Johnston, "The effects of thermomechanical history on the microstructure of a nickel-base superalloy during forging," *Materials Science & Engineering A*, vol. 668, pp. 263–270, 2016.

[107] H. Zhang, K. Zhang, S. Jiang, H. Zhou, C. Zhao, and X. Yang, "superalloy during hot deformation," *Journal of Alloys and Compounds*, vol. 623, pp. 374–385, 2015.

[108] Z.-h. Xu, M.-q. Li, and H. Li, "Plastic flow behavior of superalloy GH696 during hot deformation," *Transactions of Nonferrous Metals Society of China*, vol. 26, no. 3, pp. 712–721, 2016.

[109] L. Winberg and M. Dahlen, "Recrystallization in a powder metallurgy nickel-base superalloy," *Journal of Materials Sciences*, vol. 13, pp. 2365–2372, 1978.

[110] G. He, F. Liu, L. Huang, Z. Huang, and L. Jiang, "Controlling grain size via dynamic recrystallization in an advanced polycrystalline nickel base superalloy," *Journal of Alloys and Compounds*, vol. 701, pp. 909–919, 2017.

[111] S. Hyuk, J. Hun, H. Yu, J. Yoon, and B. Sun, "Materials Science & Engineering A Effect of cold pre-forging on the microstructure and mechanical properties of extruded Mg 8Sn 1Al 1Zn alloy," *Materials Science & Engineering A*, vol. 612, pp. 197–201, 2014.

[112] H. Mirzadeh, J. M. Cabrera, A. Najafizadeh, and P. R. Calvillo, "EBSD study of a hot deformed austenitic stainless steel," *Materials Science & Engineering A*, vol. 538, pp. 236–245, 2012.

[113] B. Li and S. Tin, "The role of deformation temperature and strain on grain boundary engineering of Inconel 600," *Materials Science & Engineering A*, vol. 603, pp. 104–113, 2014.

[114] H. Meckings and U. F. Kocks, "Kinetics of flow and strain hardening," *Acta Metallurgica*, vol. 29, pp. 1865–1875, 1981.

[115] A. Porter and B. Ralph, "The recrystallization of nickel-base superalloys," *Journal of Materials Science*, vol. 16, no. 16, pp. 707–713, 1981.

[116] J. Mccarley and S. Tin, "Utilization of hot deformation to trigger Strain Induced Boundary Migration (SIBM) in Ni-base Superalloys," *Materials Science & Engineering A*, 2018.

[117] B. Lindsley and X. Pierron, "Sub-Solvus Recrystallization Mechanisms in Udimet Alloy 720LI," in *Superalloys 2000*, pp. 59–68, 2000.

[118] S. Gyoon and Y. Bum, "Grain boundary segregation , solute drag and abnormal grain growth," *Acta Materialia*, vol. 56, pp. 3739–3753, 2008.

[119] Y. K. Y. U. Cho, D. U. K. Y. Yoon, and M. F. Henry, "The Effects of Deformation and Pre-Heat-Treatment on Abnormal Grain Growth in RENE 88 Superalloy," *Metallurgical and Materials Transactions A*, vol. 32, no. December, pp. 3077–3090, 2001.

[120] O. T. Ola, O. A. Ojo, and M. C. Chaturvedi, "Effect of deformation mode on hot ductility of a γ precipitation strengthened nickel-base superalloy," *Materials Science & Engineering A*, vol. 585, pp. 319–325, 2013.

[121] W. M. Kane, U. Krupp, T. Jacobs, and C. J. Mcmahon, "On the mechanism of quench cracking in Rene 95 nickel-based superalloy," *Materials Science & Engineering A*, vol. 402, pp. 42–46, 2005.

[122] R. P. Singh and T. E. Howson, "The Microstructural Response of As-HIP P/M U-720 to Thermomechanical Processing," in *Superalloys 1992*, pp. 93–101, 1992.

[123] C. Blankenship, Jr, M. Henry, J. Hyzak, R. Rohling, and E. Hall, "Hot-Die Forging of P/M Ni-Base Superalloys," *Superalloys 1996 (Eighth International Symposium)*, pp. 653–662, 1966.

[124] G. He, F. Liu, L. Huang, Z. Huang, and L. Jiang, "Materials Science & Engineering A Microstructure evolutions and nucleation mechanisms of dynamic recrystallization of a powder metallurgy Ni-based superalloy during hot compression," *Materials Science & Engineering A*, vol. 677, pp. 496–504, 2016.

[125] M. J. Thomas, "The Effect of Thermomechanical Process Parameters on the Microstructure and Crystallographic Texture Evolution of Near-α Aerospace Alloy Timetal ® 834 . The University of Sheffield," *Behaviour*, no. June, 2007.

[126] G. E. Dieter, H. A. Kuhn, and S. L. Semiatin, *Handbook of Workability and Process Design*. ASM International, 2003.

[127] K. J. Bockenstedt, C. M. O. Brien, R. S. Minisandram, G. J. Smith, and D. J. Bryant, "Conventionally Forged RR1000 Billet for Forged Turbine Components," *Superalloys 2016: 13th International Symposium*, pp. 479–486, 2016.

[128] D. Zhao and P. Chaudhury, "Effect of Starting Grain Size on As-Deformed Microstructure in High Temperature Deformation of Alloy 718," *Superalloys 718, 625, 706 and Various Derivatives (1994)*, pp. 303–313, 1994.

[129] J. H. Persson, D. Chen, Z. Lenrick, R. M'Saoubi, D. Gustafsson, V. Bushlya, J. Stahl, and J. Zhou, "Modelling tool life in high speed machining of AD370," *Procedia Manufacturing*, vol. 8, no. May, pp. 16–18, 2018.

[130] E. O. Ezugwu, "Key improvements in the machining of difficult-to-cut aerospace superalloys," *International Journal of Machine Tools and Manufacture*, vol. 45, no. 12-13, pp. 1353–1367, 2005.

[131] R. Arunachalam and M. Mannan, "Machinability of Nickel Based High Temperature Alloys," *Machining science and technology*, vol. 4, no. 1, pp. 127–168, 2000.

[132] Y. H. Fan, Z. P. Hao, J. Q. Lin, and Z. X. Yu, "Material response at tool-chip interface and its effects on tool wear in turning Inconel718," *Materials and Manufacturing Processes*, vol. 29, no. 11-12, pp. 1446–1452, 2014.

[133] D. Zhu, X. Zhang, and H. Ding, "Tool wear characteristics in machining of nickel-based superalloys," *International Journal of Machine Tools and Manufacture*, vol. 64, pp. 60–77, jan 2013.

[134] R. M'Saoubi, T. Larsson, J. Outeiro, Y. Guo, S. Suslov, C. Saldana, and S. Chandrasekar, "Surface integrity analysis of machined Inconel 718 over multiple length scales," *CIRP Annals - Manufacturing Technology*, vol. 61, no. 1, pp. 99–102, 2012.

[135] D. Dudzinski, V. Zerrouki, J. Vigneau, A. Devillez, A. Moufki, and D. Larrouque, "A review of developments towards dry and high speed machining of Inconel 718 alloy," *International Journal of Machine Tools and Manufacture*, vol. 44, no. 4, pp. 439–456, 2004.

[136] a. Devillez, F. Schneider, S. Dominiak, D. Dudzinski, and D. Larrouquere, "Cutting forces and wear in dry machining of Inconel 718 with coated carbide tools," *Wear*, vol. 262, pp. 931–942, 2007.

[137] R. Polvorosa, A. Suárez, L. N. L. D. Lacalle, I. Cerrillo, A. Wretland, and F. Veiga, "Tool wear on nickel alloys with different coolant pressures : Comparison of Alloy 718 and Waspaloy," *Journal of Manufacturing Processes*, vol. 26, pp. 44–56, 2017.

[138] D. D'Addona, S. J. Raykar, and M. Narke, "High Speed Machining of Inconel 718: Tool Wear and Surface Roughness Analysis," *Procedia CIRP*, vol. 62, pp. 269–274, 2017.

[139] G. R. Thellaputta, P. S. Chandra, and C. S. P. Rao, "ScienceDirect 5th International Conference of Materials Processing and Characterization (ICMPC 2016) Machinability of Nickel Based Superalloys : A Review," *Materials Today: Proceedings*, vol. 4, no. 2, pp. 3712–3721, 2017.

[140] P. Vogtel, F. Klocke, and D. Lung, "High performance machining of profiled slots in nickel-based-superalloys," *Procedia CIRP*, vol. 14, pp. 54–59, 2014.

[141] F. F. Lima, W. F. Sales, E. S. Costa, F. J. da Silva, and Á. R. Machado, "Wear of ceramic tools when machining Inconel 751 using argon and

oxygen as lubri-cooling atmospheres," *Ceramics International*, vol. 43, no. 1, pp. 677–685, 2017.

[142] F. Barthelmä, H. Frank, M. Schiffler, and A. Bartsch, "Hard Coatings to Improve the Machining of Nickel Based Materials," *Procedia CIRP*, vol. 46, pp. 294–298, 2016.

[143] A. Thakur and S. Gangopadhyay, "Dry machining of nickel-based super alloy as a sustainable alternative using TiN/TiAlN coated tool," *Journal of Cleaner Production*, vol. 129, pp. 256–268, 2016.

[144] W. Grzesik, P. Niesłony, W. Habrat, J. Sieniawski, and P. Laskowski, "Investigation of tool wear in the turning of Inconel 718 superalloy in terms of process performance and productivity enhancement," *Tribology International*, vol. 118, no. October 2017, pp. 337–346, 2018.

[145] A. Bhatt, H. Attia, R. Vargas, and V. Thomson, "Wear mechanisms of WC coated and uncoated tools in finish turning of Inconel 718," *Tribology International*, vol. 43, no. 5-6, pp. 1113–1121, 2010.

[146] M. Imran, P. T. Mativenga, A. Gholinia, and P. J. Withers, "Comparison of tool wear mechanisms and surface integrity for dry and wet micro-drilling of nickel-base superalloys," *International Journal of Machine Tools and Manufacture*, vol. 76, pp. 49–60, 2014.

[147] N. H. Razak, Z. W. Chen, and T. Pasang, "Progression of tool deterioration and related cutting force during milling of 718Plus superalloy using cemented tungsten carbide tools," *International Journal of Advanced Manufacturing Technology*, vol. 86, no. 9-12, pp. 3203–3216, 2016.

[148] N. Swain, V. Venkatesh, P. Kumar, G. Srinivas, S. Ravishankar, and H. C. Barshilia, "An experimental investigation on the machining characteristics of Nimonic 75 using uncoated and TiAlN coated tungsten carbide micro-end mills," *CIRP Journal of Manufacturing Science and Technology*, vol. 16, pp. 34–42, 2017.

[149] T. Obikawa, M. Yamaguchi, K. Funai, Y. Kamata, and S. Yamada, "Air jet assisted machining of nickel-base superalloy," *International Journal of Machine Tools and Manufacture*, vol. 61, pp. 20–26, 2012.

[150] F. Pusavec, H. Hamdi, J. Kopac, and I. Jawahir, "Surface integrity in cryogenic machining of nickel based alloyInconel 718," *Journal of Materials Processing Technology*, vol. 211, no. 4, pp. 773–783, 2011.

[151] F. Pusavec, A. Deshpande, S. Yang, R. M'Saoubi, J. Kopac, O. W. Dillon, and I. S. Jawahir, "Sustainable machining of high temperature Nickel alloy - Inconel 718: Part 2 - Chip breakability and optimization," *Journal of Cleaner Production*, vol. 87, no. 1, pp. 941–952, 2015.

[152] M. Aramesh, S. Montazeri, and S. C. Veldhuis, "A novel treatment for cutting tools for reducing the chipping and improving tool life during machining of Inconel 718," *Wear*, 2018.

[153] R. K. Ananda-Kumar, W. Moscoso-Kingsley, G. Jacob, A. Donmez, and V. Madhavan, "Machining behavior of additively manufactured and cast-wrought nickel-based superalloy (IN 625)," *Procedia Manufacturing*, vol. 26, pp. 595–606, 2018.

[154] S. Azhdari Tadavani, R. Shoja Razavi, and R. Vafaei, "Pulsed laser-assisted machining of Inconel 718 superalloy," *Optics and Laser Technology*, vol. 87, pp. 72–78, 2017.

[155] A. Thakur and S. Gangopadhyay, "State-of-the-art in surface integrity in machining of nickel-based super alloys," *International Journal of Machine Tools and Manufacture*, vol. 100, pp. 25–54, 2016.

[156] D. Umbrello, "Investigation of surface integrity in dry machining of Inconel 718," *International Journal of Advanced Manufacturing Technology*, vol. 69, no. 9-12, pp. 2183–2190, 2013.

[157] J. Sun, T. Wang, A. Su, and W. Chen, "Surface integrity and its influence on fatigue life when turning nickel alloy GH4169," *Procedia CIRP*, vol. 71, pp. 478–483, 2018.

[158] X. Wang, L. Yang, Y. Qiao, P. Guo, and S. Wang, "Cutting Characteristics and Surface Integrity in Drilling of Powder Metallurgy Nickel-based Superalloy FGH97," *Procedia CIRP*, vol. 71, pp. 370–373, 2018.

[159] F. Gunnberg, M. Escursell, and M. Jacobson, "The influence of cutting parameters on residual stresses and surface topography during hard turning of 18MnCr5 case carburised steel," *Journal of Materials Processing Technology*, vol. 174, no. 1-3, pp. 82–90, 2006.

[160] M. Anthony Xavior, A. Duchosal, and P. Jeyapandiarajan, "Experimental Investigation on Work Hardening and Residual Stress during Machining of Inconel718," *Materials Today: Proceedings*, vol. 5, no. 5, pp. 13301–13308, 2018.

[161] D. Ulutan, Y. M. Arisoy, T. Özel, and L. Mears, "Empirical modeling of residual stress profile in machining nickelbased superalloys using the sinusoidal decay function," *Procedia CIRP*, vol. 13, pp. 365–370, 2014.

[162] F. Akhavan Niaki and L. Mears, "A comprehensive study on the effects of tool wear on surface roughness, dimensional integrity and residual stress in turning IN718 hard-to-machine alloy," *Journal of Manufacturing Processes*, vol. 30, pp. 268–280, 2017.

[163] M. Girinon, F. Dumont, F. Valiorgue, J. Rech, E. Feulvarch, F. Lefebvre, H. Karaouni, and E. Jourden, "Influence of lubrication modes on residual stresses generation in drilling of 316L, 15-5PH and Inconel 718 alloys," *Procedia CIRP*, vol. 71, pp. 41–46, 2018.

[164] A. Devillez, G. Le Coz, S. Dominiak, and D. Dudzinski, "Dry machining of Inconel 718, workpiece surface integrity," *Journal of Materials Processing Technology*, vol. 211, no. 10, pp. 1590–1598, 2011.

[165] Z. H. He, X. M. Zhang, and H. Ding, "Comparison of Residual Stresses in Cryogenic and Dry Machining of Inconel 718," *Procedia CIRP*, vol. 46, pp. 19–22, 2016.

[166] J. Wang, D. Zhang, B. Wu, and M. Luo, "Numerical and Empirical Modelling of Machining-induced Residual Stresses in Ball end Milling of Inconel 718," *Procedia CIRP*, vol. 58, pp. 7–12, 2017.

[167] Y. Choi, "Influence of rake angle on surface integrity and fatigue performance of machined surfaces," *International Journal of Fatigue*, vol. 94, pp. 81–88, 2017.